SANDIA REPORT

SAND2012-3503 P
Unlimited Release
Printed May 2014

Standard Problem Exercise to Determine Containment Vessel Performance under Severe Accident Conditions

Lili Heitman, Christopher Jones, Robert Dameron, Herman Graves, and Madhumita Sircar

Prepared by
Sandia National Laboratories
Albuquerque, New Mexico 87185 and Livermore, California 94550

Sandia National Laboratories is a multi-program laboratory managed and operated by Sandia Corporation, a wholly owned subsidiary of Lockheed Martin Corporation, for the U.S. Department of Energy's National Nuclear Security Administration under contract DE-AC04-94AL85000.

Issued by Sandia National Laboratories, operated for the United States Department of Energy by Sandia Corporation.

Available to DOE and DOE contractors from
U.S. Department of Energy
Office of Scientific and Technical Information
P.O. Box 62
Oak Ridge, TN 37831

Telephone: (865) 576-8401
Facsimile: (865) 576-5728
E-Mail: reports@adonis.osti.gov
Online ordering: http://www.osti.gov/bridge

Available to the public from
U.S. Department of Commerce
National Technical Information Service
5285 Port Royal Rd.
Springfield, VA 22161

Telephone: (800) 553-6847
Facsimile: (703) 605-6900
E-Mail: orders@ntis.fedworld.gov
Online order: http://www.ntis.gov/help/ordermethods.asp?loc=7-4-0#online

SAND2012-3503 P
Unlimited Release
Printed May 2014

Standard Problem Exercise to Determine Containment Vessel Performance under Severe Accident Conditions

Lili Heitman and Christopher Jones
Structural and Thermal Analyses
Sandia National Laboratories
P.O. Box 5800
Albuquerque, New Mexico 87185-MS0744

Robert Dameron,
Moffatt & Nichol
1660 Hotel Circle North
San Diego, California 92108

Herman Graves and Madhumita Sircar
United States Nuclear Regulatory Commission
Washington, DC 20555-0001

Abstract

The Nuclear Power Engineering Corporation (NUPEC) of Japan and the US Nuclear Regulatory Commission (NRC) jointly funded a cooperative containment research program at Sandia National Laboratories (SNL) from July 1991-Deccember 2002. As part of the NUPEC, NRC program a 1:4 scale model of a prestressed concrete containment vessel (PCCV) was constructed and pressurized to failure. Using the 1:4 Scale PCCV Model as a starting point, six international organizations (AERB, EDF, FORTUM, GRS, NRC, SCANSCOT) have participated in the round robin Standard Problem Exercise #3. The results from the first phase of this exercise are presented. This exercise focused on investigating local effects of interest that have not been studied in previous efforts related to the PCCV 1:4 scale model. Using state-of-the art modeling techniques, local and global models were generated by the participants to investigate the effects of containment dilation on prestressing force, slippage of prestressing cables, steel-concrete interface, failure mechanisms, and the use of nominal versus in-situ conditions.

ACKNOWLEDGMENTS

The authors would like to thank Michael Hessheimer of SNL for his assistance in setting up these analyses, and his continued input and expertise. In addition, thanks to all the participants for participating in this standard problem exercise, we could not have gotten worthwhile results without you. Finally, thanks to the USNRC and AERB for having the vision to set up this effort, without which none of these analyses would have been completed.

CONTENTS

Acknowledgments 4

Contents 5

Figures 6

Tables 16

Executive summary 17

Nomenclature 19

1. Introduction 21
   1.1 Background 22
   1.2 Phase One Defintion 23
      1.2.1. SPE 1.1 – Tendon Forces as a Function of Containment Dilation 23
      1.2.2. SPE 1.2 – Slippage of Prestressing Cables 24
      1.2.3. SPE 1.3 – Steel-Concrete Interface 31
      1.2.4. SPE 2.4 – Failure Mechanisms 40
      1.2.1. SPE 2.5 – Differences Between Nominal Design and In-Situ Construction 49
   1.3. Documents of the SPE 54
   1.4. Organizational Schedule 54

2. Model 1 56
   2.1. Description of modeling assumptions and phenomenological models 56
   2.2. Description of Tendon Failure Criteria 59
   2.3. Pressure Milestones 59
   2.4. Deformed Shape Comparison 60
   2.5. Comparison of Tendons Stress Distribution 70
   2.6. Tendon Strain versus Pressure 76
   2.7. Radial Displacement versus Pressure 77
   2.8. Tendon Force as a Function of Containment Dilation 81
   2.9. Model 1 Conclusions 82

3. Model 2 84
   3.1. Description of Modeling Assumptions and Phenomenological Models 84
   3.2. Description of Liner Failure Criteria 86
   3.3. Pressure Milestones 87
   3.4. Deformed Shape 88
   3.5. Liner Strain Distribution 103
   3.6. Liner Strain Magnitudes at Required Locations 125
   3.7. Tendon Stress Distribution 153
      3.7.1. Hoop Tendon Nearest the Penetration Hatch 153
      3.7.2. Location at Hoop Tendon at Top of Model 2 170
   3.8. Radial Displacements as a Function of Pressure 187
   3.9. Ovalization 192
   3.10. Model 2 Conclusions 196

4. Model 3 197
   4.1. Description of Material and FEM Models 197
   4.2. Description of Model Failure Criteria 200
   4.3. Deformed Shape 200

4.4. Liner Strains 206
4.4.1. Peak Strains of Entire Liner 206
4.4.2. Average Strains at Selected Locations 216
4.5. Tendon Stress Distribution 221
4.6.4. Hoop Tendons 222
4.6.5. Vertical Tendons 236
4.6. Standard Output Location Comparisons 245
4.6.1. Displacements 245
4.6.2. Rebar Strains 253
4.6.3. Liner Strains 262
4.6.4. Tendon Strain 269
4.6.5. Tendon Forces 272
4.7. Model 3 Conclusions 273

5. Phase Two analysis defintion 275
5.1. Introduction 275
5.2. Phase Two SPE #3 Analyses 275
5.2.1. Assumptions for Heat Transfer Analysis 277
5.2.2. Material Properties and Variations Due to Temperature 280
5.2.3. Concrete Strength Degradation Versus Temperature Used in ISP – 48 280
5.2.4. Required Outputs/Results 288
5.2.5. Estimating Crack Size and Leak Areas 292
5.3. Documents of SPE #3 Phase Two 296
5.4. Organizational Schedule 296

Distribution 299

FIGURES

Figure 1. Model 1 - Tendon Behavior Model, Representing Tendons H53 and H54, Elev. 6.579 m (Refer to Dwg. # PCCV-QCON-04) 25
Figure 2. H53 Tendon Force Comparisons to Pretest (From NUPEC/NRC PCCV test at SNL) 26
Figure 3. Additional Information about Tendon Friction and Seating Losses 28
Figure 4. Concrete Creep and Shrinkage Strain 29
Figure 5. Model 2 - Local E/H Model Geometry and Boundary Conditions 34
Figure 6. Model 2 – Perspective View 35
Figure 7. Rebar Summary for Model 2 (Important to Simulating Strain Concentrations) 36
Figure 8. Tendon Stress Distribution for Model 2 37
Figure 9. Pressure versus Strain for Equipment Hatch Strain Gages 38
Figure 10. Pressure Versus Strain for Equipment Hatch Strain Gages 39
Figure 11. Liner (E/H) View Showing Strain Reports (cut from Page A-28 of NUREG/CR-6810) 40
Figure 12. Longitudinal Strain Contours and Crack Propagation for Fracture Model Analysis Starting with an Initial Crack of 0.72” and Propagating in 0.75” Increments: (a) 0.72” Crack, (b) 1.5” Crack, (c) 2.22” Crack, (d) 3.0” Crack, (e) 3.72” Crack, (f) 4.50” Crack 44

Figure 13. Liner Repair Locations 48
Figure 14: Liner Repair Locations (in Black) with Liner Tears (in Red 49
Figure 15: Liner Strains (DOR) at M/S (Ref. D-SN-P-220) 50
Figure 16: Example of Variation in Concrete Properties 51
Figure 17: Designed Concrete Cross Section 52
Figure 18: Schedule for Construction of Concrete Lifts 53
Figure 19: Comparison of Pressure Milestones 60
Figure 20: Deformed Shape at Anchorage (a) EDF/NECS at 500 x Magnification (b) FORTUM at 10 x Magnification (c) GRS at 500 x Magnification (d) NRC at 500 x Magnification (e) SCANSCOT at 500 x Magnification 61
Figure 21: Deformed Shape at Design Pressure (a) EDF/NECS at 500x (b) FORTUM at 10x (c) GRS at 500x (d) NRC at 500x (e) SCANSCOT at 500x 62
Figure 22: Deformed Shape at 1.5 x Design Pressure (a) EDF/NECS 500x (b) FORTUM at 10x (c) GRS at 500x (d) NRC at 500x (e) SCANSCOT 500x 63
Figure 23: Deformed Shape at 2 x Design Pressure (a) EDF/NECS 100x (b) FORTUM at 10x (c) GRS at 100x (d) NRC at 100x (e) SCANSCOT at 100x 64
Figure 24: Deformed Shape at 2.5 x Design Pressure (a) EDF/NECS 100x (b) FORTUM at 10x (c) GRS at 100x (d) NRC at 100x (e) SCANSCOT at 100x 65
Figure 25: Deformed Shape at 3.0 x Design Pressure (a) EDF/NECS 50x (b) FORTUM at 10x (c) GRS at 50x (d) NRC at 50x (e) SCANSCOT at 50x 66
Figure 26: Deformed Shape at 3.3 x Design Pressure (a) EDF/NECS 50x (b) FORTUM at 10x (c) GRS at 50x (d) NRC at 50x (e) SCANSCOT at 50x 67
Figure 27: Deformed Shape at 3.4 x Design Pressure (a) EDF/NECS 20x (b) FORTUM at 10x (c) GRS at 10x (d) NRC at 10x (e) SCANSCOT at 20x 68
Figure 28: Deformed Shape at 3.5 x Design Pressure (a) EDF/NECS 10x (b) FORTUM at 10x (c) NRC at 10x (d) SCANSCOT at 10x 69
Figure 29: Deformed Shape at Ultimate Pressure (a) EDF/NECS 5x ($3.6xP_d$) (b) FORTUM at 10x ($3.5xP_d$) (c) NRC at 10x ($3.8xP_d$) (d) SCANSCOT at 5x ($3.62xP_d$) 70
Figure 30: Comparison of Tendon Stress Distribution at Anchoring ($0xP_d$) 71
Figure 31: Tendon Stress Distribution at 1.0 x P_d 71
Figure 32: Tendon Stress Distribution at 1.5 x P_d 72
Figure 33: Tendon Stress Distribution at 2.0 x P_d 72
Figure 34: Tendon Stress Distribution at 2.5 x P_d 73
Figure 35: Tendon Stress Distribution at 3.0 x P_d 73
Figure 36: Tendon Stress Distribution at 3.3 x P_d 74
Figure 37: Tendon Stress Distribution at 3.4 x P_d 74
Figure 38: Tendon Stress Distribution at 3.5 x Pd 75
Figure 39: Tendon Stress Distribution at Ultimate Pressure 75
Figure 40: Tendon A Strain as a Function of Pressure at Azimuth 135^o 76
Figure 41: Tendon B Strain as a Function of Pressure at Azimuth 135^o 77
Figure 42: Radial Displacement at 0^o Azimuth 78
Figure 43: Radial Displacement at 0^o Azimuth (Zoomed In) 78
Figure 44: Radial Displacement versus Pressure at 135^o Azimuth 79
Figure 45: Radial Displacement versus Pressure at 135^o Azimuth (Zoomed In) 79
Figure 46: Radial Displacement versus Pressure at 270^o Azimuth 80
Figure 47: Radial Displacement at 270^o Azimuth (Zoomed In) 80
Figure 48: Tendon slip as reported by EDF 81
Figure 49: Tendon slip as reported by NRC 82

Figure 50: Tendon slip as reported by SCANSCOT 82
Figure 51: Pressure Milestones for Model 2a 88
Figure 52. Deformed Shape of Model 2a at Anchoring (A) AERB x500 Magnification (B) NRC x500 Magnification 89
Figure 53: Deformed Shape of Model 2a at 1xP_d (A) AERB x500 (B) NRC x500 90
Figure 54: Deformed Shape of Model 2a at 1.5xP_d (A) AERB and (B) NRC x500 91
Figure 55: Deformed Shape of Model 2a at 2.0xP_d (A) AERB and (B) NRC x100 92
Figure 56: Deformed Shape of Model 2a at 2.5xP_d (A) AERB and (B) NRC x50 93
Figure 57: Deformed Shape of Model 2a at 3.0xP_d (A) AERB and NRC x50 94
Figure 58: Deformed Shape of Model 2a at 3.3xP_d (A) AERB, (B) NRC x20 95
Figure 59: Deformed Shape of Model 2a at 3.4xP_d (A) AERB and (B) NRC x20 96
Figure 60: Deformed Shape of Model 2a at Ultimate pressure (A) AERB and (B) NRC (3.47 P_d) x500 97
Figure 61. Deformed Shape of Model 2b at Anchoring NRC x500 Magnification 98
Figure 62: Deformed Shape of Model 2b at 1xP_d NRC x500 98
Figure 63: Deformed Shape of Model 2b at 1.5xP_d NRC x500 98
Figure 64: Deformed Shape of Model 2b at 2xP_d NRC x100 99
Figure 65: Deformed Shape of Model 2b at 2.5xP_d NRC x50 99
Figure 66: Deformed Shape of Model 2b at 3xP_d NRC x50 99
Figure 67: Deformed Shape of Model 2b at 3.3xP_d NRC x20 100
Figure 68: Deformed Shape of Model 2b at 3.4xP_d NRC x20 100
Figure 69: Deformed Shape of Model 2b at Ultimate Pressure (3.47 P_d) NRC x20 100
Figure 70. Deformed Shape of Model 2c at Anchoring NRC x500 Magnification 101
Figure 71: Deformed Shape of Model 2c at 1xP_d NRC x500 101
Figure 72: Deformed Shape of Model 2c at 2xP_d NRC x500 101
Figure 73: Deformed Shape of Model 2c at 2xP_d NRC x100 102
Figure 74: Deformed Shape of Model 2c at 2.5xP_d NRC x50 102
Figure 75: Deformed Shape of Model 2c at 3xP_d NRC x50 102
Figure 76: Deformed Shape of Model 2c at 3.3xP_d NRC x20 103
Figure 77: Deformed Shape of Model 2c at 3.4xP_d NRC x20 103
Figure 78: Deformed Shape of Model 2c at Ultimate (3.47 P_d) NRC x50 103
Figure 79: Model 2a Liner Strain at Anchor (A) AERB (B) NRC (C) SCANSCOT 104
Figure 80: Model 2a Liner Strain at 1xP_d (A) AERB (B) NRC (C) SCANSCOT 105
Figure 81: Model 2a Liner Strain at 1.5xP_d (A) AERB (B) NRC (C) SCANSCOT 106
Figure 82: Model 2a Liner Strain at 2xP_d (A) AERB (B) NRC (C) SCANSCOT 107
Figure 83: Model 2a Liner Strain at 2.5xP_d (A) AERB (B) NRC (C) SCANSCOT 108
Figure 84: Model 2a Liner Strain at 3xP_d (A) AERB (B) NRC (C) SCANSCOT 109
Figure 85: Model 2a Liner Strain at 3.3xP_d (A) AERB (B) NRC (C) SCANSCOT 110
Figure 86: Model 2a Liner Strain at 3.4xP_d (A) AERB (B) NRC (C) SCANSCOT 111
Figure 87: Model 2a Liner Strain at Ultimate Pressure (A) AERB (B) NRC (3.47xP_d) (C) SCANSCOT (3.62xP_d) 112
Figure 88: Model 2b Liner Strain at Anchor (A) AERB (B) NRC (C) SCANSCOT 113
Figure 89: Model 2b Liner Strain at 1xP_d (A) AERB (B) NRC (C) SCANSCOT 114
.Figure 90: Model 2b Liner Strain at 1.5xP_d (A) AERB (B) NRC (C) SCANSCOT 115
Figure 91: Model 2b Liner Strain at 2xP_d (A) AERB (B) NRC (C) SCANSCOT 116
Figure 92: Model 2b Liner Strain at 2.5xP_d (A) AERB (B) NRC (C) SCANSCOT 117
Figure 93: Model 2b Liner Strain at 3xP_d (A) AERB (B) NRC (C) SCANSCOT 118
Figure 94: Model 2b Liner Strain at 3.3xP_d (A) NRC (B) SCANSCOT 119

Figure 95: Model 2b Liner Strain at 3.4xP_d (A) NRC (B) SCANSCOT 120
Figure 96: Model 2b Liner Strain at Ultimate Pressure (A) AERB (B) NRC (3.47xP_d) (C) SCANSCOT (3.62xP_d) 121
Figure 97: Model 2c Liner Strain at Anchor NRC 122
Figure 98: Model 2c Liner Strain at 1xP_d NRC 122
Figure 99: Model 2c Liner Strain at 1.5xP_d NRC 123
Figure 100: Model 2c Liner Strain at 2xP_d NRC 123
Figure 101: Model 2c Liner Strain at 2.5xP_d NRC 123
Figure 102: Model 2c Liner Strain at 3xP_d NRC 124
Figure 103: Model 2c Liner Strain at 3.3xP_d NRC 124
Figure 104: Model 2c Liner Strain at 3.4xP_d NRC 124
Figure 105: Model 2c Liner Strain at Ultimate Pressure (3.47xP_d) NRC 125
Figure 106: Model 2a Liner Strain Magnitude at Location 1 125
Figure 107: Model 2a Liner Strain Magnitude at Location 2 126
Figure 108: Model 2a Liner Strain Magnitude at Location 3 126
Figure 109: Model 2a Liner Strain Magnitude at Location 4 127
Figure 110: Model 2a Liner Strain Magnitude at Location 5 127
Figure 111: Model 2a Liner Strain Magnitude at Location 6 128
Figure 112: Model 2a Liner Strain Magnitude at Location 7 128
Figure 113: Model 2a Liner Strain Magnitude at Location 8 128
Figure 114: Model 2a Liner Strain Magnitude at Location 9 129
Figure 115: Model 2a Liner Strain Magnitude at Location 10 129
Figure 116: Model 2b Liner Strain Magnitude at Location 1 129
Figure 117: Model 2b Liner Strain Magnitude at Location 2 130
Figure 118: Model 2b Liner Strain Magnitude at Location 3 130
Figure 119: Model 2b Liner Strain Magnitude at Location 4 130
Figure 120: Model 2b Liner Strain Magnitude at Location 5 131
Figure 121: Model 2b Liner Strain Magnitude at Location 6 131
Figure 122: Model 2b Liner Strain Magnitude at Location 7 131
Figure 123: Model 2b Liner Strain Magnitude at Location 8 132
Figure 124: Model 2b Liner Strain Magnitude at Location 9 132
Figure 125: Model 2b Liner Strain Magnitude at Location 10 133
Figure 126: Model 2c Liner Strain Magnitude at Location 1 133
Figure 127: Model 2c Liner Strain Magnitude at Location 2 134
Figure 128: Model 2c Liner Strain Magnitude at Location 3 134
Figure 129: Model 2c Liner Strain Magnitude at Location 4 135
Figure 130: Model 2c Liner Strain Magnitude at Location 5 135
Figure 131: Model 2c Liner Strain Magnitude at Location 6 136
Figure 132: Model 2c Liner Strain Magnitude at Location 7 136
Figure 133: Model 2c Liner Strain Magnitude at Location 8 137
Figure 134: Model 2c Liner Strain Magnitude at Location 9 137
Figure 135: Model 2c Liner Strain Magnitude at Location 10 138
Figure 136: Comparison of Variability Between Models for AERB at Location 1 138
Figure 137: Comparison of Variability Between Models for NRC at Location 1 139
Figure 138: Comparison of Variability Between Models for AERB at Location 2 139
Figure 139: Comparison of Variability Between Models for NRC at Location 2 140
Figure 140: Comparison of Variability Between Models for AERB at Location 3 140
Figure 141: Comparison of Variability Between Models for NRC at Location 3 141

Figure 142: Comparison of Variability Between Models for SCANSCOT at Location 3 141
Figure 143: Comparison of Variability Between Models for AERB at Location 4 142
Figure 144: Comparison of Variability Between Models for NRC at Location 4..... 142
Figure 145: Comparison of Variability Between Models for SCANSCOT at Location 4 143
Figure 146: Comparison of Variability Between Models for AERB at Location 5 143
Figure 147: Comparison of Variability Between Models for NRC at Location 5..... 144
Figure 148: Comparison of Variability Between Models for SCANSCOT at Location 5 144
Figure 149: Comparison of Variability Between Models for AERB at Location 6 145
Figure 150: Comparison of Variability Between Models for NRC at Location 6..... 145
Figure 151: Comparison of Variability Between Models for AERB at Location 7 146
Figure 152: Comparison of Variability Between Models for NRC at Location 7..... 146
Figure 153: Comparison of Variability Between Models for AERB at Location 8 147
Figure 154: Comparison of Variability Between Models for NRC at Location 8..... 147
Figure 155: Comparison of Variability Between Models for SCANSCOT at Location 8 148
Figure 156: Comparison of Variability Between Models for AERB at Location 9 148
Figure 157: Comparison of Variability Between Models for NRC at Location 9..... 149
Figure 158: Comparison of Variability Between Models for SCANSCOT at Location 9 149
Figure 159: Comparison of Variability Between Models for AERB at Location 10 150
Figure 160: Comparison of Variability Between Models for NRC at Location 10..... 150
Figure 161: Comparison of Variability Between Models for SCANSCOT at Location 10 151
Figure 162: Model 2a Tendon Stress Distribution (Penetration Hatch) at Anchoring 152
Figure 163: Model 2a Tendon Stress Distribution (Penetration Hatch) at $1xP_d$..... 152
Figure 164: Model 2a Tendon Stress Distribution (Penetration Hatch) at $1.5xP_d$..... 153
Figure 165: Model 2a Tendon Stress Distribution (Penetration Hatch) at $2xP_d$..... 153
Figure 166: Model 2a Tendon Stress Distribution (Penetration Hatch) at $2.5xP_d$..... 154
Figure 167: Model 2a Tendon Stress Distribution (Penetration Hatch)at $3xP_d$..... 154
Figure 168: Model 2a Tendon Stress Distribution (Penetration Hatch) at $3.3xP_d$..... 155
Figure 169: Model 2a Tendon Stress Distribution (Penetration Hatch) at $3.4xP_d$..... 155
Figure 170: Model 2a Tendon Stress Distribution (Penetration Hatch) at Ultimate Pressure.... 156
Figure 171: Model 2b Tendon Stress Distribution (Penetration Hatch) at Anchoring..... 156
Figure 172: Model 2b Tendon Stress Distribution (Penetration Hatch) at $1xP_d$..... 157
Figure 173: Model 2b Tendon Stress Distribution (Penetration Hatch) at $1.5xP_d$..... 157
Figure 174: Model 2b Tendon Stress Distribution (Penetration Hatch) at $2xP_d$..... 158
Figure 175: Model 2b Tendon Stress Distribution (Penetration Hatch) at $2.5xP_d$..... 158
Figure 176: Model 2b Tendon Stress Distribution (Penetration Hatch) at $3xP_d$..... 159
Figure 177: Model 2b Tendon Stress Distribution (Penetration Hatch) at $3.3xP_d$..... 159
Figure 178: Model 2b Tendon Stress Distribution (Penetration Hatch) at $3.4xP_d$..... 160
Figure 179: Model 2b Tendon Stress Distribution (Penetration Hatch) at Ultimate Pressure.... 160
Figure 180: AERB Model 2(a-b) Tendon Stress Distribution (Penetration Hatch) at Anchoring..... 161
Figure 181: NRC Model 2(a-c) Tendon Stress Distribution (Penetration Hatch) at Anchoring 161
Figure 182: AERB Model 2(a-b) Tendon Stress Distribution (Penetration Hatch) at $1xP_d$ 162
Figure 183: NRC Model 2(a-c) Tendon Stress Distribution (Penetration Hatch) at $1xP_d$..... 162
Figure 184: AERB Model 2(a-b) Tendon Stress Distribution (Penetration Hatch) at $1.5xP_d$ 163
Figure 185: NRC Model 2(a-c) Tendon Stress Distribution (Penetration Hatch) at $1.5xP_d$..... 163
Figure 186: AERB Model 2(a-b) Tendon Stress Distribution (Penetration Hatch) at $2xP_d$ 164
Figure 187: NRC Model 2(a-c) Tendon Stress Distribution (Penetration Hatch) at $2xP_d$..... 164
Figure 188: AERB Model 2(a-b) Tendon Stress Distribution (Penetration Hatch) at $2.5xP_d$ 165

Figure 189: NRC Model 2(a-c) Tendon Stress Distribution (Penetration Hatch) at 2.5xP_d..... 165
Figure 190: AERB Model 2(a-b) Tendon Stress Distribution (Penetration Hatch) at 3xP_d 166
Figure 191: NRC Model 2(a-c) Tendon Stress Distribution (Penetration Hatch) at 3xP_d..... 166
Figure 192: NRC Model 2(a-c) Tendon Stress Distribution (Penetration Hatch) at 3.3xP_d..... 167
Figure 193: NRC Model 2(a-c) Tendon Stress Distribution (Penetration Hatch) at 3.4xP_d..... 167
Figure 194: AERB Model 2(a-b) Tendon Stress Distribution (Penetration Hatch) at Ultimate Pressure 168
Figure 195: NRC Model 2(a-c) Tendon Stress Distribution (Penetration Hatch) at Ultimate Pressure 168
Figure 196: Model 2a Tendon Stress Distribution (Top of Model) at Anchoring..... 169
Figure 197: Model 2a Tendon Stress Distribution (Top of Model) at 1xP_d 169
Figure 198: Model 2a Tendon Stress Distribution (Top of Model) at 1.5xP_d 170
Figure 199: Model 2a Tendon Stress Distribution (Top of Model) at 2xP_d 170
Figure 200: Model 2a Tendon Stress Distribution (Top of Model) at 2.5xP_d 171
Figure 201: Model 2a Tendon Stress Distribution (Top of Model) at 3xP_d 171
Figure 202: Model 2a Tendon Stress Distribution (Top of Model) at 3.3xP_d 172
Figure 203: Model 2a Tendon Stress Distribution (Top of Model) at 3.4xP_d 172
Figure 204: Model 2a Tendon Stress Distribution (Top of Model) at Ultimate Pressure 173
Figure 205: Model 2b Tendon Stress Distribution (Top of Model) at Anchoring..... 173
Figure 206: Model 2b Tendon Stress Distribution (Top of Model) at 1xP_d 174
Figure 207: Model 2b Tendon Stress Distribution (Top of Model) at 1.5xP_d 174
Figure 208: Model 2b Tendon Stress Distribution (Top of Model) at 2xP_d 175
Figure 209: Model 2b Tendon Stress Distribution (Top of Model) at 2.5xP_d 175
Figure 210: Model 2b Tendon Stress Distribution (Top of Model) at 3xP_d 176
Figure 211: Model 2b Tendon Stress Distribution (Top of Model) at 3.3xP_d 176
Figure 212: Model 2b Tendon Stress Distribution (Top of Model) at 3.4xP_d 177
Figure 213: Model 2b Tendon Stress Distribution (Top of Model) at Ultimate Pressure 177
Figure 214: AERB Model 2(a-b) Tendon Stress Distribution (Top of Model) at Anchoring 178
Figure 215: NRC Model 2(a-c) Tendon Stress Distribution (Top of Model) at Anchoring..... 178
Figure 216: AERB Model 2(a-b) Tendon Stress Distribution (Top of Model) at 1xP_d..... 179
Figure 217: NRC Model 2(a-c) Tendon Stress Distribution (Top of Model) at 1xP_d 179
Figure 218: AERB Model 2(a-b) Tendon Stress Distribution (Top of Model) at 1.5xP_d..... 180
Figure 219: NRC Model 2(a-c) Tendon Stress Distribution (Top of Model) at 1.5xP_d 180
Figure 220: AERB Model 2(a-b) Tendon Stress Distribution (Top of Model) at 2xP_d..... 181
Figure 221: NRC Model 2(a-c) Tendon Stress Distribution (Top of Model) at 2xP_d 181
Figure 222: AERB Model 2(a-b) Tendon Stress Distribution (Top of Model) at 2.5xP_d..... 182
Figure 223: NRC Model 2(a-c) Tendon Stress Distribution (Top of Model) at 2.5xP_d 182
Figure 224: AERB Model 2(a-b) Tendon Stress Distribution (Top of Model) at 3xP_d..... 183
Figure 225: NRC Model 2(a-c) Tendon Stress Distribution (Top of Model) at 3xP_d 183
Figure 226: NRC Model 2(a-c) Tendon Stress Distribution (Top of Model) at 3.3xP_d 184
Figure 227: NRC Model 2(a-c) Tendon Stress Distribution (Top of Model) at 3.4xP_d 184
Figure 228: AERB Model 2(a-b) Tendon Stress Distribution (Top of Model) at Ultimate Pressure 185
Figure 229: NRC Model 2(a-c) Tendon Stress Distribution (Top of Model) at Ultimate Pressure 185
Figure 230: Model 2a Radial Displacement as a Function of Pressure for 0^o Azimuth 186
Figure 231: Model 2a Radial Displacement as a Function of Pressure for 270^o Azimuth 186
Figure 232: Model 2a Radial Displacement as a Function of Pressure for 328^o Azimuth 187

Figure 233: Model 2b Radial Displacement as a Function of Pressure for 0^o Azimuth 187
Figure 234: Model 2b Radial Displacement as a Function of Pressure for 328^o Azimuth 188
Figure 235: AERB Model 2(a-b) Radial Displacements as a Function of Pressure for 0^o Azimuth 188
Figure 236: NRC Model 2(a-c) Radial Displacements as a Function of Pressure for 0^o Azimuth 189
Figure 237: AERB Model 2(a-b) Radial Displacement as a Function of Pressure for 328^o Azimuth 189
Figure 238: NRC Model 2(a-c) Radial Displacement as a Function of Pressure for 328^o Azimuth 190
Figure 239: Meridional Separation (gap) in Pipe Sleeve for Model 2a 190
Figure 240: Meridional Separation (gap) in Pipe Sleeve for Model 2b 191
Figure 241: Meridional Separation (gap) in Pipe Sleeve for Model 2(a-b) from AERB 191
Figure 242: Meridional Separation (gap) in Pipe Sleeve for Model 2(a-c) from NRC 192
Figure 243: Circumferential Separation (gap) in Pipe Sleeve for Model 2a 192
Figure 244: Circumferential Separation (gap) in Pipe Sleeve for Model 2b 193
Figure 245: Circumferential Separation (gap) in Pipe Sleeve for Model 2(a-b) from AERB 193
Figure 246: Circumferential Separation (gap) in Pipe Sleeve for Model 2(a-c) from NRC 194
Figure 247: Deformed Shape after Tendon Anchorage (a) AERB (b) NRC Deformation Scale x 500 199
Figure 248: Deformed Shape at 1.0 x P_d (a) AERB (c) NRC 199
Figure 249: Deformed Shape at 1.5 x P_d (a) NRC 200
Figure 250: Deformed Shape at 2.0 x P_d (a) AERB (b) NRC 200
Figure 251: Deformed Shape at 2.5 x P_d (a) NRC 201
Figure 252: Deformed Shape at 3.0 x P_d (a) AERB (b) NRC 201
Figure 253: Deformed Shape at 3.3 x P_d for NRC 202
Figure 254: Deformed Shape at 3.4 x P_d (a) AERB (b) NRC 202
Figure 255: Deformed Shape at 3.6 x P_d (a) AERB (b) FORTUM x 50 (c) NRC Deformation Scale x 20 203
Figure 256: Peak Strain at 0 x P_d (A) AERB – hoop (B) AERB - Meridional (C) FORTUM (D) NRC (E) SCANSCOT 204
Figure 257: Peak Strain at 1.0 x P_d (A) AERB – hoop (B) AERB - Meridional (C) FORTUM (D) NRC (E) SCANSCOT 205
Figure 258: Peak Strain at 1.5 x P_d (A) NRC (B) SCANSCOT 206
Figure 259: Peak Strain at 2.0 x P_d (A) AERB – hoop (B) AERB - Meridional (C) FORTUM (D) NRC (E) SCANSCOT 207
Figure 260: Peak Strain at 2.5 x P_d (A) FORTUM (B) NRC (C) SCANSCOT 208
Figure 261: Peak Strain at 3.0 x P_d (A) AERB – hoop (B) AERB - Meridional (C) FORTUM (D) NRC (E) SCANSCOT 209
Figure 262: Peak Strain at 3.3 x P_d (A) AERB – hoop (B) AERB - Meridional (C) FORTUM (D) NRC (E) SCANSCOT 210
Figure 263: Peak Strain at 3.4 x P_d (A) AERB – hoop (B) AERB - Meridional (C) FORTUM (D) NRC (E) SCANSCOT 211
Figure 264: Peak Strain at 3.5 x P_d FORTUM 212
Figure 265: Peak Strain at 3.6 x P_d (a) AERB – hoop (b) AERB - Meridional (c) FORTUM (d) NRC 213
Figure 266: Strain over Gauge Length at Location 3 Near Equipment Hatch 214
Figure 267: Strain over Gauge Length at Location 4 Near Equipment Hatch 214

Figure 268: Strain over Gauge Length at Location 5 Near Equipment Hatch..... 215
Figure 269: Strain over Gauge Length at Location 3 Near Air Lock 215
Figure 270: Strain over Gauge Length at Location 4 Near Air Lock 216
Figure 271: Strain over Gauge Length at Location 5 Near Air Lock 216
Figure 272: Strain over Gauge Length at Location 3 Near Mainsteam..... 217
Figure 273: Strain over Gauge Length at Location 4 Near Mainsteam..... 217
Figure 274: Strain over Gauge Length at Location 5 Near Mainsteam..... 218
Figure 275: Strain over Gauge Length at Location 3 Near Feed Water 218
Figure 276: Strain over Gauge Length at Location 4 Near Feed Water 219
Figure 277: Strain over Gauge Length at Location 5 Near Feed Water 219
Figure 278: Tendon Stress Distribution for Tendon #H35 at 0 x P_d..... 220
Figure 279: Tendon Stress Distribution for Tendon #H35 at 1.0 x P_d..... 221
Figure 280: Tendon Stress Distribution for Tendon #H35 at 1.5 x P_d..... 221
Figure 281: Tendon Stress Distribution for Tendon #H35 at 2.0 x P_d..... 221
Figure 282: Tendon Stress Distribution for Tendon #H35 at 2.5 x P_d..... 222
Figure 283: Tendon Stress Distribution for Tendon #H35 at 3.0 x P_d..... 222
Figure 284: Tendon Stress Distribution for Tendon #H35 at 3.3 x P_d..... 223
Figure 285: Tendon Stress Distribution for Tendon #H35 at 3.4 x P_d..... 223
Figure 286: Tendon Stress Distribution for Tendon #H35 at Ultimate Pressure..... 224
Figure 287: Tendon Stress Distribution for Tendon #H53 at 0 x P_d..... 224
Figure 288: Tendon Stress Distribution for Tendon #H53 at 1.0 x P_d..... 225
Figure 289: Tendon Stress Distribution for Tendon #H53 at 1.5 x P_d..... 225
Figure 290: Tendon Stress Distribution for Tendon #H53 at 2.0 x P_d..... 226
Figure 291: Tendon Stress Distribution for Tendon #H53 at 2.5 x P_d..... 226
Figure 292: Tendon Stress Distribution for Tendon #H53 at 3.0 x P_d..... 227
Figure 293: Tendon Stress Distribution for Tendon #H53 at 3.3 x P_d..... 227
Figure 294: Tendon Stress Distribution for Tendon #H53 at 3.4 x P_d..... 228
Figure 295: Tendon Stress Distribution for Tendon #H53 at Ultimate Pressure..... 228
Figure 296: Tendon Stress Distribution for Tendon #H68 at 0 x P_d..... 229
Figure 297: Tendon Stress Distribution for Tendon #H68 at 1.0 x P_d..... 229
Figure 298: Tendon Stress Distribution for Tendon #H68 at 1.5 x P_d..... 230
Figure 299: Tendon Stress Distribution for Tendon #H68 at 2.0 x P_d..... 230
Figure 300: Tendon Stress Distribution for Tendon #H68 at 2.5 x P_d..... 231
Figure 301: Tendon Stress Distribution for Tendon #H68 at 3.0 x P_d..... 231
Figure 302: Tendon Stress Distribution for Tendon #H68 at 3.3 x P_d..... 232
Figure 303: Tendon Stress Distribution for Tendon #H68 at 3.4 x P_d..... 232
Figure 304: Tendon Stress Distribution for Tendon #H68 at Ultimate Pressure..... 233
Figure 305: Tendon Stress Distribution for Tendon #V37 at 0 x P_d..... 234
Figure 306: Tendon Stress Distribution for Tendon #V37 at 1.0 x P_d..... 234
Figure 307: Tendon Stress Distribution for Tendon #V37 at 1.5 x P_d..... 235
Figure 308: Tendon Stress Distribution for Tendon #V37 at 2.0 x P_d..... 235
Figure 309: Tendon Stress Distribution for Tendon #V37 at 2.5 x P_d..... 236
Figure 310: Tendon Stress Distribution for Tendon #V37 at 3.0 x P_d..... 236
Figure 311: Tendon Stress Distribution for Tendon #V37 at 3.3 x P_d..... 237
Figure 312: Tendon Stress Distribution for Tendon #V37 at 3.4 x P_d..... 237
Figure 313: Tendon Stress Distribution for Tendon #V37 at 3.6 x P_d..... 238
Figure 314: Tendon Stress Distribution for Tendon #V46 at 0 x P_d..... 238
Figure 315: Tendon Stress Distribution for Tendon #V46 at 1.0 x P_d..... 239

Figure 316: Tendon Stress Distribution for Tendon #V46 at 1.5 x P_d 239
Figure 317: Tendon Stress Distribution for Tendon #V46 at 2.0 x P_d 240
Figure 318: Tendon Stress Distribution for Tendon #V46 at 2.5 x P_d 240
Figure 319: Tendon Stress Distribution for Tendon #V46 at 3.0 x P_d 241
Figure 320: Tendon Stress Distribution for Tendon #V46 at 3.3 x P_d 241
Figure 321: Tendon Stress Distribution for Tendon #V46 at 3.4 x P_d 242
Figure 322: Tendon Stress Distribution for Tendon #V46 at Ultimate Pressure 242
Figure 323: Displacement Versus Pressure at SOL #1 (Vertical Displacement at Top of Basemat) 243
Figure 324: Displacement Versus Pressure at SOL #2 (Radial Displacement at Base of Cylinder) 244
Figure 325: Displacement Versus Pressure at SOL #3 (Radial Displacement at Base of Cylinder) 244
Figure 326: Displacement Versus Pressure at SOL #4 (Radial Displacement at Base of Cylinder) 244
Figure 327: Displacement Versus Pressure at SOL #5 (Radial Displacement at E/H Elevation) 245
Figure 328: Displacement Versus Pressure at SOL #6 (Radial Displacement at Midheight) 245
Figure 329: Displacement Versus Pressure at SOL #7 (Radial Displacement at Springline) 246
Figure 330: Displacement Versus Pressure at SOL #8 (Vertical Displacement at Springline).. 246
Figure 331: Displacement Versus Pressure at SOL #9 (Radial Displacement at Dome 45^o)..... 247
Figure 332: Displacement Versus Pressure at SOL #10 (Vertical Displacement at Dome 45^o) 247
Figure 333: Displacement Versus Pressure at SOL #11 (Vertical Displacement at Dome Apex) 248
Figure 334: Displacement Versus Pressure at SOL #12 (Radial Displacement at Midheight of Buttress) 248
Figure 335: Displacement Versus Pressure at SOL #13 (Radial Displacement at Springline of Buttress) 249
Figure 336: Displacement Versus Pressure at SOL #14 (Radial Displacement at Center of E/H) 249
Figure 337: Displacement Versus Pressure at SOL #15 (Radial Displacement at Center of A/L) 250
Figure 338: Rebar Strain Versus Pressure at SOL #16 250
Figure 339: Rebar Strain Versus Pressure at SOL #17 251
Figure 340: Rebar Strain Versus Pressure at SOL #18 251
Figure 341: Rebar Strain Versus Pressure at SOL #19 251
Figure 342: Rebar Strain Versus Pressure at SOL #20 252
Figure 343: Rebar Strain Versus Pressure at SOL #21 252
Figure 344: Rebar Strain Versus Pressure at SOL #22 (Hoop Strain of Outer Rebar at Midheight) 253
Figure 345: Rebar Strain Versus Pressure at SOL #23 (Meridional Strain of Outer Rebar at Midheight) 253
Figure 346: Rebar Strain Versus Pressure at SOL #24 (Hoop Strain of Outer Rebar at Springline) 253
Figure 347: Rebar Strain Versus Pressure at SOL #25 (Meridional Strain of Inner Rebar at Springline) 254
Figure 348: Rebar Strain Versus Pressure at SOL #26 (Meridional Strain of Outer Rebar at Springline) 254

Figure 349: Rebar Strain Versus Pressure at SOL #27 (Hoop Strain of Outer Rebar at Dome 45°) 255
Figure 350: Rebar Strain Versus Pressure at SOL #28 (Meridional Strain of Inner Rebar at Dome 45°) 255
Figure 351: Rebar Strain Versus Pressure at SOL #29 (Meridional Strain of Outer Rebar at Dome 45°) 256
Figure 352: Rebar Strain Versus Pressure at SOL #30 256
Figure 353: Rebar Strain Versus Pressure at SOL #31 257
Figure 354: Rebar Strain Versus Pressure at SOL #32 257
Figure 355: Rebar Strain Versus Pressure at SOL #33 257
Figure 356: Liner Strain Versus Pressure at SOL #34 258
Figure 357: Liner Strain Versus Pressure at SOL #35 258
Figure 358: Liner Strain Versus Pressure at SOL #36 (Meridional Strain of Inside of Liner at Base of Cylinder) 259
Figure 359: Liner Strain Versus Pressure at SOL #37 (Hoop Strain of Inside of Liner at Base of Cylinder) 259
Figure 360: Liner Strain Versus Pressure at SOL #38 (Meridional Strain of Inside of Liner at Midheight) 259
Figure 361: Liner Strain Versus Pressure at SOL #39 (Hoop Strain of Inside of Liner at Midheight) 260
Figure 362: Liner Strain Versus Pressure at SOL #40 (Meridional Strain of Inside of Liner at Springline) 260
Figure 363: Liner Strain Versus Pressure at SOL #41 (Hoop Strain of Inside of Liner at Springline) 261
Figure 364: Liner Strain Versus Pressure at SOL #42 (Meridional Strain of Inside of Liner at Dome Apex) 261
Figure 365: Liner Strain Versus Pressure at SOL #43 262
Figure 366: Liner Strain Versus Pressure at SOL #44 262
Figure 367: Liner Strain Versus Pressure at SOL #45 263
Figure 368: Liner Strain Versus Pressure at SOL #46 263
Figure 369: Tendon Strain Versus Pressure at SOL #48 (Hairpin, Tendon V37 at Tendon Apex) 263
Figure 370: Tendon Strain Versus Pressure at SOL #49 (Hairpin, Tendon V46 at Tendon Springline) 264
Figure 371: Tendon Strain Versus Pressure at SOL #50 (Hoop, Tendon H53 at Mid-Tendon) 264
Figure 372: Tendon Strain Versus Pressure at SOL #51 (Hoop, Tendon H53 at ¼ Tendon) 265
Figure 373: Tendon Strain Versus Pressure at SOL #52 (Hoop, Tendon H53 Near Buttress)... 265
Figure 374: Tendon Strain Versus Pressure at SOL #53 (Hoop, Tendon H35 Between E/H and A/L) 266
Figure 375: Tendon Force Versus Pressure at SOL #54 (Hairpin, Tendon V37 at Tendon Gallery) 266
Figure 376: Tendon Strain Versus Pressure at SOL #55 (Hoop, Tendon H53 at Buttress) 267
Figure 377: Model 4 – Case 1 Saturated Steam Pseudo-Time History 270
Figure 378: Model 4 – Case 2 Station Black-Out Time History 271
Figure 379: Axisymmetric Model with Thermal Boundary Conditions 273
Figure 380: Axisymmetric Model Thermal Gradients 274
Figure 381: Thermal Gradient Locations 274
Figure 382: Concrete Compression Strength Ratio vs. Temperature (Used for ISP-48) 275

Figure 383: Steel Yield Strength and Modulus Ratio vs. Temperature (used for ISP-48) 276
Figure 384: Stress-Strain Curves for Typical Hot-Rolled Steel at Elevated Temperatures [?] .. 277
Figure 385: Reduction Factors for the Stress-Strain Relationship of Carbon Steel at Elevated Temperatures 278
Figure 386: Determination of Strain-Hardening of Carbon Steel at Elevated Temperatures (Figure A.2 Refers to A.2 in 279
Figure 387: Alternate Stress-Strain Relationships for Steel 281
Figure 388: Idealization of Stress-Strain For Concrete at Elevated Temperatures per Eurocode 2 281
Figure 389: Liner View Showing SOL Strain Reports – Also Shown for Reference in Planning Global Liner Strain Map 286
Figure 390: LST Calculated Leak Rates at 1.5, 2.0, and 2.5 P_d 287
Figure 391: LST – Estimated Leak Rates (2.5-3.1 P_d) 288
Figure 392: Estimated Terminal Leak Rates 289
Figure 393: Schematic of a Containment Performance Model 291

TABLES

Table 1. Tendon Stress Distribution for Standard Tendon Behavior Analysis (Includes Seating Losses and Assumed Linearly Varying with Azimuth In-Between Points) ... 26
Table 2. Concrete Creep and Shrinkage Strains 30
Table 3. Applied Strain Demands and Imposed Crack Propagation Steps for Trials (a), (b), and (c) 45
Table 4. Liner Tear Details 46
Table 5: Differences Between Design and In-Situ Properties for the Liner 54
Table 6: Meeting schedule for round robin activities 55
Table 7: Model Detail Comparison 57
Table 8: Comparison of Material Models 58
Table 9: Tendon failure criteria 59
Table 10: Pressure Milestones 59
Table 11: Model Detail Comparison 85
Table 12: Comparison of Material Models 86
Table 13: Liner failure criteria 87
Table 14: Pressure Milestones for Model 2a 87
Table 15: Model Detail Comparison 196
Table 16: Comparison of Material Models 197
Table 17: Tendon failure criteria 198
Table 18: Liner failure criteria 198
Table 19: Data Points for Strength Degradation Versus Temperature 275
Table 20: Reduction Factors for Stress-Strain Relationship of Carbon Steel at Elevated Temperatures 277
Table 21: Values for the Main Parameters of the Stress-Strain Relationships of Normal Weight Concrete with Siliceous or Calcareous Aggregates Concrete at Elevated Temperatures 281
Table 22: Standard Output Location Definitions 283

EXECUTIVE SUMMARY

Research into the integrity of containment structures for nuclear power plants has been conducted in multiple international Round Robin analyses. These analyses have contributed to the understanding of the role of containment in ensuring the safe operation of nuclear power plants. One of the most comprehensive experimental efforts, testing of a 1:4 scale PCCV, was conducted at SNL, primarily under the sponsorship of the NRC. Building upon the research efforts made in the pre- and post- test analyses, and the ISP 48, the SPE #3 has been set up to provide the opportunity for participants to further the state-of-the-art in modeling of prestressed concrete containments. Following the ISP 48 and 1:4 scale PCCV efforts, there was interest in investigating local effects and questions that had been unanswered previously due to modeling and computational limitations at the time and scope limitations of the previous efforts. At the kick off meeting of the SPE#3, held in Mumbai, India, the scope of the first phase of the SPE#3 was agreed upon. There was an interest in investigating the effects of containment dilation on prestressing force, slippage of prestressing cables, steel-concrete interface, failure mechanisms, and the use of nominal versus in-situ conditions.

These areas of investigation, and proposed models to be used in the analyses were determined by those participants who participated in the kick-off meeting. The participants of the kick-off meeting included (in alphabetical order):

- Atomic Energy Regulatory Board of India
- Bhabha Atomic Research Center of India
- Électricité de France of France
- FORTUM of Finland
- Gesellschaft Für Anlagen-und Reaktorsicherheit of Germany
- Indira Gandhi Center of Atomic Research of India
- Nuclear Power Corporation Ltd. Of India
- US Nuclear Regulatory Commission, Sandia National Laboratory, and Moffatt & Nichol of The United States of America
- SCANSCOT of Sweden

The participants agreed to create three models to investigate the local effects mentioned above. Two of the models were to be local models, and the third was to be a full 3-D model. The first local model, a fundamental tendon behavior model, consists of two hoop tendons, assumed to be unaffected by penetration stiffness discontinuities in the wall. This model will allow participants to investigate tendon forces as a function of containment dilation and tendon slippage. The second local model investigates the equipment hatch, and allows participants to further investigate tendon force as a function of containment dilation and tendon slippage, while also allowing participants to investigate the steel-concrete interface and failure mechanisms in the liner. The final full 3-D model will allow participants to investigate all of the local effects, and set the stage for the second phase of the analyses which will focus on leak rates as a function of pressure.

This report provides a comparison of the modeling approaches and results of all of the participants. Chapter 1 provides a description of the three models, as well as a list of the expected results from the participants. Chapter 2 compares the methods used by the participants for Model 1, and the subsequent results called for in the problem definition. Chapter 3 compares

Model 2, and Chapter 4 compares Model 3. Chapter 5 provides a description of the second phase of the analyses, which has yet to be completed. Each participant wrote a report summarizing their modeling efforts. Those are included in the appendices, and organized alphabetically.

NOMENCLATURE

AERB	Atomic Energy Regulatory Board
A/L	Airlock
AMEC	AMEC Power & Process
BARC	Bhabha Atomic Research Center
BWR	Boiling Water Reactor
Δs	Anchorage Slip
E	Young's Modulus
E/H	Equipment Hatch
Ep	Plastic Hardening Modulus
EDF	Électricité de France
FEM	Finite Element Method
fgu	Guaranteed Ultimate Tensile Strength
FY	Fiscal Year
GRS	Gesellschaft Für Anlagen-und Reaktorsicherheit
IGCAR	Indira Gandhi Center of Atomic Research
ISP	International Standard Problem
NPCIL	Nuclear Power Corporation (India) Ltd.
NRC	See USNRC
NUPEC	Nuclear Power Engineering Corporation of Japan
ρ	Density
PCCV	Prestressed Concrete Containment Vessel
Pd	Design Pressure
PWR	Pressurized Water Reactor (?)
SCANSCOT	Scanscot Technology
σt	Tensile Yield Strength
SCV	Steel Containment Vessel
SNL	Sandia National Laboratory
SOL	Standard Output Location
SPE	Standard Problem Exercise
T0	Initial Prestressing Force
μ	Coefficient of Friction
USNRC	United States Nuclear Regulatory Agency
ν	Poisson Ratio

1. INTRODUCTION

Research into the integrity of containment structures for nuclear power plants has been conducted in multiple international Round Robin analyses. These analyses have contributed to the understanding of the role of containment in ensuring the safe operation of nuclear power plants. One of the most comprehensive experimental efforts, testing of a 1:4 scale PCCV, was conducted at SNL, under the sponsorship of the NRC and NUPEC. Building upon the research efforts made in the pre- and post- test analyses, and the ISP 48, the SPE #3 has been set up to provide the opportunity for participants to further the state-of-the-art in modeling of prestressed concrete containment vessels. Following the ISP 48 and 1:4 scale PCCV efforts, there was interest in investigating local effects and questions that had been unanswered previously due to modeling and computational limitations at the time and scope limitations of the previous efforts. At the kick off meeting of the SPE#3, held in Mumbai, India, the scope of the first phase of the SPE#3 was agreed upon. There was an interest in investigating the effects of containment dilation on prestressing force, slippage of prestressing cables, steel-concrete interface, failure mechanisms, and the use of nominal versus in-situ conditions in modeling.

These areas of investigation, and proposed models to be used in the analyses were determined by those participants who participated in the kick-off meeting. The participants of the kick-off meeting included (in alphabetical order):

- Atomic Energy Regulatory Board of India
- Bhabha Atomic Research Center of India
- Électricité de France of France
- FORTUM of Finland
- Gesellschaft Für Anlagen-und Reaktorsicherheit of Germany
- Indira Gandhi Center of Atomic Research of India
- Nuclear Power Corporation Ltd. Of India
- NRC/SNL/M&N of The United States of America
- SCANSCOT of Sweden

The participants agreed to create three models to investigate the local effects mentioned above. Two of the models were to be local models, and the third was to be a full 3-D model. The first local model, a fundamental tendon behavior model, consists of two hoop tendons, assumed to be unaffected by penetration stiffness discontinuities in the wall. This model will allow participants to investigate tendon forces as a function of containment dilation and tendon slippage. The second local model investigates the equipment hatch, and allows participants to further investigate tendon force as a function of containment dilation and tendon slippage, while also allowing participants to investigate the steel-concrete interface and failure mechanisms in the liner. The final full 3-D model will allow participants to investigate all of the local effects, and set the stage for the second phase of the analyses which will focus on leak rates as a function of pressure.

This report provides a comparison of the modeling approaches and results of all of the participants. The rest of Chapter 1 provides a description of the required models to be built, as well as a list of the expected results from the participants. Chapter 2 compares the methods used by the participants for Model 1, and the subsequent results called for in the problem definition. Chapter 3 compares Model 2, and Chapter 4 compares Model 3. Chapter 5 provides a

description of the second phase of the analyses, which has yet to be completed. Each participant wrote a report summarizing their modeling efforts. Those are included in the appendices, and organized alphabetically.

1.1 Background

Research into the integrity of containment structures for nuclear power plants has been conducted in both internal and international Round Robin analyses. While the contributions of each of these efforts to the understanding of the role of containment in ensuring the safe operation of nuclear power plants is important, the most comprehensive experimental effort has been conducted at Sandia National Laboratories, primarily under the sponsorship of the Nuclear Regulatory Commission. NUREG/CR 6906, "Containment Integrity Research at Sandia National Laboratories: An Overview," summarizes the major results of the experimental efforts, the observations and insights gained from the analytical efforts for more than 25 years of containment integrity research at SNL. Prior to pressure testing the scale models, a number of regulatory and research organizations were invited to participate in a pre-test Round Robin analysis to perform predictive modeling of the response of scale models to over pressurization. Seventeen organizations responded and agreed to participate in the pre-test Round Robin analysis activities. The purpose of the Containment Integrity Research at SNL was to provide a forum for researchers in the area to apply current stat-of-the-art analysis methodologies to predicting capacity of steel, reinforced, and pre-stressed concrete containment vessels.

As noted above, this work is related to the NRC-sponsored Containment Integrity Programs at SNL. These programs investigated the behavior of light water reactor (LWR) containment buildings under loadings that exceed the design basis or so-called "severe" accident loads. A combination of experimental and analytical studies was employed in these programs. Initially, over-pressurization tests of several scale model containment buildings were conducted under FIN A1817, "Concrete Containment Experiments," and FIN A1249, "Experiments on Containment Models under Extreme Loading Conditions." Separate tests of typical containment penetrations were conducted under FIN A 1375, "Integrity of Containment Penetrations under Sever Accident Loads." Tests of electrical penetration assemblies (EPAs), a personnel airlock, bellows, a pressure0unseating equipment hatch, and the seals and gaskets used in penetrations were included in this program.

In FY91, a cooperative program on containment integrity under sever accident conditions between the NRC and the Nuclear Power Engineering Corporation (NUPEC) of Japan was begun. Testing and analyses of a steel containment vessel (SCV) model representative of a BWR, Mk-11 containment and a prestressed concrete containment vessel model, as used in some large, dry, PWR containments, were funded by the NRC.

Efforts were also made to assess the seismic capacity of containment structures. SNL performed pre- and post-test analyses of shaking table tests of a 1:10-scale prestressed concrete containment model and a 1:8 scale reinforced concrete containment model. These models were constructed and the tests were conducted by NUPEC at their Tadotsu Engineering Laboratory. The insights gained from analyzing the response of these test models were used to estimate the seismic capacities of typical US containments. The effects of aging-related degradation on containment capacity to resist severe accident pressures were investigated.

All of the aforementioned research efforts are being used to set the foundation for the current AERB/USNRC sponsored SPE #3. The 1:4 Scale Prestressed Concrete Containment Vessel built and pressure tested to failure by NUPEC, the USNRC, and SNL between 1998 and 2000 is the experimental model which is being used to test the FEM models against in the current SPE #3. Analytical models are meant to improve on modeling techniques developed for the pre- and post-test analyses, and the ISP #48, which also used the 1:4 Scale PCCV as the experimental basis for its FEM models. This exercise was set up as part of the U.S.-India Civil Nuclear Cooperation Agreement, and provides all participants the opportunity to improve the current state-of-the-art in the modeling of prestressed concrete containment vessels subject to severe loads.

1.2 Phase One Defintion

At the kick-off meeting for the standard problem exercise (SPE) on the performance of containment vessels under severe accident conditions, it was agreed that the SPE round robin exercise would build on previous round robin analyses of the NRC/NUPEC 1:4-Scale Prestressed Concrete Containment Vessel model tests. Additionally, some of the SPE participants conducted analyses for the ISP-48. A goal that emerged from the kick-off meeting was to focus on questions still unanswered by the ISP-48. This section is meant to specify the details of the SPE analyses to be performed, and recap decisions made at the kick-off meeting.

The round robin analysis on containment vessel performance will consist of two rounds of analyses, and three review meetings, in addition to the kick-off meeting. The primary source of physical test data remains the Sandia/NRC/NUPEC 1:4 Scale PCCV Test, but the introduction of other research or published ancillary test data is welcomed in furthering the aims of the SPE work.

The remainder of this chapter is organized as follows. The work phases and topics of study printed in the original SPE invitation are shown in italics. The actual finite element model definitions, boundary conditions and loads, and instructions to analysts, which emerged from the kick-off meeting are presented in normal typeface, as Models 1, 2, 3.

Phase One of the SPE, whose focus is the further examination of those local effects which were observed to require more study in the previous round robin analyses, will include an examination into the effects of containment dilation on prestressing force, slippage of prestressing cables, steel-concrete interface, failure mechanisms, and the use of nominal versus in-situ conditions in the previous round robin analyses. Analysis results from this phase may also help in calibrating the model in phase 2 of the analyses.

Within Phase 1, local models will be developed and analyzed. Following completion of local model analysis, a full 3d model incorporating the local model methods and lessons learned will be evaluated.

1.2.1. SPE 1.1 – Tendon Forces as a Function of Containment Dilation

Some important observations made in the previous Round Robin Analyses hosted by SNL concerned the nature of hoop tendon measurements as pressure increased within the model. It was noted that when pressure overcame prestress, tendon stress distributions changed from the classical angular friction design assumption to an approximately uniform distribution; then they

stayed fairly uniform at most higher pressures. Toward the end of the test, some tendon interior forces slightly exceeded the force at the anchor. The pre- and post-test analyses resulted in poor agreement in the hoop tendon stress distributions despite the good agreement with radial displacements. The overprediction of dome and overall vertical displacements and anchor forces, in addition to the underprediction of interior gage stresses, warrant further examination. Participants will be asked to analytically explore tendon forces as a function of containment dilation.

1.2.2. SPE 1.2 – Slippage of Prestressing Cables

It was also observed that the apparent strain increases in the tendons corresponding to the force/strain gage readings are significantly larger (e.g. 0.48% versus 0.35%) than the strain that corresponds purely to radial expansion Figure 2. This could only be explained by force redistribution associated with sliding. Thus the position of the tendon relative to the concrete must be allowed to change after initial prestress in order to adequately simulate tendon behavior during over-pressurization.

It was seen through test measurements and analytically that tendon friction is important to the tendon behavior, but traditional friction design formulas that predict tendon stress distribution begin to break down once pressurization exceeds the pressure that overcomes prestress. The coefficient of angular friction appears to lessen, allowing sliding and force redistribution as the vessel expands, but more importantly, some parts of the tendon are forced to reverse direction of travel relative to the duct, reverse it from the direction of travel experienced during prestressing.

Cylinder hoop tendon data shows evidence that angular friction forces were overcome by differential tendon forces resulting in the tendons sliding, relative to the ducts, during pressurization. The measurements indicate that the shape of the tendon stress profile completely changes during pressurization. The increase in tendon strain, which is greater than the corresponding cylinder wall hoop strain, implies that portions of the tendons are slipping in order for higher deformation at other azimuths to be accommodated. The participants will be asked to investigate the slippage of prestressing cables.

1.2.4.1 Model 1: Tendon Behavior Model

The aforementioned italicized narrative describes two topics related to tendon behavior, as stated in the SPE proposal. At the kick off meeting, SPE participants agreed to combine these topical studies into one analysis series based on a fundamental tendon behavior model (Model 1). The model is illustrated in Figure 1. It consists of two hoop tendons, assumed to be unaffected by penetration stiffness discontinuities in the wall.

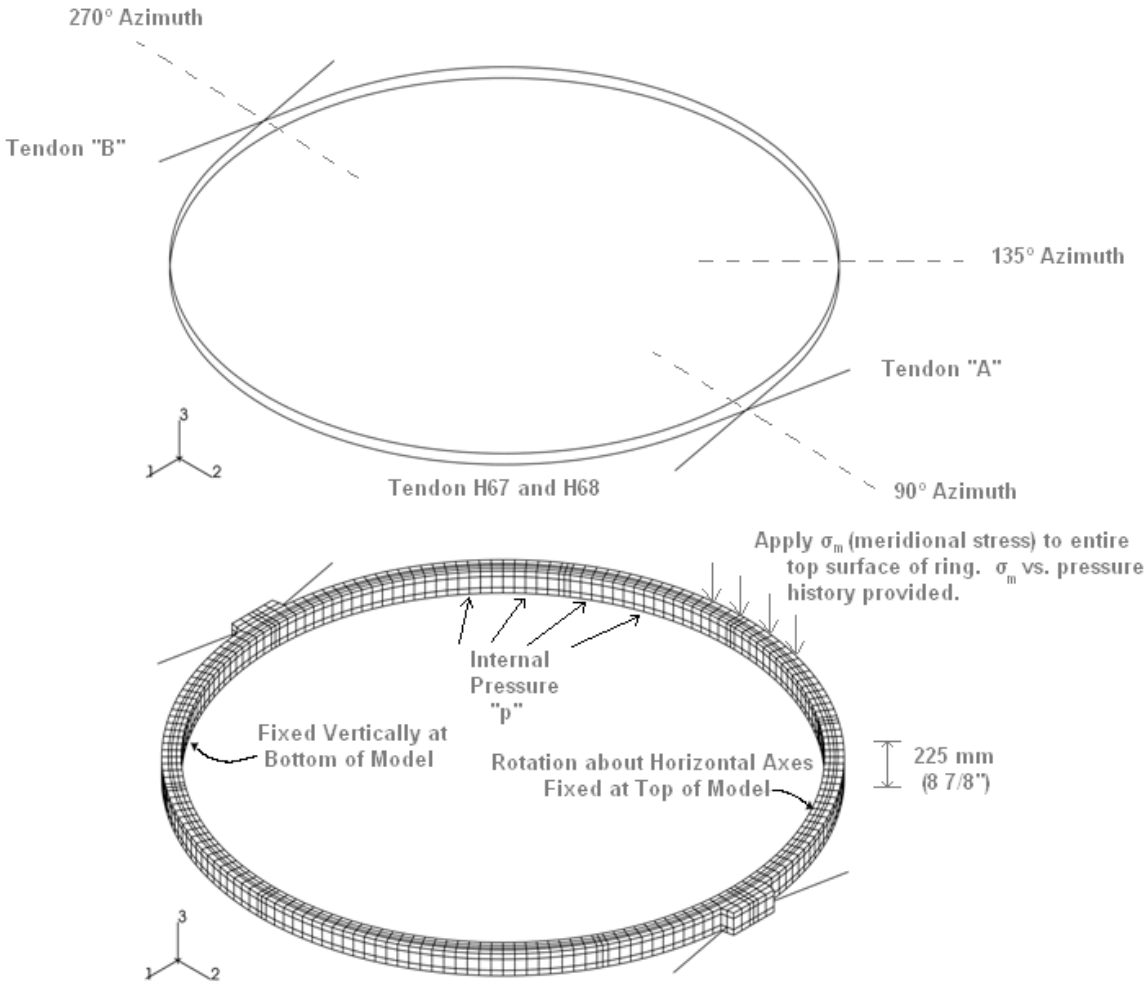

Figure 1. Model 1 - Tendon Behavior Model, Representing Tendons H53 and H54, Elev. 6.579 m (Refer to Dwg. # PCCV-QCON-04)

Boundary conditions and pressure will be applied the same by all participants, and these are specified in the Figure. The minimum requirement for this task is a pressure analysis up to prediction of ultimate limit state. In a separate analysis, application of temperature effects will be optional. Participants are asked to use best tools and efforts available (with due consideration to constraints on funding and computational resources) to include simulation of friction and pressure-response related changes to tendon stress distribution, in their analysis. Analytical representation of losses (from all sources) is optional, but encouraged. Attempts have been made to quantify the losses measured in the lead-up time to the test. Some postulation of magnitude of components of losses is required and is open to further discussion. However, the sum total of losses is measured and known. In an effort for all participants to begin their pressure analysis from the same basis, and same initial tendon stress distribution, the black lines (with dashed line anchor set), as shown in Figure 2 and tabulated in Table 1, are prescribed as the starting point for the exercise. The pretest tendon data for H53 can be found on the data-CD already distributed to participants.

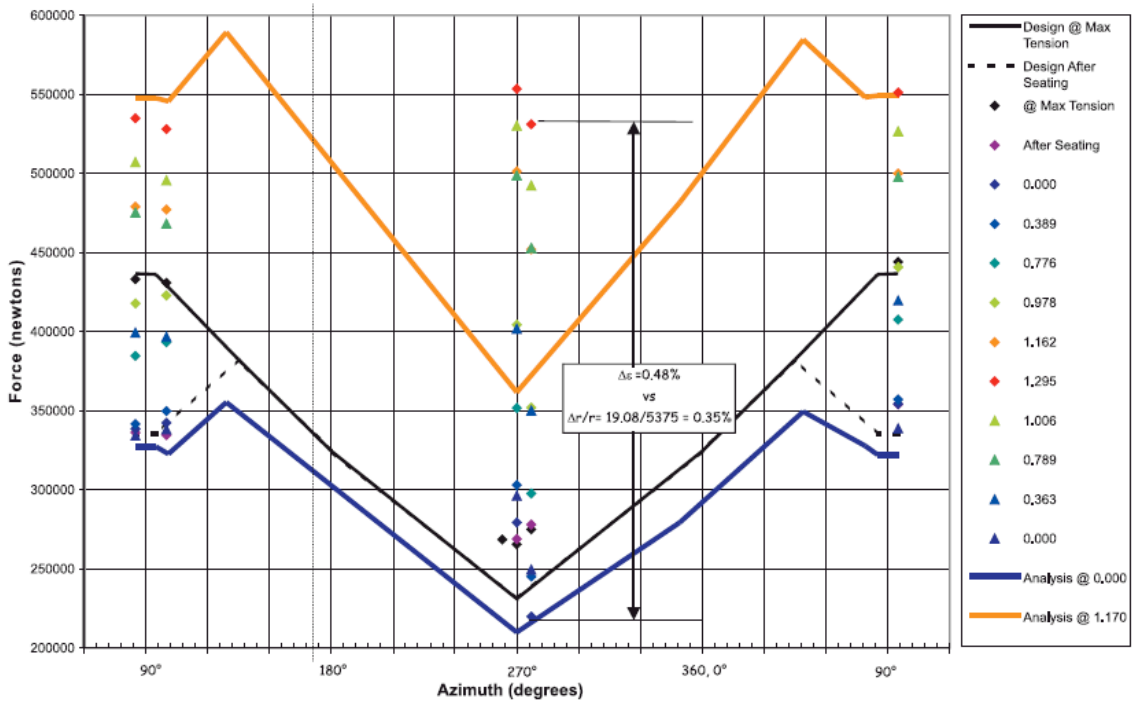

Figure 2. H53 Tendon Force Comparisons to Pretest (From NUPEC/NRC PCCV test at SNL)

Table 1. Tendon Stress Distribution for Standard Tendon Behavior Analysis (Includes Seating Losses and Assumed Linearly Varying with Azimuth In-Between Points)

AZIMUTH	FORCE (NEWTON)
365	334,292
355	334,625
315	381,526
270	323,648
180	230,512
90	323,648
45	381,526
5	334,625
-5	334,292

Tendon, rebar and concrete material stress-strain assumptions should follow that tabulated in Appendix 1 of NUREG/CR-6810. Additional discussion about tendon losses is provided below, based on excerpts from Sandia's post-test analysis report for the 1:4 Scale PCCV (NUREG/CR-6809), which is provided on the SPE website.

The prestressing tendon tensioning data shows that the average hoop tendon seating loss is 3.95 mm when averaged over all hoop tendons *and* when averaged over H35 to H72 (it appears that

the cables H35 to H72 are representative of all the prestress cables, and there was not a significant difference in behavior of these cables compared to the rest of the model). Therefore, it was decided to use 3.95 mm for the seating loss on all hoop tendons. This put the seating loss zone of influence at 39.5 degrees from the buttress centerline. This assumption appears to agree fairly well with the strain gage data points on the hoop tendons that were instrumented (H35, H53, and H68). The measured strains/forces at the midpoints of H53 and H68 imply that the angular friction may be a little smaller than the design value (0.18 versus 0.21), but the H35 measurements show that near penetrations where the tendon path curves around the penetrations, the effective angular friction may be higher than the design value. For the tendons represented in the 3DCM, it was assumed that the design value 0.21 (as measured by NUPEC in separate mock-up tests) would provide a reasonable average of the varying conditions that occur in the cylinder-midheight region. For local modeling of the Equipment Hatch, although it would be possible to input different hoop tendon stresses in each tendon, it was decided to use the average load cell value of 32.89T (72.5 kips) that existed at the July 6 measurement. The load cell measurements for H40 and H58 appear unreasonably low compared to the jacking forces and an average force seems more appropriate. The final hoop tendon stress profiles produced are shown in Figure 3.

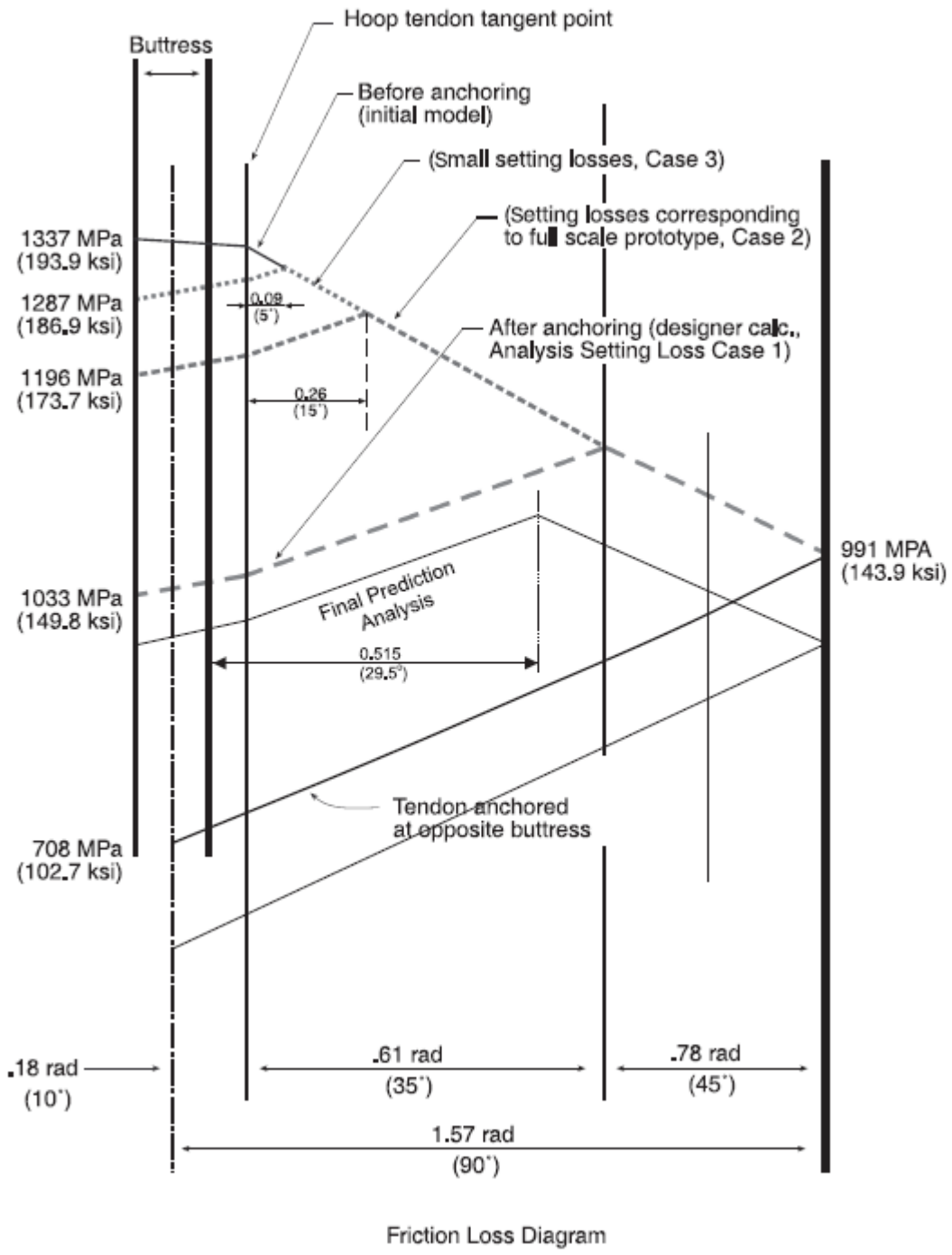

Figure 3. Additional Information about Tendon Friction and Seating Losses

Concrete creep and shrinkage strains are shown in Figure 4and in Table 2. Judging by the minimal change in the tendon forces between May and July prior to the LST, the effects of creep and shrinkage appeared to be much smaller than anticipated. It is difficult, however, to isolate the creep response from other time-dependent effects, such as temperature. Since creep effects will tend to be largest within the first 30 to 60 days after prestressing, using the July 6 measured prestress values accounts for time-dependent effects reasonably well. In general, the initial levels

of prestress arrived at are lower than those measured on individual tendons by between 3% and 10%. This should accommodate creep effects that may have occurred between July 6 and September 26 (LST time of test).

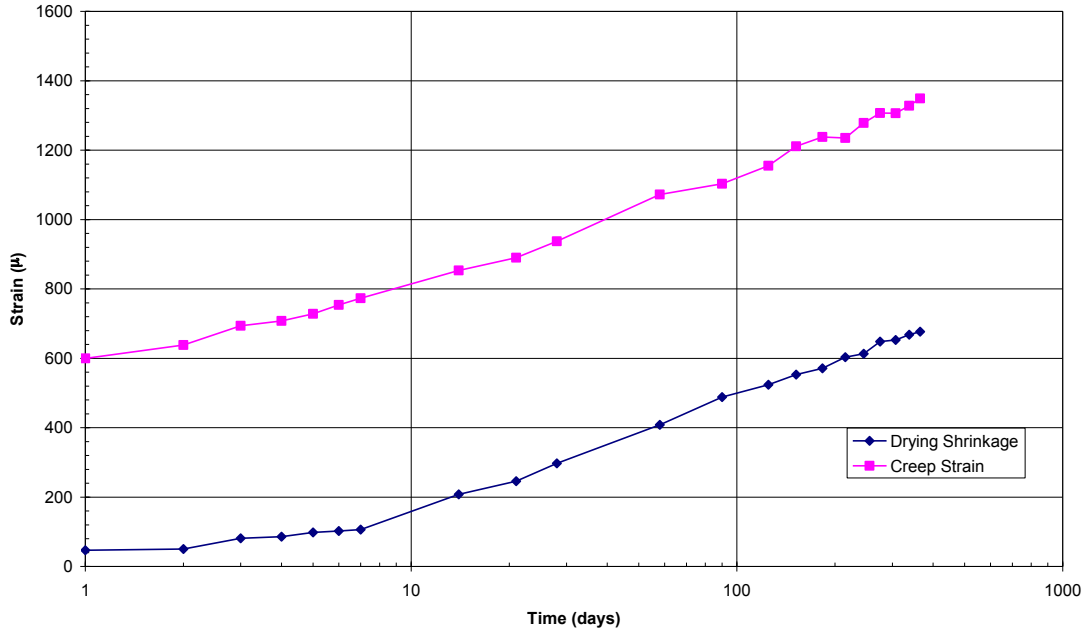

Figure 4. Concrete Creep and Shrinkage Strain

Table 2. Concrete Creep and Shrinkage Strains

Time (days)	Time after Loading (days)	Drying Shrinkage Strain	Post Loading Strain	Load-induced Strain	Creep Strain = Post Loading Strain - Initial Elastic Strain	Creep Coefficient = Creep Strain / Elastic Strain	Applied Stress (kgf/cm2)	Applied Stress (psi)	Load-induced Strain per Applied Stress (kgf/cm2)	Load-induced Strain per Applied Stress (psi)
0							0	0		
28	0	0	508	508			176	2500	2.89	0.203
29	1	47	600	553	92	0.18	176	2500	3.15	0.221
30	2	50	638	588	130	0.26	176	2500	3.34	0.235
31	3	81	694	613	186	0.37	176	2500	3.49	0.245
32	4	86	708	622	200	0.39	176	2500	3.54	0.249
33	5	98	728	630	220	0.43	176	2500	3.58	0.252
34	6	102	754	652	246	0.48	176	2500	3.71	0.261
35	7	106	773	667	265	0.52	176	2500	3.79	0.267
42	14	208	853	645	345	0.68	176	2500	3.67	0.258
49	21	246	890	644	382	0.75	176	2500	3.66	0.258
56	28	297	937	640	429	0.84	176	2500	3.64	0.256
86	58	408	1072	664	564	1.11	176	2500	3.78	0.266
118	90	488	1103	615	595	1.17	176	2500	3.50	0.246
153	125	524	1155	631	647	1.27	176	2500	3.59	0.252
180	152	553	1211	658	703	1.38	176	2500	3.74	0.263
211	183	571	1238	667	730	1.44	176	2500	3.79	0.267
243	215	603	1235	632	727	1.43	176	2500	3.59	0.253
273	245	613	1278	665	770	1.52	176	2500	3.78	0.266
303	275	648	1307	659	799	1.57	176	2500	3.75	0.264
335	307	653	1306	653	798	1.57	176	2500	3.71	0.261
366	338	668	1328	660	820	1.61	176	2500	3.75	0.264
393	365	677	1349	672	841	1.66	176	2500	3.82	0.269

The SPE participants are expected to produce the following results for Model 1.

1.2.4.2 Required output/Results for Model 1

1.1 Description of modeling assumptions and phenomenological models

1.2 Description of tendon failure criteria used

1.3 Pressure Milestones. Applied pressure when:

1.3.1 Concrete hoop stress (at 135^o azimuth) equals zero

1.3.2 Concrete hoop cracking cccurs (at 135^o azimuth)

Tendon A reaches 1% strain (at 135^o azimuth)

1.3.3 Tendon B reaches 1% strain (at 135^o azimuth)

1.3.4 Tendon A reaches 2% strain (at 135^o azimuth)

1.3.5 Tendon B reaches 2% strain (at 135^o azimuth)

1.4 Deformed shape and tendon stress distribution at P = 0 (prestress applied); 1 x P_d; 1.5 P_d; 2 P_d; 2.5 P_d; 3 P_d; 3.3 P_d; 3.4 P_d; Ultimate Pressure

1.5 Description of observations about tendon force as a function of containment dilation and tendon slippage

1.2.3. SPE 1.3 – Steel-Concrete Interface

Separations were observed surrounding containment penetrations during testing of the PCCV structure. Many of the highest strains recorded during the limit state test (LST) were near the Mainstream (M/S) and Feedwater (F/W) penetrations, but also near the edge of the wall embossment of the Equipment Hatch. Even at locations which were designed to be identical in geometry, there was a wide variation in peak strain data. These variations were most likely due to slight variations in liner thickness (due to manufacturing and weld repair grinding), gage position relative to the collar/weld, material properties (including welding heat effects), etc. Of particular interest is the separation between the concrete and sleeves, the stress concentrations that lead to liner tearing, and the development of potential leak paths using strain information. The participants will be asked to quantify the risk associated with the formation of a gap as a function of a potential leak path.

1.2.4.1 Model 2: Local Model of Equipment Hatch

Similar to SPE topics 1.1 and 1.2, SPE 1.3 will encompass the study of different aspects of Steel-Concrete Interface using one local analysis model (Model 2). The topics are: (1) ovalizations of concrete versus steel, looking at displacement and the leakage this could cause, and (2) slippage between the liner and the concrete, and the influence of this behavior on potential tearing and leakage. The decision was made to investigate the equipment hatch in a local model.

During the kick-off meeting, a third aspect of Steel-Concrete Interface was introduced: a study of rebar stress-strain specified versus stress-strain characteristics in the FE model (because concrete can influence this representation). This will also be addressed with Model 2 with a view toward

applying lessons learned to final global analysis. On the subject of liner slip, data from the 1/6 scale steel model may also be used.

The geometry and boundary condition assumptions of the local E/H model (Model 2) specified for all participants to use is shown in Figure 5, Figure 6, and Figure 7 (the numbering D16, D19, etc. refer to the numbering of the rebar found in the drawings of NUREG/CR-6810 – specifically the drawing labeled Opening Rebar Details (E/H)). Please refer to the drawings in NUREG/CR-6810 for a more detailed description of the geometry. Tendon stress distributions are shown in Figure 8. Similar to Model 1, participants may implement the starting tendon stress distribution using any means they wish, but at the start of pressure loading, all participants' analyses should have a common set of initial conditions. The boundary conditions are symmetry at the azimuth-324-degrees and Azimuth-18-degrees planes, and quasi-symmetry at the bottom and top of the model, i.e., $U_z = 0$ at the bottom, and the statically determinant meridonal stress applied at the top (as indicated in Figure 6). An additional required condition along the top of the model is that all nodes must stay in a plane, and the plane is not allowed to rotate about the tangential (theta) direction. Using this boundary condition allows the application of vertical prestress, without causing local distortions at the ends of the tendons at the top of the model. As a plane, the top of the model is still free to deform vertically, under the action of the meriodional applied stress, and the model response.

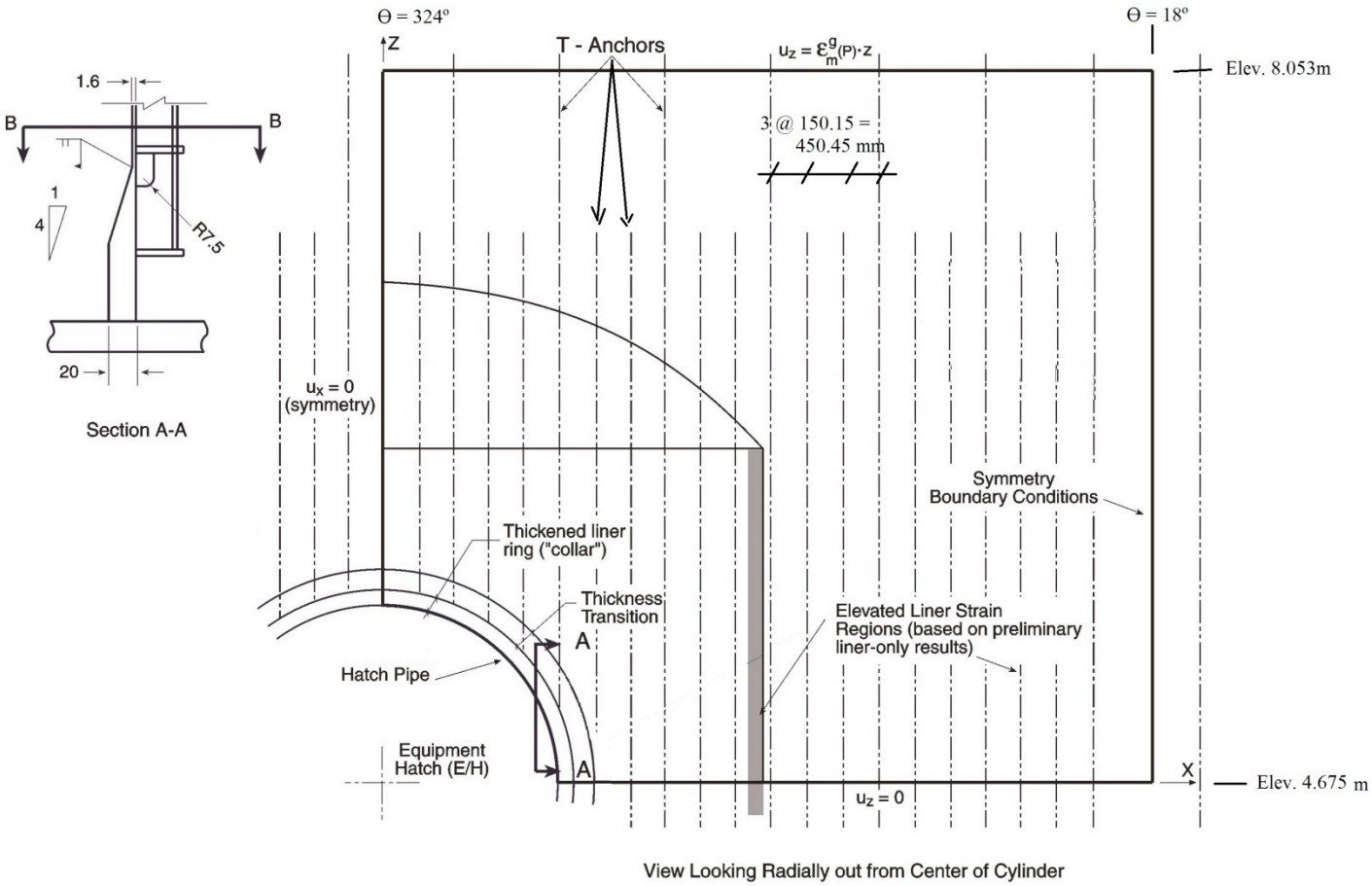

Detailed Liner Analysis Near E/H (View from Inside PCCV Looking Out Radially)

Figure 5. Model 2 - Local E/H Model Geometry and Boundary Conditions

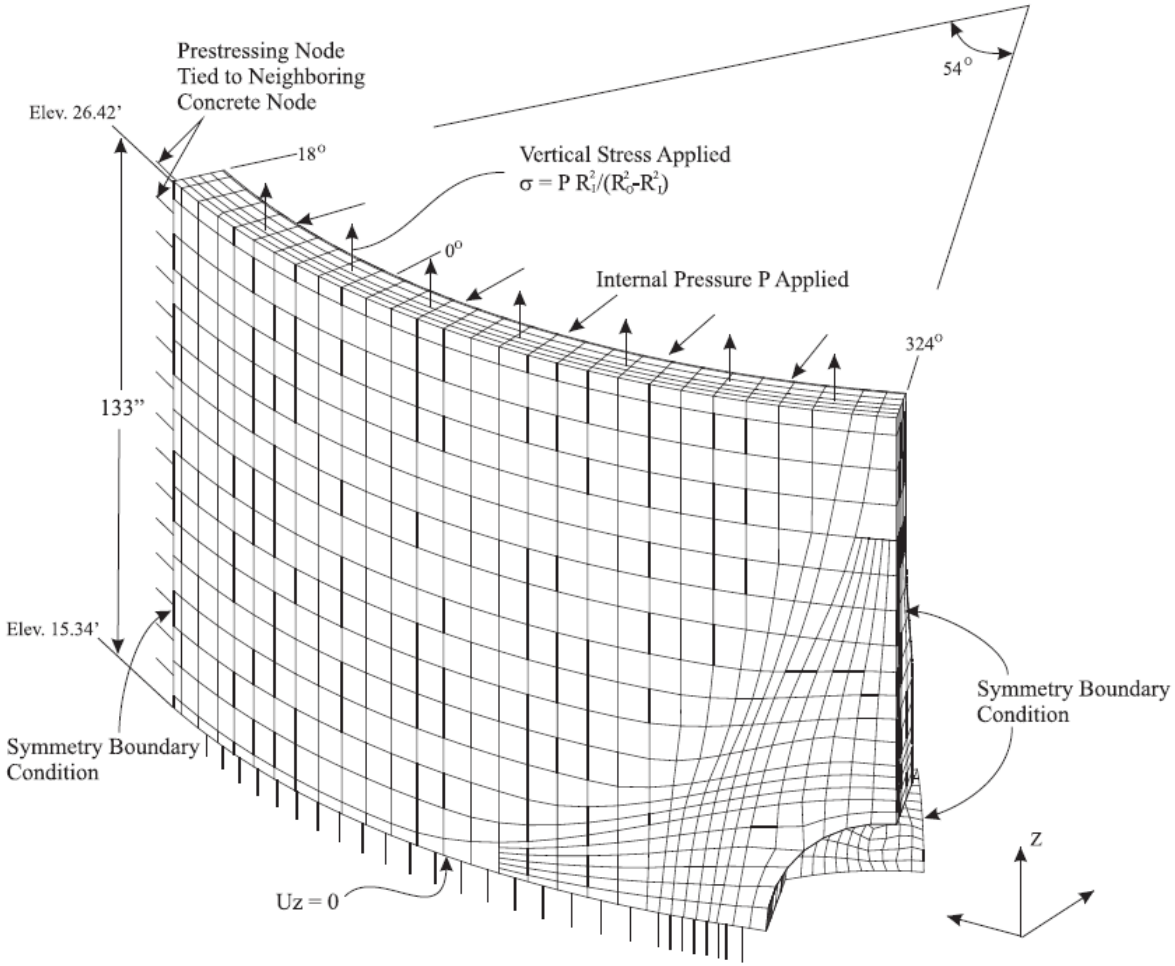

Figure 6. Model 2 – Perspective View

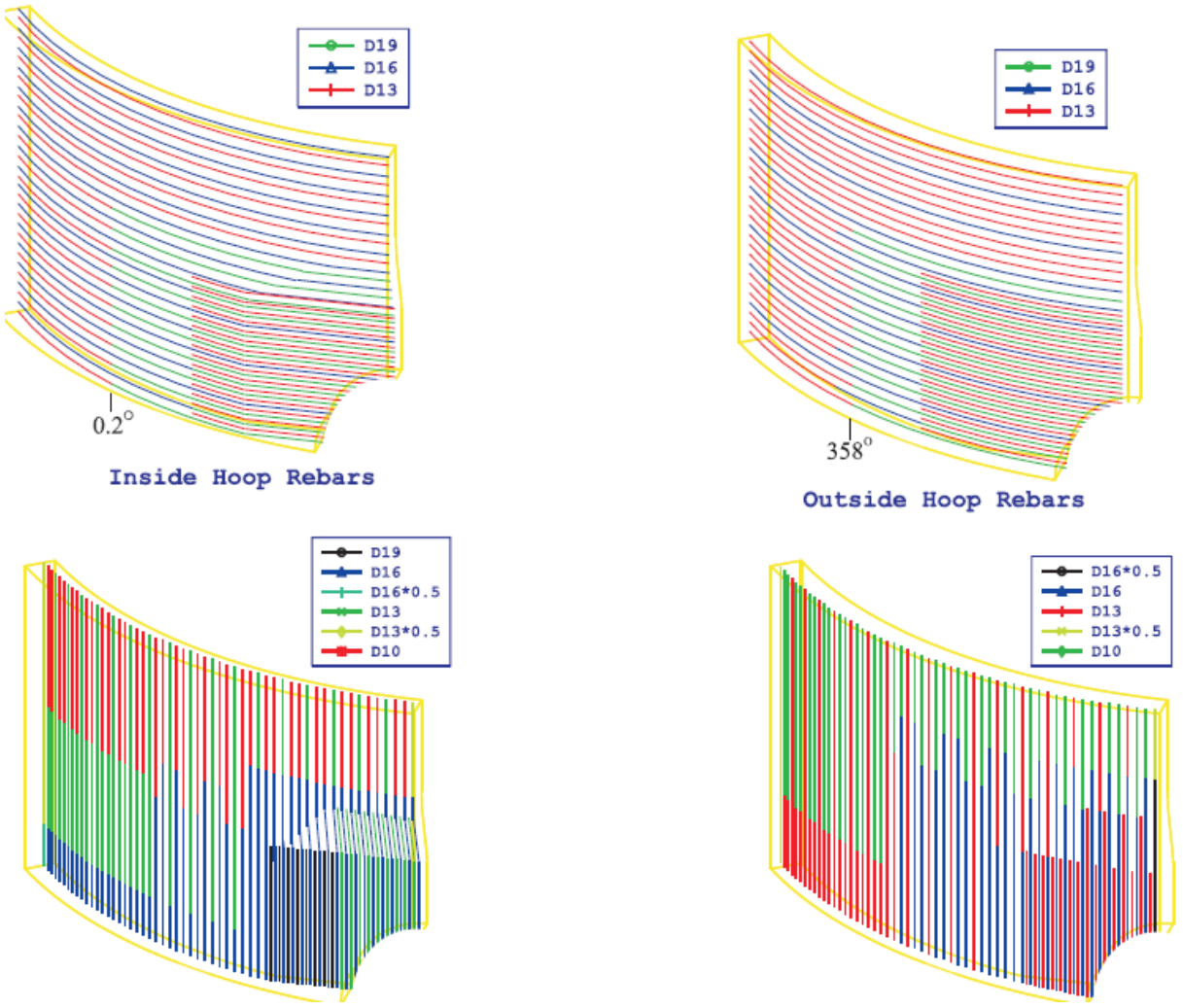

Figure 7. Rebar Summary for Model 2 (Important to Simulating Strain Concentrations)

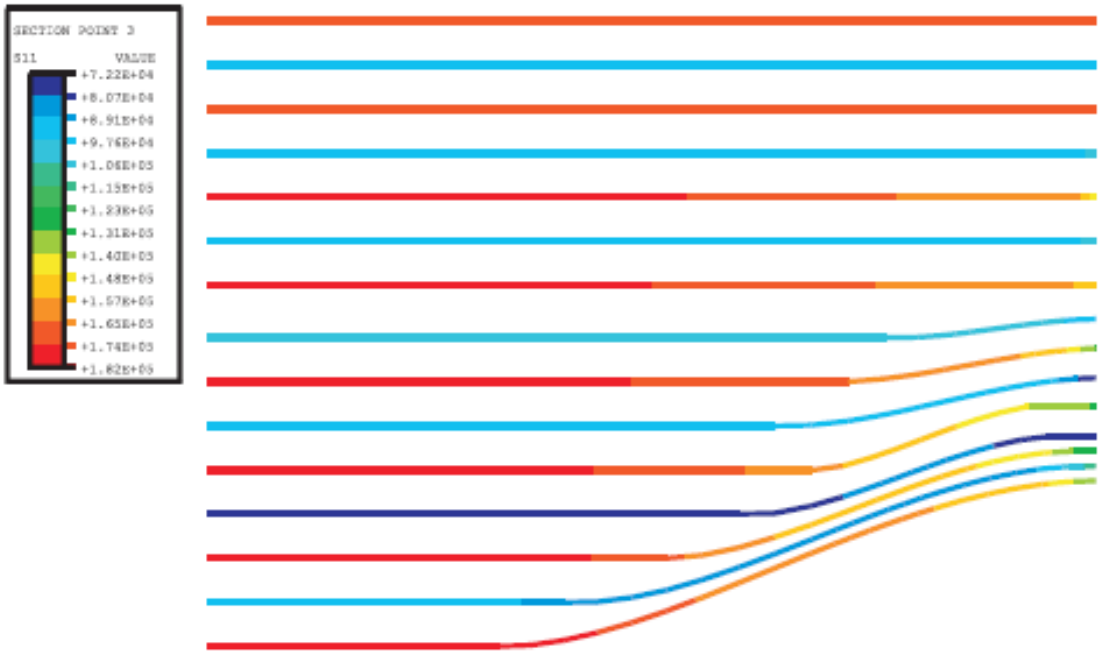

Figure 8. Tendon Stress Distribution for Model 2

It should be noted that the tendons shown in Figure 6 and Figure 8 are represented "2 for 1", based on a simplifying FE modeling assumption made in Sandia's post-test analysis work (as published in NUREG-CR/6809). Participants may follow this modeling strategy, or may model every tendon. Further, for purposes of studying the liner-concrete interaction problem, we recommend that a simplifying assumption can be made as to the initial distribution of stress in the tendons of this local model. It is important to characterize the difference between the initial stress in the "A" tendons (which are anchored at the 90-degree azimuth) and the "B" tendons (which are anchored at the 270-degree azimuth), but it is not critically important to model the changing distribution of stress across this local model. Thus, we recommend using the following initial stresses in the tendons:

A-tendons: 165,000 psi (1138 MPa)

B-tendons: 90,000 psi (621 MPa)

As with Model 1, tendon friction may be represented using the best method available to the analyst, and if it is represented, then initial tendon stress distributions will be variable. But the average tendon stresses within the model should be approximately those specified here.

Several of the liner strain gages in the vicinity of the E/H showed elevated strains, as indicated in Figure 9. Further, a number of tears were observed after the LST (as shown in Figure 10).

These strain gages (and possibly others), and the existence of tears #7, 8, 12, 13, 14, 15, and 18 are important to this SPE study model, and their locations are encompassed by it. The primary stress/strain concentration locations were observed to occur along the juncture between the standard wall (liner), and wall embossment (liner anchors and stiffeners), and also along a vertical line in the vicinity of 0-degree to 6-degree azimuth which corresponds to a "step-down" reduction in the steel area of the circumferential rebar (See Figure 7). For this reason, it is important for analysts to represent the rebar areas correctly, and analysts are directed to review the PCCV-Model drawings to make the correct assumptions.

Figure 11 shows key locations for reporting the liner strain selected for the Model 2 Exercise. The objectives in choosing these locations are:

1. To choose a relatively long gage length over which to report strain in order to eliminate differences between analysts due to mesh size.

2. To focus on key aspects of liner-concrete interaction.

3. Establish a framework for conducting a fracture-mechanics based liner failure prediction.

The locations are numbered 1 through 10, and the boundaries are defined by the liner anchors. This is logical, especially for the case where the liner slips freely between anchors because, for such a case, liner hoop strain will likely be nearly uniform between anchors. At the large anchor spacing, the gage length is, therefore, 450.45 mm, and at the small spacing, it is 150.15 mm. At the smaller spacing, analysts are requested to report three separate strain values, i.e., at locations 3a, 3b, 3c, 4a, 4b, 4c, 5a, 5b, 5c, 8a, 8b, 8c, 9a, 9b, 9c, 10a, 10b, 10c.

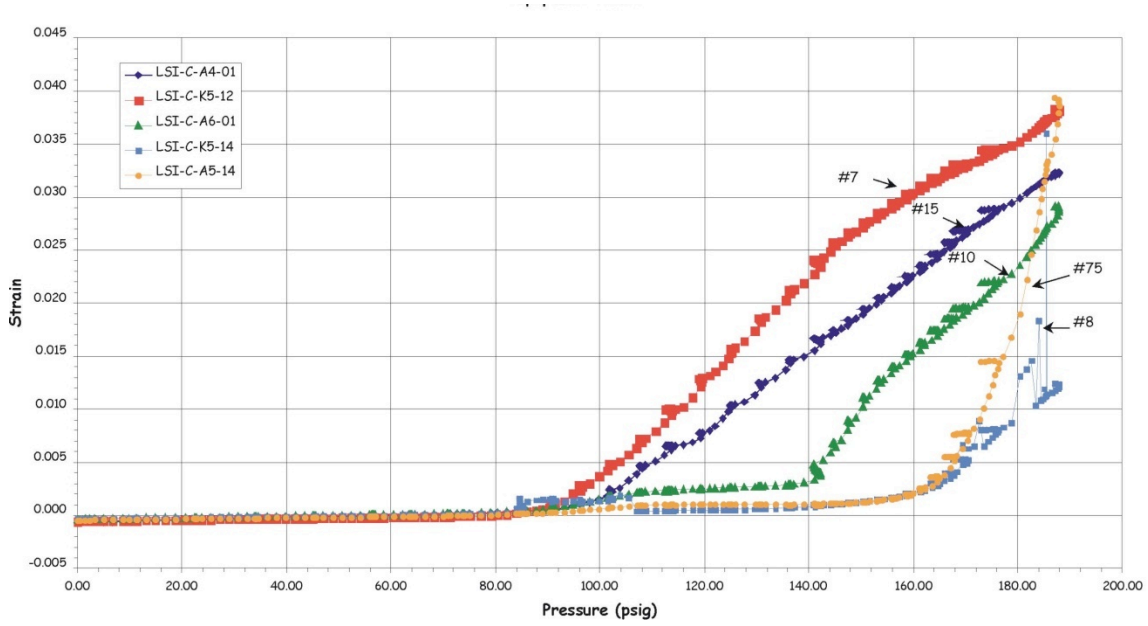

Figure 9. Pressure versus Strain for Equipment Hatch Strain Gages

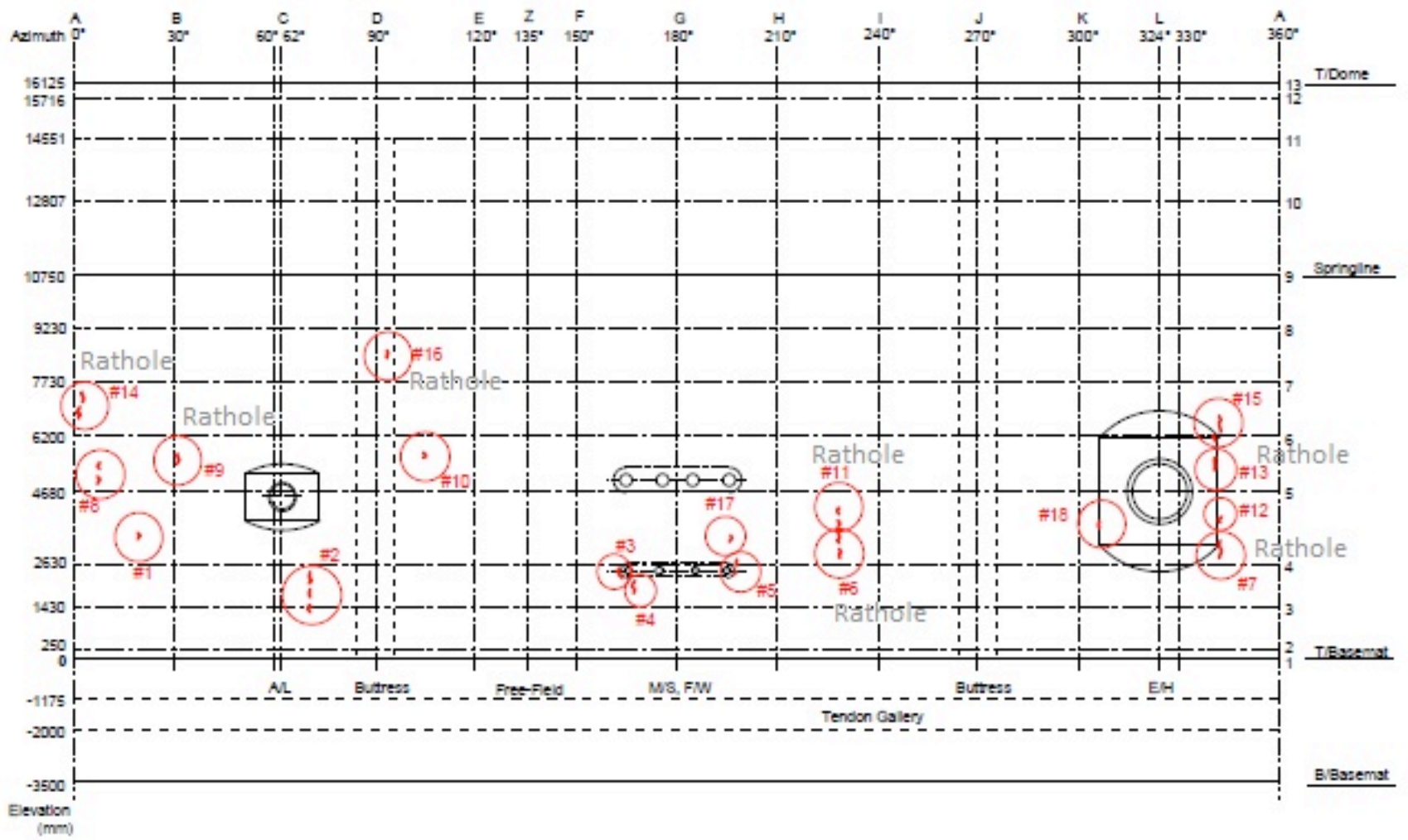

Figure 10. Pressure Versus Strain for Equipment Hatch Strain Gages

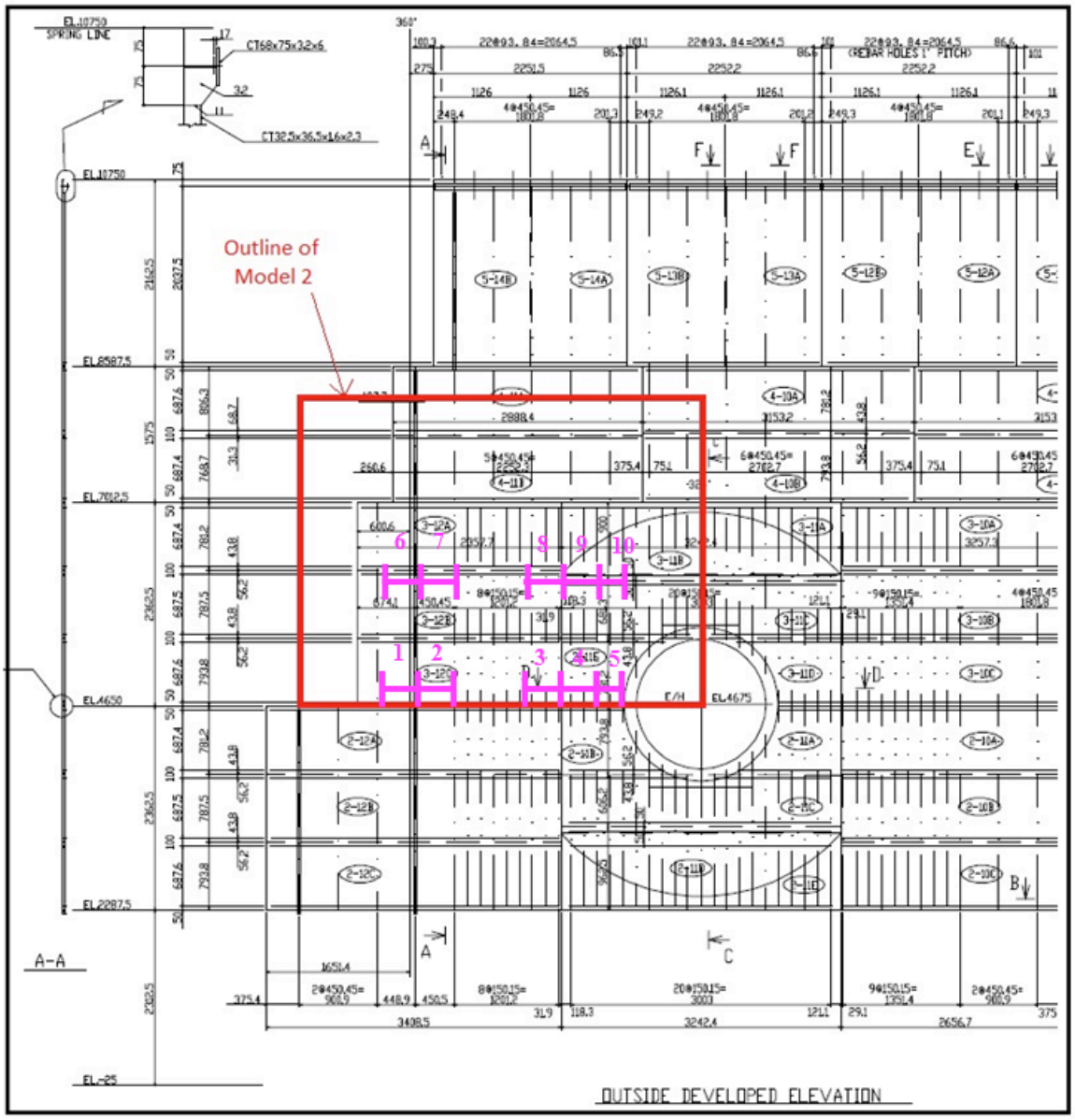

Figure 11. Liner (E/H) View Showing Strain Reports (cut from Page A-28 of NUREG/CR-6810)

To further the state-of-knowledge on the subject of liner-concrete slippage, we suggest that the local E/H model be analyzed with a minimum of 2 (plus one optional) sets of liner-concrete interaction assumptions:

1. Liner assumed bonded (no-slip) to concrete

2. Liner only connected to concrete at anchors, free-slip in between

3. Best estimate connection and consideration of friction (Optional – It is up to the participants to determine what they feel is the best method of representing the connection and friction.)

By presenting results using two or three parameter sensitivities, the SPE will, hopefully, arrive at conclusions about the importance of these aspects of behavior on liner tearing and leakage, and on analytical prediction of the same.

1.2.4.2 Required Outputs/Results for Model 2

2.1 Description of modeling assumptions and phenomenological models

2.2 Description of liner failure criteria used

2.3 Pressure Milestones. Applied pressure when:

- 2.3.1 Concrete hoop cracking occurs, and report where
- 2.3.2 First tendon reaches 1% strain, and report where

2.4 Deformed shape and liner strain distribution at P = 0 (prestress applied); 1 x P_d; 1.5 P_d; 2 P_d; 2.5 P_d; 3 P_d; 3.3 P_d; 3.4 P_d; Ultimate Pressure

2.5 Liner strain magnitudes (hoop direction) at locations indicated in Figure 11. Ovalization: plot change in diameter of hatch and adjacent concrete, in hoop direction, versus pressure

2.6 Ovalization: plot change in diameter of hatch and adjacent concrete, in meridional direction, versus pressure

1.2.4. SPE 2.4 – Failure Mechanisms

During the PCCV test, tearing in the liner was observed (See LinerTears.doc). Of interest is the characterization of the liner tearing mechanism. The applicability of a fracture mechanics approach versus ductile failure approach needs further investigation. Ultimately, the participants need to determine how to predict tears in the liner from the finite element model strains. To this end, they need to determine if there are areas where fracture mechanics can be applied to predicting the size of liner tears or if the tears should be characterized with a ductility-based failure criteria (such as the Davis Triaxility Factor approach).

This SPE topic should be considered in the results assessment for both Model 2 (previously described) and Model 3. Doing this will help introduce liner failure prediction in a stepwise approach, starting from a simpler model, and ending in the global prediction model. The following discussion provides some background on a possible approach to applying fracture mechanics to the PCCV liner.

The state-of-the-art for predicting tearing for steel shells comprised of plates, weld seams, stiffeners and other details consists of two fundamental types of failure criteria:

1. Strain-based failure criteria applied to unflawed steel material and components;

2. Fracture-based failure methods applied to postulated flaws, which are commonly found in welded steel shell structures

Both are highly relevant to PCCV liners, but both have different information requirements about the material, the strain state, and the conditions surrounding a potential crack. Failure Criteria Type 2 is more demanding in terms of information required. But for PCCVs, it may be a better predictor of "failure," because it guides the prediction of failure size, while Criteria Type 1 does not. Further, investigation of the PCCV's welding records show that weld flaws were prevalent. Fractures are possible, and strain conditions sufficient to cause fracture occur at potentially hundreds of locations. It would be inconceivable to analyze all possible locations. What is needed is an approximate procedure, or "transfer function", for correlating J-based fracture prediction to strains in the PCCV Liner. The following outlines such a procedure.

Ultimately, this also leads to prediction of liner tear lengths and opening areas versus strain in the liner. The final step from prediction of J for a typical "flawed" piece of liner, to prediction of specific numbers and sizes of cracks, requires the addition of a statistical assessment of the existence of flaws. This can also be done in a systematic way, but for the SPE, will not be addressed until Phase 2.

Development of strain-to-J-mapping (or "transfer function") is illustrated in the figures provided herein. Explanation requires basic understanding of calculation of the "J-Integral" shown below, and the concept of $J_{critical}$ as a toughness measure in the material.

Fracture models can be developed as simple, separate FE models with extremely fine mesh, appropriate to embedding small initial cracks into the models, calculating J-integrals, and propagating these cracks. The illustrations show a strain contour result, which is intended to show the plasticity "hot spots" that occur at the postulated crack tips, qualitatively speaking. Note that the spread of plasticity from the crack tip out into the previously non-yielded material occurs along paths at an angle of between 30 and 45 degrees to the circumferential line. This is not a surprising result since plasticity spreads according to a Mises Yield condition which in two (or three) dimensions, trends along lines of maximum octahedral shear stress.

The fracture sub models need to have a standardized length. In the case of the PCCV, it could be the length between liner anchors, for example. This length would become a gage-length for strain mapping, and it should be relatively immune from differences between analysts that occur due to mesh size in Models 2 or 3 of the SPR. It can be defined or viewed in different ways: the integration of strain from the crack to the edge of the fracture sub model, or the differential longitudinal displacement of the shell nodes in the FE model – divided by the gage length, or the integration of strain across the gage length of the FE model. Using this gage length to define a strain measure common to the fracture geometry, the fracture analysis results can be cast in terms of J versus strain.

The crack propagation threshold needs to be established, but say for example it is J_{cr} = 350 in-lb/in^2); values such as this come from fracture toughness testing.

1.2.4.1 Fracture Propagation and Arrest; Predicting Crack Lengths

Typical crack propagation analyses are shown below.

The stepwise procedure that has been developed specifically for this work is outlined below.

1. Fracture Model analyzed with no crack propagation (green curve on the plot).

2. Fracture Model set-up to propagate the crack at the strain step corresponding to J reaching J_{cr}. Cracks are advanced (in ABAQUS) by element "deaths" of the row of elements extending from the crack-tip. The elements die, causing stress and strain redistribution, but at the same time, additional increments of displacement are applied to the edges of the sub model. The analysis is set up to advance the crack tip AND add driving strain during individual steps; ABAQUS automatically chooses solution sub-increments, and equilibrium is reached at the end of the step before going on to a new step (new propagation).
3. Sub-increments in this example are crack advances of 3/8" on each end of the crack, or a total of ¾". (In the fracture models, the mesh-size is 0.03", and the cracks are advanced equally at both crack-tips, so an even-number of elements must be "removed," thus the crack extension increments are even-multiples of 0.03", i.e., 0.72", 1.5", 2.22", etc.).
4. The total strain driving the fracture model is divided into two parts: ε_{cr} (the strain demand when J first reaches J_{cr}); and ε_{pr} (the additional strain that is driving further propagation). The premise for crack extension length (and crack arrest) is that for the kind of loading this structure will experience, and the geometric aspects (for example, the fact that the steel shell remains tied to the concrete at the T-anchors), the crack will only propagate as long as additional driving strain is present, and as long as conditions at the crack tip still meet or exceed $J_{cr.}$ When the driving strain is used up, crack propagation will stop.
5. An initial estimate of the total crack extension length is made, in multiples of ¾". ε_{pr} is divided by the number of ¾" long crack extension steps. The analysis is performed and J is plotted versus strain. If J remains above J_{cr}, this means the crack should have extended further, so Step 5 is repeated for a longer crack extension length. This process is repeated until J remains at or below $J_{cr.}$ The crack extension length corresponding to the final analysis in the series (which meets the J criteria) is the final crack length.

Example:
Returning to the discussion for Fracture Model 2 and the preceding plot,

$\varepsilon_{cr} = 0.0016$; and $\varepsilon_{pr} = 0.0016$;

the fact they are equal is coincidental, and review of other cases shows this to be true.
Analysis Trial 1 (crack extension of 1.5" to a total length of 2.22") produced the purple curve; J is exceeding $J_{cr.}$ Analysis Trial 2 (crack extension of 3" to a total length of 3.75") produced the dark blue curve; J is still slightly exceeding $J_{cr.}$ Analysis trial 3 (crack extension of 3.75" to a total length of 4.5") produced the red curve; J is approximately flat at $J_{cr.}$

Figure 12 also shows the strain increments applied in the analysis, and this provides further detail about the procedure. The basic procedure is the same in all cases. Figure 12 also provides the final Crack Length versus Strain, and the Crack Opening (inches) and Crack Opening Area (sq. inches), so the final result of the procedure becomes tables of crack lengths and openings versus longitudinal "driving" strain (

Table 3). The following figures and discussion provide some observations about the additional cases.
Reference for J-Integral Analysis procedures: ABAQUS Theory Manual

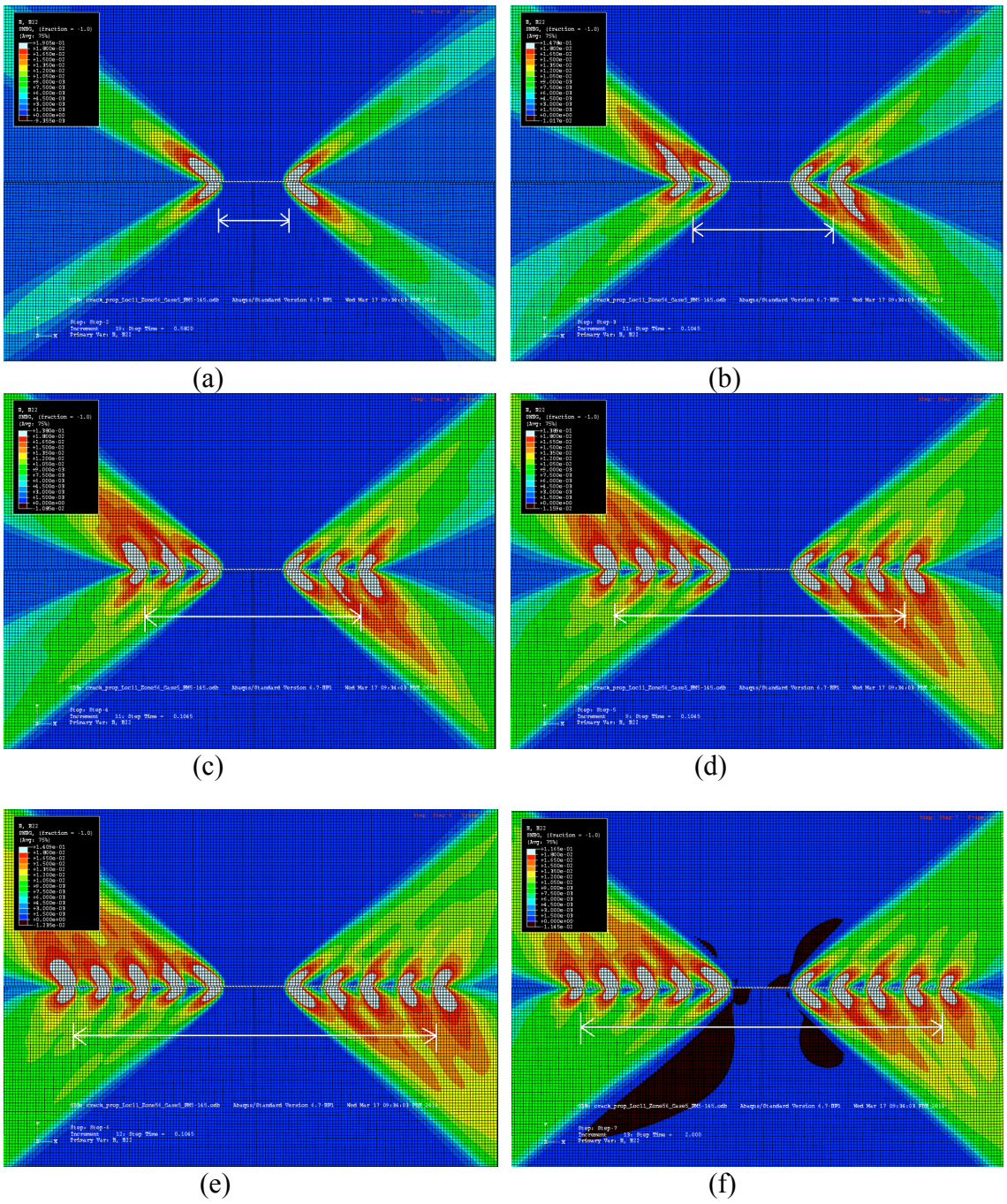

Figure 12. Longitudinal Strain Contours and Crack Propagation for Fracture Model Analysis Starting with an Initial Crack of 0.72" and Propagating in 0.75" Increments: (a) 0.72" Crack, (b) 1.5" Crack, (c) 2.22" Crack, (d) 3.0" Crack, (e) 3.72" Crack, (f) 4.50" Crack

Table 3. Applied Strain Demands and Imposed Crack Propagation Steps for Trials (a), (b), and (c)

(a)			
Analysis Step	Averaged Strain	J-Value	Crack Length
1	0.00160	350	0.72
2	0.00240	360	1.5
3	0.00320	370	2.22
Strain Increment	**0.0008**		

(b)			
Analysis Step	Averaged Strain	J-Value	Crack Length
1	0.00160	350	0.72
2	0.00200	410	1.5
3	0.00240	415	2.22
4	0.00280	430	3
5	0.00320	430	3.72
Strain Increment	**0.0004**		

(c)					
Analysis Step	Averaged Strain	J-value	Crack Length (in.)	Crack Width (in.)	Crack Area ($in.^2$)
1	0.00160	350	0.72	0.0083	0.0138
2	0.00192	360	1.5	0.0157	0.0328
3	0.00224	370	2.22	0.0230	0.0567
4	0.00256	375	3	0.0305	0.0873
5	0.00288	370	3.72	0.0376	0.1230
6	0.00320	375	4.5	0.0450	0.1725
Strain Increment	**0.00032**				

The general arrangement of the 1:4 Scale PCCV liner is shown on page A-23 of NUREG/CR-6810. Liner panels were prefabricated and welded in Japan. These panels typically encompassed three vertical rings of individual plate segments, with an area of approximately $3m^2$. The panels were transported to Sandia National Laboratories, and then field welded on site. The plate block layout and weld locations (both shop and field) in the cylinder and dome of the PCCV are shown on pages A-25, A-34, and A-36 of NUREG/CR-6810. The majority of the liner anchors were shop-welded to the liner in Japan. The layout of the liner anchors is shown on page A-24, and pages A-26 through A-34 of NUREG/CR-6810.

Following the completion of the LST, a map of the liner tears was compiled, and is shown in Figure 5-77 on page 5-64 of NUREG/CR-6810. A metallurgical analysis was performed on samples of the liner removed from areas where tears occurred. A detailed description of this analysis can be found in Appendix L of NUREG/CR-6810. Please refer to the appendix for a description of each tear, photos of the tears from the inside and outside of the liner, and conclusions concerning liner quality and composition. Table 4 summarizes the tear lengths and liner thicknesses in the area surrounding the tears. No crack widths were measured during or after the test.

Table 4. Liner Tear Details

LOCATION OF TEAR	TEAR LENGTH ESTIMATE (MM)	TEAR LENGTH MEASURED (CM)	RANGE OF LINER THICKNESSES IN AREA SURROUNDING TEARS (WHERE AVAILABLE) (MM)
1	28	4	1.32 - 1.82
2-1	68	8	
2-2	73	8	1.22 - 1.91
2-3	157	18	
3	270	>15	1.41 - 1.73
4-1	67	11	1.32 - 1.78
4-2	26	4	1.04 - 1.4
4-3	123	14	1.09 - 1.78
5-1	40	4	1.31 - 1.66
5-2	71	8	1.27 - 1.64
6-1	112	10	1.31 - 1.8
6-2	118	7	1.1 - 1.81
7	228	23	1.28 - 1.81
8-1	62	6	1.24 - 1.83
8-2	43	4	0.86 - 1.81
9	123	13	1.37 - 1.83
10	18	1.5	1.37 - 1.85
11-1	100	10	1.45 - 1.8
11-2	74	6	1.55 - 1.8
12	63	5	1.37 - 1.8
13	92	9	1.14 - 1.8
14-1	77	8	1.07 - 1.81
14-2	120	13	1.23 - 1.81
15	83	10	1.25 - 1.81
16	87	8	1.37 - 1.78
17	15	3	0.66 - 1.83

Of note from the metallurgical analyses performed on the PCCV liner is that tearing tended to occur where significant amounts of grinding was done for repair welding. Twenty-six liner tears were observed to result from the PCCV testing, and seven of these tears were associated with structural features such as feedwater penetrations. The tears appear to have been caused by thinning of the liner due to grinding, which allowed localized plastic deformation to occur before the onset of general plasticity in the majority of the liner. The geometric features of the liner were also thought to have played a role in the formation of tears. The first tears occurred around the equipment hatch, where not as much grinding had been done. The global strain at which tearing occurred is ~0.4% (NUREG/CR-6810 – Appendix L)

The location of the liner repairs is shown in Figure 13. Please refer to the attached document LinerRepairs.doc for pictures of each repair, as well as a detailed description of each repair. An overlay of the liner tears and liner repairs is shown in Figure 14.

At strain concentration locations within the liner, the very localized strain distributions leading up to and causing liner tearing is very complex. It is not always simulated well by local analysis, nor is it possible to place enough strain gages or be fortunate enough to place gages directly on tear locations to sufficiently map these local strain fields. Some data from the test is available, though, as shown in the plotted strain results from the family of gages near the Main-Steam penetrations (Figure 15). In the SPE Model 3, participants are not being asked to match or compare to a given "highly localized" strain measurement. Instead they are asked to provide strains versus pressure at critical locations in the containment, but defined over a standardized gage length.

It is up to the individual participant to determine how they wish to use the weld repair and metallurgical data and the local strain measurements, and which failure prediction approach to use. Some suggestions on how to consider the thinning of the liner due to grinding for repair welding is to reduce the thickness of the elements in those section which had liner repairs, using a reduced strain failure limit in the sections where repair occurred, etc.

1.2.4.2 Model 3: Global Analysis Model

Model 3 is a Global Analysis Model aimed at incorporating lessons learned from Model Exercises 1 and 2, and at providing PCCV response information at any and all locations of the structure. Particular emphasis, however, is to be placed on providing liner strain mapping information to be used in the more comprehensive failure (liner tearing and leakage) prediction exercises being discussed in the SPE than have heretofore been performed in the PCCV test analyses, or in the ISP-48 exercise. Because computational and funding resources vary, and so do the goals and objectives of the participants, the specifics about the model are not prescribed. Models can be axisymmetric, 3d shell, solid, etc. However, a 3D representation is strongly encouraged because axisymmetric results alone will only provide a limited set of strain information, and this information is important for the remainder of the exercise. Specific output points may be refined somewhat at a later date, but for model planning, participants should plan to report response data versus pressure for the "55 standard output locations" originally requested of the 1:4 Scale model round-robin exercise (see the appendices and website for these definitions).

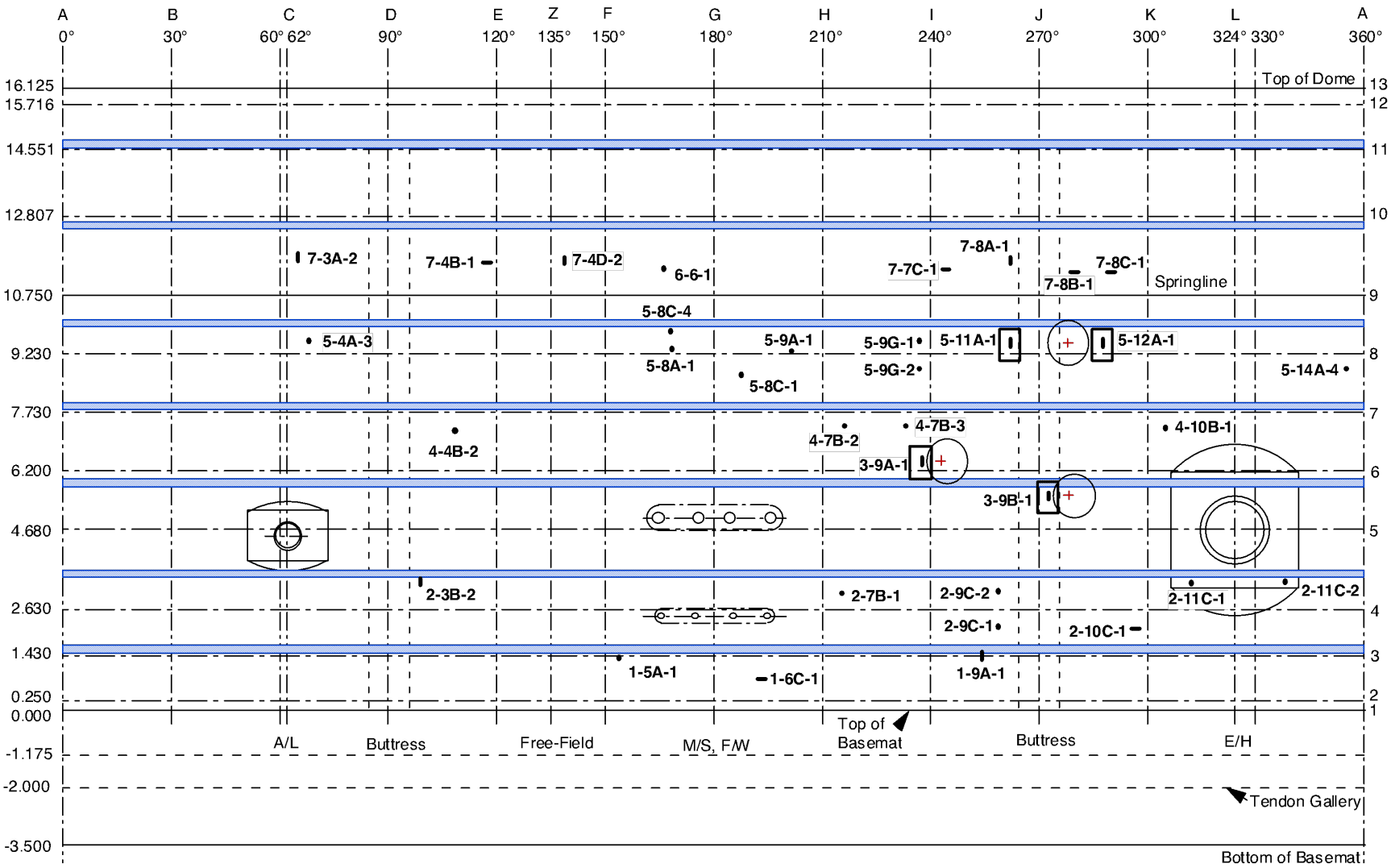

Figure 13. Liner Repair Locations

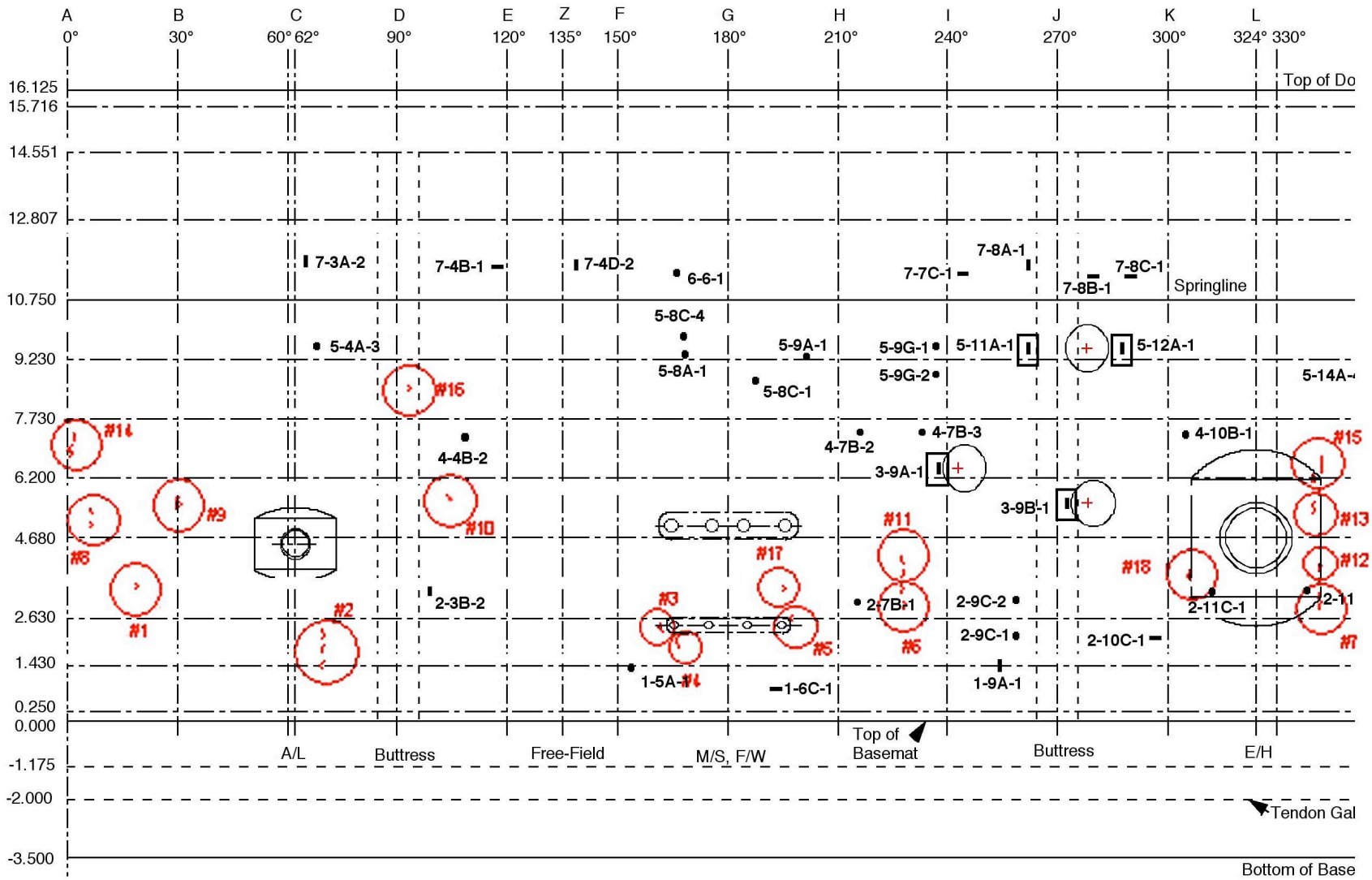

Figure 14: Liner Repair Locations (in Black) with Liner Tears (in Red

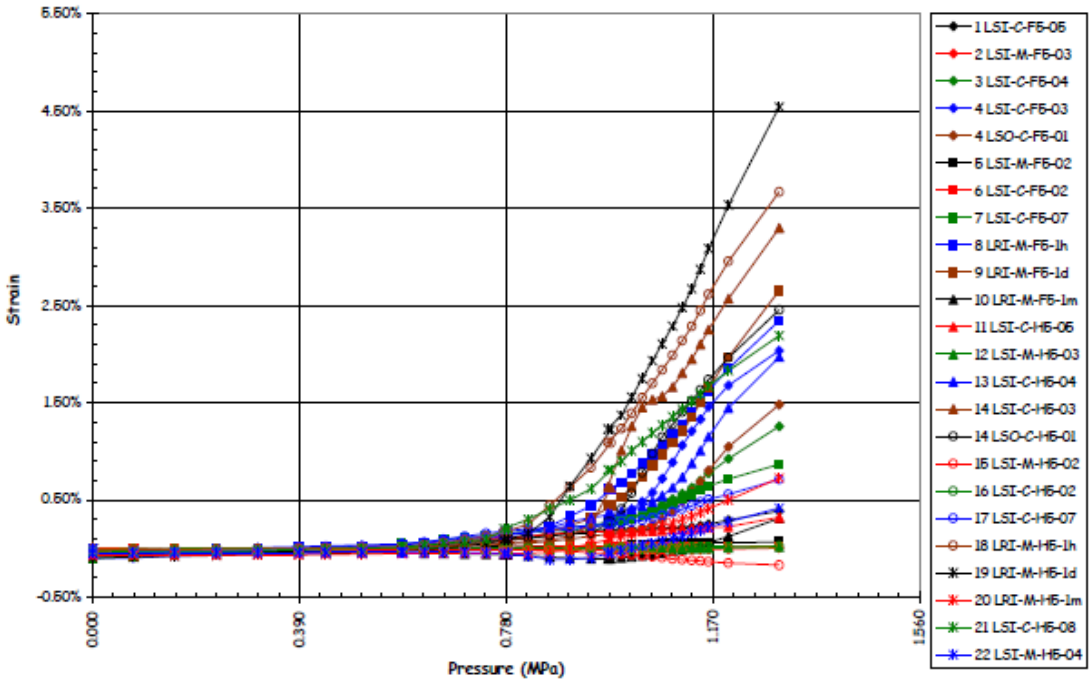

Figure 15: Liner Strains (DOR) at M/S (Ref. D-SN-P-220)

1.2.4.3 Required Outputs/Results for Model 3:

1.3 Description of failure prediction model or criteria selected for use

1.4 Assumptions made in geometric modeling, and model description

1.5 A subset of the response information defined by the "55 standard output locations" of the 1:4 Scale PCCV round-robin exercise; subset is to be determined later, but participants should plan models accordingly. At a minimum, the displacement transducer/data plots portion of the 55 Standard Output Locations are required.

1.6 Contour plot of peak strains in the liner during the LST at the pressure milestones: P = 0 (prestress applied); 1 x P_d; 1.5 P_d; 2 P_d; 2.5 P_d; 3 P_d; 3.3 P_d; 3.4 P_d; Ultimate Pressure

1.7 Average strains over 450.45 mm regions as were shown in Figure 11, locations 3, 4, 5, but with similar locations adjacent to all other penetrations, plotted as a function of pressure. The intent is for these strains to be over a standardized gage length, which is defined by the spacing between liner anchors.).

1.2.1. SPE 2.5 – Differences Between Nominal Design and In-Situ Construction

In the initial pre-test Round Robin Analysis (completed in 2000), participants were provided with detailed design drawings and material properties. Upon construction of the PCCV, participants were provided with the in-situ construction details (where different from design). Of interest is the use of the in-situ material properties and geometric details versus nominal design values in

analysis. Many participants made little to no changes to the analytical models for the pre-test and post-test analyses. This part of the Round Robin Analysis Containment Exercise would like participants to examine the significance of variation from design in geometric and material property values in analytical results. The participants will examine scatter in data, non-uniformity of tendon forces, geometric irregularities, deviations in material properties, friction losses, and initial conditions from a probabilistic rather than deterministic framework. To this end, the participant will present containment capacity as a cumulative distribution function, incorporating the aspects mentioned in Sections 4.1.1 through 4.1.4.

It is up to the participant to determine the significance of scatter in data. Potential areas of investigation are (but not limited to) scatter in material testing data and scatter in measured response to loading. One such example of scatter in material data can be seen in Figure 16.

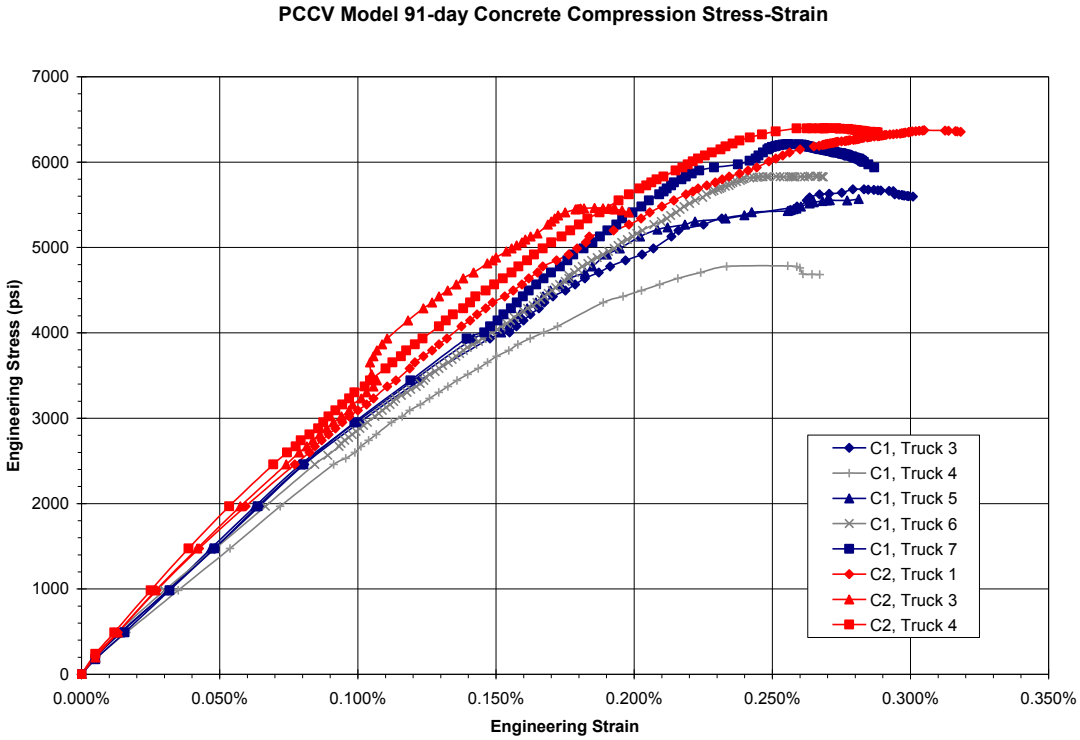

Figure 16: Example of Variation in Concrete Properties

In the data-CD provided from NUREG/CR-6810, the recorded measurements on the tendons are reported. It is up to the participant to determine how to investigate the effects of non-uniformity of tendon forces, and friction losses on the structural behavior of the model.

In past modeling efforts, most participants used the design geometry (Appendix A of NUREG/CR-6810) for model development. Participants have the opportunity to investigate the differences found in-situ from design. Appendix C of NUREG/CR-6810 contains the as-built survey of the PCCV model.

The participants have the opportunity to investigate the influence of initial conditions on the PCCV containment capacity. Possible initial conditions to be included in this effort are state of prestressing, ambient temperature at time of testing, etc. The data gathered during the testing of the PCCV Model was corrected for temperature affects as discussed in Appendix J of NUREG/CR-6810.

In past analysis efforts concerning the NRC/NUPEC PCCV Model Test, participants have frequently used the design material properties, rather than those tested. An example of this is for the concrete material modeling, where most participants used the design strengths for the concrete pours shown in Figure 17. Chapter 2 discusses the design and construction of the PCCV model, and includes the design material properties. It is suggested (but not limited to or required) that participants investigate fabrication variations in the material properties.

	Concrete Pour Completion Date	Specified Strength F_c' (MPa)
F1	2-12-97	29.42
F2	2-28-97	29.42
$F3_A$	5-8-97	29.42
$F3_B$	5-8-97	44.13
F4	7-2-97	44.13
	Planned Date	F_c' (MPa)
C1	(11-98)	44.13
C2	(12-98)	44.13
C3	(1-99)	44.13
C4	(1-99)	44.13
D1	(2-99)	44.13
D2	(4-99)	44.13
D3	(5-99)	44.13
F5	(5-00)	29.42
F6	(5-00)	44.13

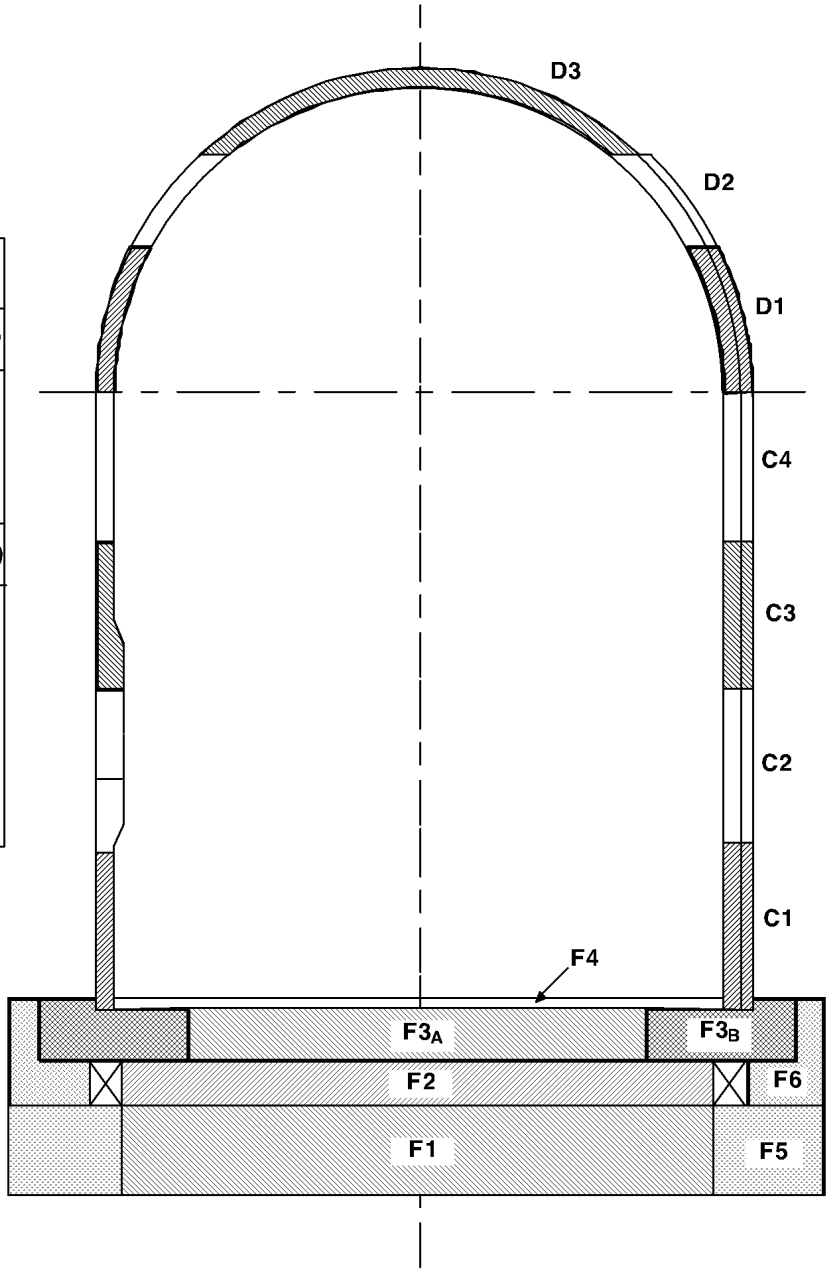

Figure 17: Designed Concrete Cross Section

Figure 18 shows the concrete lifts as poured during the construction of the PCCV model. The concrete properties were tested for each lift, and the results are reported in Appendix B of NUREG/CR-6810 on pages B-13 through B-16. Additionally, stress/strain curves at varying stages of the testing effort, and creep data for lift C2 are reported on pages B-17 through B-26 of NUREG/CR-6810. Variations in curing conditions due to schedule, as well as inherent variations in concrete fabrication resulted in variance of the strength characteristics of the concrete.

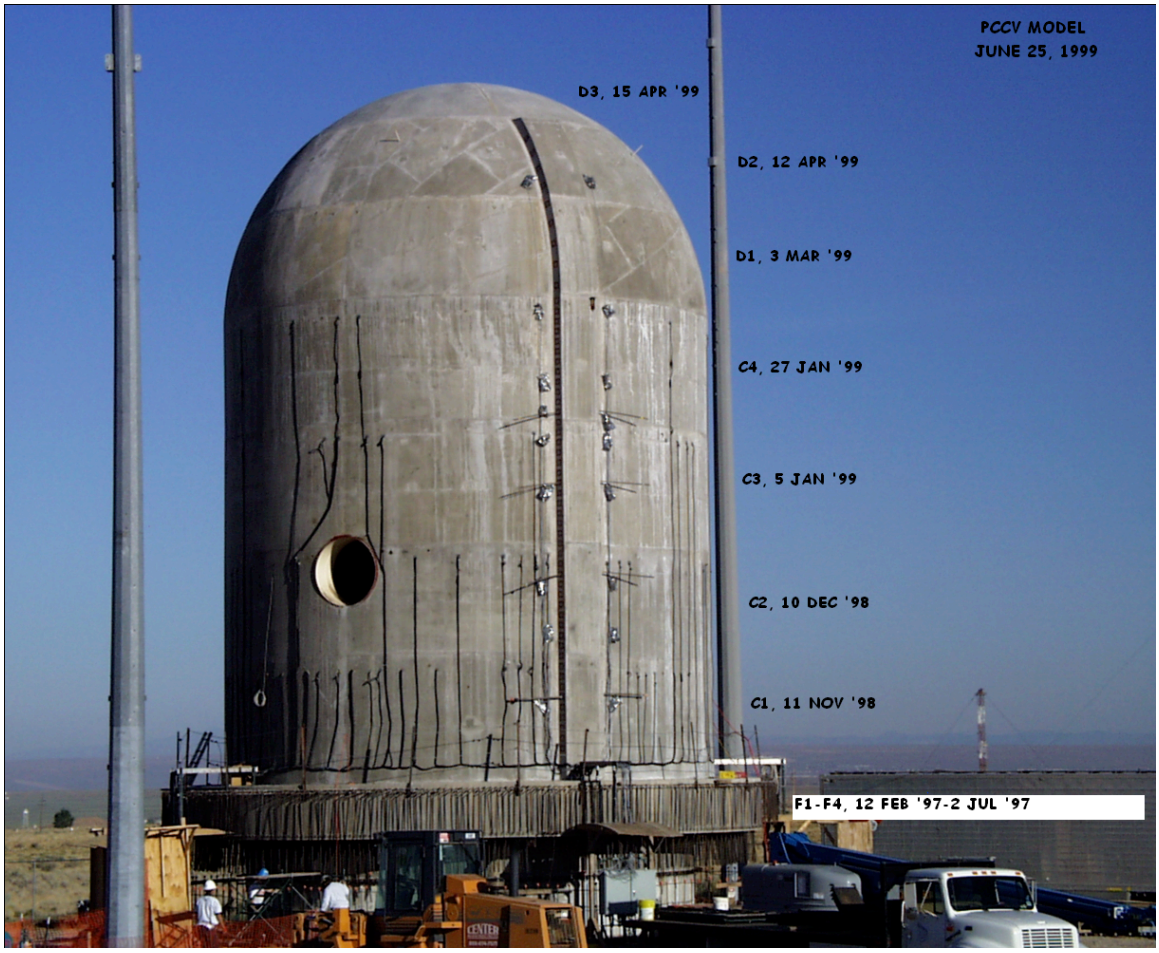

Figure 18: Schedule for Construction of Concrete Lifts

In addition to differences between design and in-situ properties for the concrete, the in-situ liner properties differed from design. Table 5 shows some of those differences. Variations in rebar and tendon material properties are listed in Appendix B of NUREG/CR-6810 (B-35 through B-54 and B-55 through B-64 respectively).

Table 5: Differences Between Design and In-Situ Properties for the Liner

Material Property	Design	In-Situ
Yield Strength – MPa (ksi)	225 (33) (min)	383 (55)
Ultimate Tensile Strength – MPa (ksi)	410 to 490 (59 to 71)	498 (72)
Elongation	21% min	33%
Thickness	1.8mm	0.86 – 1.85 mm[1]

[1] This range is the range of thicknesses measured in the areas surrounding the liner tears; it is not the range of thickness in the liner prior to the test.

1.2.4.1 Required Outputs/Results for Studies of Differences between Design and In-Situ properties.

This model is optional, so the required outputs are too. But the following suggestions are provided.

1. Discussion of parameters investigated (as determined by each participant)

2. List of range of values for each parameter investigated

3. Average peak hoop strain in critical regions shown in Figure 11 (and adjacent to other penetrations) for pressures P = 0 (prestress applied); 1 x P_d; 1.5 P_d; 2 P_d; 2.5 P_d; 3 P_d; 3.3 P_d; 3.4 P_d; 4.

4. Consider constructing strain response versus pressure as a lognormal distribution, as was constructed in the following Reference: Dameron, R.A., R.S. Dunham, Y.R. Rashid, and H.T. Tang. "Conclusions of the EPRI Concrete Containment Research Program." *Nuclear Engineering and Design*, 125, 1991, pgs. 41-55

1.3. Documents of the SPE

In conjunction with completing the aforementioned analyses, participants were asked to document, in the form of two reports, results from each phase of the Round Robin Analyses. The reports provide the input for the appendices of this document.

1.4. Organizational Schedule

The schedule for the meetings and calculations was as follows (as now modified and agreed to at the SPE kick-off meeting):

Table 6: Meeting schedule for round robin activities

EVENT	DATES
Initial Workshop (Mumbai, India)	June 30-July 2, 2010
White Paper Finalization	August 6, 2010
Milestone Verification of Tendon and Equipment Hatch	December 1, 2010
Return Results from Milestone Evaluation	December 21, 2010
Format For Documentation Sent Out	December 21, 2010
Phase 1 Meeting After Completion of Phases 1.1-1.3 (**Tentative** – San Diego, USA)[2]	January 6-8, 2011 (Not Conducted)
Phase One Calculations and Documentation Due	March 15, 2011
Phase One Review Meeting (Washington, D.C.)	April 14-15, 2011
Phase Two Calculations and Documentation Due	April 27, 2012
Final Workshop (Calcutta, India) Following SMiRT-21 at New Delhi	March 27-29, 2012
Final Report	June 2012

[2] The San Diego meeting was tentative. It was not to be held unless it is determined that there is enough variability in participant analyses to warrant an additional meeting prior to the Phase One Review Meeting in Washington D.C.

2. MODEL 1

As mentioned previously, the SPE #3 has been broken into two phases. Model One is meant to be a tool to investigate the local effects of interest in Phase One, specifically, in the effects of containment dilation on prestressing force, and the slippage of prestressing cables. The analysts were requested to apply two load cases to the model, pressure only, and a pressure and temperature (saturated steam) load.

The required output and results from Model 1 are listed below. These results were agreed upon at the Phase One kick-off meeting, held in Mumbai, India. All participants were asked for these outputs as a means of comparing results.

1. Description of modeling assumptions and phenomenological models
2. Description of tendon failure criteria used
3. The following pressure milestones, applied pressure when:
    a. Concrete hoop stress (at 135^{o} azimuth) equals zero
    b. Concrete hoop cracking occurs (at 135 ^{o} azimuth)
    c. Tendon A reaches 1% strain (at 135 ^{o} azimuth)
    d. Tendon B reaches 1% strain (at 135 ^{o} azimuth)
    e. Tendon A reaches 2% strain (at 135 ^{o} azimuth)
    f. Tendon B reaches 2% strain (at 135 ^{o} azimuth)
4. Deformed shape and tendon stress distribution at P= 0 (Prestress Applied); 1 x P_d; 1.5 x P_d; 2 x P_d; 2.5 x P_d; 3 x P_d; 3.3 x P_d; 3.4 x P_d; Ultimate Pressure
5. Tendon A and B strain at 135 ^{o} azimuth versus pressure
6. Radial displacements versus pressure at azimuth: 135 ^{o}, 0 ^{o}, 270 ^{o}
7. Description of observations about tendon force as a function of containment dilation and tendon slippage

The following sections provide a comparison of the different participant's results.

2.1. Description of modeling assumptions and phenomenological models

A comparison of the different modeling software and modeling set-up is listed below in Table 7. Each participant was free to use any FEM software they so chose, and to represent the geometry described in Figure 1 as needed.

Table 7: Model Detail Comparison

MODELING DETAILS	EDF	FORTUM	GRS	NRC	SCANSCOT
FEM Tool	Code_Aster Implicit Algorithm	Abaqus 6.10 Implicit Dynamic	ANSYS with DYNARDO Material Models	Abaqus Standard FE	Abaqus Explicit 6.9 and Abaqus Standard 6.9
Concrete Element Type	8 Node Hex Element	Shell Elements (S4R)		Hex Elements (C3D8R)	Hex Elements (C3D8R)
Concrete Element Count		420		2220	
Rebar Element Type	Linear 4-node Shell Element with Uniaxial Behavior	Rebar Layer		Rebar Layer (SFM3D4R)	Rebar Layer
Rebar Element Count				1488	
Liner Element Type	Linear 4-node Shell Element with Uniaxial Behavior	Shell Elements (S4R)		Shell Elements (S4R)	Shell Elements (S4R)
Liner Element Count		420		708	
Tendon Element Type	Linear 2-Node Truss Element	Truss Elements (T3D2)		Beam Elements (B31)	Truss Elements (T3D2)
Tendon Element Count		138		226	
Concrete / Liner Interaction				Tied	Tied
Tendon / Concrete Interaction	Friction Element Connects Coincident Nodes	Connector Elements (CONN3D2)		Node –Line Defined by 2 Nodes with Friction (0.21)	Contact Surfaces with Friction (0.22)
Concrete / Rebar Interaction		Embedded		Embedded	Embedded

A comparison of the material models is provided in Table 8.

Table 8: Comparison of Material Models

MATERIAL	EDF	FORTUM	GRS	NRC	SCANSCOT
Concrete Model	Non-Liner Damage Mechanics	Concrete Damage Plasticity		Concrete Damage Plasticity	Brittle Cracking Model
Concrete Parameters of Note	E = 26,900 MPa ν = 0.21 σ_t = 2.4 MPa ρ = 2,176 kg/m^3	E = 28,000 MPa ν = 0.2 σ_t = MPa ρ = 2500kg/m^3 Ep = MPa		E = 33,000 MPa ν = 0.2	E=26,800 MPa
Rebar	Non-Linear Elasto-Plastic	Elasto-Plastic		Elasto-Plastic	Elasto-Plastic
Rebar Parameters of Note	E = 185,000 MPa ν = 0.3 σ_t = 445-460 MPa ρ = 7,850 kg/m^3 Ep = 1,250-1,350 MPa	E = 200,000 MPa ν = 0.3 σ_t = MPa ρ = 7,850 kg/m^3 Ep = MPa		E = 200,000 MPa ν = 0.3	E = 185,000 MPa ν = σ_t = 460 MPa ρ = kg/m^3 Ep = MPa
Liner	Non-Linear Elasto-Plastic	Elasto-Plastic		Elasto-Plastic	
Liner Parameters of Note	E = 210,000 MPa ν = 0.3 σ_t = 400 MPa ρ = 7,850 kg/m^3 Ep = 700 MPa	E = 219,000 MPa ν = 0.3 σ_t = MPa ρ = 7,850 kg/m^3 Ep = MPa		E = 200,000 MPa ν = 0.3	E = 220,000 MPa ν = σ_t = 383 MPa ρ = kg/m^3 Ep = MPa
Tendon	Non-Linear Elasto-Plastic	Elasto-Plastic		Elasto-Plastic	
Tendon Parameters of Note	E = 191,000 MPa ν = 0.3 σ_t = 1,750 MPa ρ = 7,850 kg/m^3 Ep = 3,350 MPa f_{gu} = 1,857 MPa μ = 0.21 Δs = 3.95 mm T_0 = 444 kN	E = 191,000 MPa ν = 0.3 σ_t = MPa ρ = 7,850 kg/m^3 Ep = MPa f_{gu} = MPa μ = Δs = mm T_0 = kN		E = 195,000 MPa ν = 0.3	

2.2. Description of Tendon Failure Criteria

The critical parameter for predicting tendon failure appears to be the axial strain in the tendon of interest. The participants in the present study were requested to provide the tendon failure criteria used when predicting the failure of the tendons in Model 1 from their simulations. The participants all selected tendon failure criteria in reasonable agreement with one another. Three participants (Fortum, NRC, and SCANSCOT) specified the actual ultimate tensile strain to predict failure, while one participant (EDF) specified the ultimate tensile stress as well as the assumed yield stress and the elastic and hardening moduli. The tendon failure strain was calculated from these parameters. The ultimate strain for the prestressing tendons in Model 1 used by all the participants are presented below in Table 9.

Table 9: Tendon failure criteria

	EDF	FORTUM	GRS	NRC	SCANSCOT
Tendon Failure Criteria (ultimate strain)	4.1%	4%		3.8%	3.7%

2.3. Pressure Milestones

The pressure milestones as reported by each participant are shown below in Table 10 and in Figure 19. In general, the results from all the participants agree well with one another. The greatest differences occurred for milestone two, initial cracking of the concrete, and for milestones five and six, two percent strain in the tendons.

Table 10: Pressure Milestones

MILESTONE	PRESSURE (MPA, X P_D)				
	EDF/NECS	FORTUM	GRS	NRC	SCANSCOT
Concrete Hoop Stress (at 135° azimuth) Equals Zero	0.57, 1.5	0.55, 1.4	0.5, 1.3	0.6, 1.4	0.5, 1.4
Concrete Hoop Cracking Occurs (at 135° azimuth)	0.78, 2.0	0.74, 1.9	0.74, 1.9	0.7, 1.8	0.6, 1.6
Tendon A Reaches 1% Strain (at 135° azimuth)	1.31, 3.4	1.29, 3.3	1.35, 3.5	1.3, 3.3	1.3, 3.3
Tendon B Reaches 1% Strain (at 135° azimuth)	1.31, 3.4	1.29, 3.3	1.32, 3.4	1.3, 3.4	1.3, 3.3
Tendon A Reaches 2% Strain (at 135° azimuth)	1.33, 3.4	1.33, 3.4	1.42, 3.6	1.4, 3.7	1.4, 3.5
Tendon B Reaches 2% Strain (at 135° azimuth)	1.33, 3.4	1.33, 3.4	1.42, 3.6	1.4, 3.7	1.4, 3.5

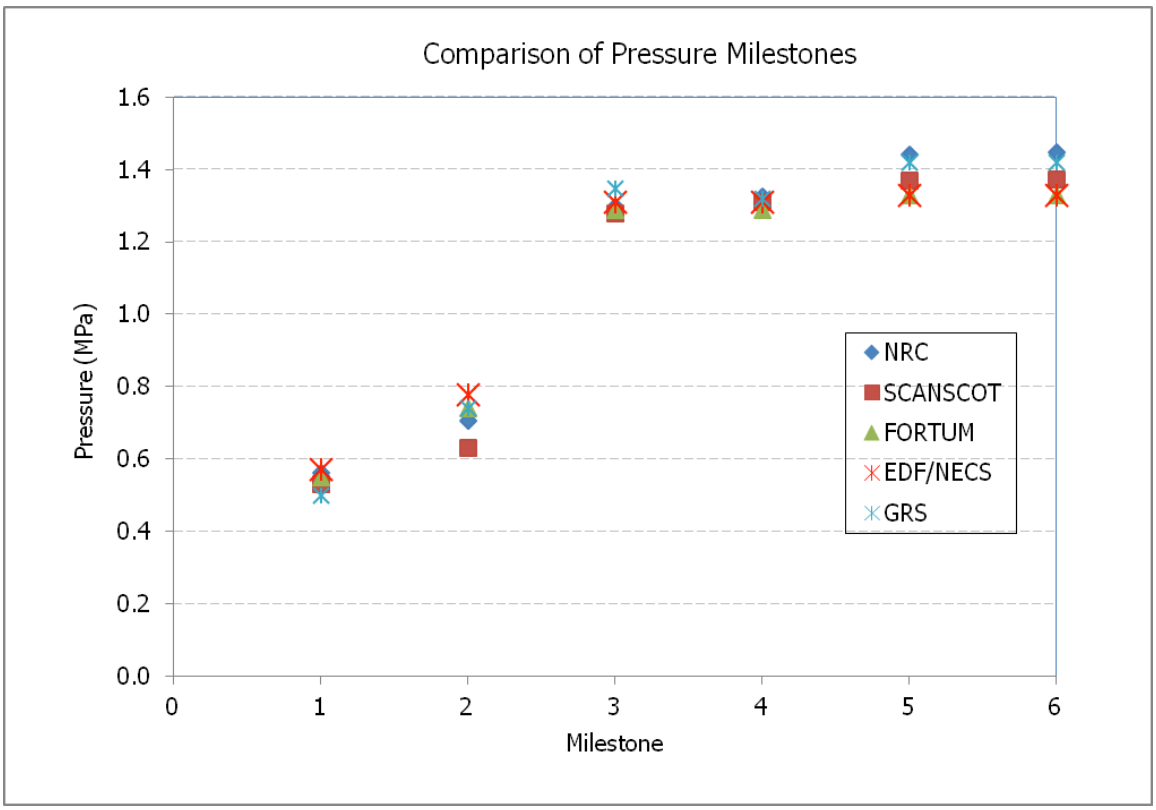

Figure 19: Comparison of Pressure Milestones

2.4. Deformed Shape Comparison

The comparison of the deformed shapes for Model 1 at pressure milestones for all participants can be found in Figure 20 through Figure 29. Unfortunately, the deformation scale factors applied by each participant at each pressure milestone are not uniform and therefore, the individual plots may appear to differ greatly. In general however, the results from all the participants agree well with one another at all pressure levels. For the final pressure milestones, deformed shape plots were not furnished by AERB and therefore Figure 25 and Figure 29 only include four plots. Finally, it should be noted that the final pressure milestone for each participant varied due according to each participant's particular model.

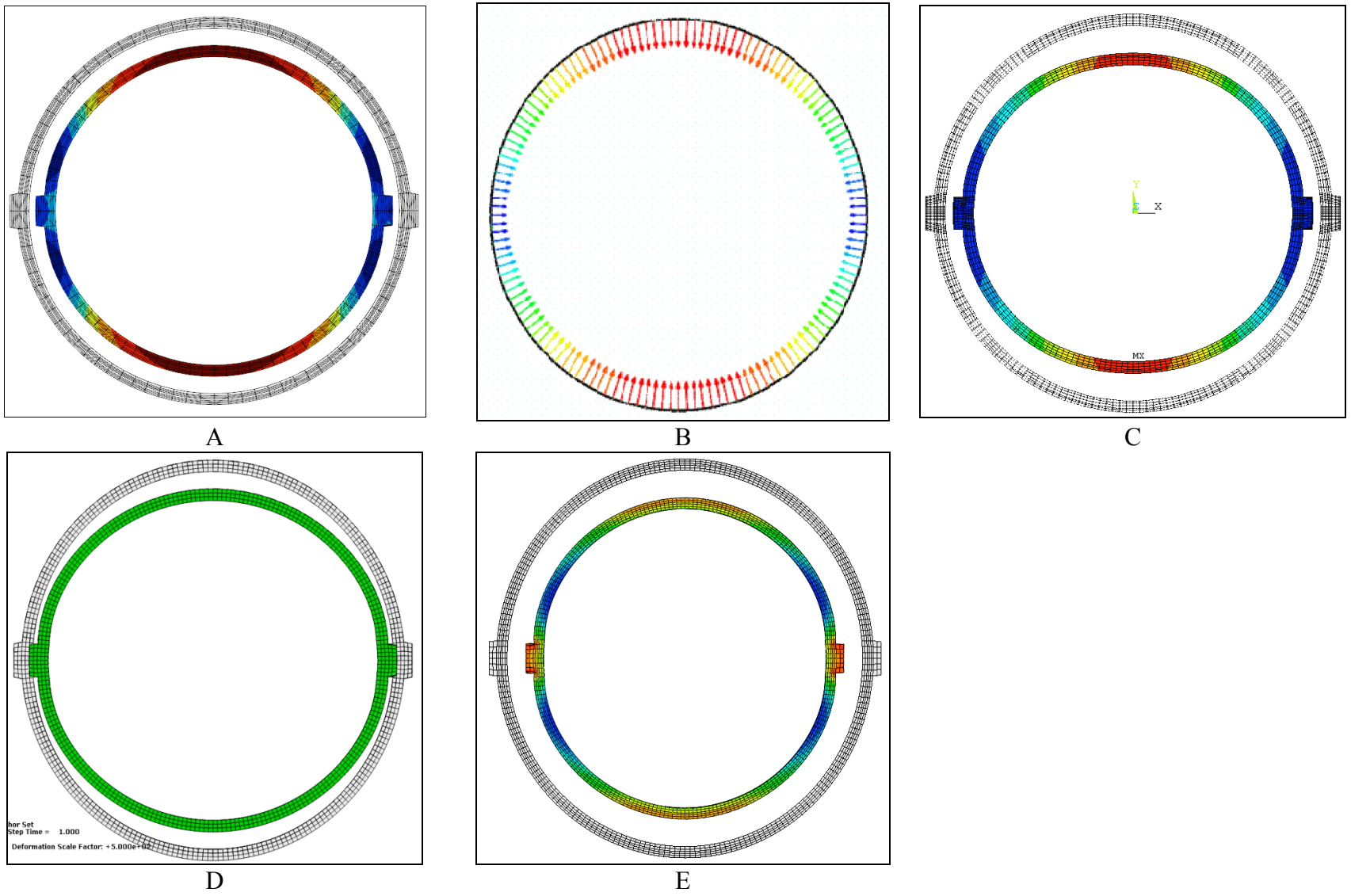

Figure 20: Deformed Shape at Anchorage (a) EDF/NECS at 500 x Magnification (b) FORTUM at 10 x Magnification (c) GRS at 500 x Magnification (d) NRC at 500 x Magnification (e) SCANSCOT at 500 x Magnification

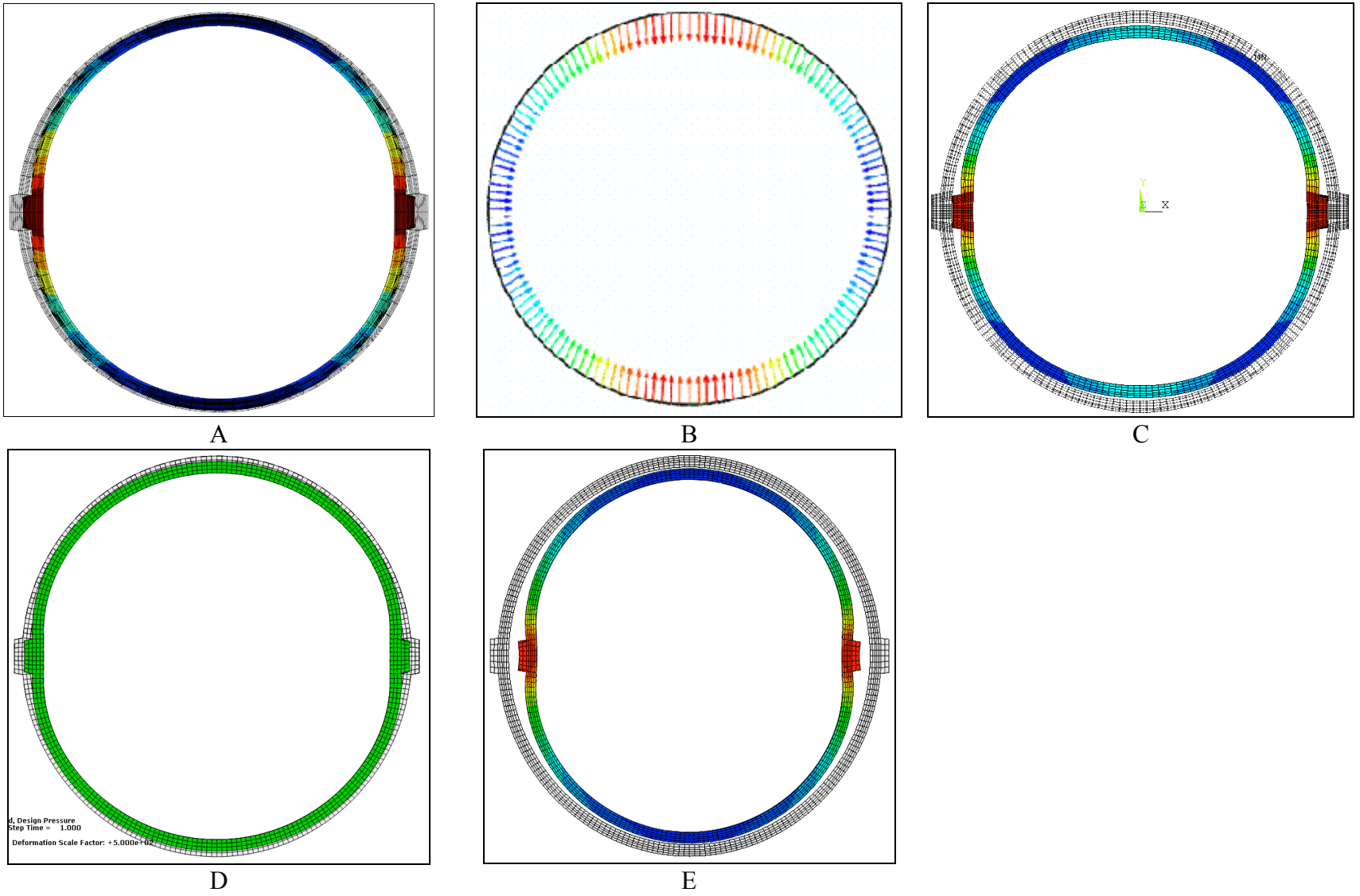

Figure 21: Deformed Shape at Design Pressure (a) EDF/NECS at 500x (b) FORTUM at 10x (c) GRS at 500x (d) NRC at 500x (e) SCANSCOT at 500x

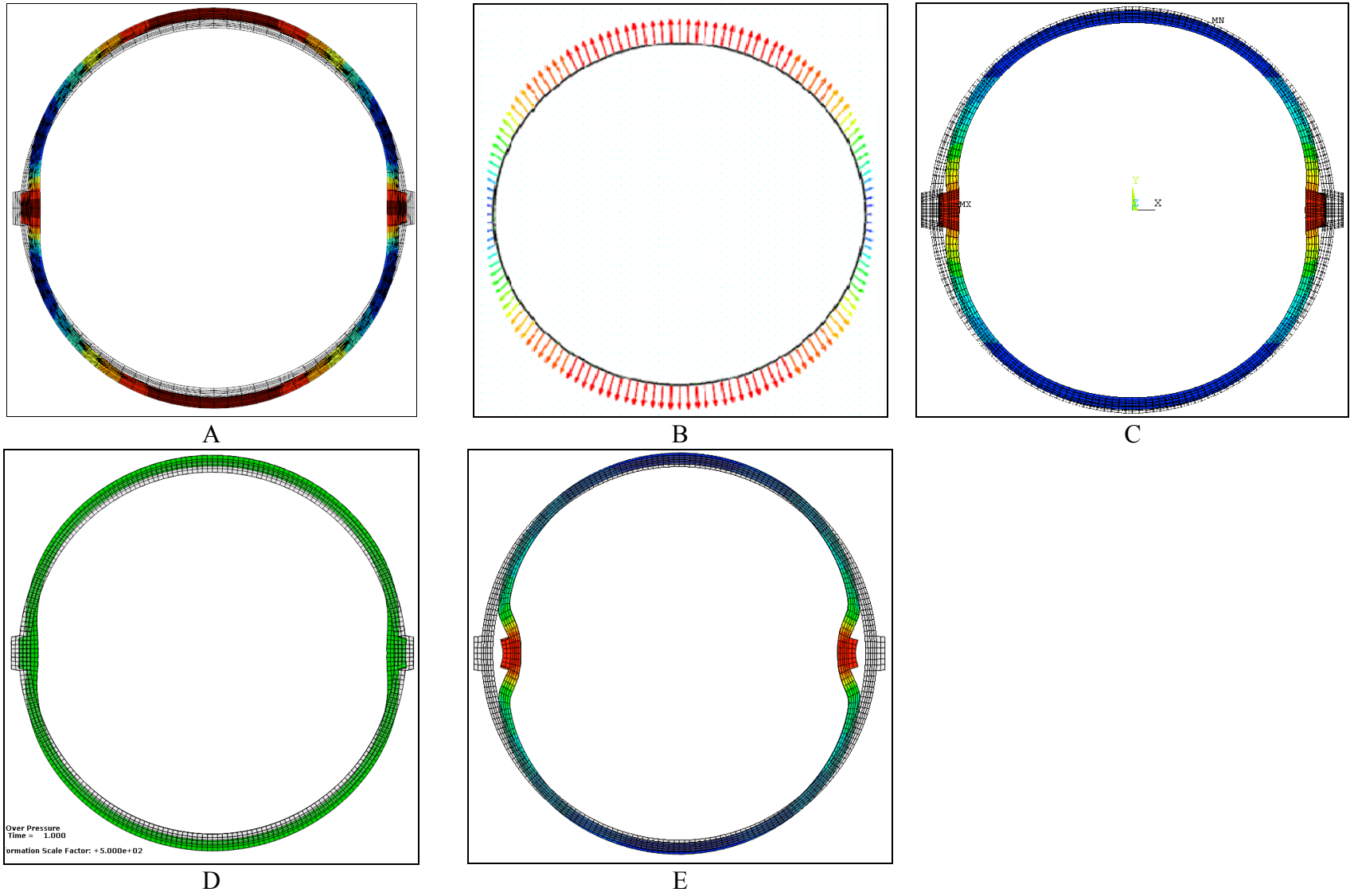

Figure 22: Deformed Shape at 1.5 x Design Pressure (a) EDF/NECS 500x (b) FORTUM at 10x (c) GRS at 500x (d) NRC at 500x (e) SCANSCOT 500x

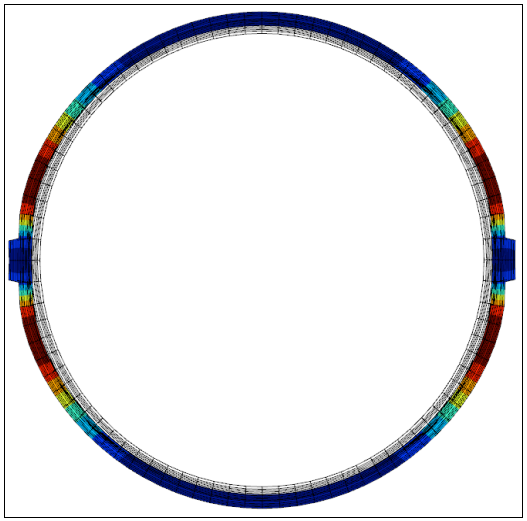

A

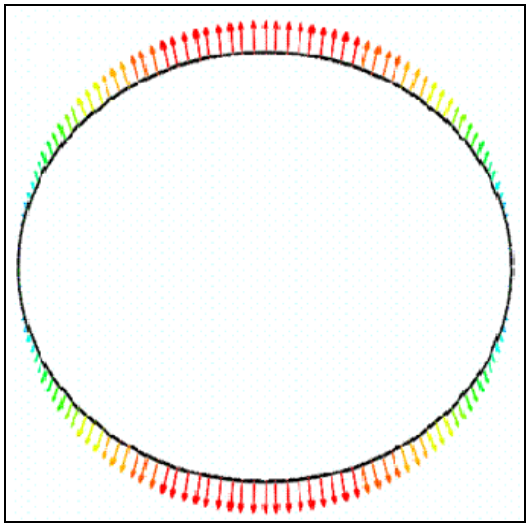

B

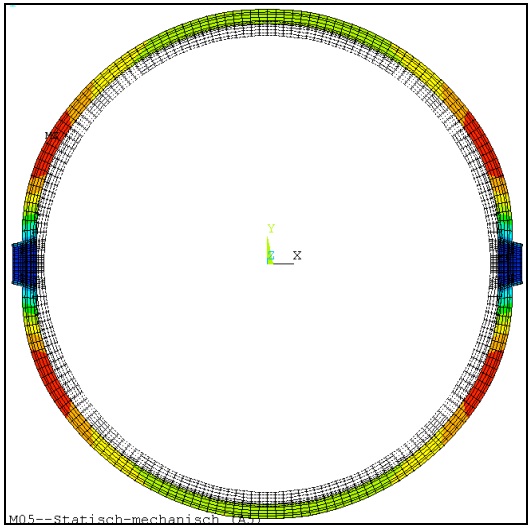

C

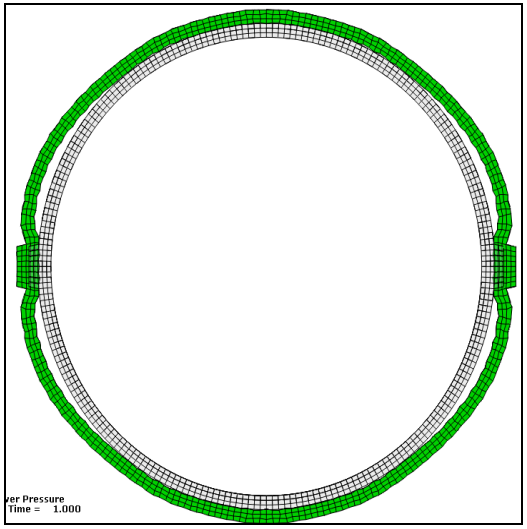

D

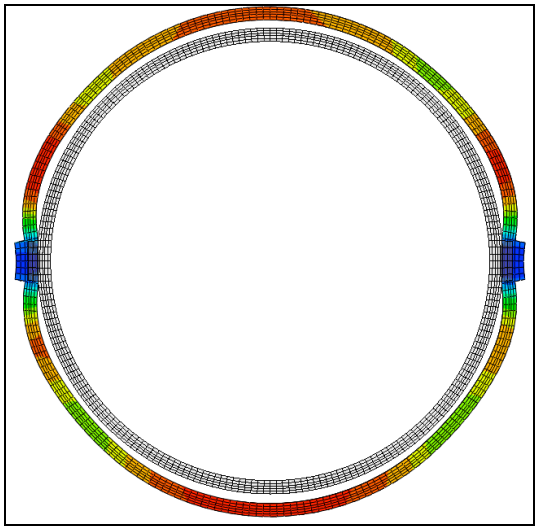

E

Figure 23: Deformed Shape at 2 x Design Pressure (a) EDF/NECS 100x (b) FORTUM at 10x (c) GRS at 100x (d) NRC at 100x (e) SCANSCOT at 100x

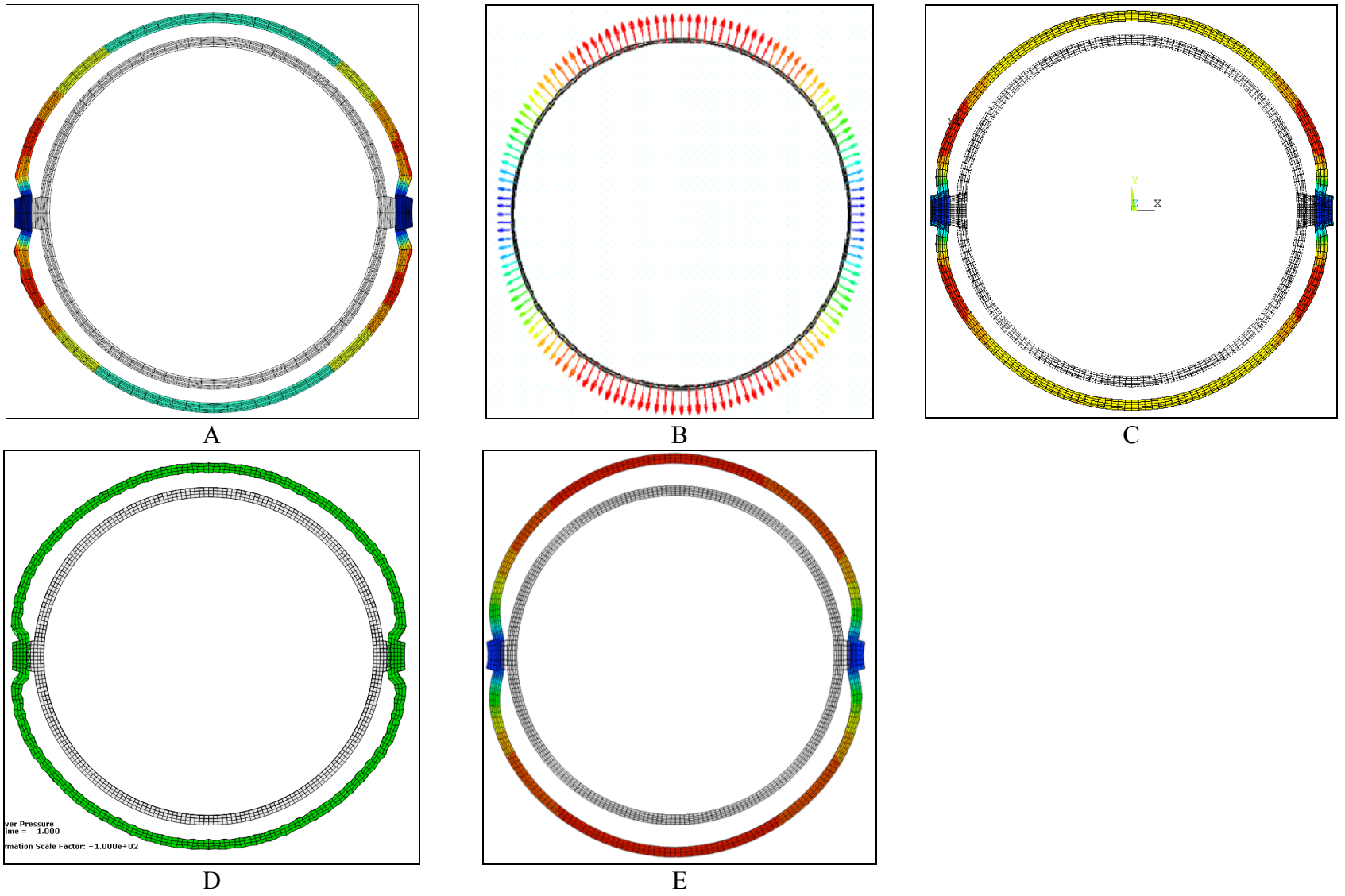

Figure 24: Deformed Shape at 2.5 x Design Pressure (a) EDF/NECS 100x (b) FORTUM at 10x (c) GRS at 100x (d) NRC at 100x (e) SCANSCOT at 100x

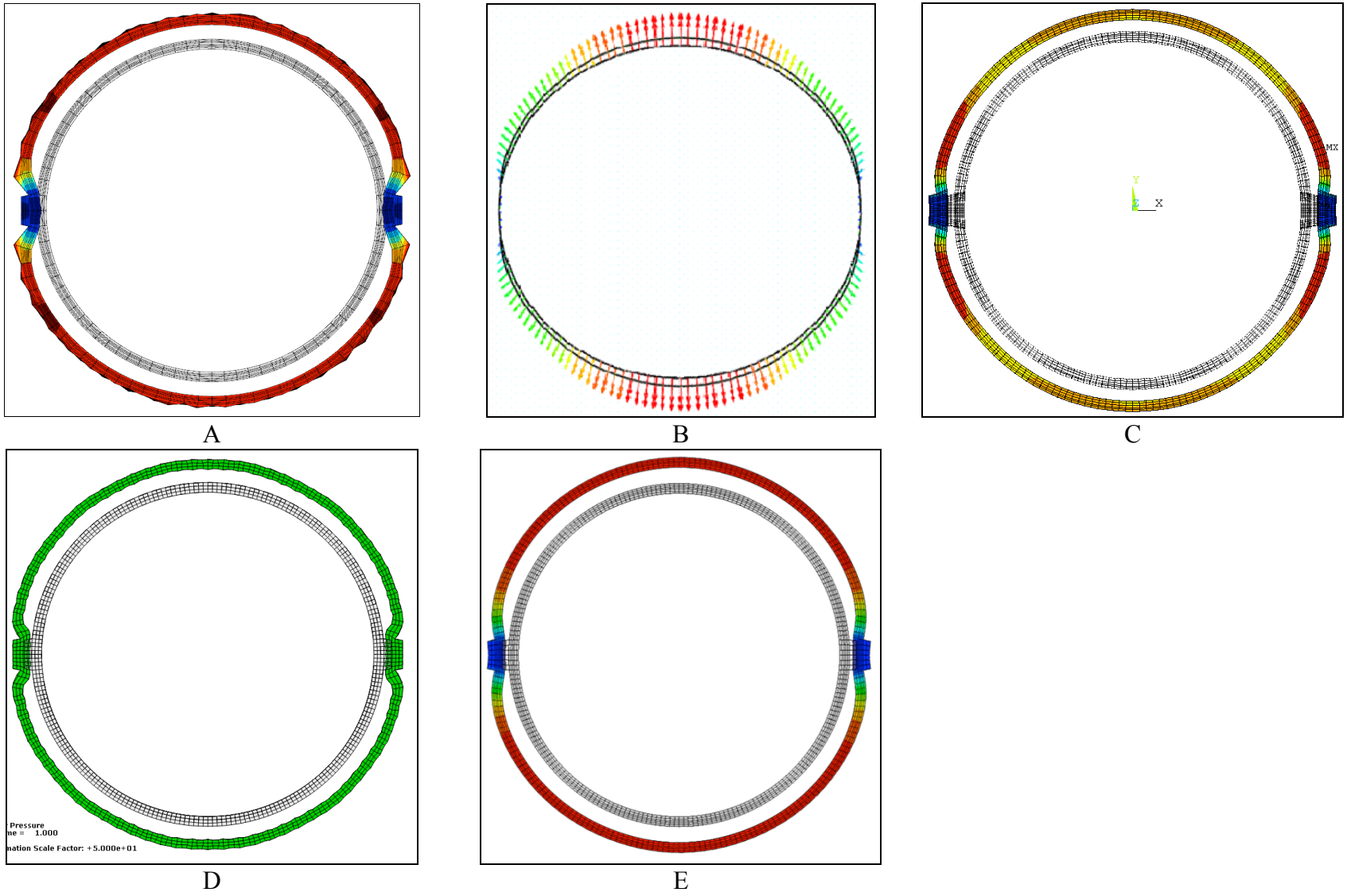

Figure 25: Deformed Shape at 3.0 x Design Pressure (a) EDF/NECS 50x (b) FORTUM at 10x (c) GRS at 50x (d) NRC at 50x (e) SCANSCOT at 50x

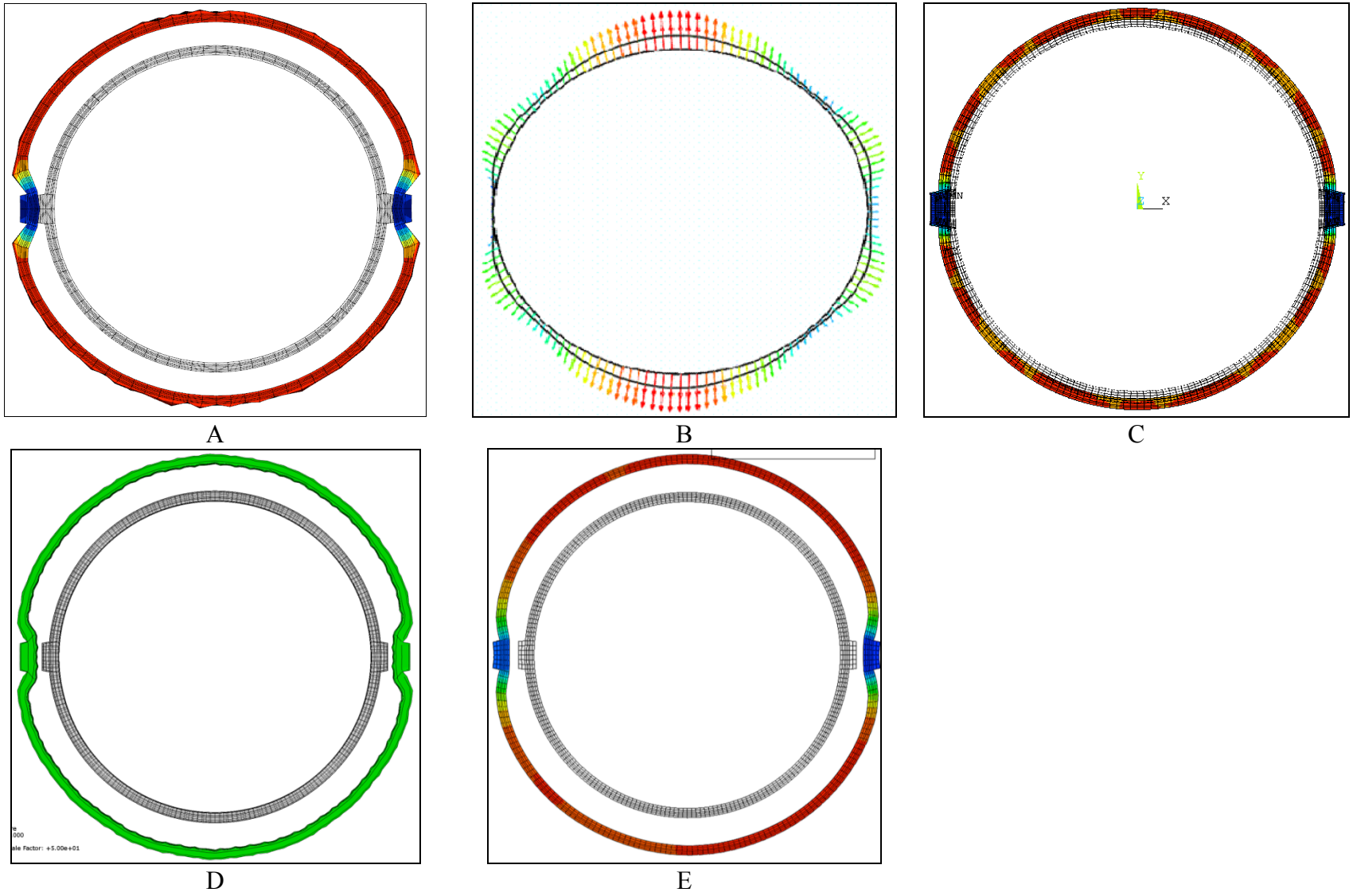

Figure 26: Deformed Shape at 3.3 x Design Pressure (a) EDF/NECS 50x (b) FORTUM at 10x (c) GRS at 50x (d) NRC at 50x (e) SCANSCOT at 50x

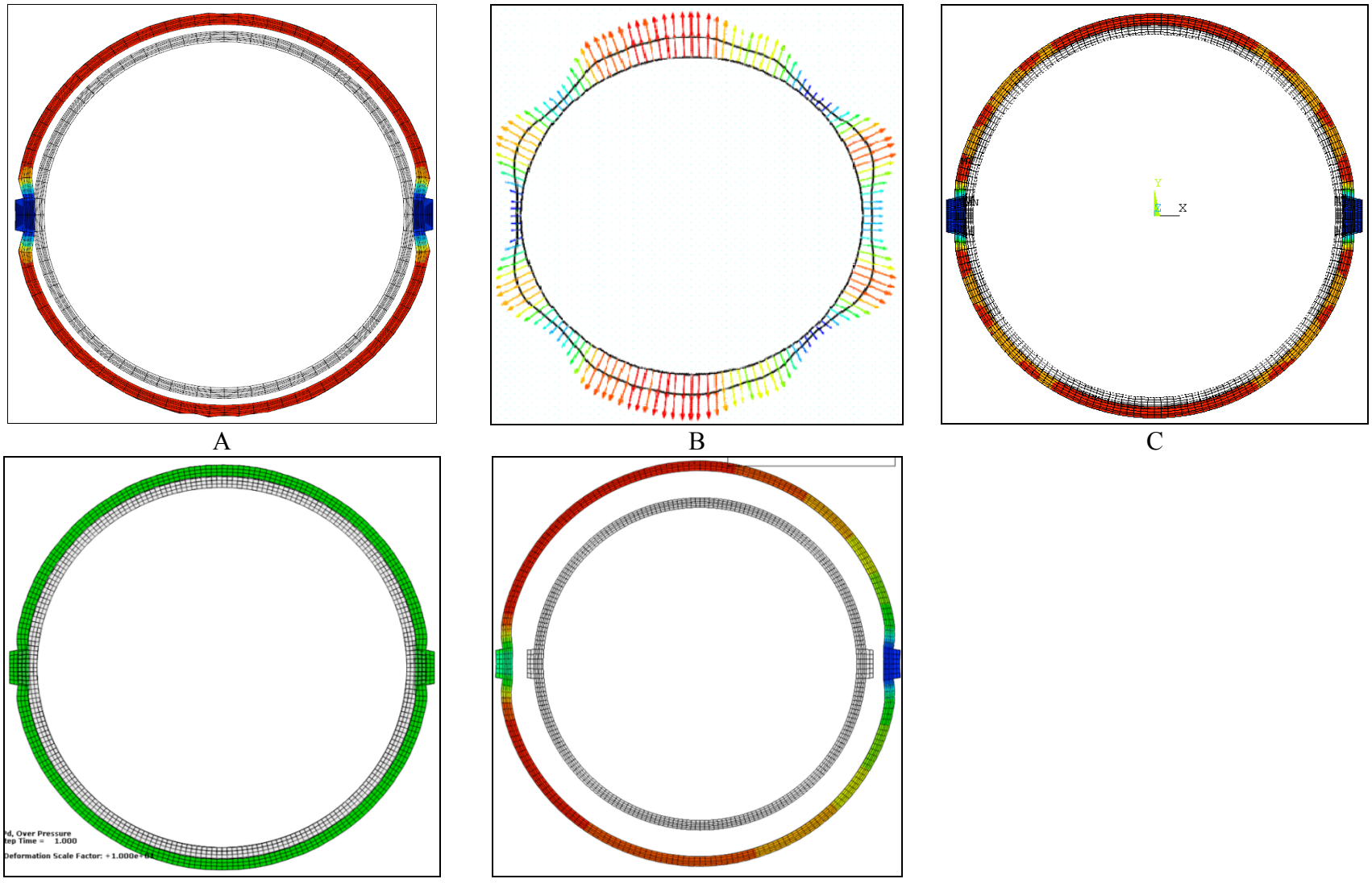

Figure 27: Deformed Shape at 3.4 x Design Pressure (a) EDF/NECS 20x (b) FORTUM at 10x (c) GRS at 10x (d) NRC at 10x (e) SCANSCOT at 20x

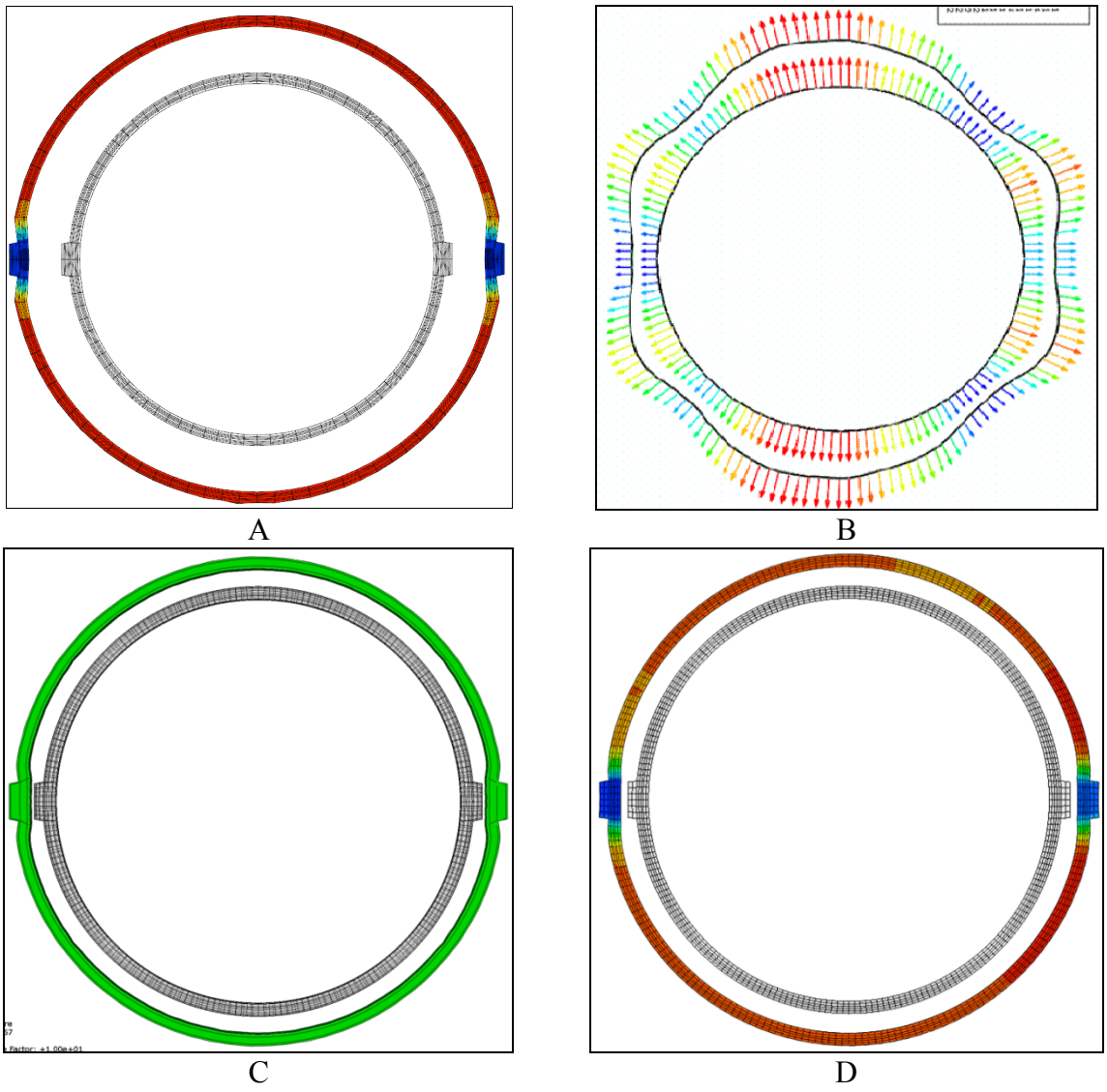

Figure 28: Deformed Shape at 3.5 x Design Pressure (a) EDF/NECS 10x (b) FORTUM at 10x (c) NRC at 10x (d) SCANSCOT at 10x

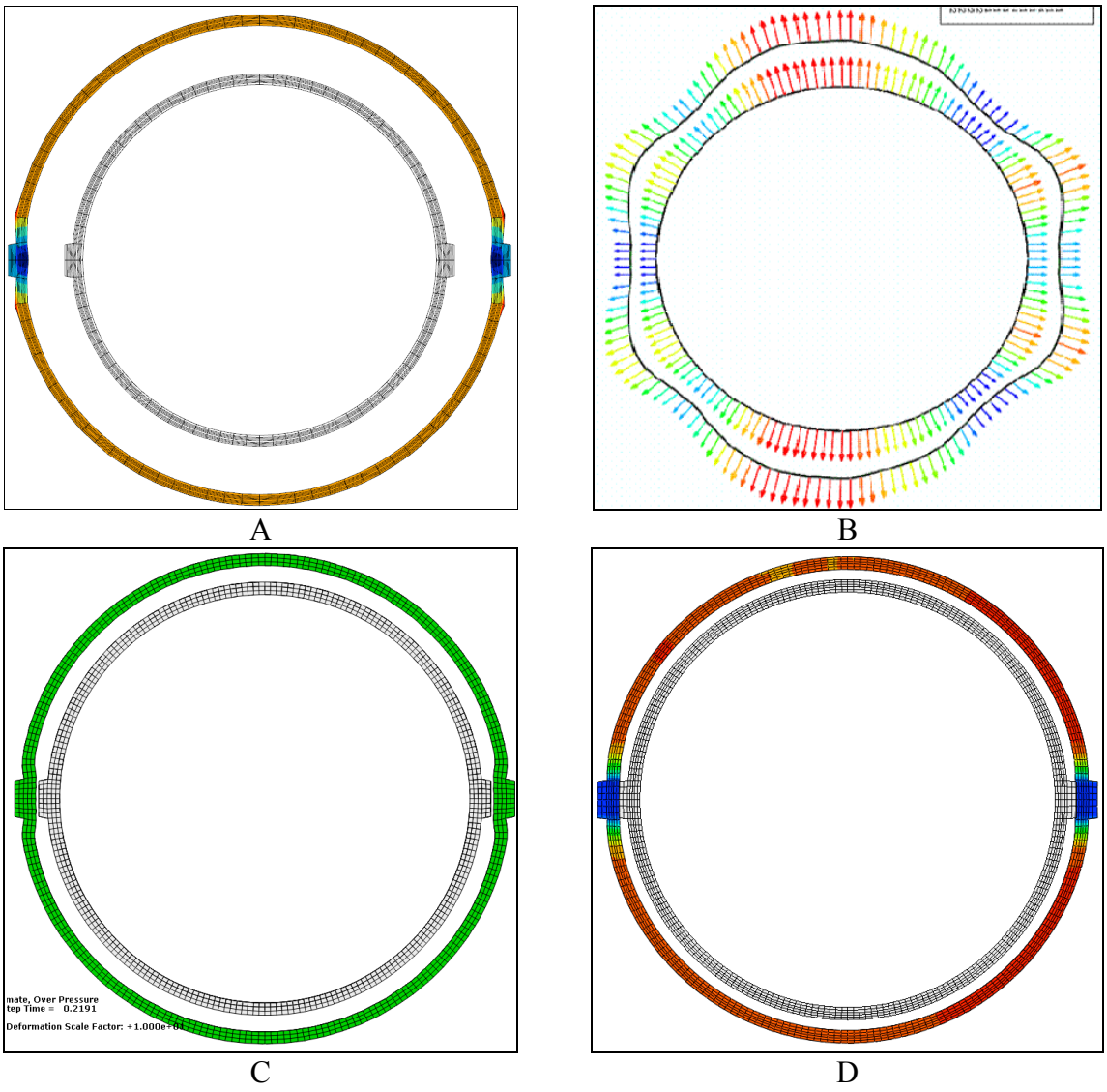

Figure 29: Deformed Shape at Ultimate Pressure (a) EDF/NECS 5x (3.6xP_d) (b) FORTUM at 10x (3.5xP_d) (c) NRC at 10x (3.8xP_d) (d) SCANSCOT at 5x (3.62xP_d)

2.5. Comparison of Tendons Stress Distribution

The distributions of tendon stress furnished by each participant are consolidated and plotted below in Figure 30 through Figure 39. The abscissa and ordinate for each plot below maintains a constant range to facilitate comparison between plots. It is interesting to note that through the application of realistic tendon friction, all participants were able to obtain realistic shapes for the tendon stress distribution.

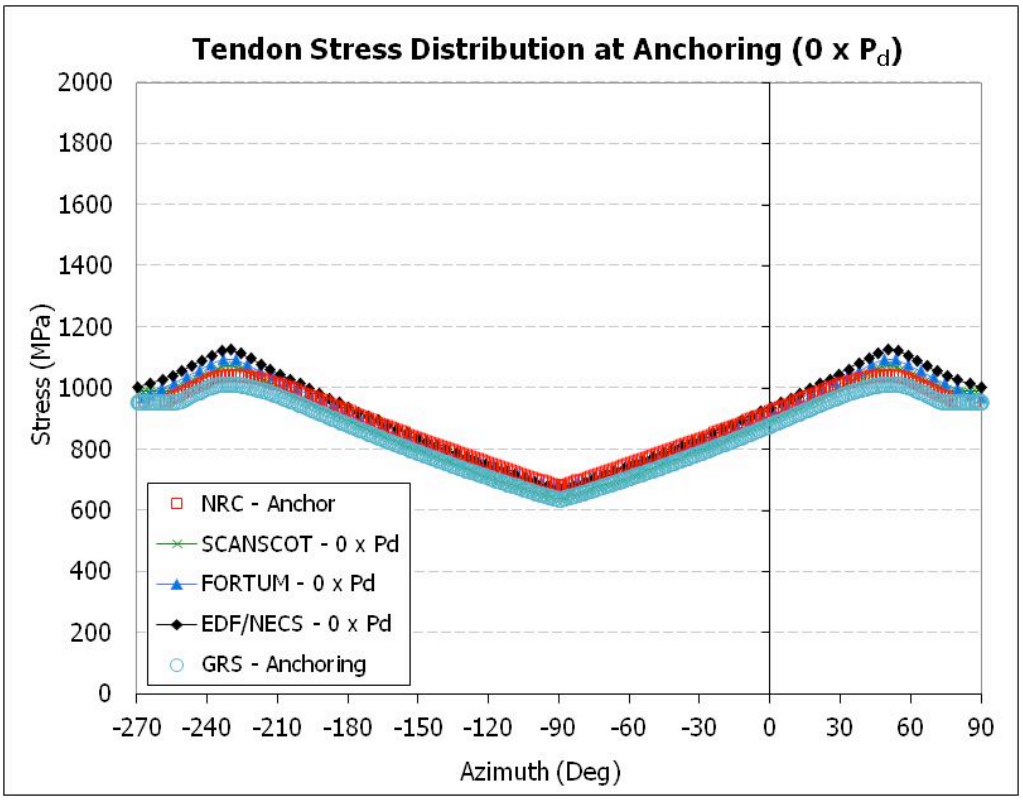

Figure 30: Comparison of Tendon Stress Distribution at Anchoring (0xP_d)

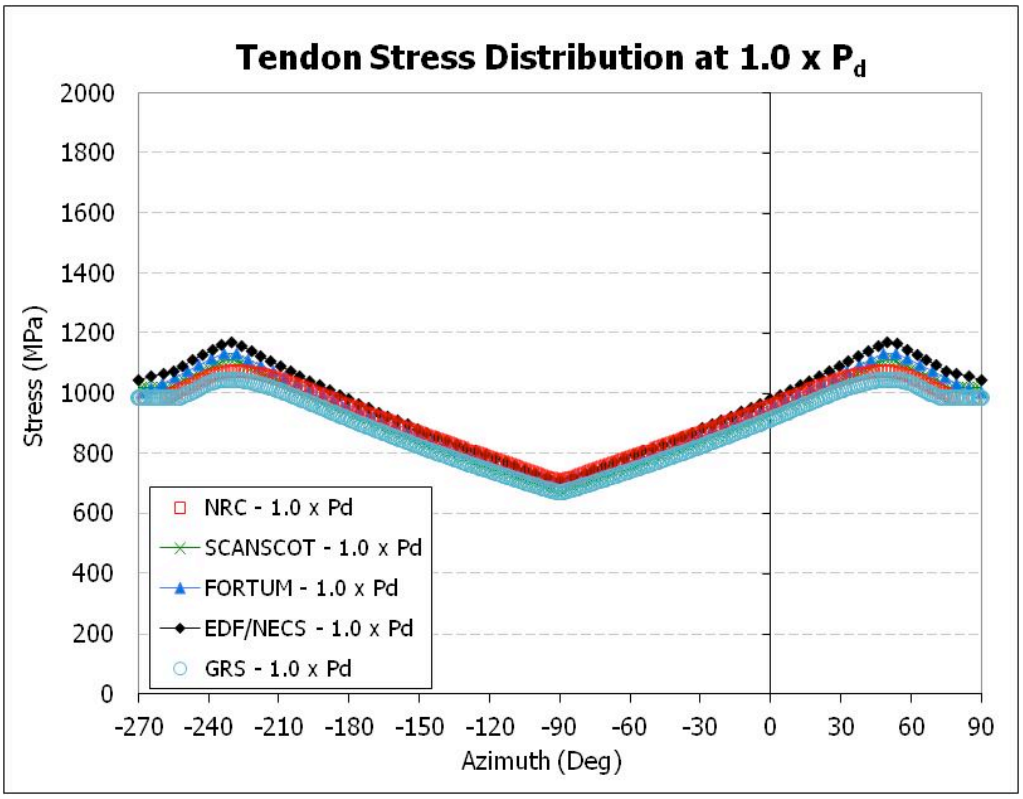

Figure 31: Tendon Stress Distribution at 1.0 x P_d

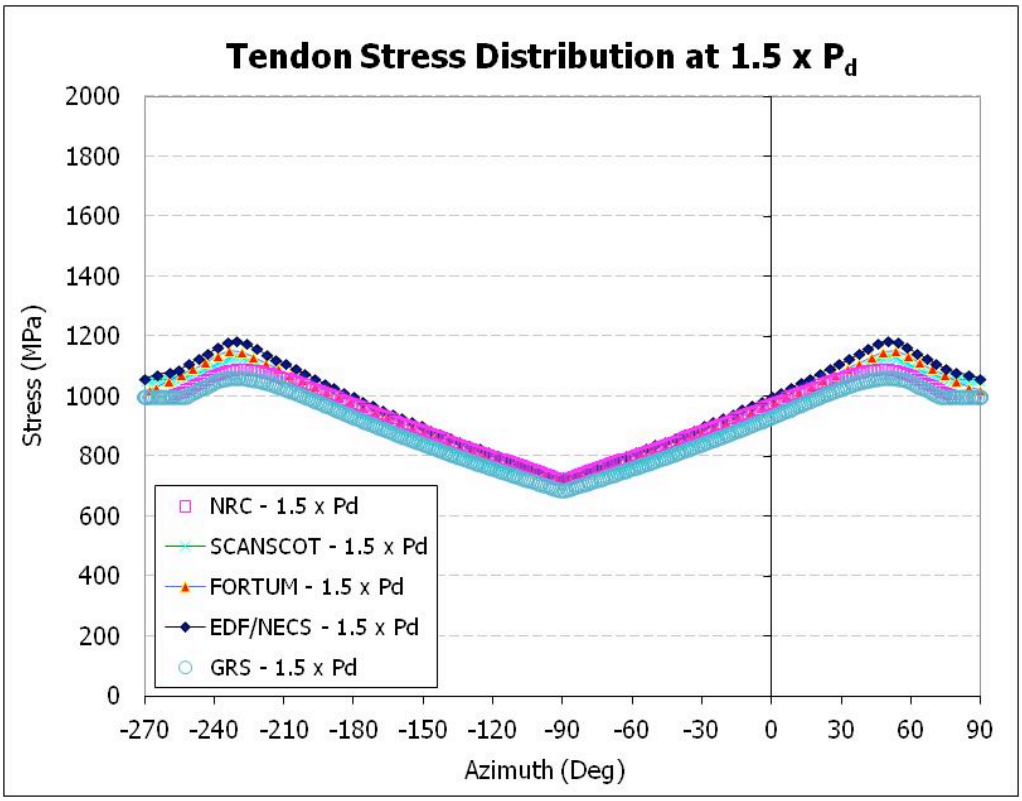

Figure 32: Tendon Stress Distribution at 1.5 x P_d

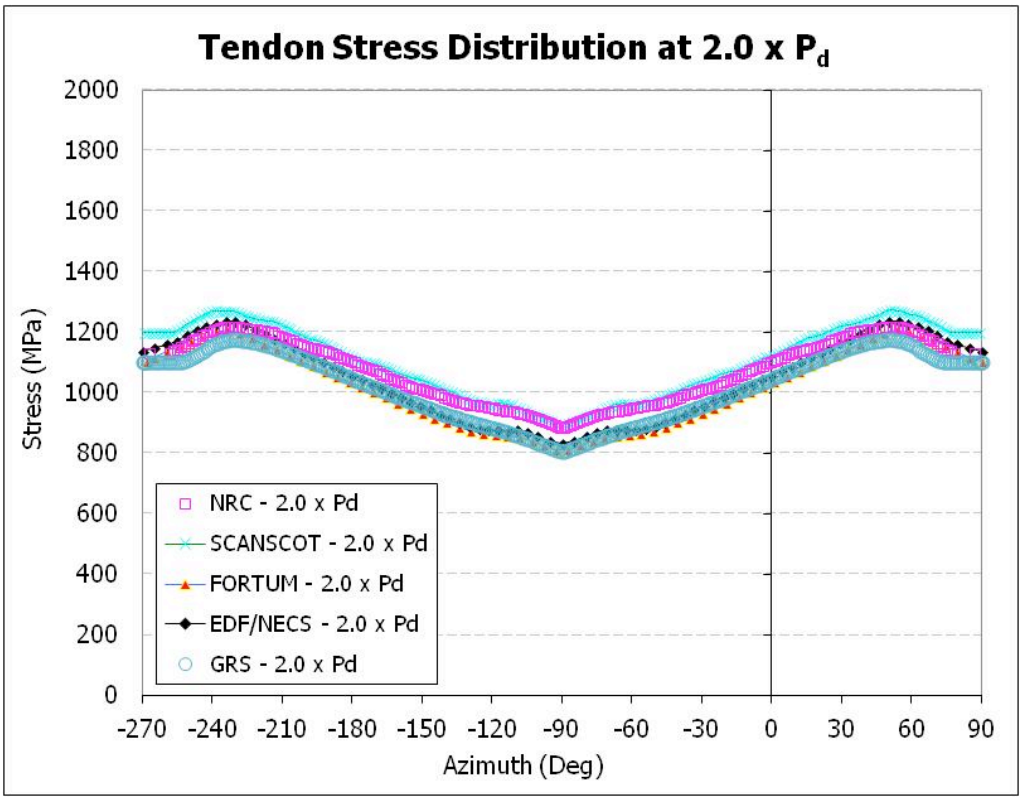

Figure 33: Tendon Stress Distribution at 2.0 x P_d

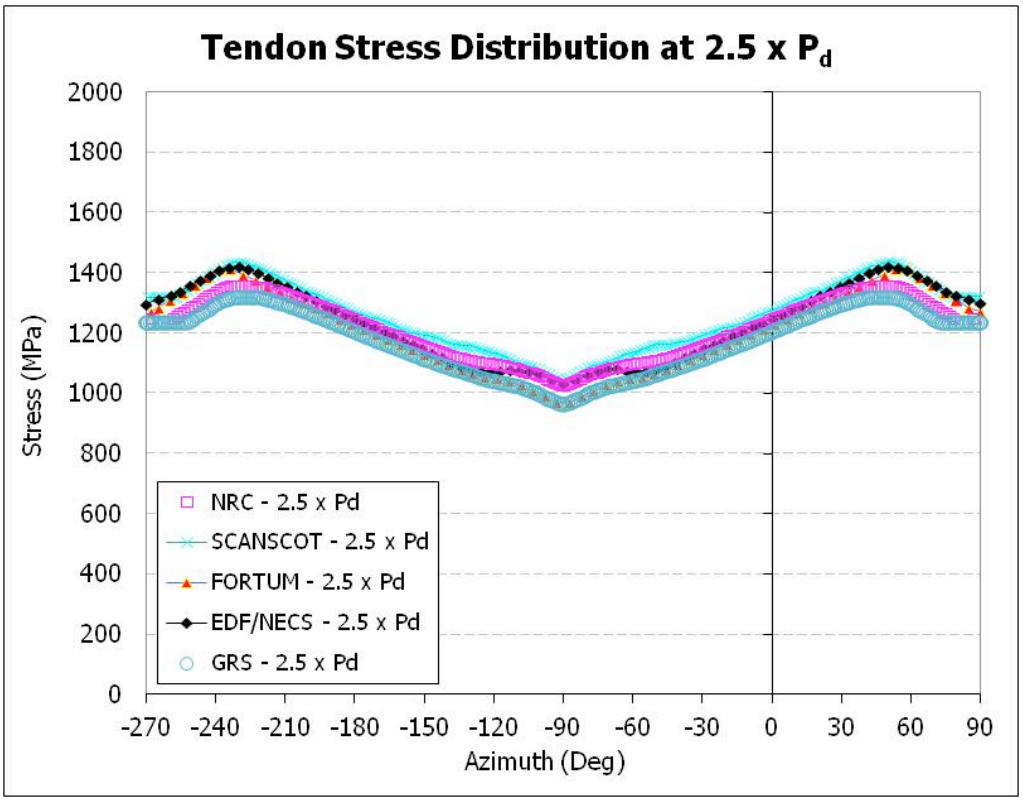

Figure 34: Tendon Stress Distribution at 2.5 x P_d

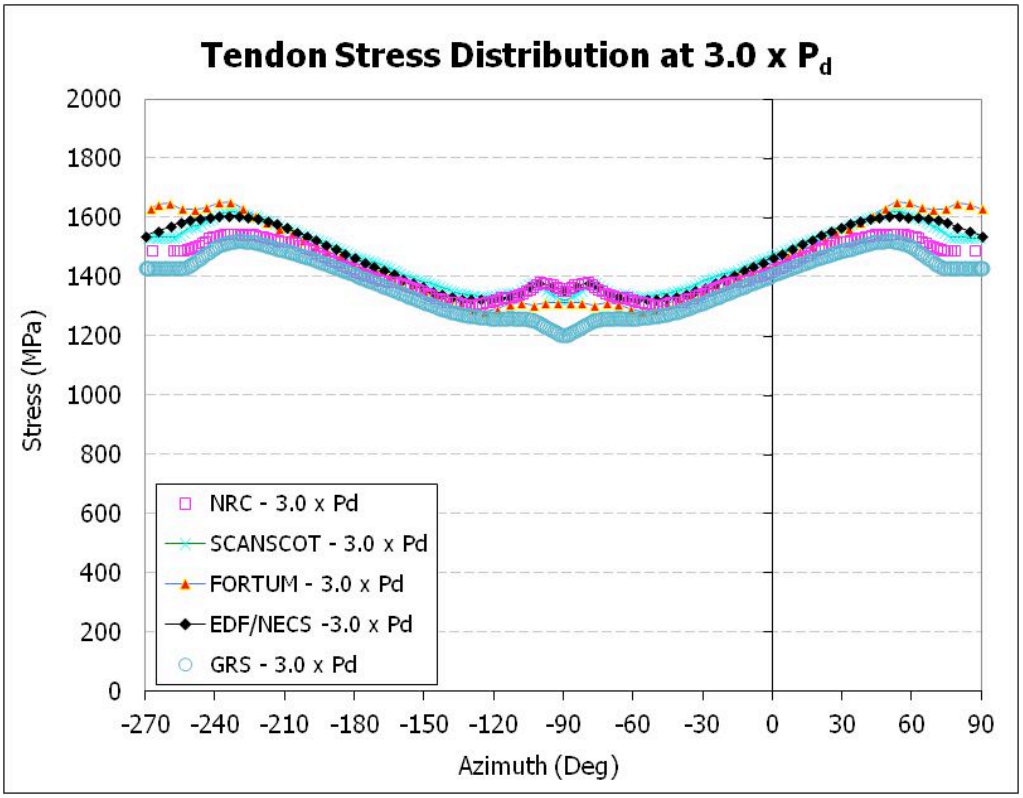

Figure 35: Tendon Stress Distribution at 3.0 x P_d

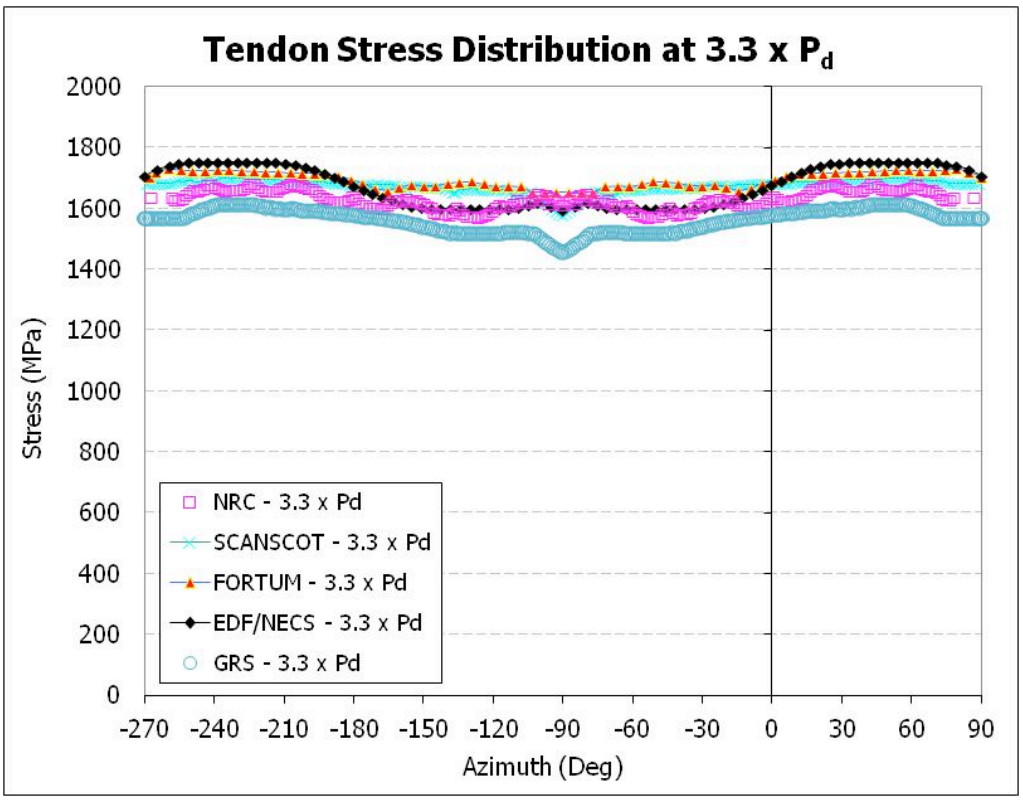

Figure 36: Tendon Stress Distribution at 3.3 x P_d

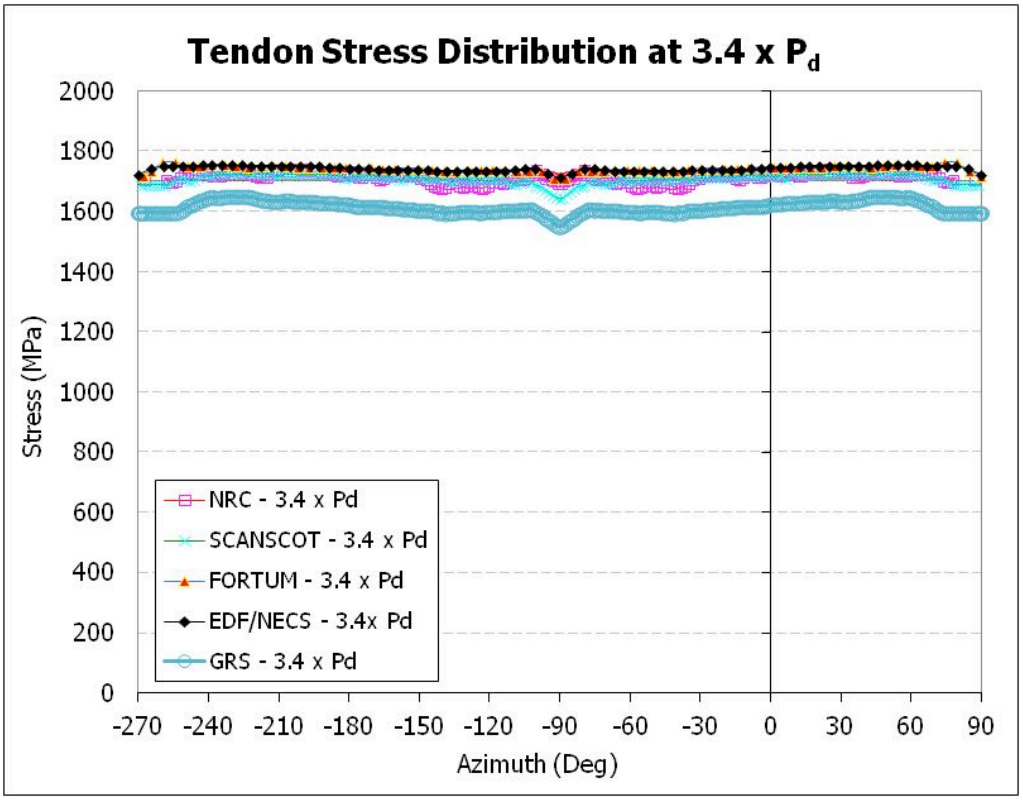

Figure 37: Tendon Stress Distribution at 3.4 x P_d

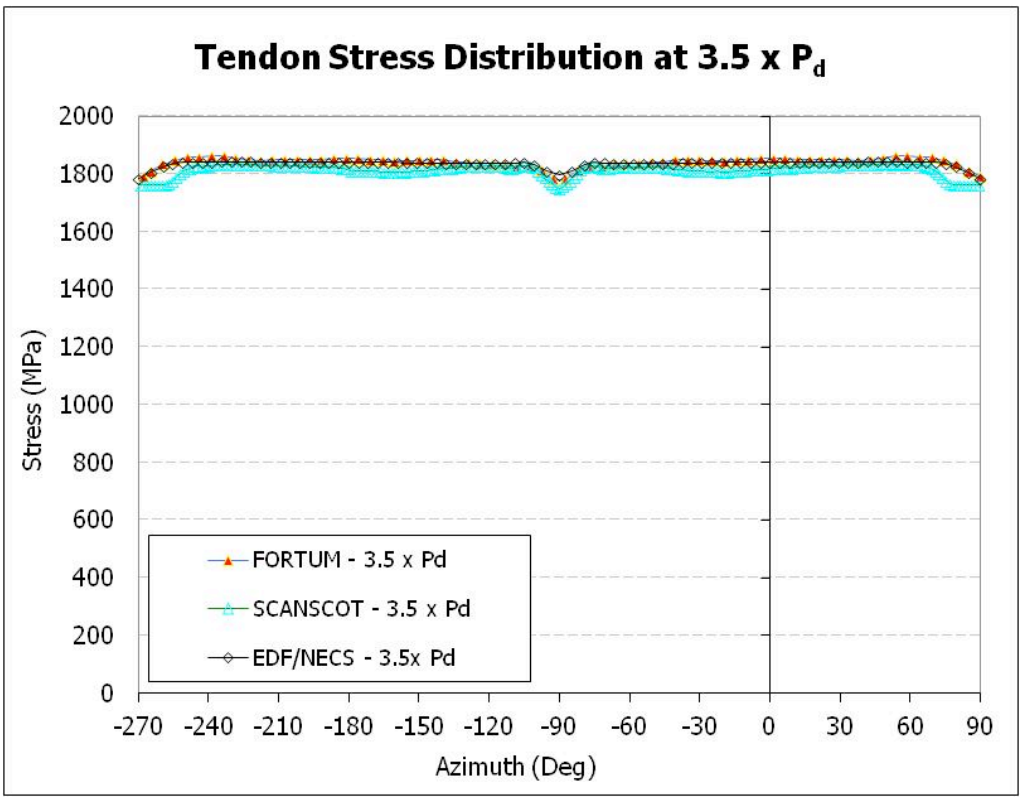

Figure 38: Tendon Stress Distribution at 3.5 x Pd

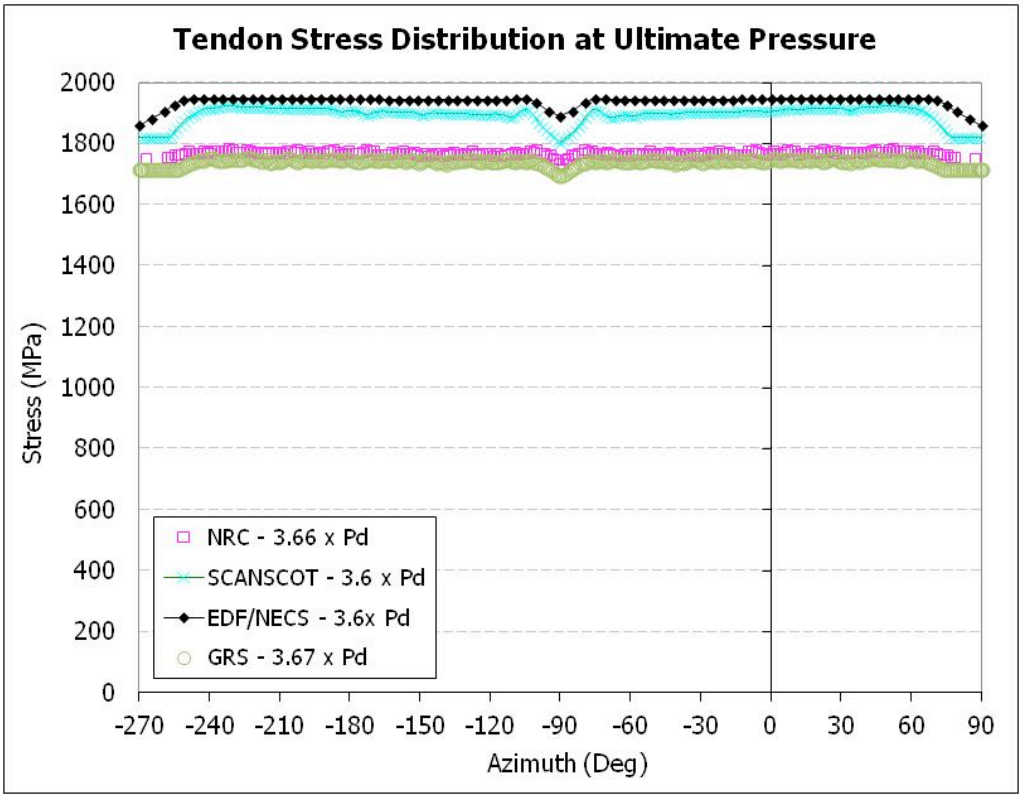

Figure 39: Tendon Stress Distribution at Ultimate Pressure

2.6. Tendon Strain versus Pressure

Tendon Strain versus pressure at Azimuth 135° was requested from all participants. This azimuth corresponds to the "free-field" section of the PCCV. The tendon strain at Azimuth 135° for Tendon A can be found below in Figure 40 while the strain in Tendon B can be found in Figure 41. For both tendons, the results from all the participants agree well up to approximately 1.3 MPa where significant differences emerge. This pressure corresponds roughly with the failure of the 1:4 Scale PCCV test.

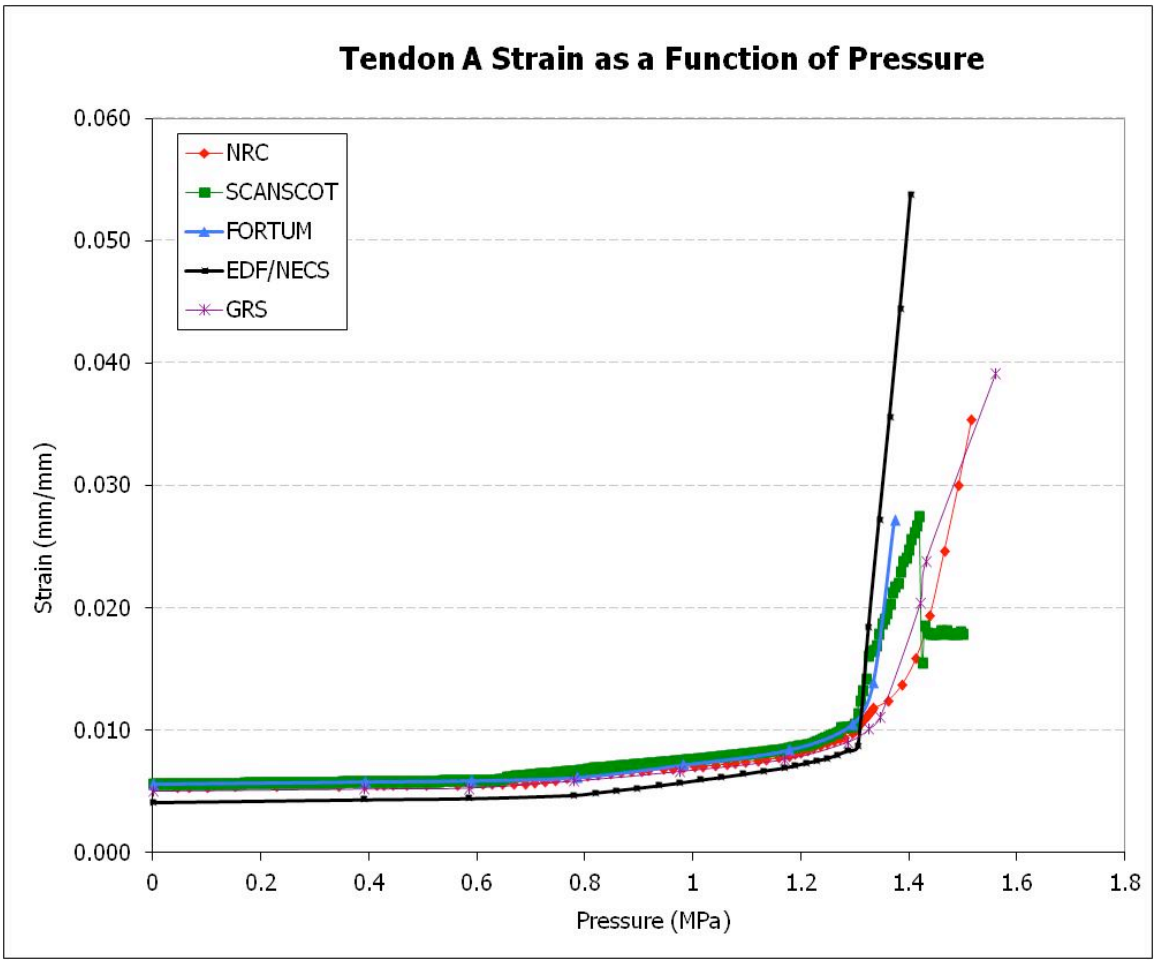

Figure 40: Tendon A Strain as a Function of Pressure at Azimuth 135°

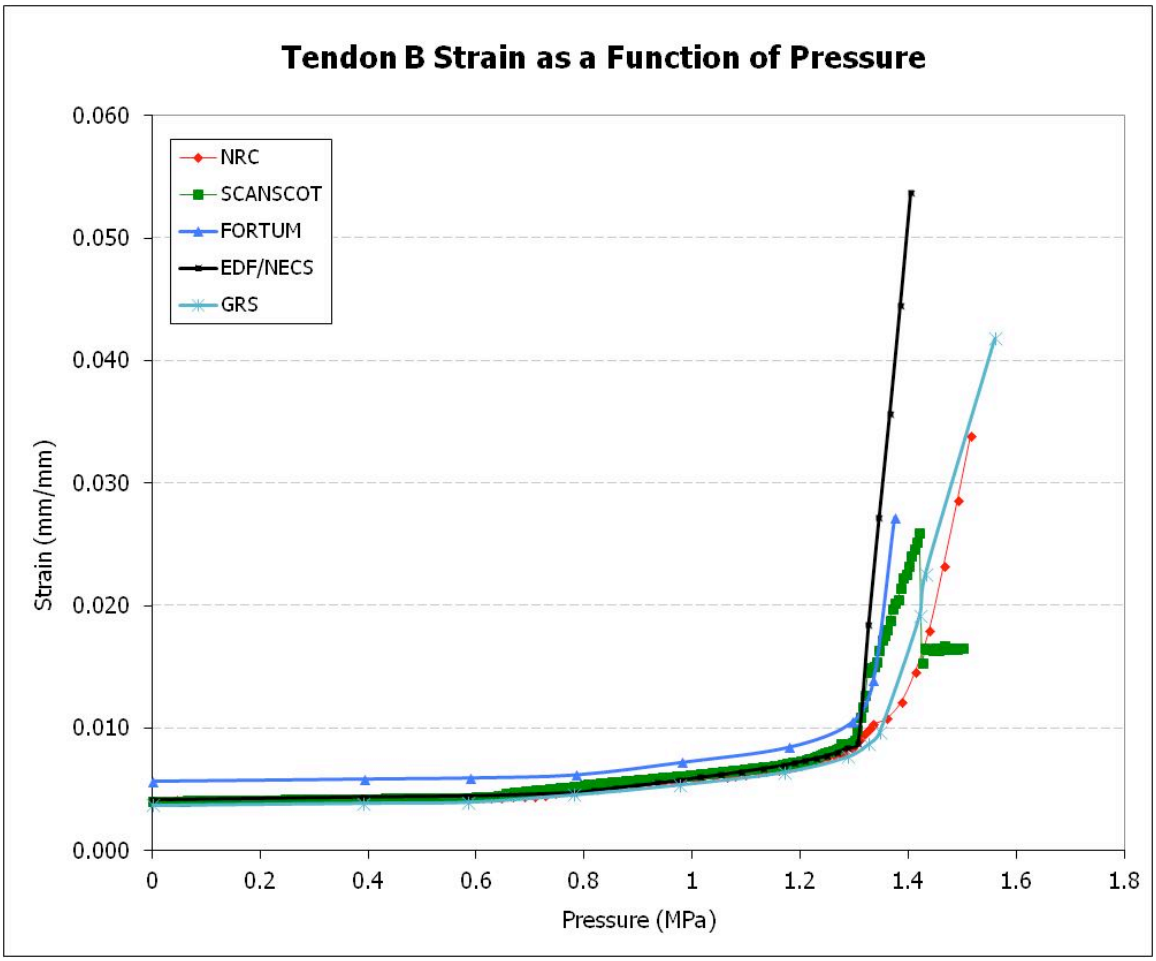

Figure 41: Tendon B Strain as a Function of Pressure at Azimuth 135°

2.7. Radial Displacement versus Pressure

The participants were asked to provide plots of radial displacement versus pressure at three Azimuths (135°, 0°, and 270°). These comparisons can be found below in Figure 42 through Figure 47. For each azimuth, there exist two plots, one with the full displacement range and one with a reduced displacement range to focus on the differences (if any) between the participant's responses. In general the results from all the participants agreed very well up until approximately 1.3 MPa when the structure becomes unstable and achieving convergence with the codes becomes more difficult.

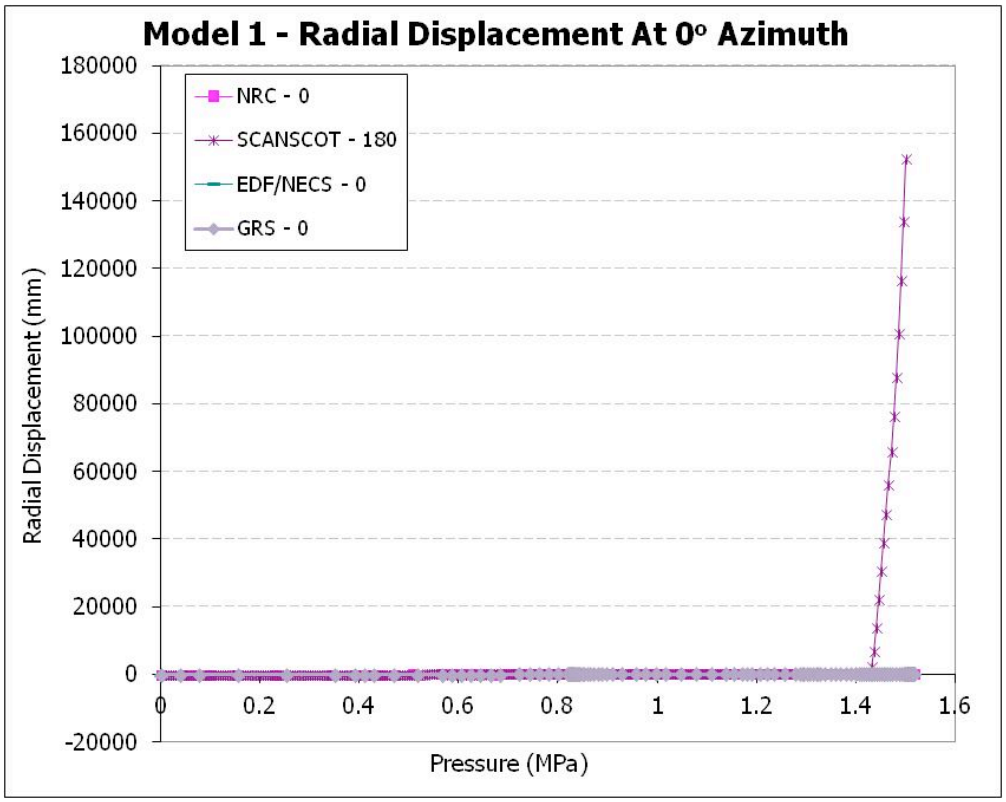

Figure 42: Radial Displacement at 0° Azimuth

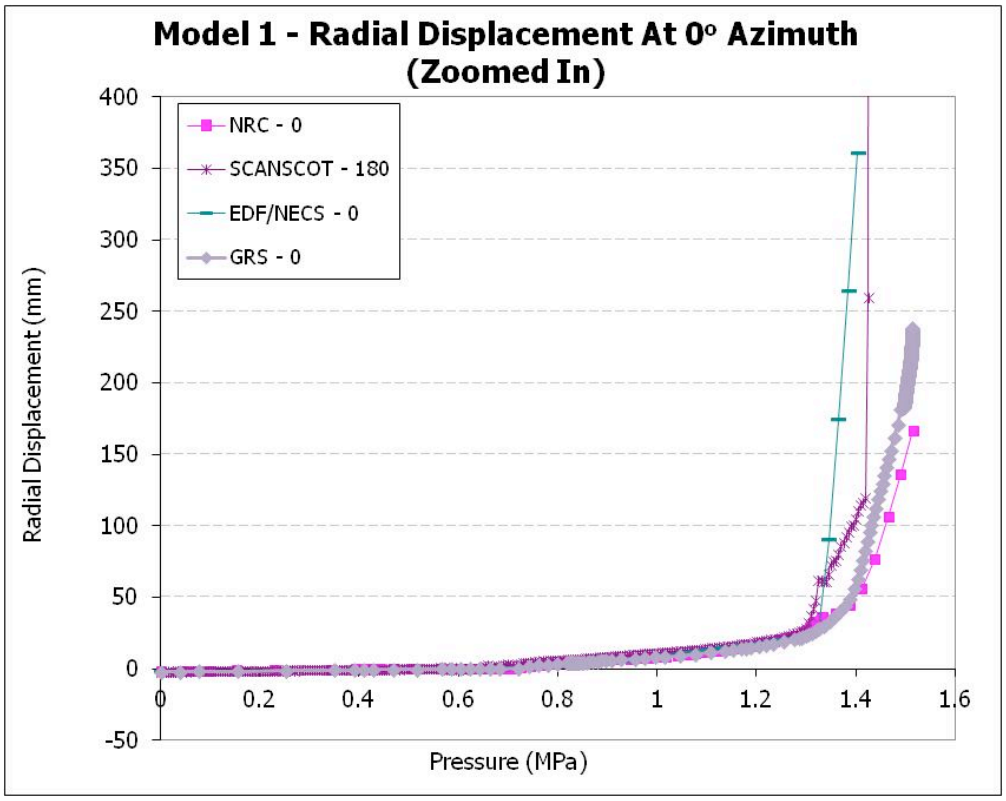

Figure 43: Radial Displacement at 0° Azimuth (Zoomed In)

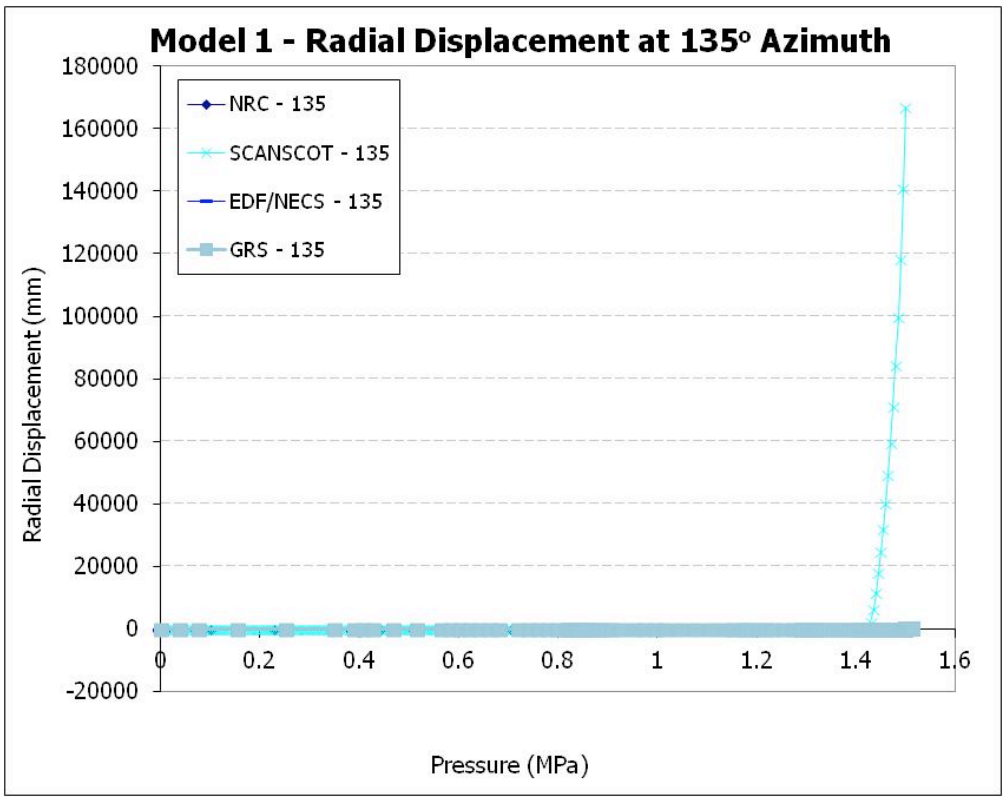

Figure 44: Radial Displacement versus Pressure at 135° Azimuth

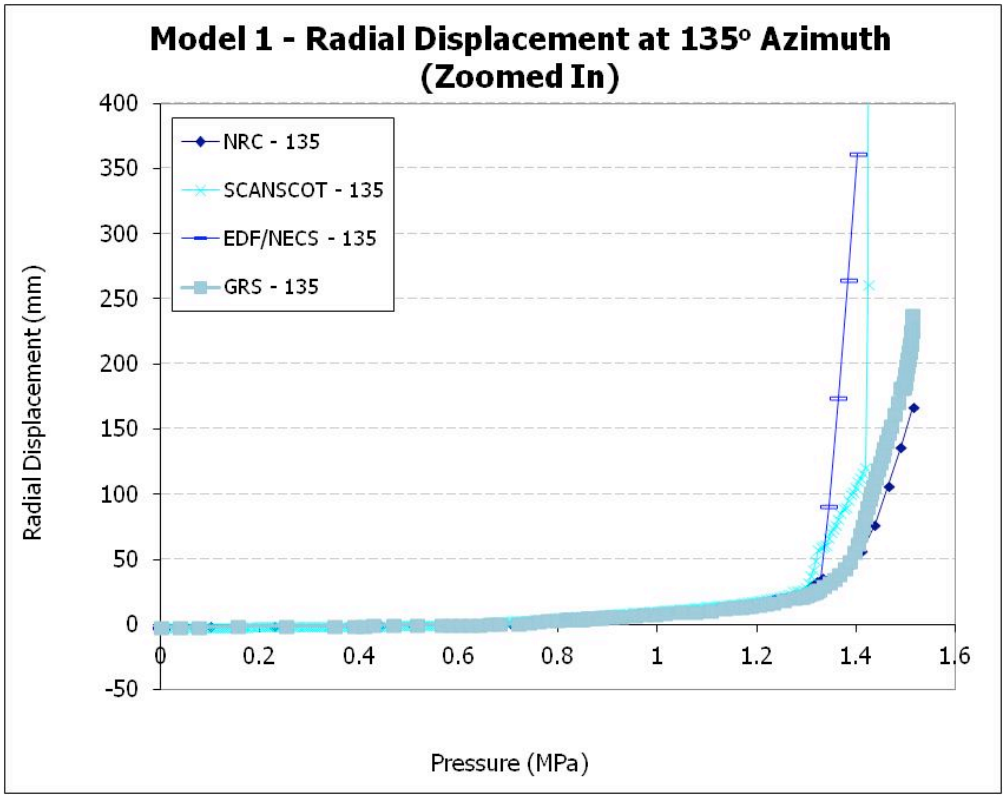

Figure 45: Radial Displacement versus Pressure at 135° Azimuth (Zoomed In)

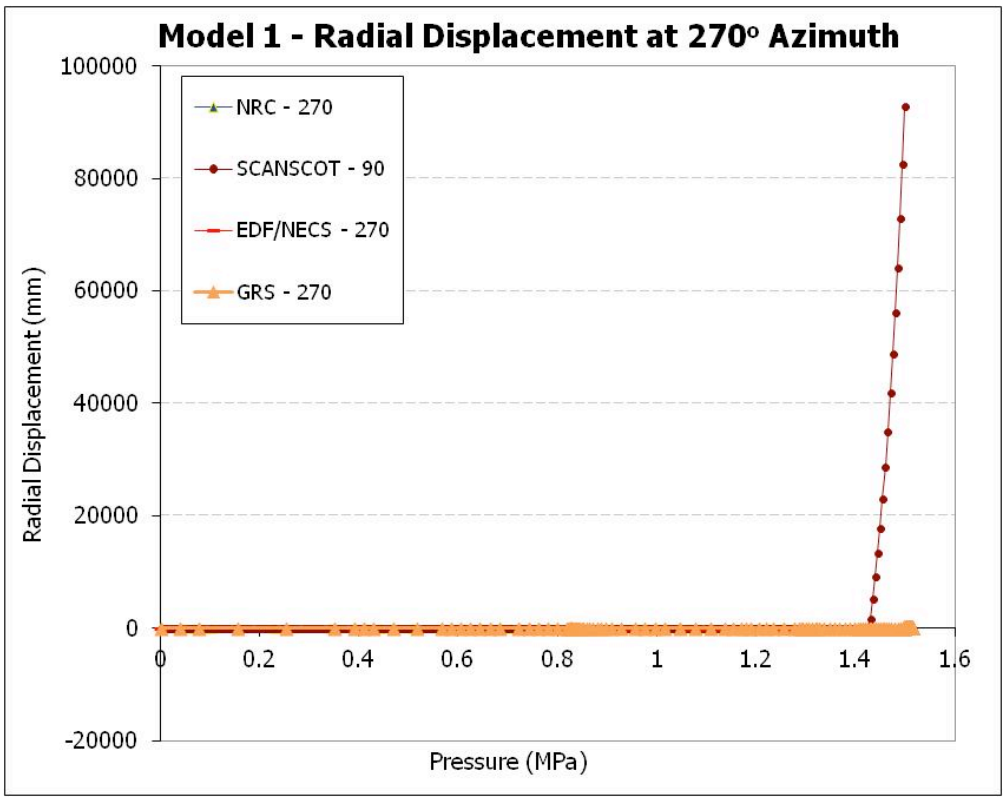

Figure 46: Radial Displacement versus Pressure at 270° Azimuth

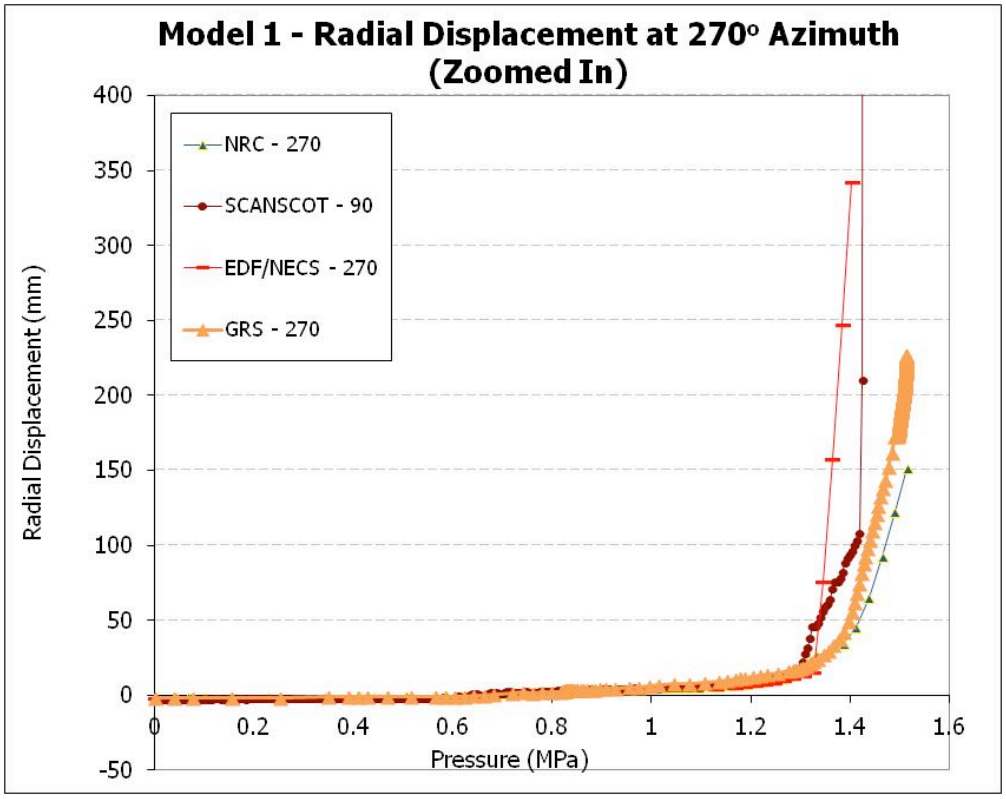

Figure 47: Radial Displacement at 270° Azimuth (Zoomed In)

2.8. Tendon Force as a Function of Containment Dilation

It has been observed from the scale model testing that the tendon force distribution tends to flatten as the internal pressure increases and the containment vessel dilates. This flattening of the distribution is attributed to tendon slip within the tendon ducts that alleviates the distribution of force along the length of each tendon. Several of the participants (EDF, NRC, and SCANSCOT) provided information with respect to tendon slippage and this information is presented in Figure 48 through Figure 50. In general, these results agree with the notion of increased tendon slippage contributing to the flattening of the tendon force distribution as the internal pressure increases.

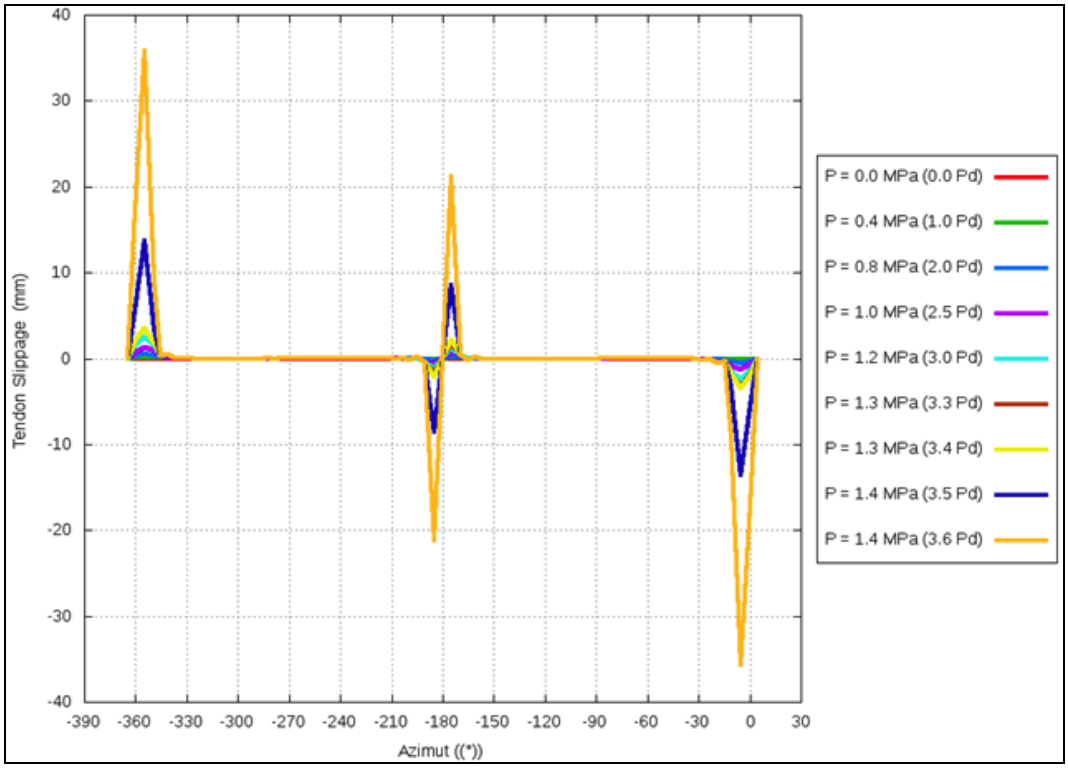

Figure 48: Tendon slip as reported by EDF

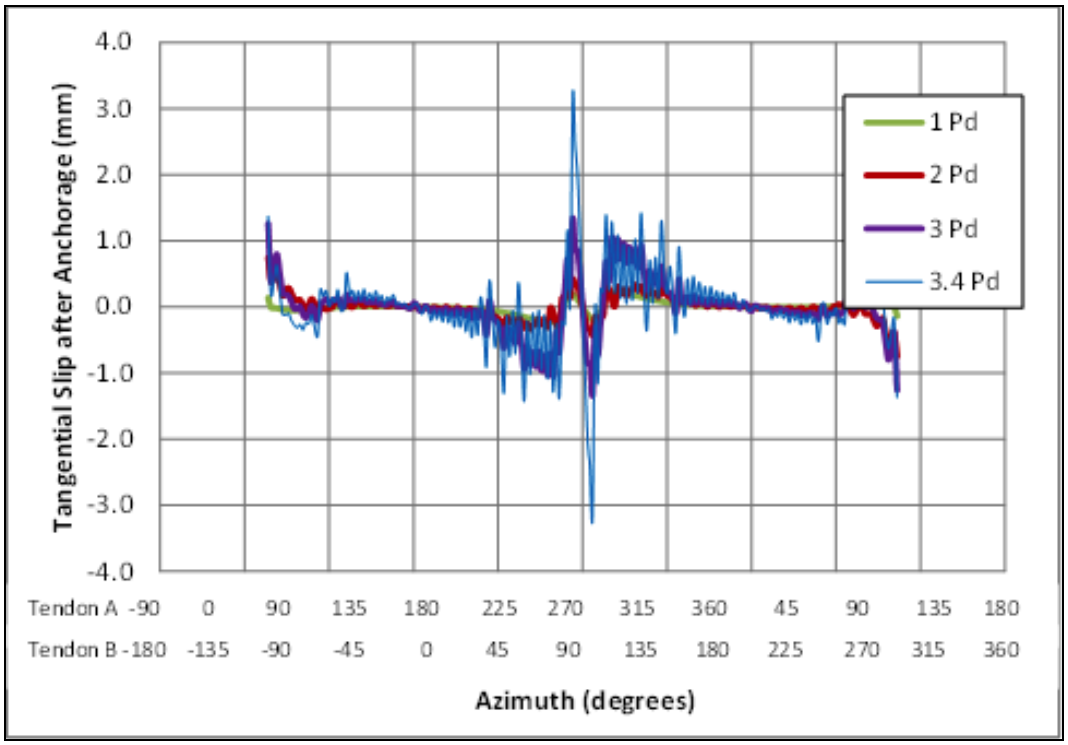

Figure 49: Tendon slip as reported by NRC

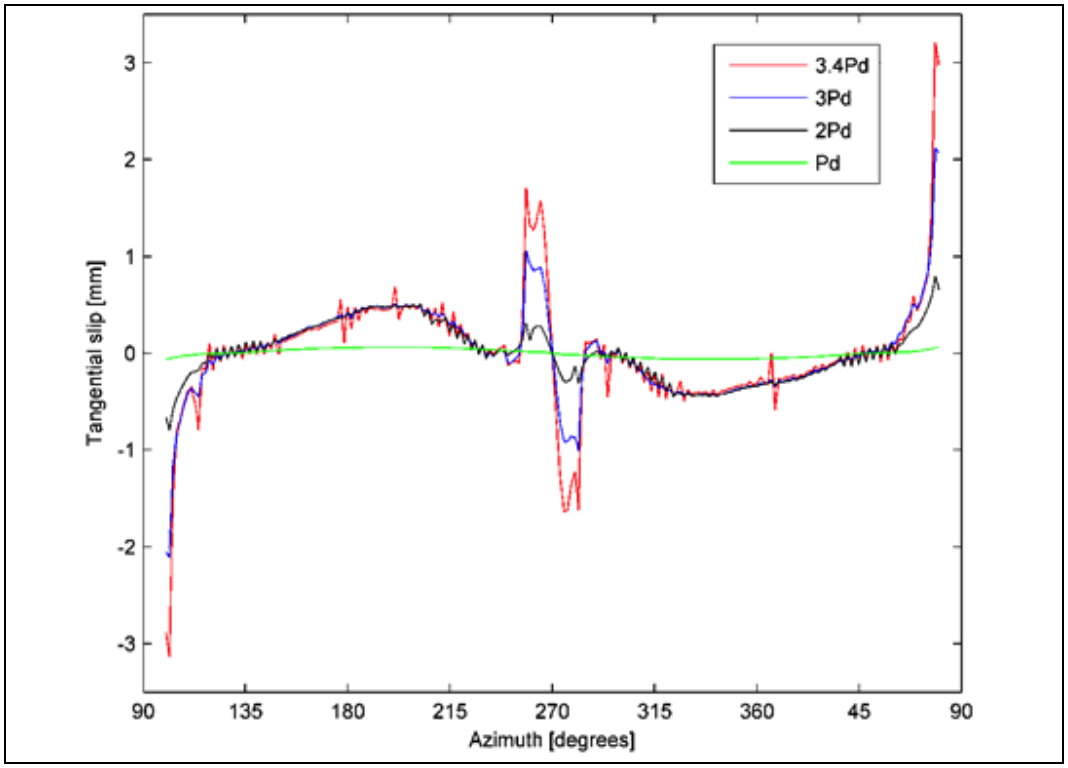

Figure 50: Tendon slip as reported by SCANSCOT

2.9. Model 1 Conclusions

Model 1 results were submitted by EDF, FORTUM, GRS, NRC and SCANSCOT. Some variability in modeling technique was observed between the participants, most notably in the method of modeling the rebar and the tendons. NRC, SCANSCOT, and FORTUM used embedded rebar layers while EDF chose uniaxial shell elements to model the rebar in Model 1. Similarly EDF, FORTUM, and SCANSCOT chose truss elements to model the tendons while NRC chose beam elements. Additionally relatively minor differences were observed in the specific values used for the material properties for Model 1. It is suspected that the variation in modeling approach and the minor differences in the input material properties likely account for the variations noted in the results for Model 1.

The pressure milestones submitted by the participants indicate good agreement from the participants with a few small exceptions. For example, SCANSCOT indicated a slightly lower internal pressure for the onset of concrete cracking while EDF and FORTUM indicated slightly lower internal pressure levels at 2% strain in the tendons.

The deformed shape comparisons indicated good agreement between all participants, particularly near the design pressure for the structure. The variations between the participants in the deformed shape at all pressure levels are small, however, and the agreement between participants for the deformed shapes are good.

The tendon stress profiles, tendon strain versus pressure plots, and radial displacement versus pressure plots indicate very good agreement between the participants, particularly up to approximately 3.0-3.3 x P_d. Past this point in the pressurization, the models begin to become somewhat unstable as supported by the termination of the Limit State Test in the NUPEC/NRC 1:4 Scale PCCV Test at 3.3 x P_d. Additionally, several participants verified the slipping of the tendons with internal pressure as the source of the observed flattening of the tendon force versus location plots at high pressures.

3. MODEL 2

As noted previously, the participants were requested to create a local model of the equipment hatch (Figure 5-Figure 6). The participants were asked to represent the contact to the liner in three different methods, a fully tied case, connection only along the anchors, and a best representation approach to be left up to each participant to determine. The desired output for the Model 2s are as follows:

1. Description of Modeling Assumptions and Phenomenological Models
2. Description of Liner Failure Criteria Used
3. Pressure Milestones, Applied Pressure When:
    a. Concrete Hoop Cracking Occurs and Location
    b. First Tendon Reaches 1% Strain and Location
4. Deformed Shape at P =0, $1xP_d$, $1.5xP_d$, $2xP_d$, $2.5xP_d$,, $3xP_d$,, $3.3xP_d$,, $3.4xP_d$,, Ultimate Pressure
5. Tendon Stress distribution at P =0, $1xP_d$, $1.5xP_d$, $2xP_d$, $2.5xP_d$,, $3xP_d$,, $3.3xP_d$,, $3.4xP_d$,, Ultimate Pressure for:
    a. Hoop Tendon Nearest the Penetration Hatch
    b. Hop Tendon at Top of Model 2
6. Liner Strain Magnitudes (Hoop Direction) at Locations 1-10 in Figure 11.
7. Radial Displacements Versus Pressure at Azimuth 328^o (centered on the hatch), 0^o, and 270^o at the same elevation as the Hatch CL (Elevation 4680mm)
8. Plot Ovalization (Separation which Occurs Between Concrete and Pipe Sleeve) Versus Pressure in Circumferential and Meridional Direction
9. Provide Commentary About Observed Differences Between Model 2a, 2b, and 2c.

3.1. Description of Modeling Assumptions and Phenomenological Models

A comparison of the different modeling software and modeling set-up is listed below in Table 11. Each participant was free to use any FEM software they so chose, and to represent the geometry for Model 2 as needed.

Table 11: Model Detail Comparison

MODELING DETAILS	AERB	NRC	SCANSCOT
FEM Tool	Abaqus	Abaqus Standard FE	Abaqus Explicit 6.9 and Abaqus Standard 6.9
Concrete Element Type	Hex Elements (C3D8R)	Hex Elements (C3D8R)	Hex Elements (C3D8R)
Rebar Element Type	Rebar Layer	Rebar Layer (SFM3D4R)	Rebar Layer
Liner Element Type	Linear 4-node Shell Element with Uniaxial Behavior	Shell Elements (S4R)	Shell Elements (S4R)
Tendon Element Type	Linear 2-Node Truss Element	Beam Elements (B31)	Truss Elements (T3D2)
Tendon / Concrete Interaction	Embedded	Tendons inside tendon ducts	Contact Surfaces with Friction (0.22)
Concrete / Rebar Interaction	Embedded	Embedded	Embedded

A comparison of the material models is provided in Table 12. In general, there is good agreement between the material parameters chosen by the participants.

Table 12: Comparison of Material Models

MATERIAL	AERB	NRC	SCANSCOT
Concrete Model	Damage Plasticity Concrete	Concrete Damage Plasticity	Brittle Cracking Model
Concrete Parameters of Note	E = 26,900 MPa ν = 0.21 σ_t = 2.4 MPa ρ = 2,176 kg/m^3	E = 33,000 MPa ν = 0.2	E=26,800 MPa ν = 0.2
Rebar	Non-Linear Elasto-Plastic	Elasto-Plastic	Elasto-Plastic
Rebar Parameters of Note	E = 185,000 MPa ν = 0.3 σ_t = 445-460 MPa ρ = 7,850 kg/m^3 Ep = 1,250-1,350 MPa	E = 200,000 MPa ν =0.3 σ_t = 498 MPa	E = 185,000 MPa ν =0.3 σ_t = 460 MPa
Liner	Metal Plasticity	Elasto-Plastic	Elasto-Plastic
Liner Parameters of Note	E = 210,000 MPa ν = 0.3 σ_t = 400 MPa ρ = 7,850 kg/m^3 Ep = 700 MPa	E = 200,000 MPa ν =0.3 σ_t = 498 MPa	E = 220,000 MPa ν =0.3 σ_t = 383 MPa
Tendon	Non-Linear Elasto-Plastic	Elasto-Plastic	Elasto-Plastic
Tendon Parameters of Note	E = 191,000 MPa ν = 0.3 σ_t = 1,750 MPa ρ = 7,850 kg/m^3 Ep = 3,350 MPa f_{gu} = 1,857 MPa μ = 0.21 Δs = 3.95 mm T_0 = 444 kN	E = 200,000 MPa ν = 0.3 σ_t = 1875 MPa	E = 191,000 MPa ν = 0.3 σ_t = 1680 MPa

3.2. Description of Liner Failure Criteria

The model failure parameter of interest in Model 2 was liner tearing. This failure criteria is not as straightforward as the dominant failure mechanism in Model 1, tendon rupture. Because the liner experiences a bi-axial state of stress, determining the particular onset of tearing is

somewhat complicated. The methods used by the participants for Model 2 are identified in Table 13.

Table 13: Liner failure criteria

	AERB	NRC	SCANSCOT
Tendon Failure Criteria (ultimate strain)		Biaxial Stress based (Davis Triaxiality Factor)	Biaxial Stress based (Davis Triaxiality Factor)

3.3. Pressure Milestones

For Model 2 several pressure milestones were requested from all participants. These milestones and the participant specific responses are presented in Table 14. The agreement between the responses of the participants is not as good as in Model 1 and perhaps this is to be expected due to the more complicated nature of Model 2 in comparison to Model 1.

Table 14: Pressure Milestones for Model 2a

MILESTONE	PRESSURE (MPA, PD)			
	AERB	GRS	NRC	SCANSCOT
1. Concrete Hoop Cracking Occurs	(0.64, 1.64)	(0.6, 1.54)	(0.585, 1.49)	(0.52, 1.33)
Location of Milestone 1	0° Azimuth	Above and Below Equipment Hatch	0° Azimuth	0° Azimuth
2. Tendon Reaches 1% Strain	Not Reached	(1.15, 2.95) (1.3, 3.33)	(1.362, 3.47)	(1.32, 3.38)
Location of Milestone 2	None	H37, 324°, z=5583mm V47, 41°, z=240mm	0° Azimuth	0° Azimuth

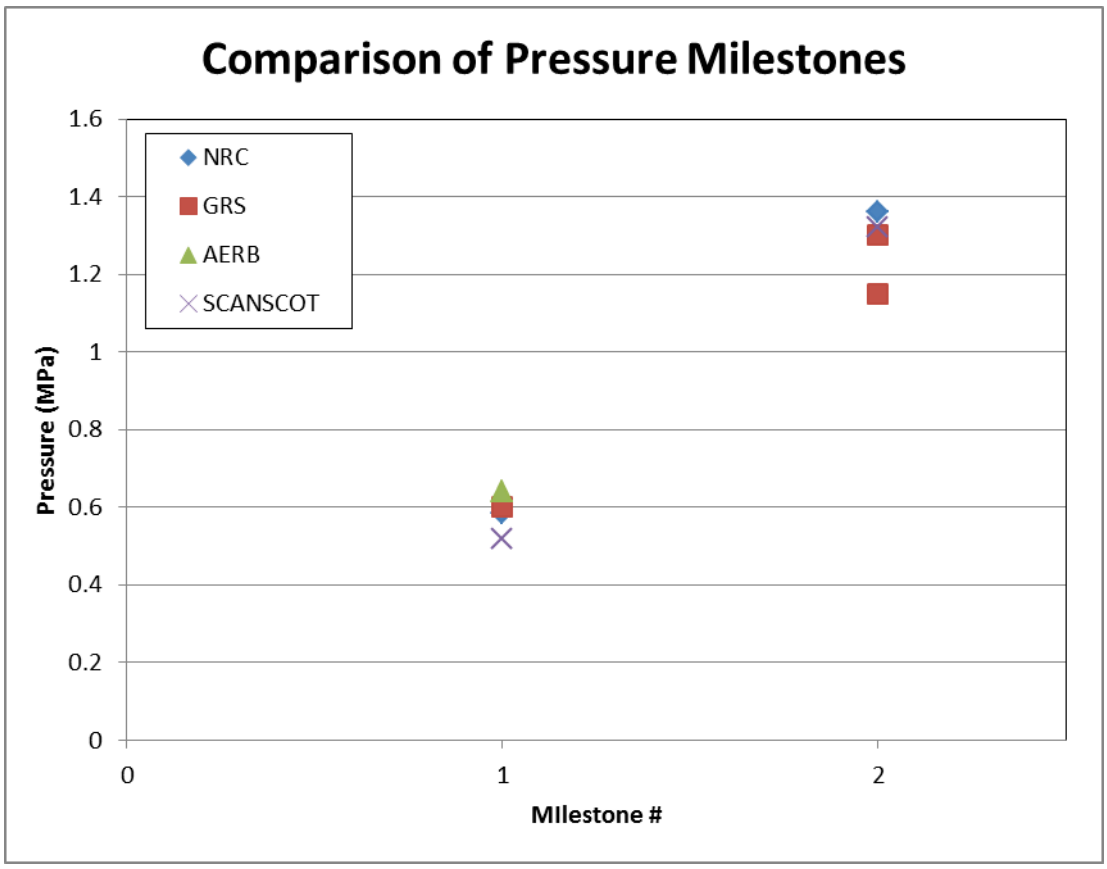

Figure 51: Pressure Milestones for Model 2a

3.4. Deformed Shape

The plots of deformed shape, as provided by each participant, are shown below. The deformed shape plots for Model 2a are shown in Figure 52 through Figure 60. The shape plots demonstrated similar behavior between the participants' Model 2a. The deformed shape plots for Model 2b can be found in Figure 61 through Figure 69 while the deformed shape plots for Model 2c can be found in Figure 70 through Figure 78.

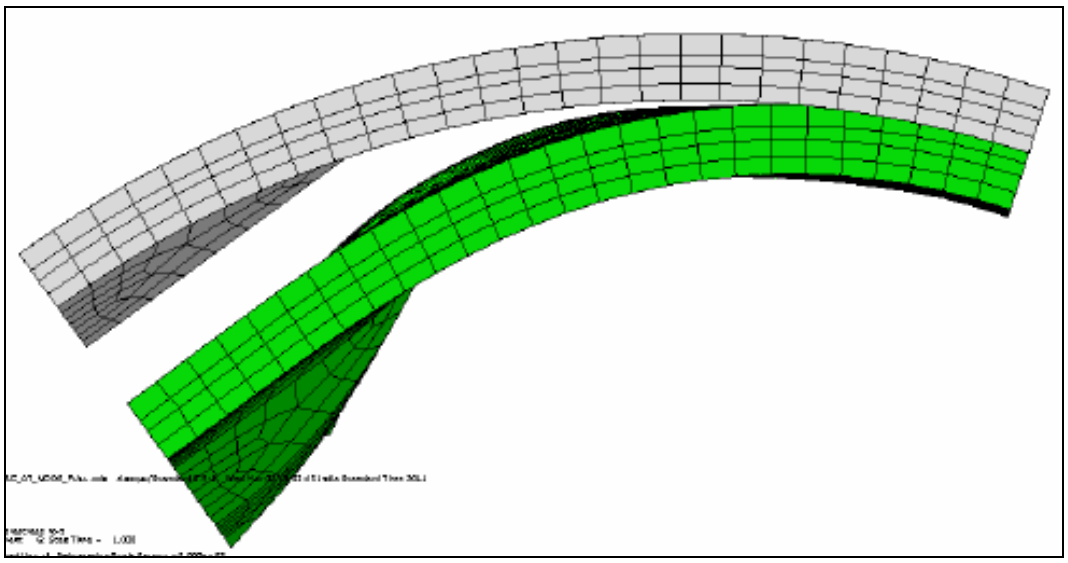

A

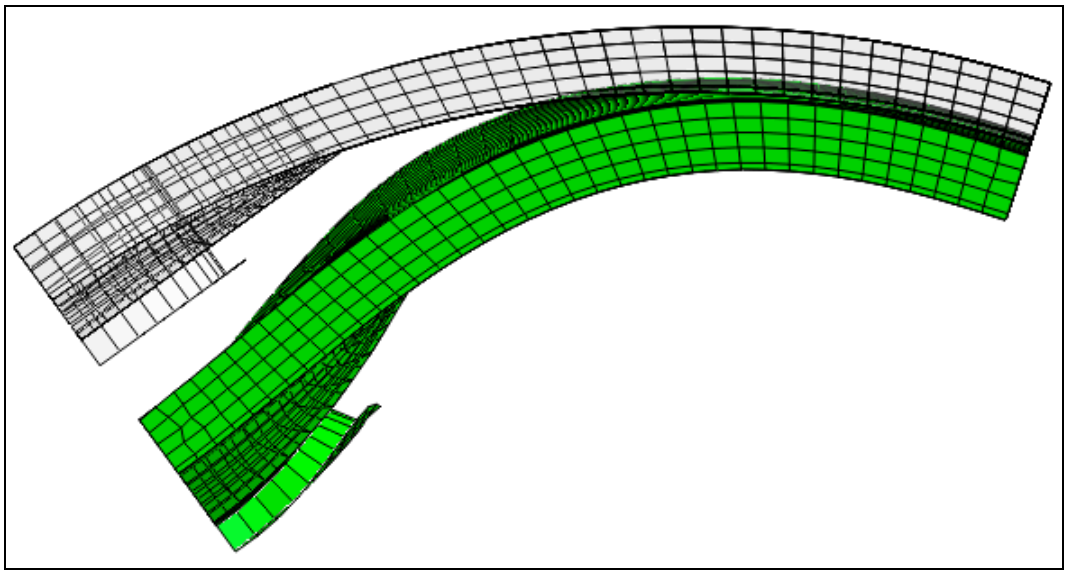

B

Figure 52. Deformed Shape of Model 2a at Anchoring (A) AERB x500 Magnification (B) NRC x500 Magnification

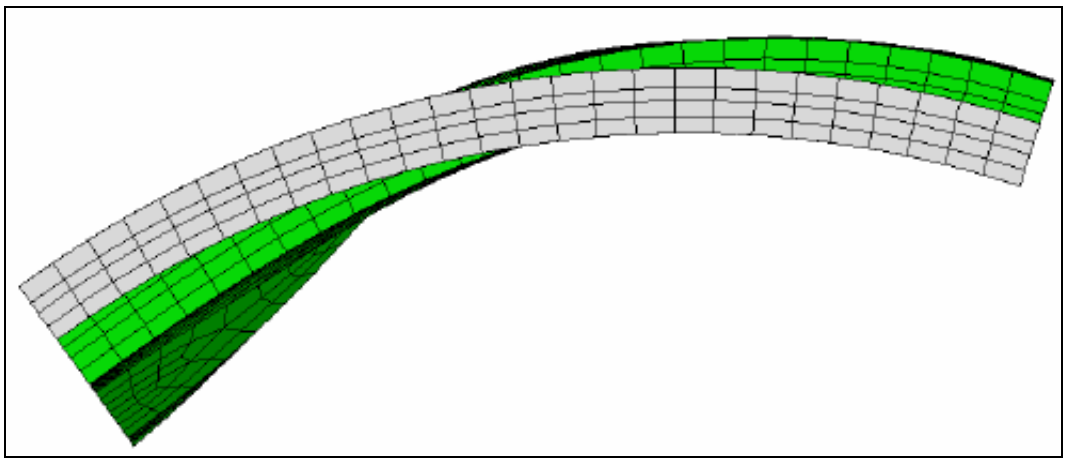

A

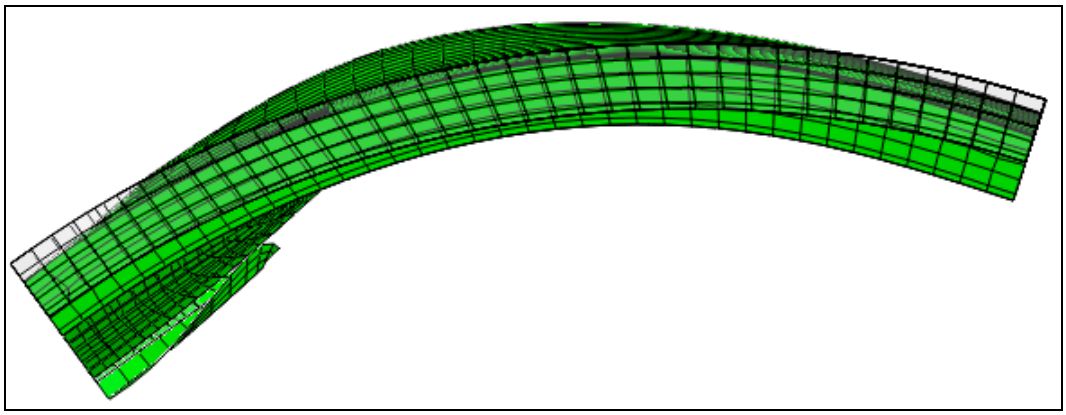

B

Figure 53: Deformed Shape of Model 2a at $1xP_d$ (A) AERB x500 (B) NRC x500

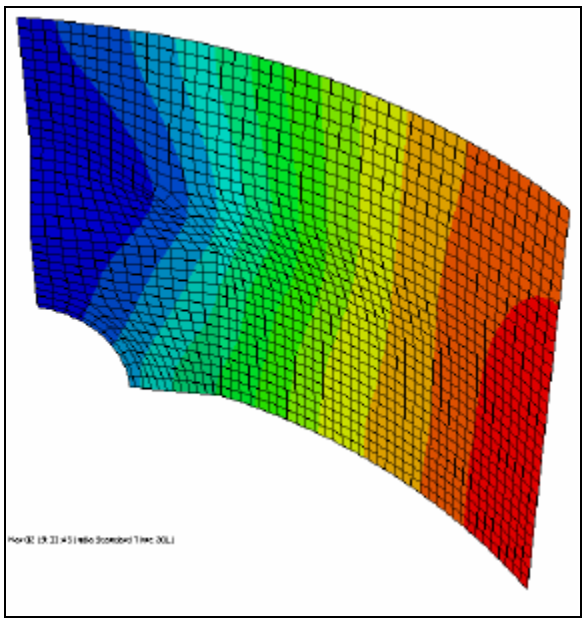

A

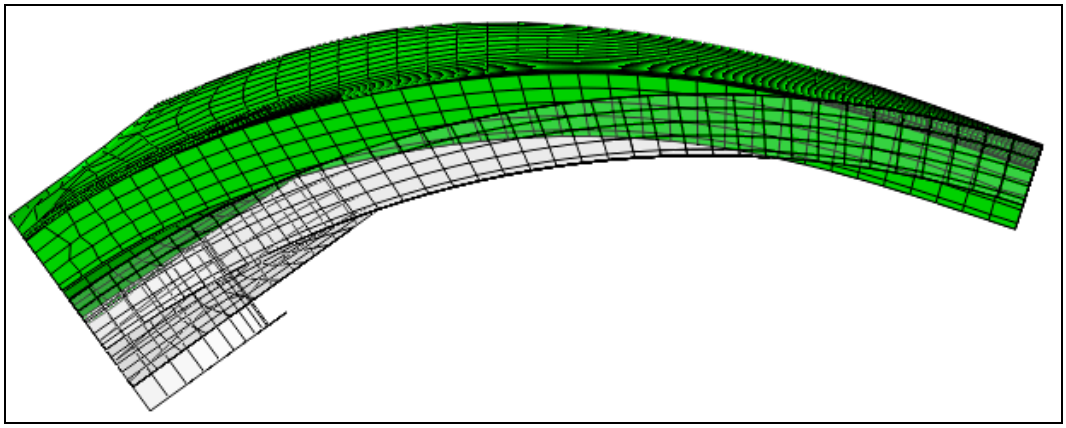

B

Figure 54: Deformed Shape of Model 2a at 1.5xP_d (A) AERB and (B) NRC x500

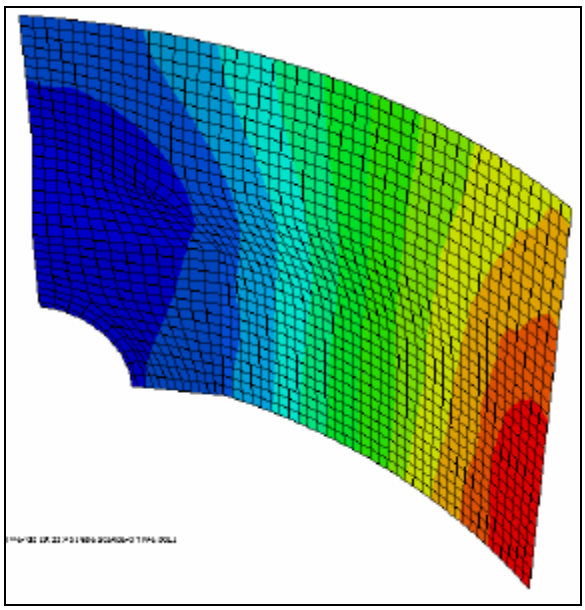

A

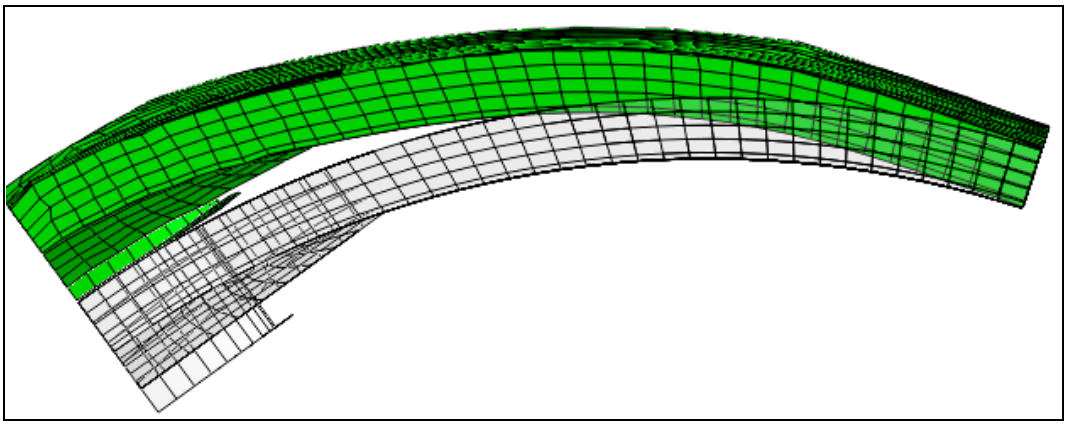

B

Figure 55: Deformed Shape of Model 2a at 2.0xP_d (A) AERB and (B) NRC x100

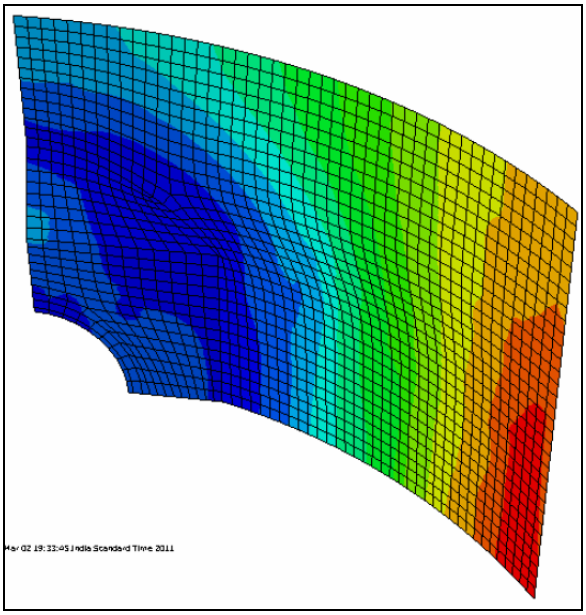

A

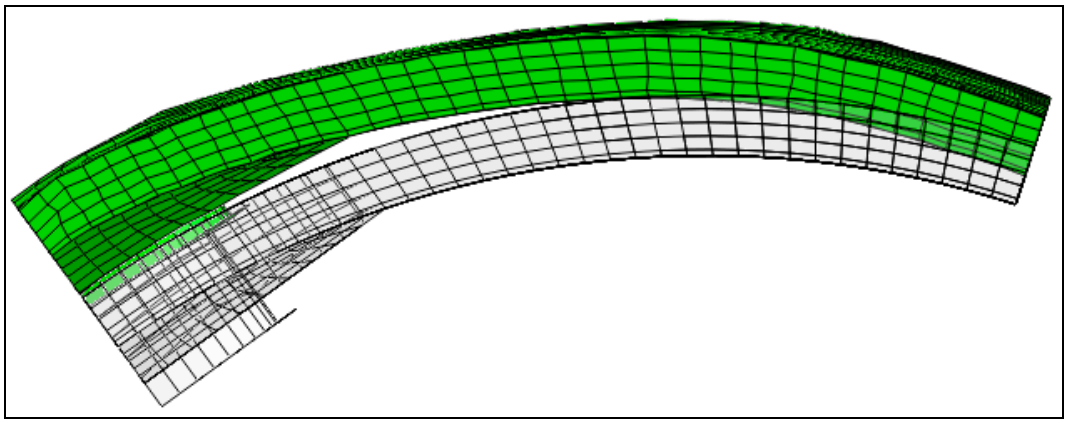

B

Figure 56: Deformed Shape of Model 2a at 2.5xP_d (A) AERB and (B) NRC x50

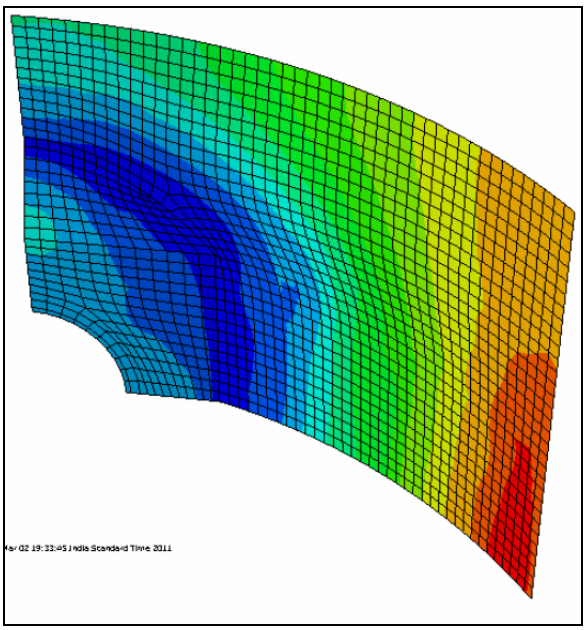

A

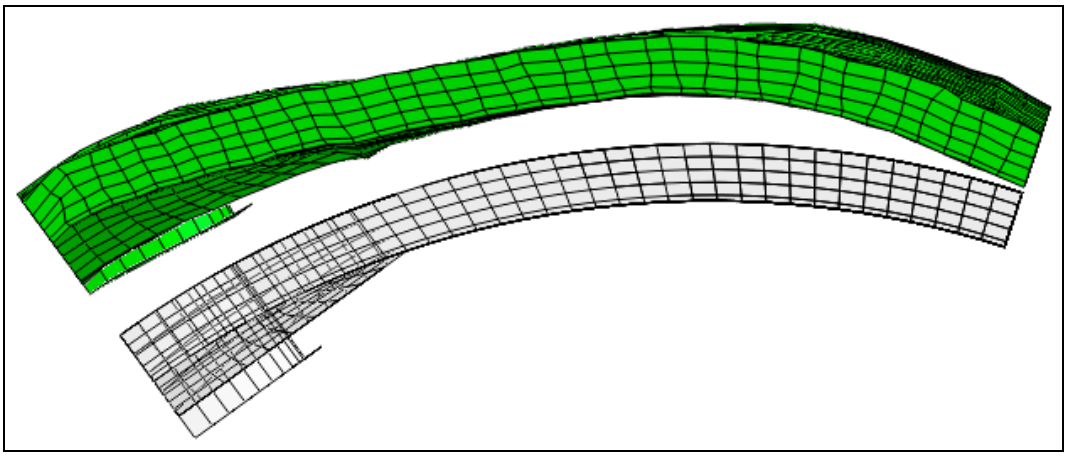

B

Figure 57: Deformed Shape of Model 2a at 3.0xP_d (A) AERB and NRC x50

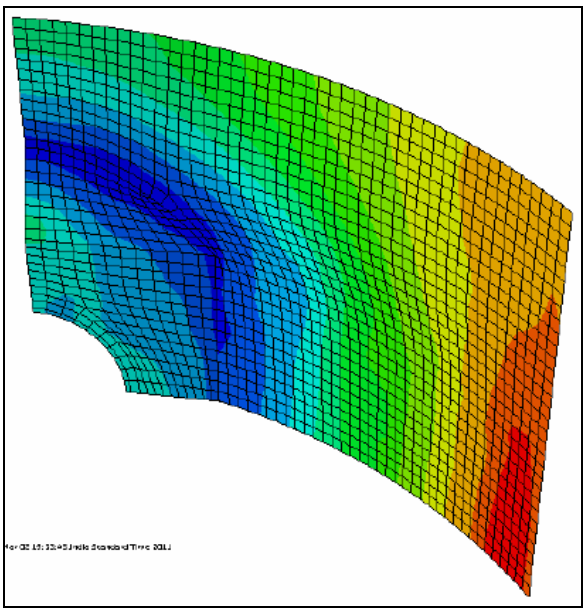

A

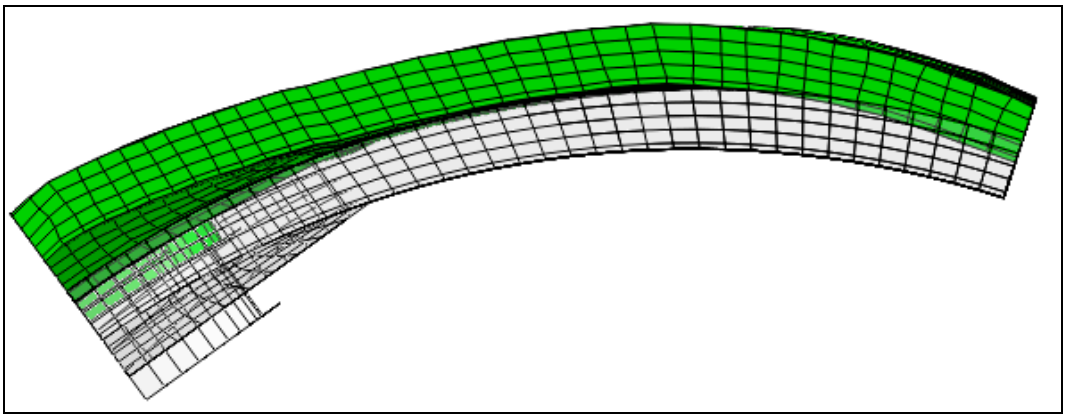

B

Figure 58: Deformed Shape of Model 2a at 3.3xP_d (A) AERB, (B) NRC x20

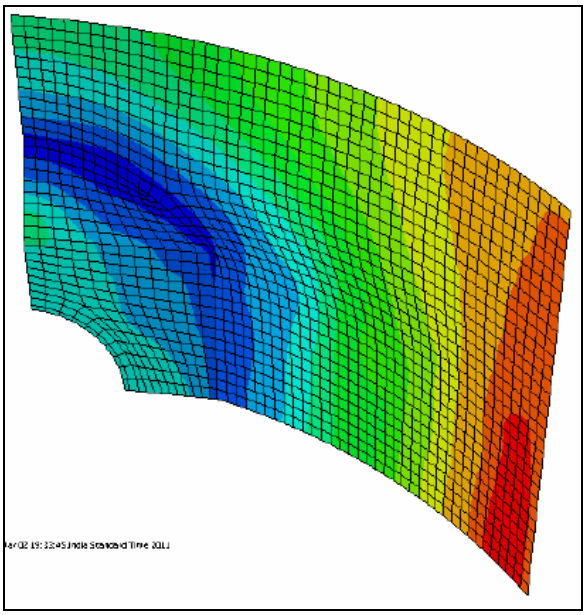

A

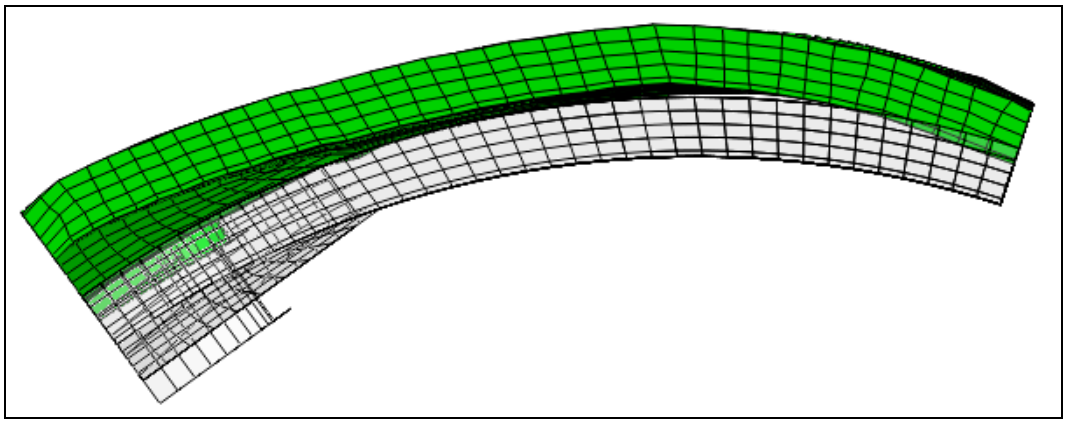

B

Figure 59: Deformed Shape of Model 2a at 3.4xP_d (A) AERB and (B) NRC x20

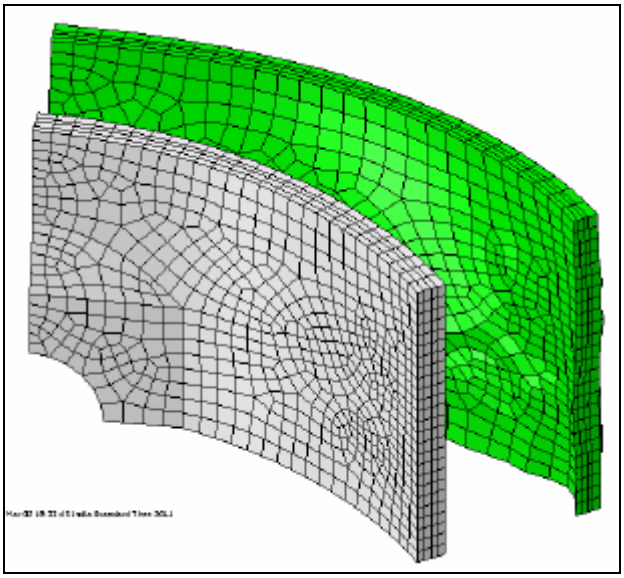

A

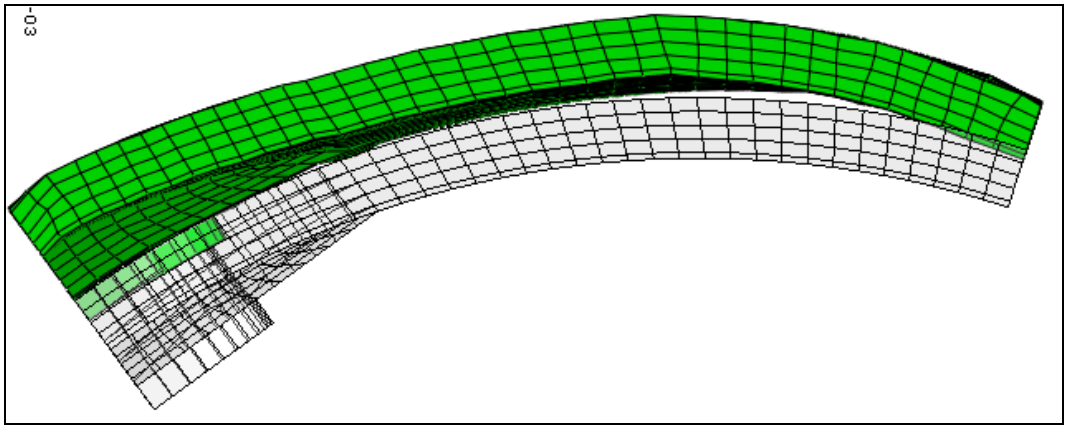

B

Figure 60: Deformed Shape of Model 2a at Ultimate pressure (A) AERB and (B) NRC (3.47 P_d) x500

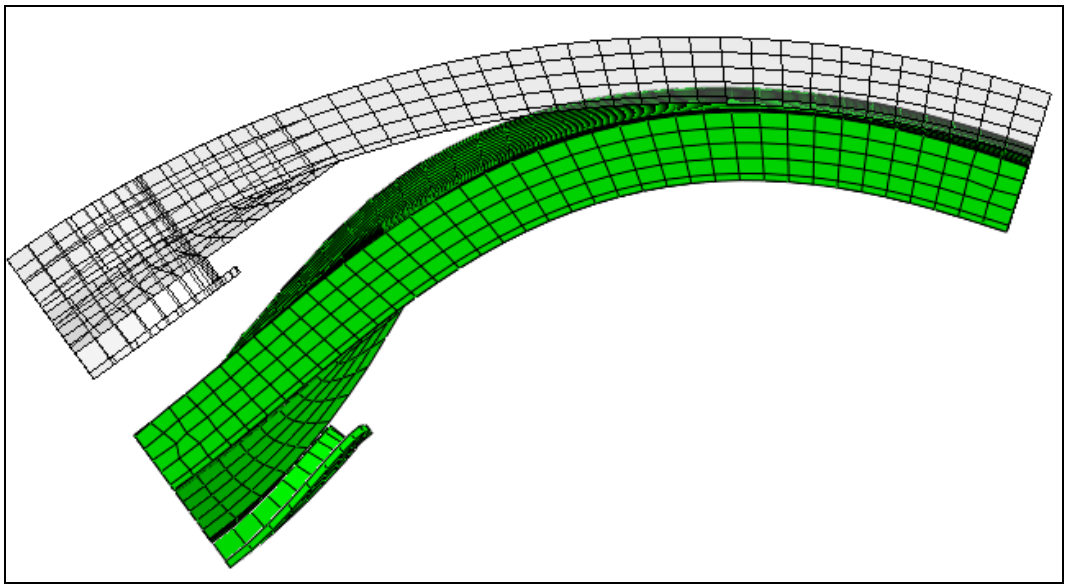

Figure 61. Deformed Shape of Model 2b at Anchoring NRC x500 Magnification

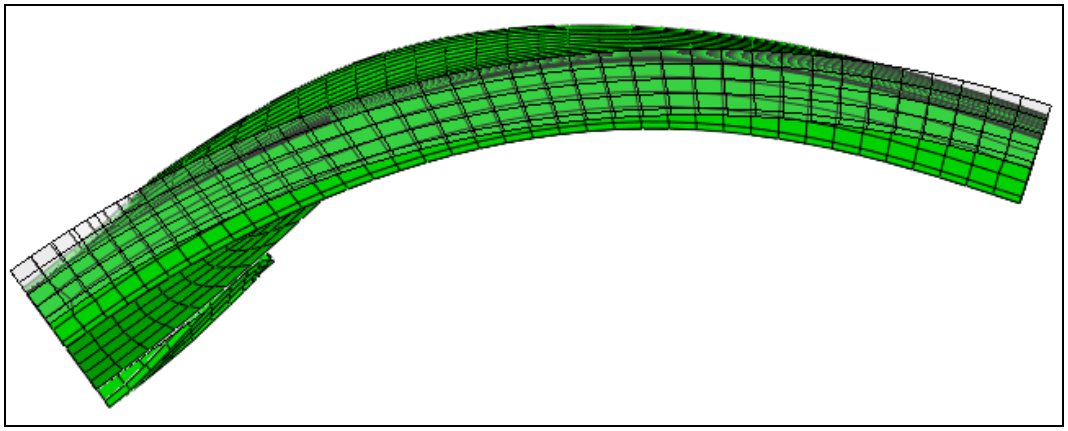

Figure 62: Deformed Shape of Model 2b at 1xP_d NRC x500

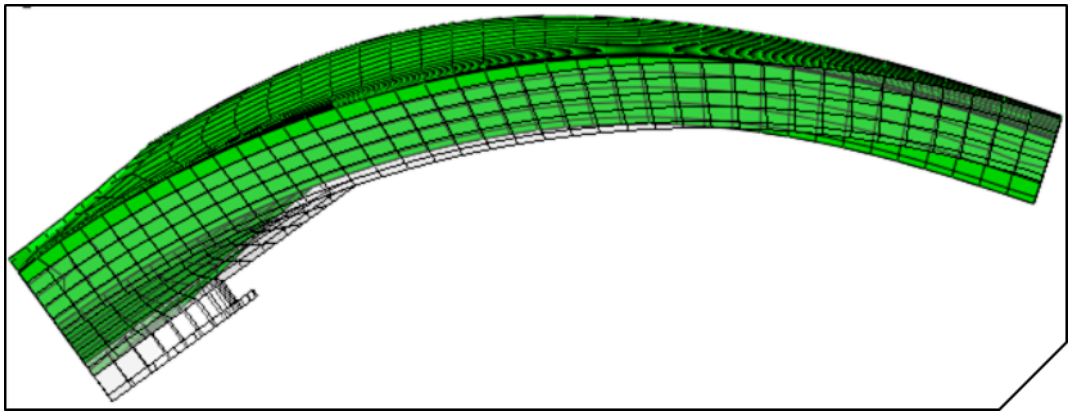

Figure 63: Deformed Shape of Model 2b at 1.5xP_d NRC x500

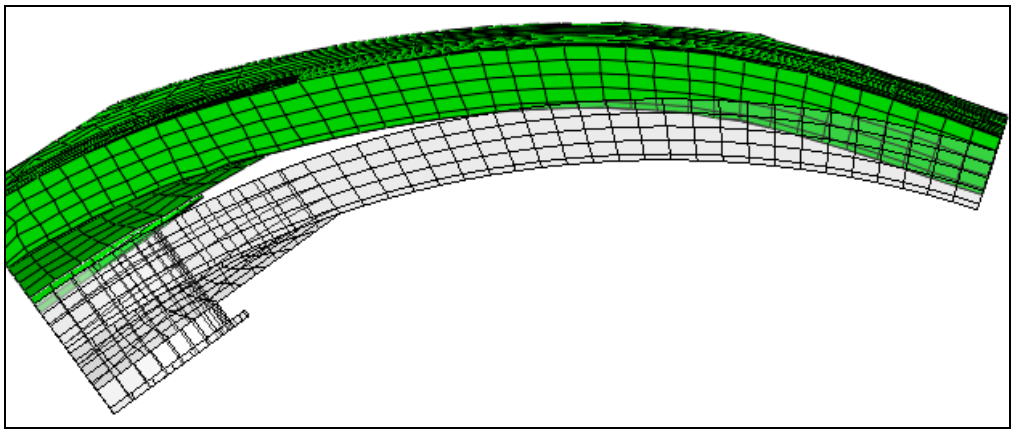

Figure 64: Deformed Shape of Model 2b at 2xP_d NRC x100

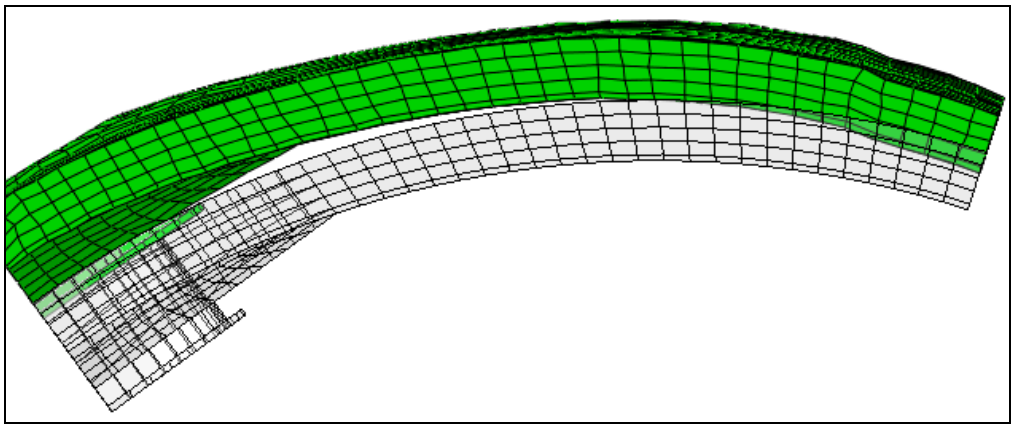

Figure 65: Deformed Shape of Model 2b at 2.5xP_d NRC x50

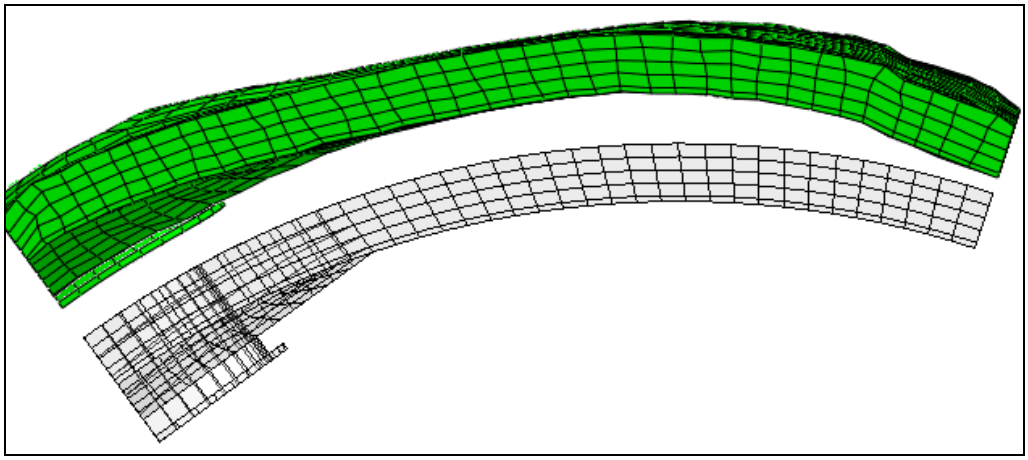

Figure 66: Deformed Shape of Model 2b at 3xP_d NRC x50

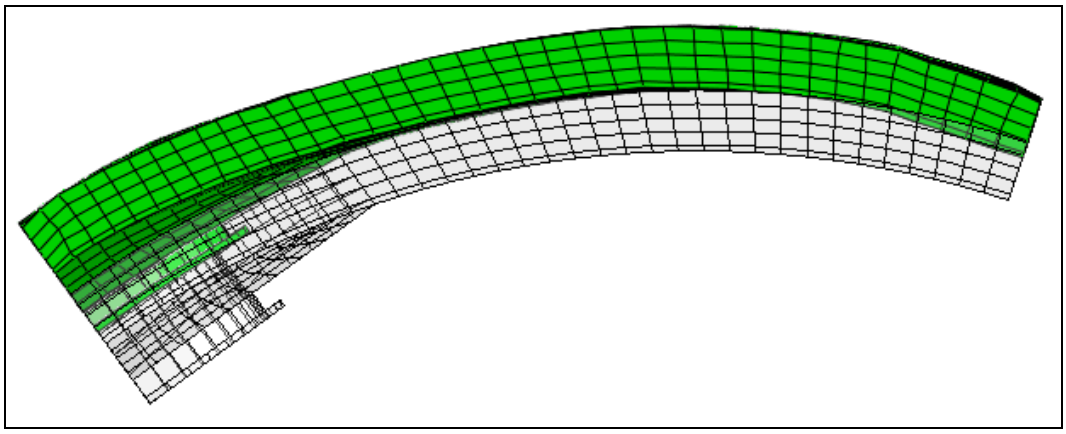

Figure 67: Deformed Shape of Model 2b at 3.3xP_d NRC x20

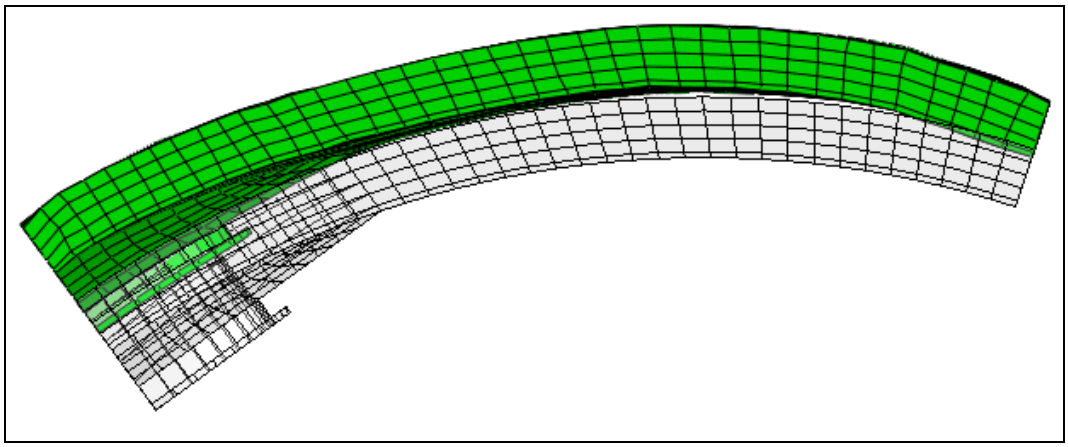

Figure 68: Deformed Shape of Model 2b at 3.4xP_d NRC x20

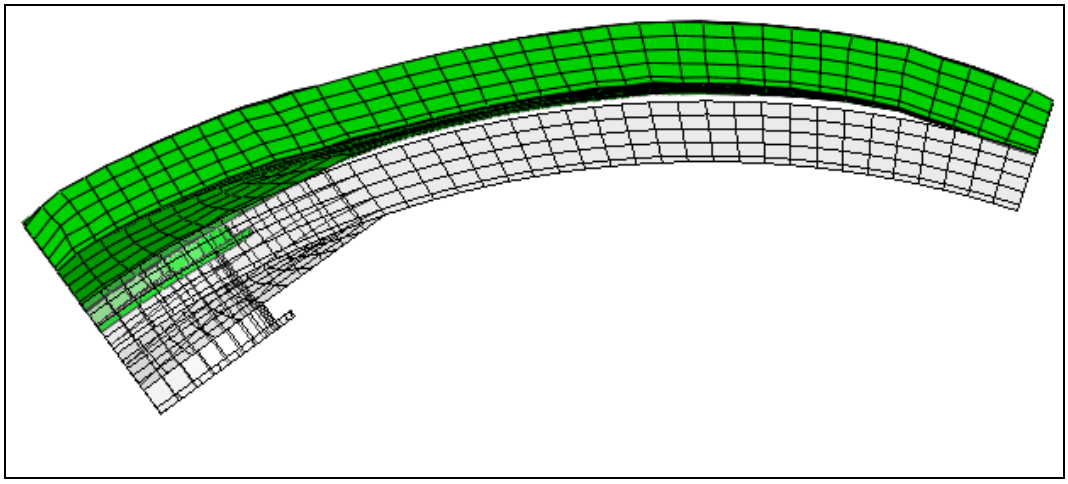

Figure 69: Deformed Shape of Model 2b at Ultimate Pressure (3.47 P_d) NRC x20

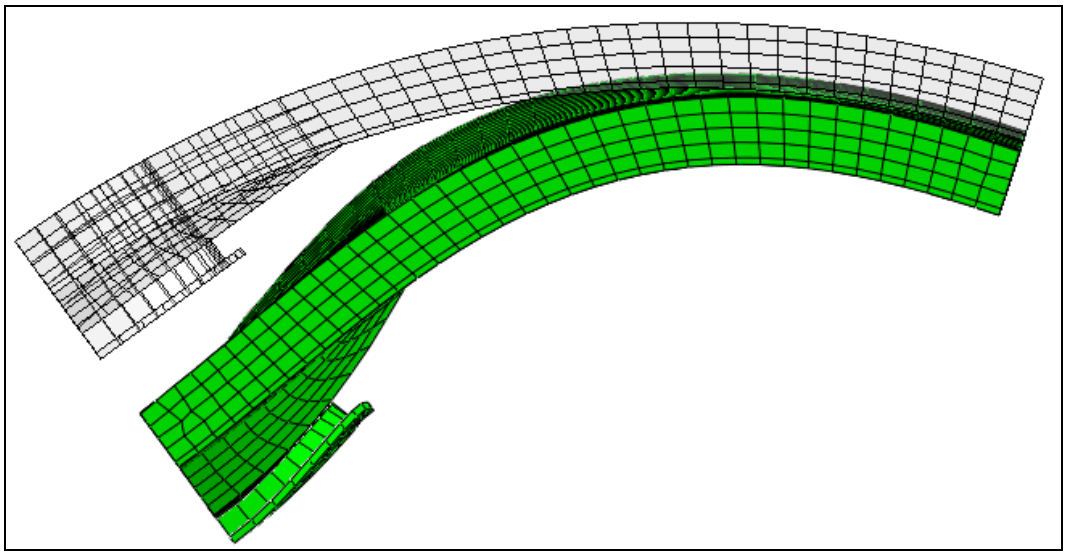

Figure 70. Deformed Shape of Model 2c at Anchoring NRC x500 Magnification

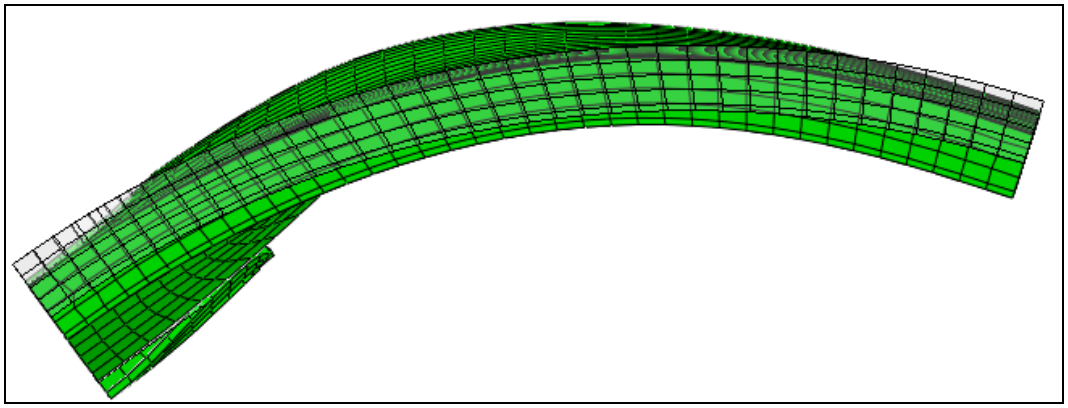

Figure 71: Deformed Shape of Model 2c at 1xP_d NRC x500

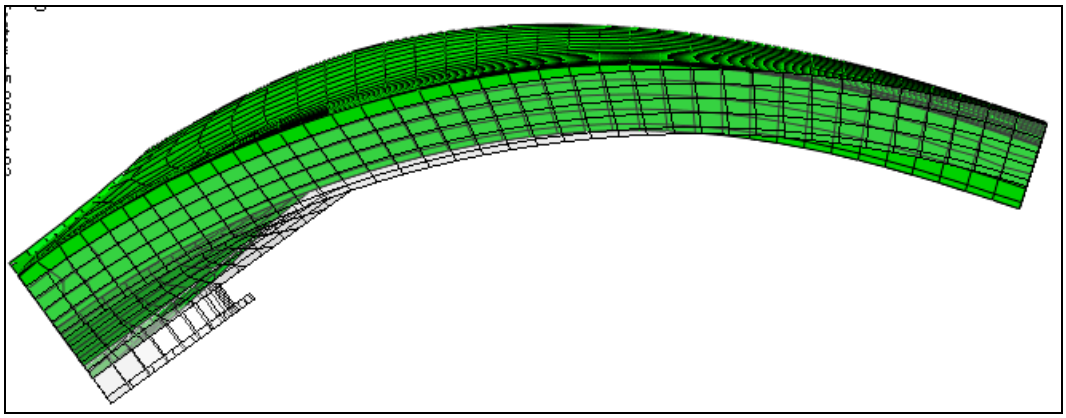

Figure 72: Deformed Shape of Model 2c at 2xP_d NRC x500

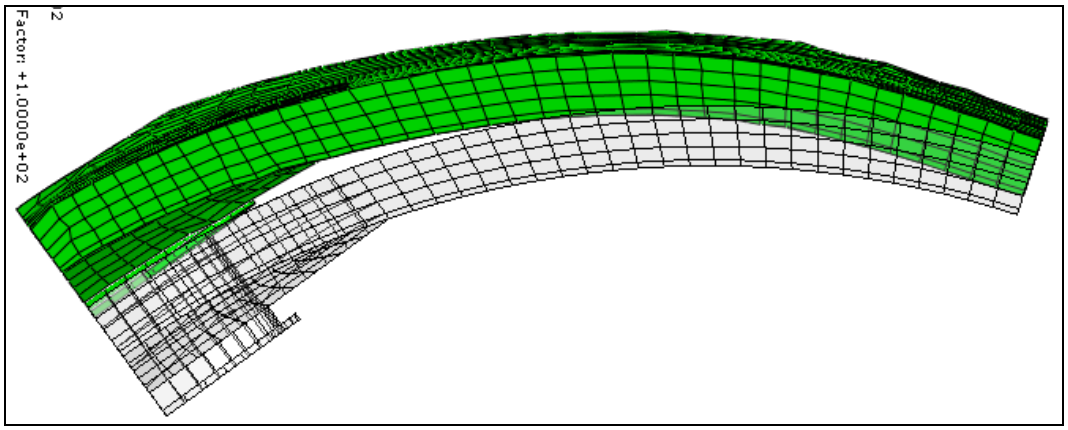

Figure 73: Deformed Shape of Model 2c at 2xP_d NRC x100

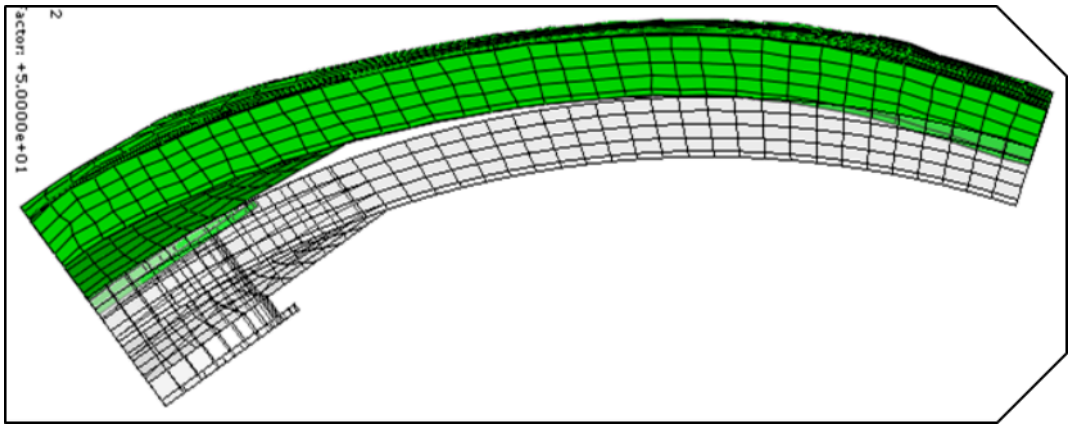

Figure 74: Deformed Shape of Model 2c at 2.5xP_d NRC x50

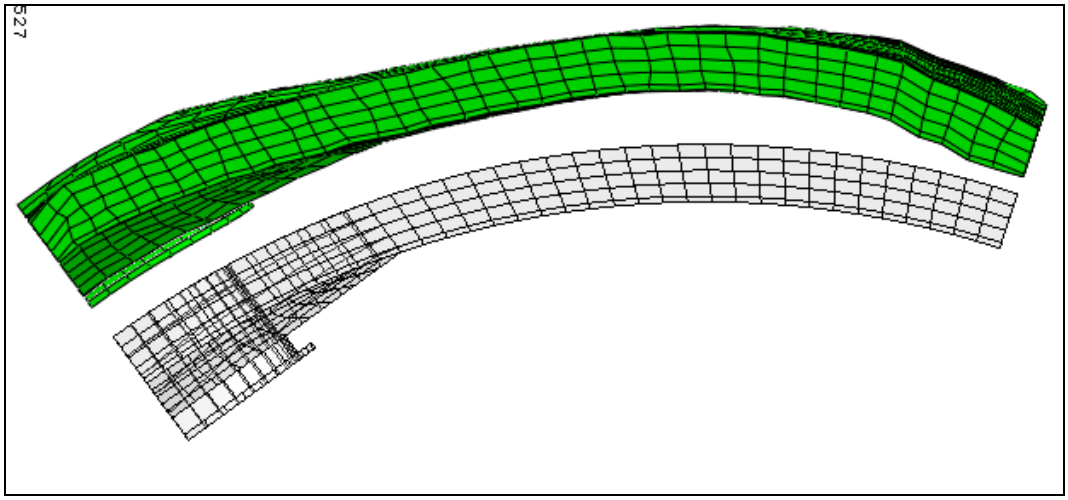

Figure 75: Deformed Shape of Model 2c at 3xP_d NRC x50

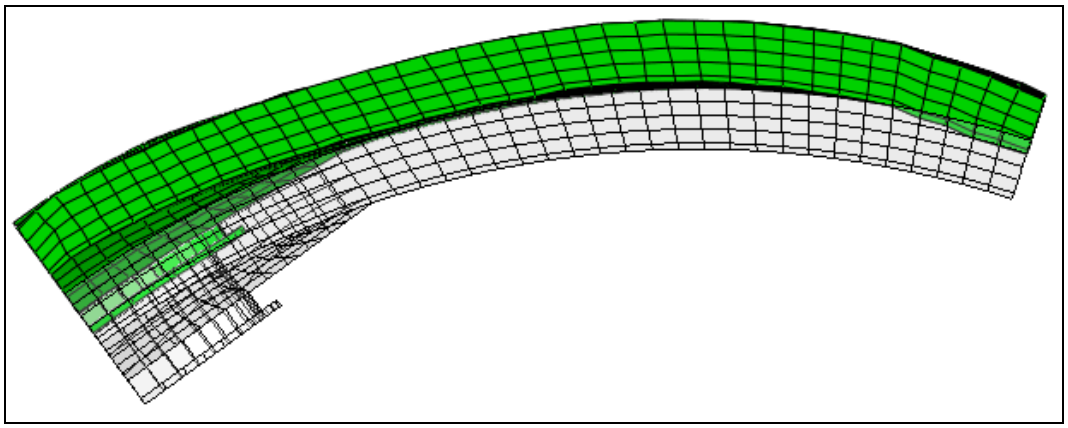

Figure 76: Deformed Shape of Model 2c at 3.3xP_d NRC x20

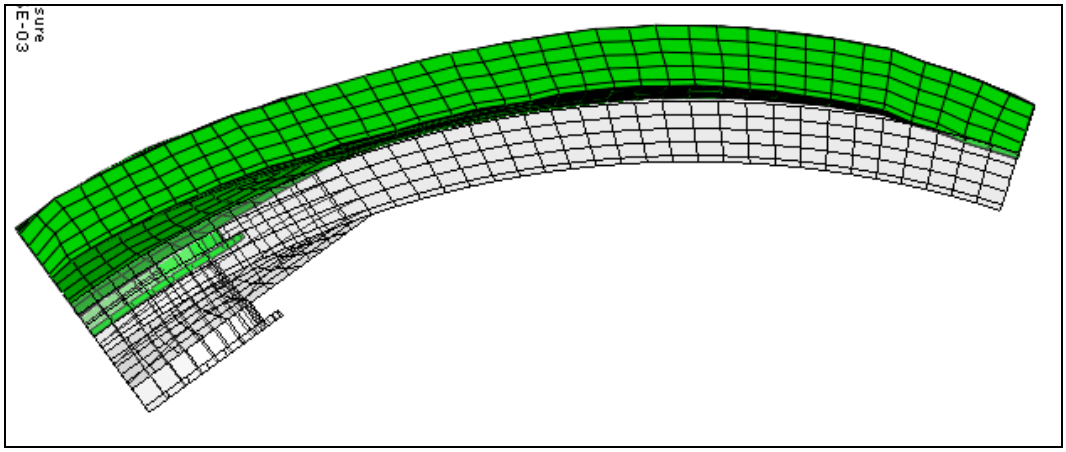

Figure 77: Deformed Shape of Model 2c at 3.4xP_d NRC x20

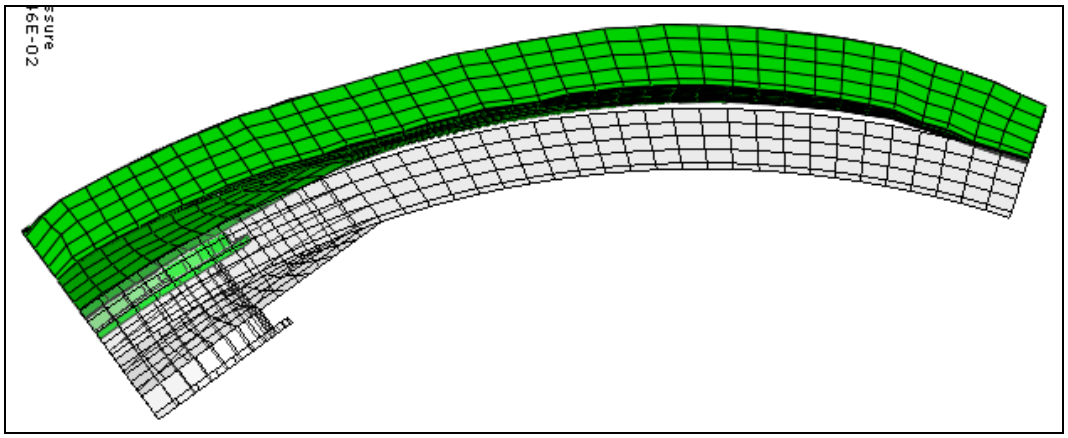

Figure 78: Deformed Shape of Model 2c at Ultimate (3.47 P_d) NRC x50

3.5. Liner Strain Distribution

The participants were requested to provide liner strain magnitudes and locations for Model 2. The participants chose to provide this information in the form of contour plots outputted from the FEA software. The liner strain contour plots from the participants can be found in Figure 79 through Figure 105.

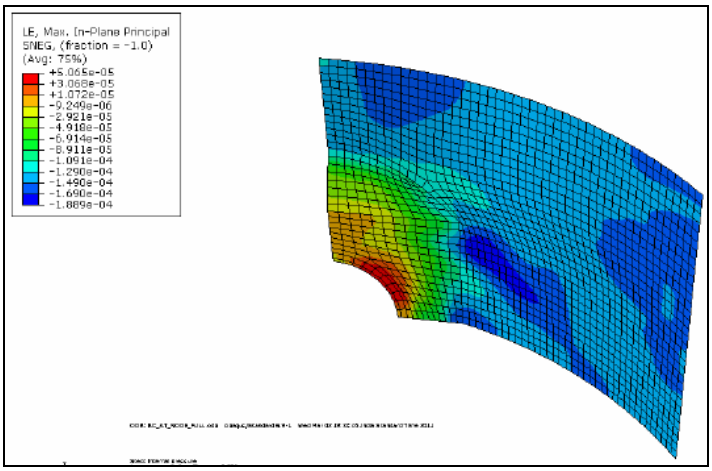

A

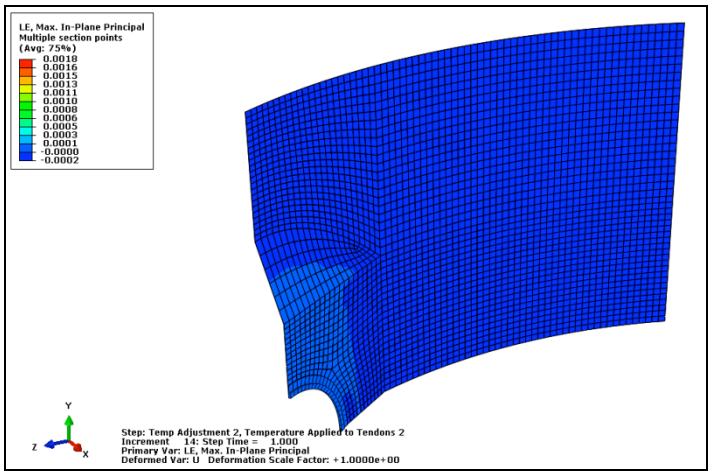

B

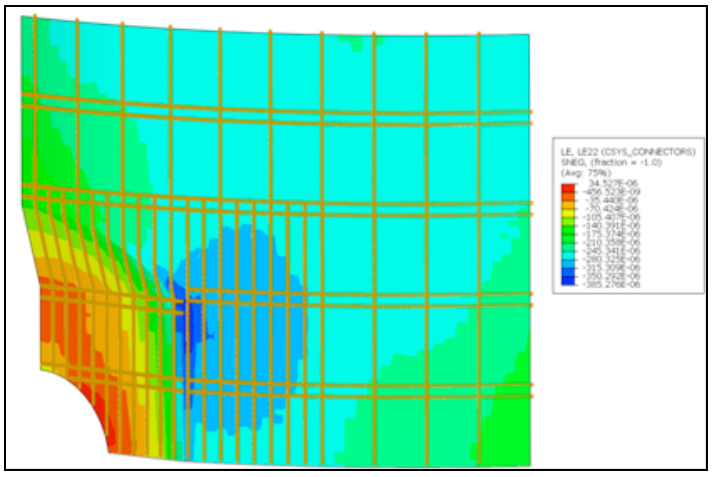

C

Figure 79: Model 2a Liner Strain at Anchor (A) AERB (B) NRC (C) SCANSCOT

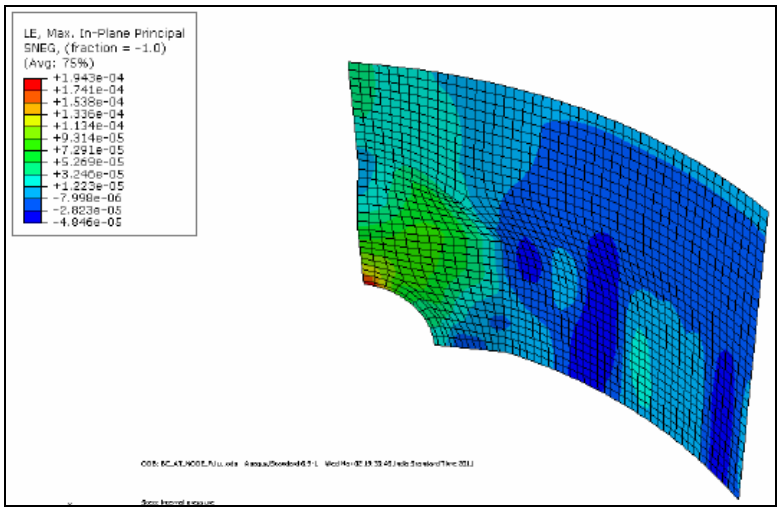

A

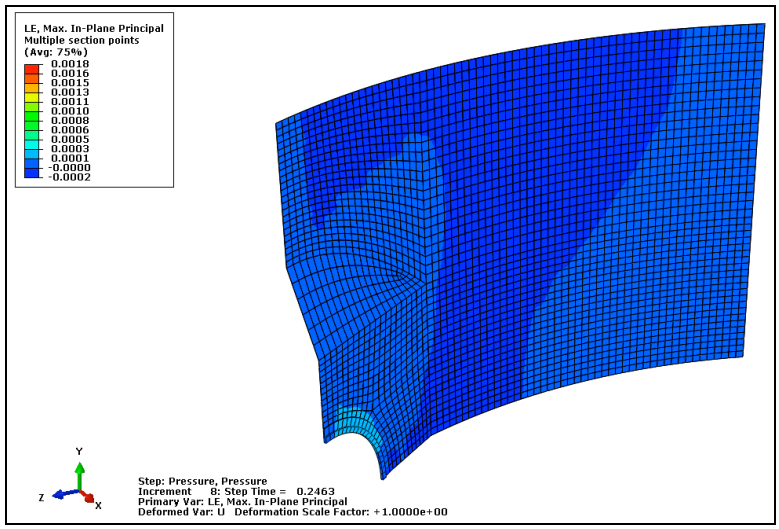

B

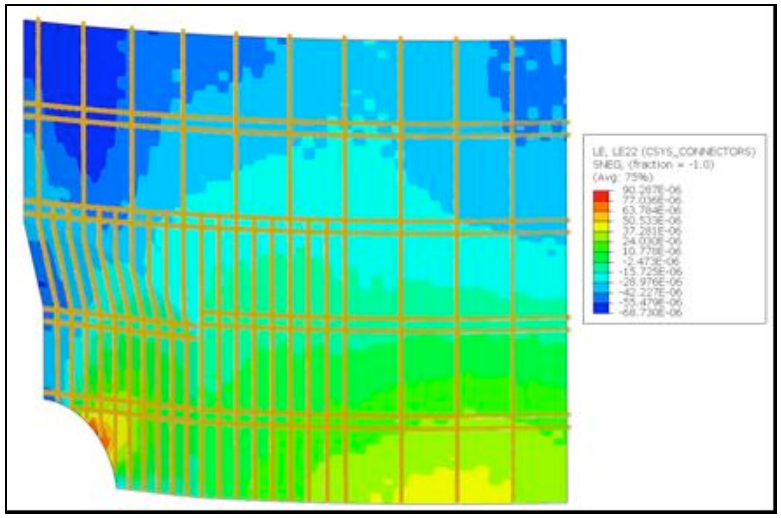

C

Figure 80: Model 2a Liner Strain at 1xP_d (A) AERB (B) NRC (C) SCANSCOT

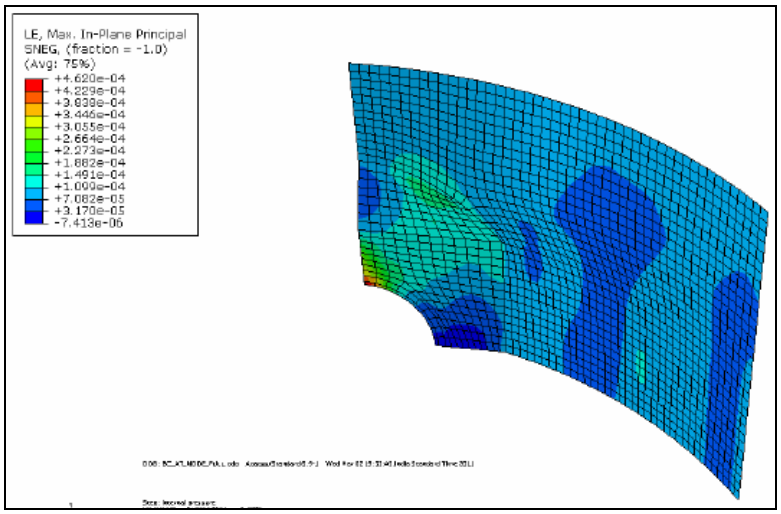

A

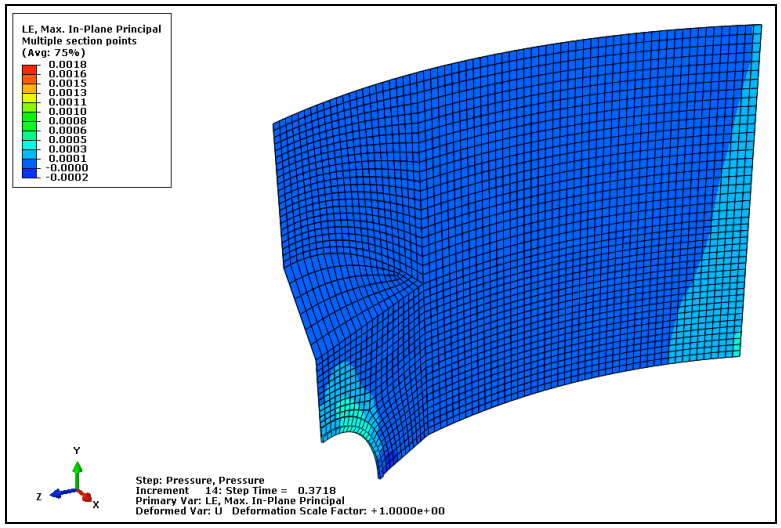

B

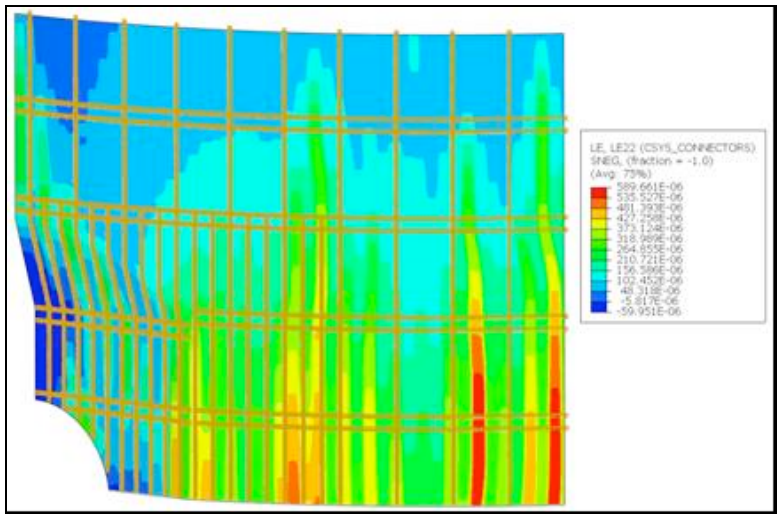

C

Figure 81: Model 2a Liner Strain at 1.5xP_d (A) AERB (B) NRC (C) SCANSCOT

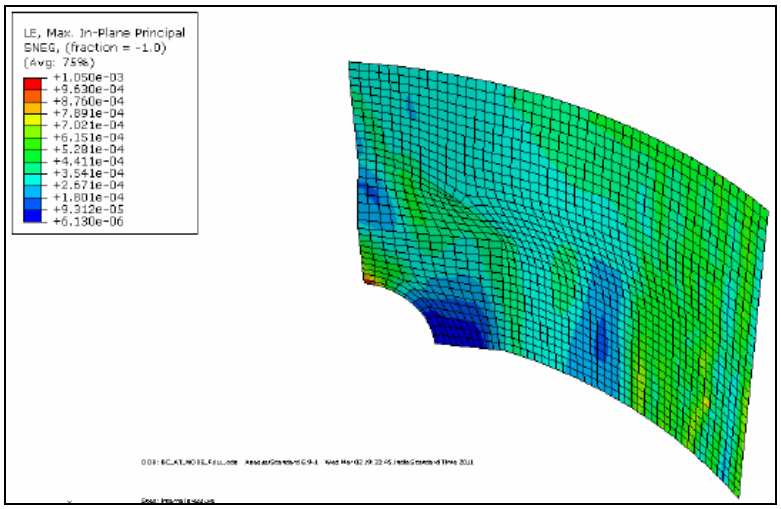

A

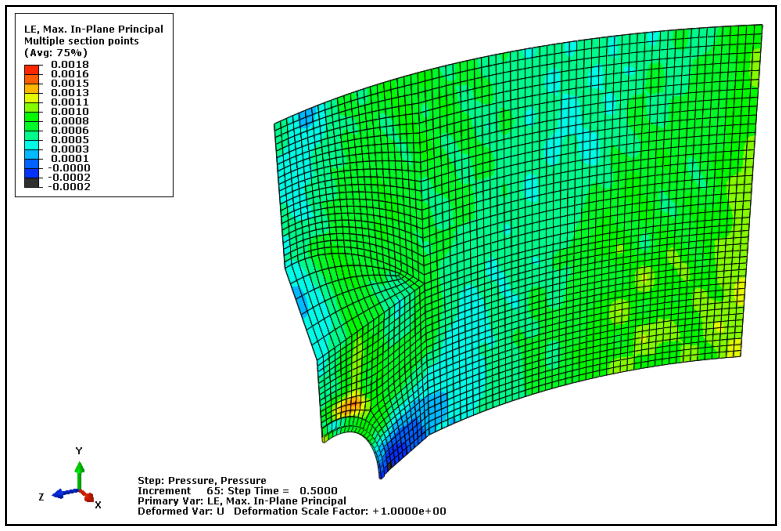

B

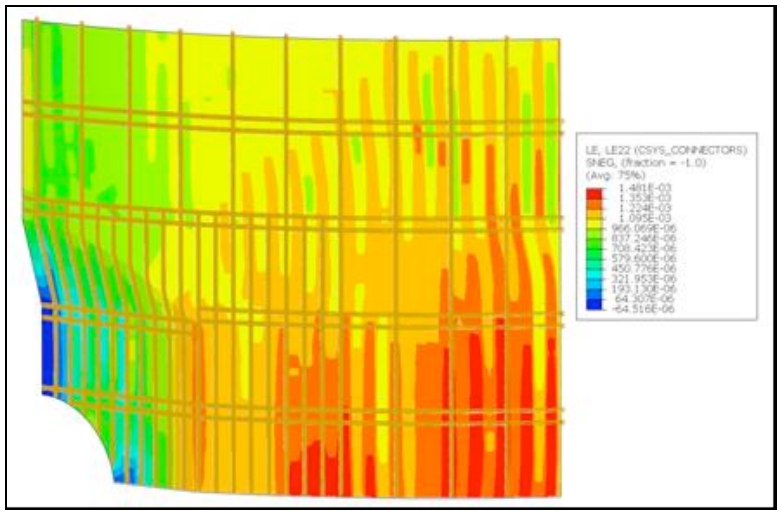

C

Figure 82: Model 2a Liner Strain at 2xP_d (A) AERB (B) NRC (C) SCANSCOT

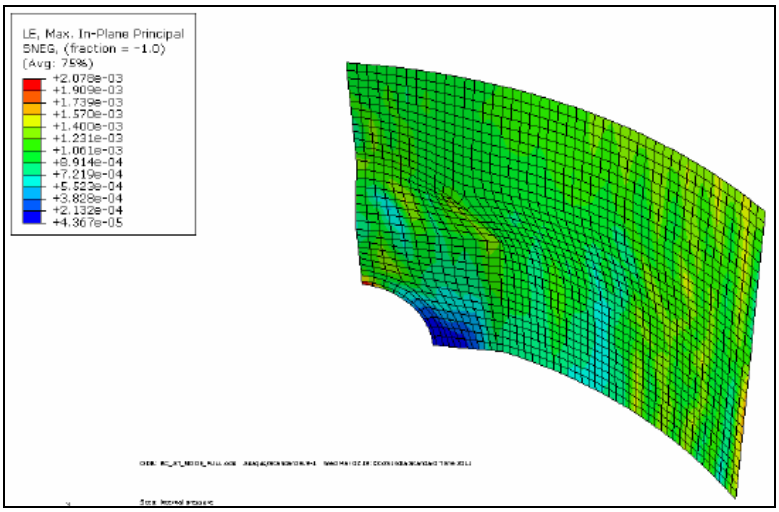

A

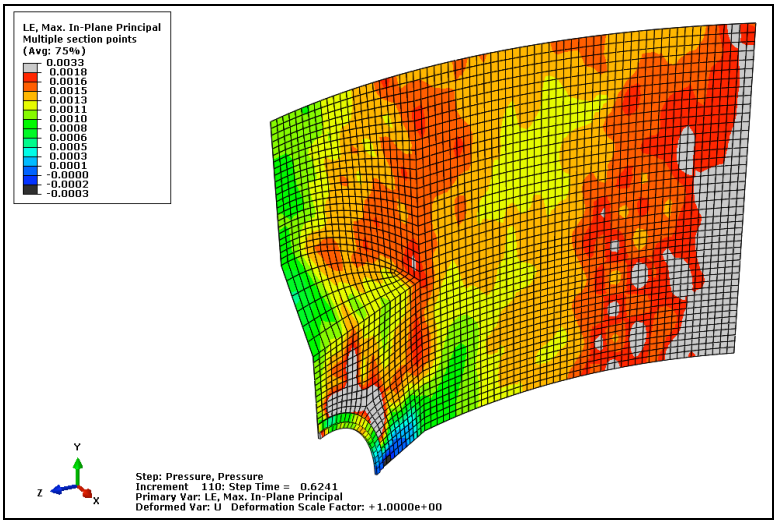

B

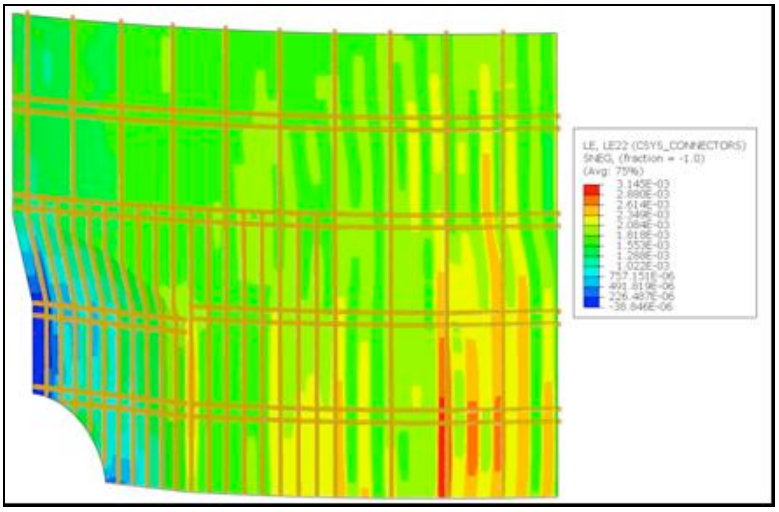

C

Figure 83: Model 2a Liner Strain at 2.5xP_d (A) AERB (B) NRC (C) SCANSCOT

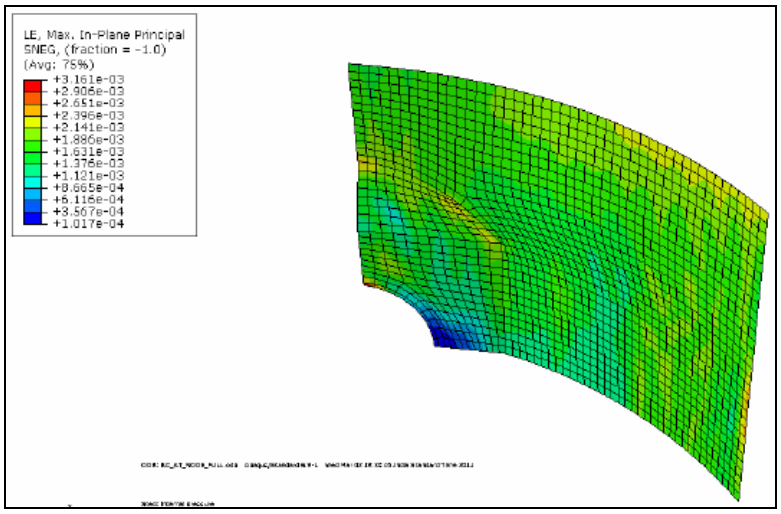

A

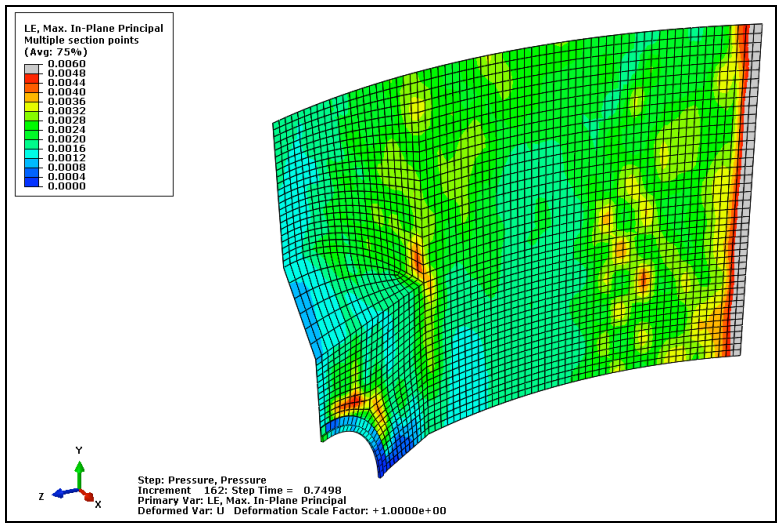

B

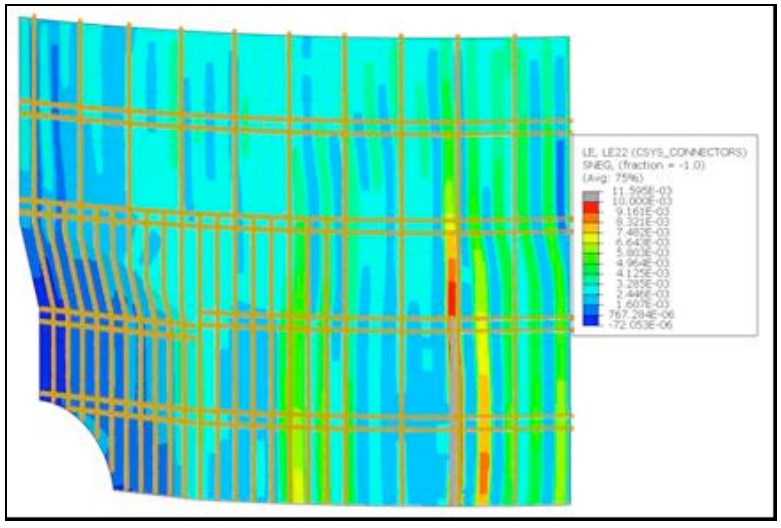

C

Figure 84: Model 2a Liner Strain at 3xP_d (A) AERB (B) NRC (C) SCANSCOT

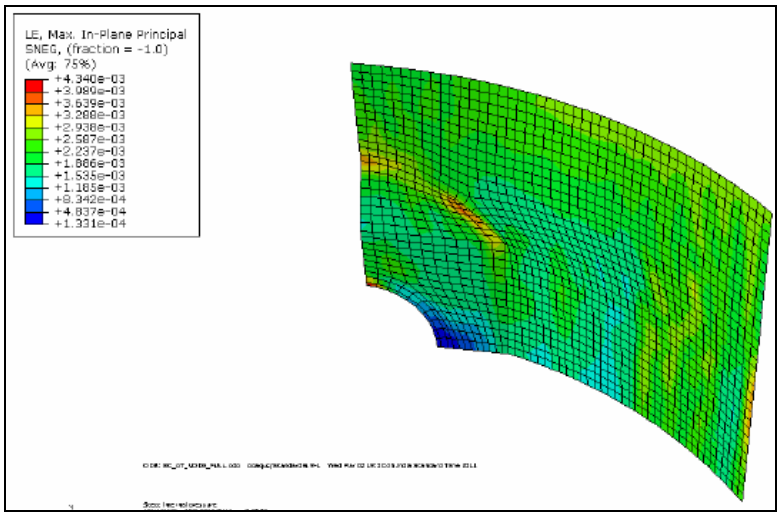

A

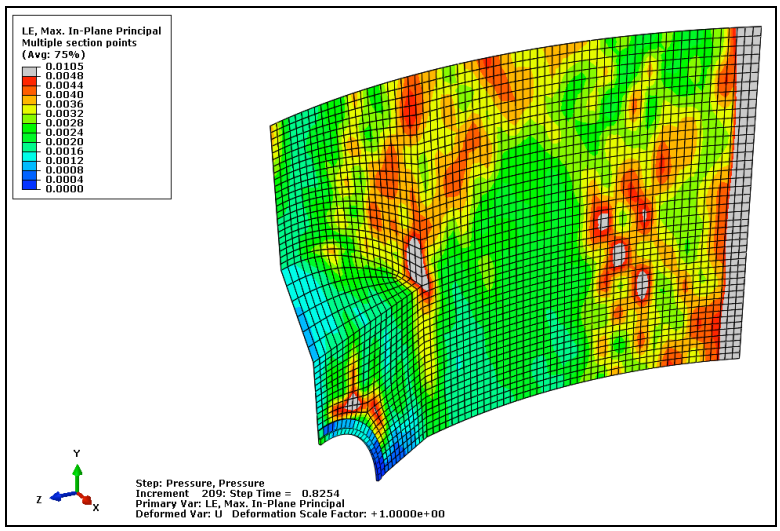

B

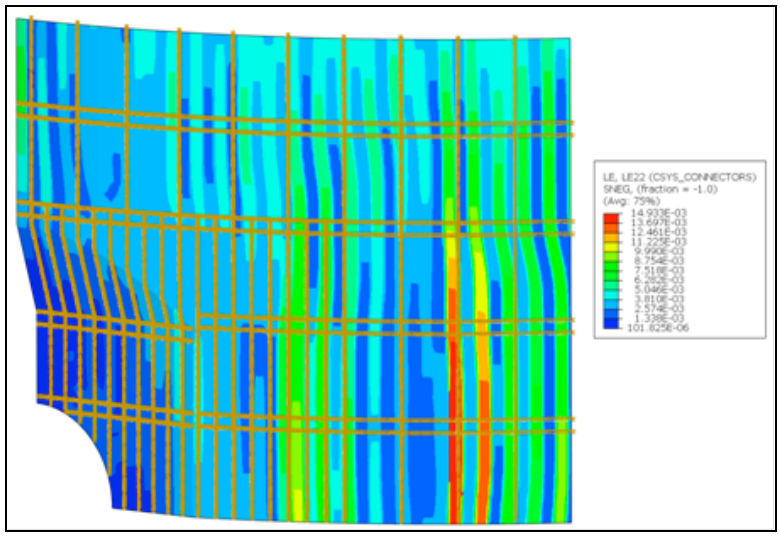

C

Figure 85: Model 2a Liner Strain at 3.3xP_d (A) AERB (B) NRC (C) SCANSCOT

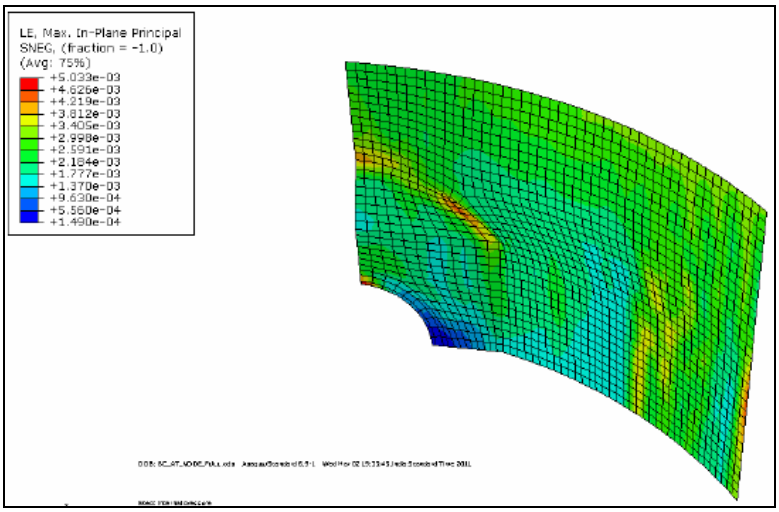

A

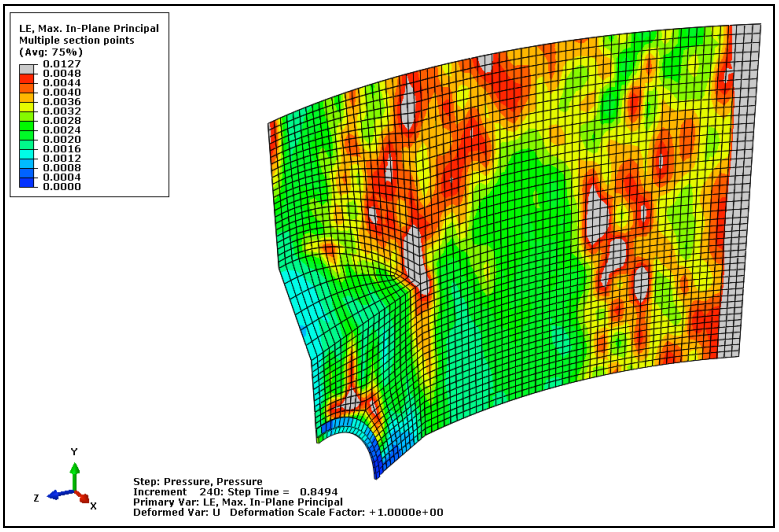

B

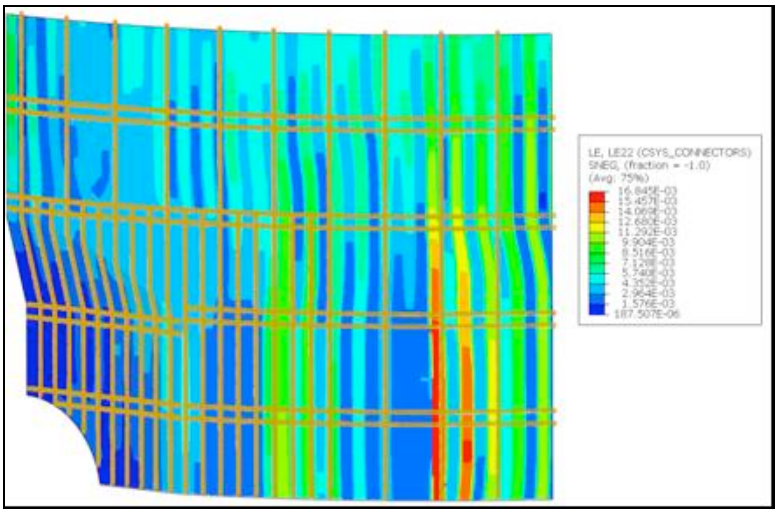

C

Figure 86: Model 2a Liner Strain at 3.4xP_d (A) AERB (B) NRC (C) SCANSCOT

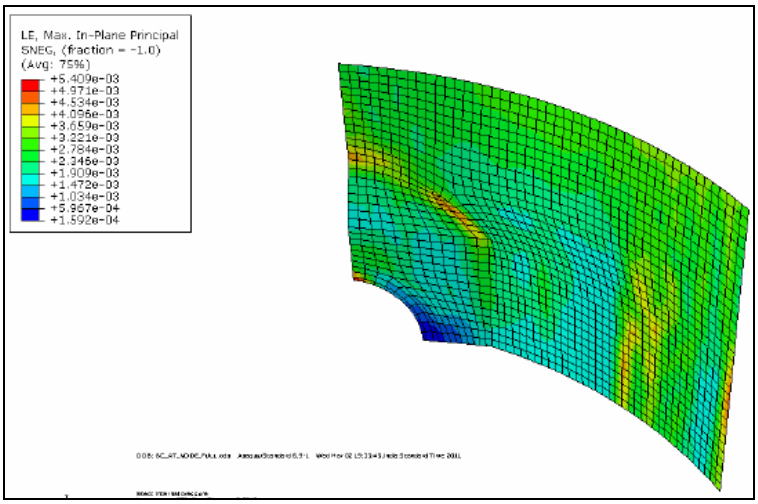

A

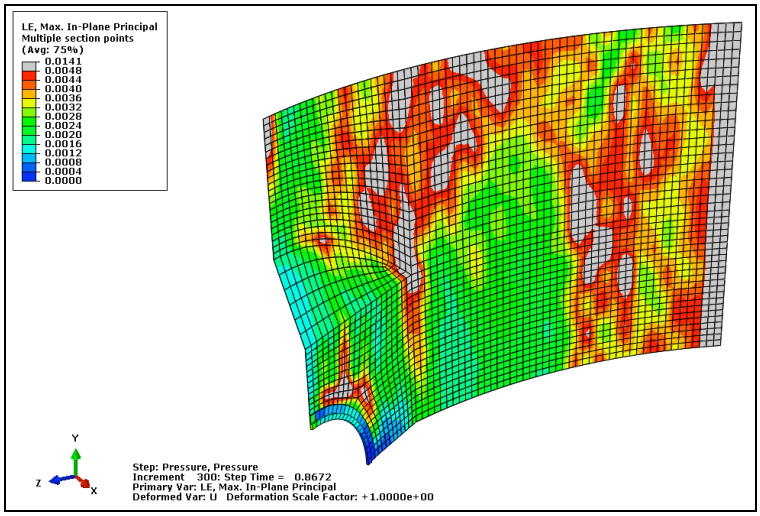

B

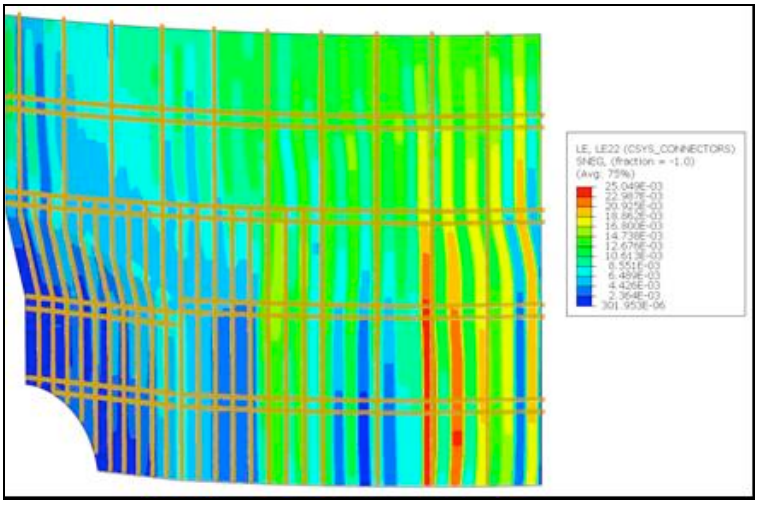

C

Figure 87: Model 2a Liner Strain at Ultimate Pressure (A) AERB (B) NRC (3.47xP_d) (C) SCANSCOT (3.62xP_d)

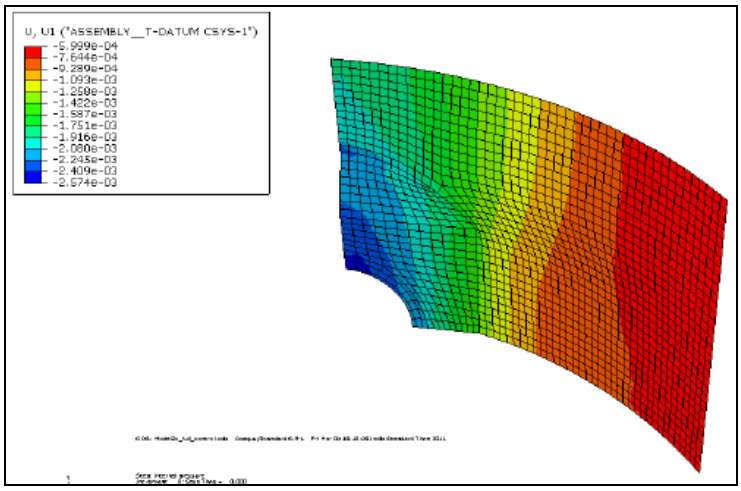

A

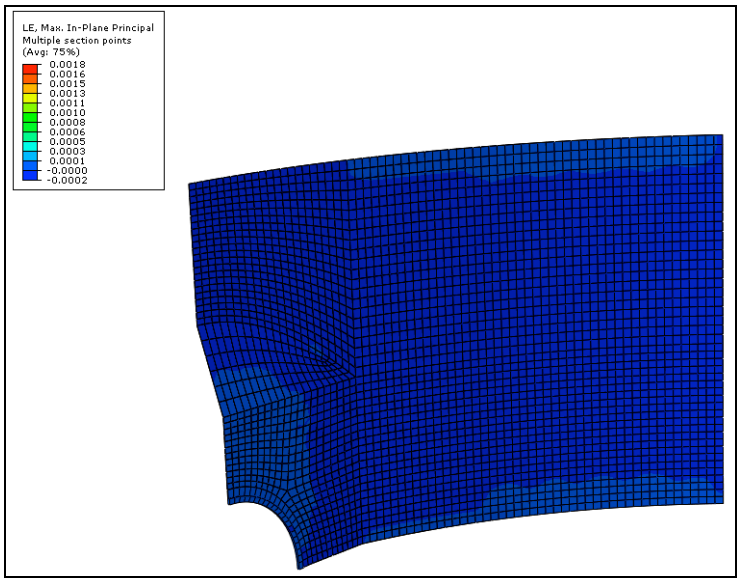

B

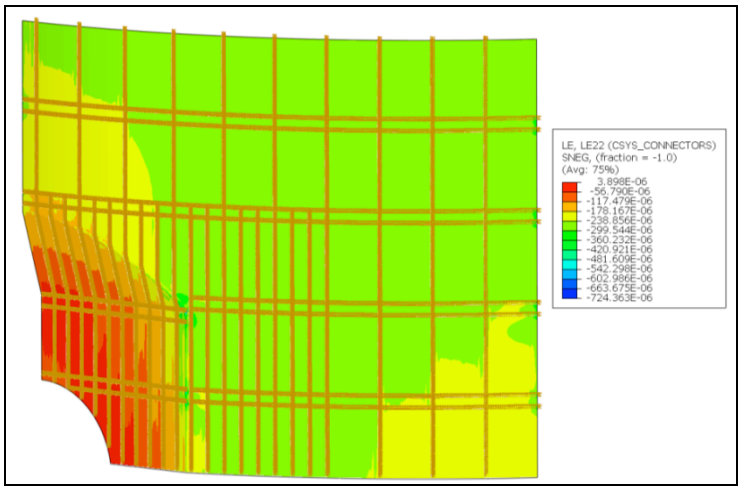

C

Figure 88: Model 2b Liner Strain at Anchor (A) AERB (B) NRC (C) SCANSCOT

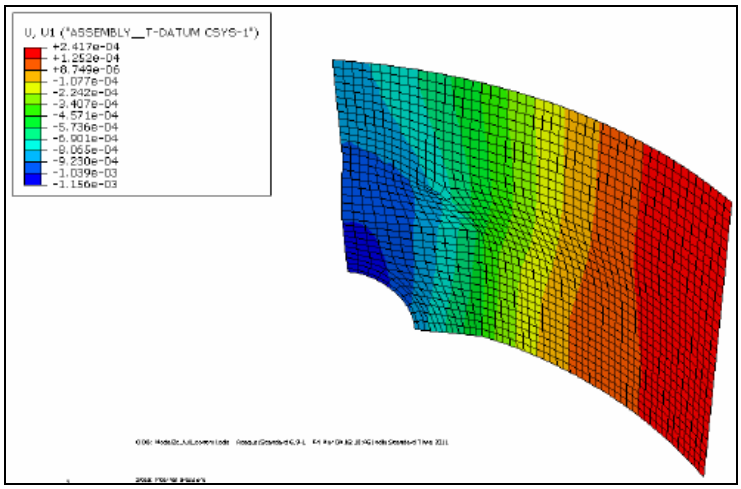

A

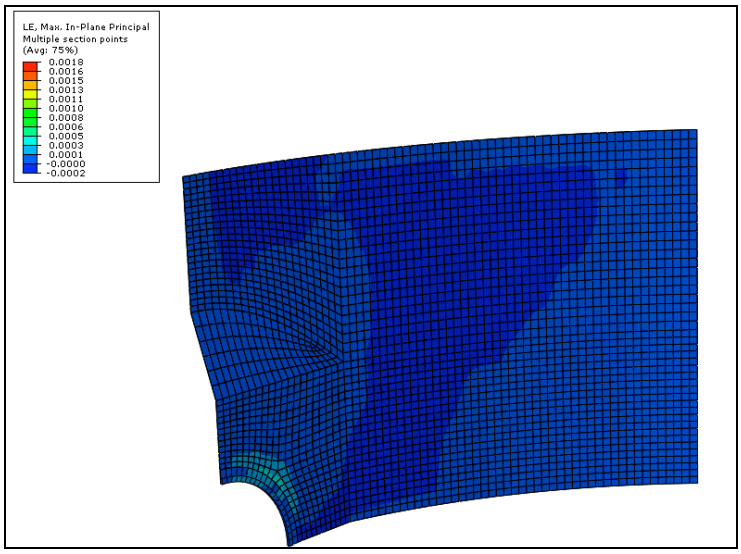

B

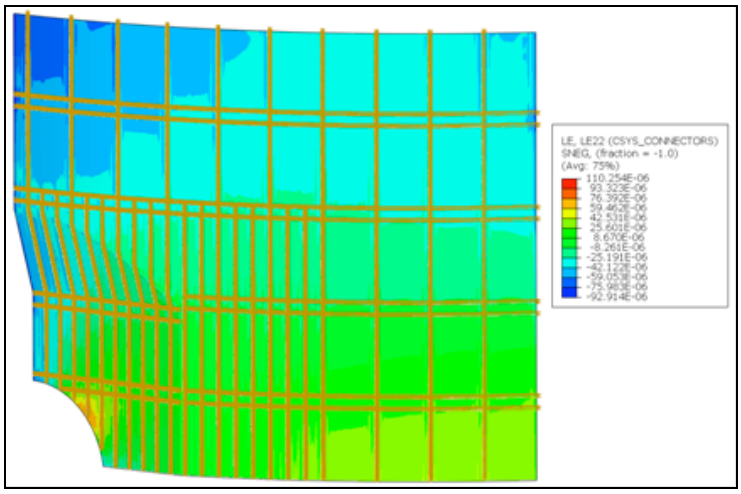

C

Figure 89: Model 2b Liner Strain at 1xP_d (A) AERB (B) NRC (C) SCANSCOT

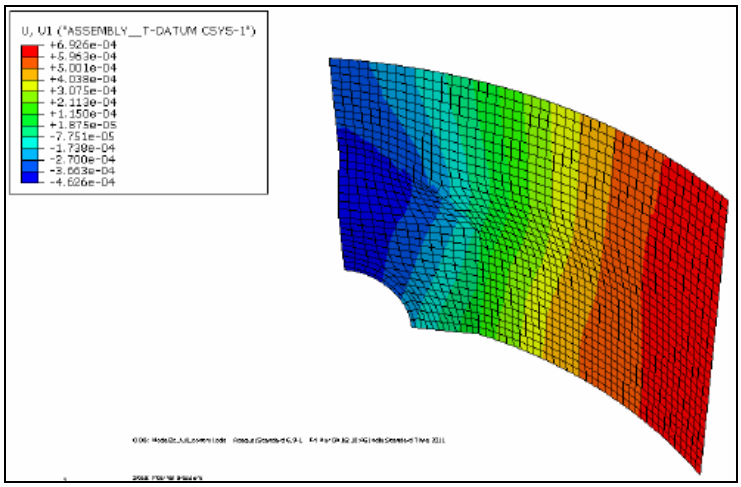

A

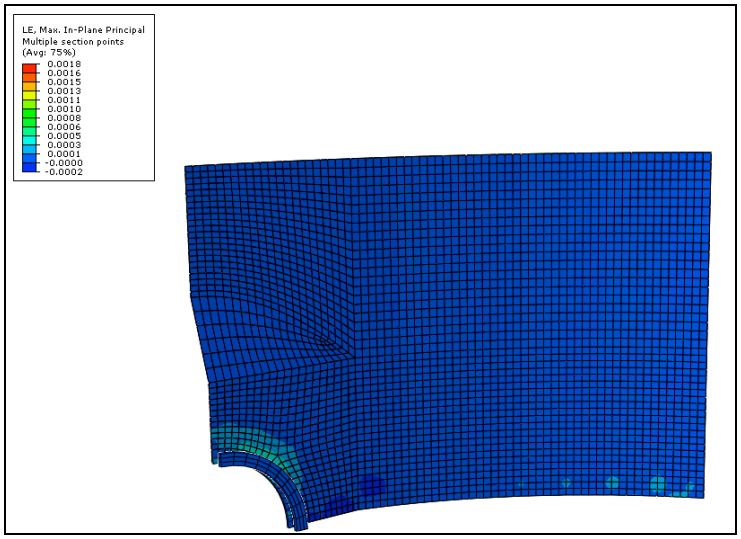

B

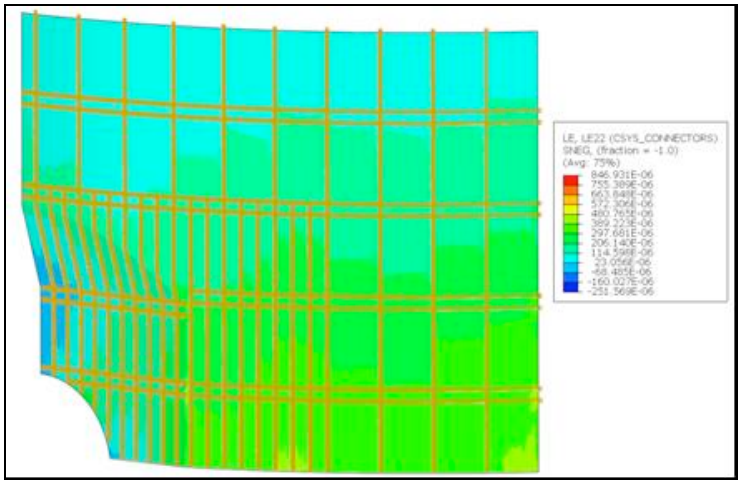

C

.Figure 90: Model 2b Liner Strain at 1.5xP_d (A) AERB (B) NRC (C) SCANSCOT

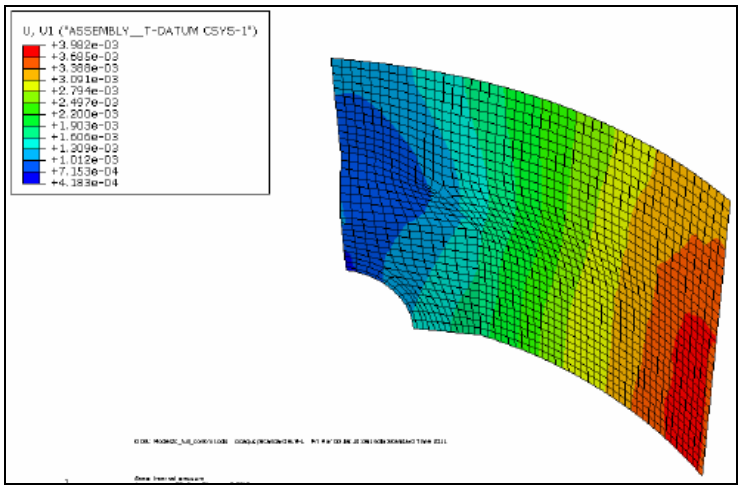

A

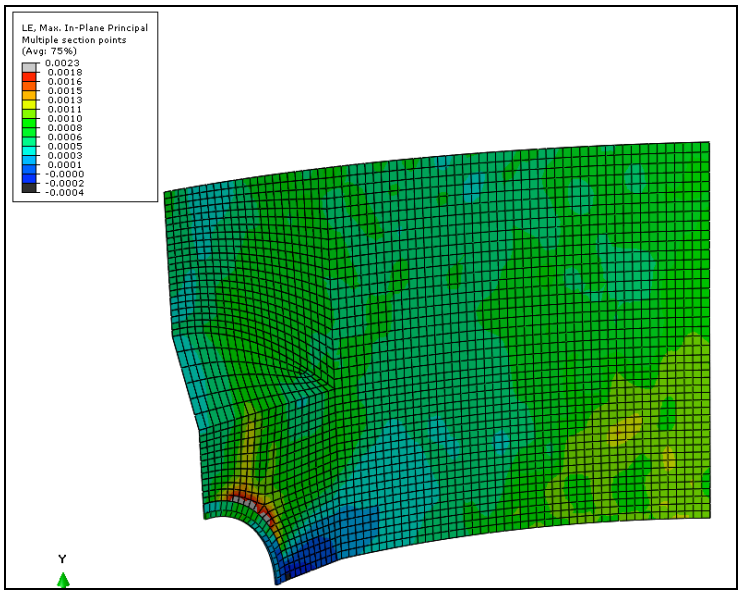

B

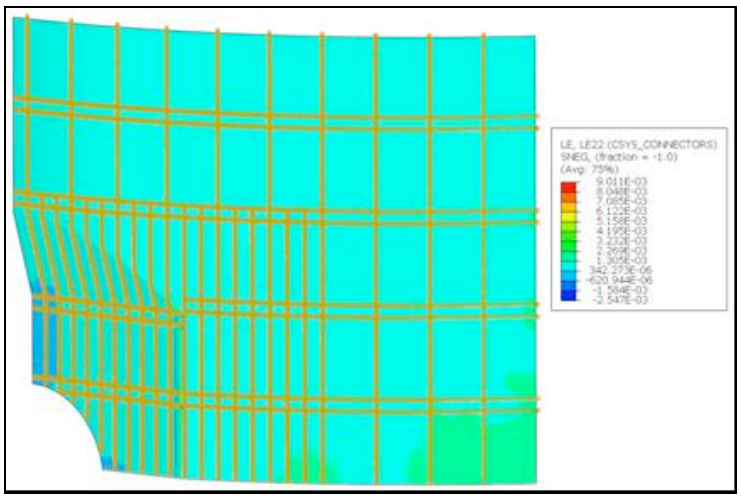

C

Figure 91: Model 2b Liner Strain at 2xP_d (A) AERB (B) NRC (C) SCANSCOT

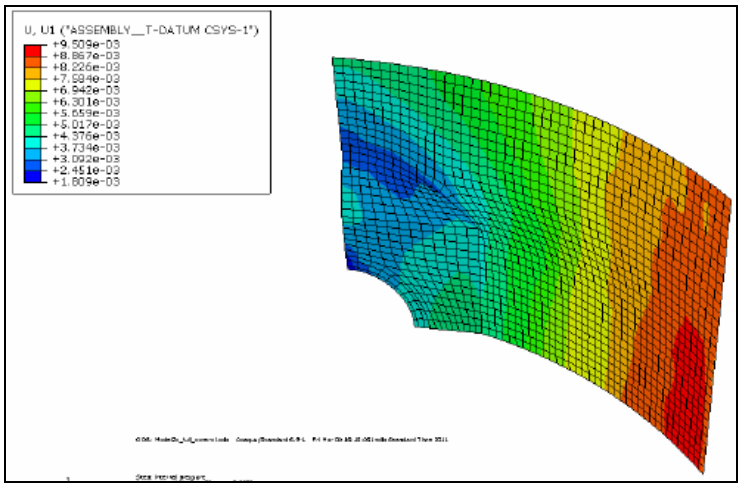

A

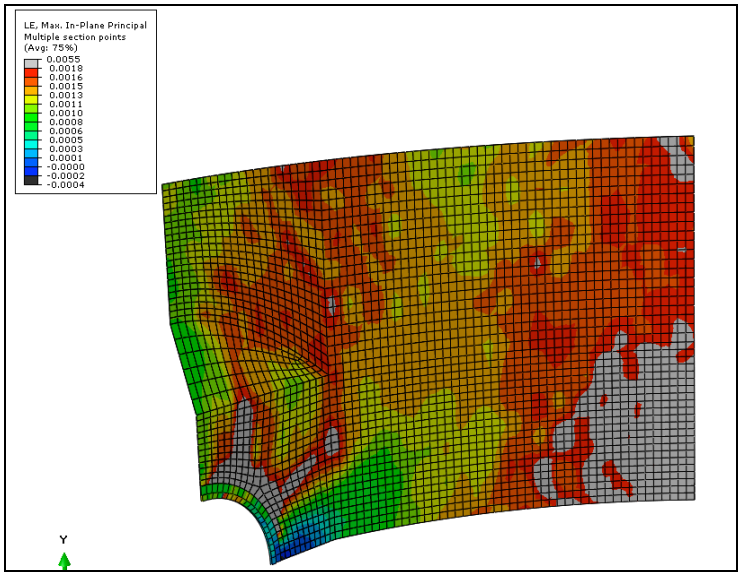

B

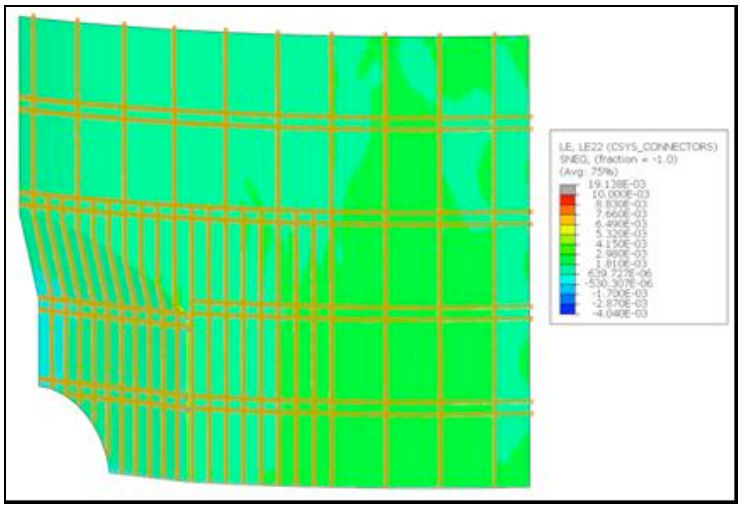

C

Figure 92: Model 2b Liner Strain at 2.5xP_d (A) AERB (B) NRC (C) SCANSCOT

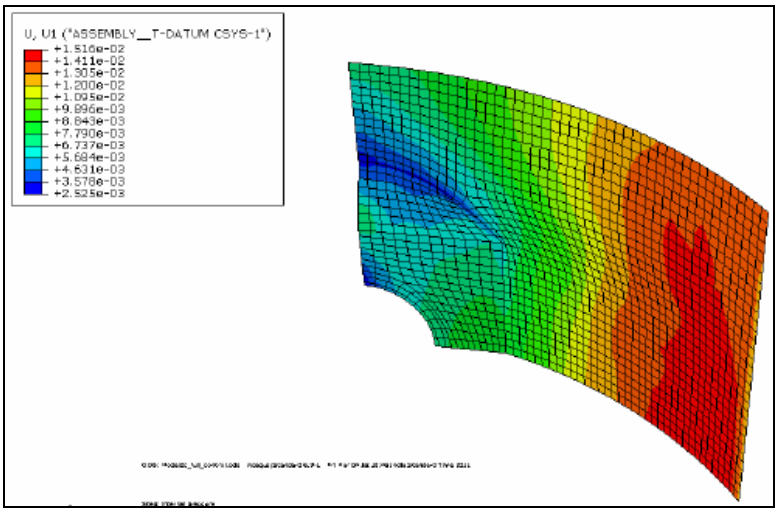

A

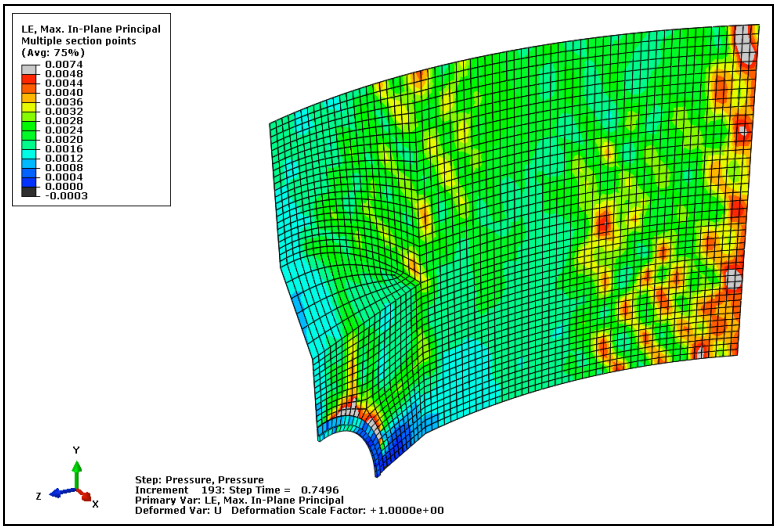

B

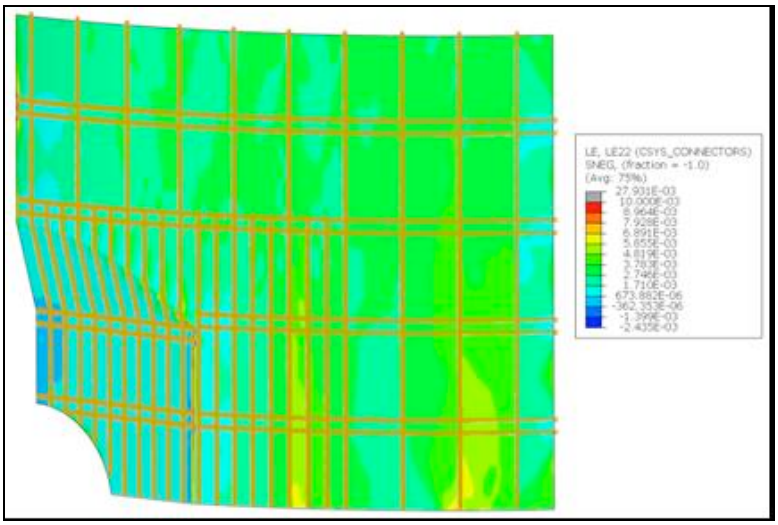

C

Figure 93: Model 2b Liner Strain at 3xP_d (A) AERB (B) NRC (C) SCANSCOT

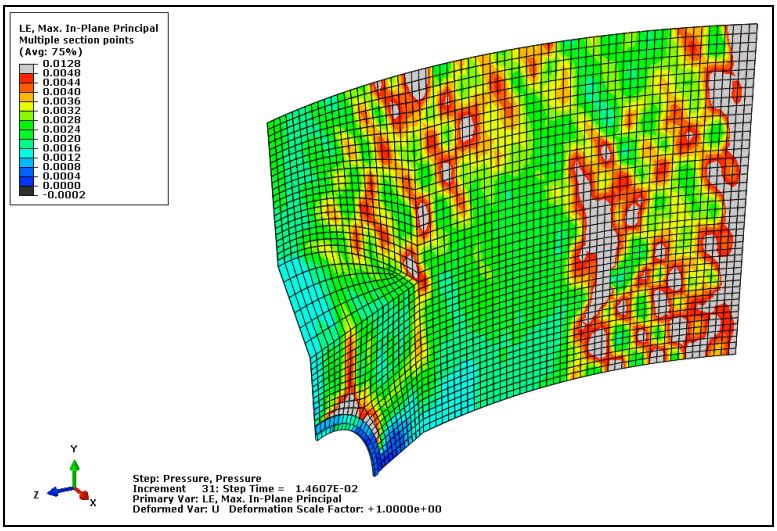

A

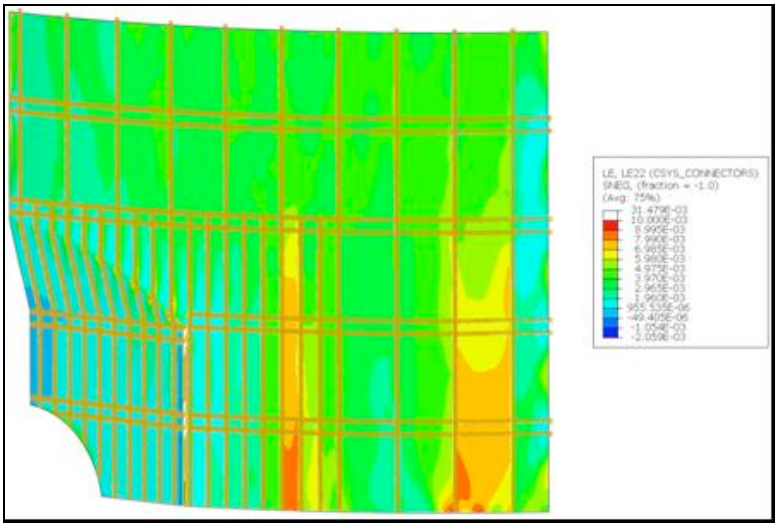

B

Figure 94: Model 2b Liner Strain at 3.3xP_d (A) NRC (B) SCANSCOT

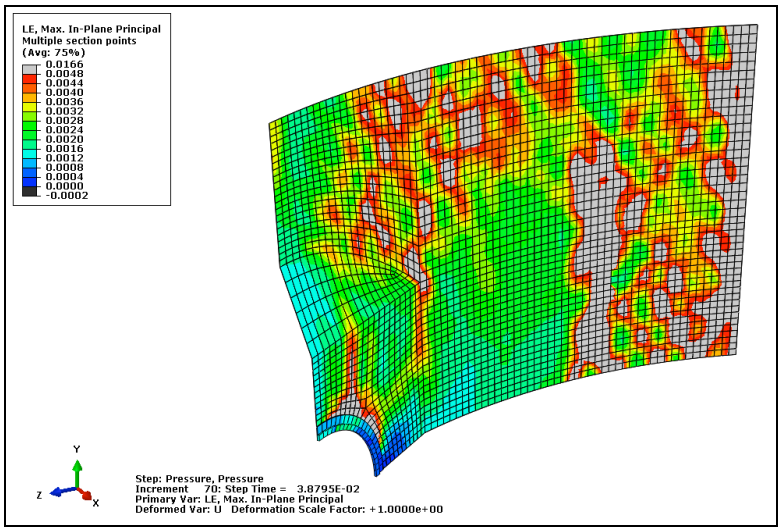

A

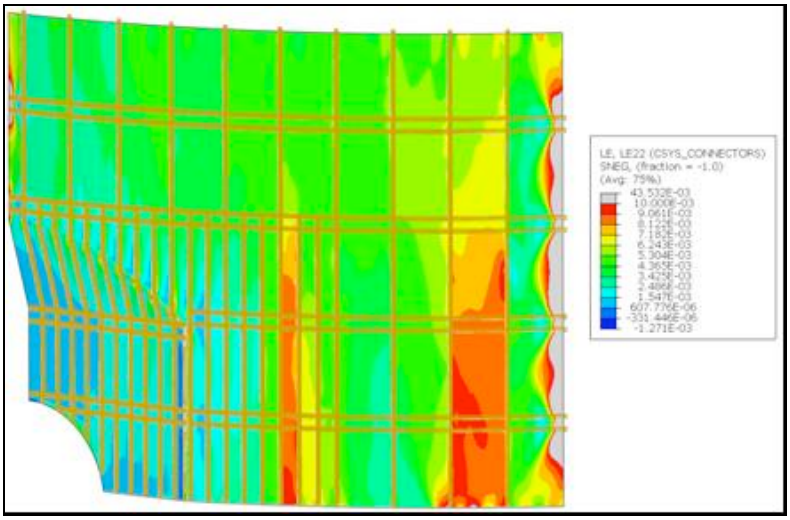

B

Figure 95: Model 2b Liner Strain at 3.4xP_d (A) NRC (B) SCANSCOT

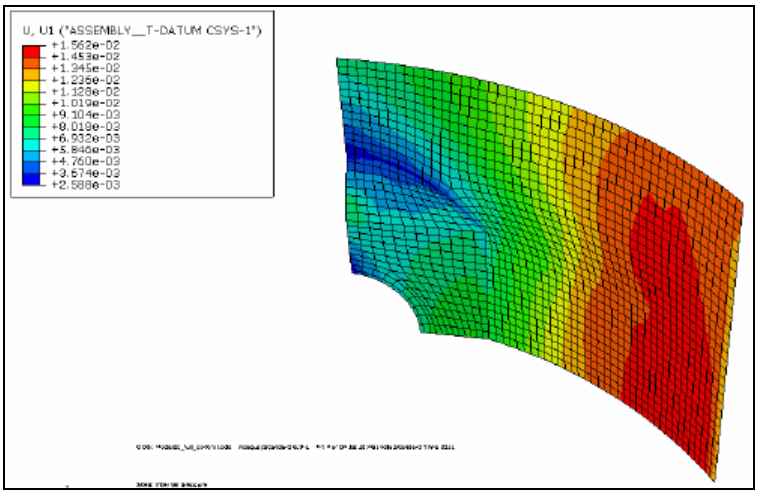

A

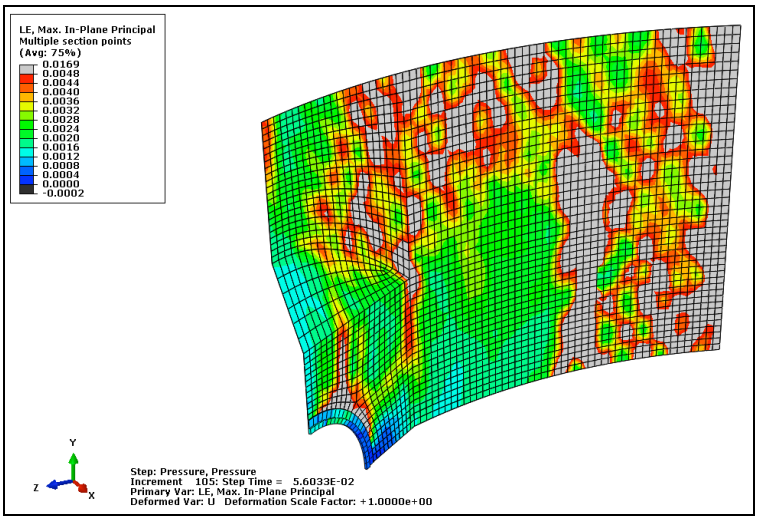

B

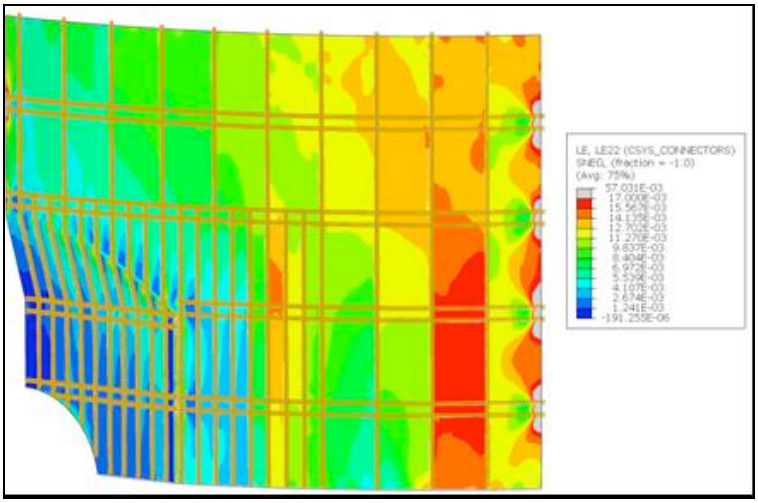

C

Figure 96: Model 2b Liner Strain at Ultimate Pressure (A) AERB (B) NRC (3.47xP_d) (C) SCANSCOT (3.62xP_d)

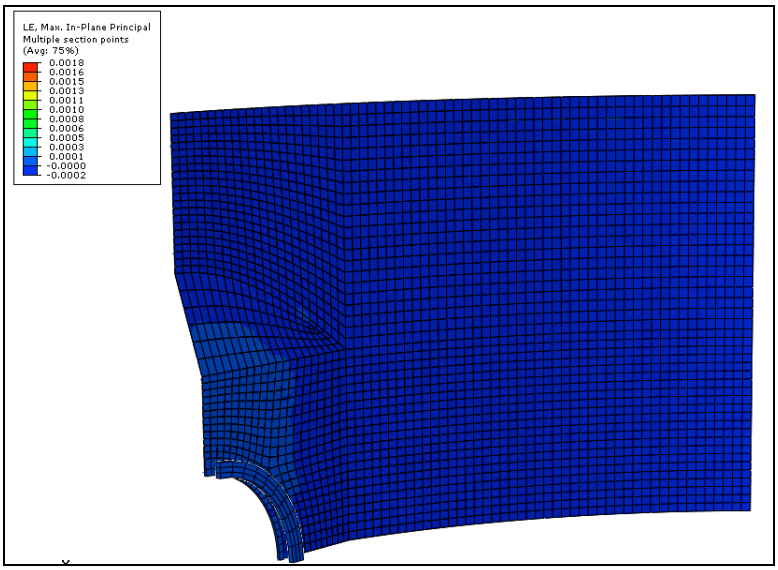

Figure 97: Model 2c Liner Strain at Anchor NRC

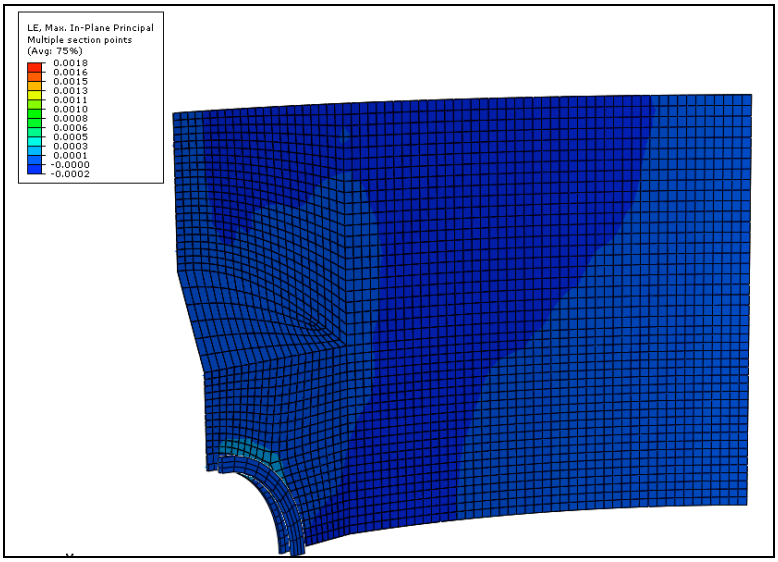

Figure 98: Model 2c Liner Strain at 1xP_d NRC

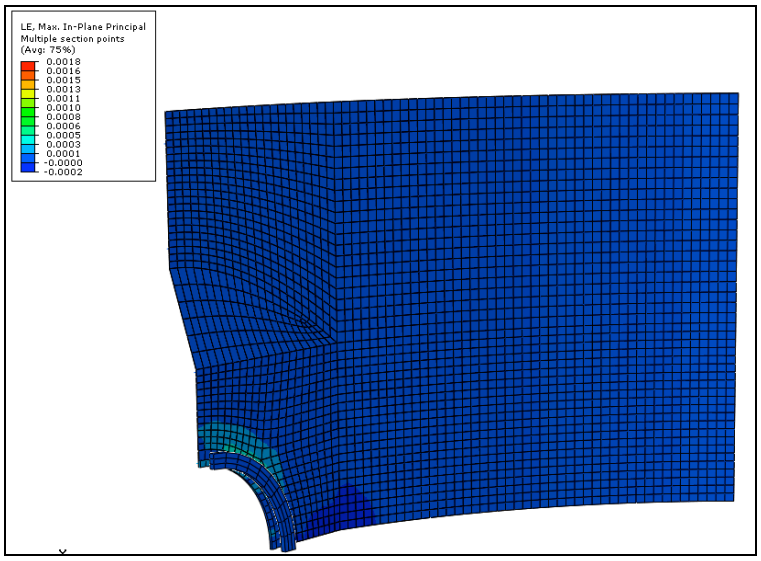

Figure 99: Model 2c Liner Strain at 1.5xP_d NRC

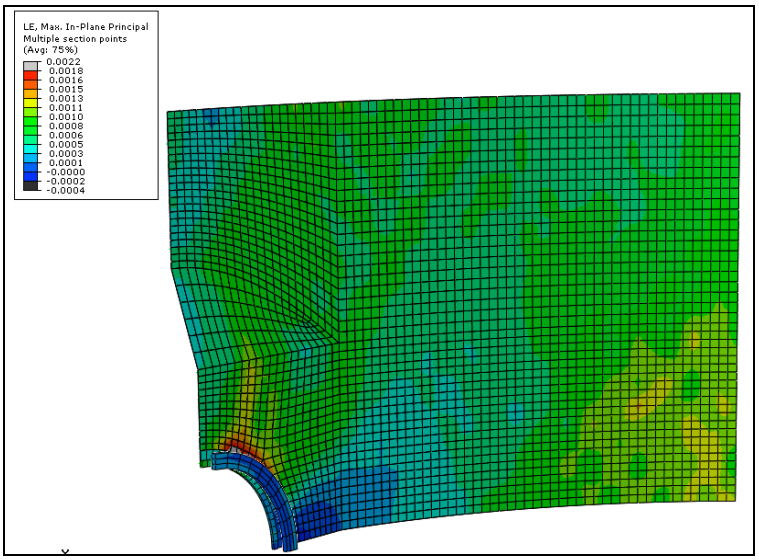

Figure 100: Model 2c Liner Strain at 2xP_d NRC

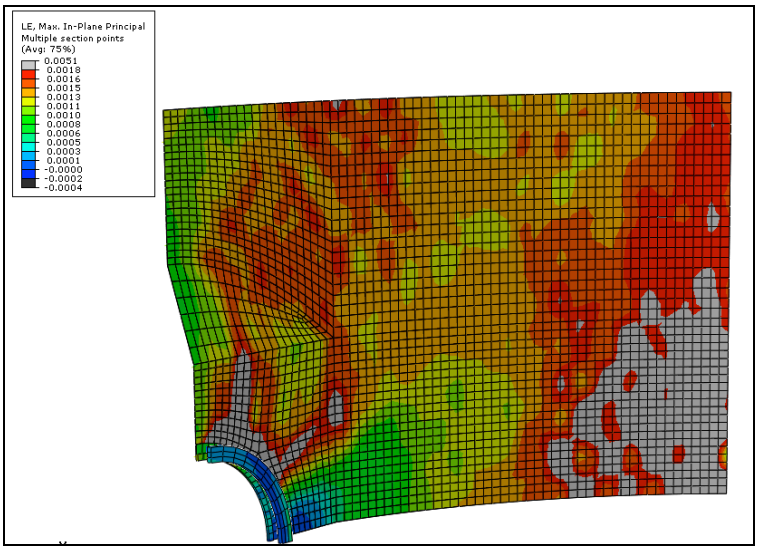

Figure 101: Model 2c Liner Strain at 2.5xP_d NRC

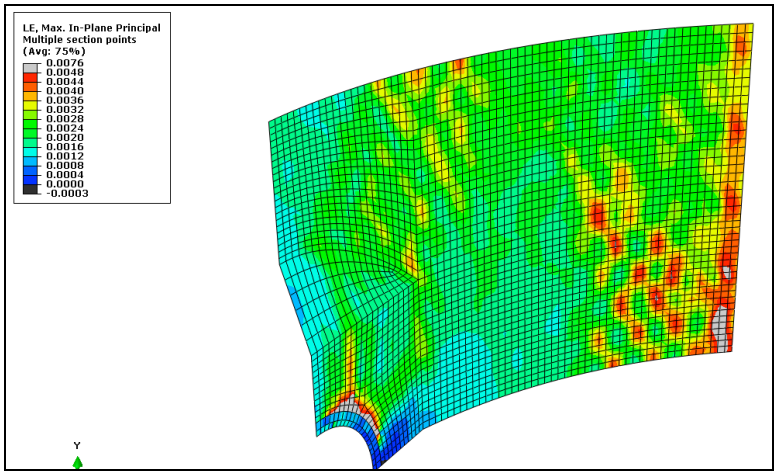

Figure 102: Model 2c Liner Strain at 3xP_d NRC

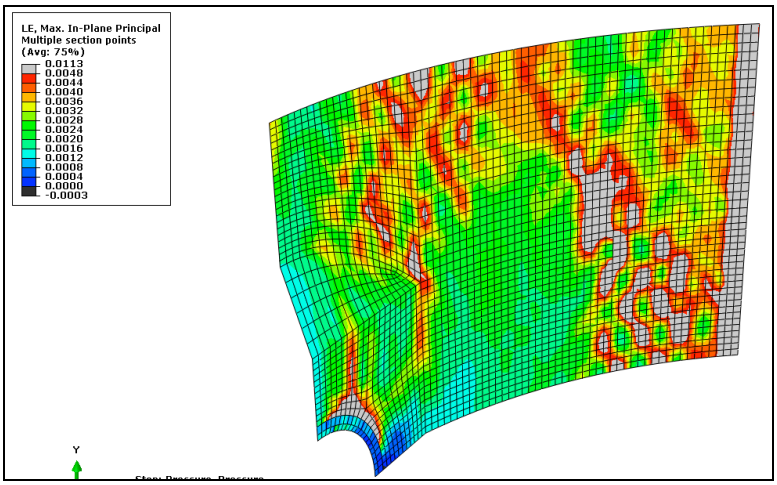

Figure 103: Model 2c Liner Strain at 3.3xP_d NRC

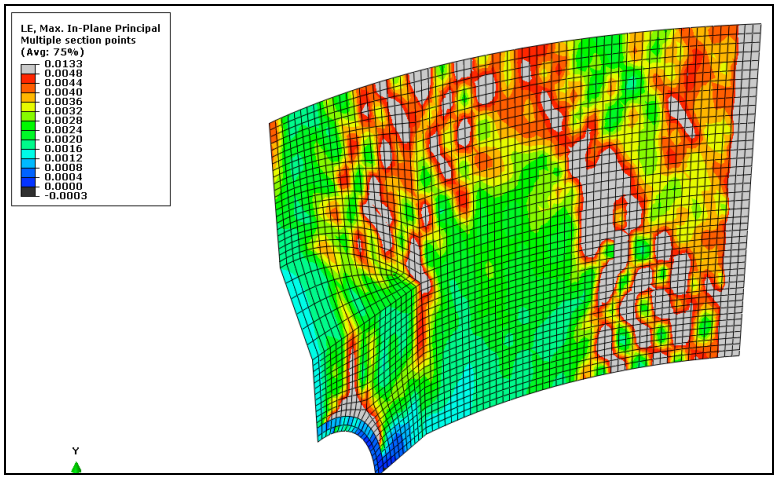

Figure 104: Model 2c Liner Strain at 3.4xP_d NRC

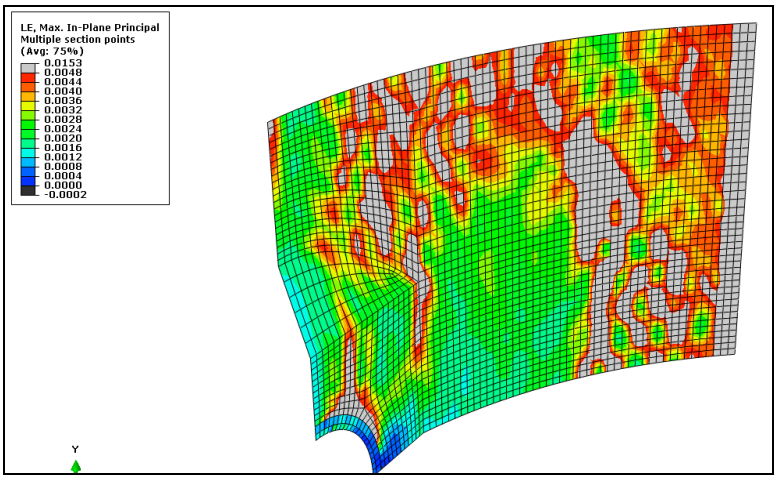

Figure 105: Model 2c Liner Strain at Ultimate Pressure ($3.47xP_d$) NRC

3.6. Liner Strain Magnitudes at Required Locations

The participants were required to provide strain magnitude values for several locations specified in Figure 11. The participants' responses are plotted together for each location as a function of internal pressure. The location specific strain versus pressure plots for Model 2a are located in Figure 106 through Figure 115. Similarly the analogous plots from Model 2b and Model 2c are found in Figure 116 through Figure 125 and Figure 126 through Figure 135 respectively. Finally, as a way of comparing the different versions of Model 2, Figure 136 through Figure 161 show location specific strain versus pressure plots for a specific location and participant. These plots indicate the influence of the differing assumptions in the versions of Model 2.

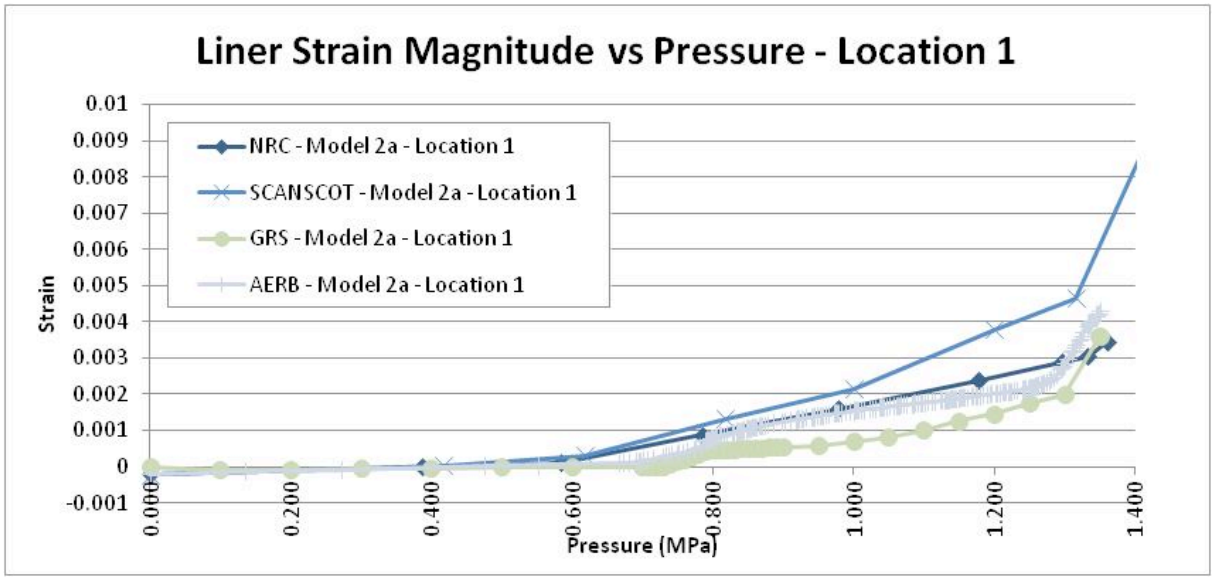

Figure 106: Model 2a Liner Strain Magnitude at Location 1

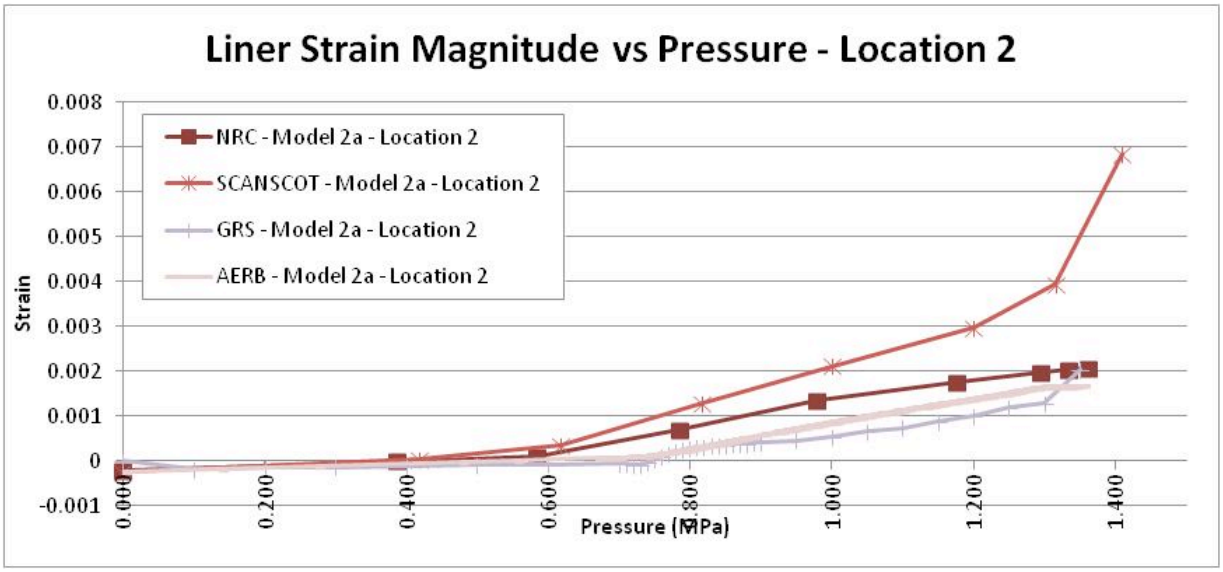

Figure 107: Model 2a Liner Strain Magnitude at Location 2

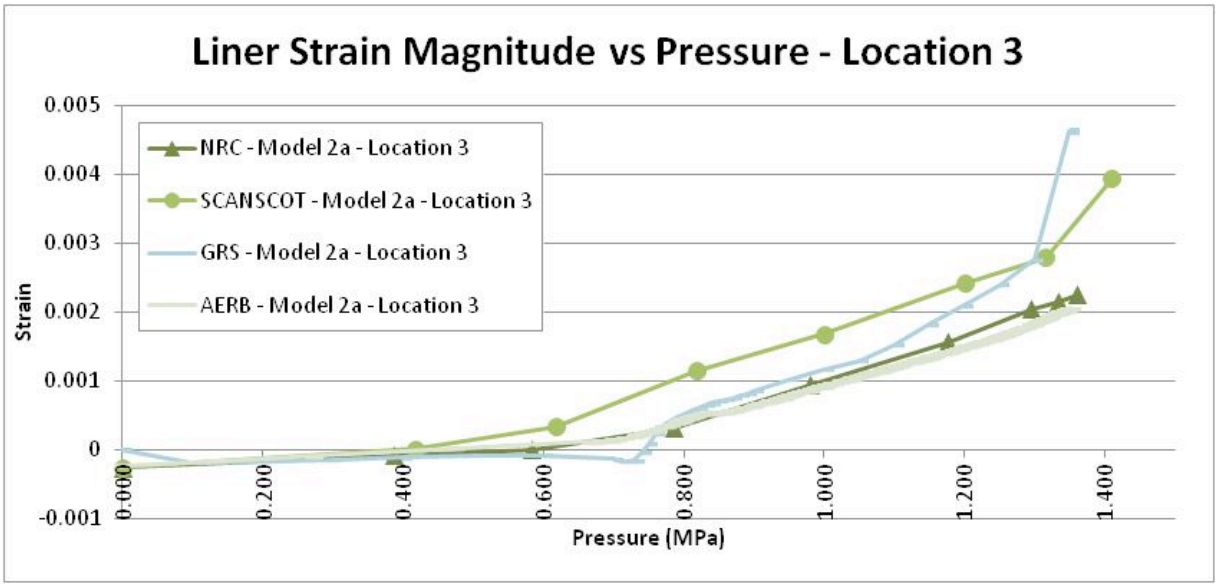

Figure 108: Model 2a Liner Strain Magnitude at Location 3

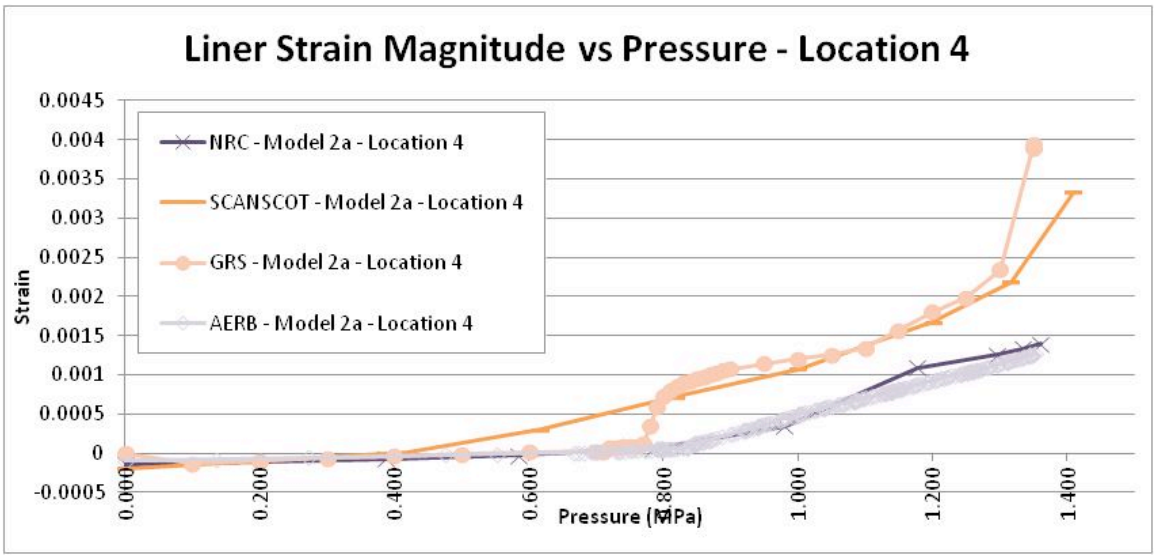

Figure 109: Model 2a Liner Strain Magnitude at Location 4

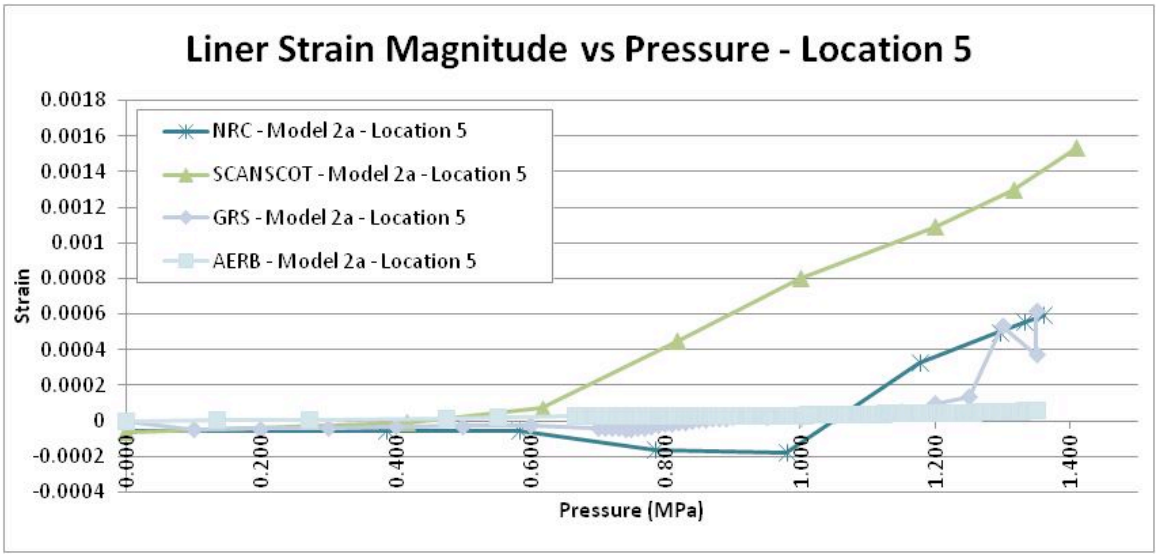

Figure 110: Model 2a Liner Strain Magnitude at Location 5

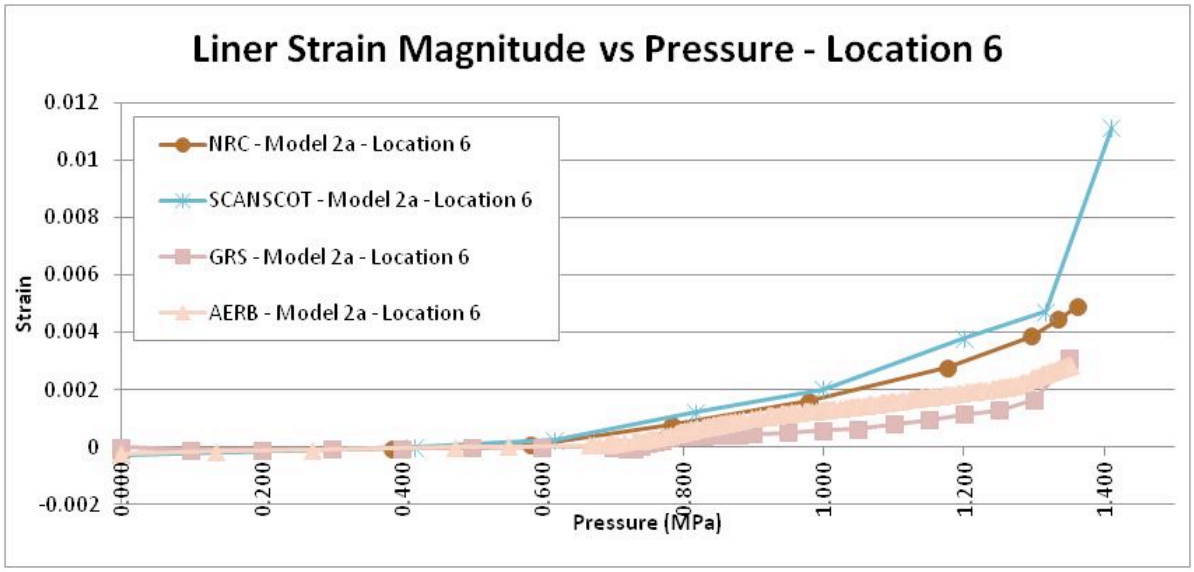

Figure 111: Model 2a Liner Strain Magnitude at Location 6

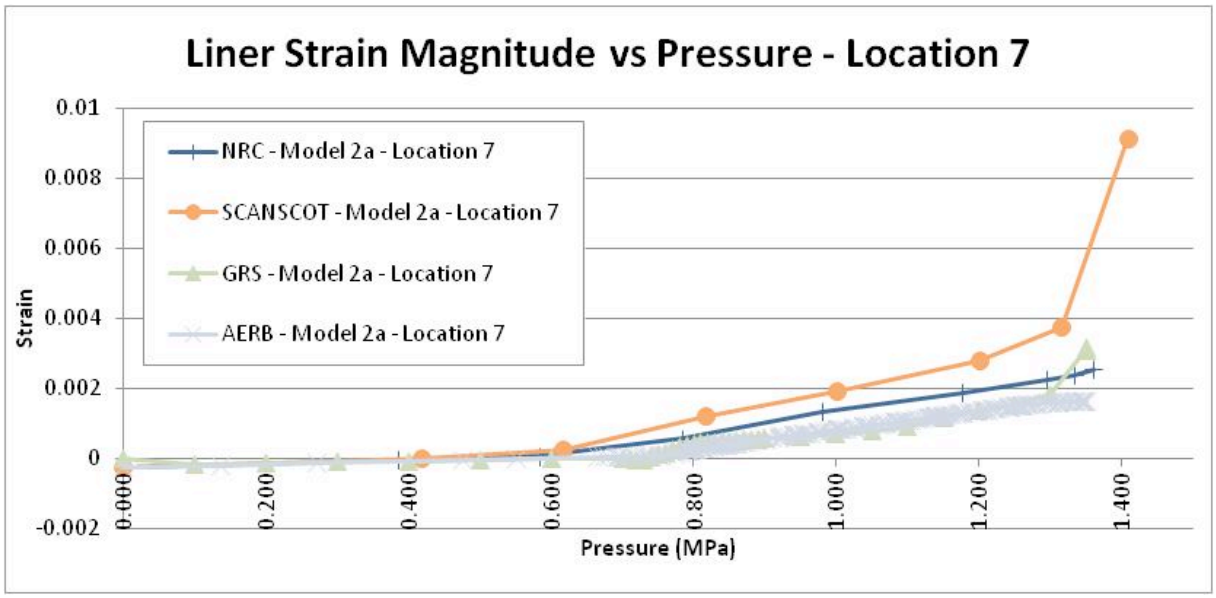

Figure 112: Model 2a Liner Strain Magnitude at Location 7

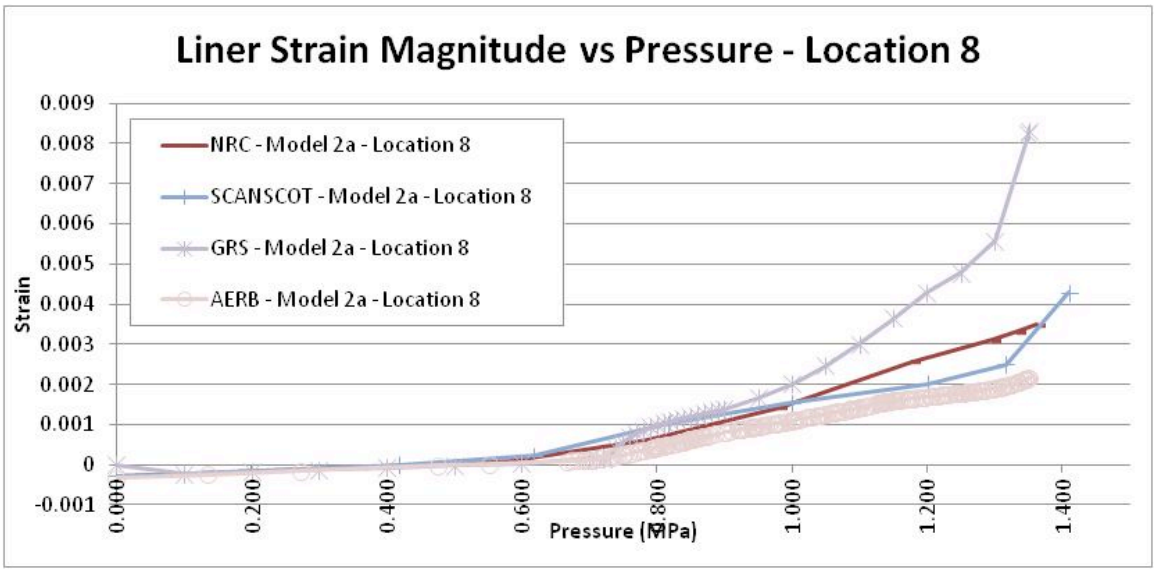

Figure 113: Model 2a Liner Strain Magnitude at Location 8

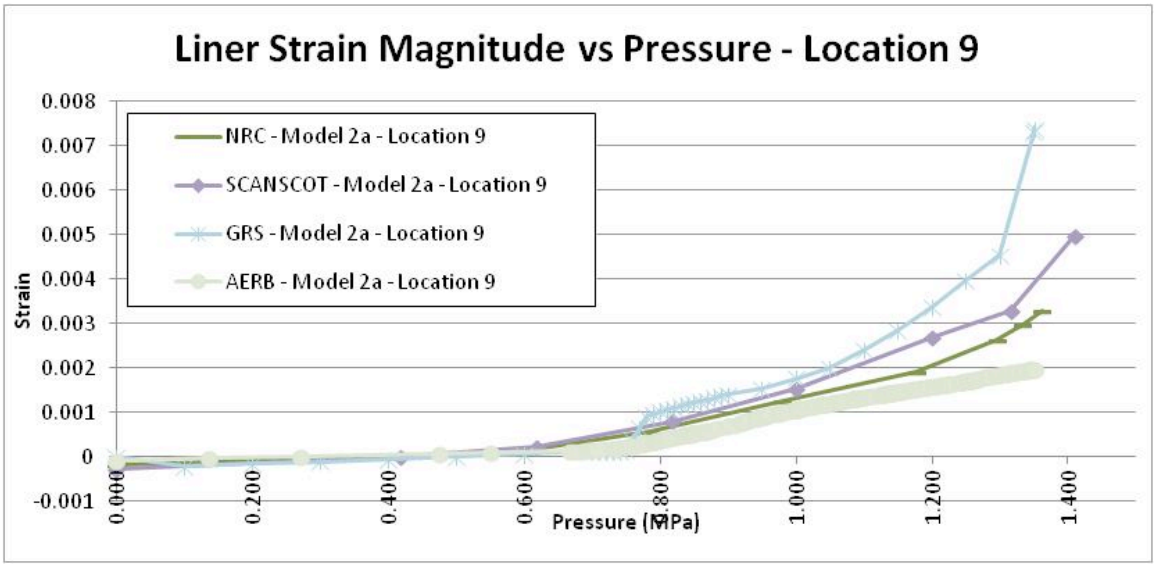

Figure 114: Model 2a Liner Strain Magnitude at Location 9

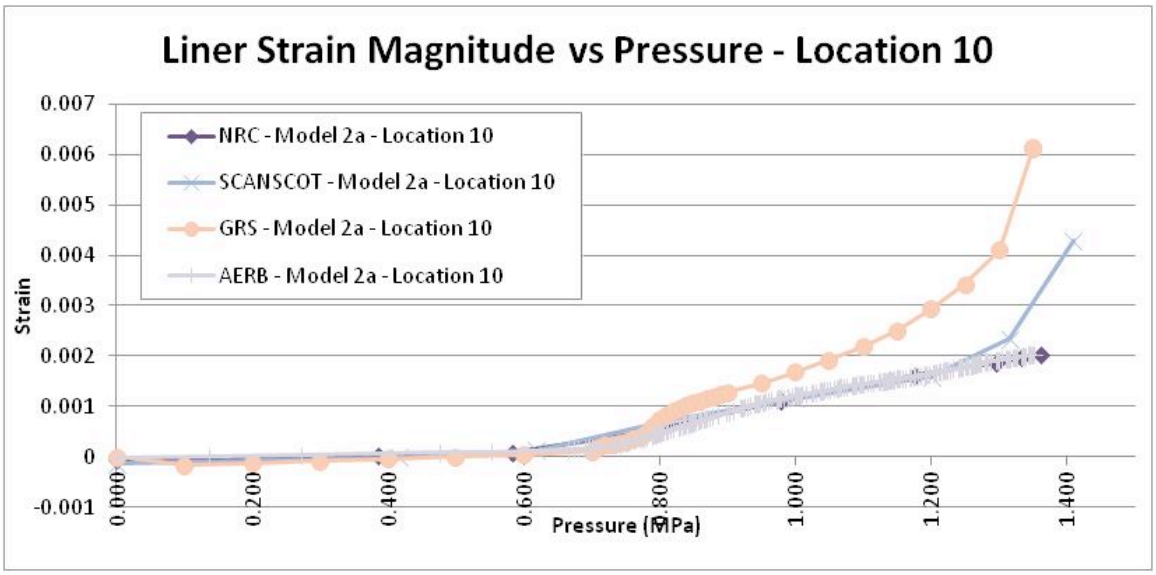

Figure 115: Model 2a Liner Strain Magnitude at Location 10

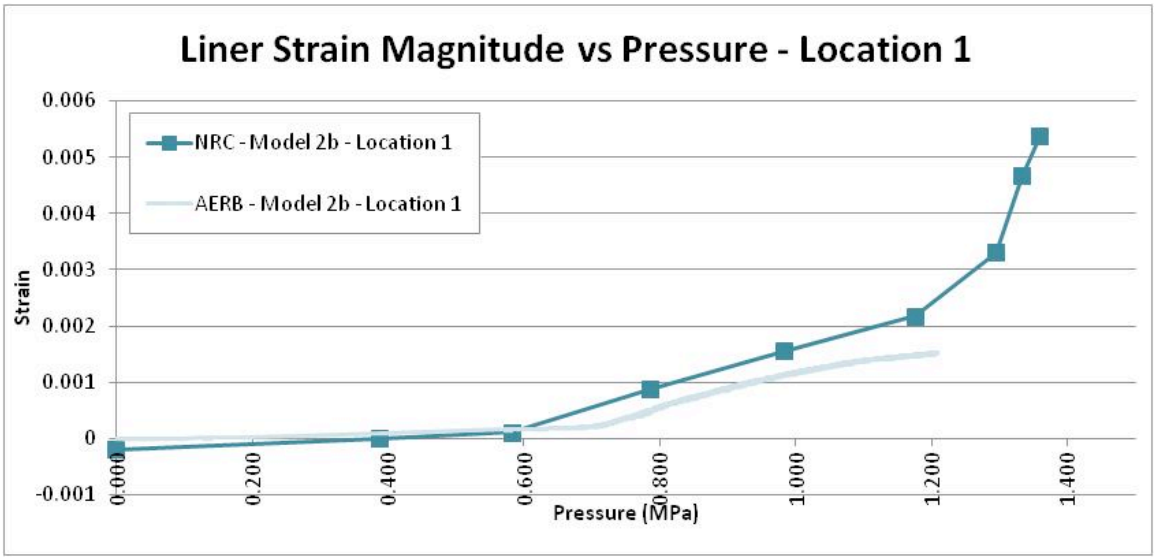

Figure 116: Model 2b Liner Strain Magnitude at Location 1

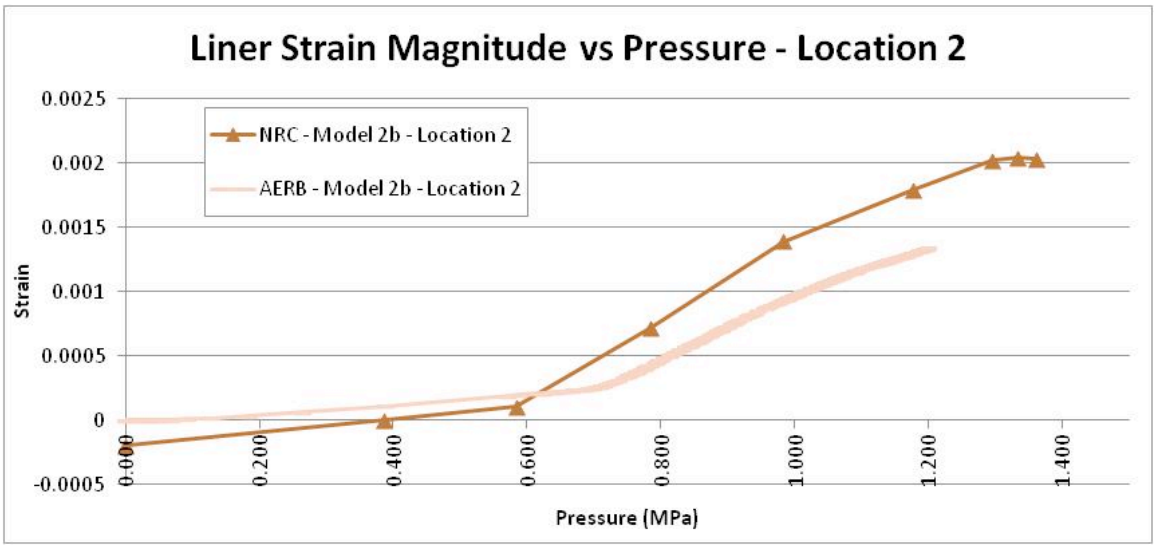

Figure 117: Model 2b Liner Strain Magnitude at Location 2

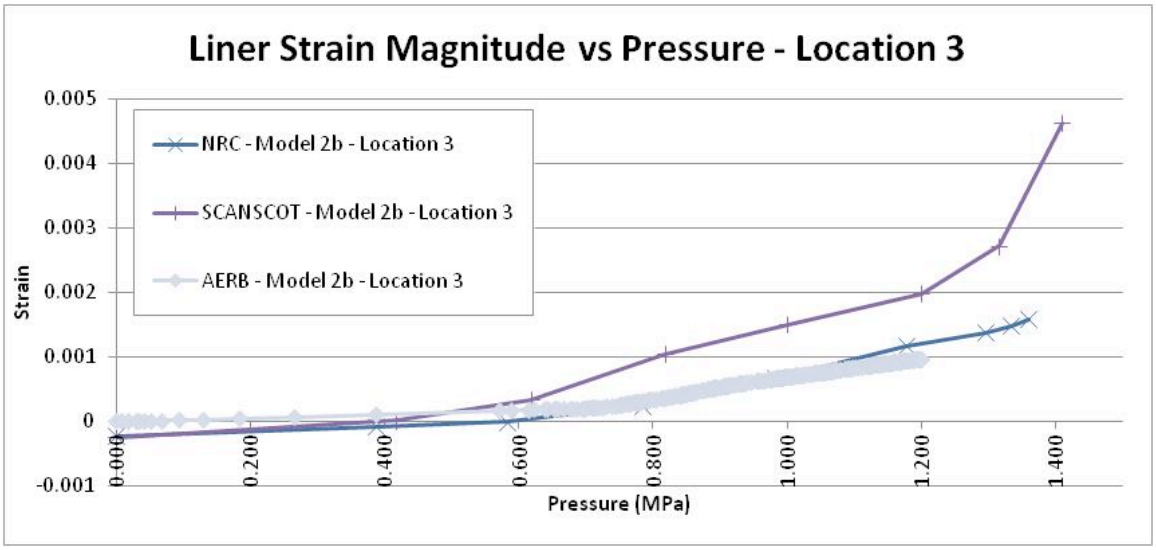

Figure 118: Model 2b Liner Strain Magnitude at Location 3

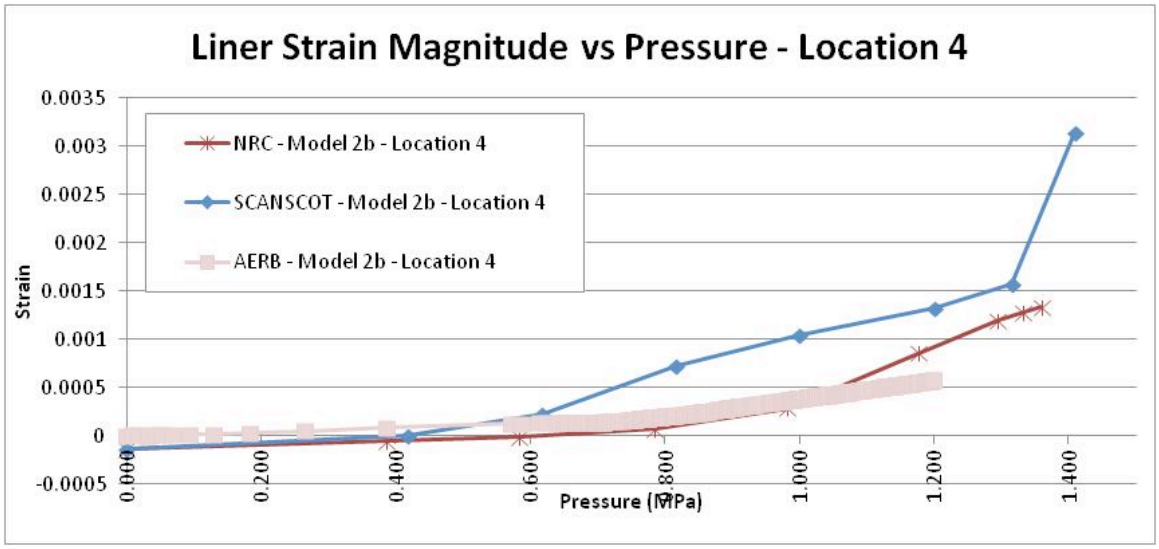

Figure 119: Model 2b Liner Strain Magnitude at Location 4

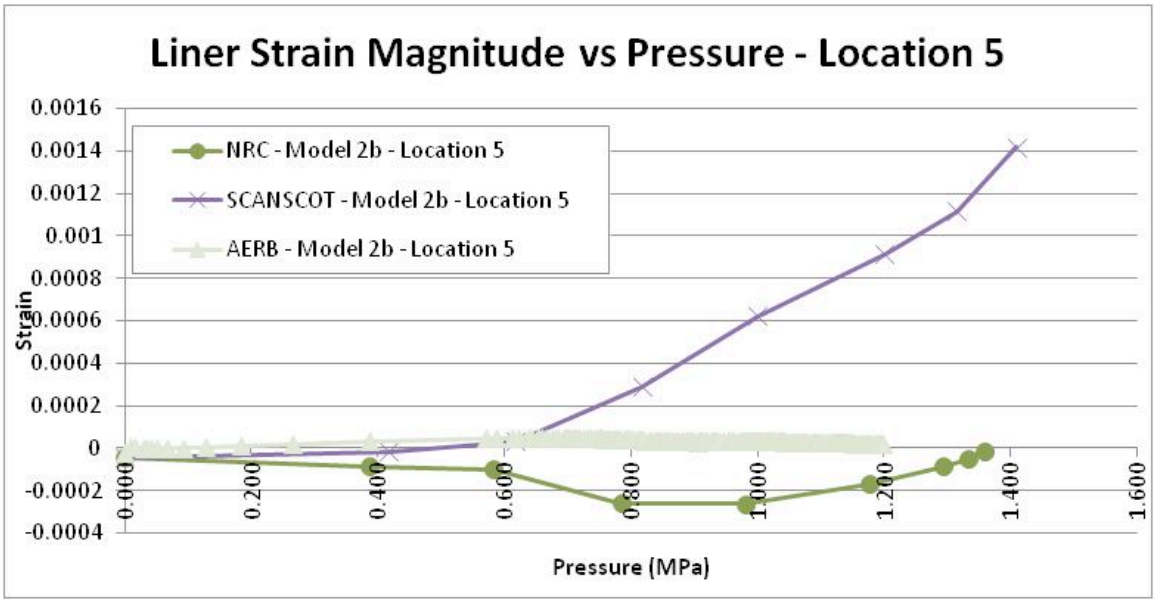

Figure 120: Model 2b Liner Strain Magnitude at Location 5

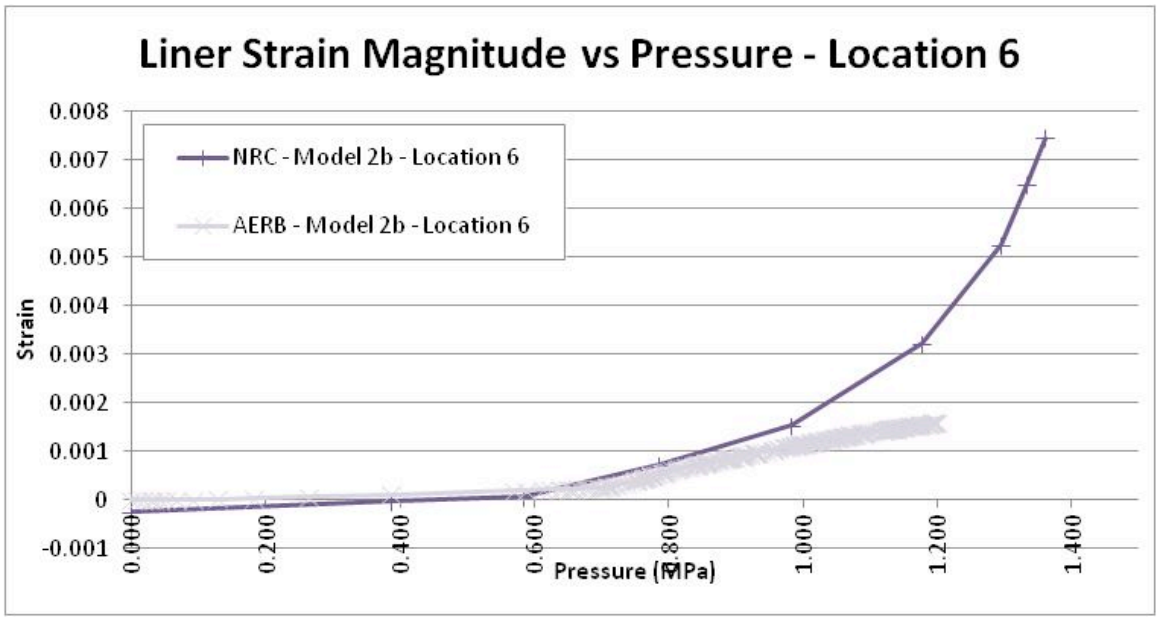

Figure 121: Model 2b Liner Strain Magnitude at Location 6

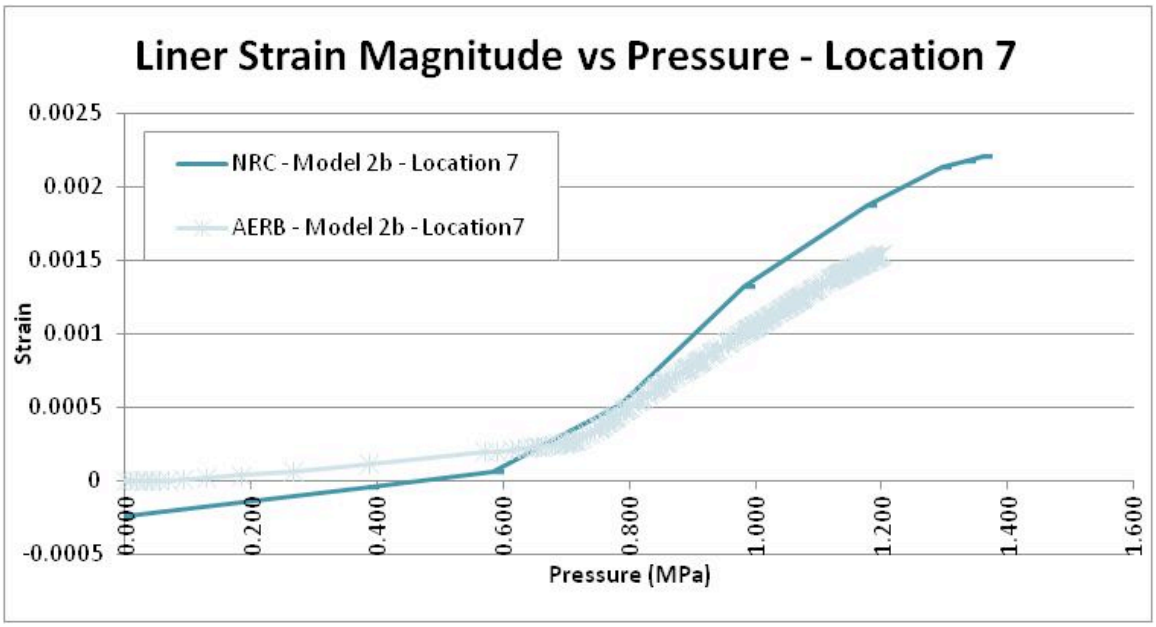

Figure 122: Model 2b Liner Strain Magnitude at Location 7

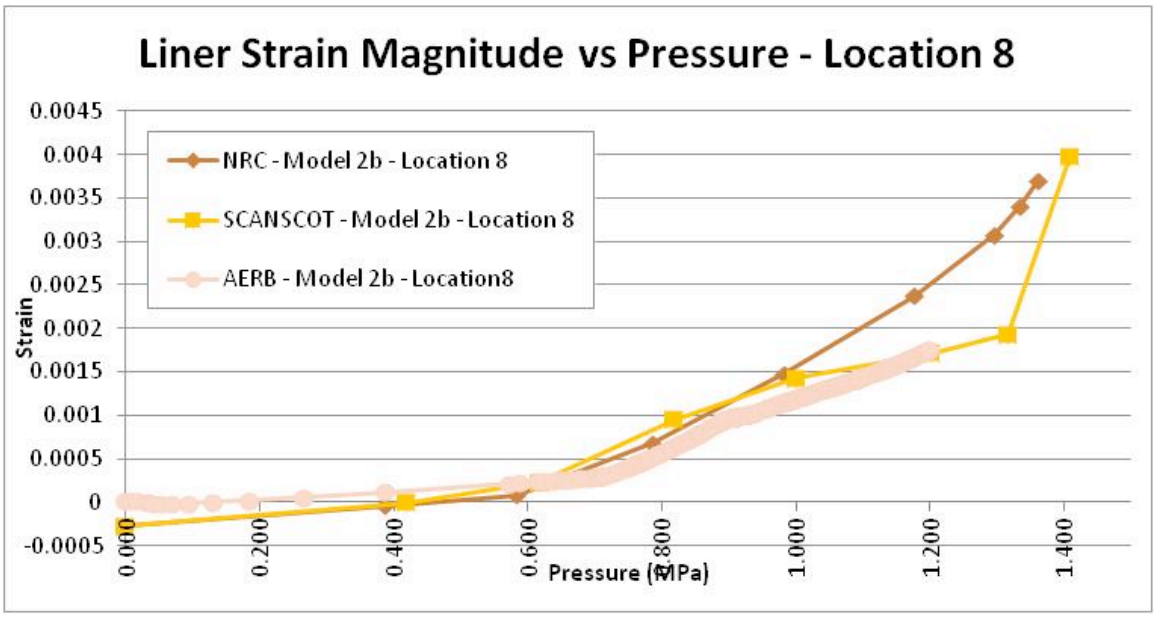

Figure 123: Model 2b Liner Strain Magnitude at Location 8

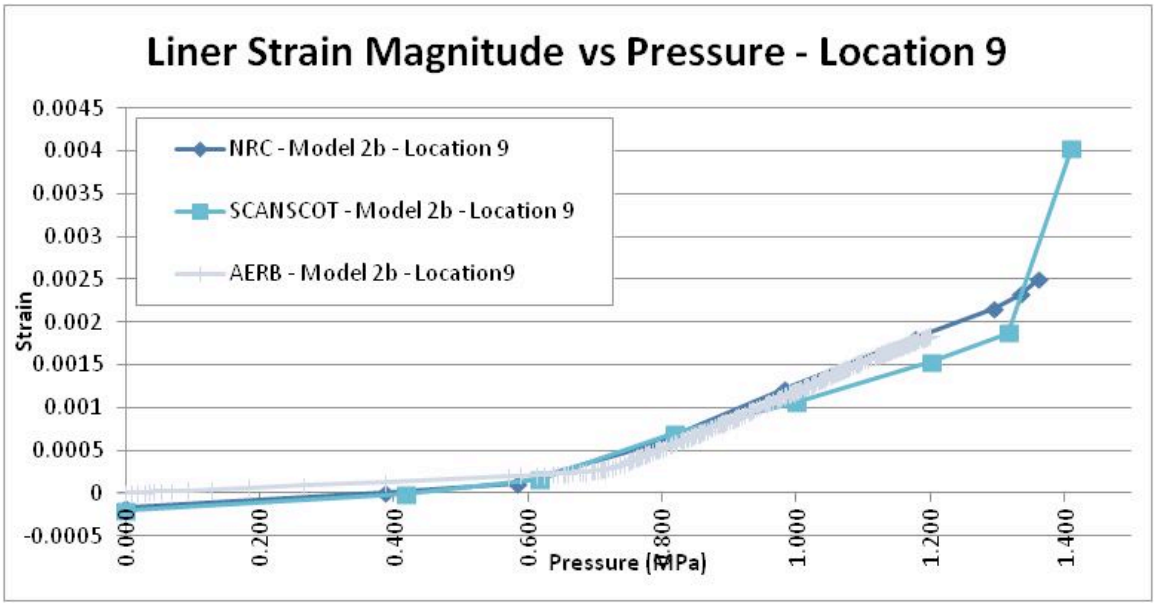

Figure 124: Model 2b Liner Strain Magnitude at Location 9

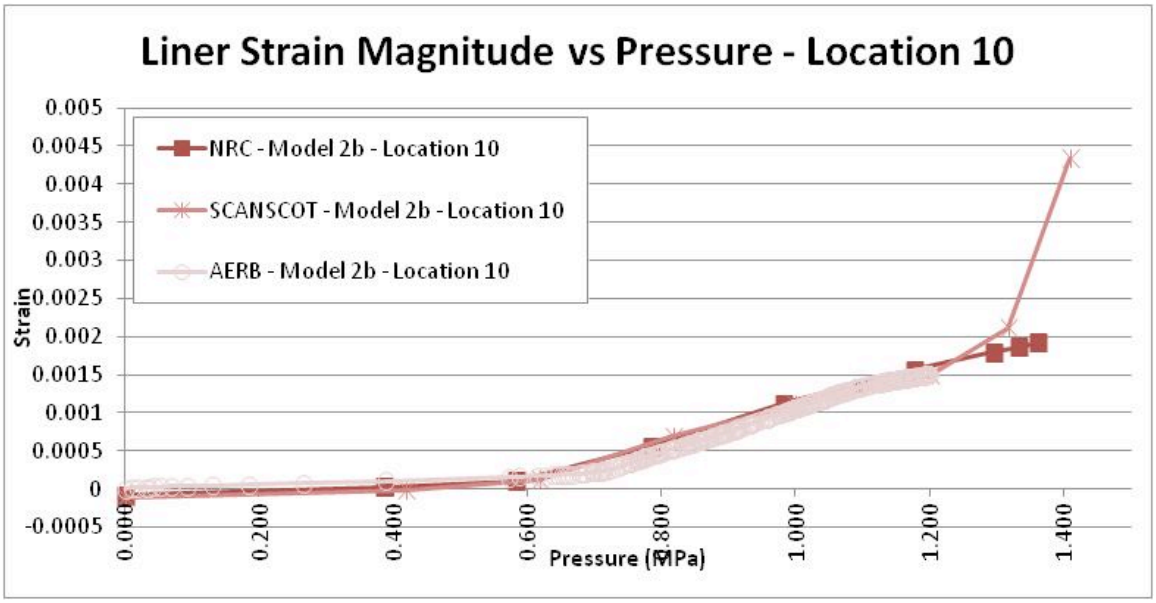

Figure 125: Model 2b Liner Strain Magnitude at Location 10

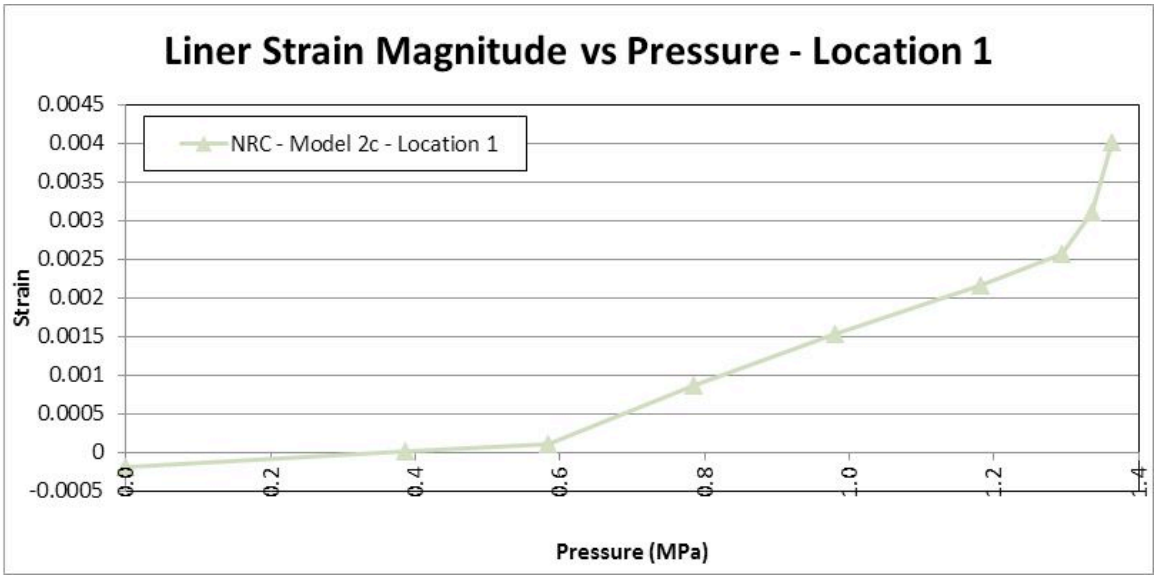

Figure 126: Model 2c Liner Strain Magnitude at Location 1

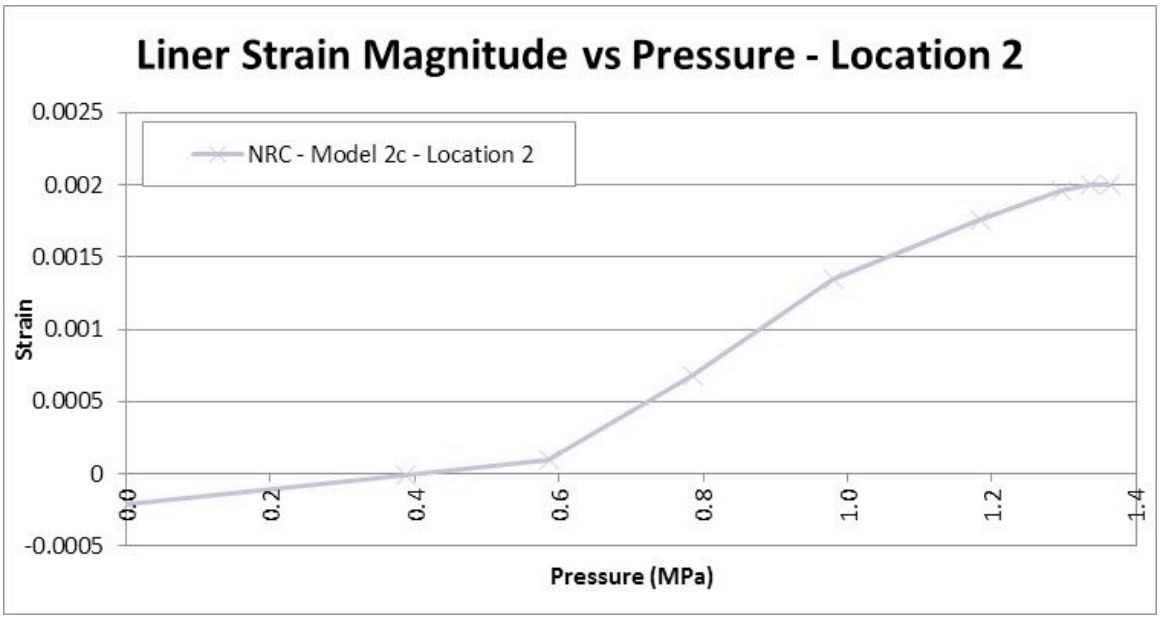

Figure 127: Model 2c Liner Strain Magnitude at Location 2

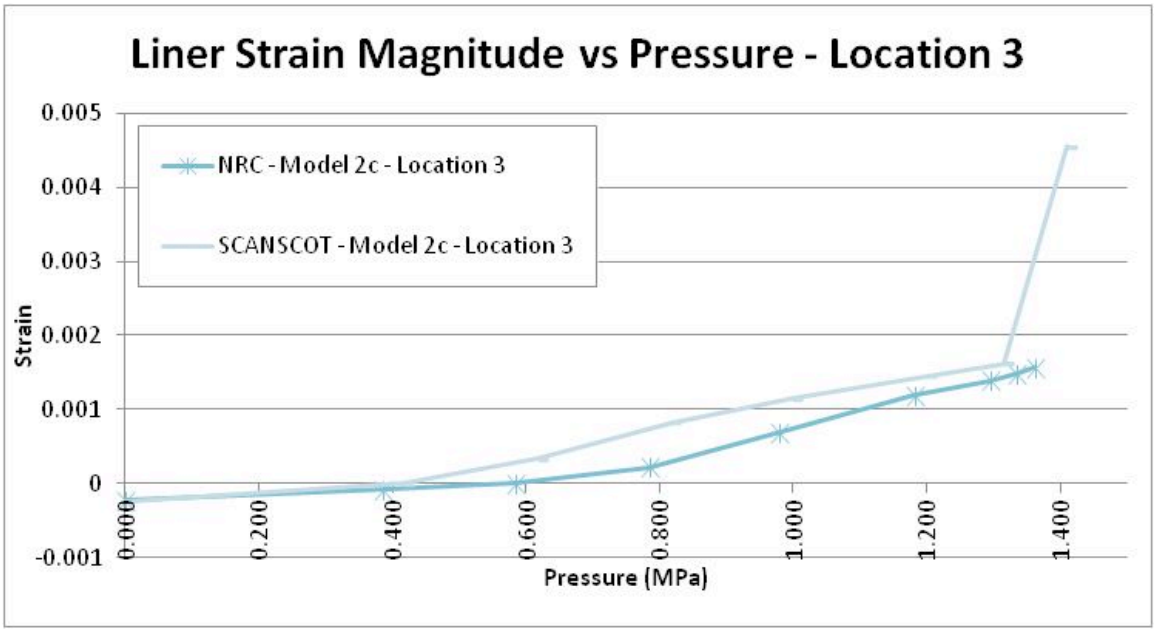

Figure 128: Model 2c Liner Strain Magnitude at Location 3

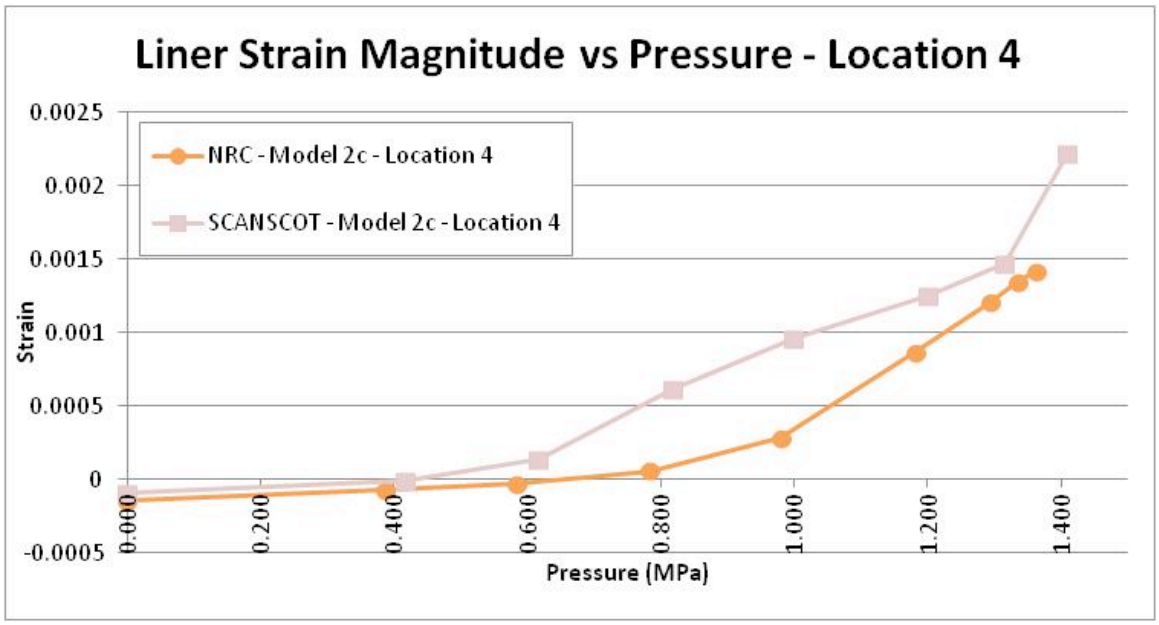

Figure 129: Model 2c Liner Strain Magnitude at Location 4

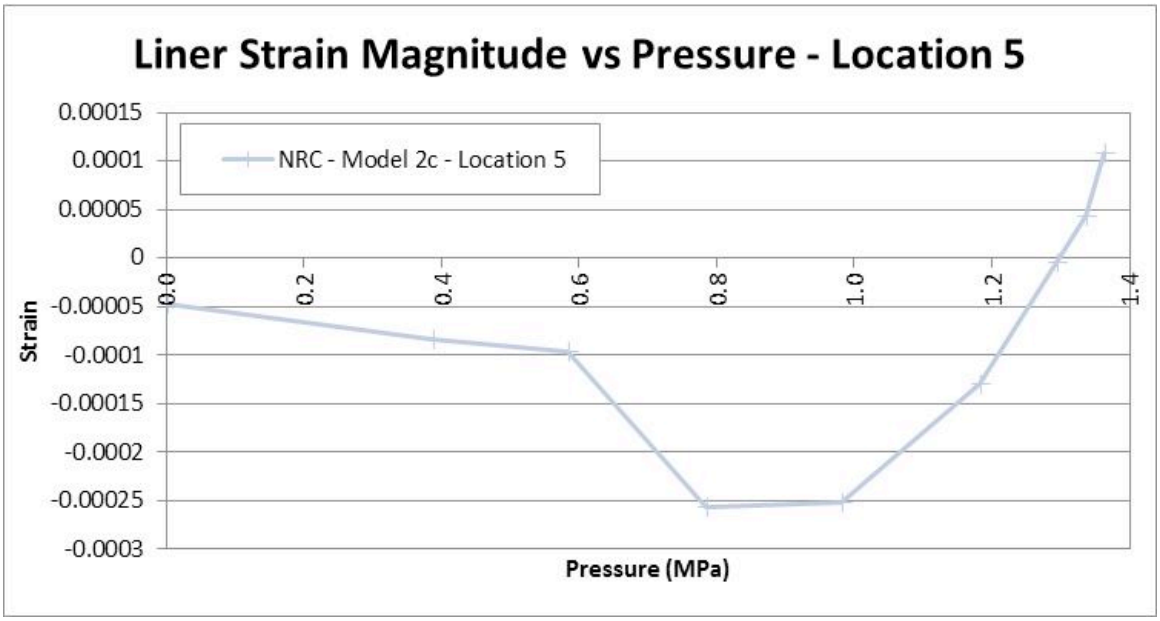

Figure 130: Model 2c Liner Strain Magnitude at Location 5

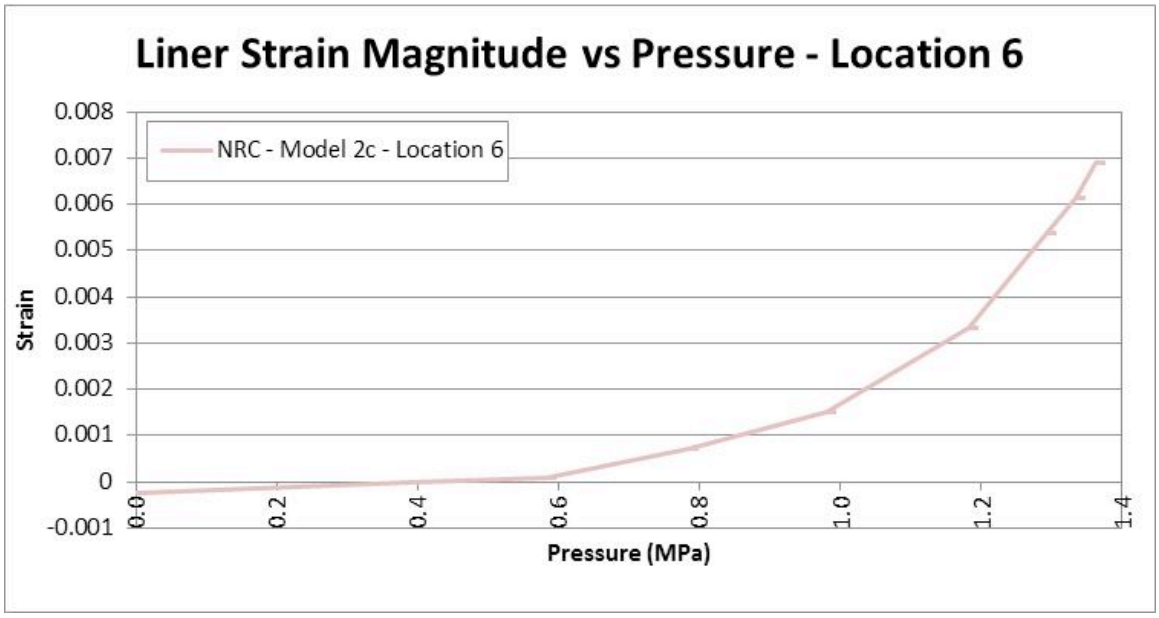

Figure 131: Model 2c Liner Strain Magnitude at Location 6

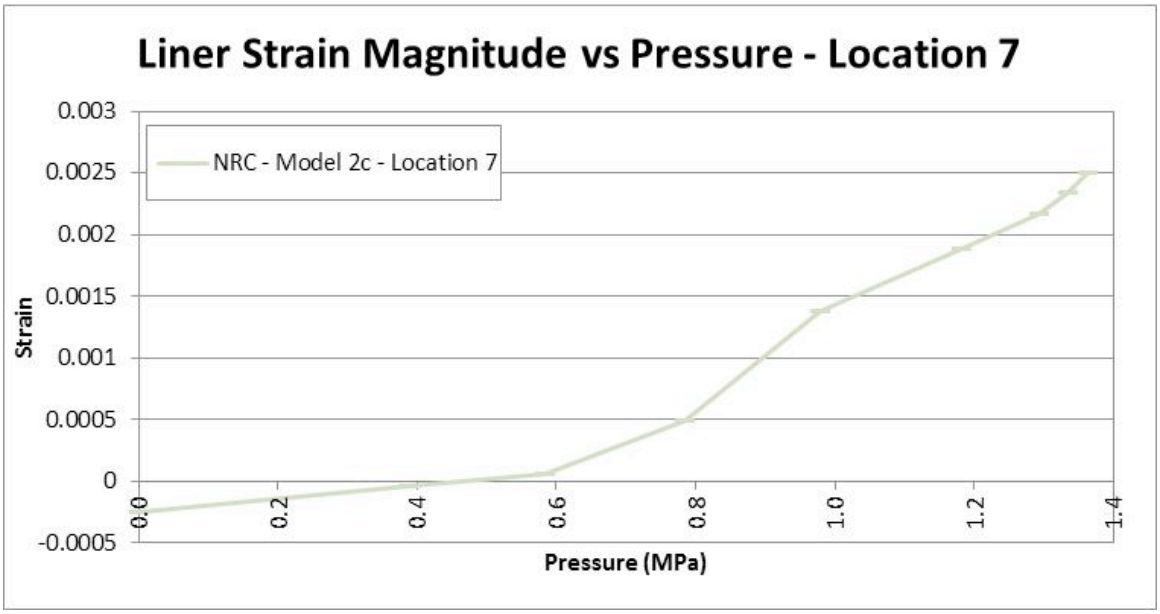

Figure 132: Model 2c Liner Strain Magnitude at Location 7

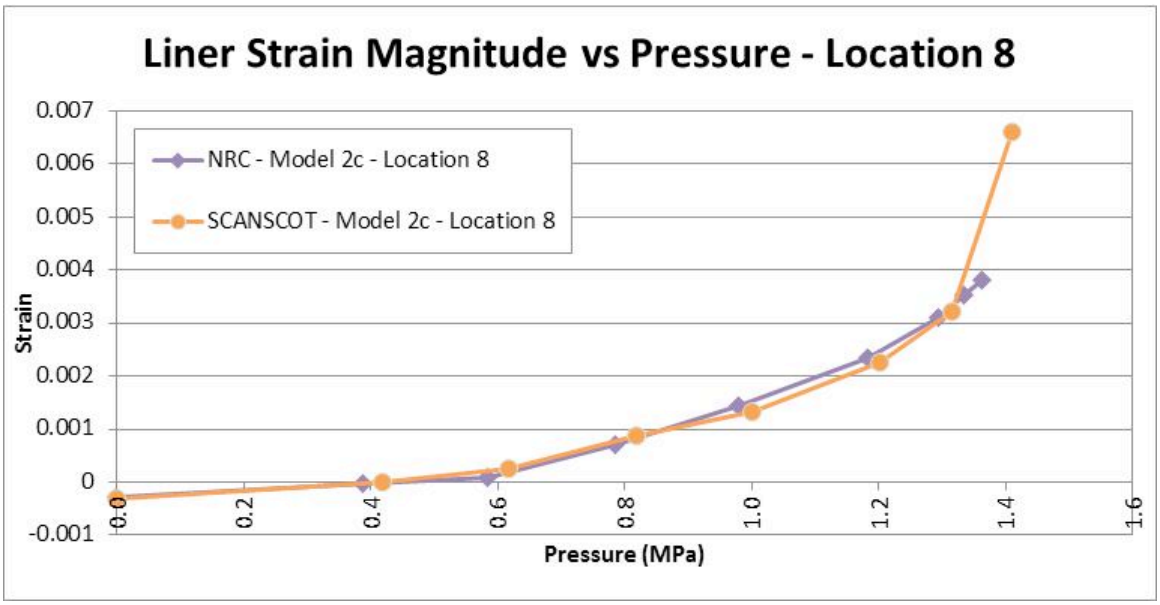

Figure 133: Model 2c Liner Strain Magnitude at Location 8

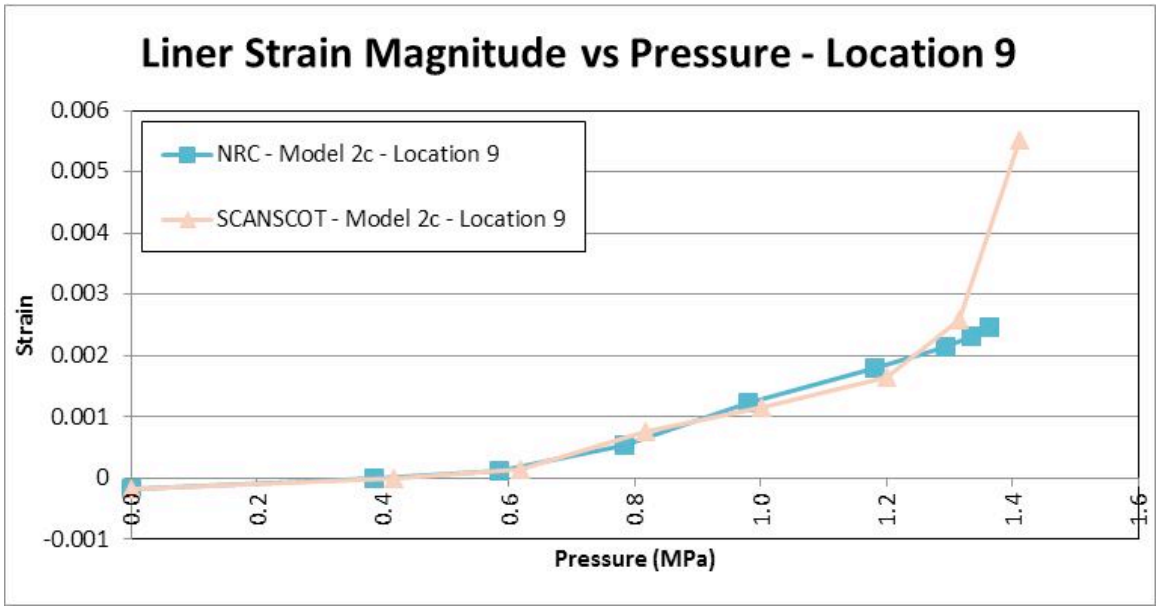

Figure 134: Model 2c Liner Strain Magnitude at Location 9

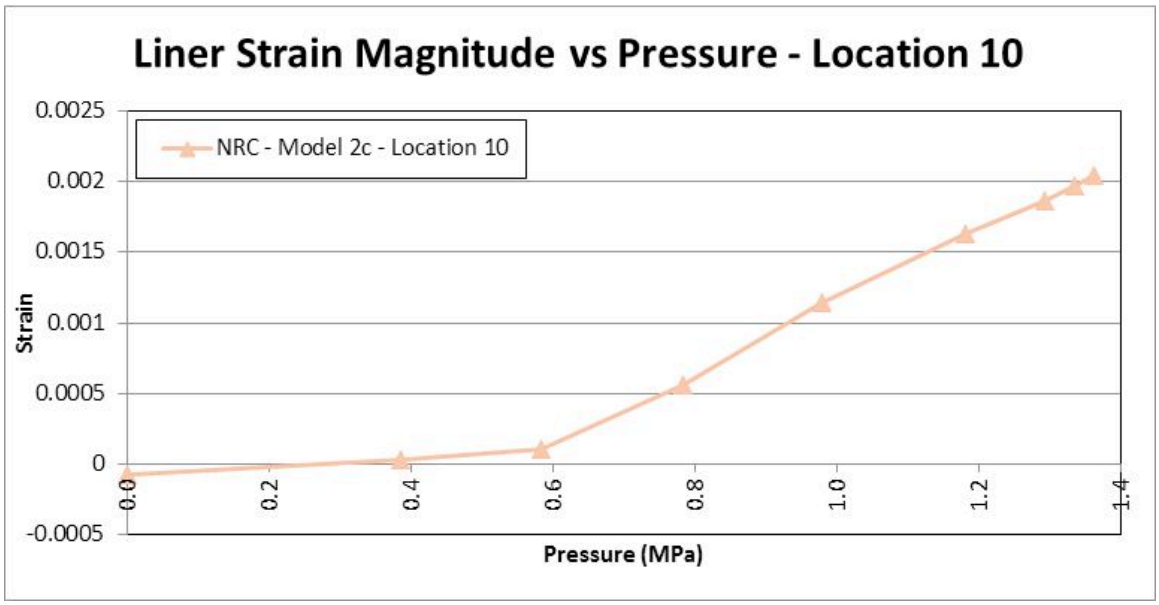

Figure 135: Model 2c Liner Strain Magnitude at Location 10

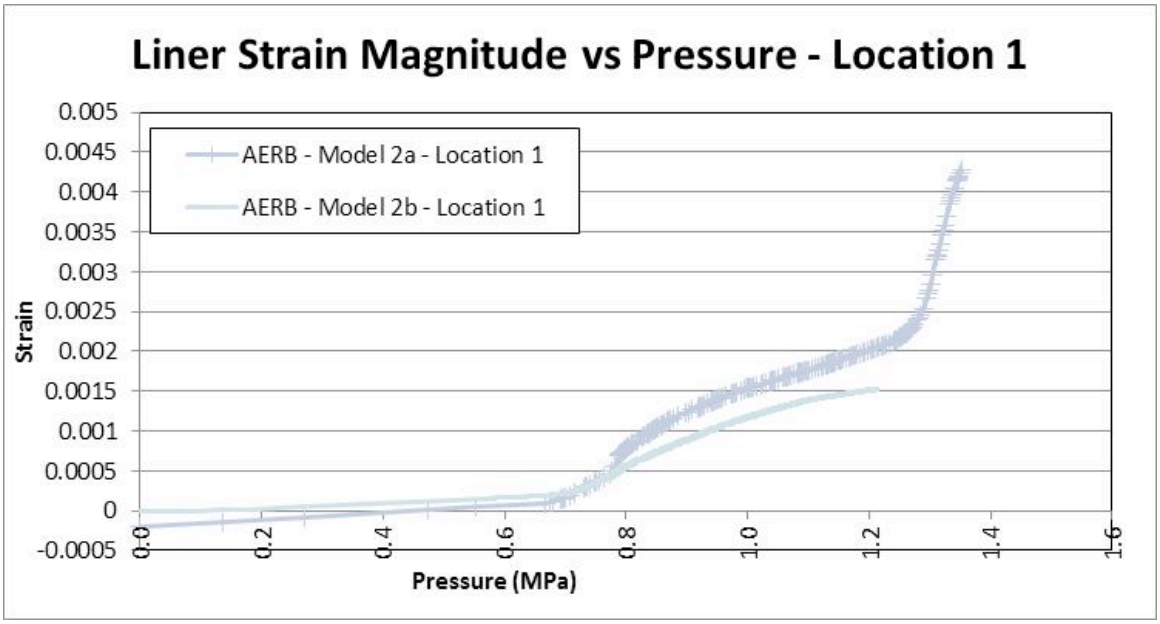

Figure 136: Comparison of Variability Between Models for AERB at Location 1

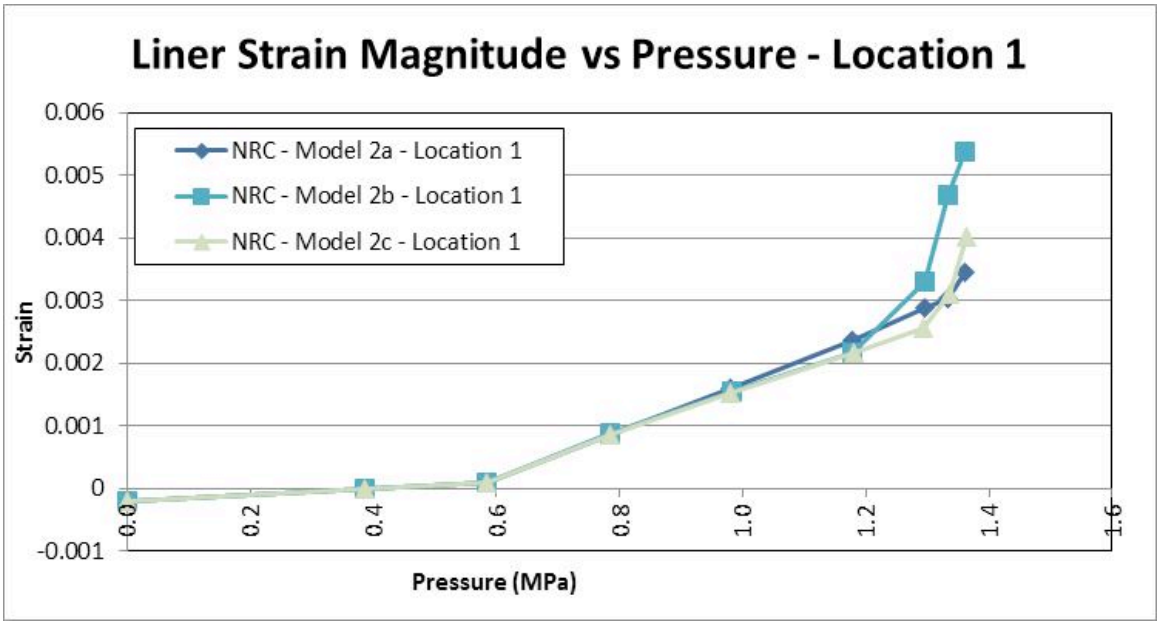

Figure 137: Comparison of Variability Between Models for NRC at Location 1

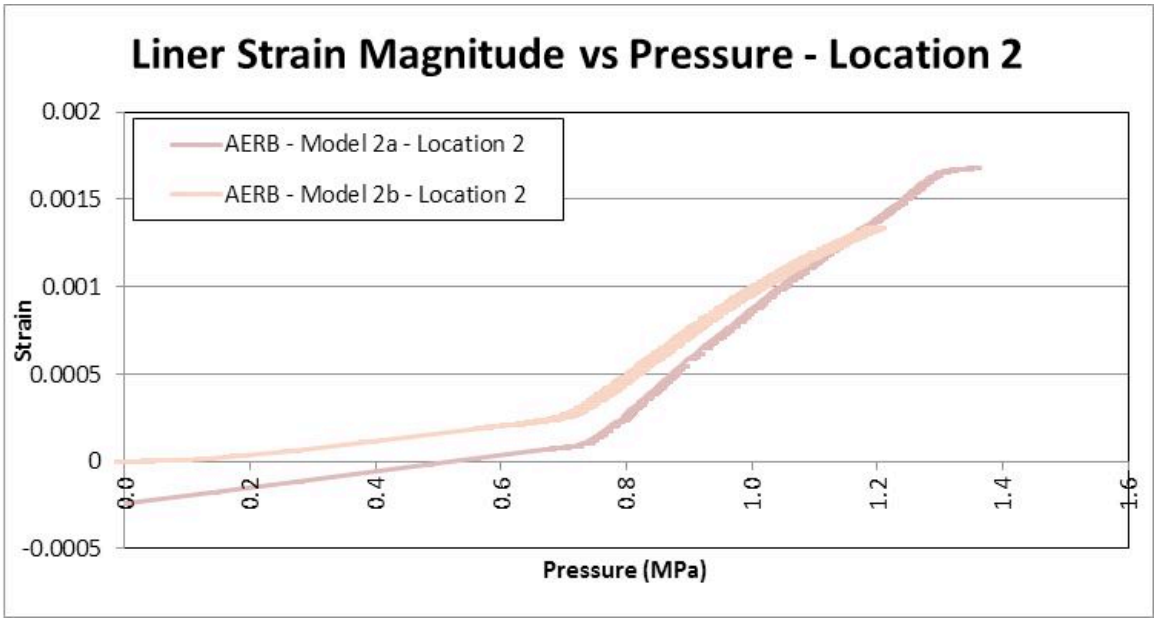

Figure 138: Comparison of Variability Between Models for AERB at Location 2

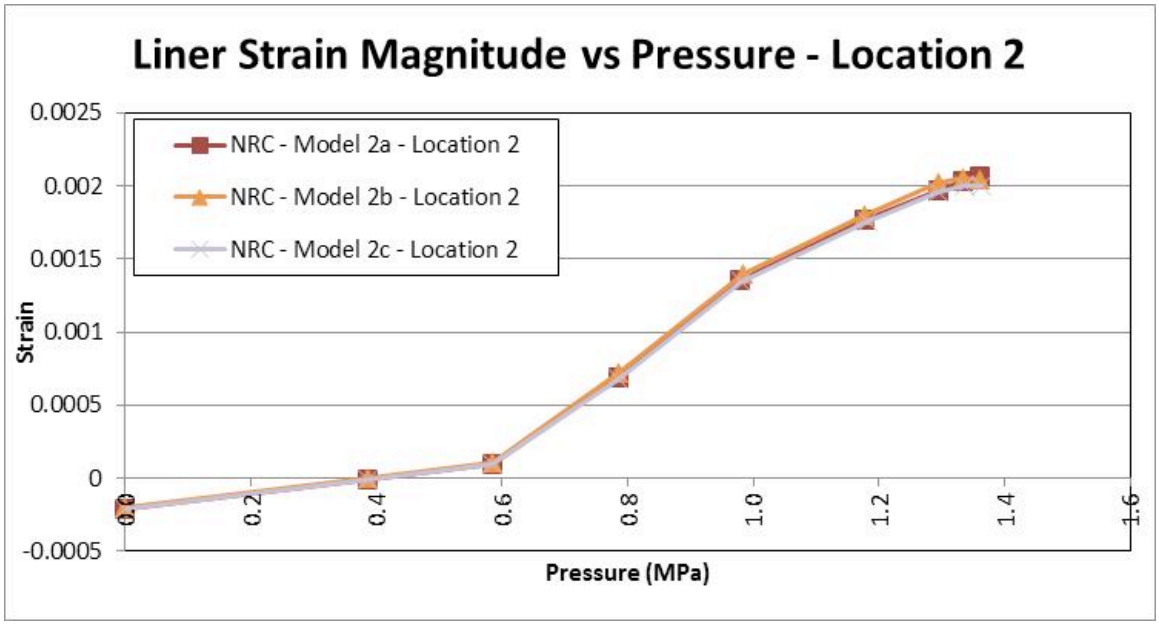

Figure 139: Comparison of Variability Between Models for NRC at Location 2

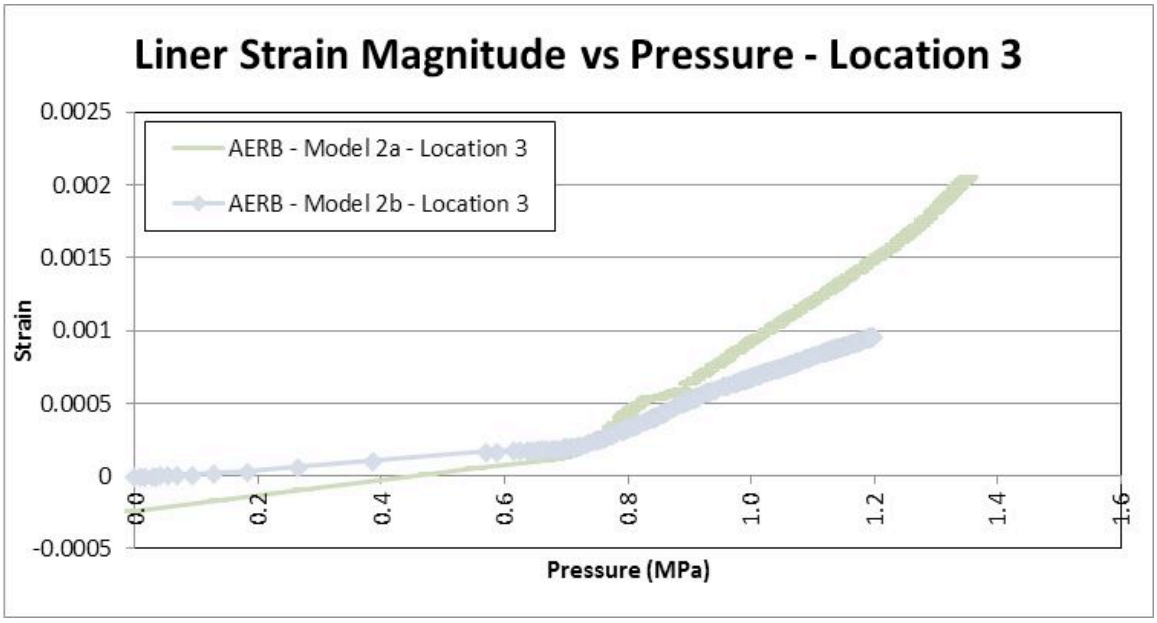

Figure 140: Comparison of Variability Between Models for AERB at Location 3

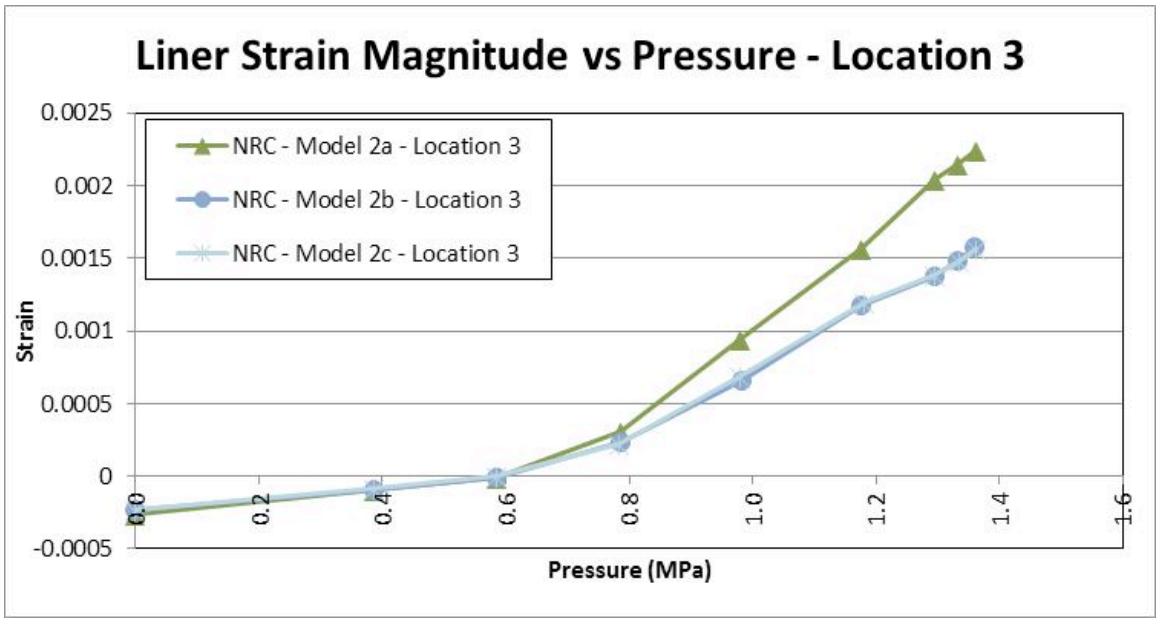

Figure 141: Comparison of Variability Between Models for NRC at Location 3

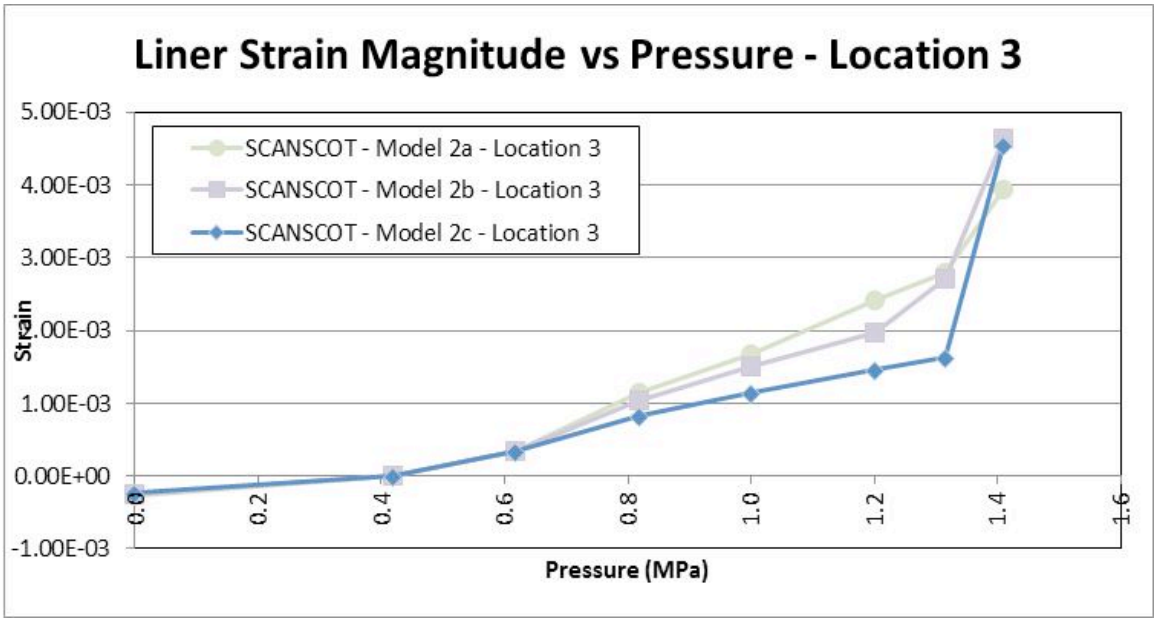

Figure 142: Comparison of Variability Between Models for SCANSCOT at Location 3

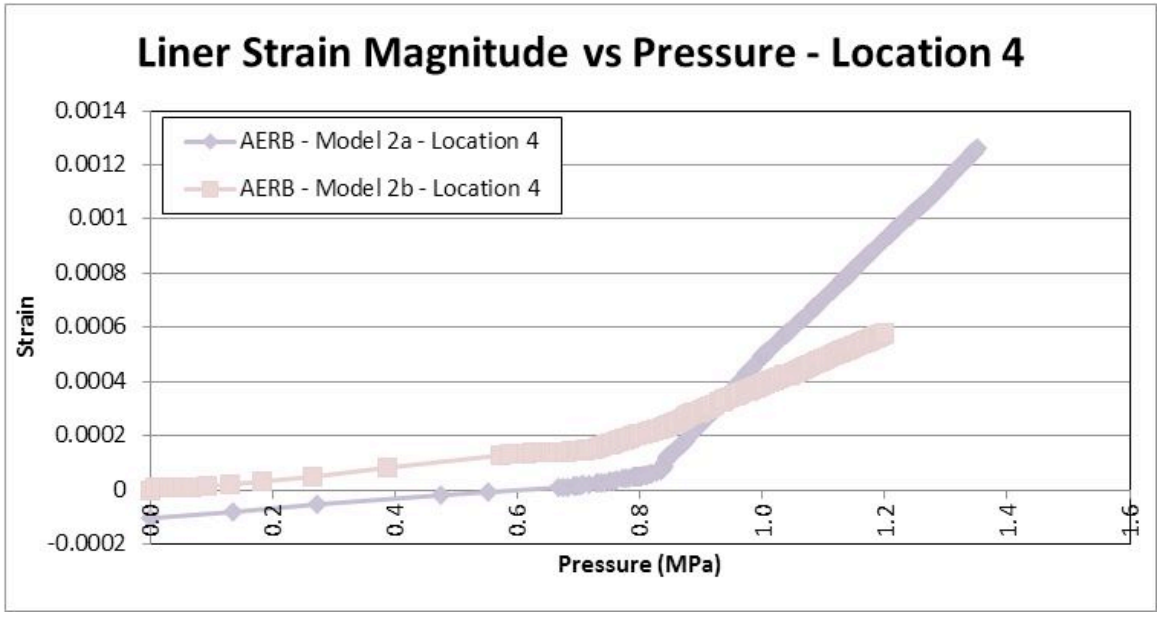

Figure 143: Comparison of Variability Between Models for AERB at Location 4

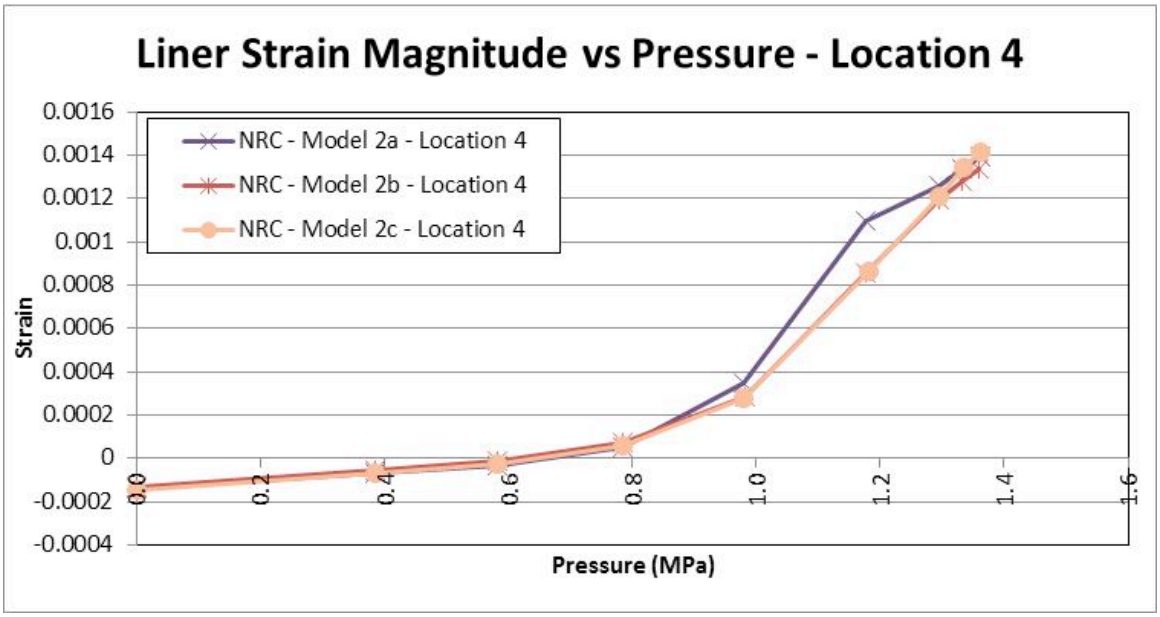

Figure 144: Comparison of Variability Between Models for NRC at Location 4

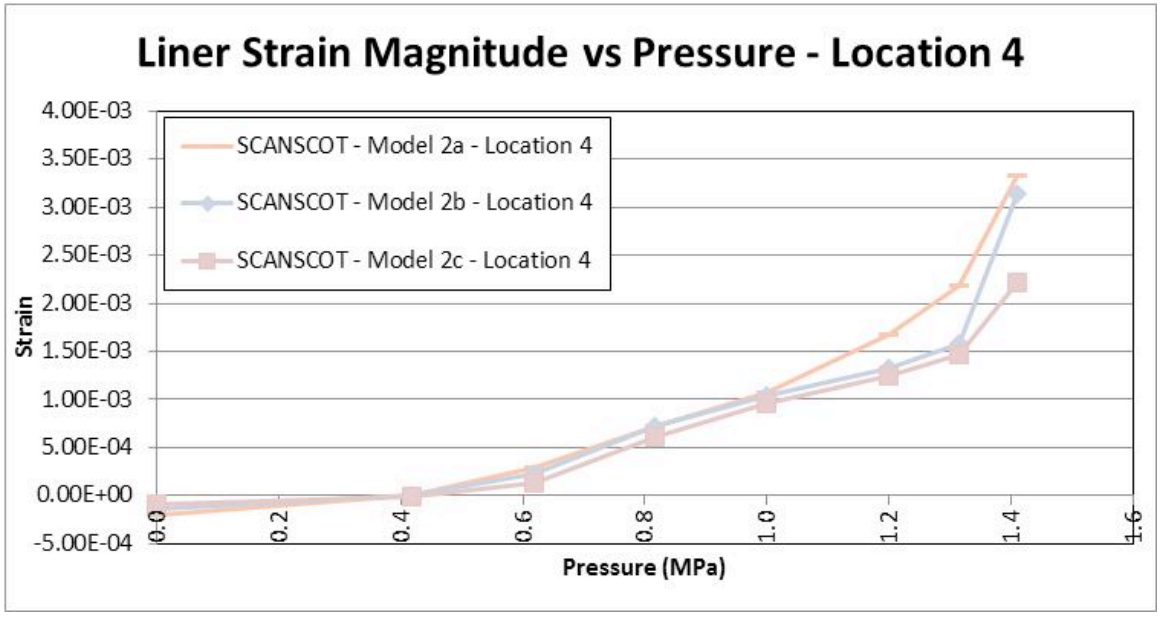

Figure 145: Comparison of Variability Between Models for SCANSCOT at Location 4

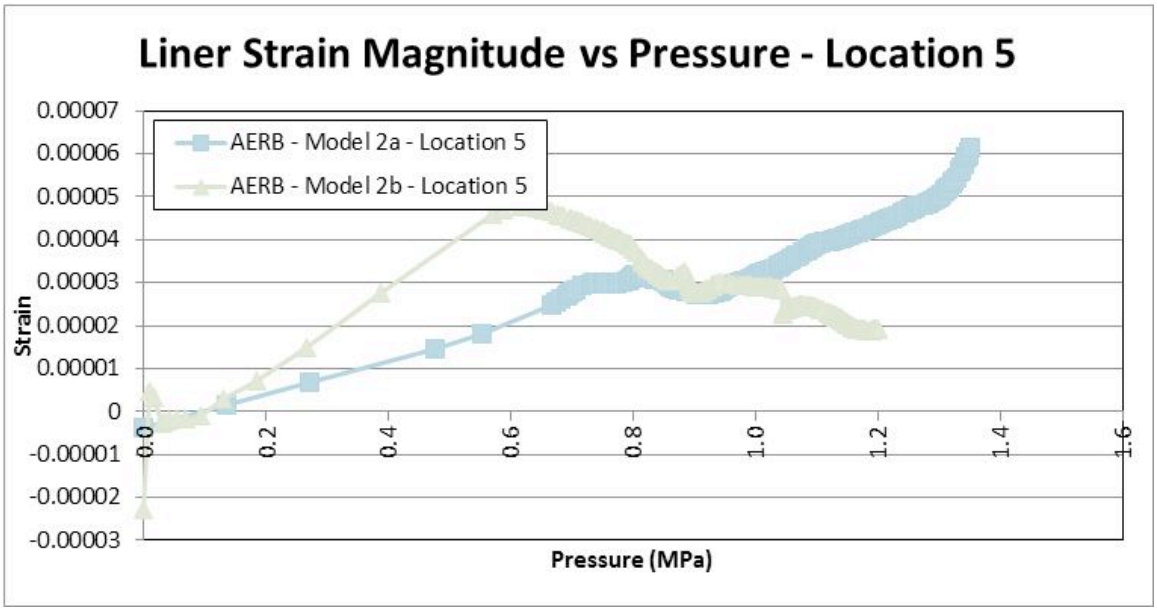

Figure 146: Comparison of Variability Between Models for AERB at Location 5

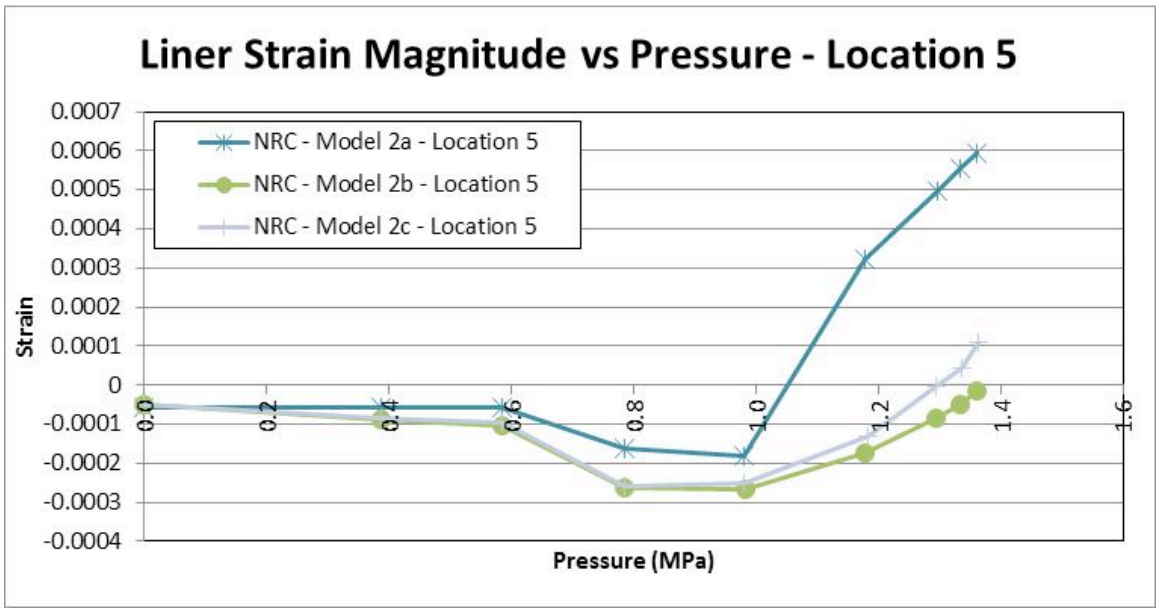

Figure 147: Comparison of Variability Between Models for NRC at Location 5

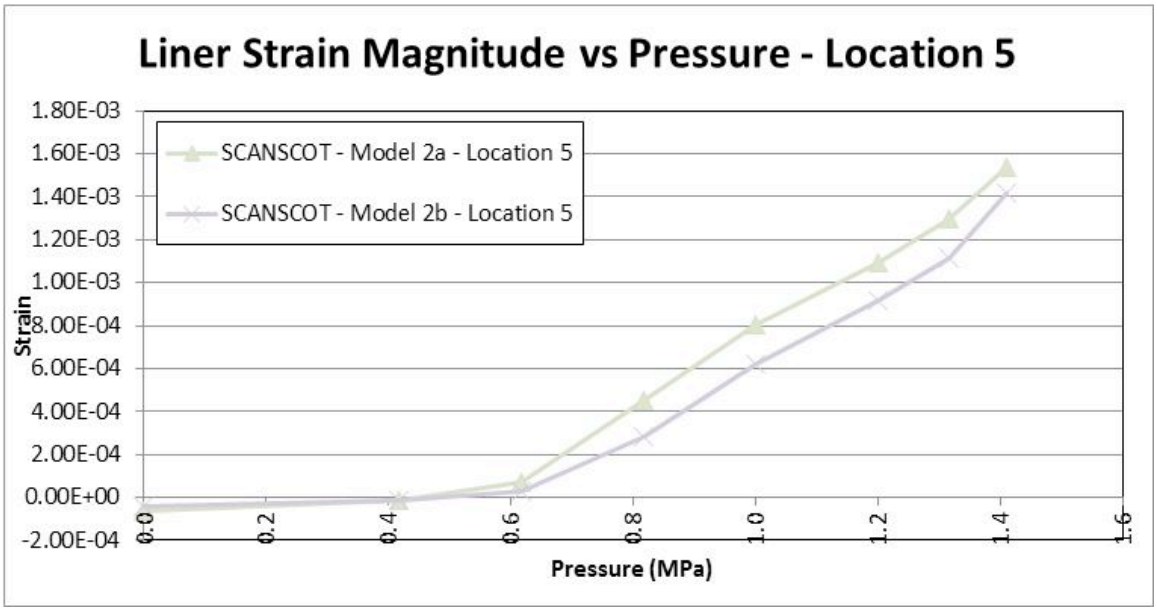

Figure 148: Comparison of Variability Between Models for SCANSCOT at Location 5

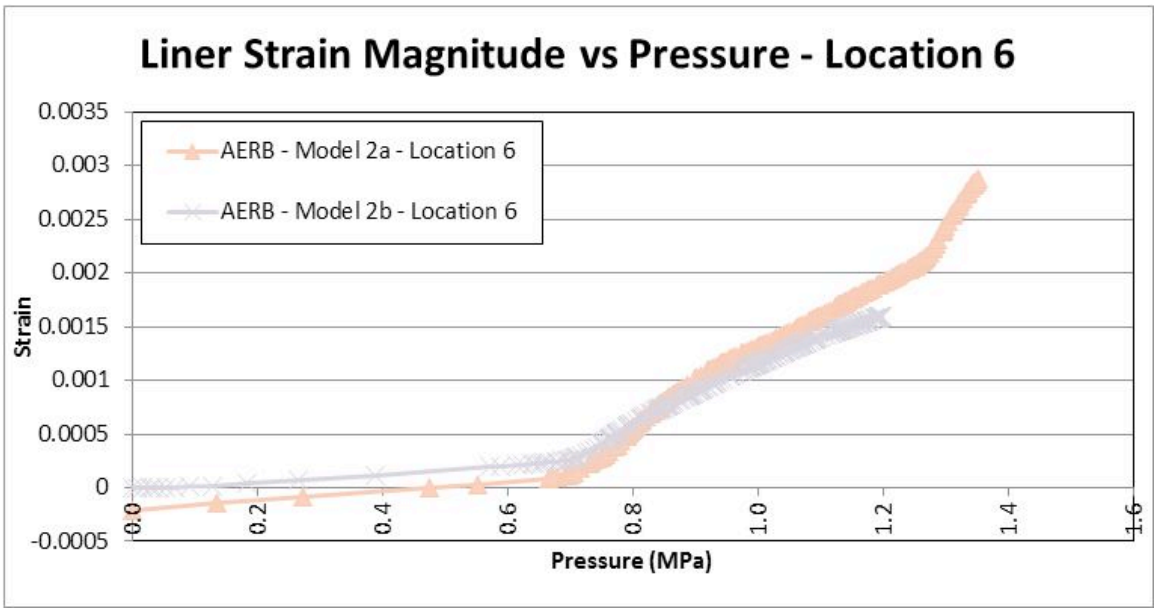

Figure 149: Comparison of Variability Between Models for AERB at Location 6

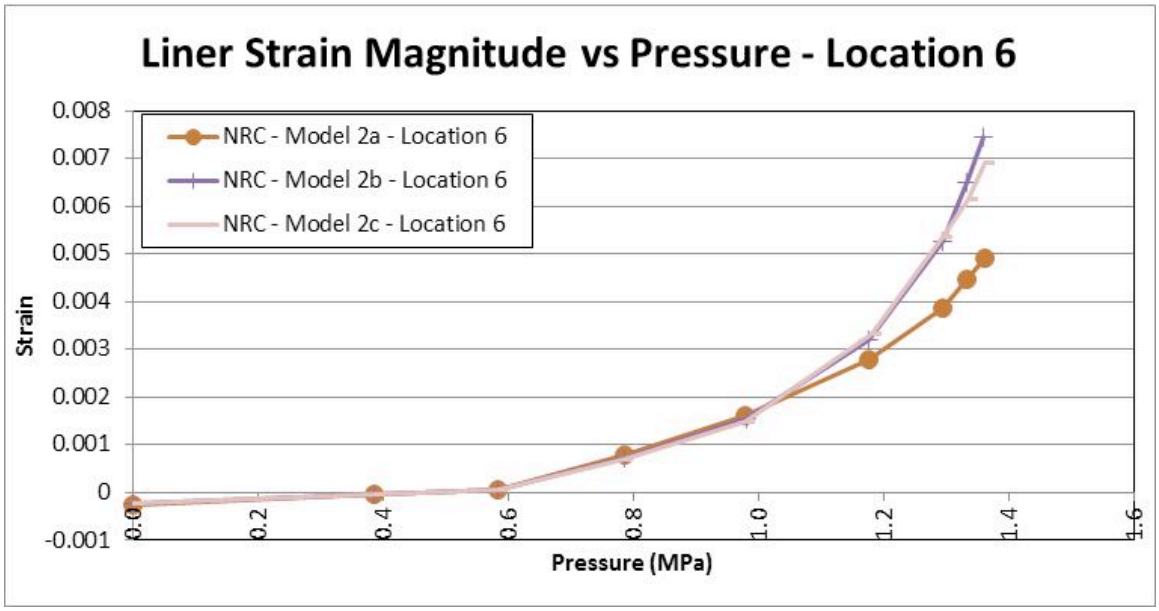

Figure 150: Comparison of Variability Between Models for NRC at Location 6

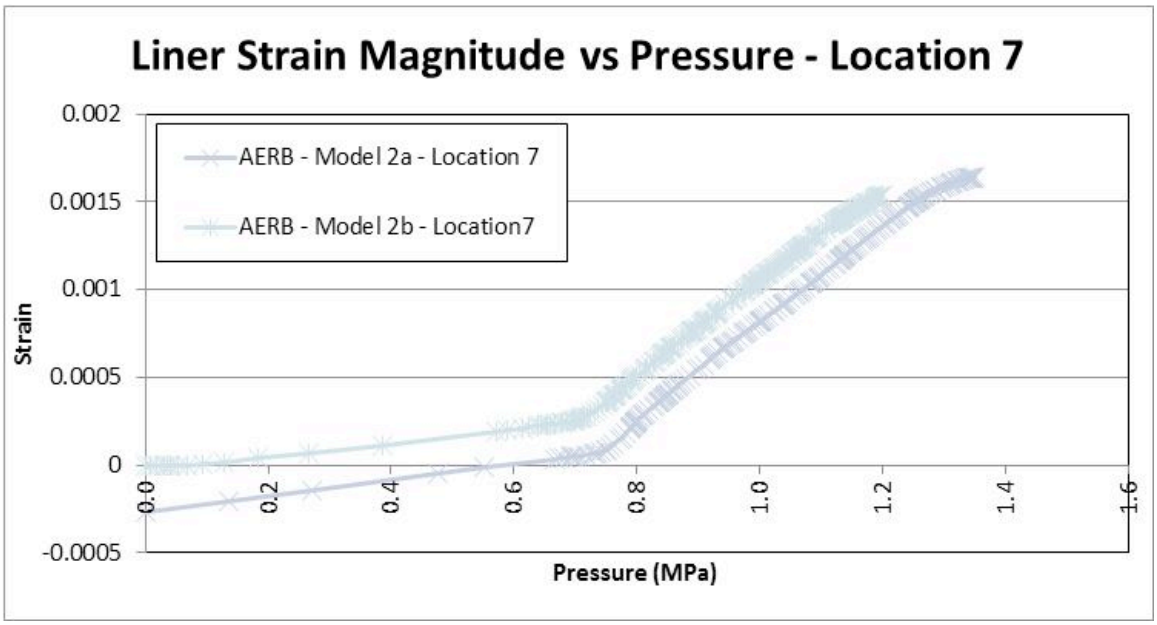

Figure 151: Comparison of Variability Between Models for AERB at Location 7

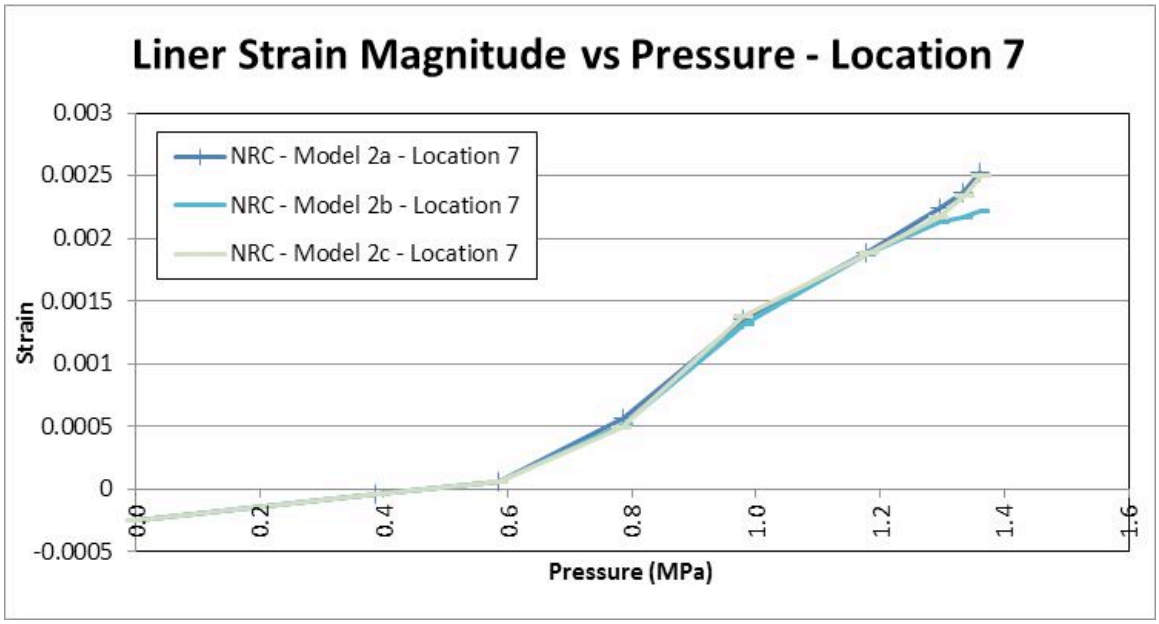

Figure 152: Comparison of Variability Between Models for NRC at Location 7

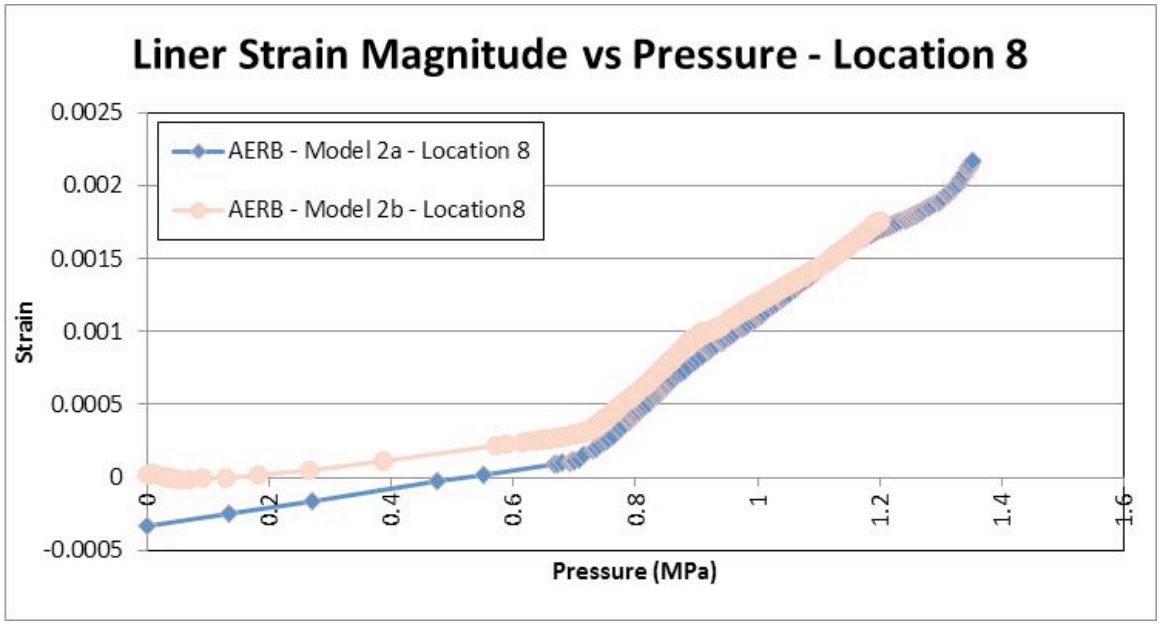

Figure 153: Comparison of Variability Between Models for AERB at Location 8

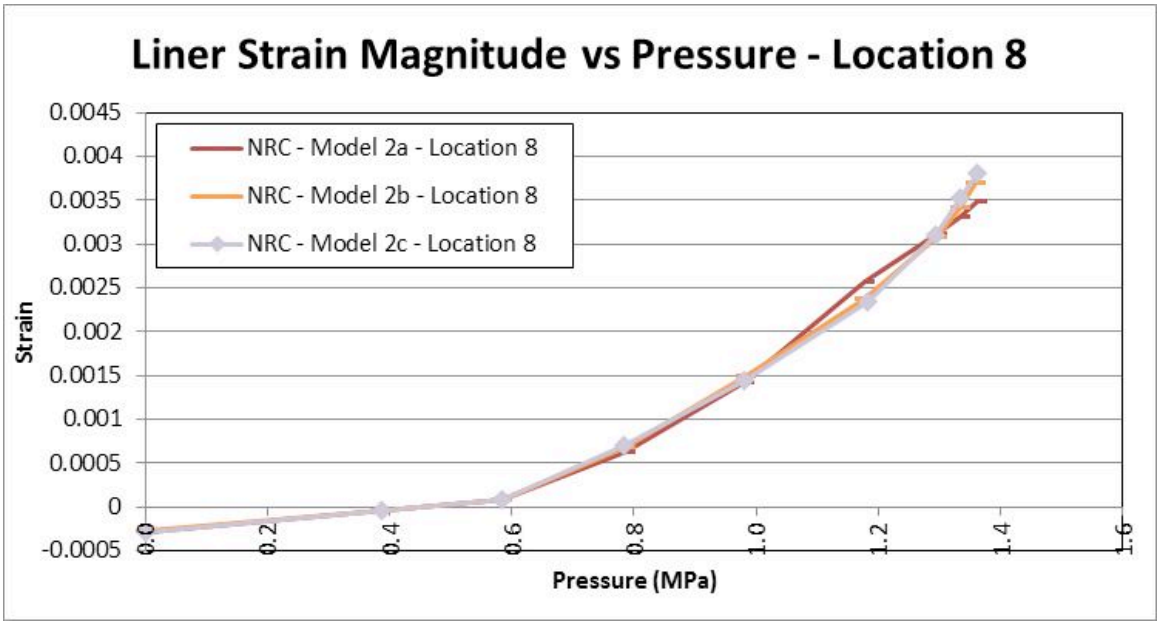

Figure 154: Comparison of Variability Between Models for NRC at Location 8

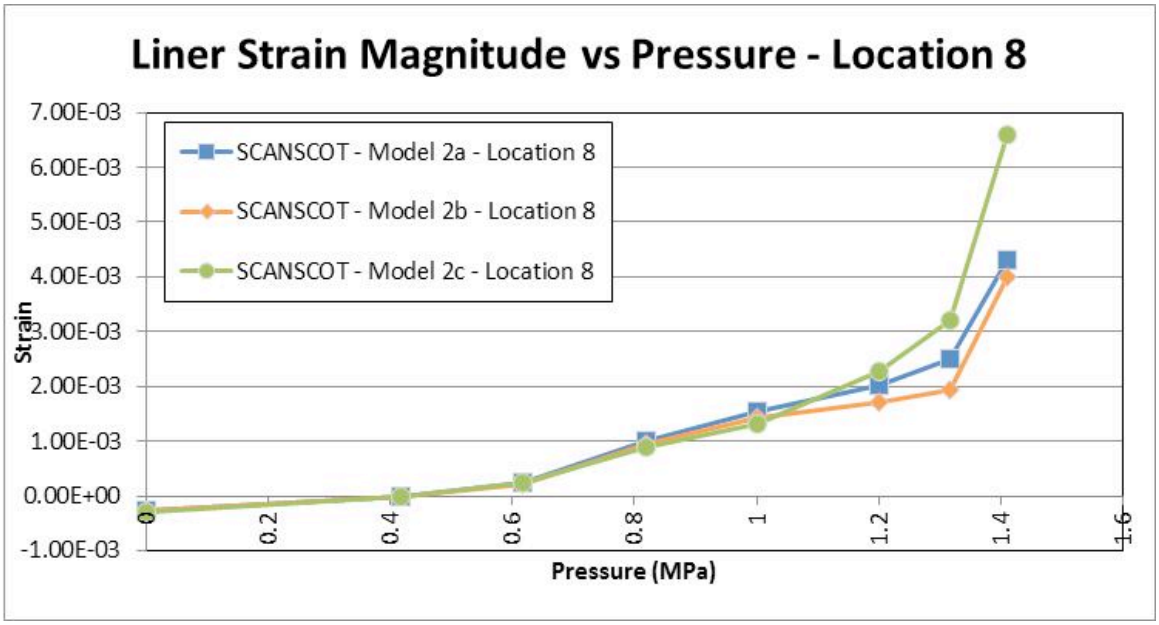

Figure 155: Comparison of Variability Between Models for SCANSCOT at Location 8

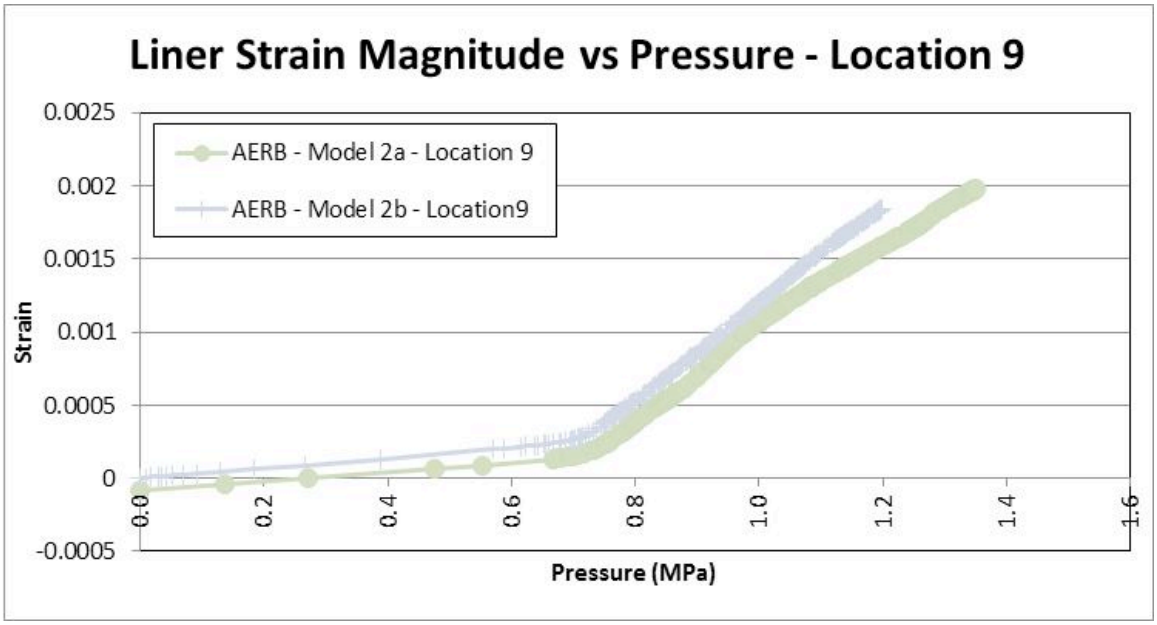

Figure 156: Comparison of Variability Between Models for AERB at Location 9

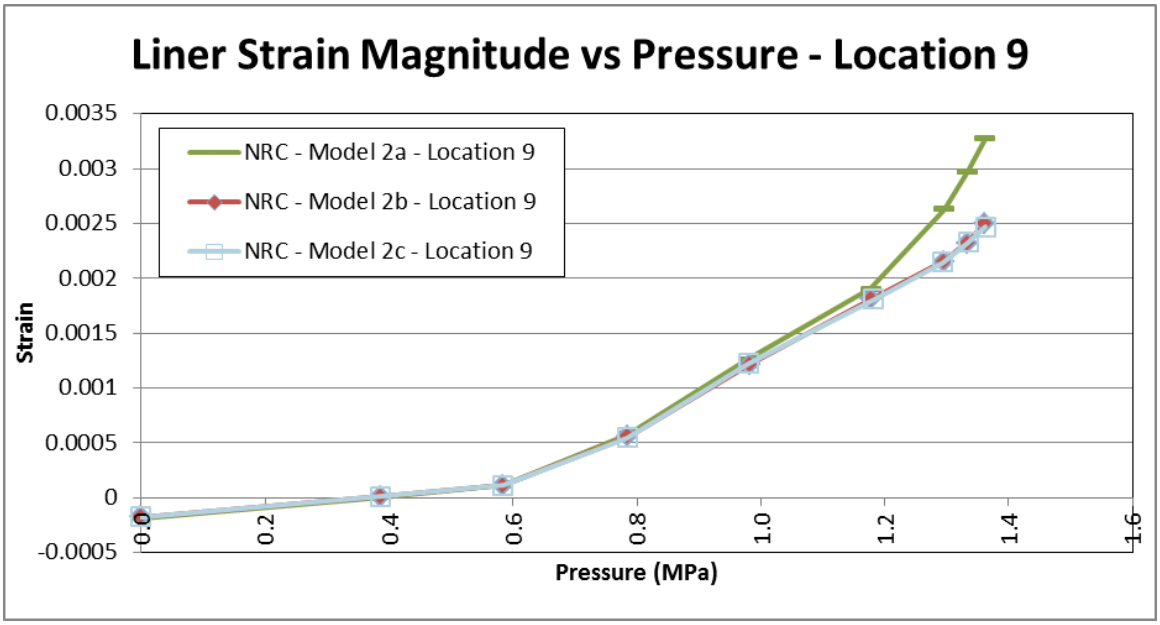

Figure 157: Comparison of Variability Between Models for NRC at Location 9

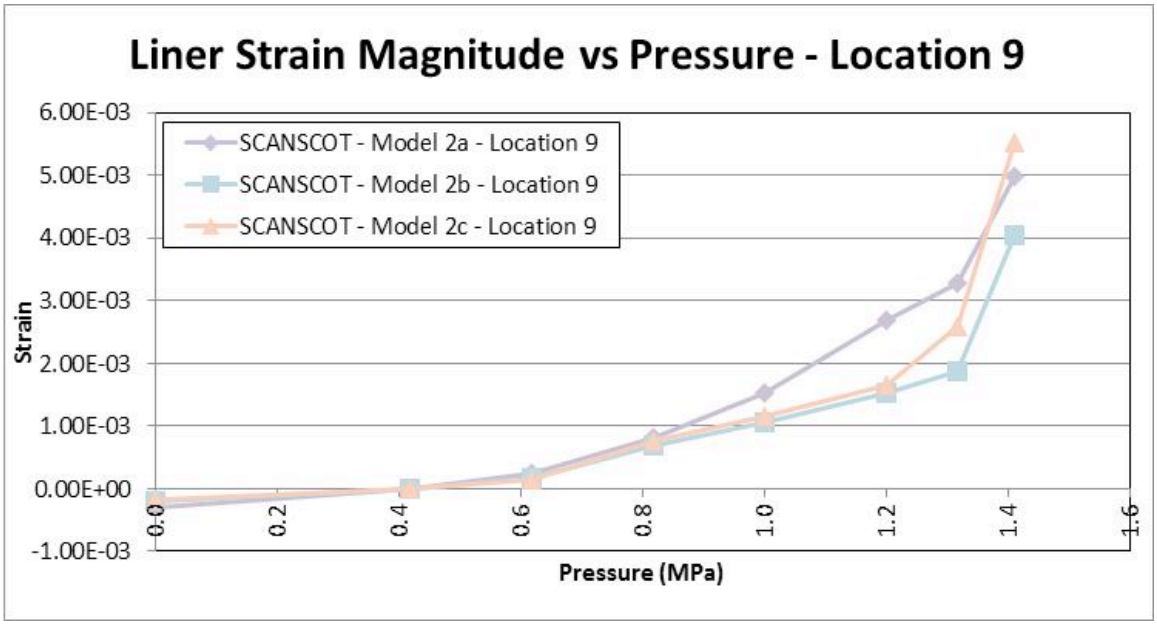

Figure 158: Comparison of Variability Between Models for SCANSCOT at Location 9

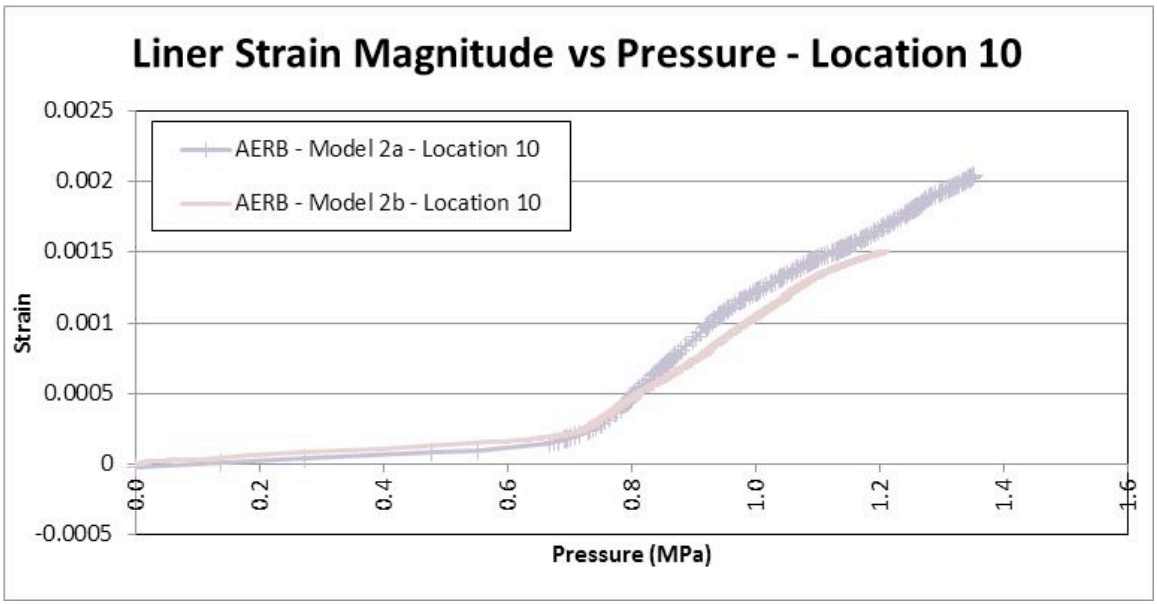

Figure 159: Comparison of Variability Between Models for AERB at Location 10

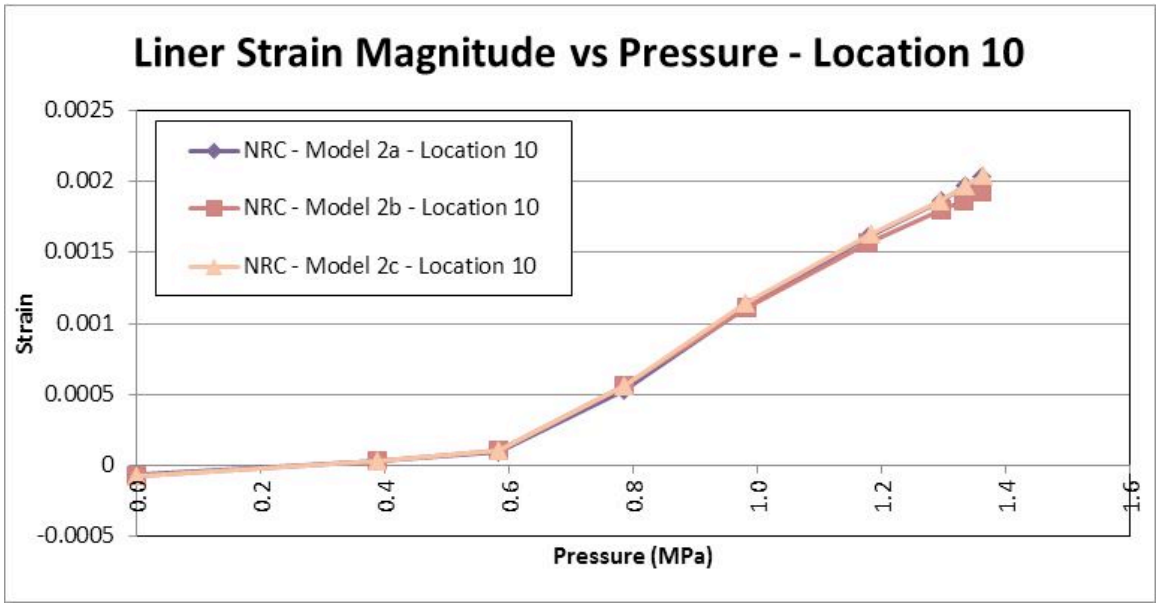

Figure 160: Comparison of Variability Between Models for NRC at Location 10

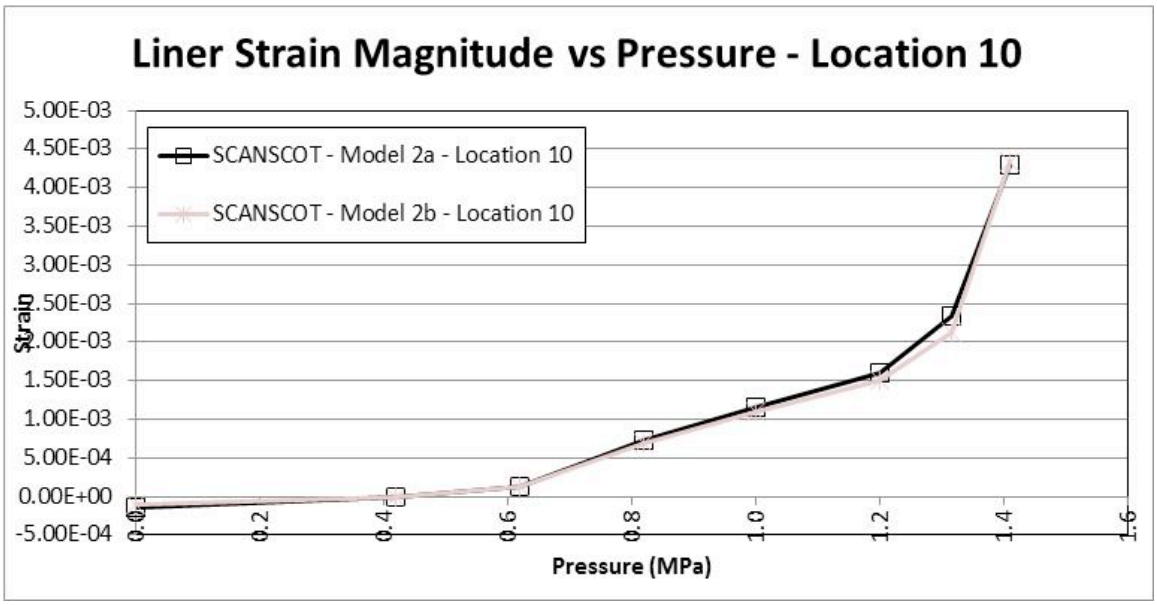

Figure 161: Comparison of Variability Between Models for SCANSCOT at Location 10

3.7. Tendon Stress Distribution

In addition to the liner strain magnitudes and locations, the participants were requested to provide tendon stress distributions for the pressure milestones specified above. These tendon stress profiles for Model 2 are presented in Figure 162 through Figure 229. These figures are subdivided into two subsections corresponding to the location of the tendons that are being investigated. The first tendon of interest is the hoop tendon nearest the penetration hatch and the second tendon of interest is the tendon at the extreme top of Model 2.

3.7.1. Hoop Tendon Nearest the Penetration Hatch

The tendon stress distributions provided by the participants for the hoop tendon nearest the penetration hatch are presented in Figure 162 through Figure 195. The participant provided results agree well with one another in most cases. It should be noted that the abscissa and ordinate for these plots retains a constant scale to facilitate comparison between figures.

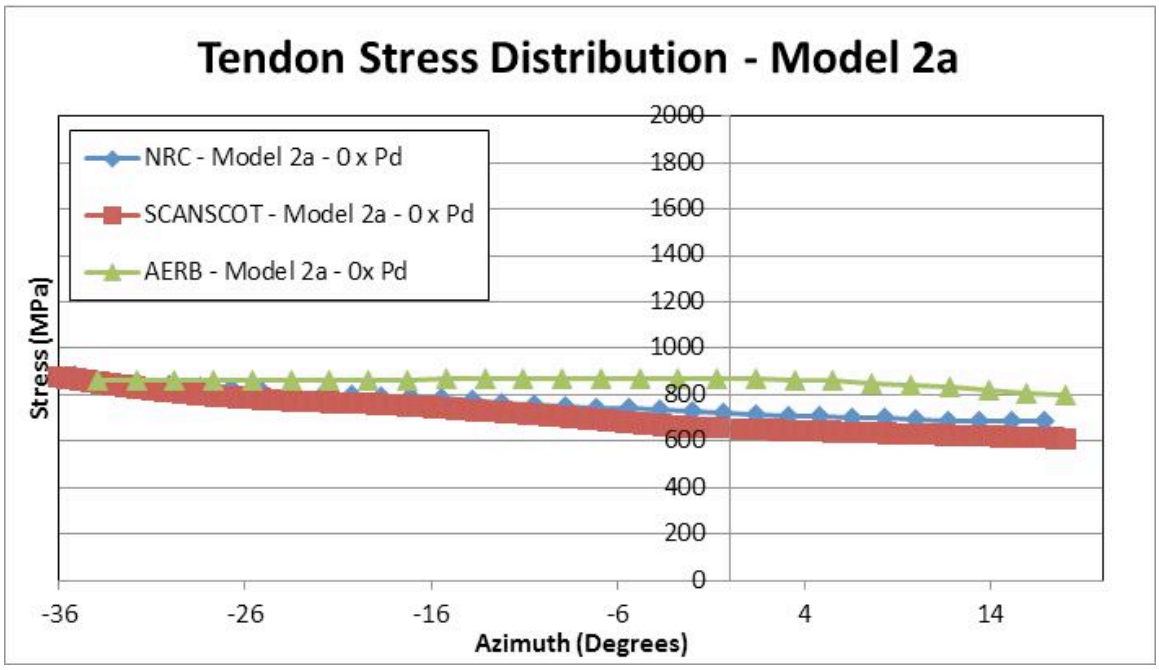

Figure 162: Model 2a Tendon Stress Distribution (Penetration Hatch) at Anchoring

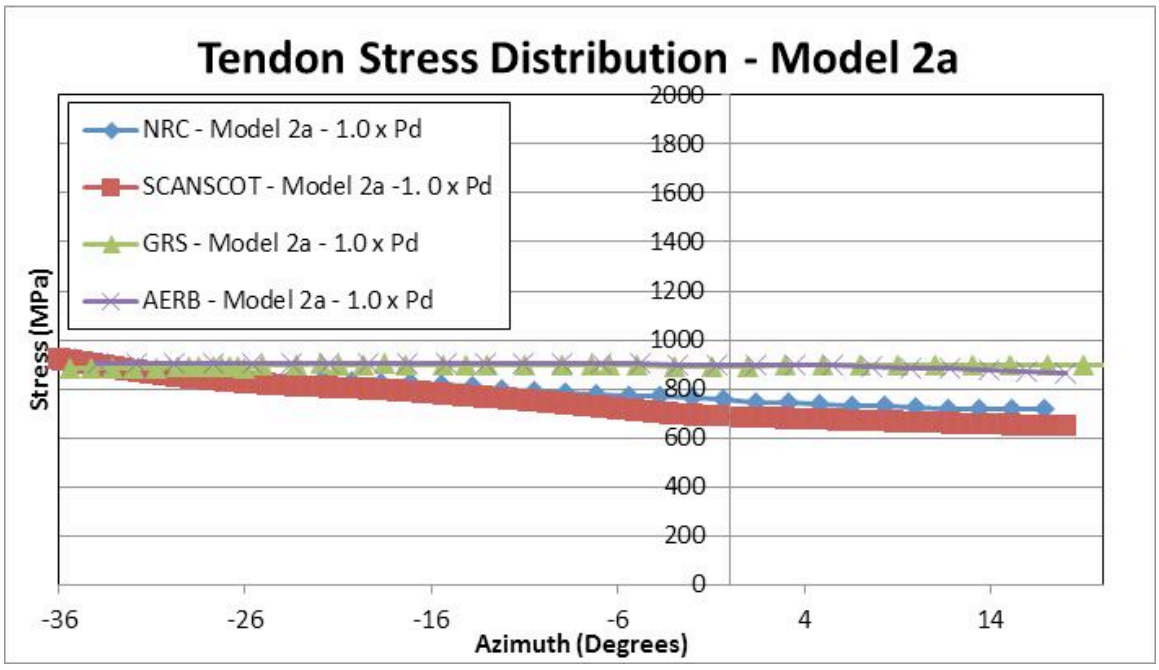

Figure 163: Model 2a Tendon Stress Distribution (Penetration Hatch) at 1xP_d

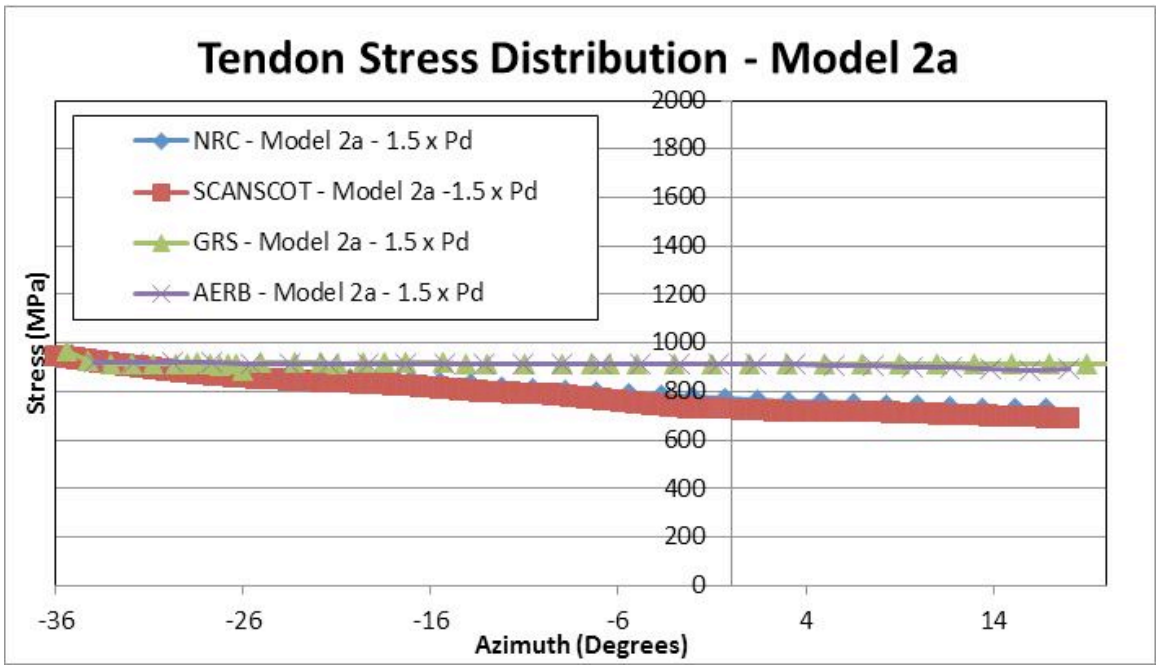

Figure 164: Model 2a Tendon Stress Distribution (Penetration Hatch) at 1.5xP_d

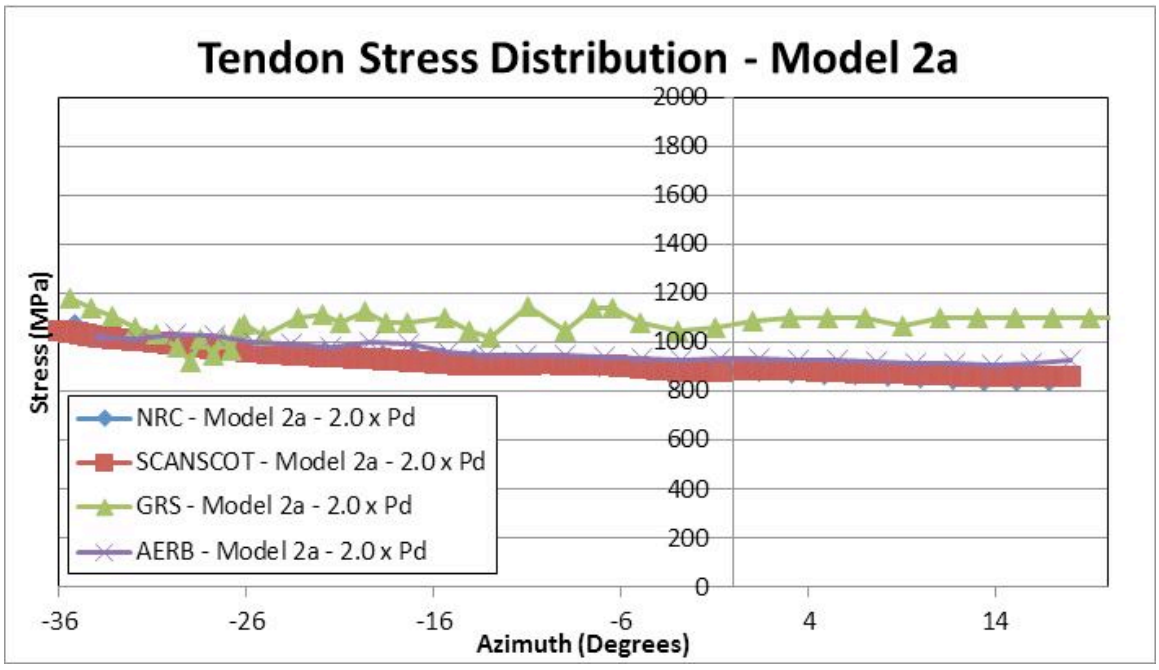

Figure 165: Model 2a Tendon Stress Distribution (Penetration Hatch) at 2xP_d

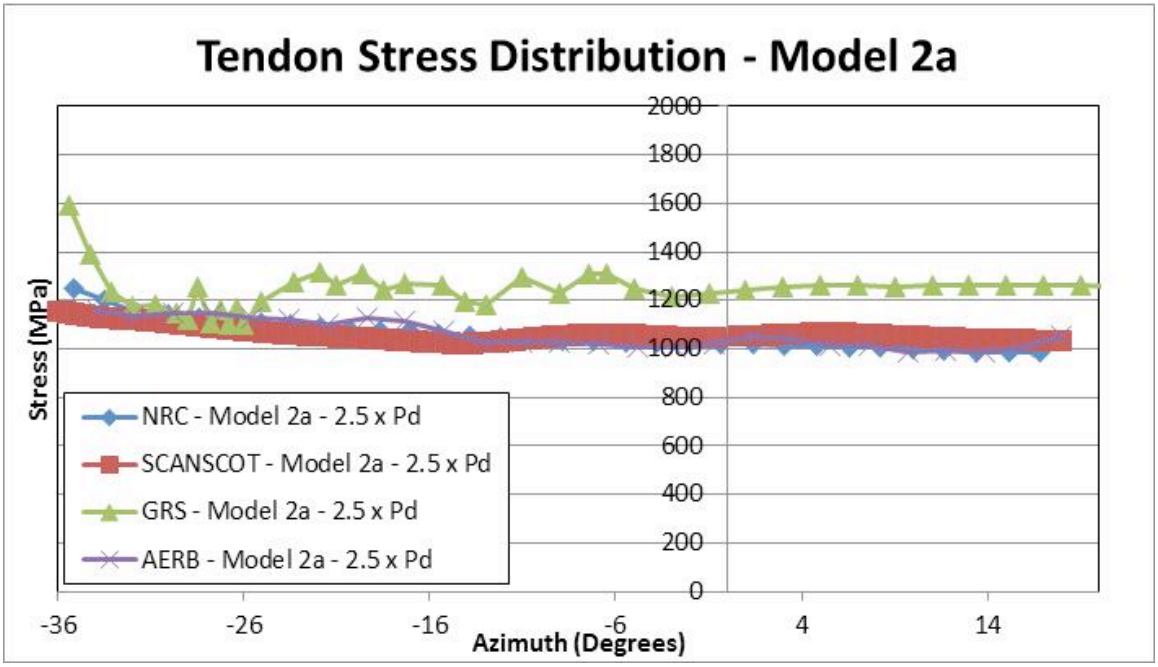

Figure 166: Model 2a Tendon Stress Distribution (Penetration Hatch) at 2.5xP_d

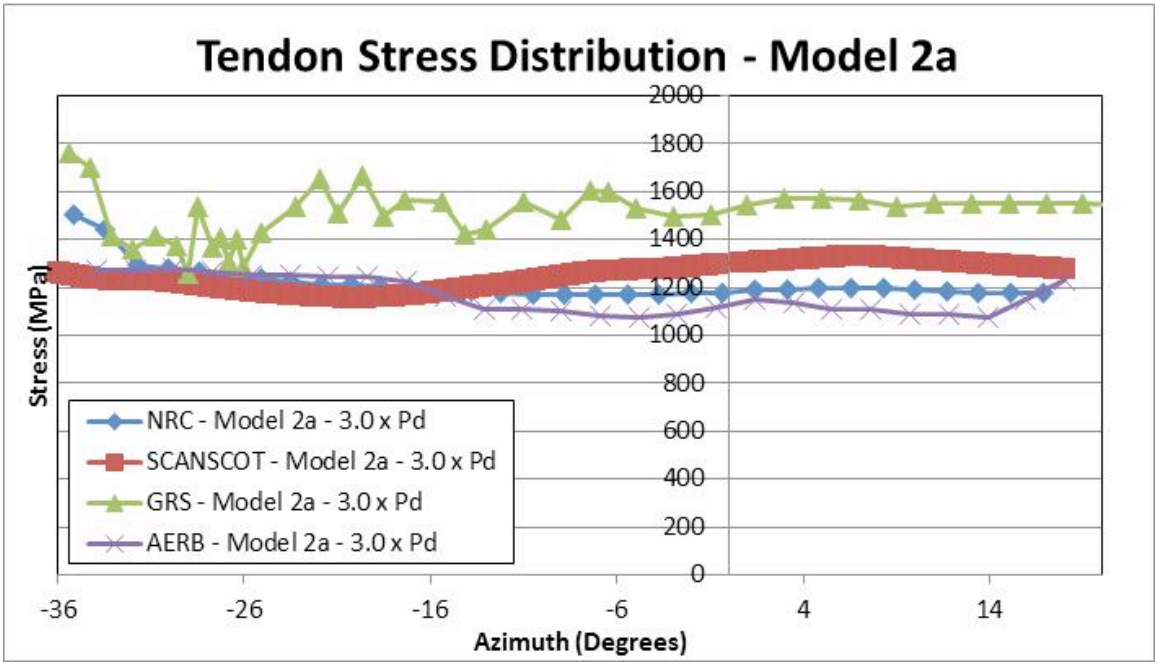

Figure 167: Model 2a Tendon Stress Distribution (Penetration Hatch)at 3xP_d

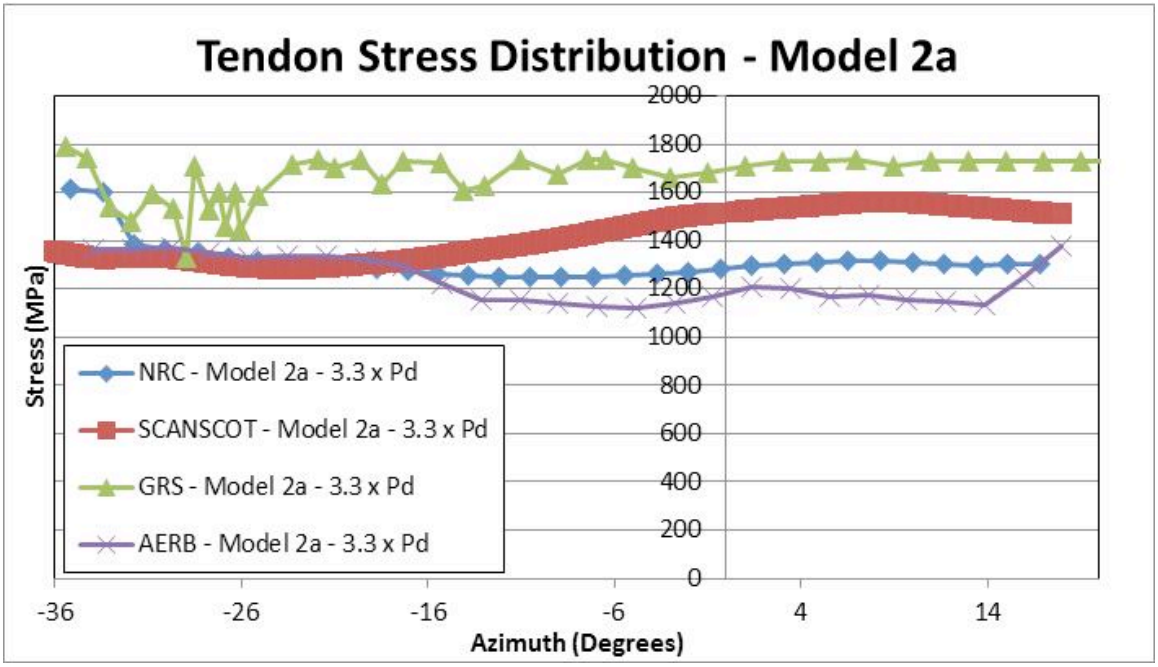

Figure 168: Model 2a Tendon Stress Distribution (Penetration Hatch) at 3.3xP_d

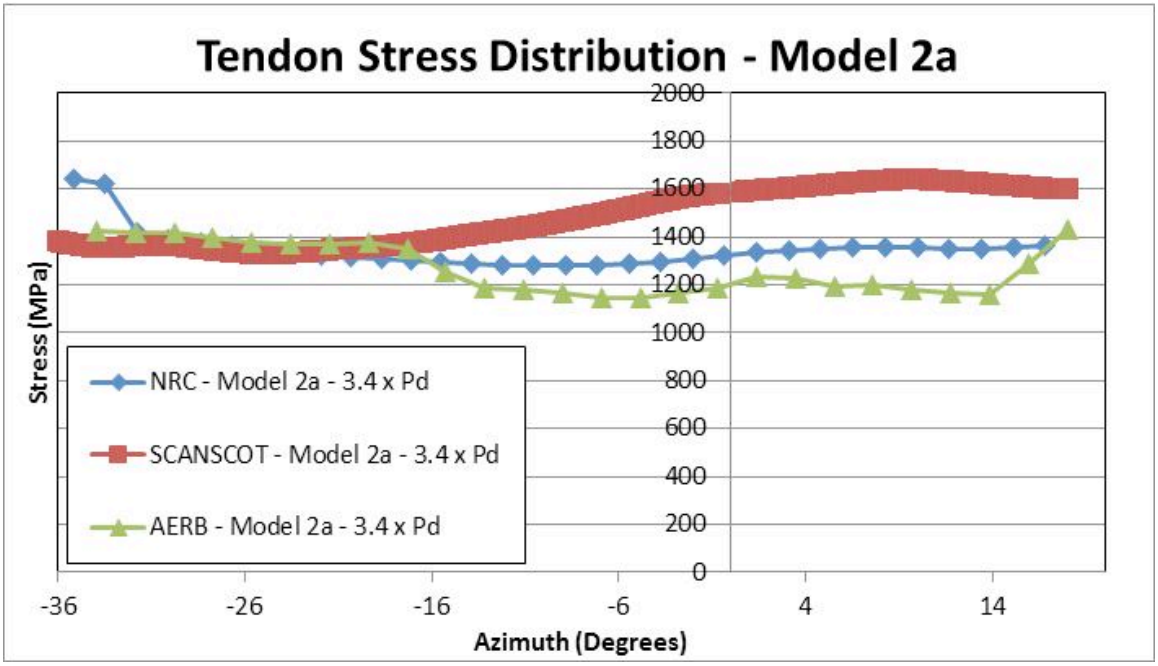

Figure 169: Model 2a Tendon Stress Distribution (Penetration Hatch) at 3.4xP_d

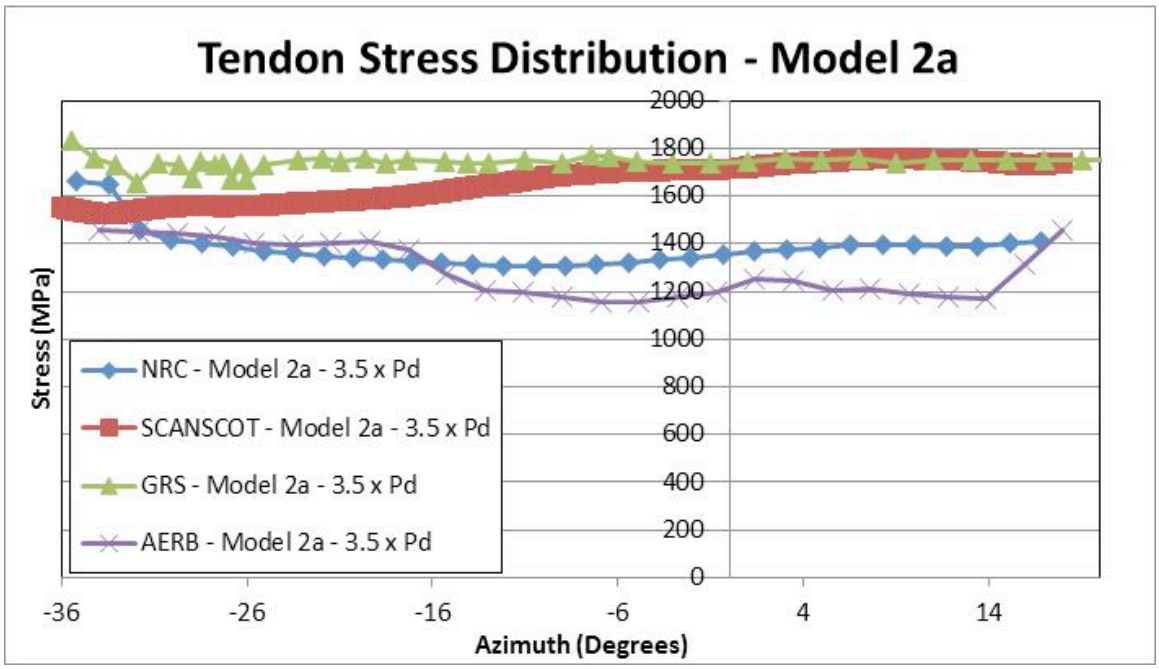

Figure 170: Model 2a Tendon Stress Distribution (Penetration Hatch) at Ultimate Pressure

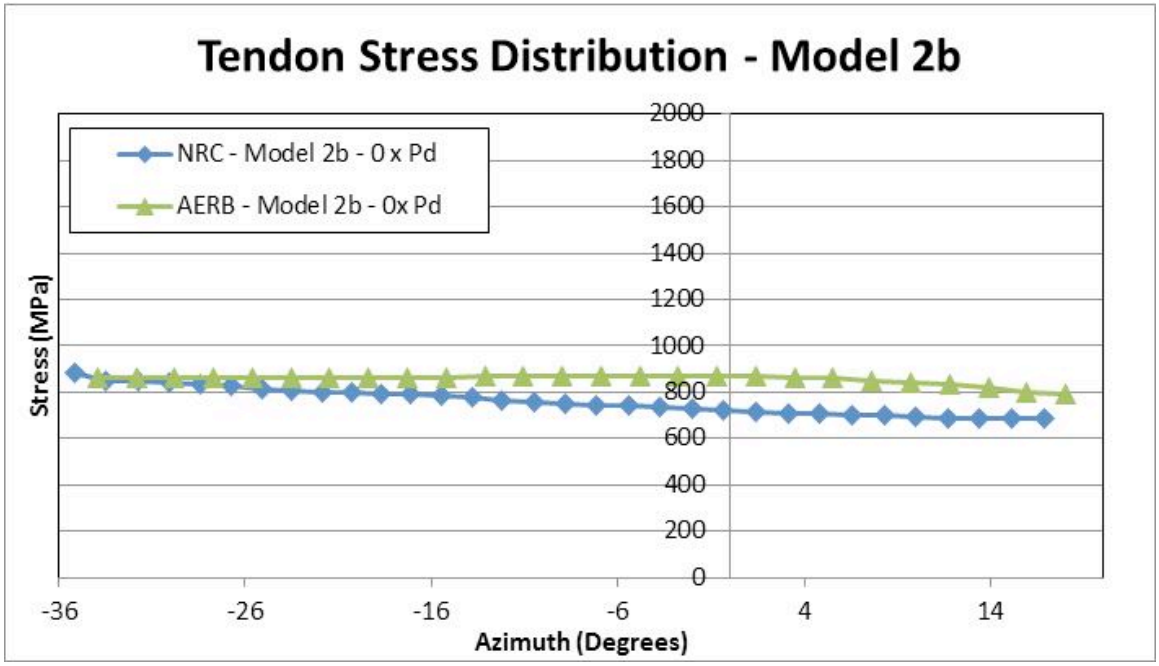

Figure 171: Model 2b Tendon Stress Distribution (Penetration Hatch) at Anchoring

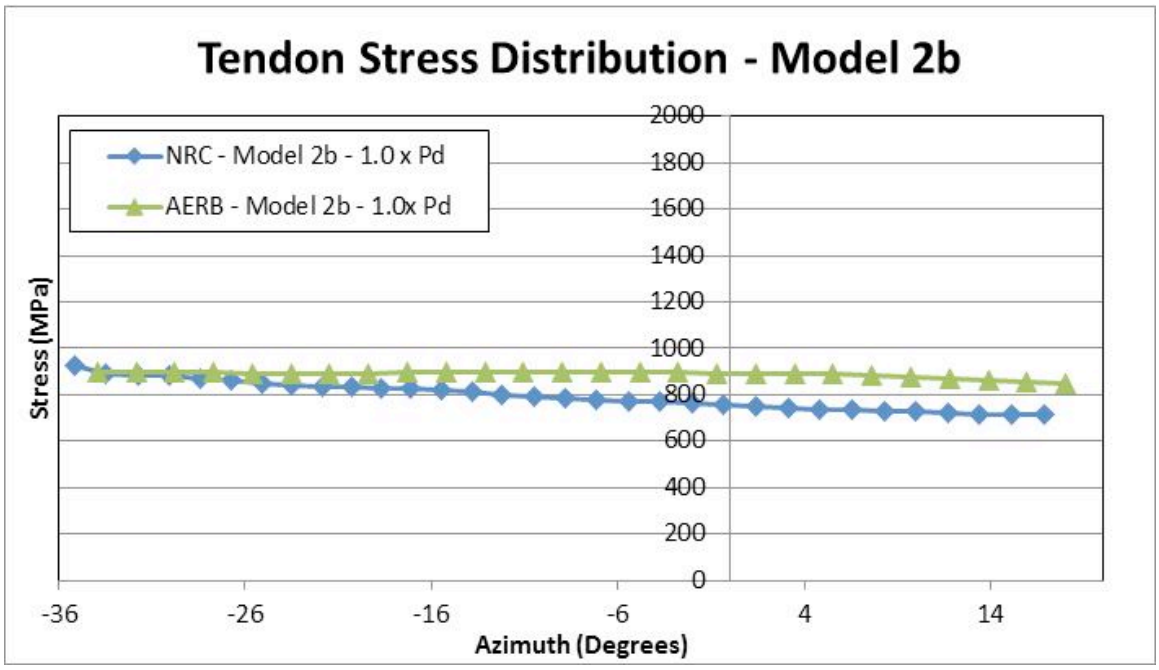

Figure 172: Model 2b Tendon Stress Distribution (Penetration Hatch) at 1xP_d

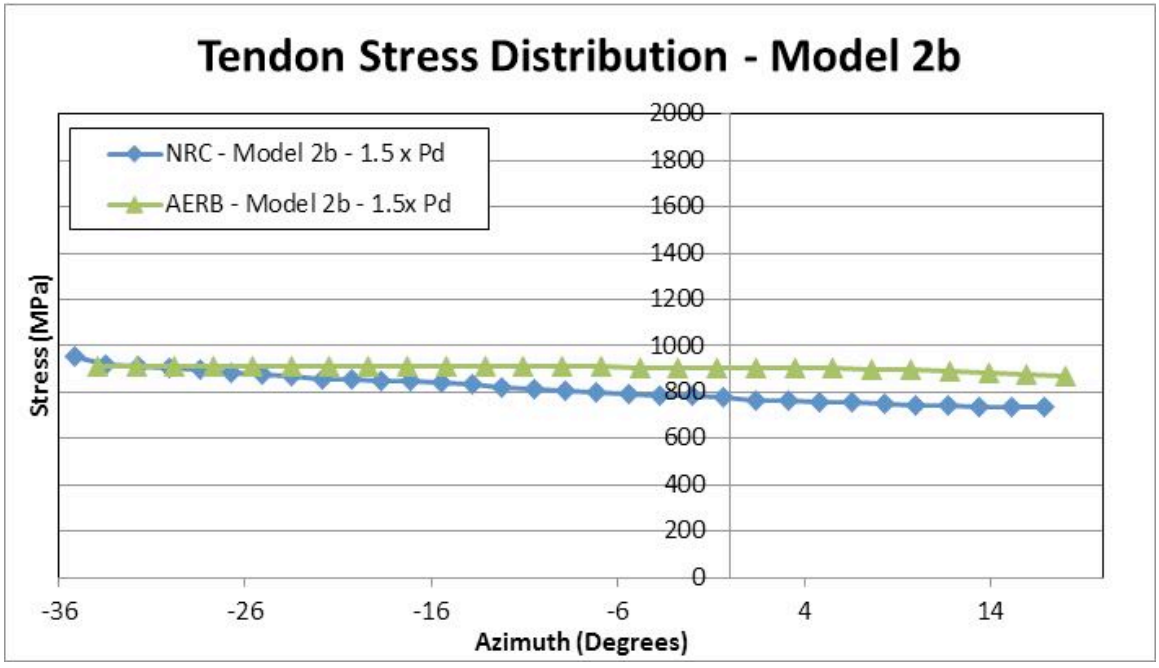

Figure 173: Model 2b Tendon Stress Distribution (Penetration Hatch) at 1.5xP_d

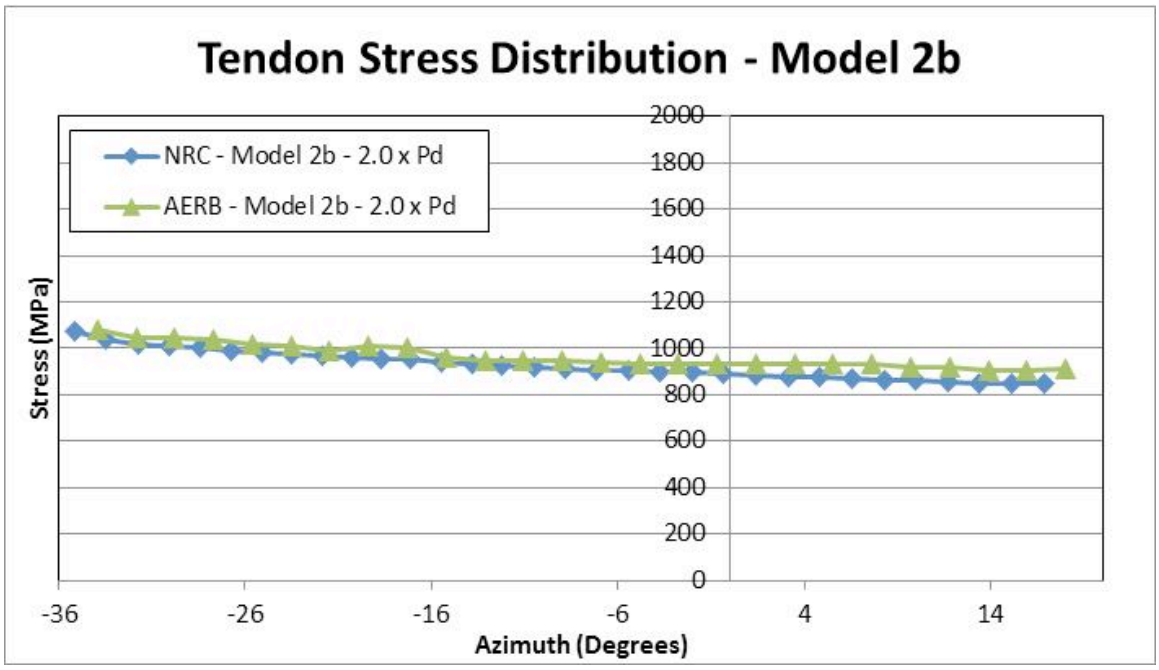

Figure 174: Model 2b Tendon Stress Distribution (Penetration Hatch) at 2xP_d

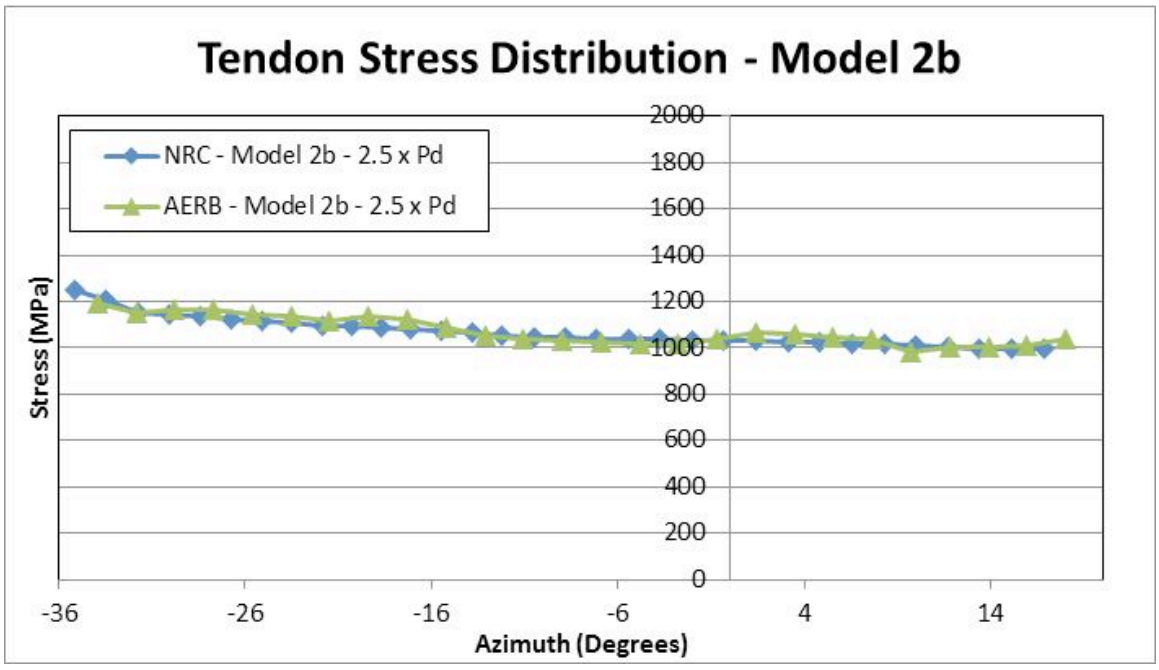

Figure 175: Model 2b Tendon Stress Distribution (Penetration Hatch) at 2.5xP_d

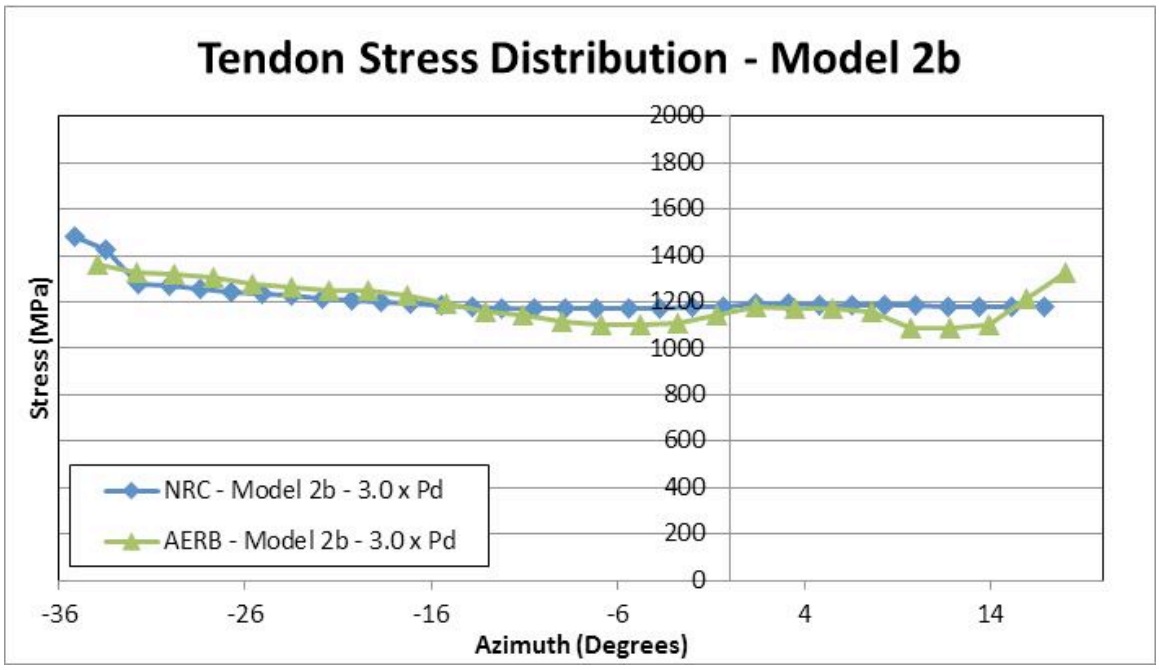

Figure 176: Model 2b Tendon Stress Distribution (Penetration Hatch) at 3xP_d

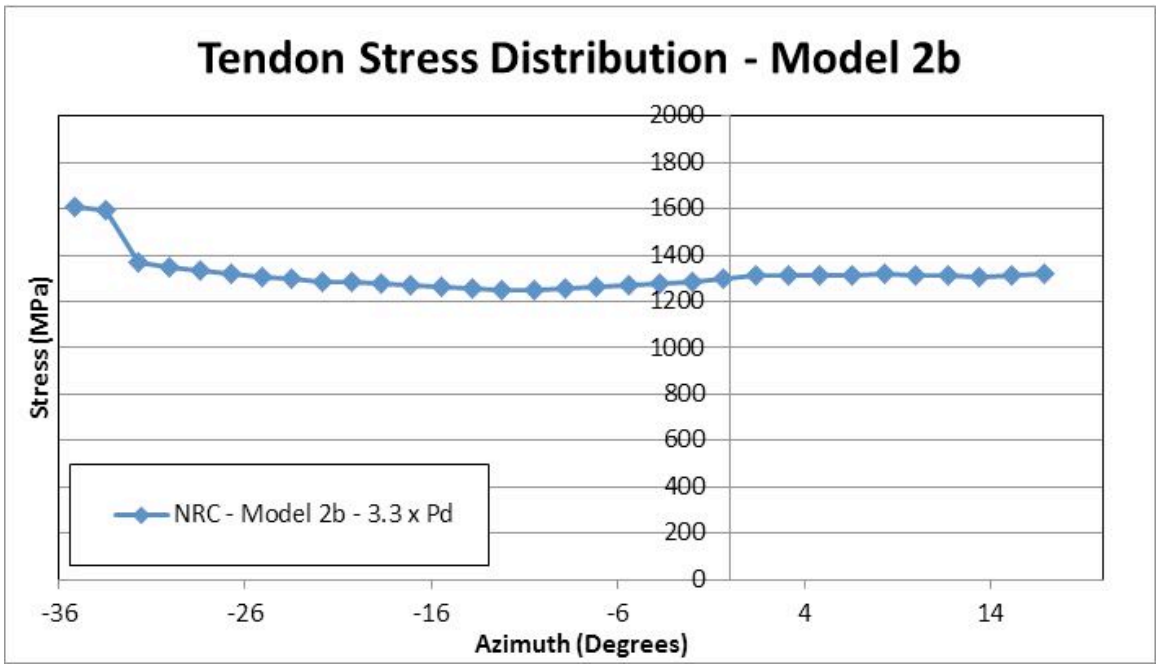

Figure 177: Model 2b Tendon Stress Distribution (Penetration Hatch) at 3.3xP_d

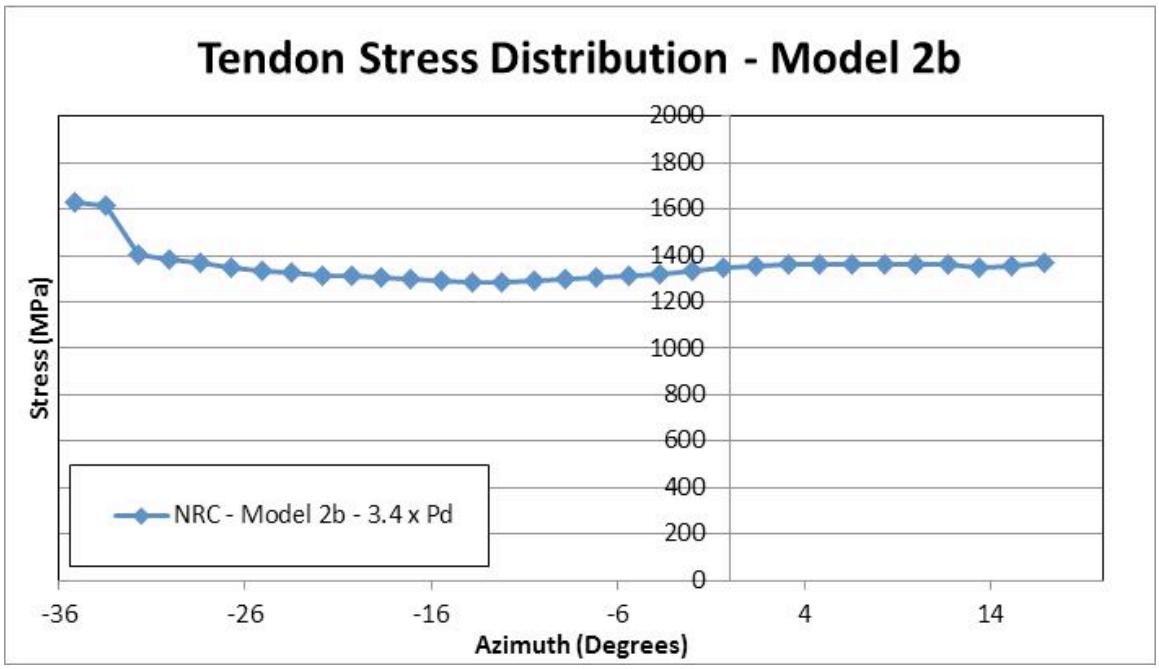

Figure 178: Model 2b Tendon Stress Distribution (Penetration Hatch) at 3.4xP_d

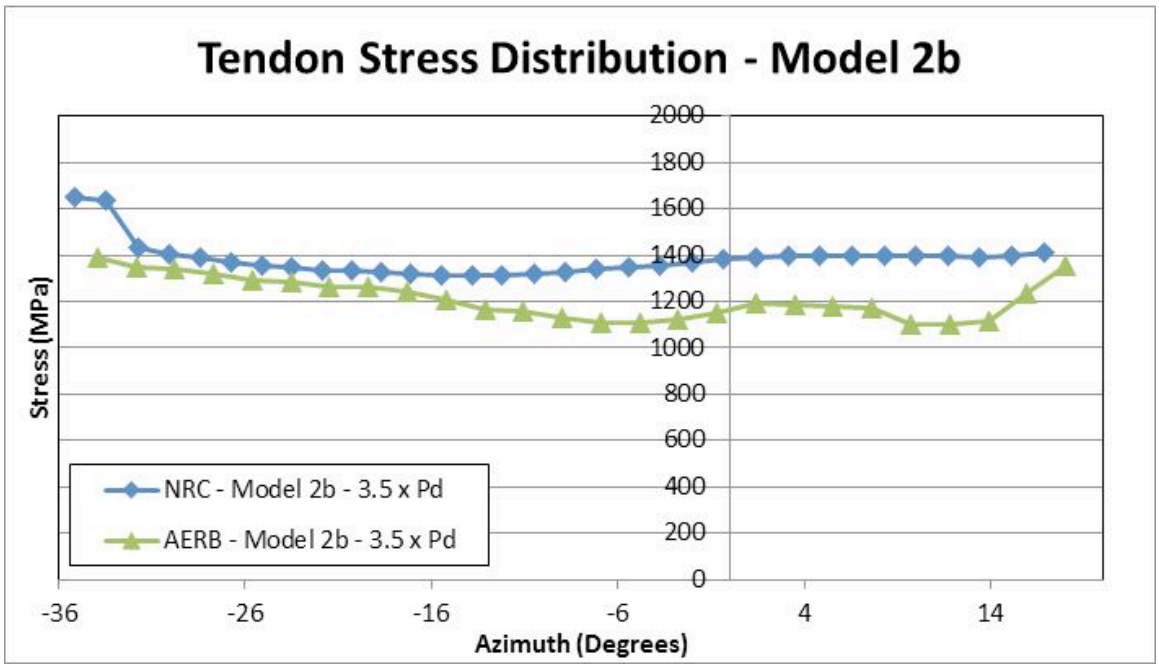

Figure 179: Model 2b Tendon Stress Distribution (Penetration Hatch) at Ultimate Pressure

A comparison of models 2a-2c for each pressure load is presented below for each participant where data was available. These plots are useful for evaluating the specific differences between the individual model 2a – 2c. These comparisons are plotted in Figure 180 through Figure 195.

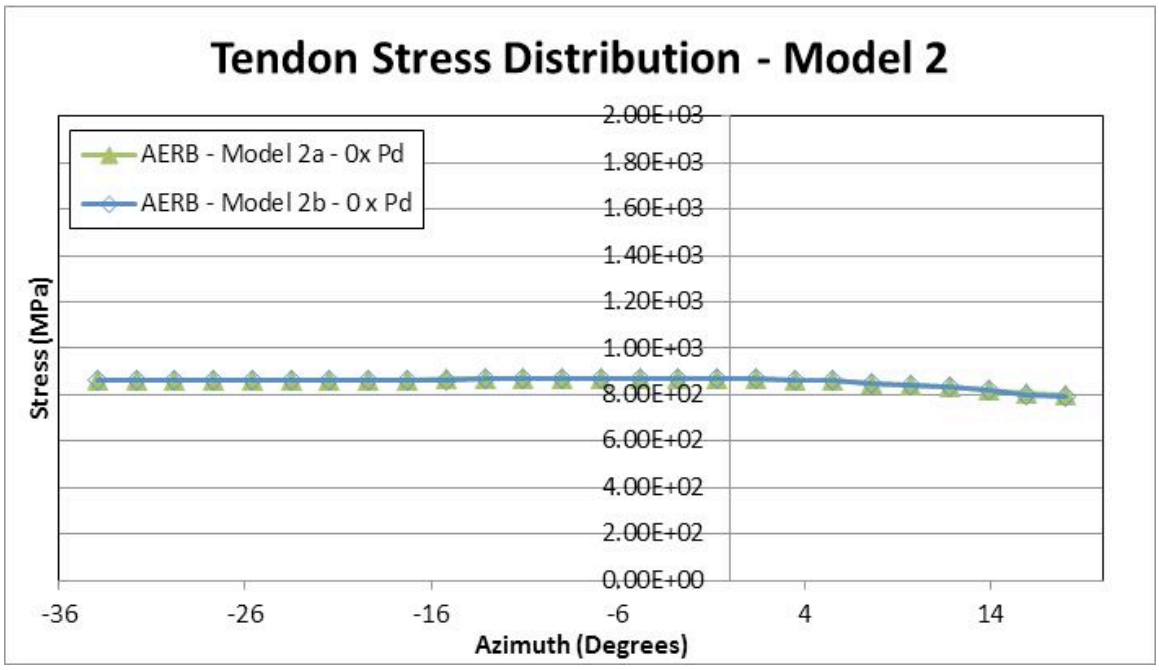

Figure 180: AERB Model 2(a-b) Tendon Stress Distribution (Penetration Hatch) at Anchoring

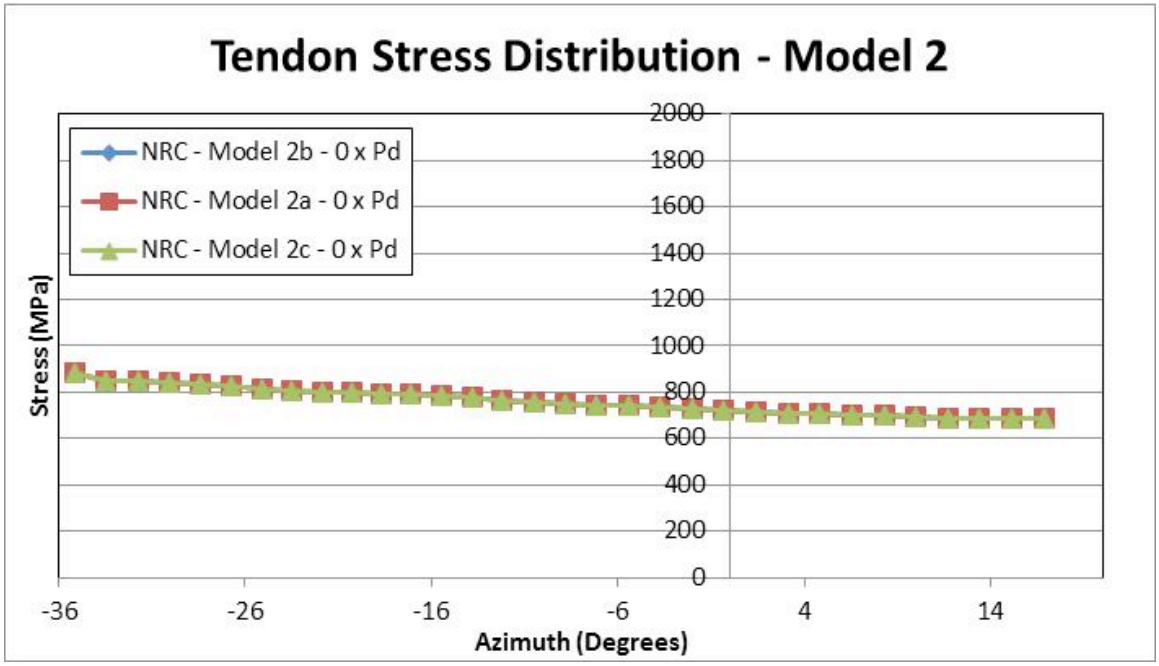

Figure 181: NRC Model 2(a-c) Tendon Stress Distribution (Penetration Hatch) at Anchoring

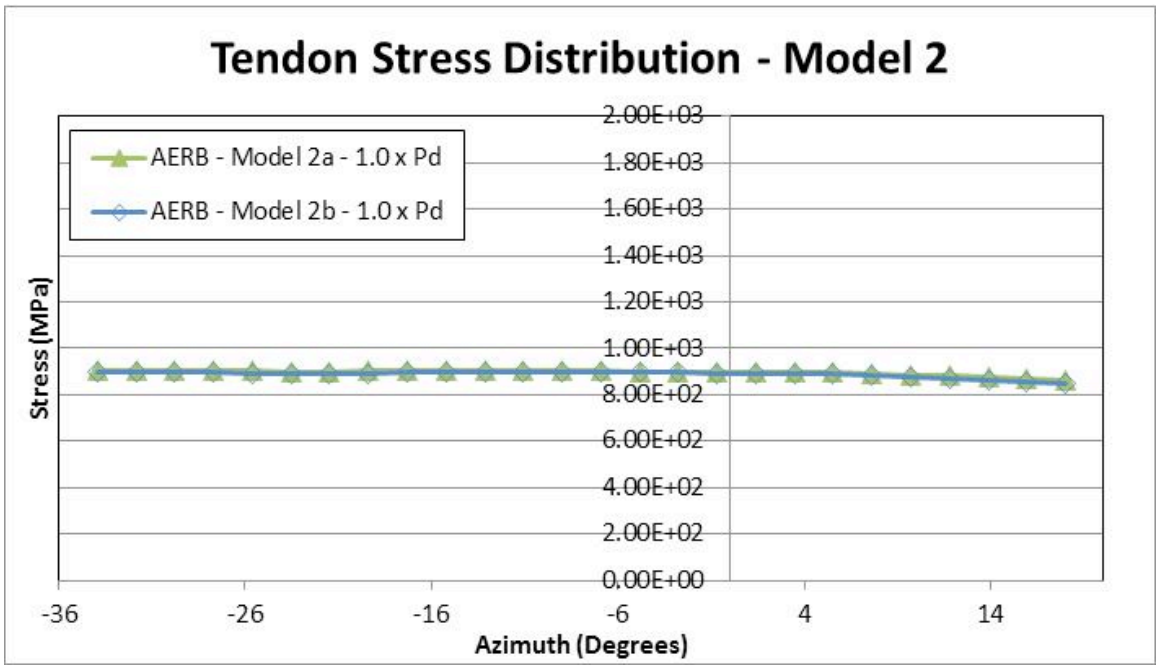

Figure 182: AERB Model 2(a-b) Tendon Stress Distribution (Penetration Hatch) at 1xP_d

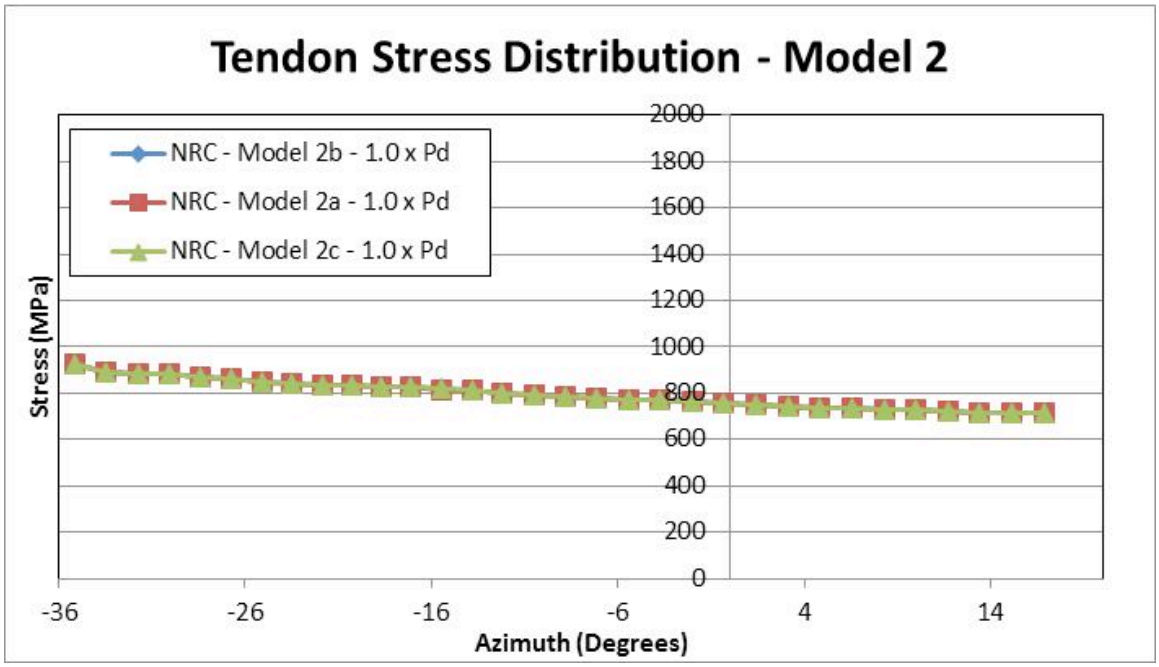

Figure 183: NRC Model 2(a-c) Tendon Stress Distribution (Penetration Hatch) at 1xP_d

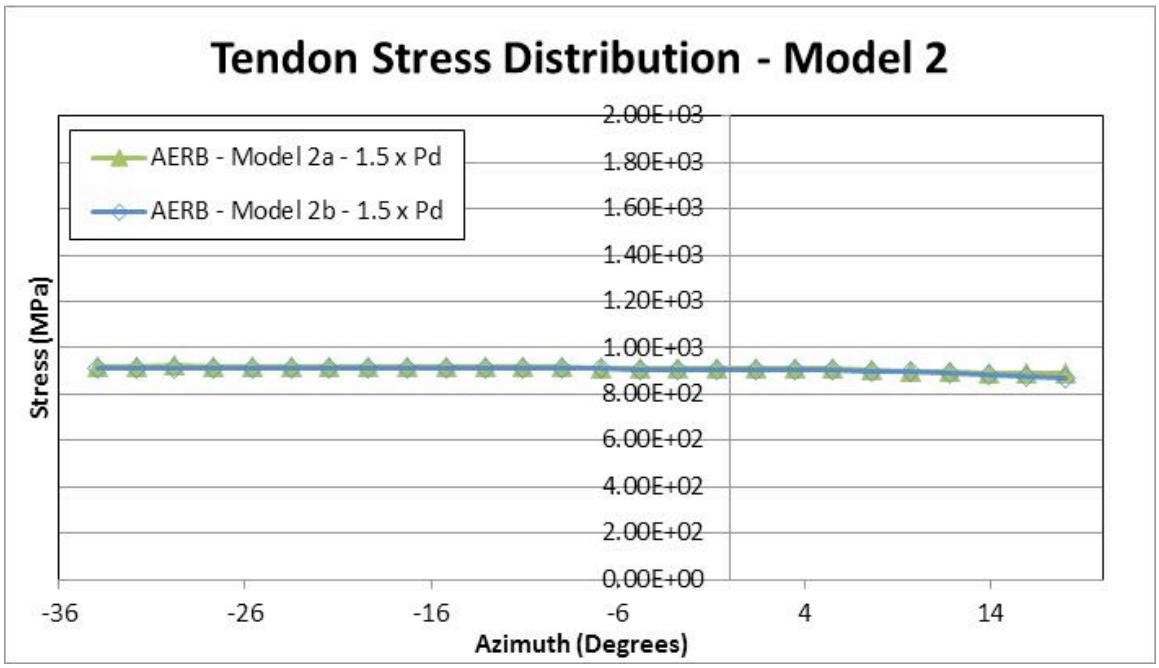

Figure 184: AERB Model 2(a-b) Tendon Stress Distribution (Penetration Hatch) at 1.5xP_d

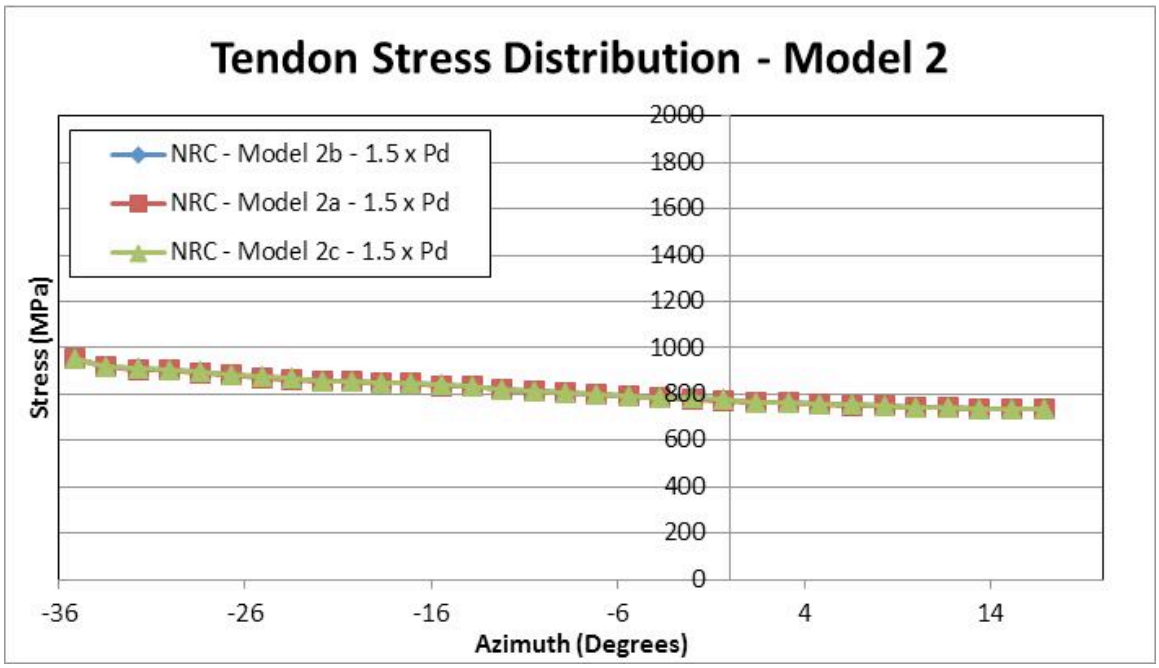

Figure 185: NRC Model 2(a-c) Tendon Stress Distribution (Penetration Hatch) at 1.5xP_d

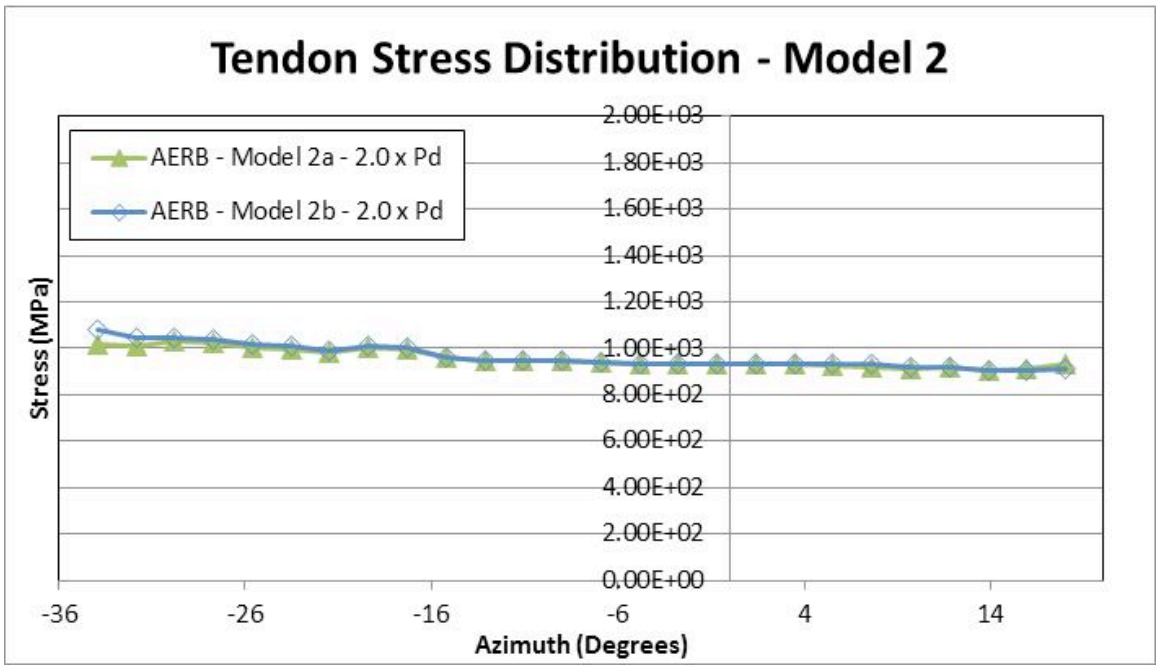

Figure 186: AERB Model 2(a-b) Tendon Stress Distribution (Penetration Hatch) at 2xP_d

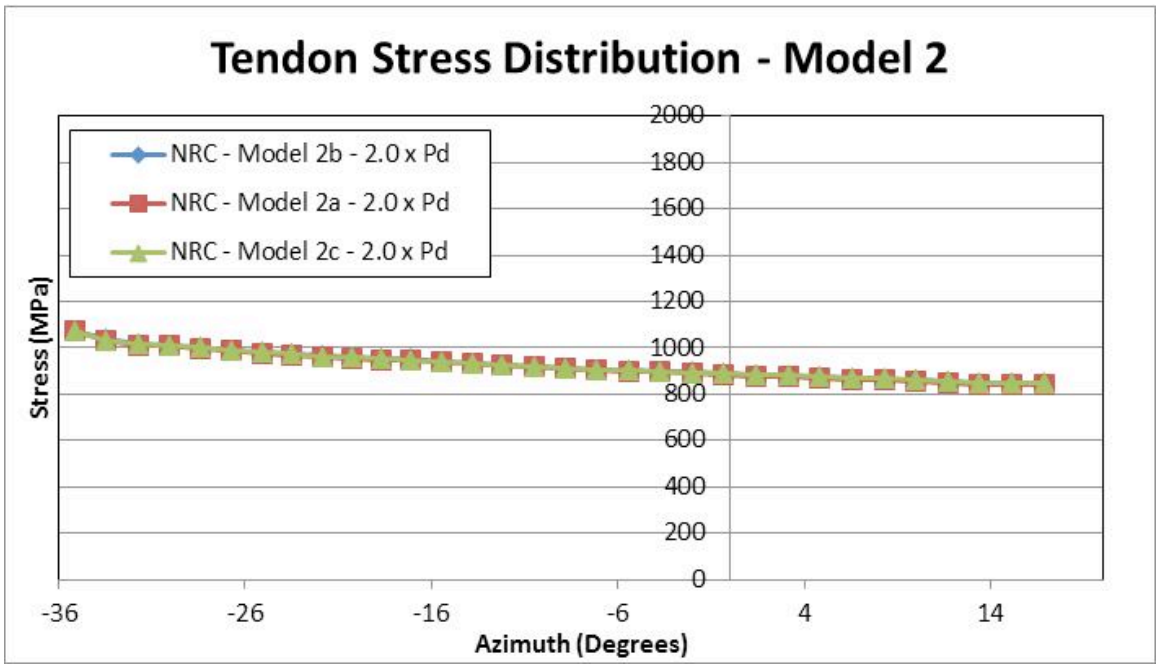

Figure 187: NRC Model 2(a-c) Tendon Stress Distribution (Penetration Hatch) at 2xP_d

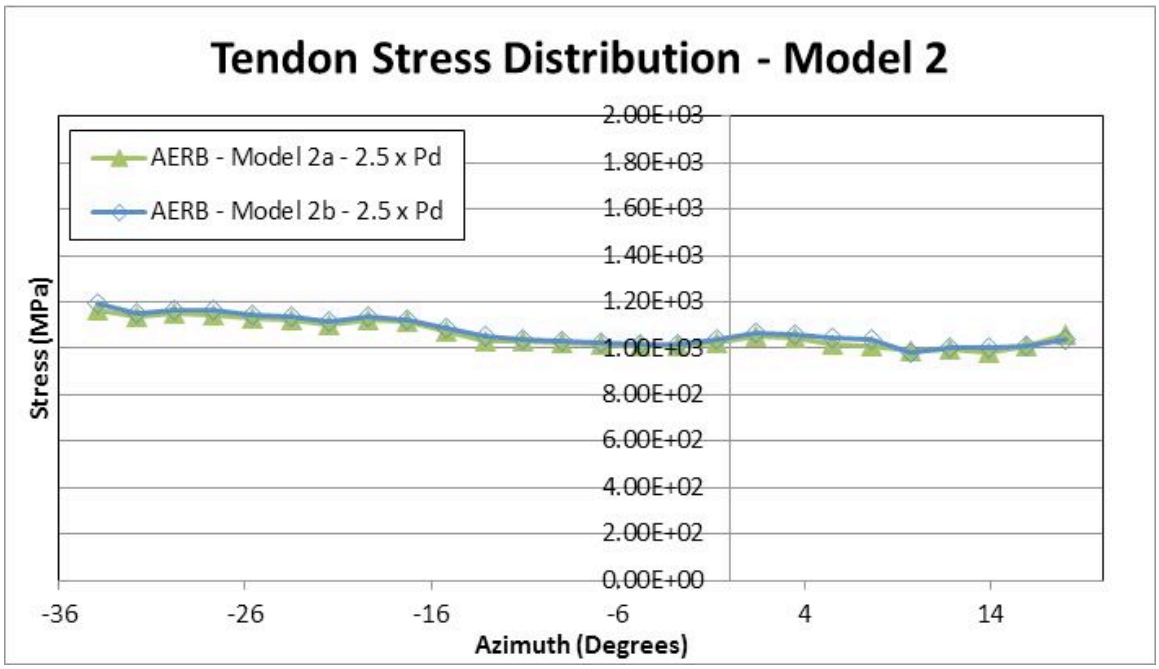

Figure 188: AERB Model 2(a-b) Tendon Stress Distribution (Penetration Hatch) at 2.5xP_d

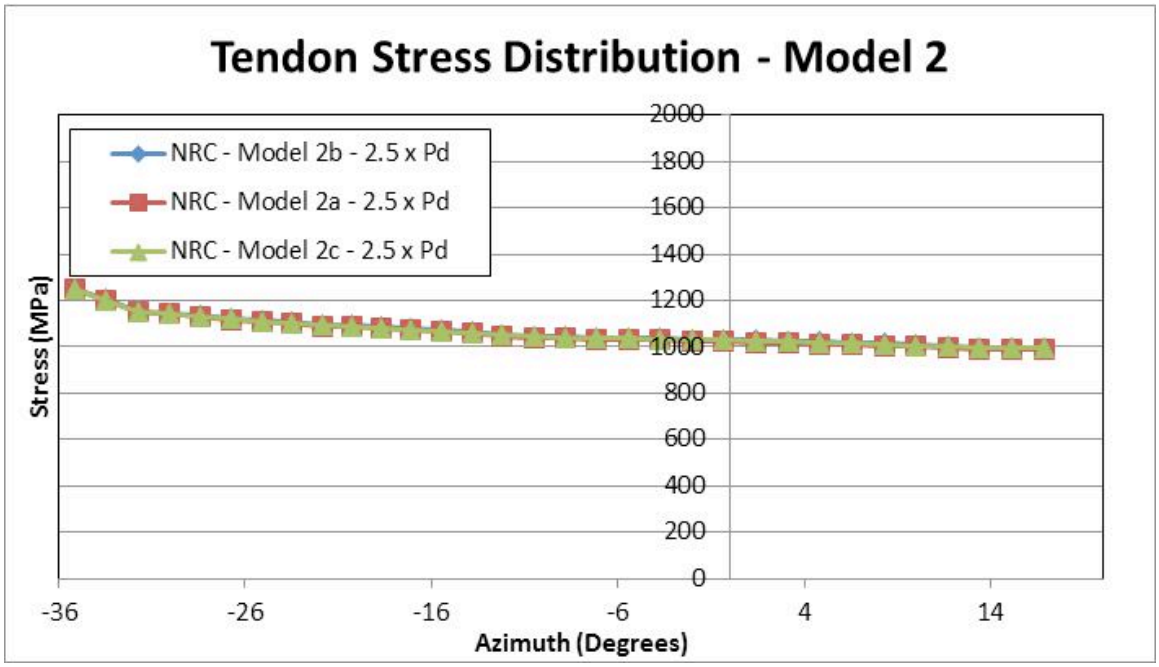

Figure 189: NRC Model 2(a-c) Tendon Stress Distribution (Penetration Hatch) at 2.5xP_d

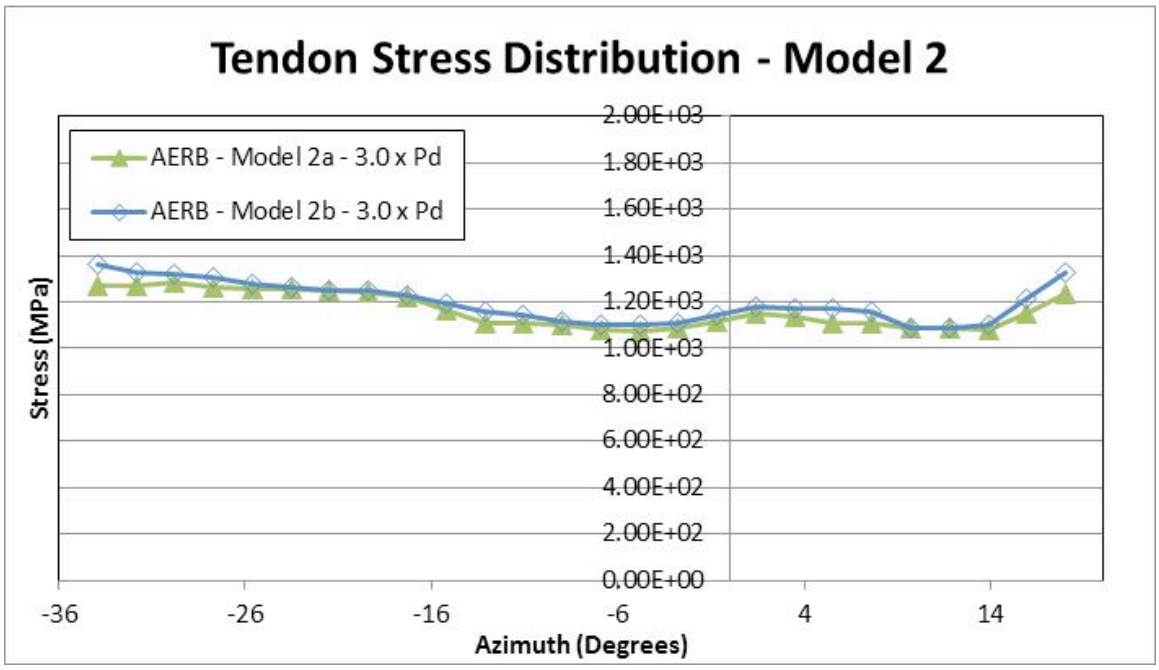

Figure 190: AERB Model 2(a-b) Tendon Stress Distribution (Penetration Hatch) at 3xP_d

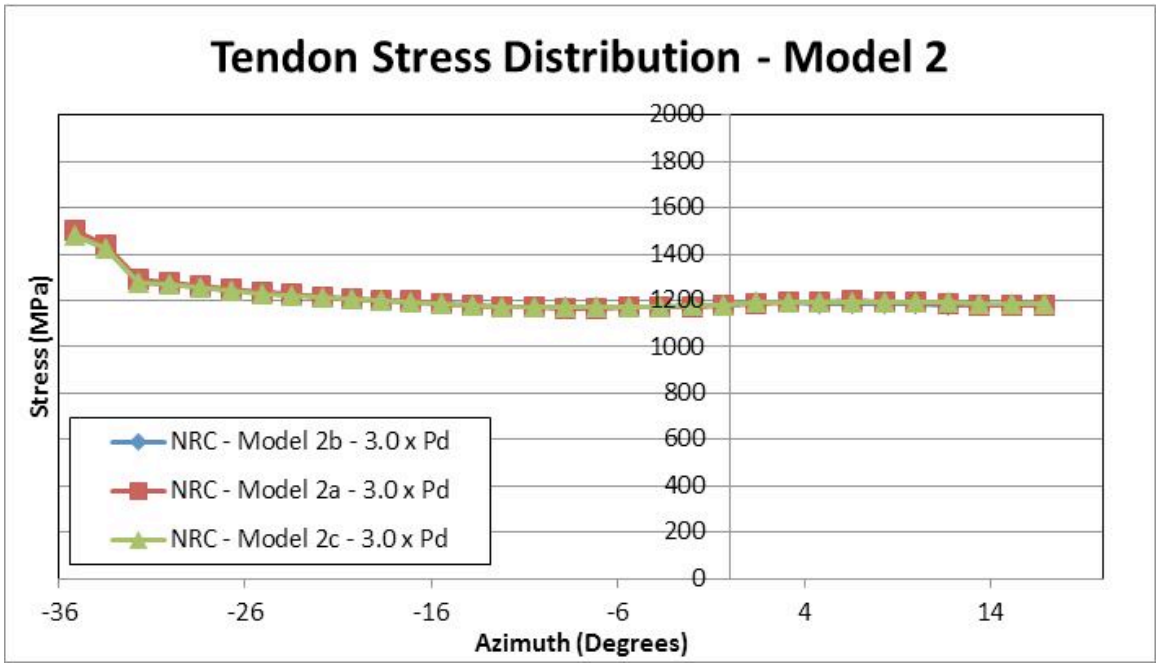

Figure 191: NRC Model 2(a-c) Tendon Stress Distribution (Penetration Hatch) at 3xP_d

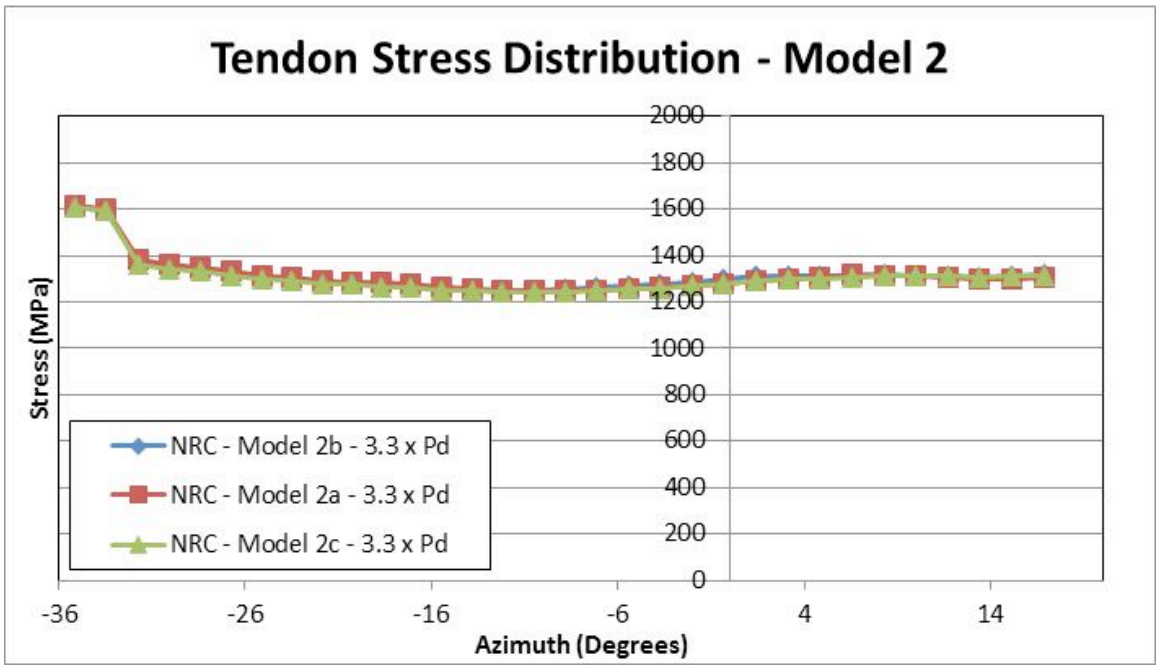

Figure 192: NRC Model 2(a-c) Tendon Stress Distribution (Penetration Hatch) at 3.3xP_d

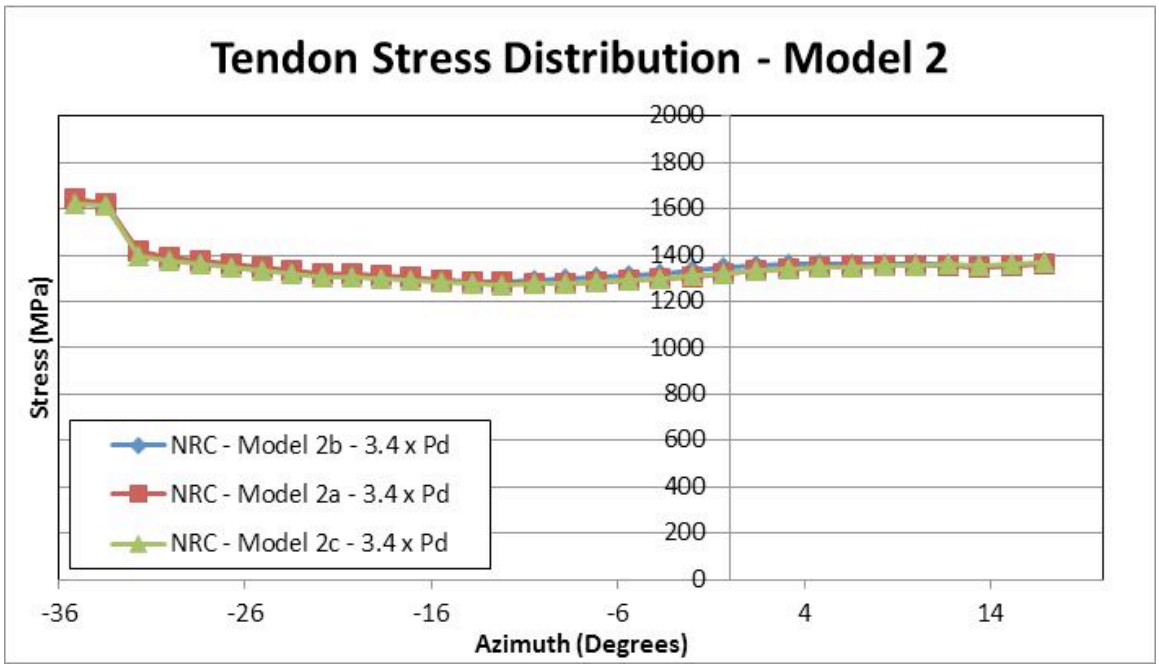

Figure 193: NRC Model 2(a-c) Tendon Stress Distribution (Penetration Hatch) at 3.4xP_d

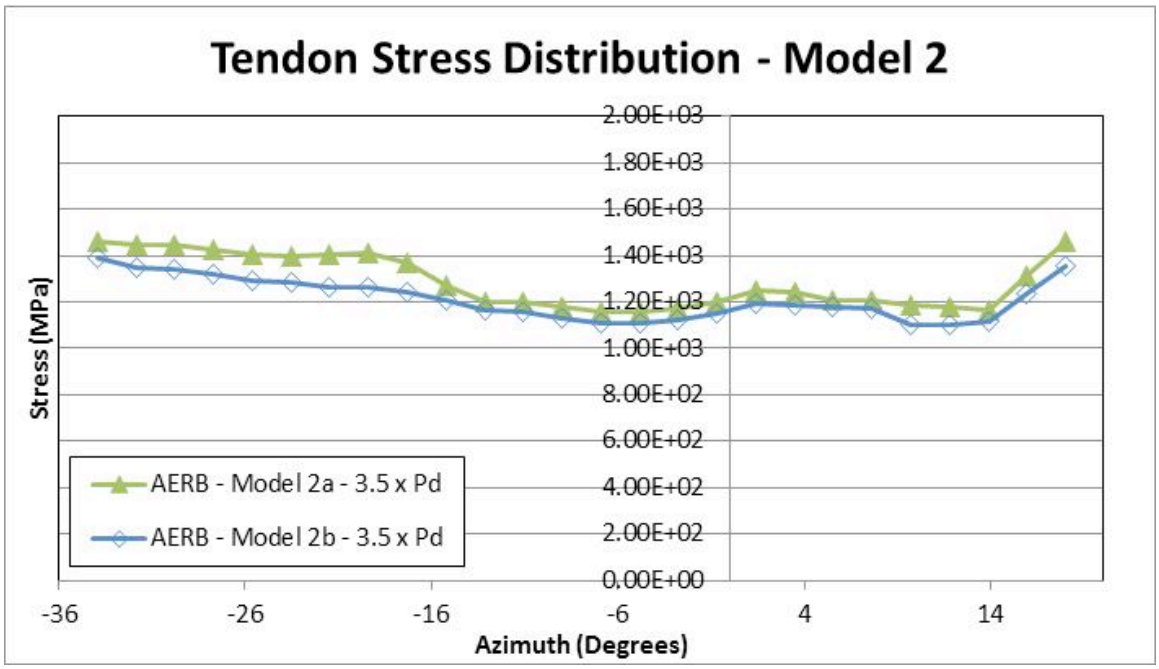

Figure 194: AERB Model 2(a-b) Tendon Stress Distribution (Penetration Hatch) at Ultimate Pressure

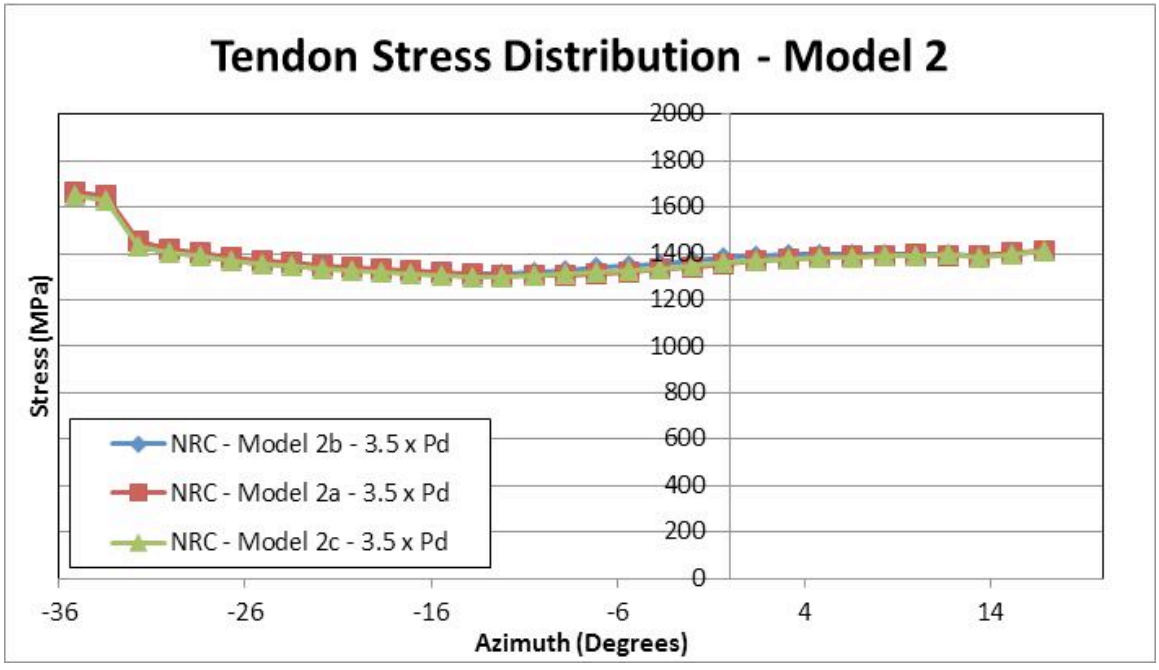

Figure 195: NRC Model 2(a-c) Tendon Stress Distribution (Penetration Hatch) at Ultimate Pressure

3.7.2. Location at Hoop Tendon at Top of Model 2

The tendon stress distributions for the hoop tendon at the top of Model 2 are presented in Figure 196 through Figure 229. As in the previous section, the abscissa and the ordinate are maintained on constant scales to facilitate comparison between the plots.

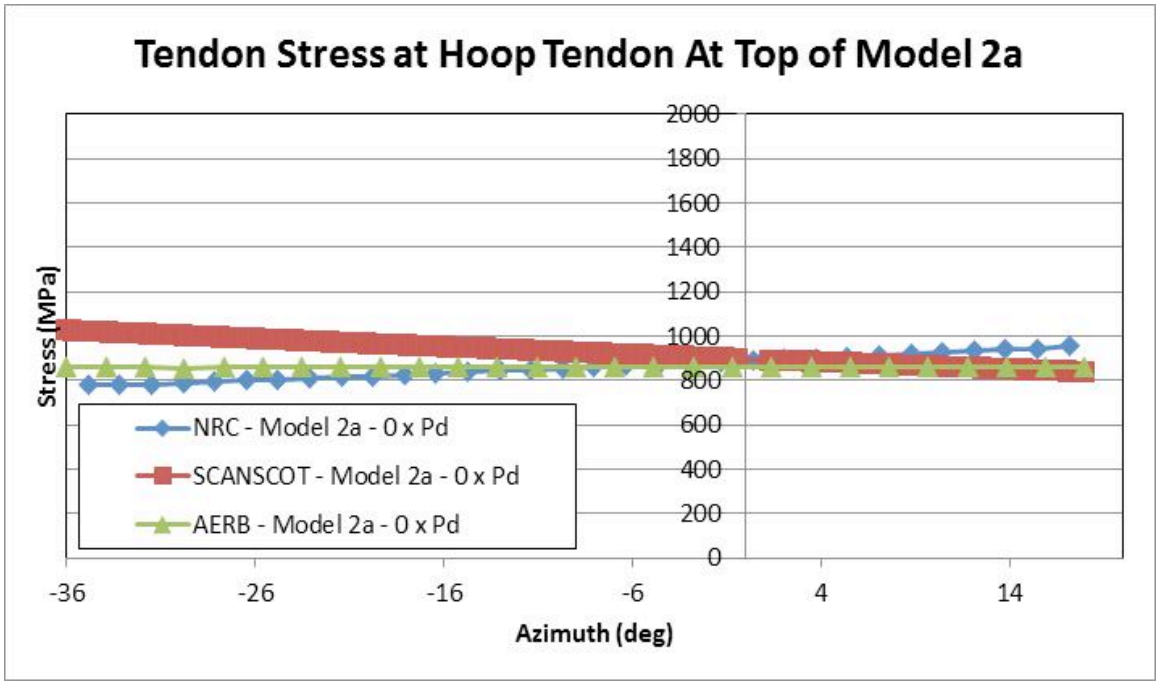

Figure 196: Model 2a Tendon Stress Distribution (Top of Model) at Anchoring

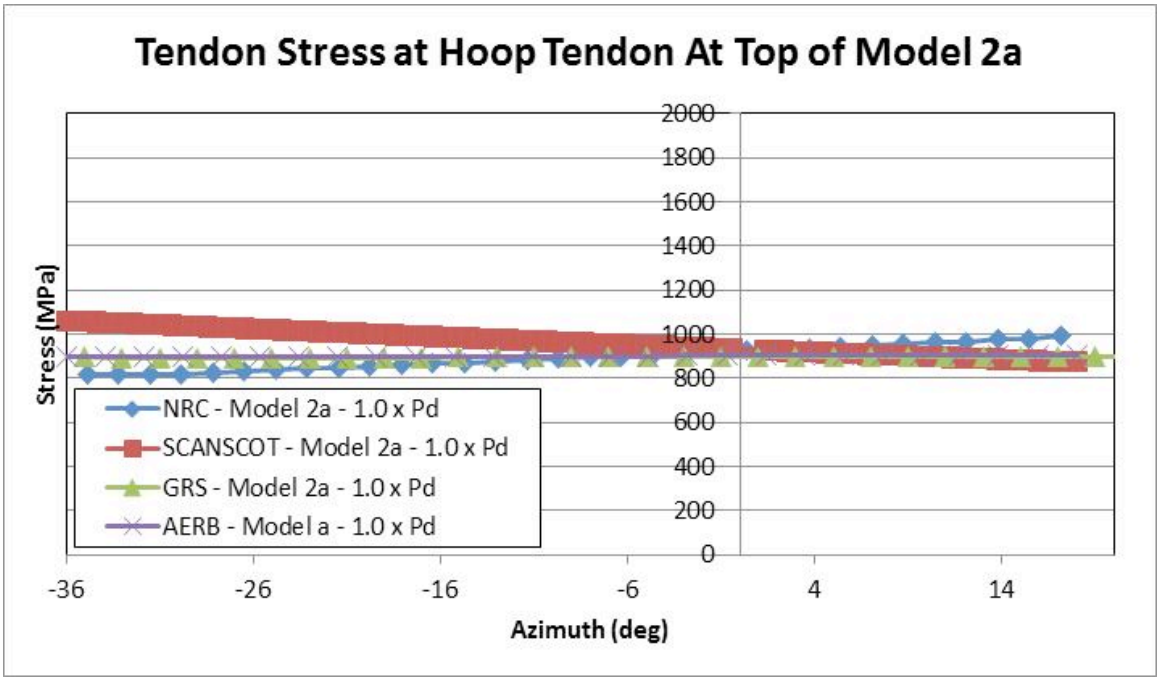

Figure 197: Model 2a Tendon Stress Distribution (Top of Model) at 1xP_d

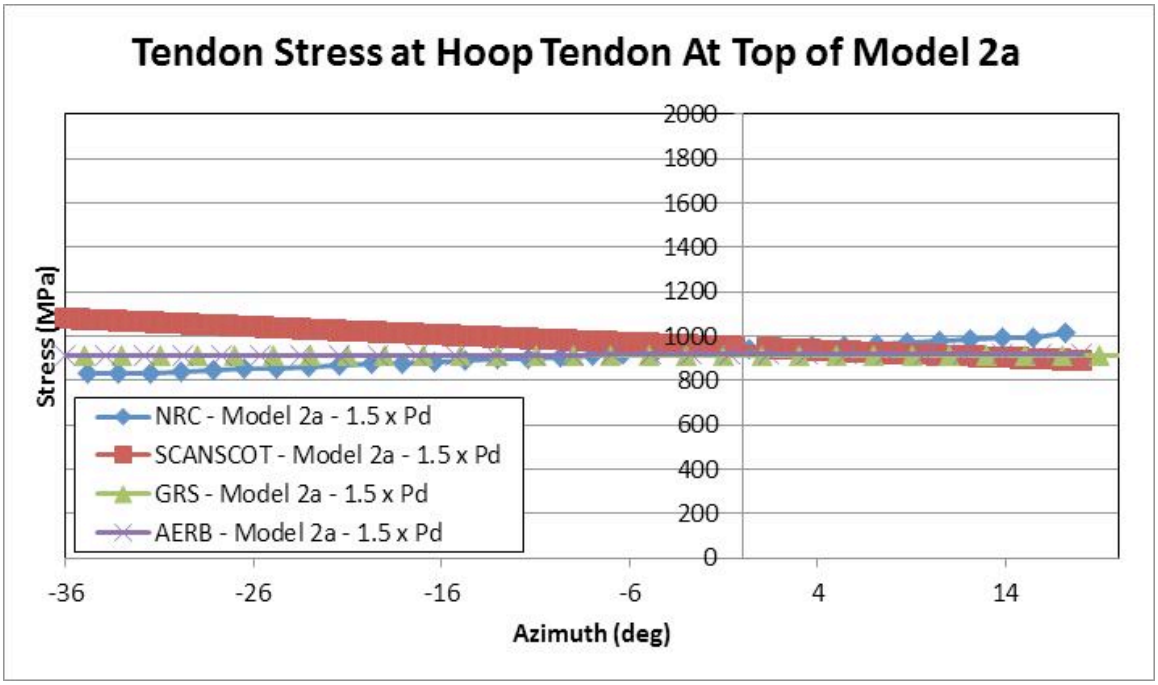

Figure 198: Model 2a Tendon Stress Distribution (Top of Model) at 1.5xP_d

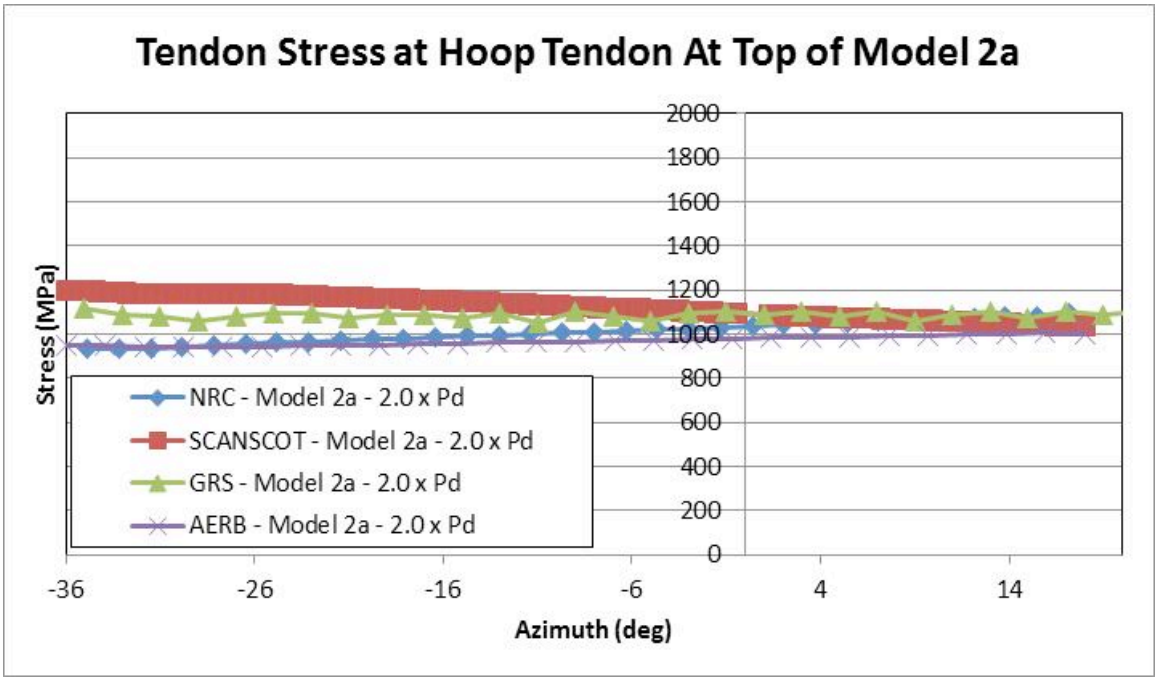

Figure 199: Model 2a Tendon Stress Distribution (Top of Model) at 2xP_d

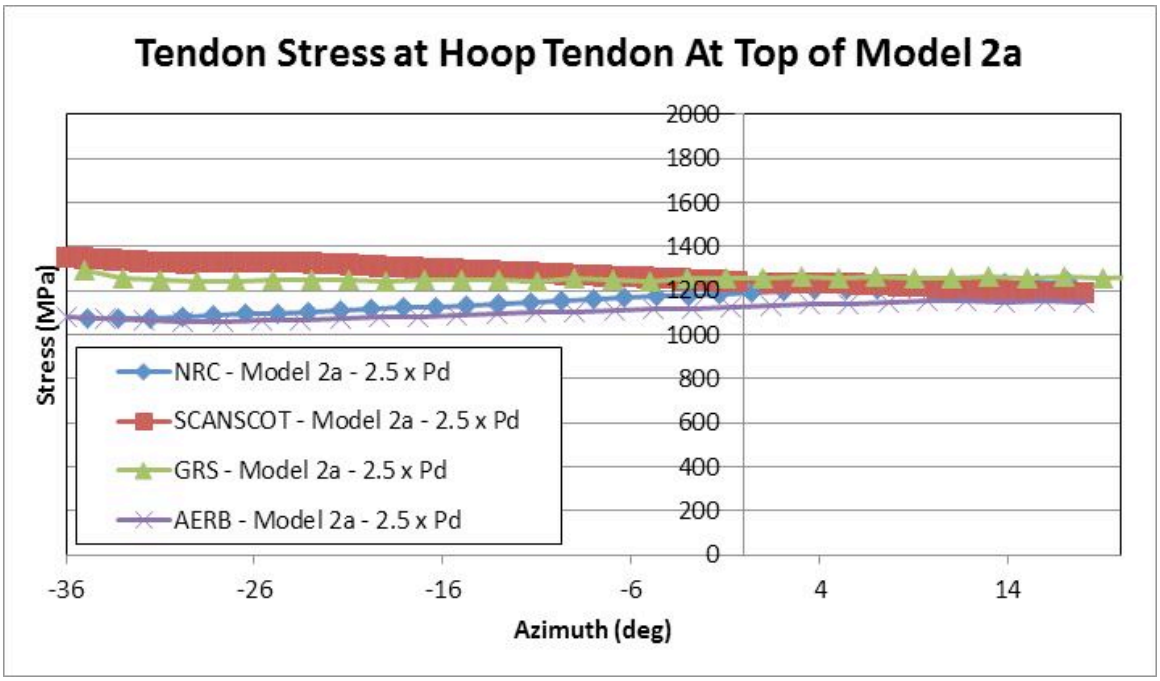

Figure 200: Model 2a Tendon Stress Distribution (Top of Model) at 2.5xP_d

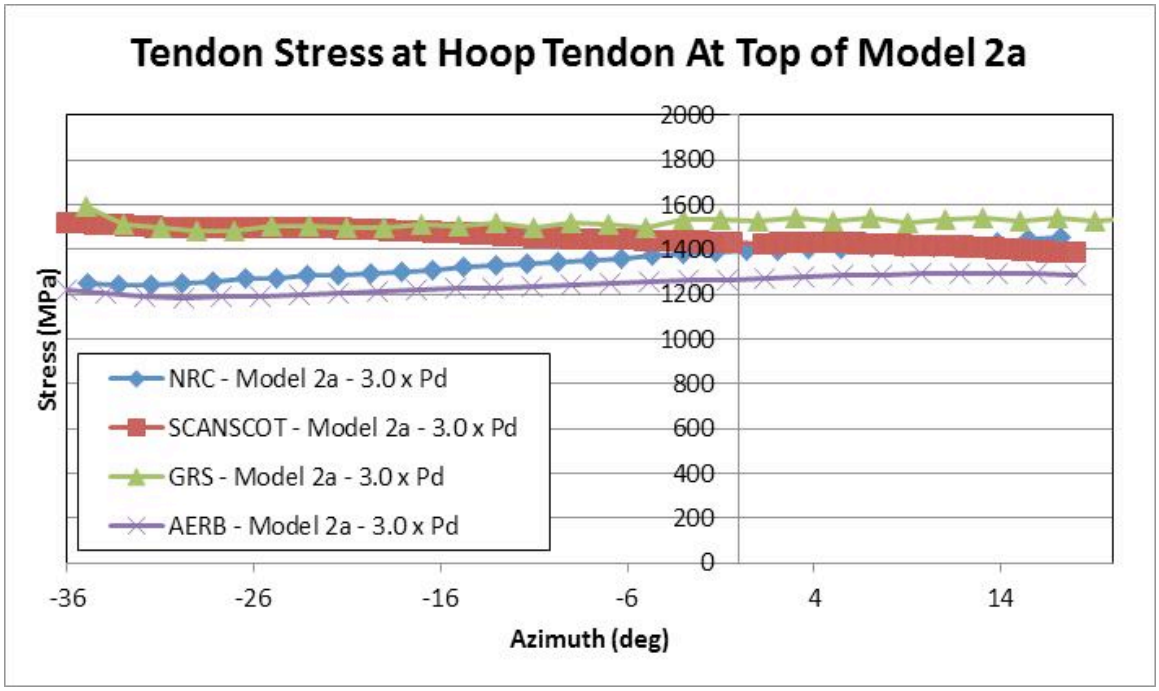

Figure 201: Model 2a Tendon Stress Distribution (Top of Model) at 3xP_d

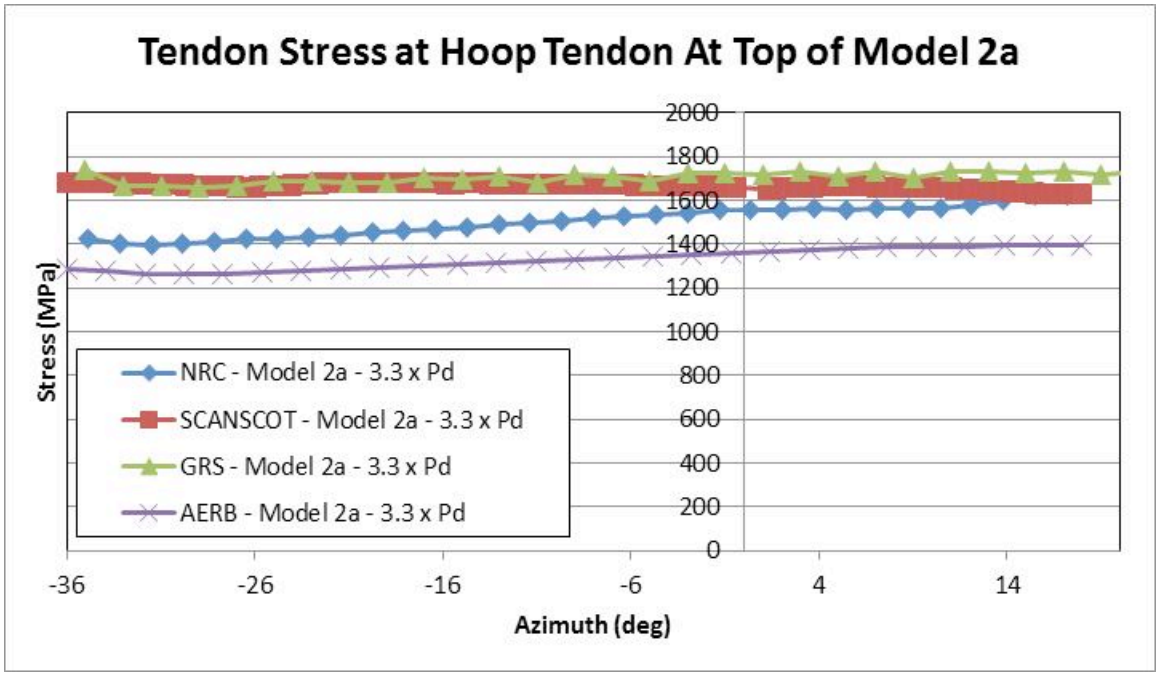

Figure 202: Model 2a Tendon Stress Distribution (Top of Model) at 3.3xP_d

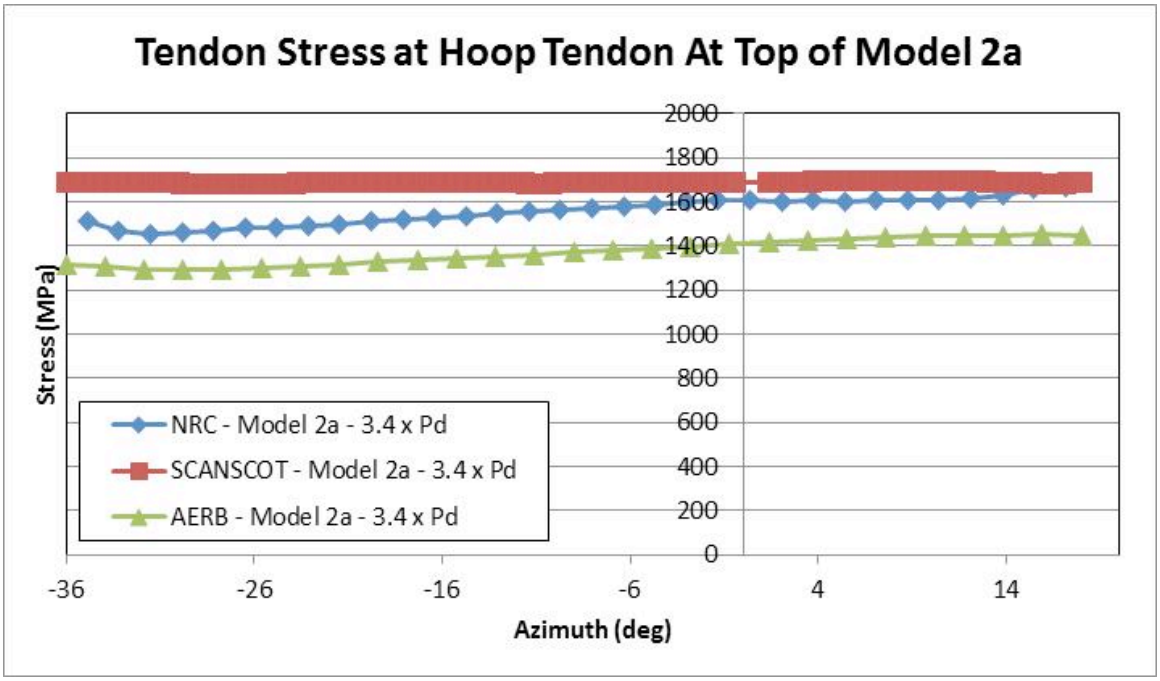

Figure 203: Model 2a Tendon Stress Distribution (Top of Model) at 3.4xP_d

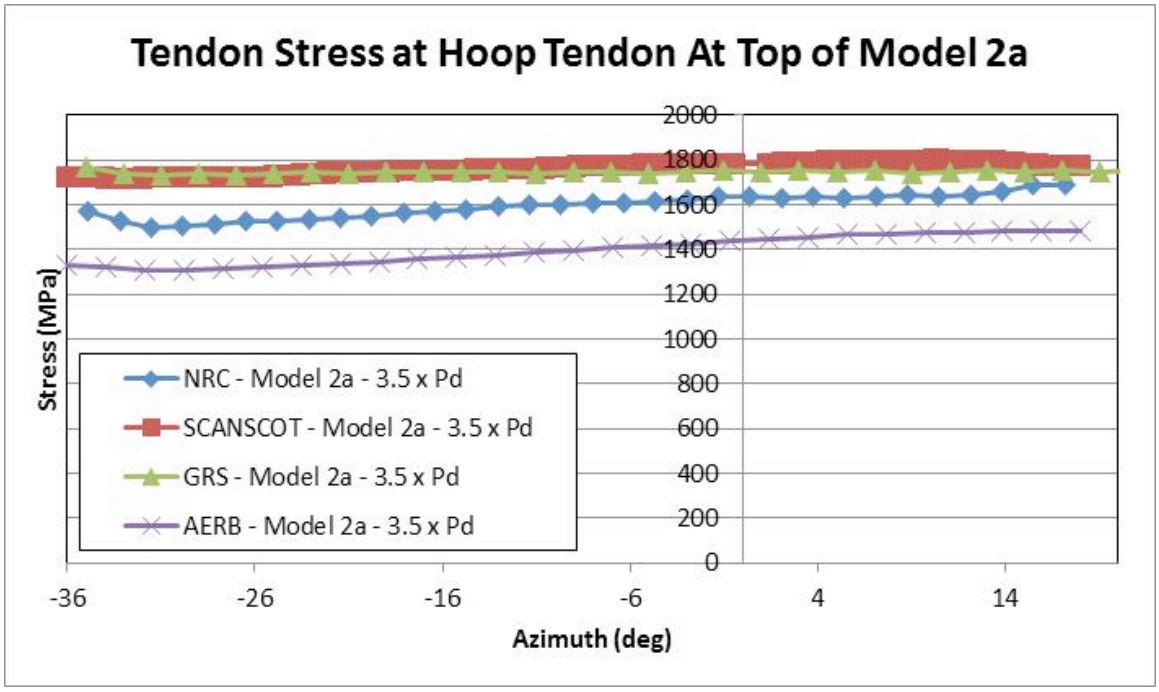

Figure 204: Model 2a Tendon Stress Distribution (Top of Model) at Ultimate Pressure

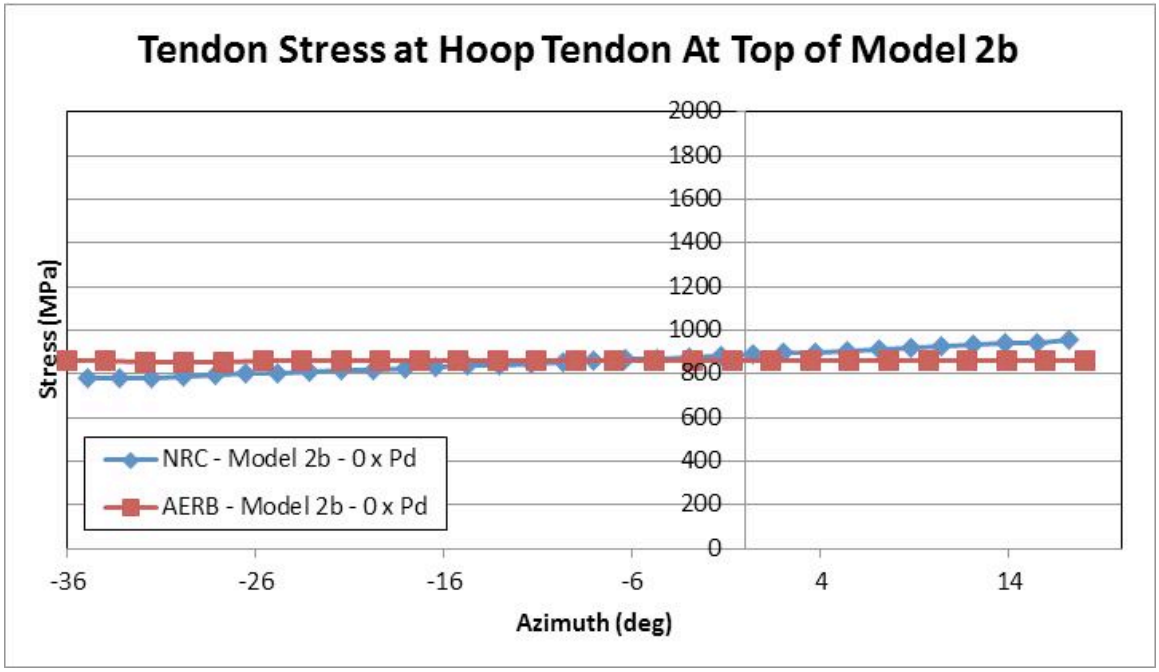

Figure 205: Model 2b Tendon Stress Distribution (Top of Model) at Anchoring

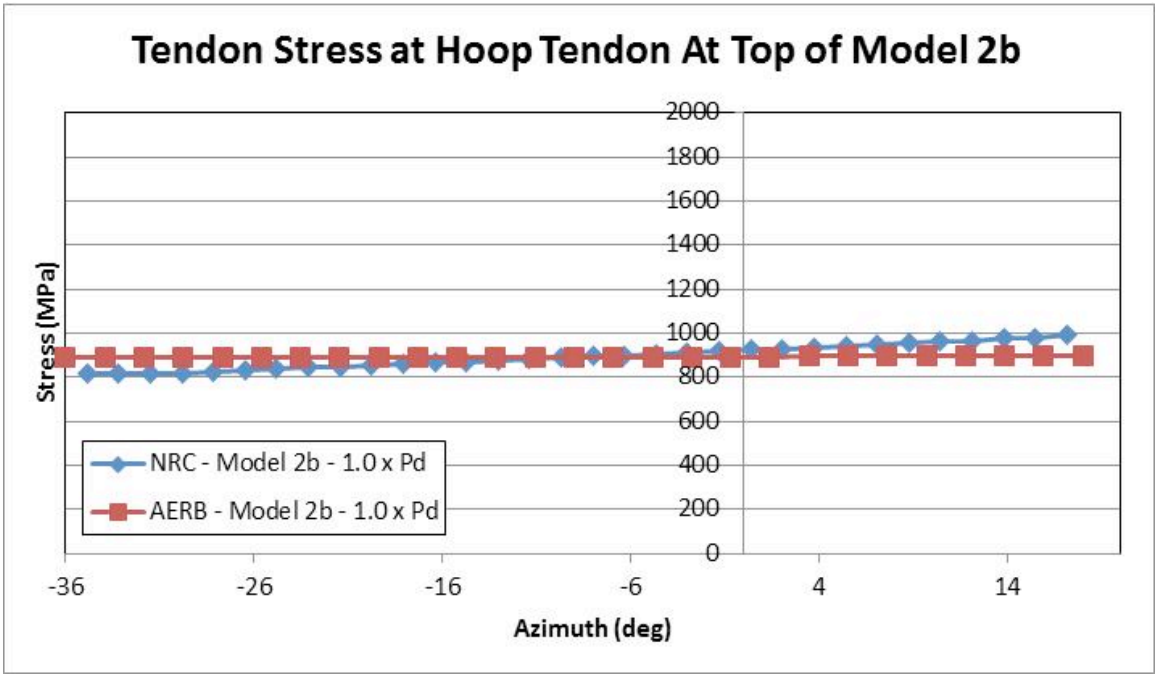

Figure 206: Model 2b Tendon Stress Distribution (Top of Model) at 1xP_d

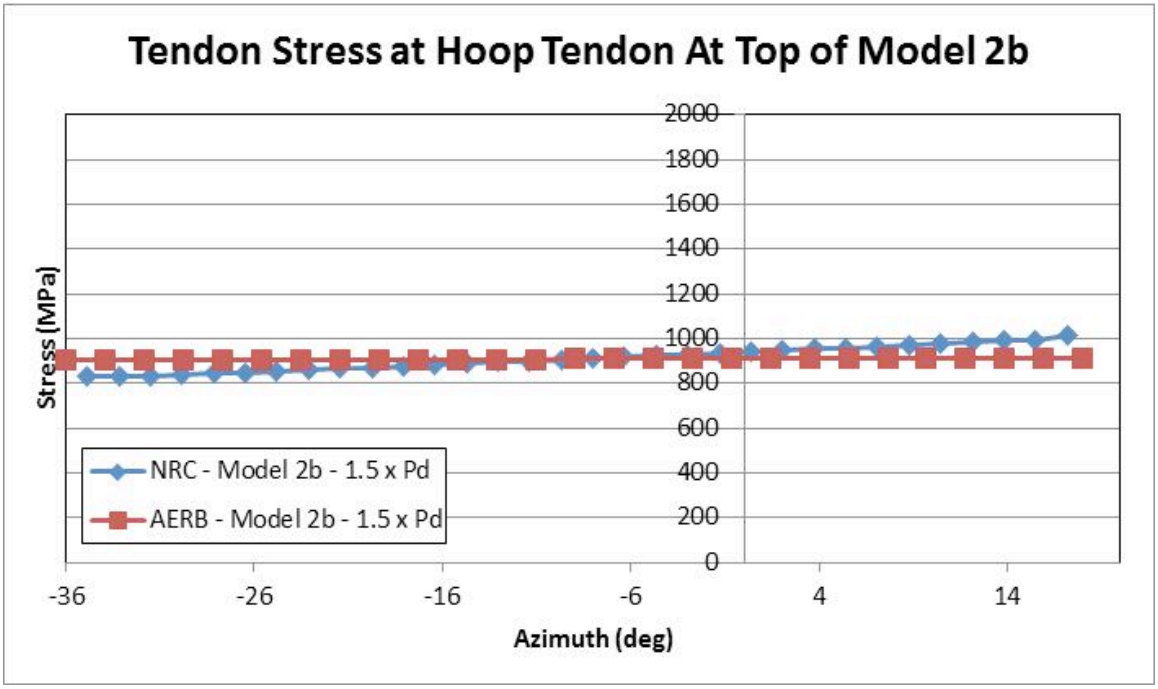

Figure 207: Model 2b Tendon Stress Distribution (Top of Model) at 1.5xP_d

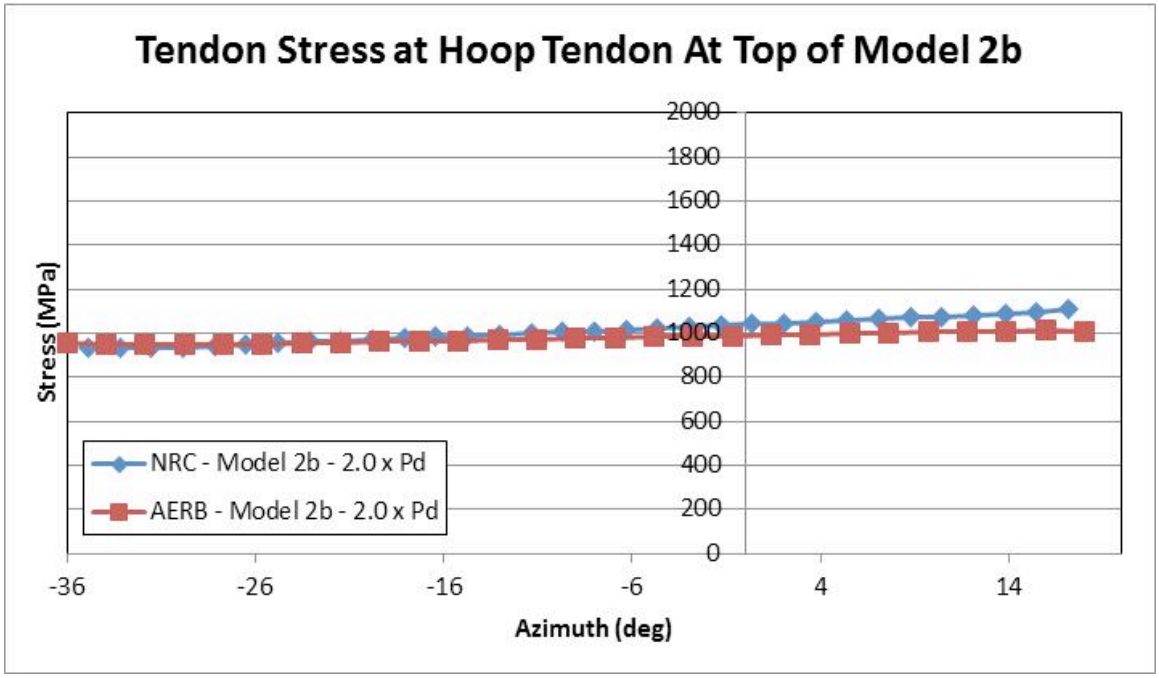

Figure 208: Model 2b Tendon Stress Distribution (Top of Model) at 2xP_d

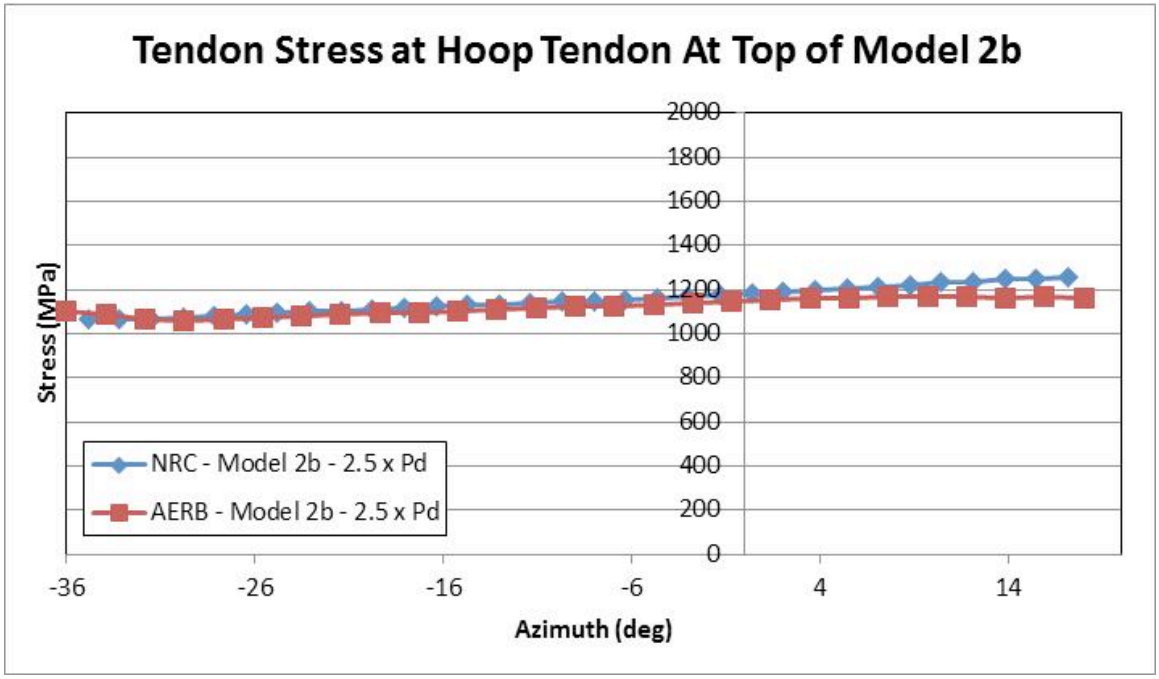

Figure 209: Model 2b Tendon Stress Distribution (Top of Model) at 2.5xP_d

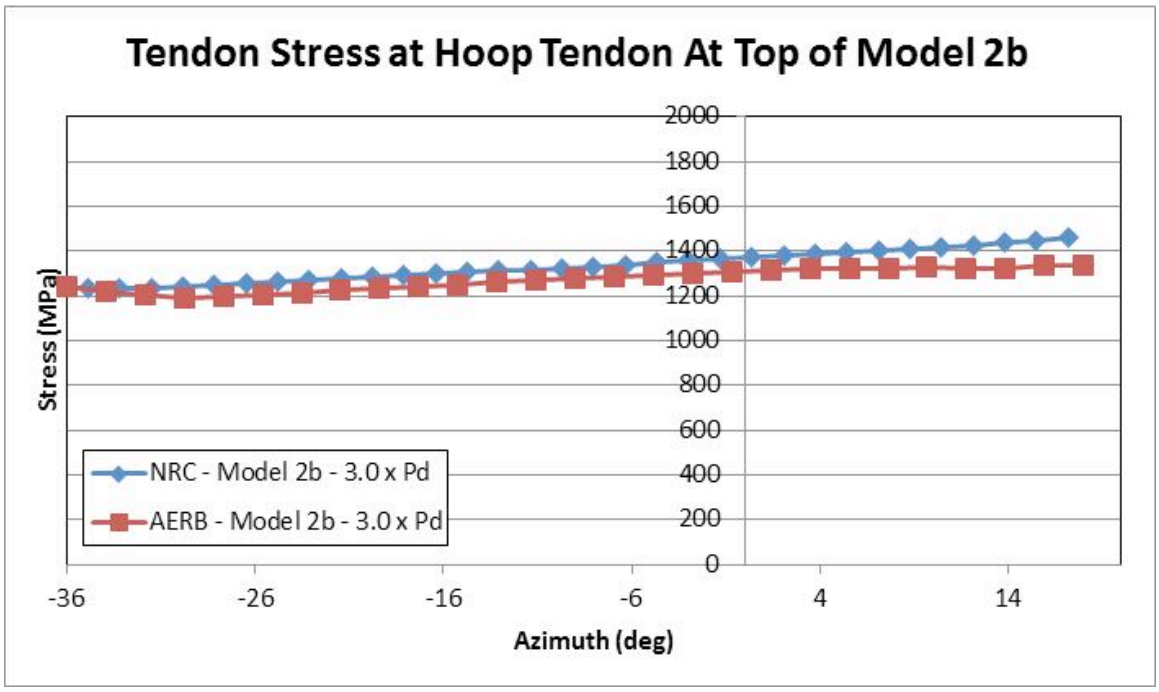

Figure 210: Model 2b Tendon Stress Distribution (Top of Model) at 3xP_d

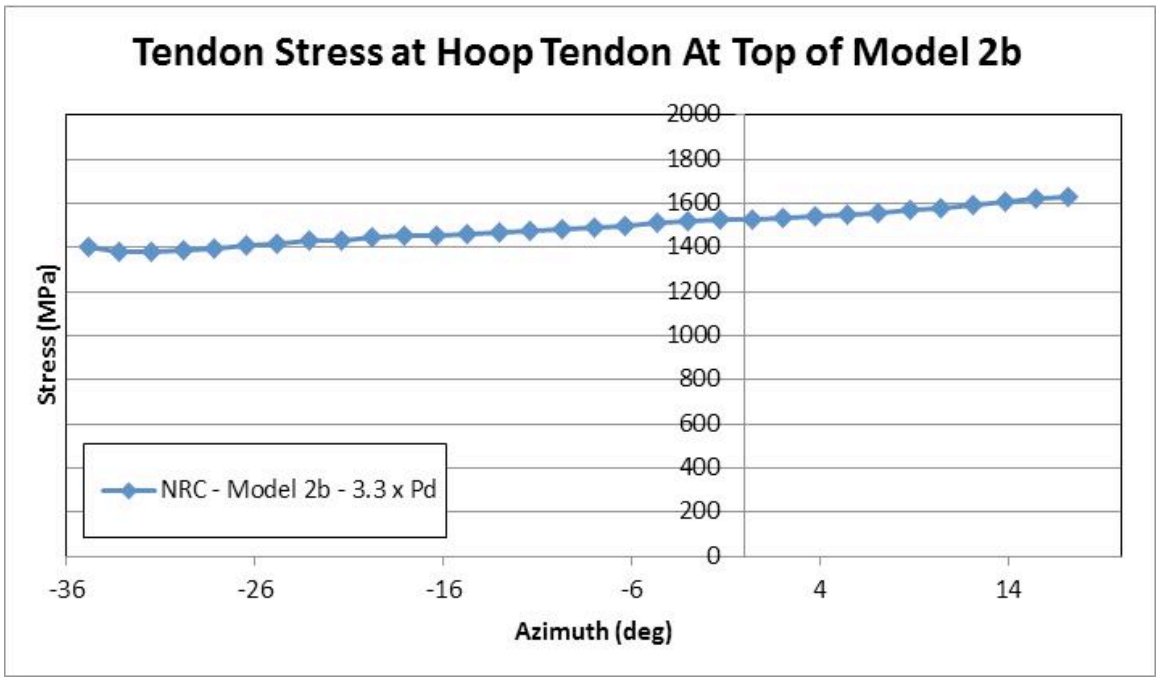

Figure 211: Model 2b Tendon Stress Distribution (Top of Model) at 3.3xP_d

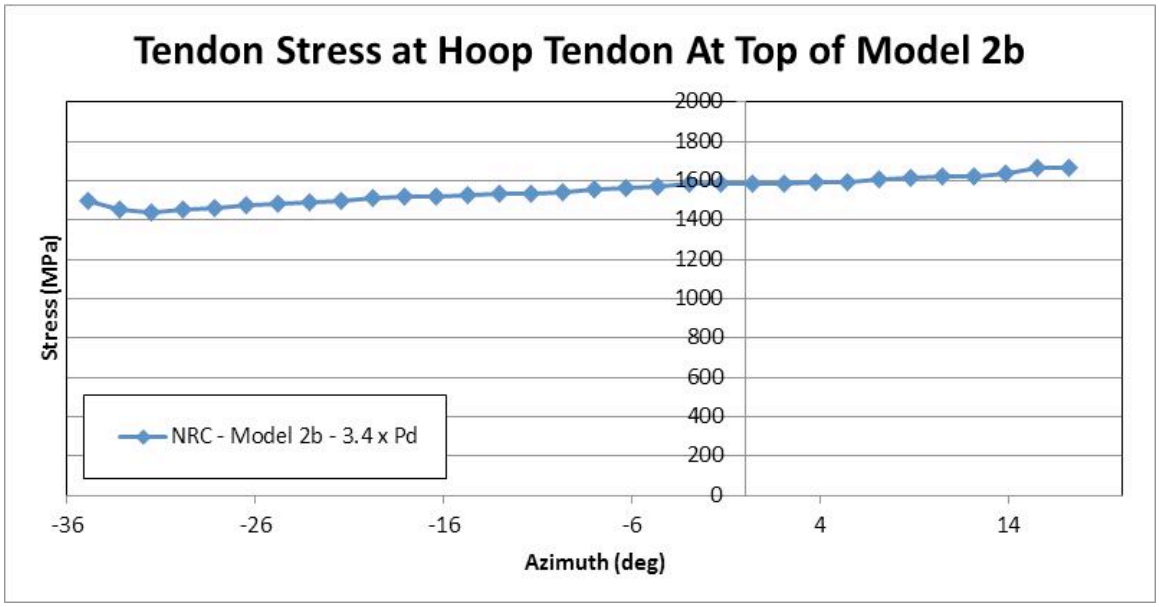

Figure 212: Model 2b Tendon Stress Distribution (Top of Model) at 3.4xP_d

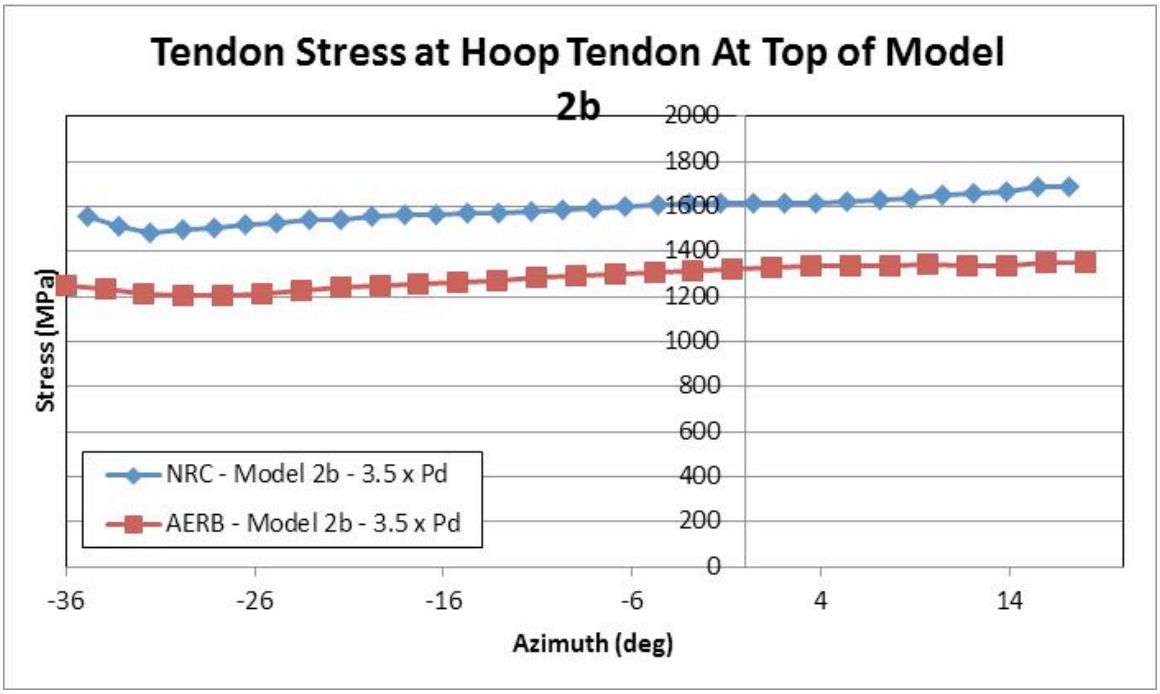

Figure 213: Model 2b Tendon Stress Distribution (Top of Model) at Ultimate Pressure

A comparison of models 2a-2c for each pressure load is presented below for each participant where data was available. These comparison plots are presented in Figure 214 through Figure 229.

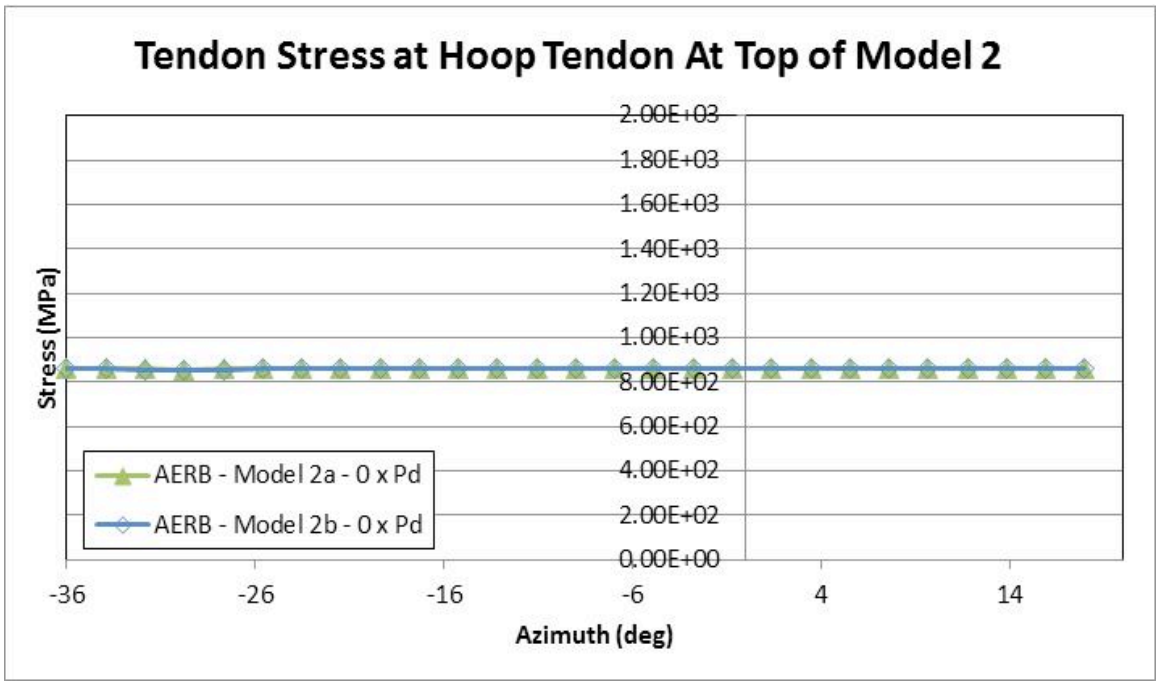

Figure 214: AERB Model 2(a-b) Tendon Stress Distribution (Top of Model) at Anchoring

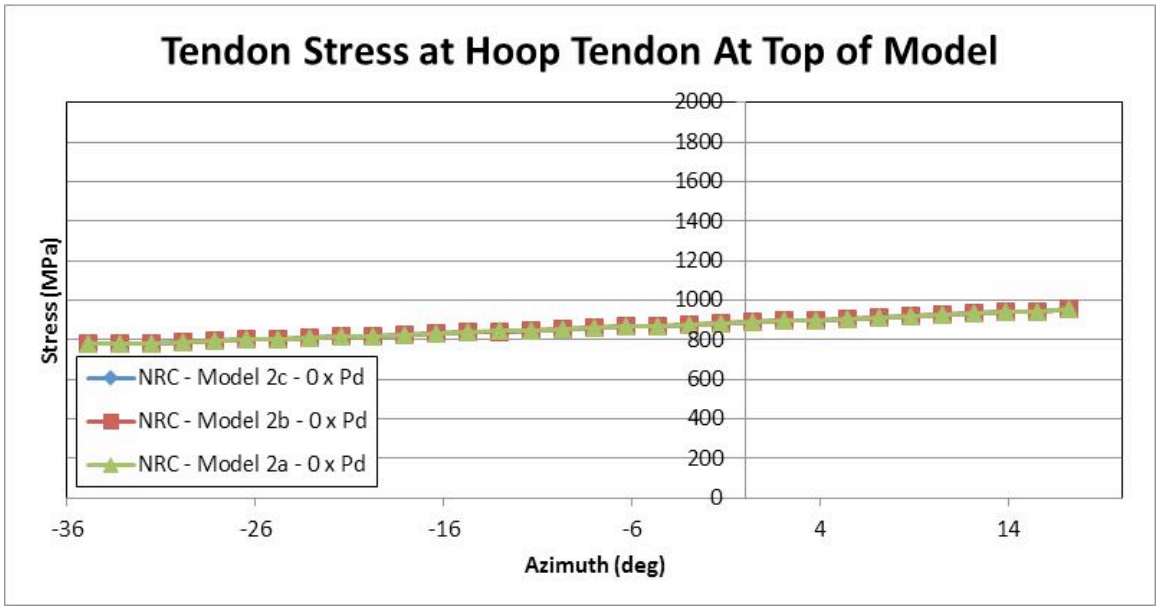

Figure 215: NRC Model 2(a-c) Tendon Stress Distribution (Top of Model) at Anchoring

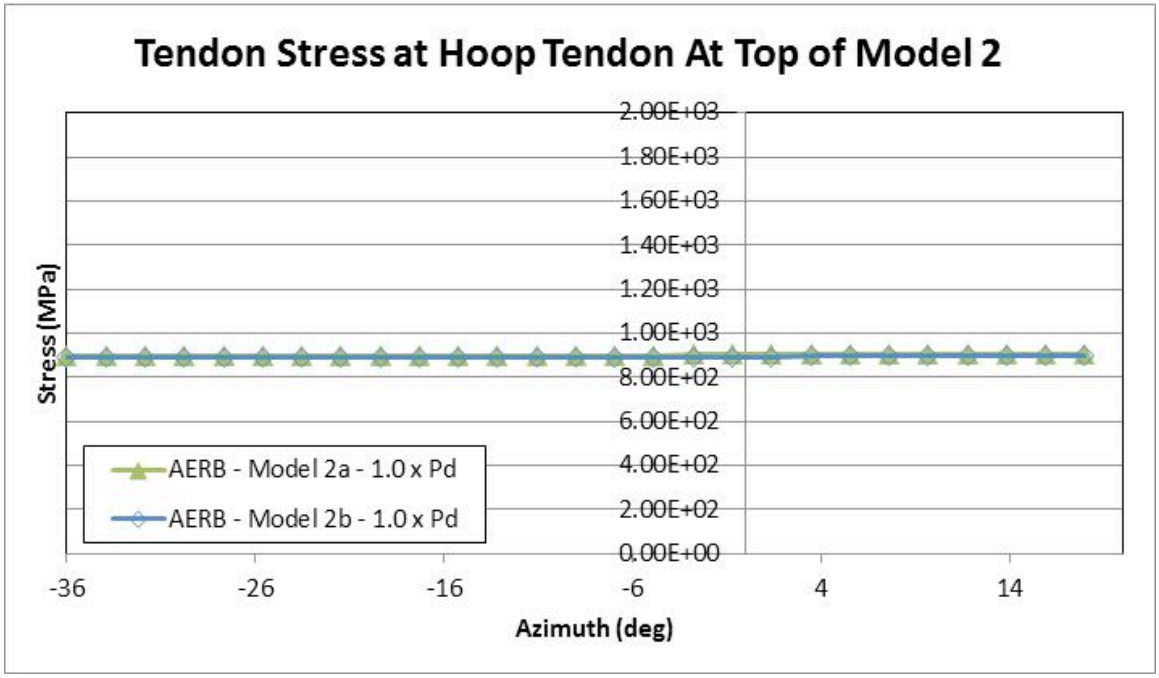

Figure 216: AERB Model 2(a-b) Tendon Stress Distribution (Top of Model) at 1xP_d

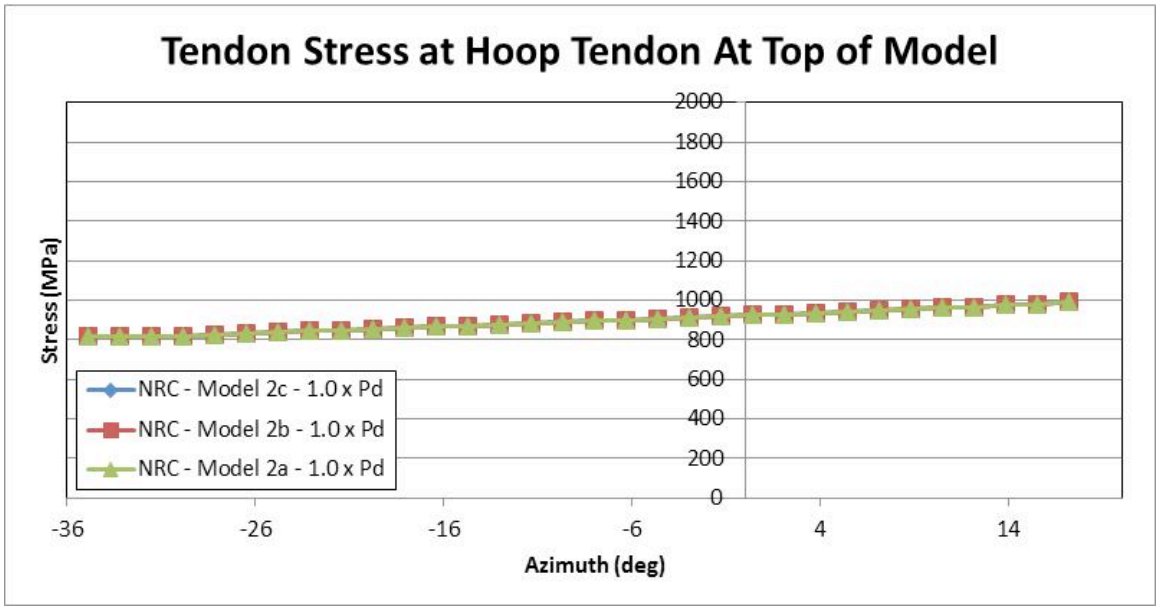

Figure 217: NRC Model 2(a-c) Tendon Stress Distribution (Top of Model) at 1xP_d

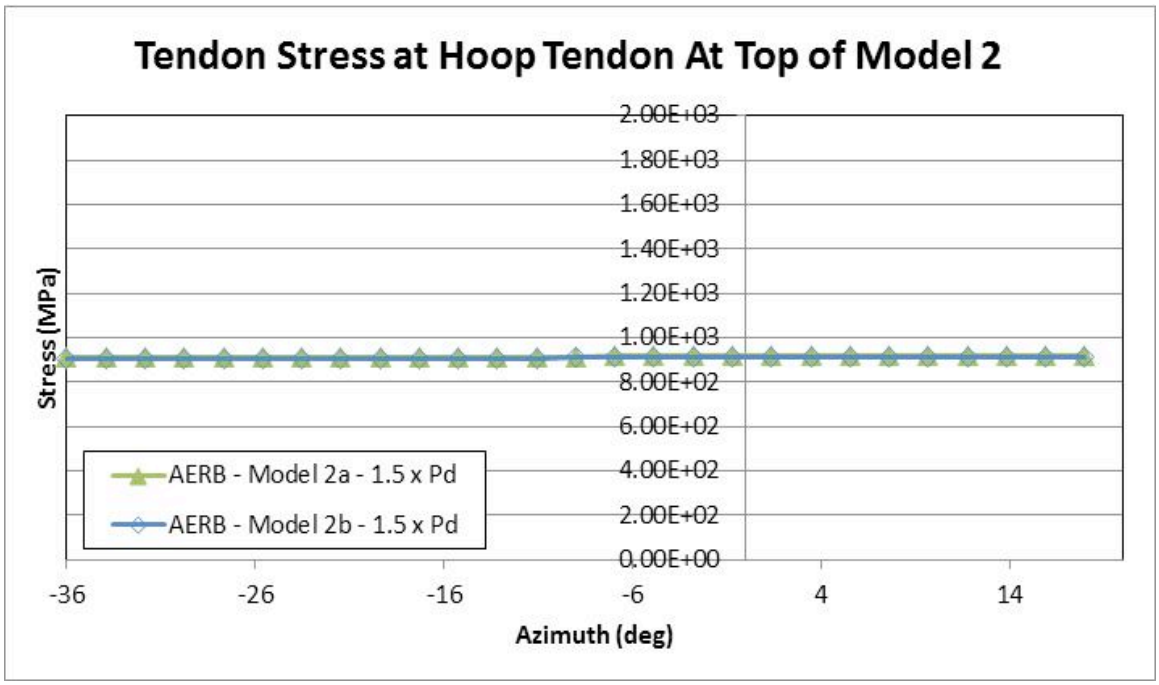

Figure 218: AERB Model 2(a-b) Tendon Stress Distribution (Top of Model) at 1.5xP_d

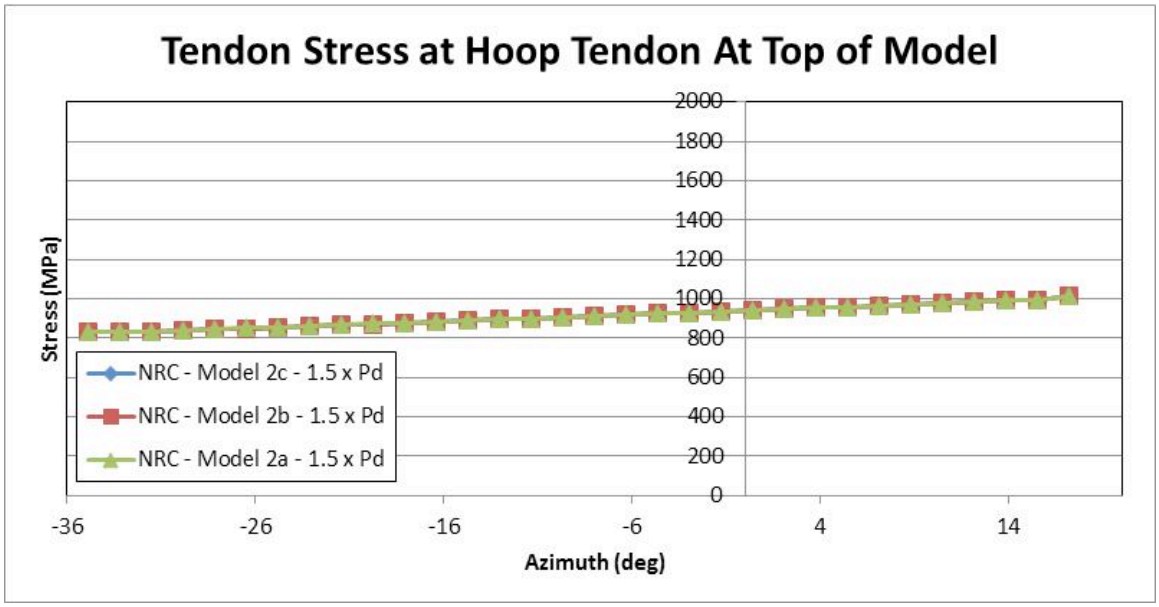

Figure 219: NRC Model 2(a-c) Tendon Stress Distribution (Top of Model) at 1.5xP_d

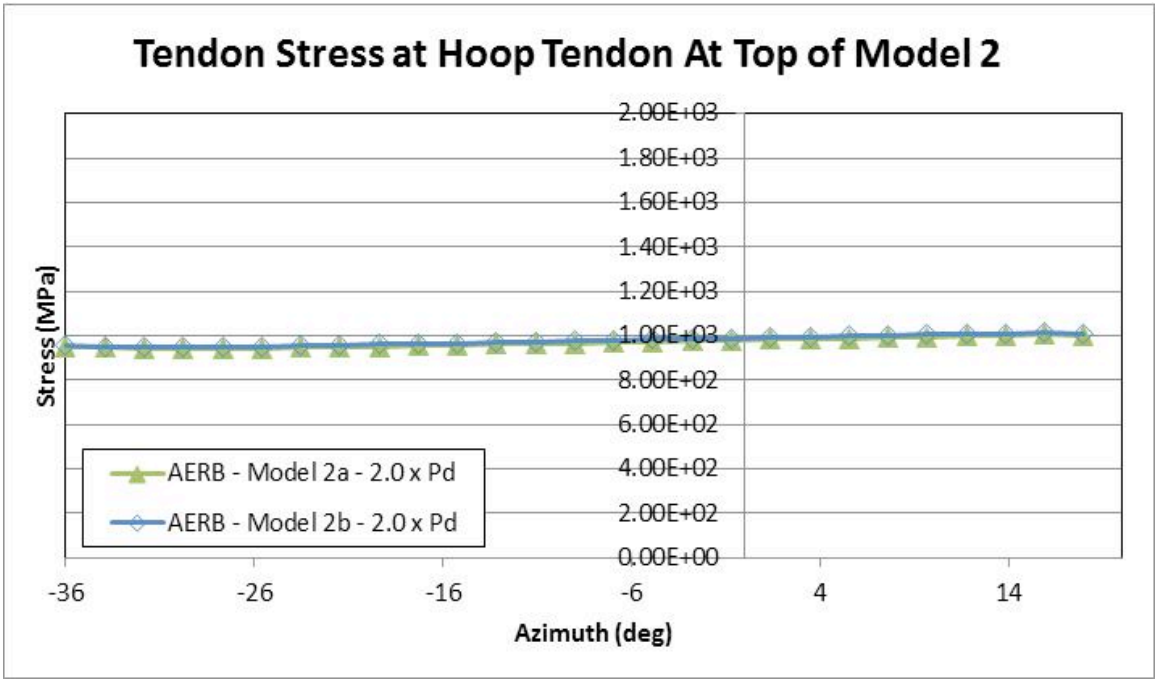

Figure 220: AERB Model 2(a-b) Tendon Stress Distribution (Top of Model) at $2xP_d$

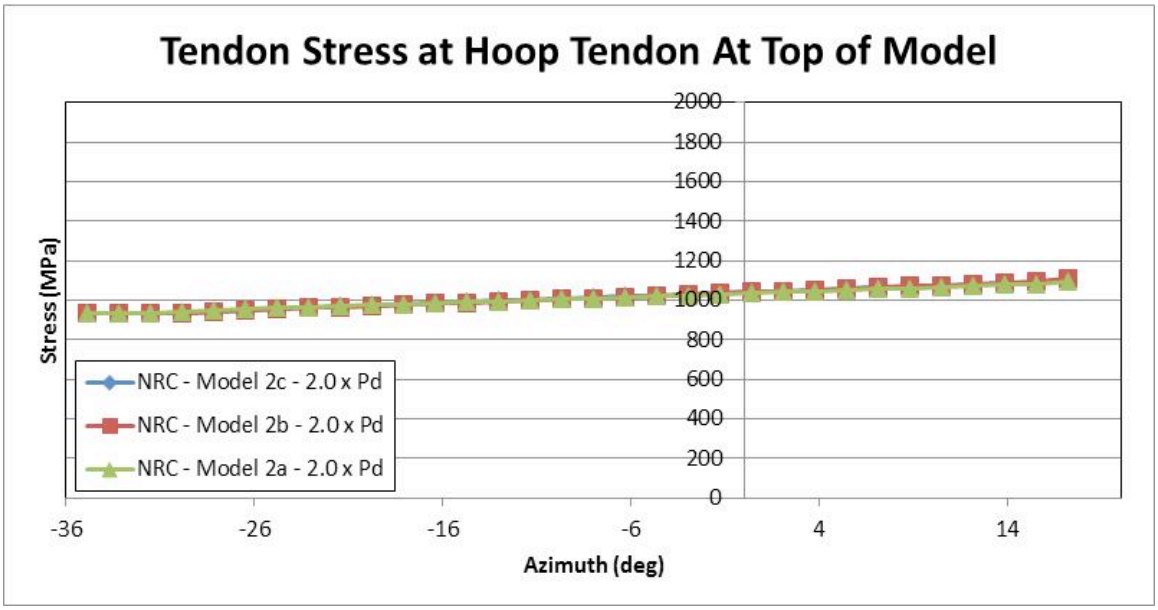

Figure 221: NRC Model 2(a-c) Tendon Stress Distribution (Top of Model) at $2xP_d$

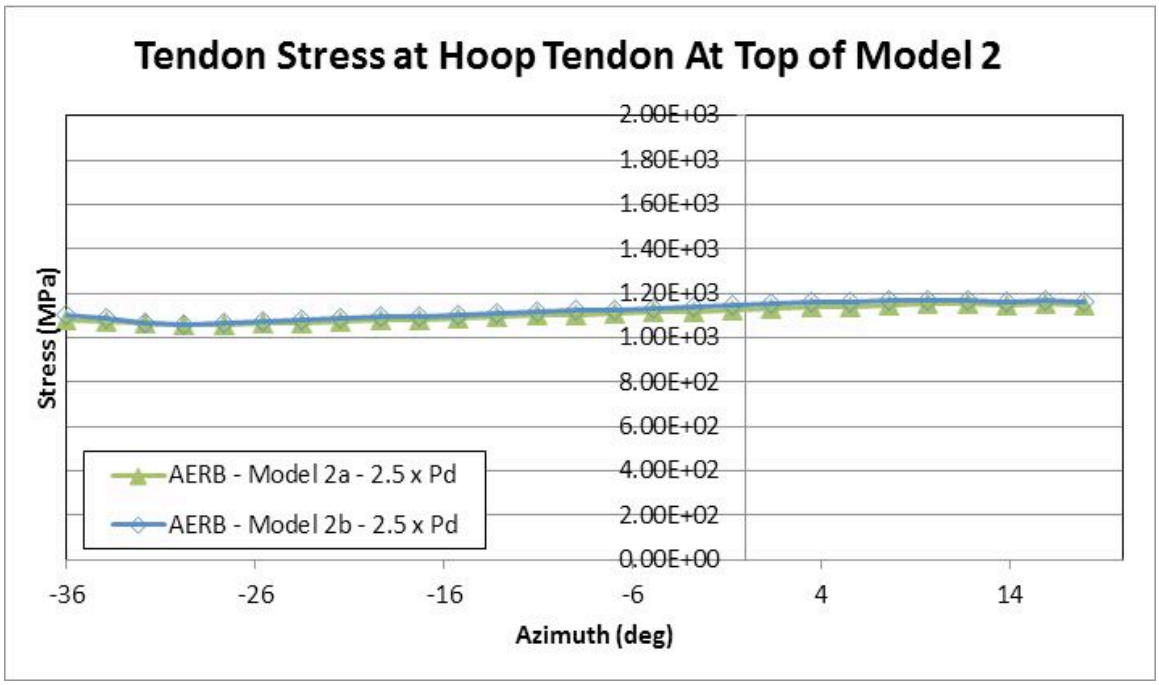

Figure 222: AERB Model 2(a-b) Tendon Stress Distribution (Top of Model) at 2.5xP_d

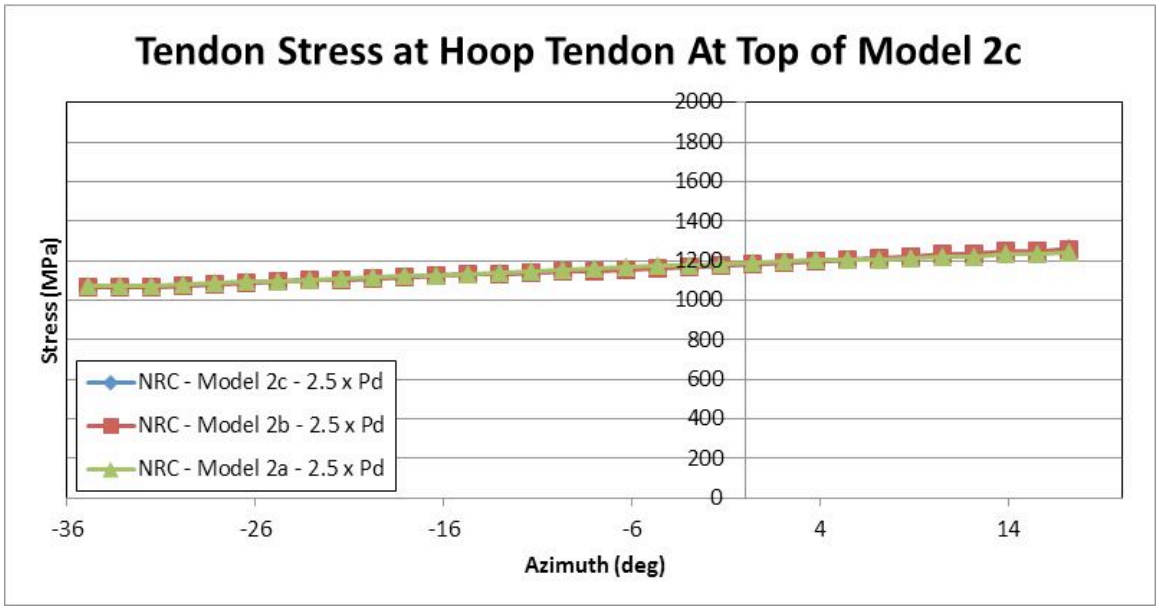

Figure 223: NRC Model 2(a-c) Tendon Stress Distribution (Top of Model) at 2.5xP_d

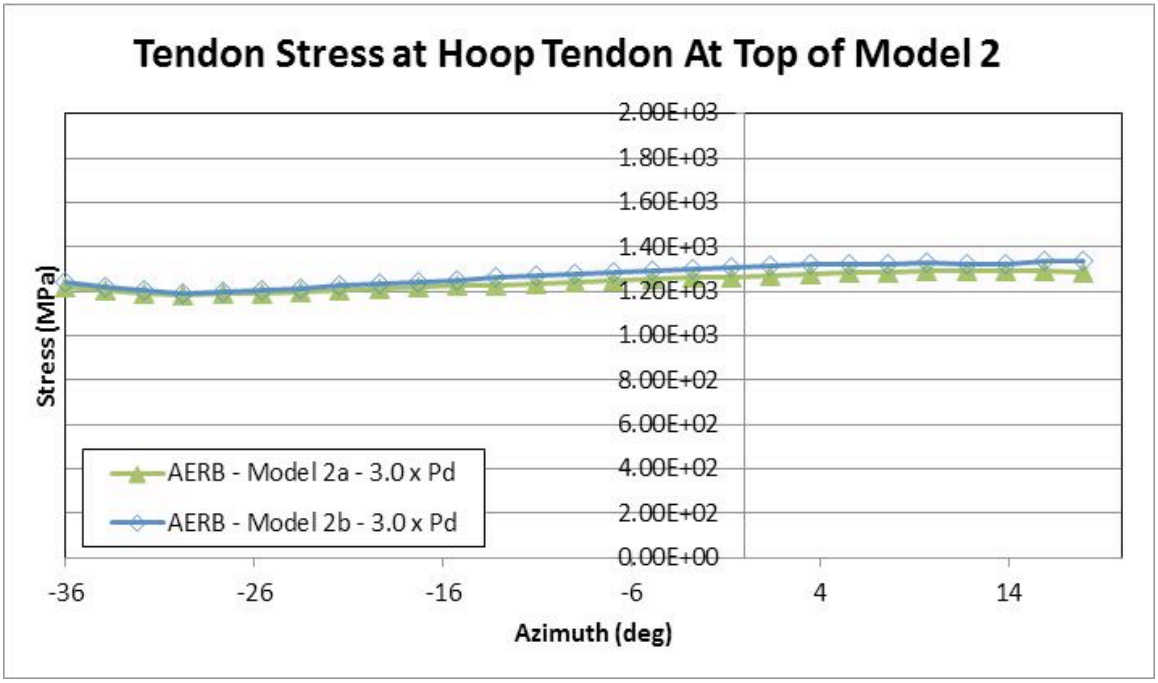

Figure 224: AERB Model 2(a-b) Tendon Stress Distribution (Top of Model) at 3xP_d

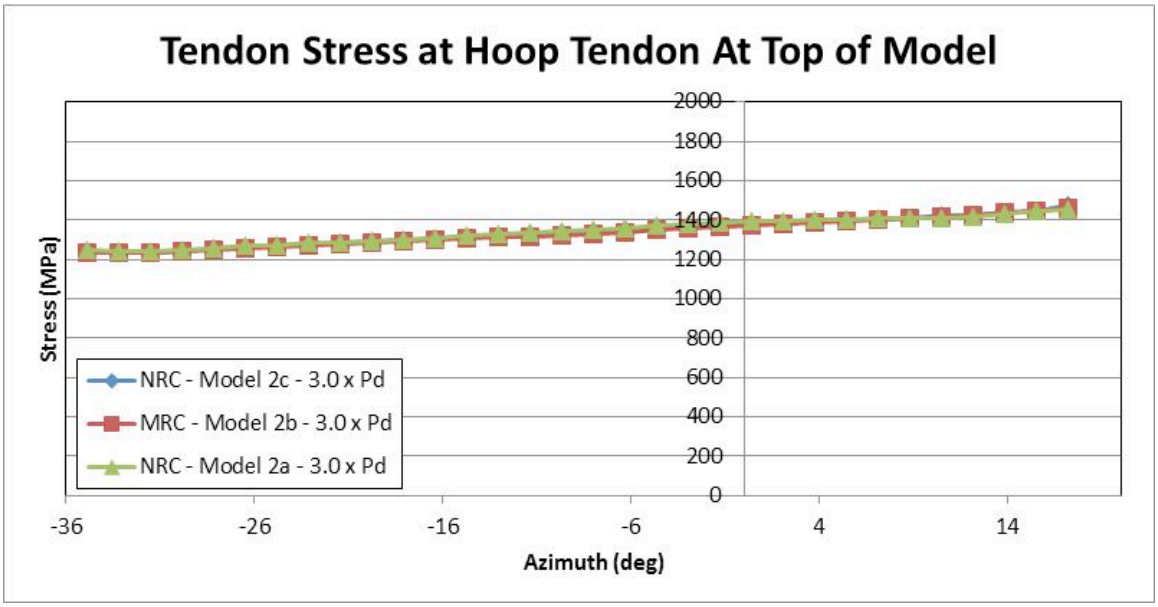

Figure 225: NRC Model 2(a-c) Tendon Stress Distribution (Top of Model) at 3xP_d

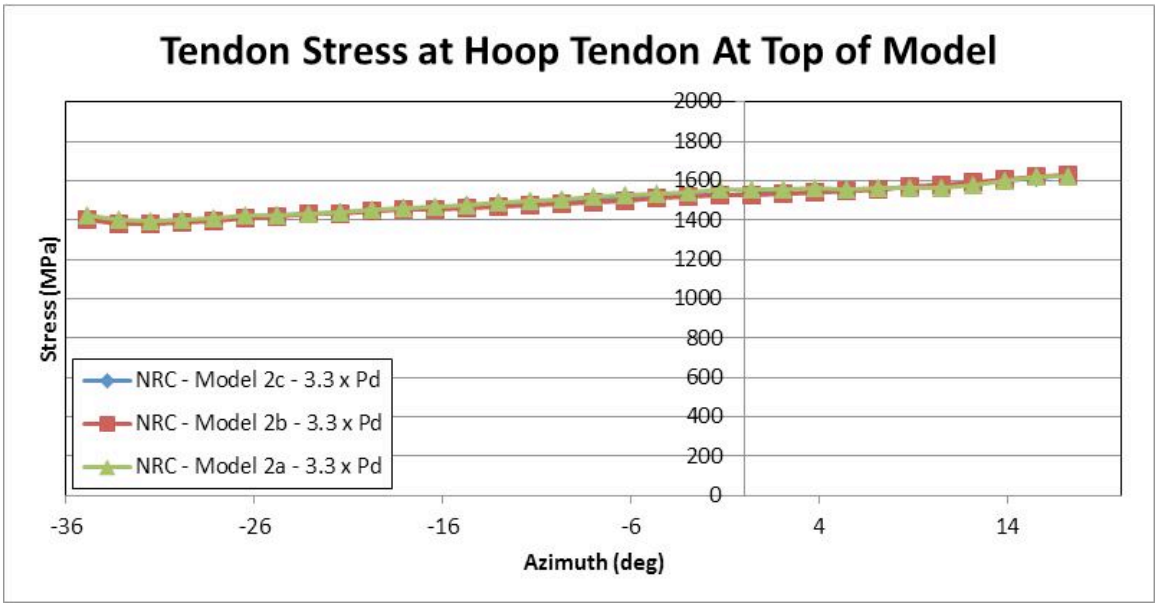

Figure 226: NRC Model 2(a-c) Tendon Stress Distribution (Top of Model) at 3.3xP_d

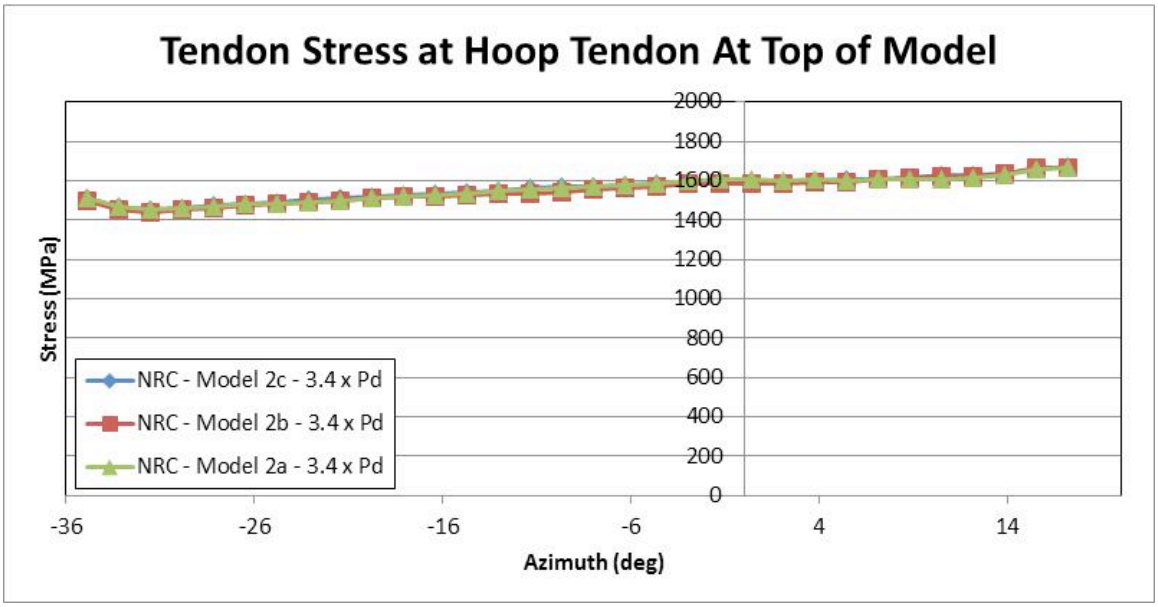

Figure 227: NRC Model 2(a-c) Tendon Stress Distribution (Top of Model) at 3.4xP_d

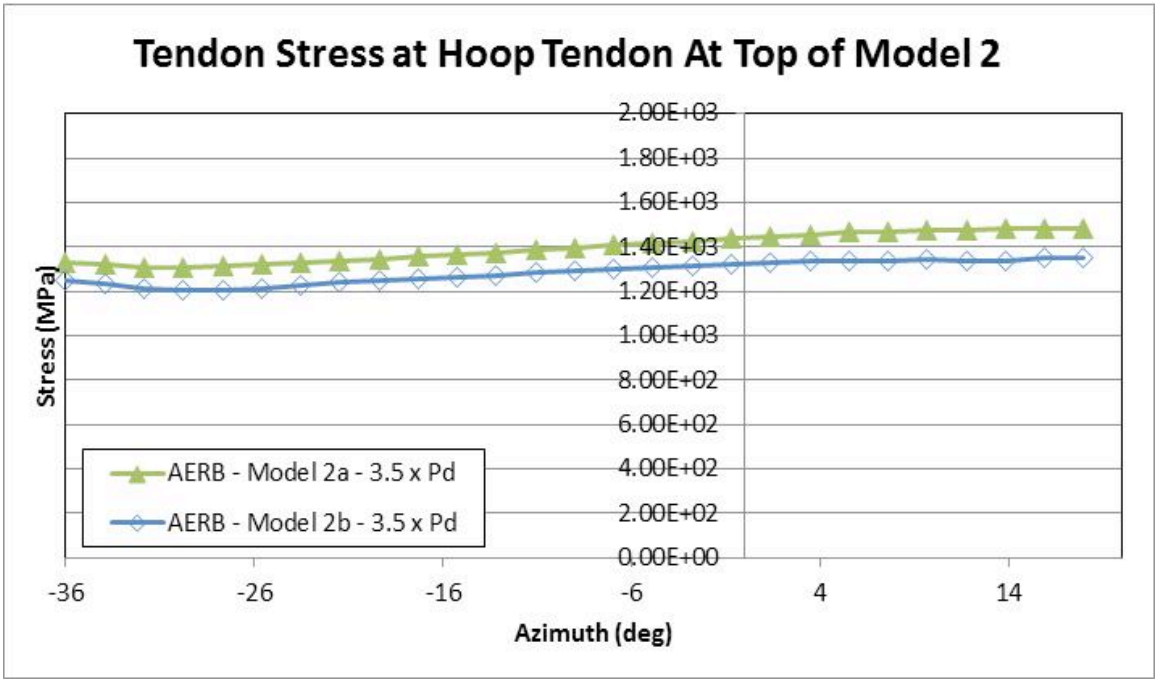

Figure 228: AERB Model 2(a-b) Tendon Stress Distribution (Top of Model) at Ultimate Pressure

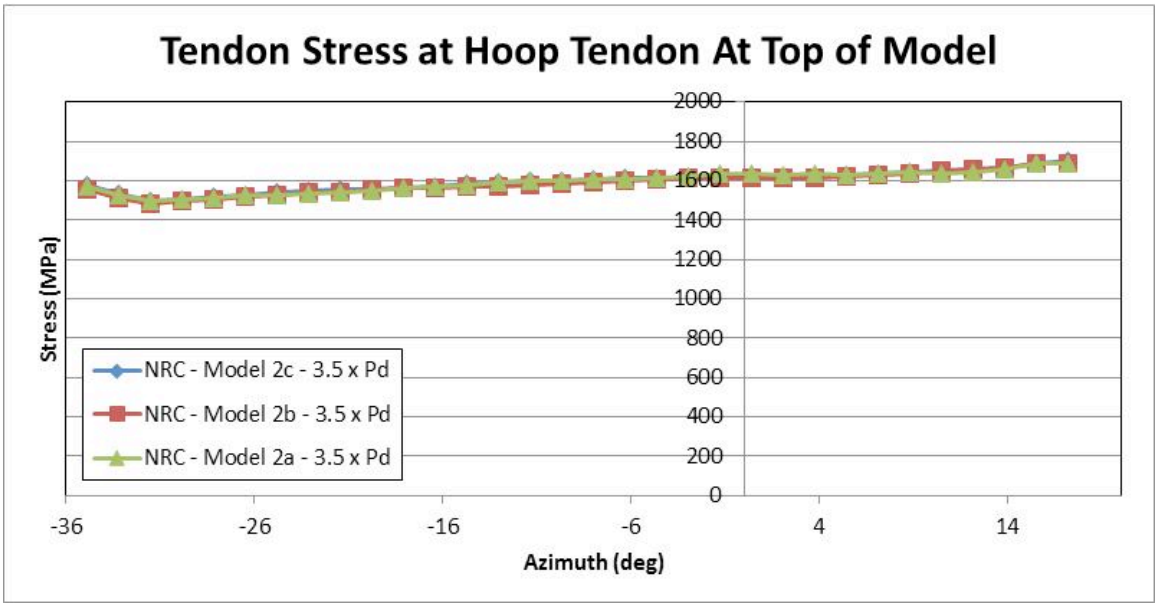

Figure 229: NRC Model 2(a-c) Tendon Stress Distribution (Top of Model) at Ultimate Pressure

3.8. Radial Displacements as a Function of Pressure

The radial displacement for Model 2, as reported by the participants, are summarized in Figure 230 through Figure 238. The plots are presented with displacement in millimeters as a function of internal pressure. Similar to Model 1, the responses from the participants agree well at the lower pressure levels with greater differences noted at the higher pressures. Additionally the figures below are location specific with each plot corresponding to a specific azimuth on the model.

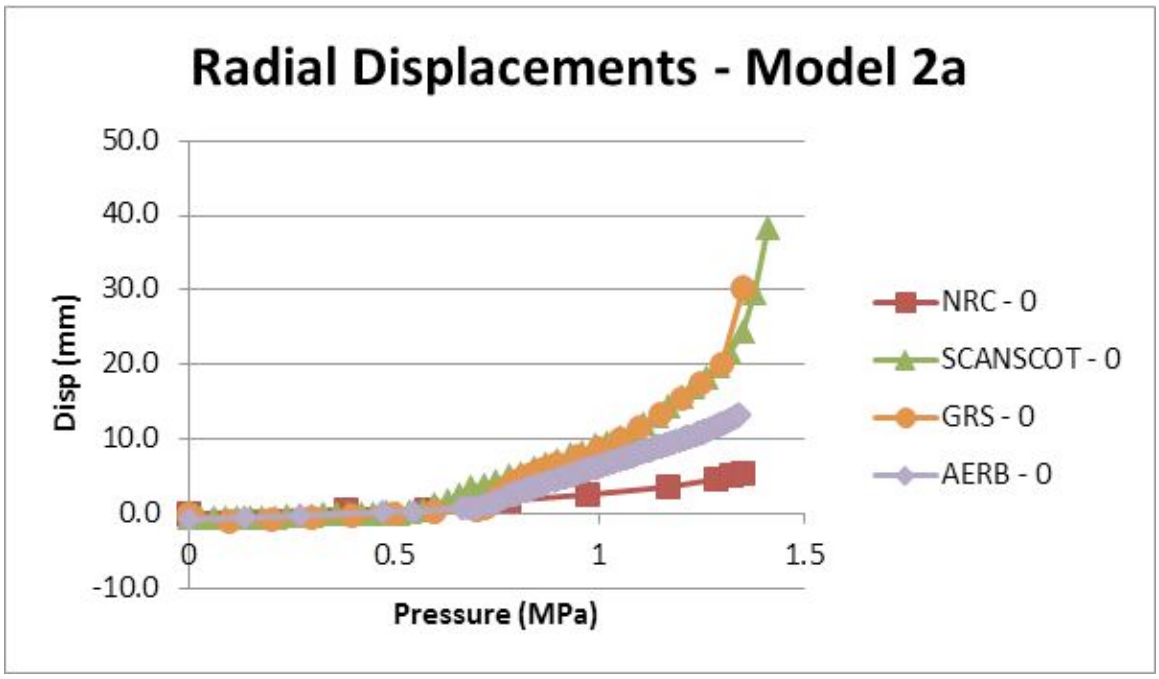

Figure 230: Model 2a Radial Displacement as a Function of Pressure for 0° Azimuth

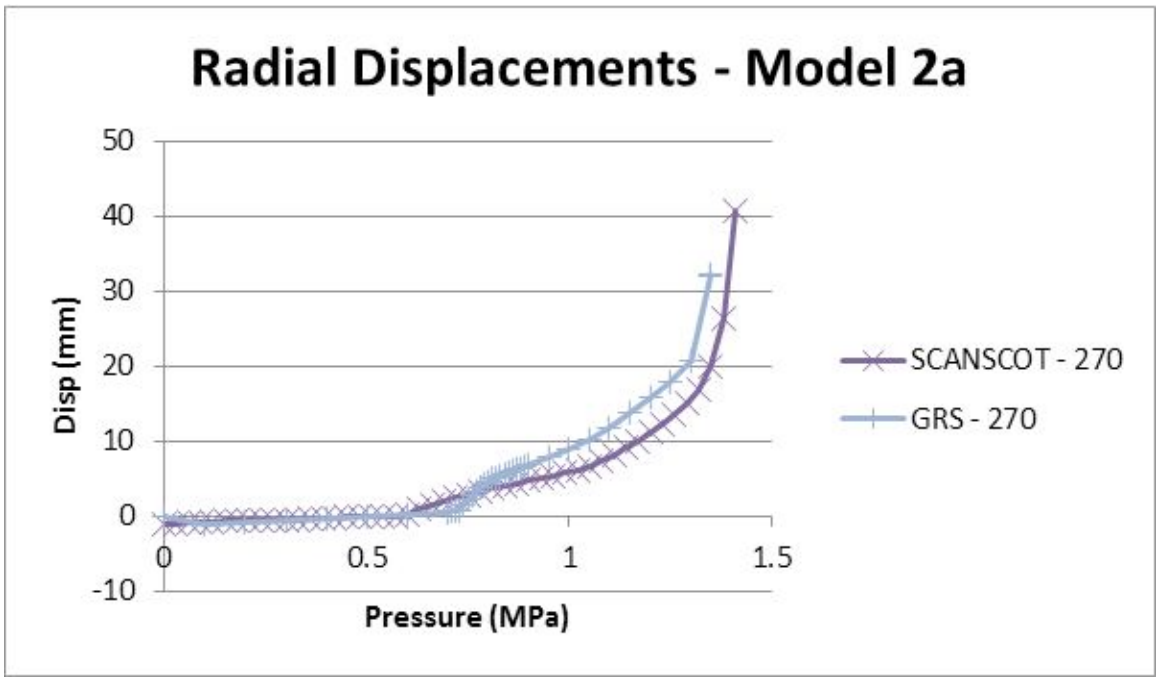

Figure 231: Model 2a Radial Displacement as a Function of Pressure for 270° Azimuth

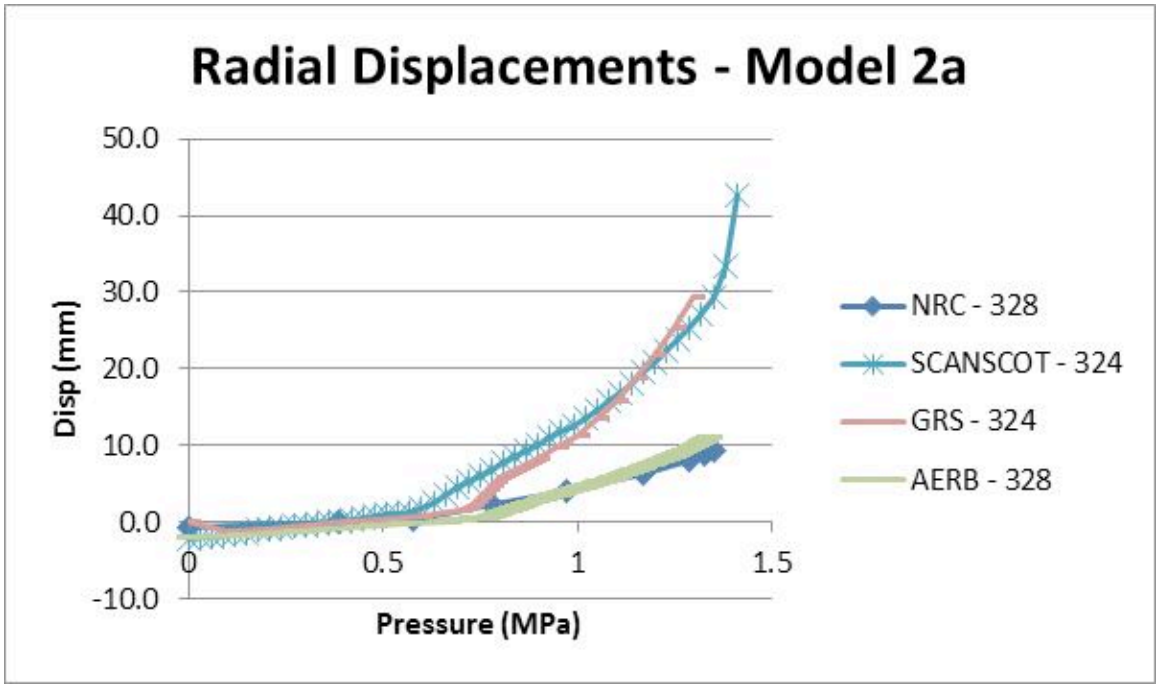

Figure 232: Model 2a Radial Displacement as a Function of Pressure for 328° Azimuth

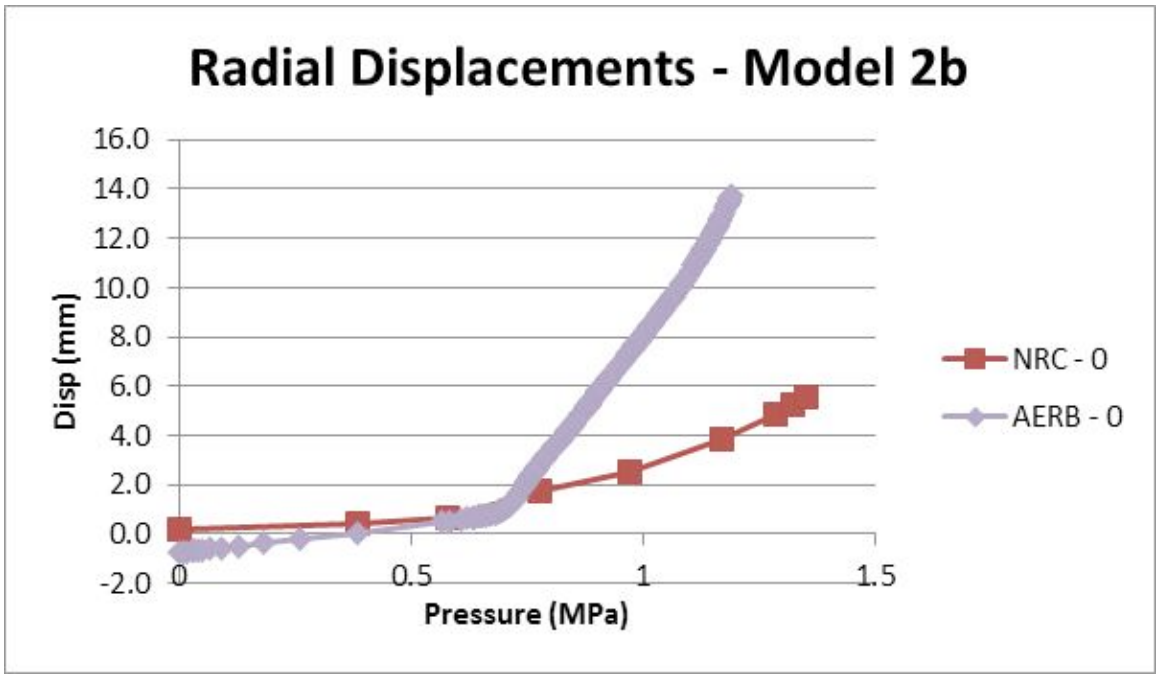

Figure 233: Model 2b Radial Displacement as a Function of Pressure for 0° Azimuth

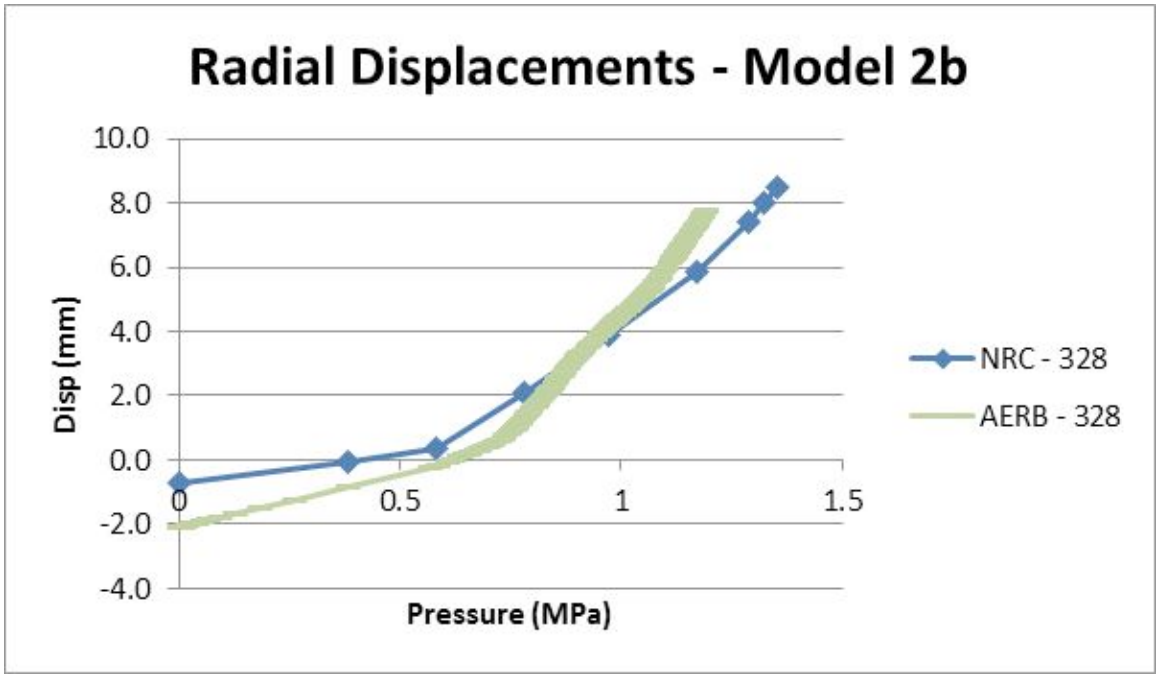

Figure 234: Model 2b Radial Displacement as a Function of Pressure for 328° Azimuth

A comparison of radial displacements for Models 2a-2c as completed by each participant as provided is presented below.

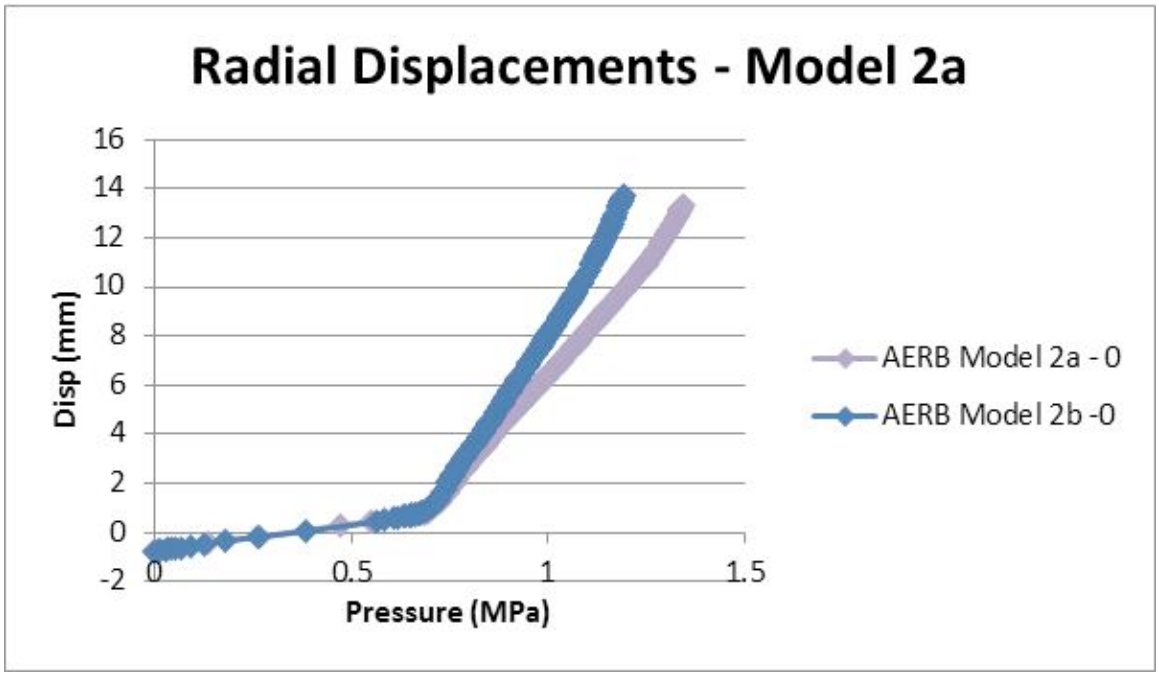

Figure 235: AERB Model 2(a-b) Radial Displacements as a Function of Pressure for 0° Azimuth

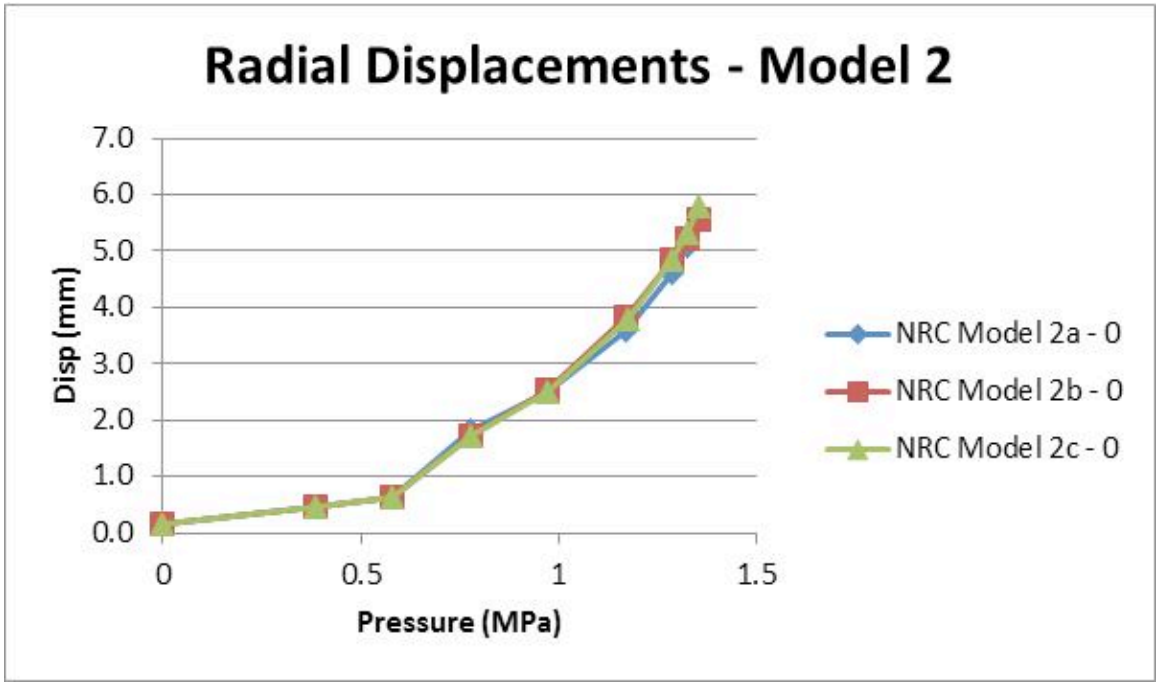

Figure 236: NRC Model 2(a-c) Radial Displacements as a Function of Pressure for 0° Azimuth

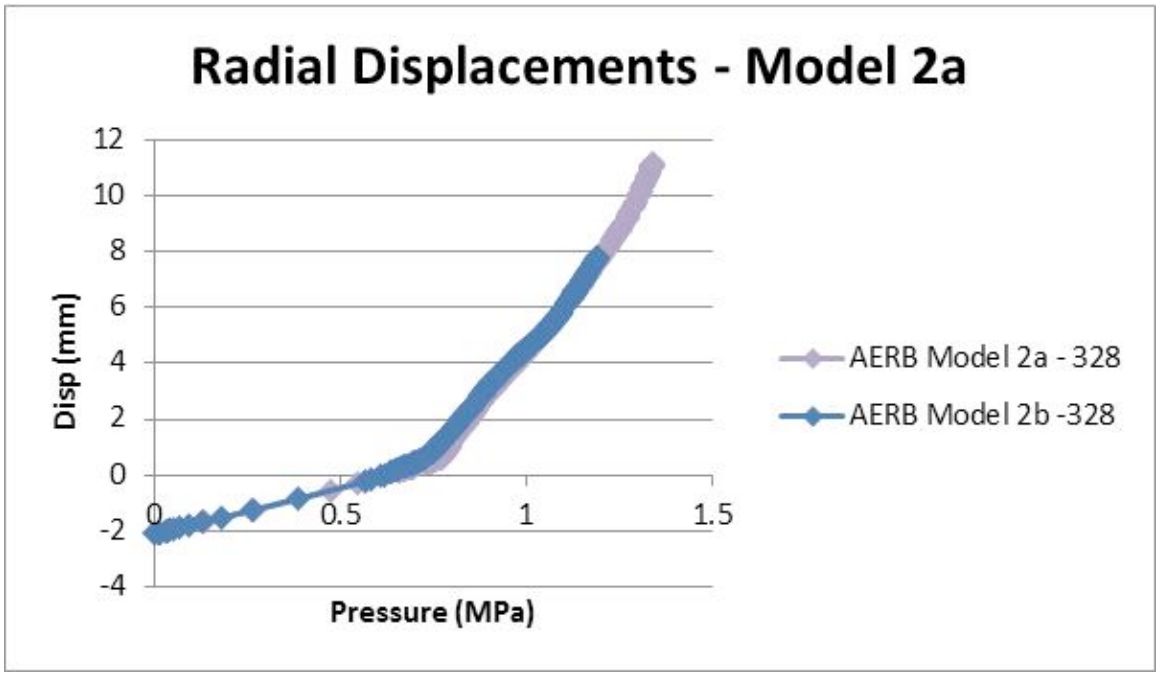

Figure 237: AERB Model 2(a-b) Radial Displacement as a Function of Pressure for 328° Azimuth

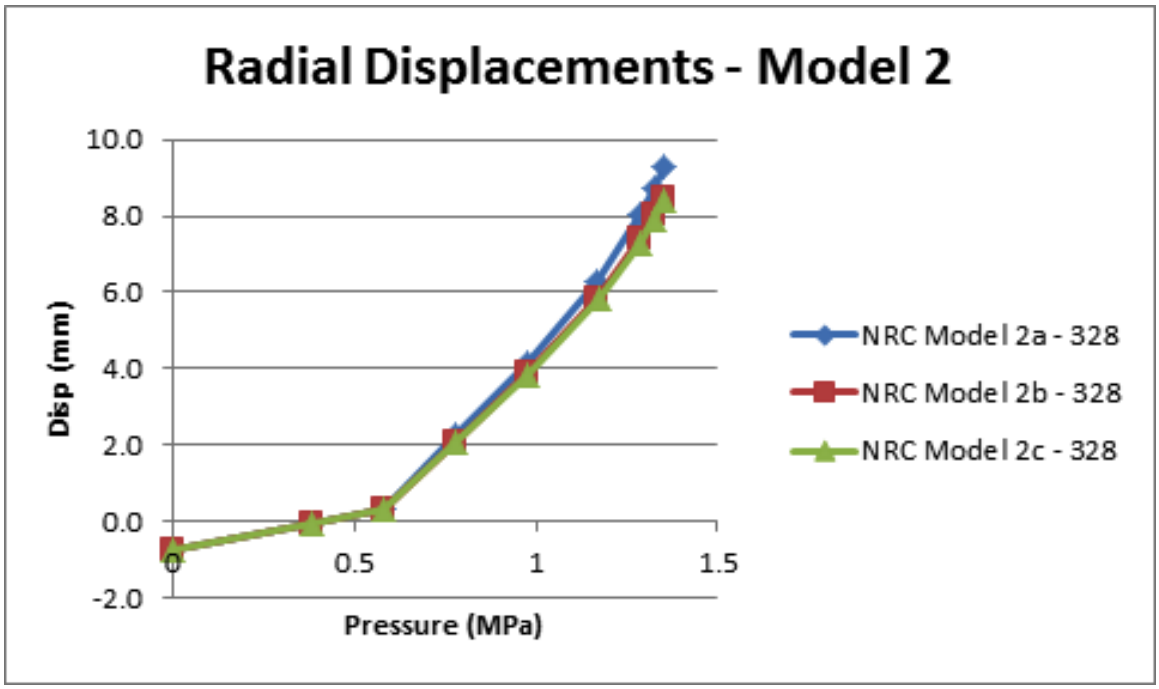

Figure 238: NRC Model 2(a-c) Radial Displacement as a Function of Pressure for 328° Azimuth

3.9. Ovalization

Pipe separation is plotted below in Figure 239 through Figure 246. Because only the NRC provided ovalization data for Model 2c, a comparison was made between Models 2a, 2b, and 2c. These comparisons are provided in Figure 245 and Figure 246.

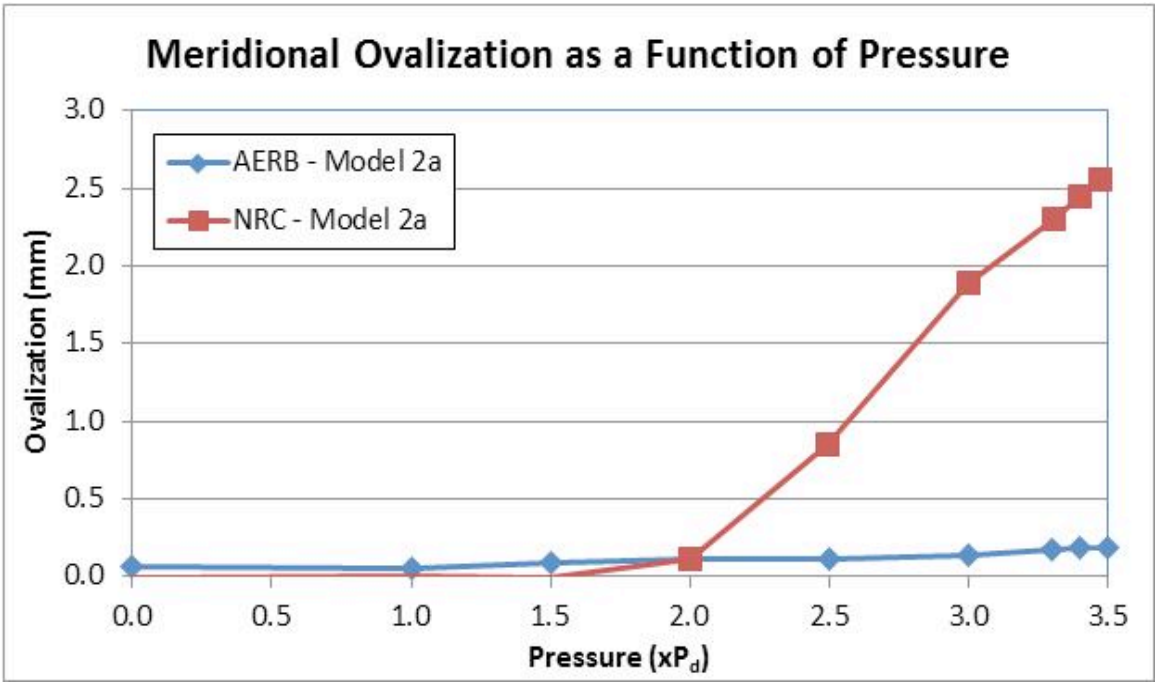

Figure 239: Meridional Separation (gap) in Pipe Sleeve for Model 2a

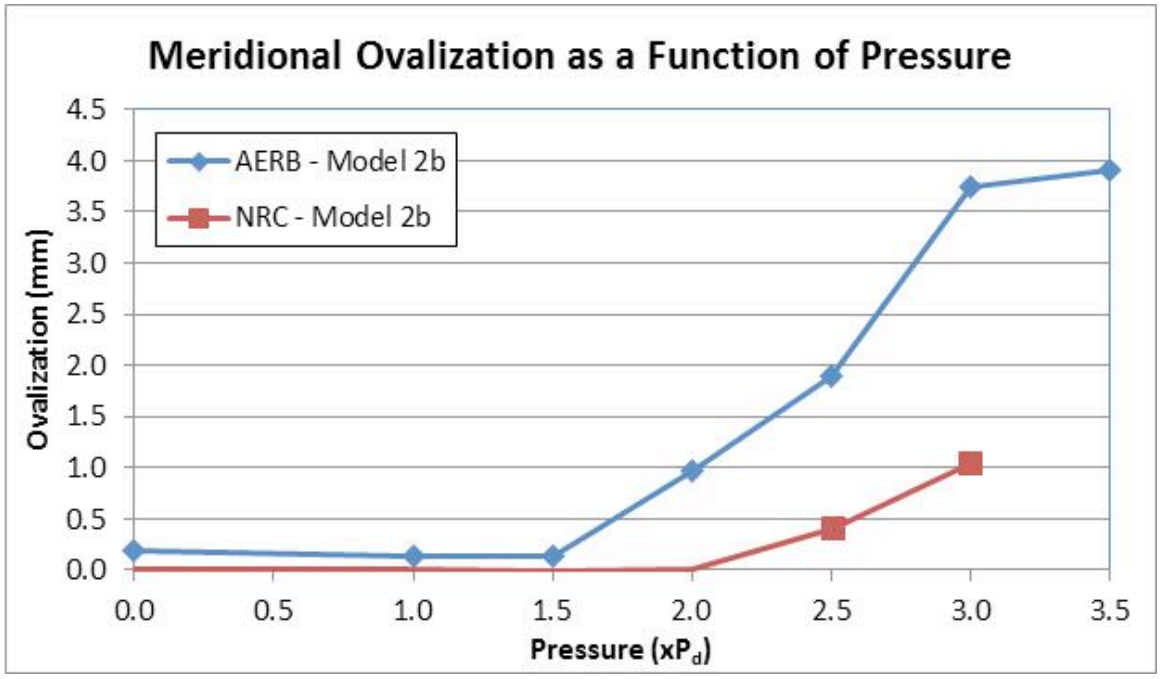

Figure 240: Meridional Separation (gap) in Pipe Sleeve for Model 2b

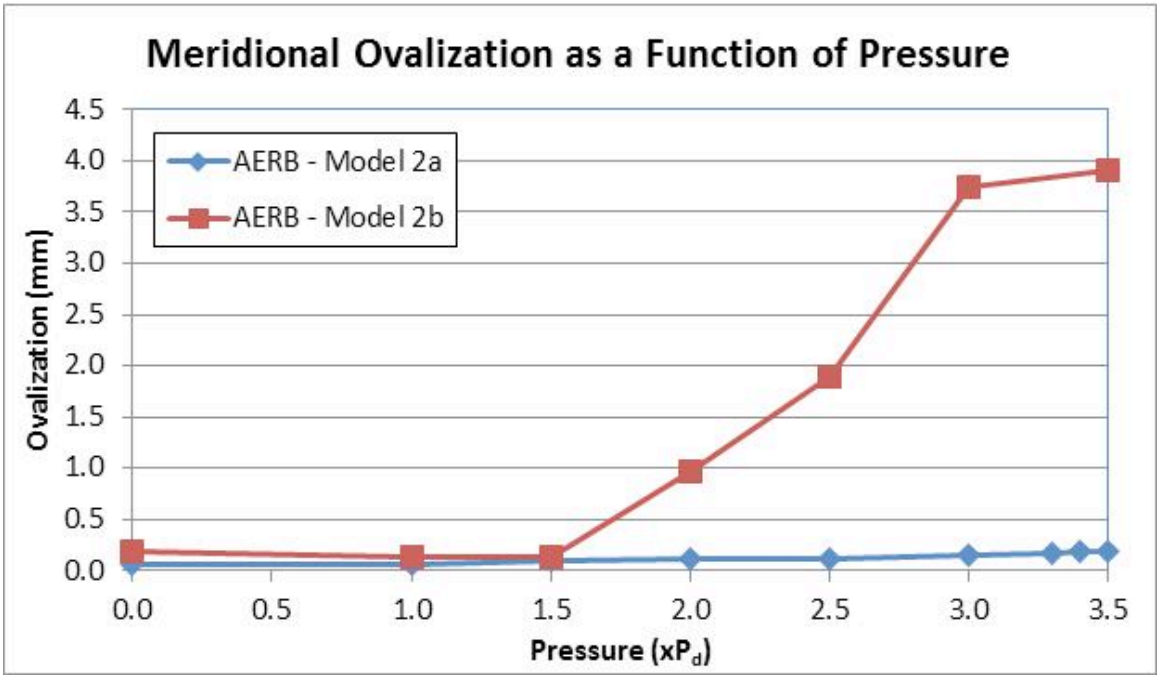

Figure 241: Meridional Separation (gap) in Pipe Sleeve for Model 2(a-b) from AERB

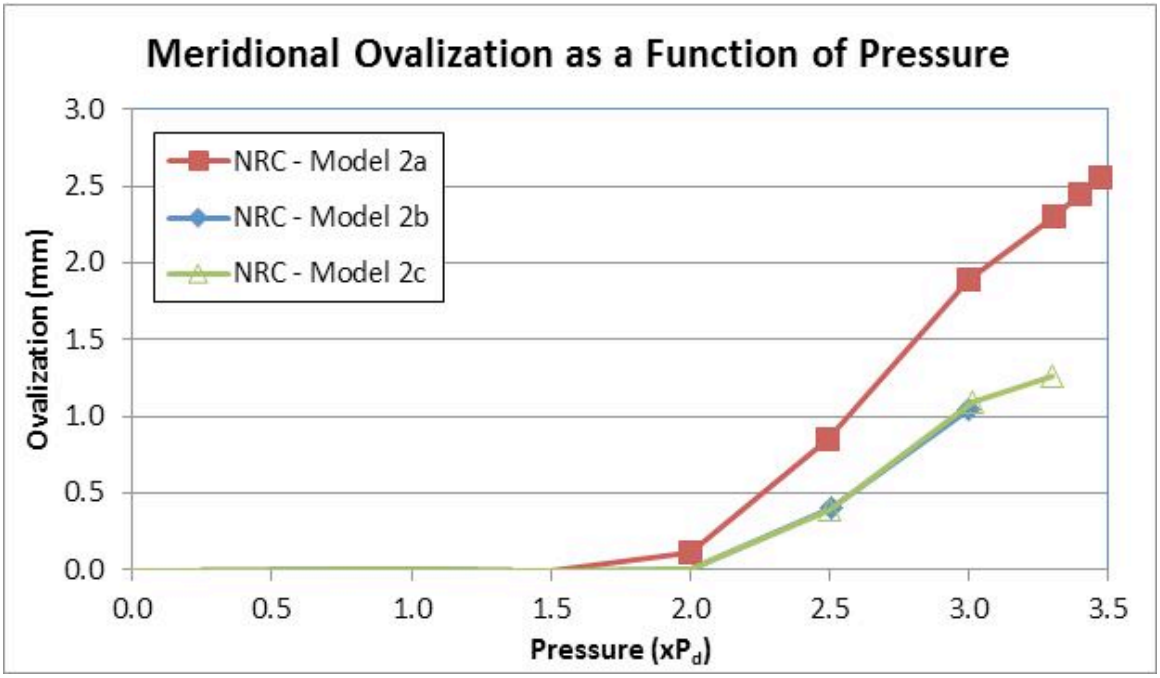

Figure 242: Meridional Separation (gap) in Pipe Sleeve for Model 2(a-c) from NRC

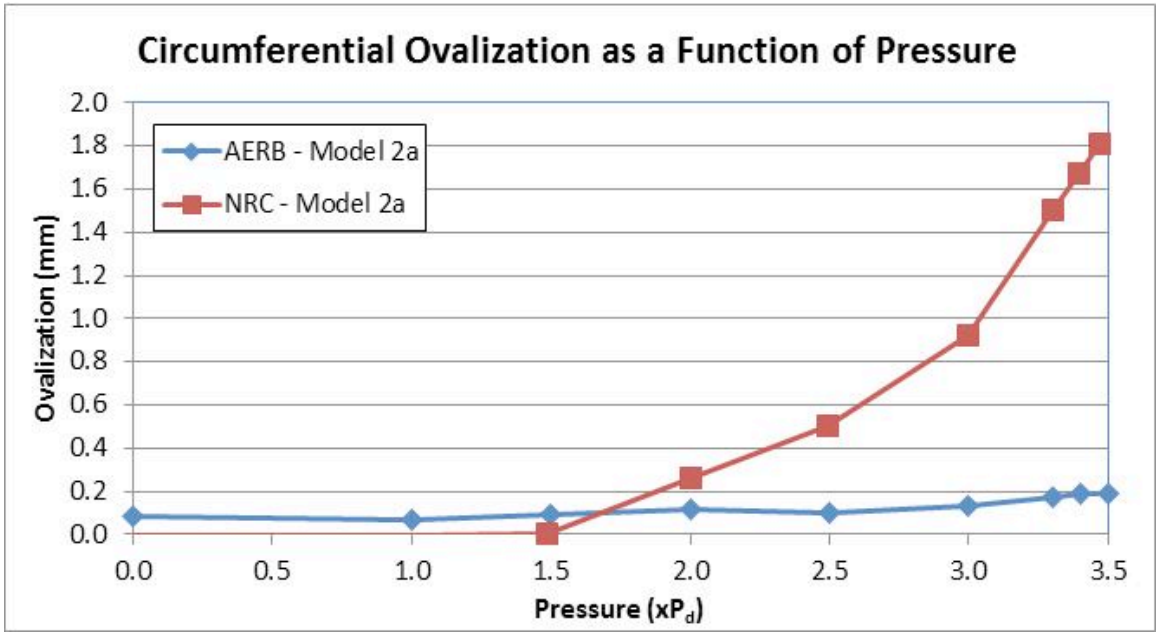

Figure 243: Circumferential Separation (gap) in Pipe Sleeve for Model 2a

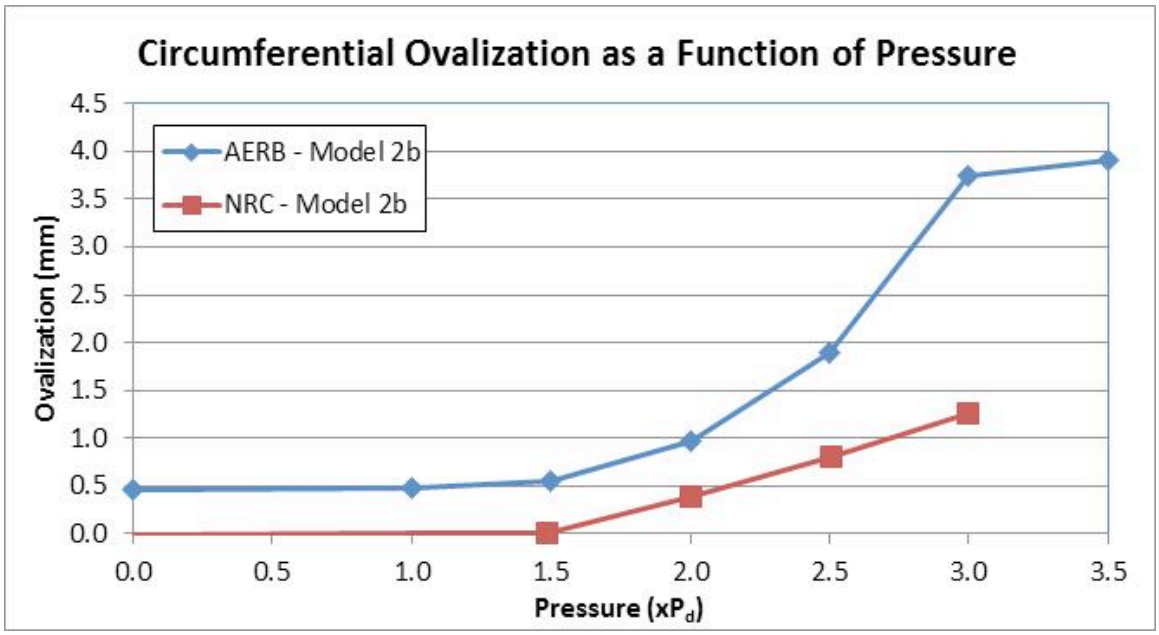

Figure 244: Circumferential Separation (gap) in Pipe Sleeve for Model 2b

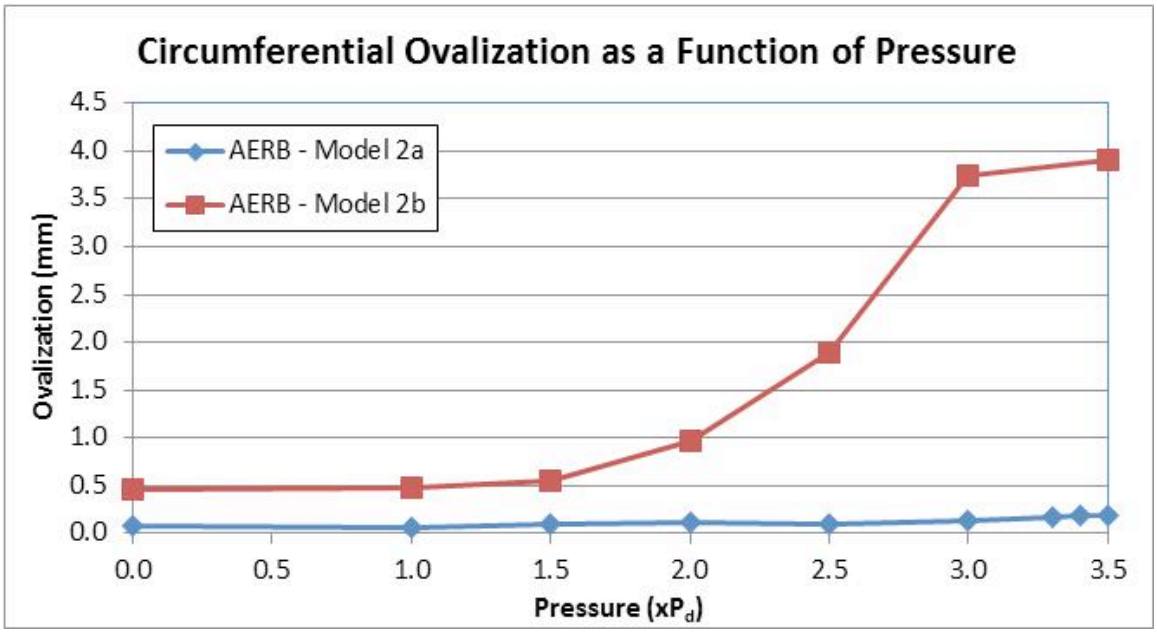

Figure 245: Circumferential Separation (gap) in Pipe Sleeve for Model 2(a-b) from AERB

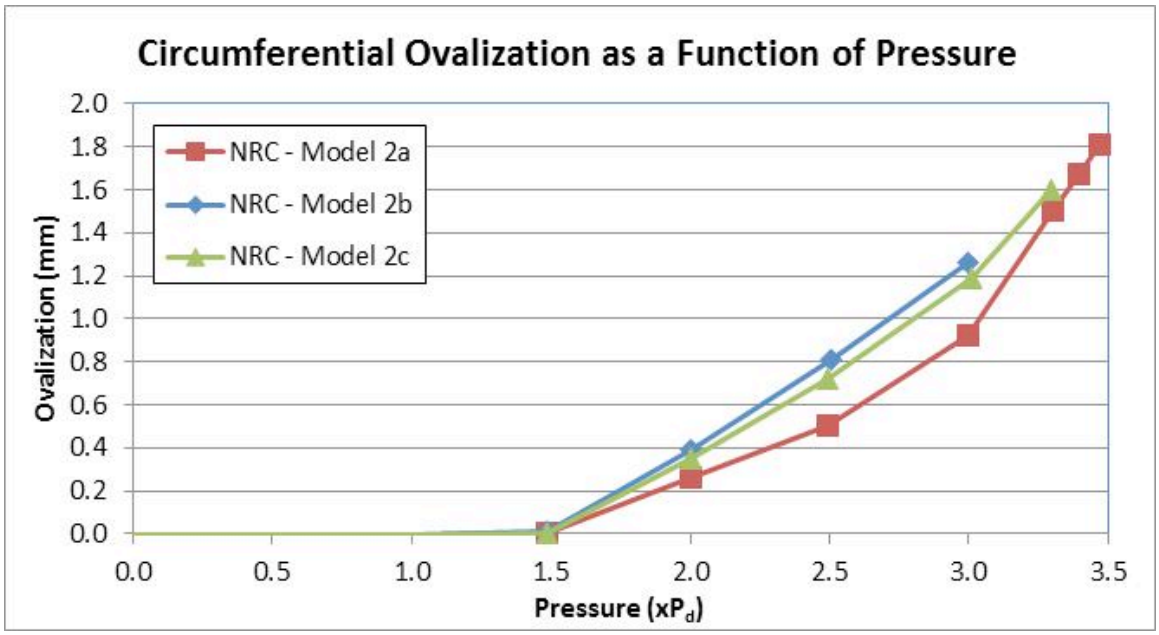

Figure 246: Circumferential Separation (gap) in Pipe Sleeve for Model 2(a-c) from NRC

3.10. Model 2 Conclusions

Model 2 results were submitted by AERB, GRS, NRC, and SCANSCOT. Some variability in modeling technique was observed between the participants, most notably in the method of modeling the tendons. AERB modeled the tendons as embedded in the concrete while NRC and SCANSCOT each used contact surfaces with friction to allow the tendons to move relative to the concrete. Additionally relatively minor differences were observed in the specific values used for the material properties for Model 2. It is suspected that the variation in modeling approach and the minor differences in the input material properties likely account for the variations noted in the results for Model 1.

The pressure milestones submitted by the participants indicate good agreement from the participants with a few small exceptions. For example, SCANSCOT indicated a slightly lower internal pressure for the onset of concrete cracking while GRS indicated slightly lower internal pressure levels at 2% strain in the tendons.

The deformed shape comparisons indicated good agreement between all participants, particularly near the design pressure for the structure. The variations between the participants in the deformed shape at all pressure levels are small, however, and the agreement between participants for the deformed shapes are good.

The tendon stress profiles, tendon strain versus pressure plots, and radial displacement versus pressure plots indicate very good agreement between the participants, particularly up to approximately 3.0-3.3 x P_d. Past this point in the pressurization, the models begin to become somewhat unstable as supported by the termination of the Limit State Test in the NUPEC/NRC 1:4 Scale PCCV Test at 3.3 x P_d. Additionally, several participants verified the slipping of the tendons with internal pressure as the source of the observed flattening of the tendon force versus location plots at high pressures.

4. MODEL 3

As mentioned previously, Model 3 is a global analysis model aimed at incorporating lessons learned from Model exercises 1 and 2, and at providing PCCV response information at any and all locations of the structure. One of the major areas of interest in Model 3 is characterizing strain in the liner, to be used in comprehensive failure prediction, which will be key to the successful completion of Phase 2. The participants were asked to provide the following output for direct comparison:

1. Description of failure prediction model or criteria selected for use
2. Assumptions made in geometric modeling , and model description
3. Contour plots of peak strains in the liner during the LST at the pressure milestones: P=0, 1 x P_d, 1 x P_d, 1.5 x P_d, 2 x P_d, 2.5 x P_d, 3 x P_d, 3.3 x P_d, 3.4 x P_d, and Ultimate Pressure
4. Average stains over 540.45 mm regions as shown in Figure 11, at locations 3, 4, and 5, for each penetration, as a function of pressure
5. Tendon stress distribution at P=0, 1 x P_d, 1 x P_d, 1.5 x P_d, 2 x P_d, 2.5 x P_d, 3 x P_d, 3.3 x P_d, 3.4 x P_d, and Ultimate Pressure for
    a. Hoop tendons #H35, H53, and H68
    b. Vertical tendons #V37 and V46
6. Plots of response versus pressure for Standard Output Locations
    a. SOL 1-15 (displacements)
    b. SOL 22-29 (rebar strains)
    c. SOL 36-42 (liner strains)
    d. SOL 48-55 (tendon strains and stresses)

4.1. Description of Material and FEM Models

A comparison of the different modeling software and modeling set-up is listed below in Table 15. Each participant was free to use any FEM software they so chose, and to represent the geometry for Model 3 as needed.

Table 15: Model Detail Comparison

MODELING DETAILS	AERB	FORTUM	NRC	SCANSCOT
FEM Tool	Abaqus	Abaqus 6.10 Implicit Dynamic	Abaqus Standard FE	Abaqus Explicit 6.9 and Abaqus Standard 6.9
Concrete Element Type	Hex Elements (C3D8R)	Shell Elements (S4R)	Hex Elements (C3D8R)	Hex Elements (C3D8R)
Rebar Element Type	Rebar Layer	Rebar Layer	Rebar Layer (SFM3D4R)	Rebar Layer
Liner Element Type	Linear 4-node Shell Element with Uniaxial Behavior	Shell Elements (S4R)	Shell Elements (S4R)	Shell Elements (S4R)
Tendon Element Type	Linear 2-Node Truss Element	Truss Elements (T3D2)	Beam Elements (B31)	Truss Elements (T3D2)
Tendon / Concrete Interaction	Embedded	Connector Elements (CONN3D2)	Tendons inside tendon ducts	Contact Surfaces with Friction (0.22)
Concrete / Rebar Interaction	Embedded	Embedded	Embedded	Embedded

A comparison of the material models is provided in Table 16. In general, there is good agreement between the material parameters chosen by the participants.

Table 16: Comparison of Material Models

MATERIAL	AERB	FORTUM	NRC	SCANSCOT
Concrete Model	Damage Plasticity Concrete	Concrete Damage Plasticity	Concrete Damage Plasticity	Brittle Cracking Model
Concrete Parameters of Note	E = 26,900 MPa ν = 0.21 σ_t = 2.4 MPa ρ = 2,176 kg/m^3	E = 28,000 MPa ν = 0.2 σ_t = MPa ρ = 2500kg/m^3 Ep = MPa	E = 33,000 MPa ν = 0.2	E=26,800 MPa ν = 0.2
Rebar	Non-Linear Elasto-Plastic	Elasto-Plastic	Elasto-Plastic	Elasto-Plastic
Rebar Parameters of Note	E = 185,000 MPa ν = 0.3 σ_t = 445-460 MPa ρ = 7,850 kg/m^3 Ep = 1,250-1,350 MPa	E = 200,000 MPa ν = 0.3 σ_t = MPa ρ = 7,850 kg/m^3 Ep = MPa	E = 200,000 MPa ν =0.3 σ_t = 498 MPa	E = 183,000 MPa ν =0.3 σ_t = 460 MPa
Liner	Metal Plasticity	Elasto-Plastic	Elasto-Plastic	Elasto-Plastic
Liner Parameters of Note	E = 210,000 MPa ν = 0.3 σ_t = 400 MPa ρ = 7,850 kg/m^3 Ep = 700 MPa	E = 219,000 MPa ν = 0.3 σ_t = MPa ρ = 7,850 kg/m^3 Ep = MPa	E = 200,000 MPa ν =0.3 σ_t = 498 MPa	E = 220,000 MPa ν =0.3 σ_t = 383 MPa
Tendon	Non-Linear Elasto-Plastic	Elasto-Plastic	Elasto-Plastic	Elasto-Plastic
Tendon Parameters of Note	E = 191,000 MPa ν = 0.3 σ_t = 1,750 MPa ρ = 7,850 kg/m^3 Ep = 3,350 MPa f_{gu} = 1,857 MPa μ = 0.21 Δs = 3.95 mm T_0 = 444 kN	E = 191,000 MPa ν = 0.3 σ_t = MPa ρ = 7,850 kg/m^3 Ep = MPa f_{gu} = MPa μ = Δs = mm T_0 = kN	E = 195,000 MPa ν = 0.3 σ_t = 1875 MPa	E = 191,000 MPa ν = 0.3 σ_t = 1680 MPa

4.2. Description of Model Failure Criteria

The critical parameter for predicting tendon failure appears to be the axial strain in the tendon of interest. The participants in the present study were requested to provide the tendon failure criteria used when predicting the failure of the tendons in Model 3 from their simulations. The participants all selected tendon failure criteria in reasonable agreement with one another. All participants (AERB, Fortum, NRC, and SCANSCOT) specified the actual ultimate tensile strain to predict failure. The tendon failure strain was calculated from these parameters. The ultimate strain for the prestressing tendons in Model 3 used by all the participants are presented below in Table 17.

Table 17: Tendon failure criteria

	AERB	FORTUM	NRC	SCANSCOT
Tendon Failure Criteria (ultimate strain)	4.1%	4%	3.8%	3.7%

The model failure parameter of interest in Model 3 was liner tearing. This failure criteria is not as straightforward as the dominant failure mechanism in Model 1, tendon rupture. Because the liner experiences a bi-axial state of stress, determining the particular onset of tearing is somewhat complicated. The methods used by the participants for Model 3 are identified in Table 18.

Table 18: Liner failure criteria

	AERB	FORTUM	NRC	SCANSCOT
Tendon Failure Criteria (ultimate strain)			Biaxial Stress based (Davis Triaxiality Factor)	Biaxial Stress based (Davis Triaxiality Factor)

4.3. Deformed Shape

Several participants provided deformed shape plots for Model 3 at the usual pressure milestones. These deformed shape plots can be found in Figure 247 through Figure 255. Similar to the deformed shape plots from Model 1, the different scaling factors used by the various participants limit the initial comparability of the figures. Nonetheless, the general shape of the deformed models does indicate some difference between the participants.

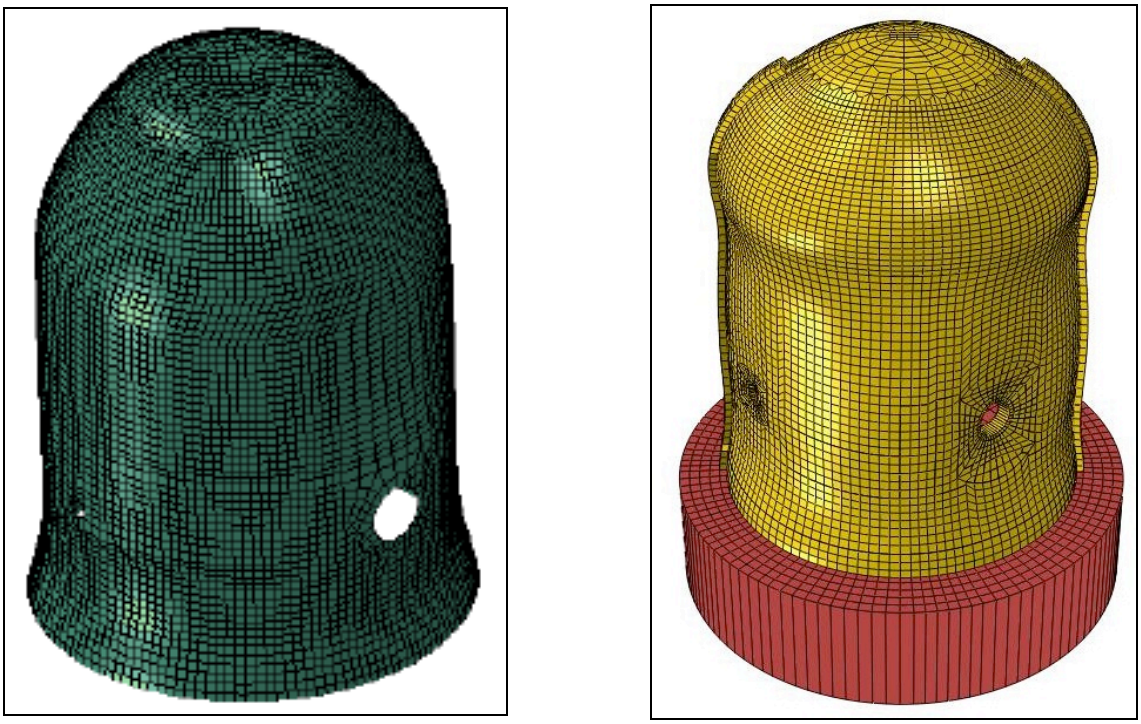

A B

Figure 247: Deformed Shape after Tendon Anchorage (a) AERB (b) NRC Deformation Scale x 500

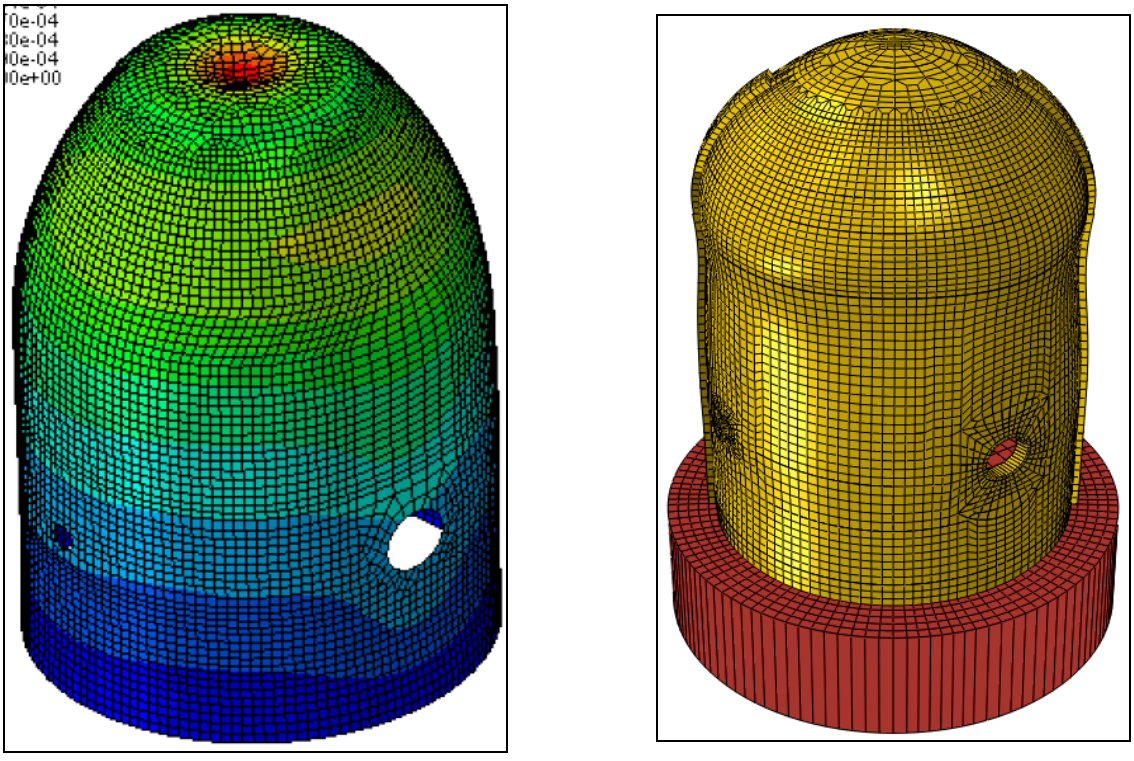

A B

Figure 248: Deformed Shape at 1.0 x P_d (a) AERB (c) NRC

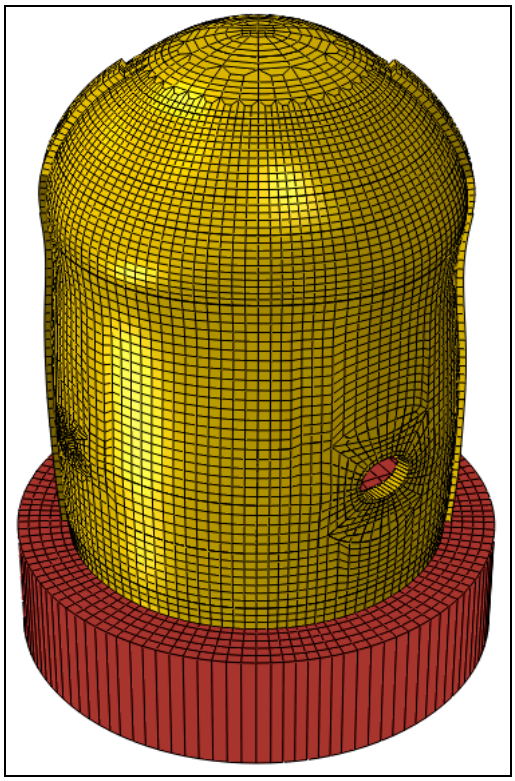

A B

Figure 249: Deformed Shape at 1.5 x P_d (a) NRC

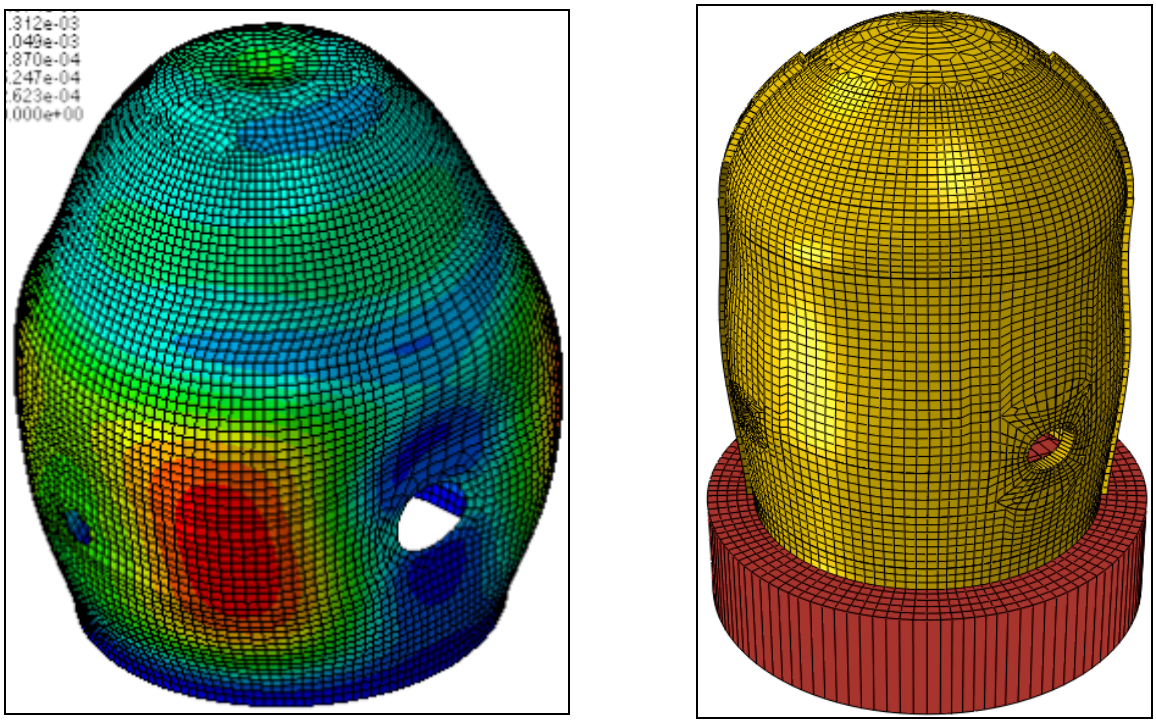

A B

Figure 250: Deformed Shape at 2.0 x P_d (a) AERB (b) NRC

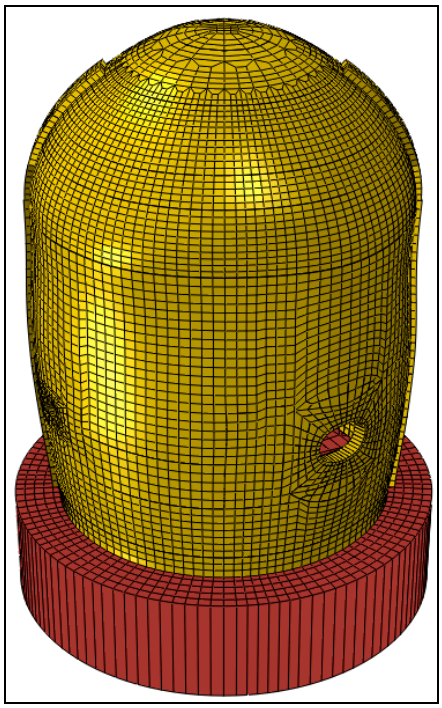

A B

Figure 251: Deformed Shape at 2.5 x P_d (a) NRC

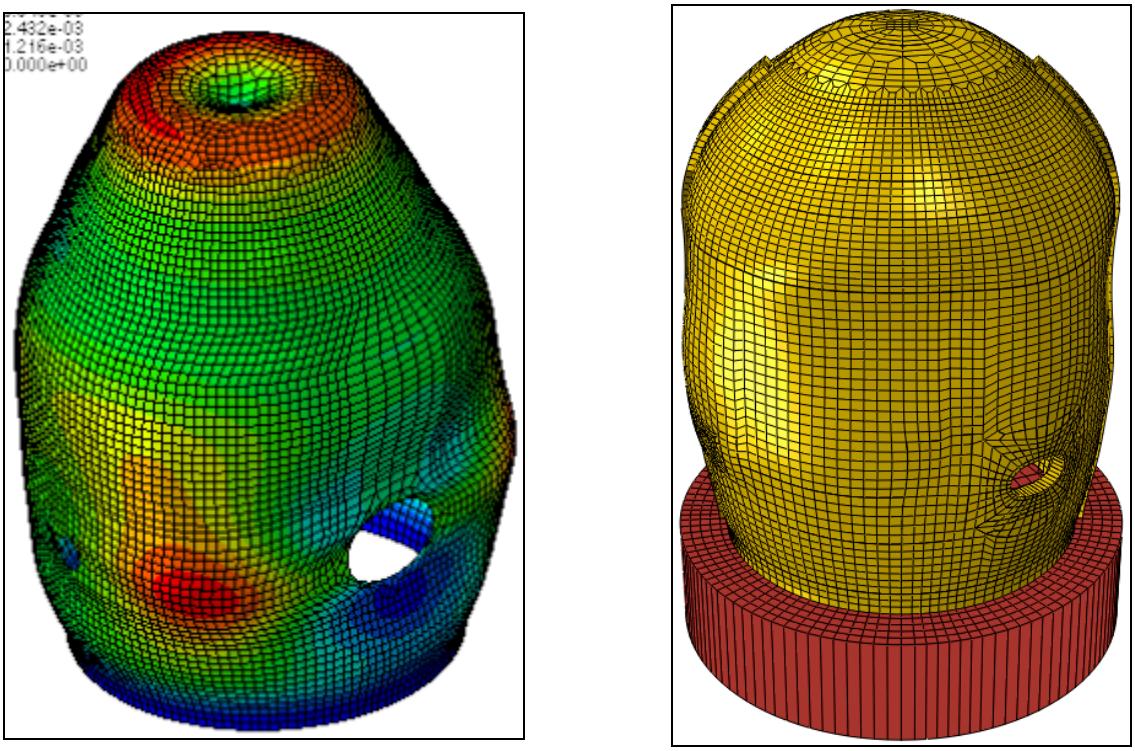

A B

Figure 252: Deformed Shape at 3.0 x P_d (a) AERB (b) NRC

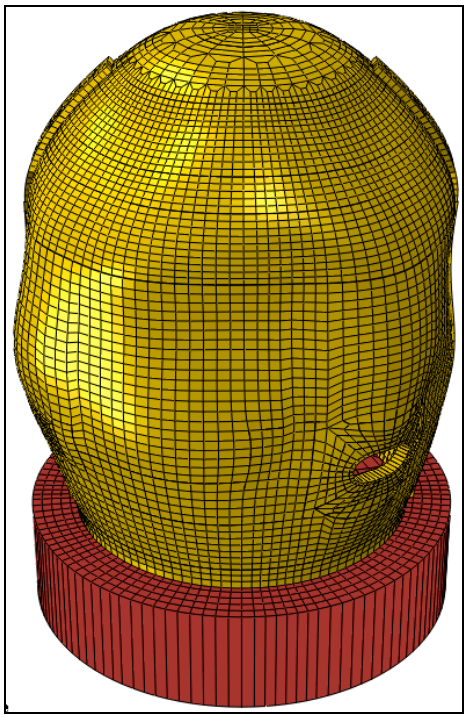

Figure 253: Deformed Shape at 3.3 x P_d for NRC

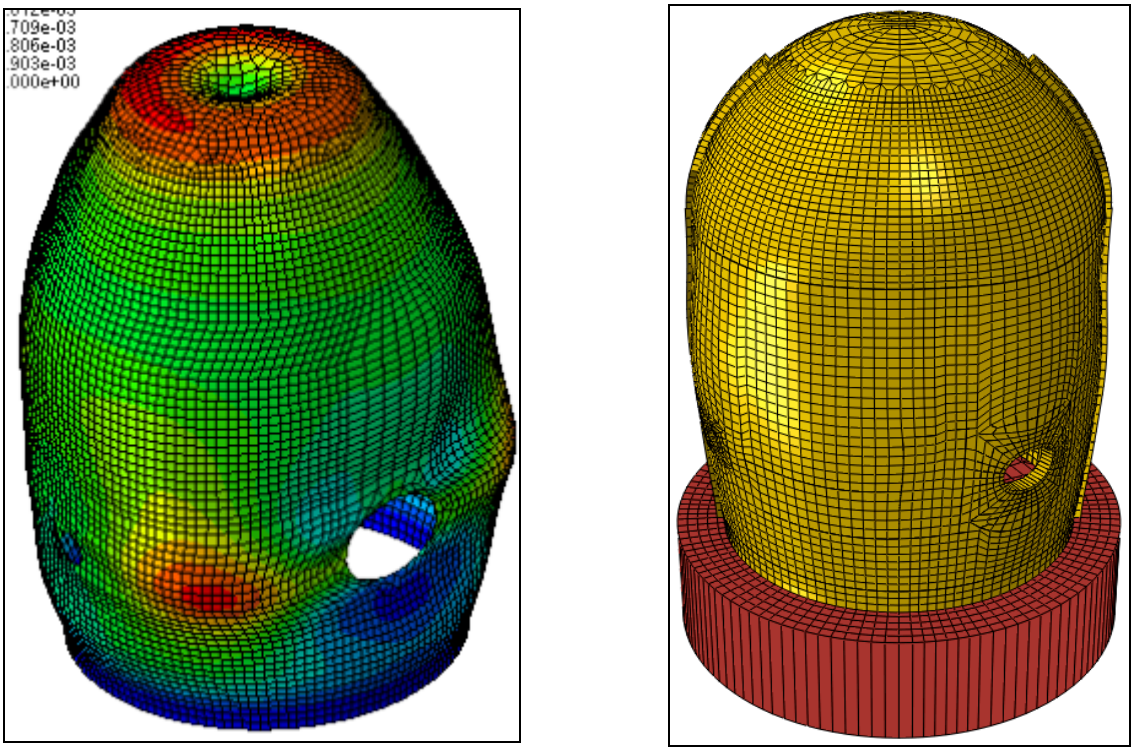

A B

Figure 254: Deformed Shape at 3.4 x P_d (a) AERB (b) NRC

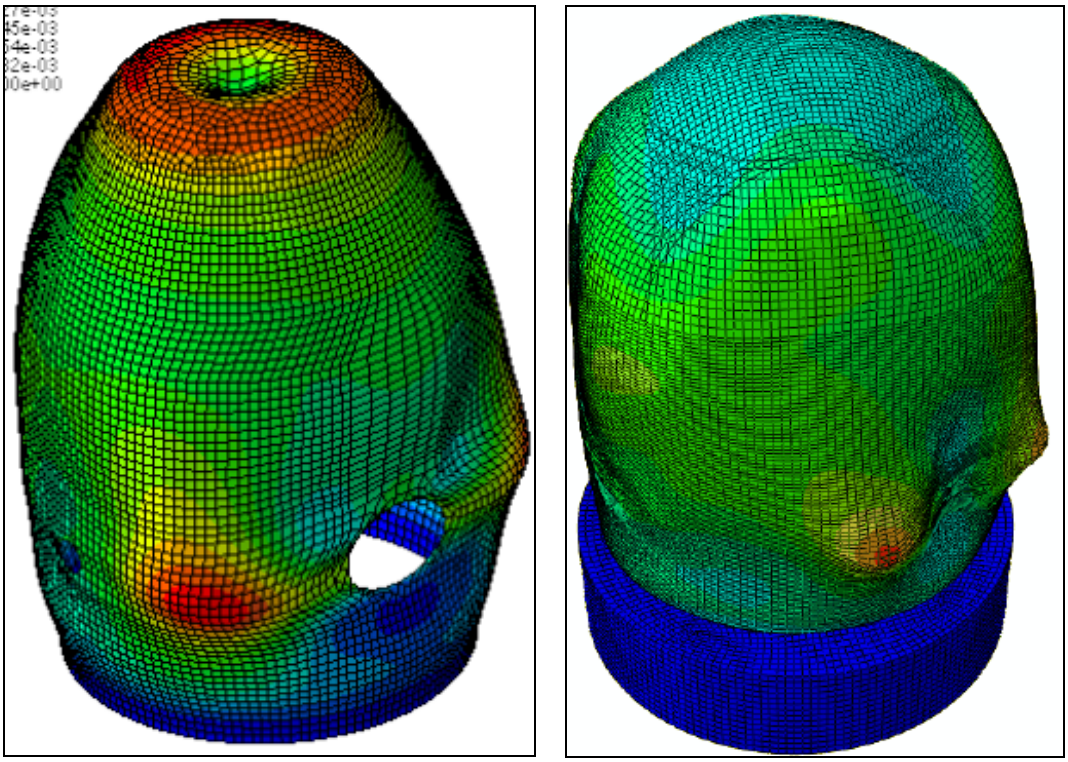

A B

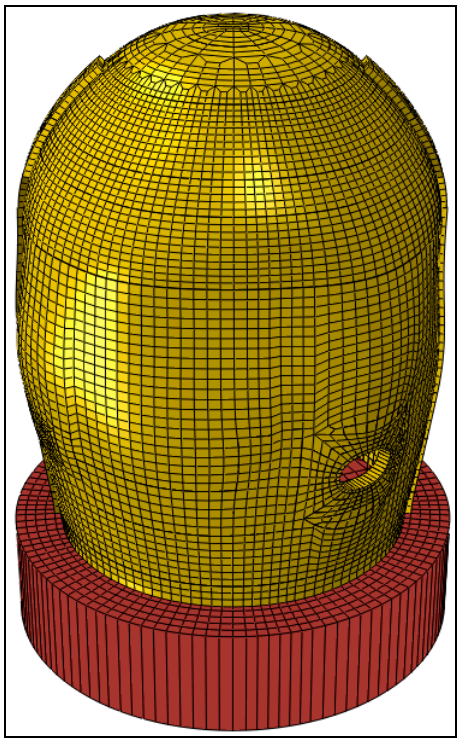

C

Figure 255: Deformed Shape at 3.6 x P_d (a) AERB (b) FORTUM x 50 (c) NRC Deformation Scale x 20

4.4. Liner Strains

4.4.1. Peak Strains of Entire Liner

Contour plots of peak strains in the liner at the pressure milestones can be found in Figure 256 through Figure 265. Perhaps of greatest interest in the peak strain plots are the general frequency and locations of the "hot spots" in the liner. For all participants, the peak strains occur near the various discontinuities in the model. This is in agreement with the experimental testing from the PCCV test.

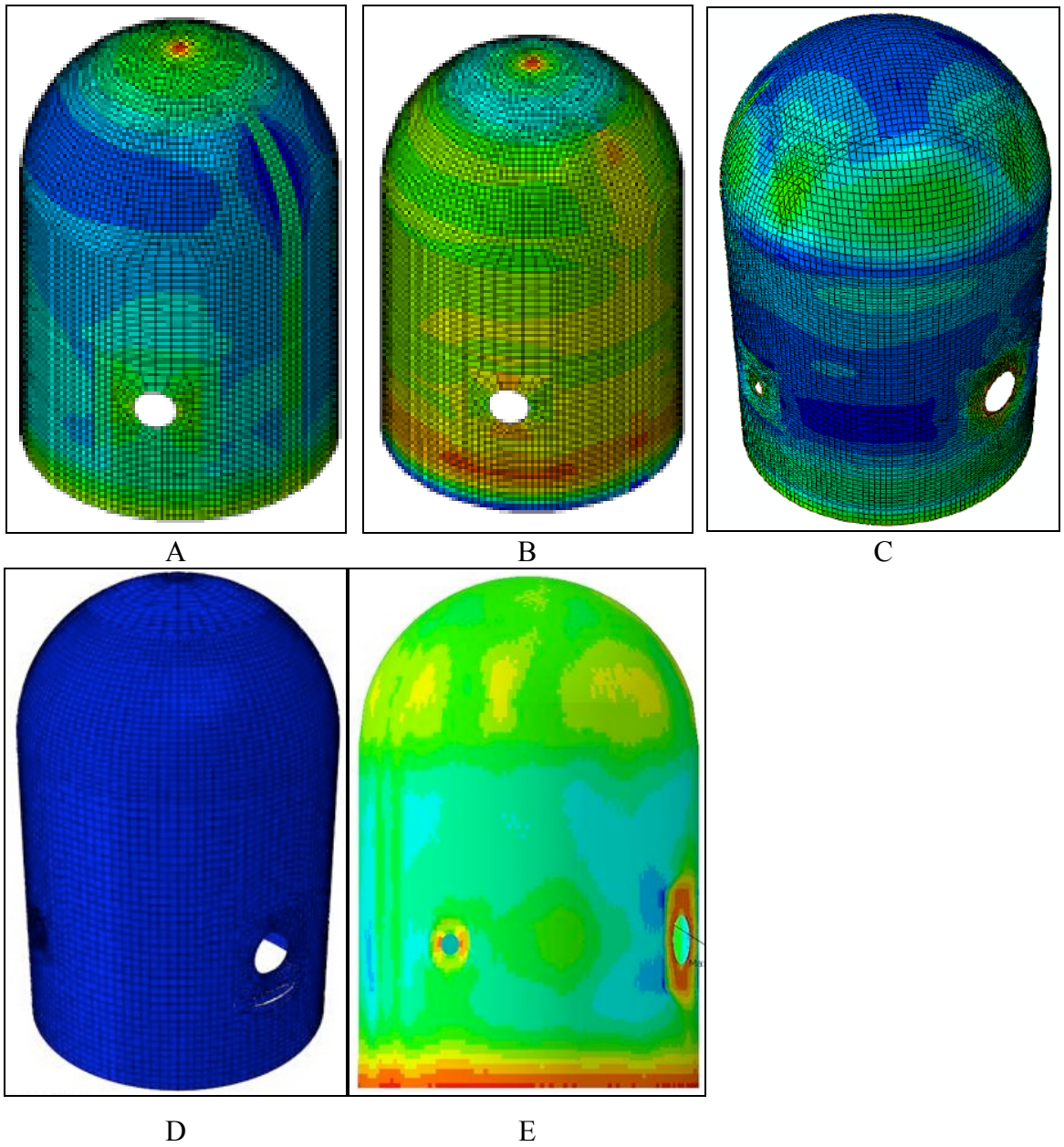

Figure 256: Peak Strain at 0 x P_d (A) AERB – hoop (B) AERB - Meridional (C) FORTUM (D) NRC (E) SCANSCOT

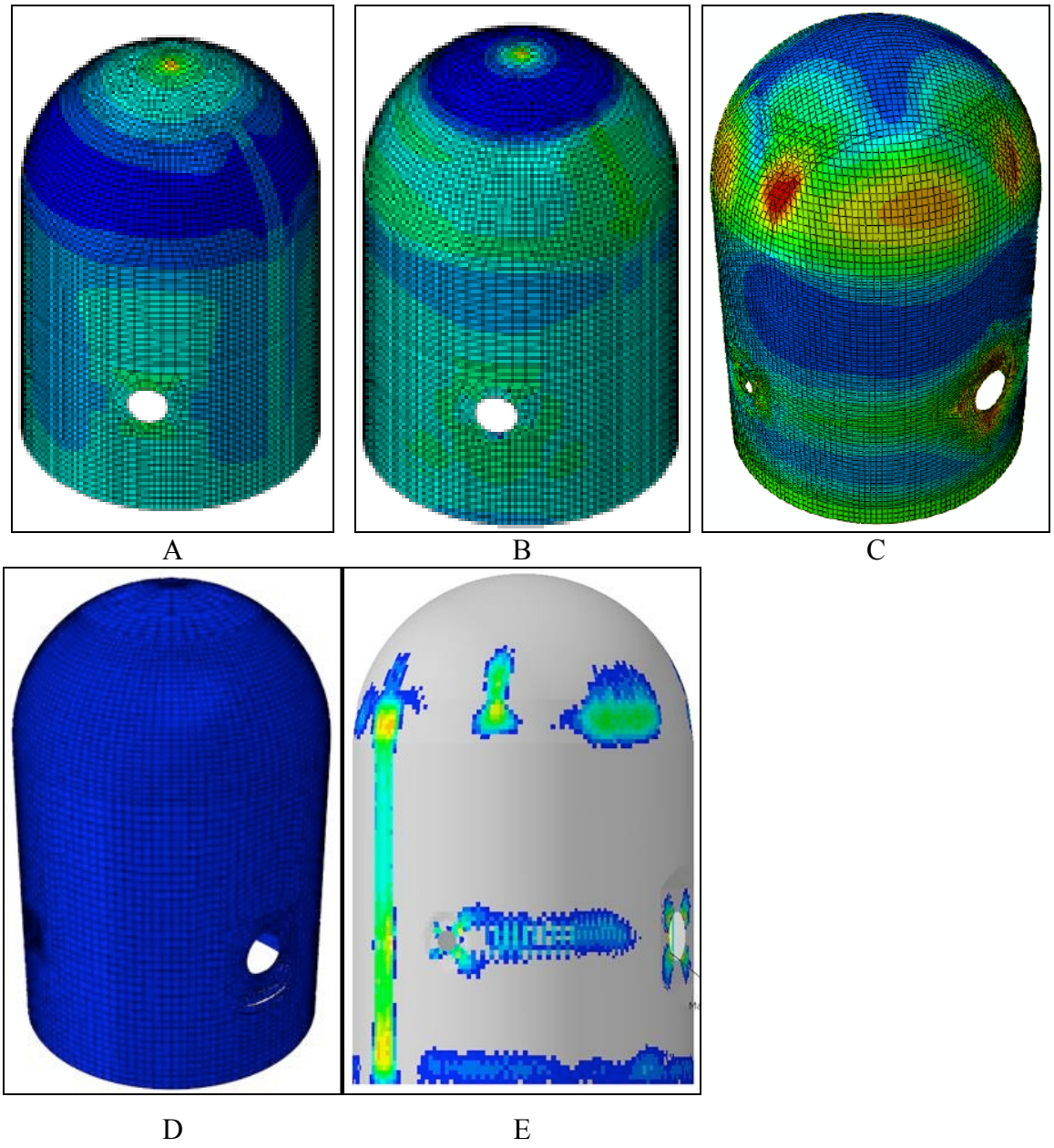

Figure 257: Peak Strain at 1.0 x P_d (A) AERB – hoop (B) AERB - Meridional (C) FORTUM (D) NRC (E) SCANSCOT

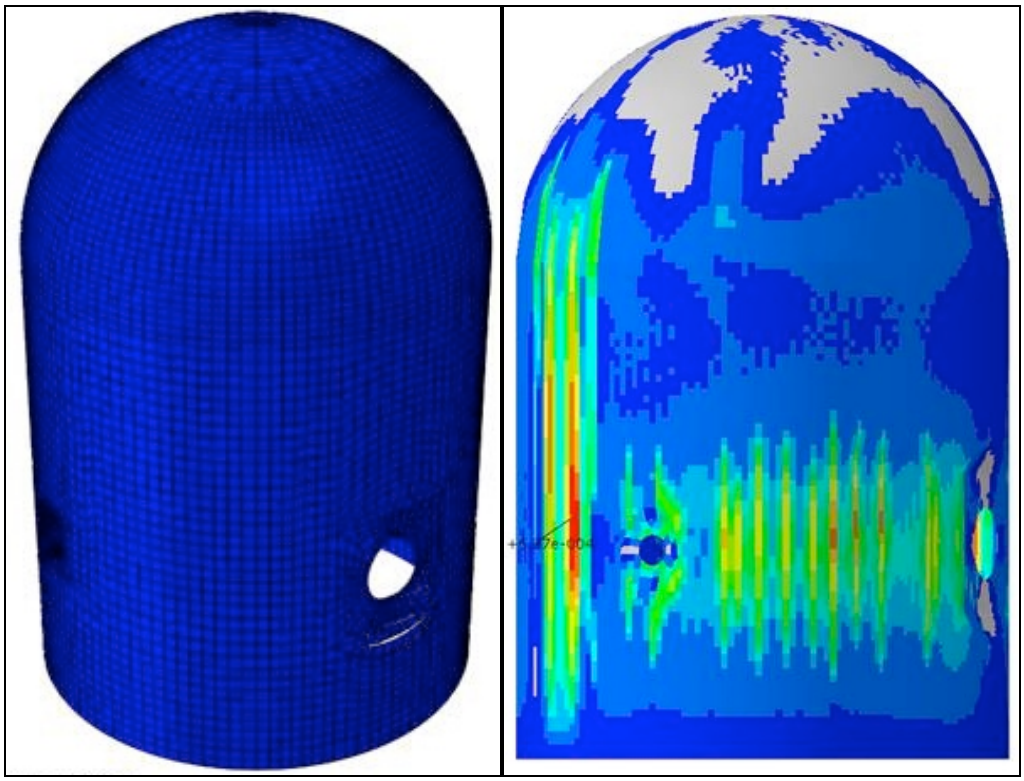

A B

Figure 258: Peak Strain at 1.5 x P_d (A) NRC (B) SCANSCOT

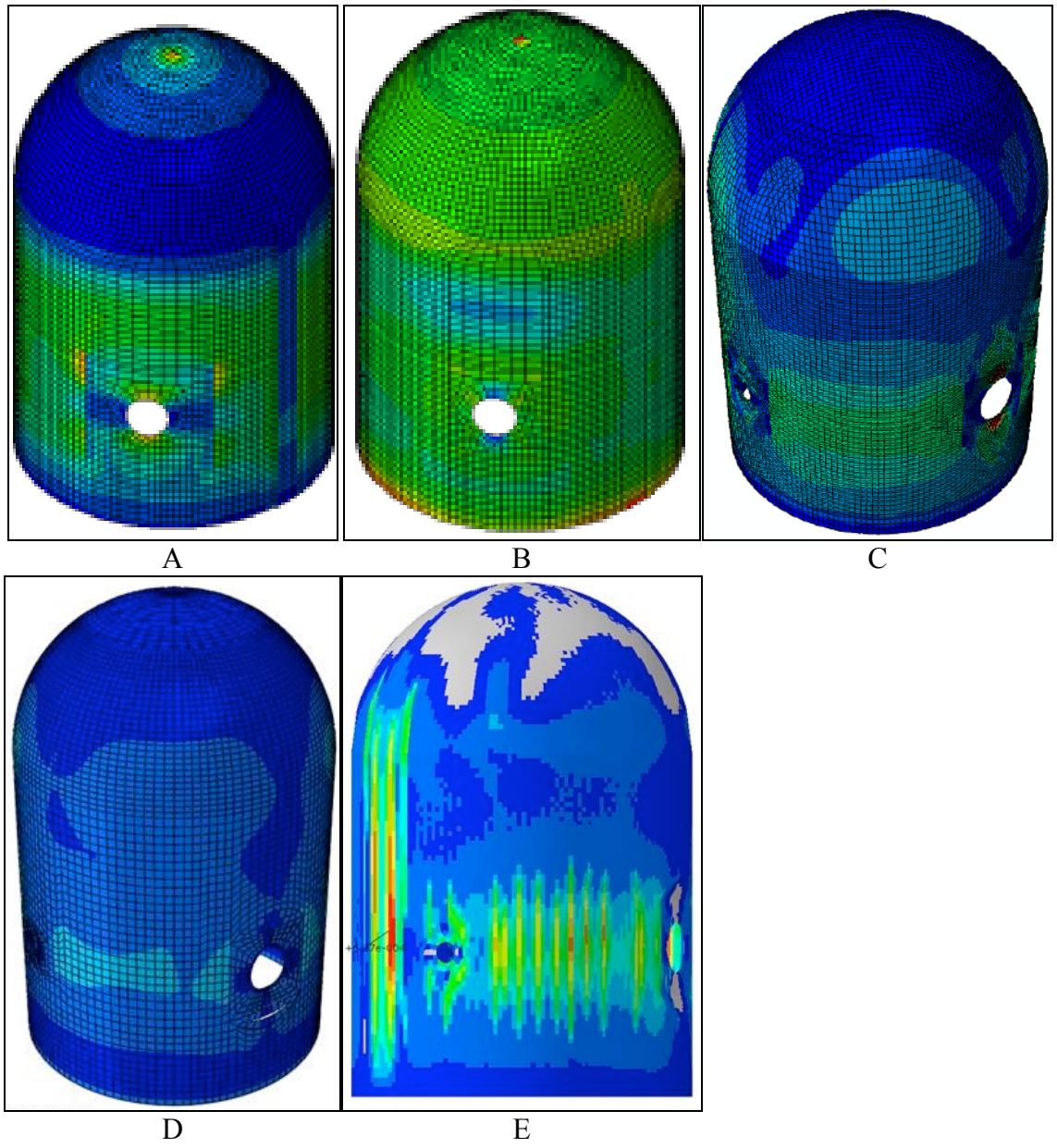

Figure 259: Peak Strain at 2.0 x P_d (A) AERB – hoop (B) AERB - Meridional (C) FORTUM (D) NRC (E) SCANSCOT

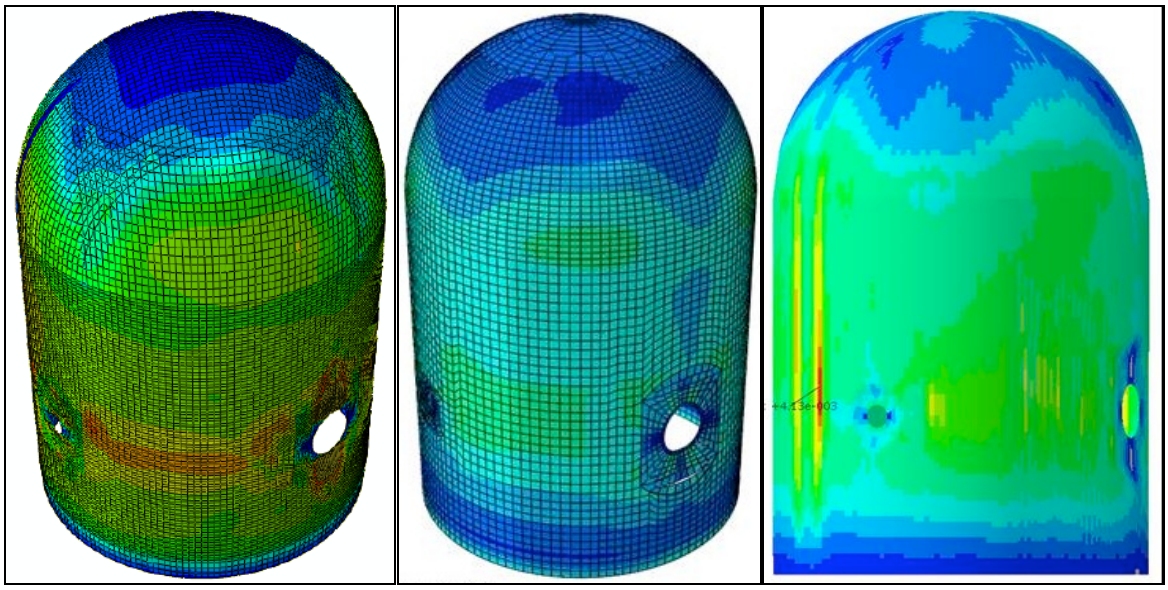

A B C

Figure 260: Peak Strain at 2.5 x P_d (A) FORTUM (B) NRC (C) SCANSCOT

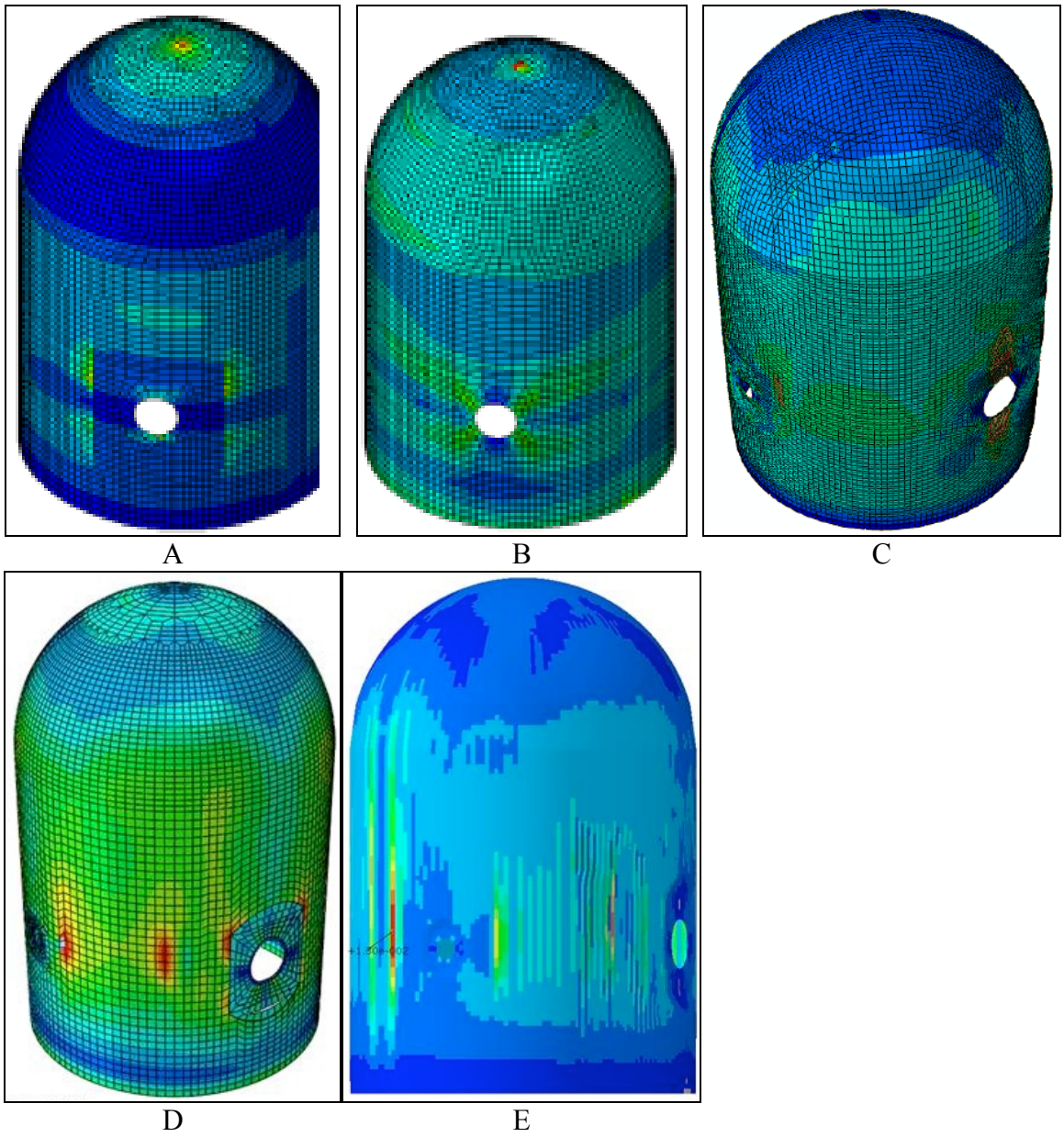

Figure 261: Peak Strain at 3.0 x P_d (A) AERB – hoop (B) AERB - Meridional (C) FORTUM (D) NRC (E) SCANSCOT

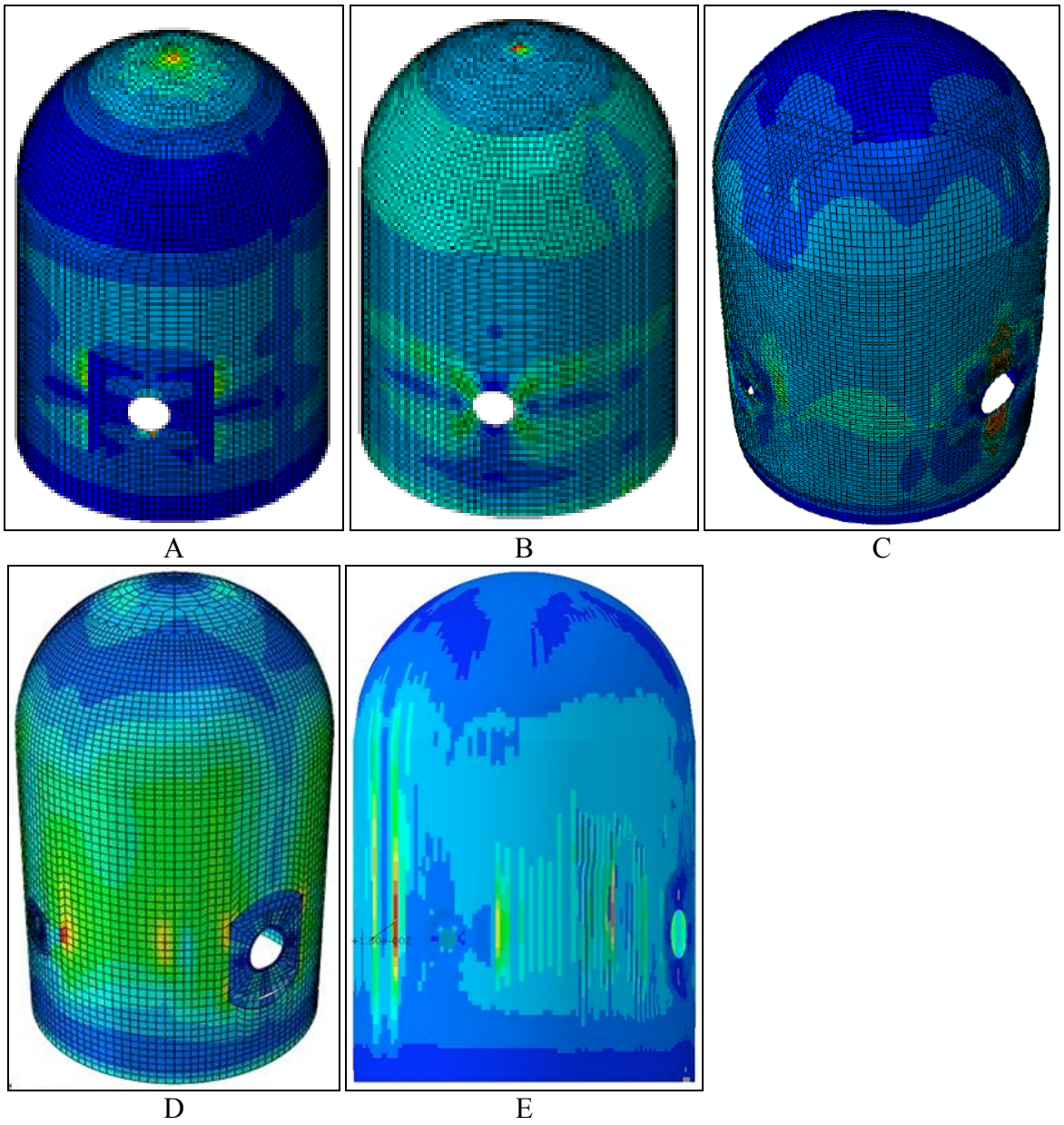

Figure 262: Peak Strain at 3.3 x P_d (A) AERB – hoop (B) AERB - Meridional (C) FORTUM (D) NRC (E) SCANSCOT

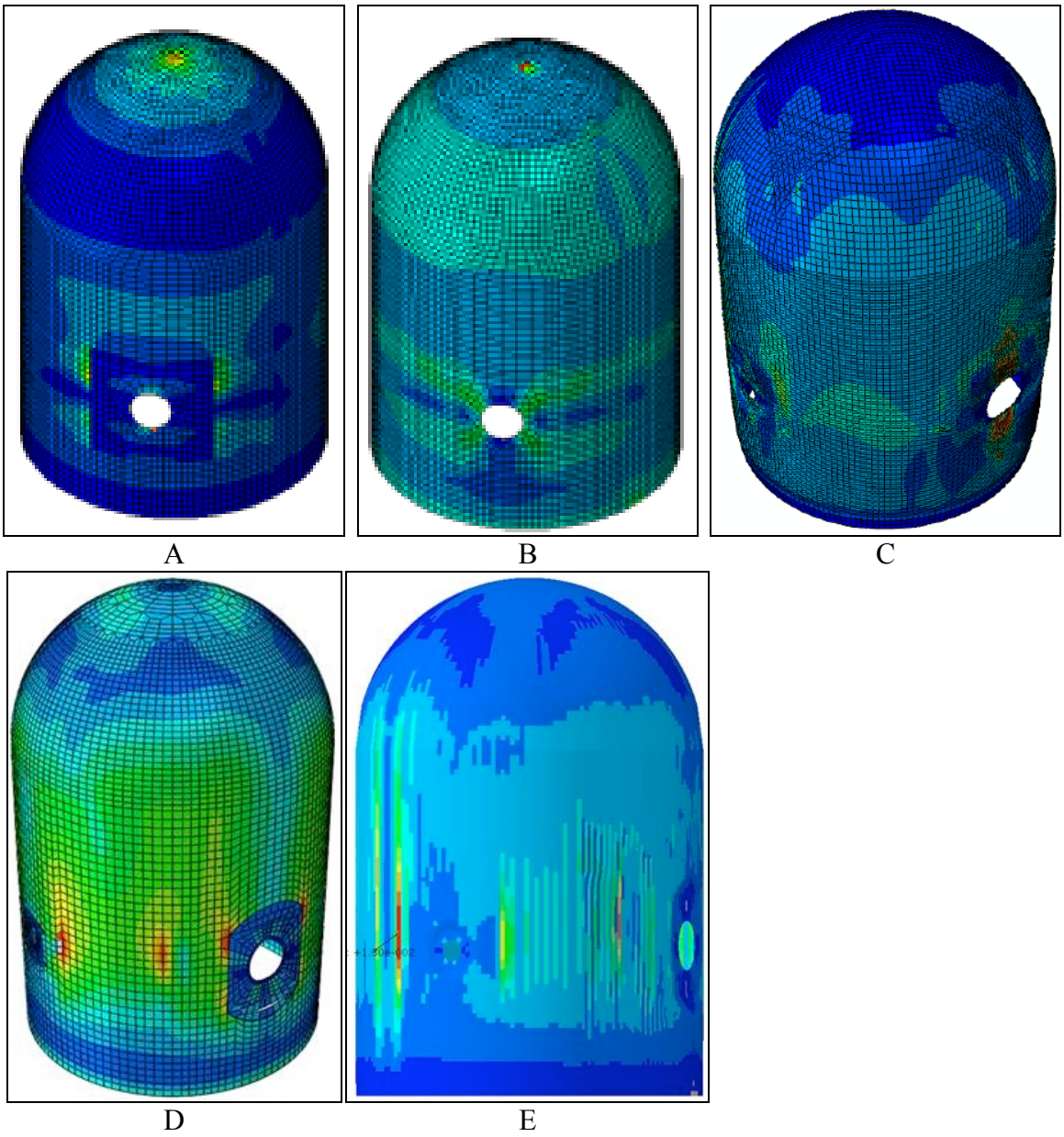

Figure 263: Peak Strain at 3.4 x P_d (A) AERB – hoop (B) AERB - Meridional (C) FORTUM (D) NRC (E) SCANSCOT

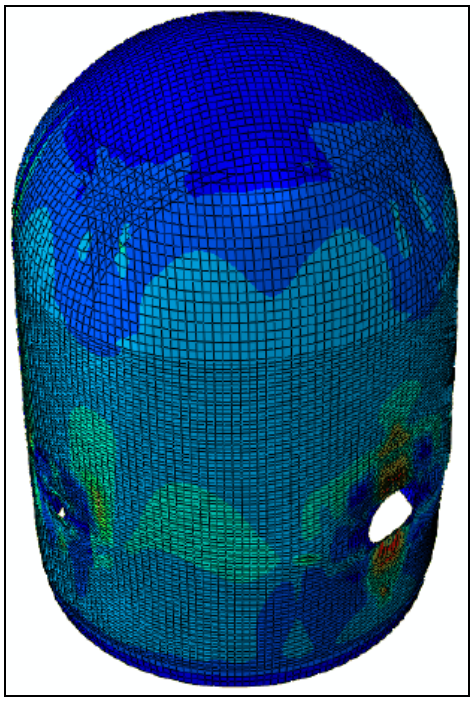

Figure 264: Peak Strain at 3.5 x P_d FORTUM

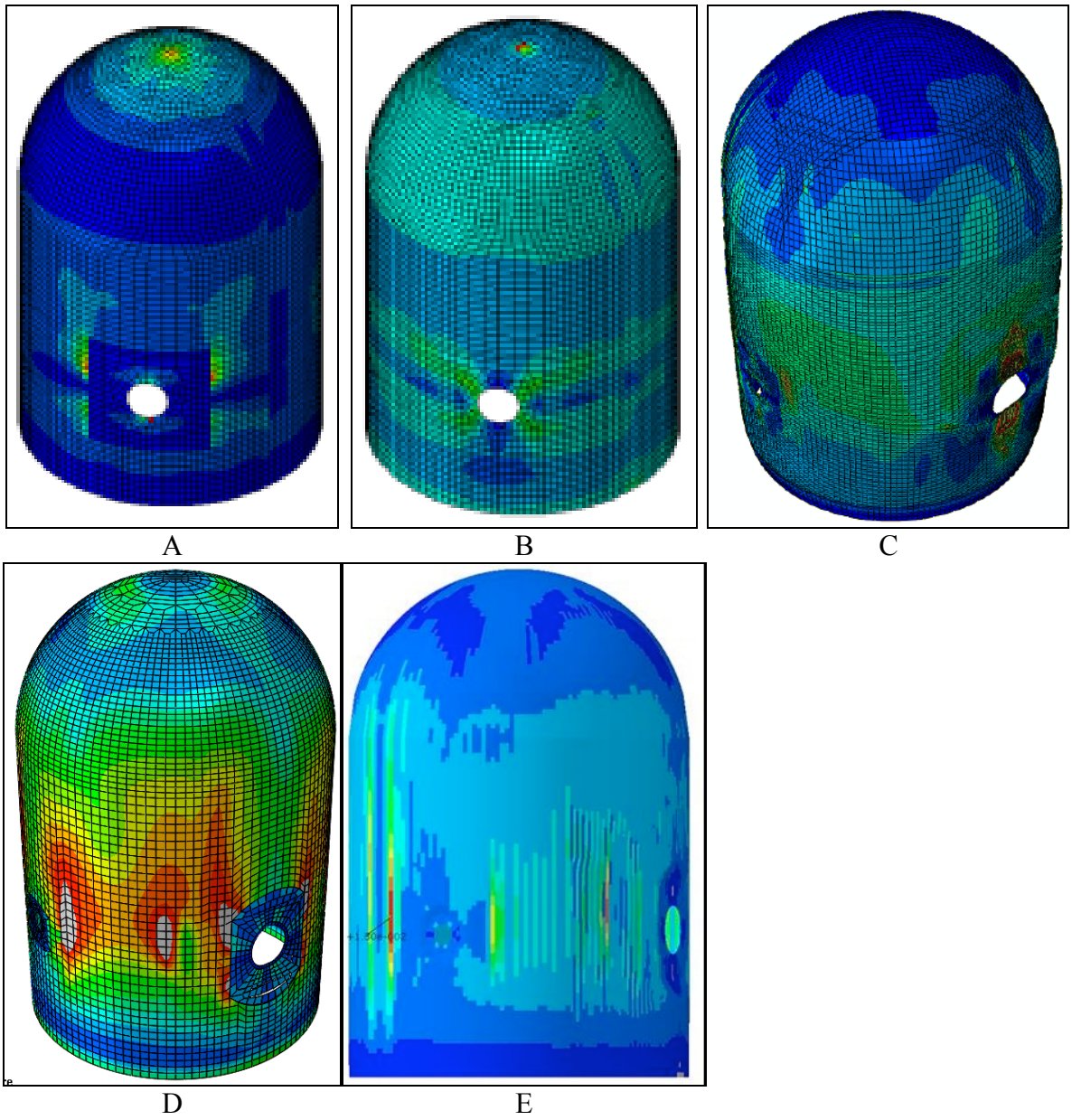

Figure 265: Peak Strain at 3.6 x P_d (a) AERB – hoop (b) AERB - Meridional (c) FORTUM (d) NRC

4.4.2. Average Strains at Selected Locations

In this section, more data is expected from the participants and therefore, the presentation of the figures has been postponed, pending the receipt of this data.

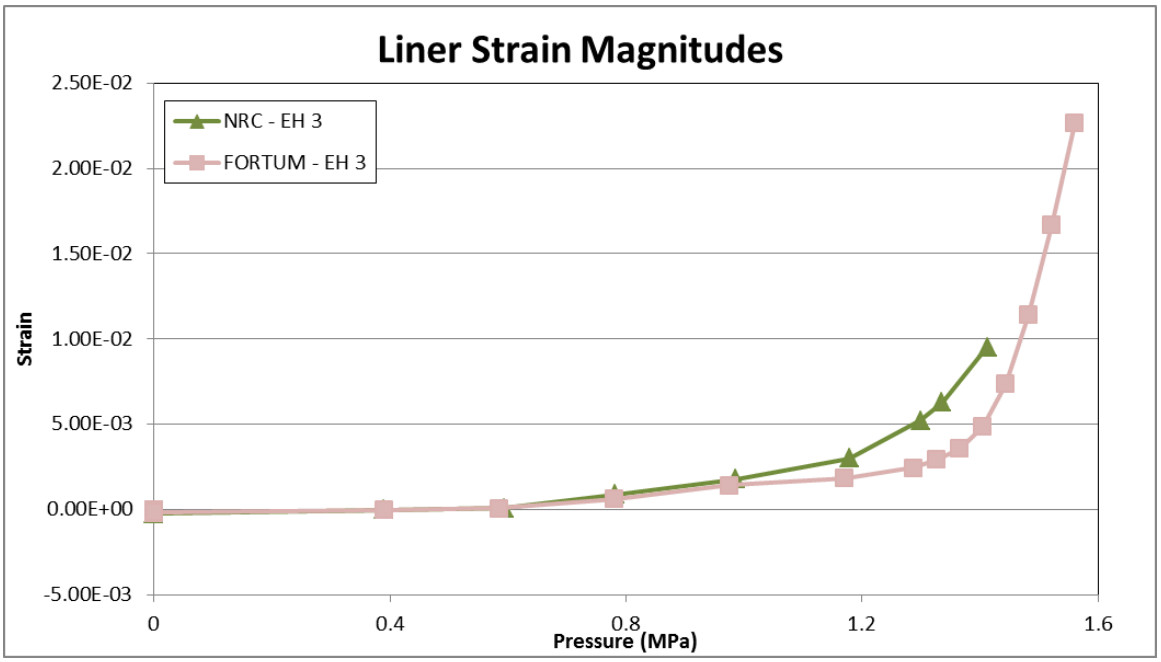

Figure 266: Strain over Gauge Length at Location 3 Near Equipment Hatch

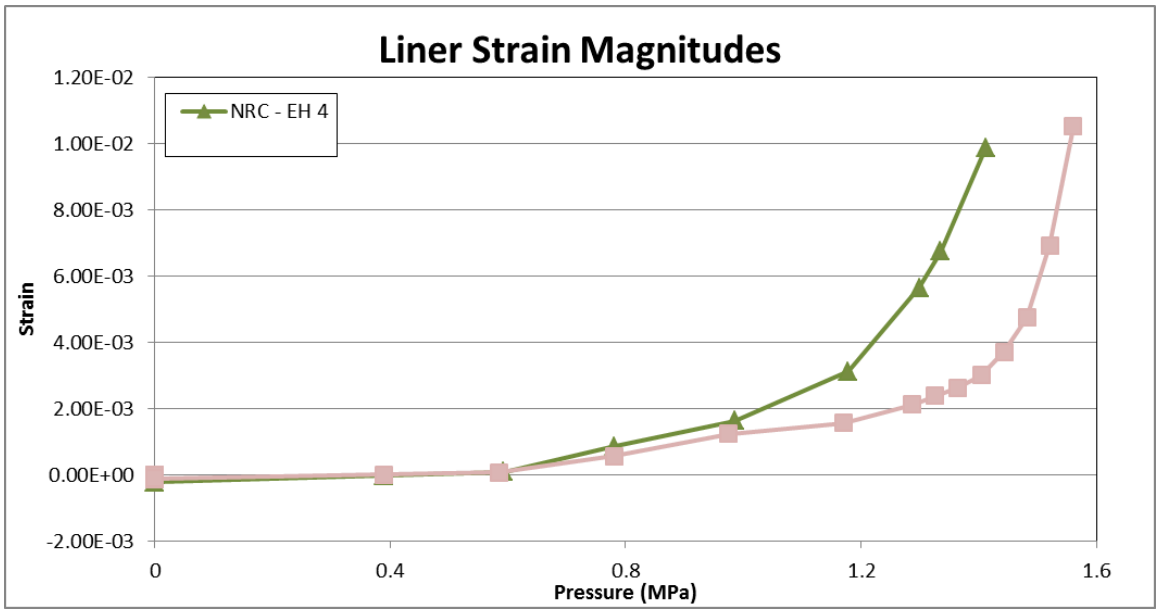

Figure 267: Strain over Gauge Length at Location 4 Near Equipment Hatch

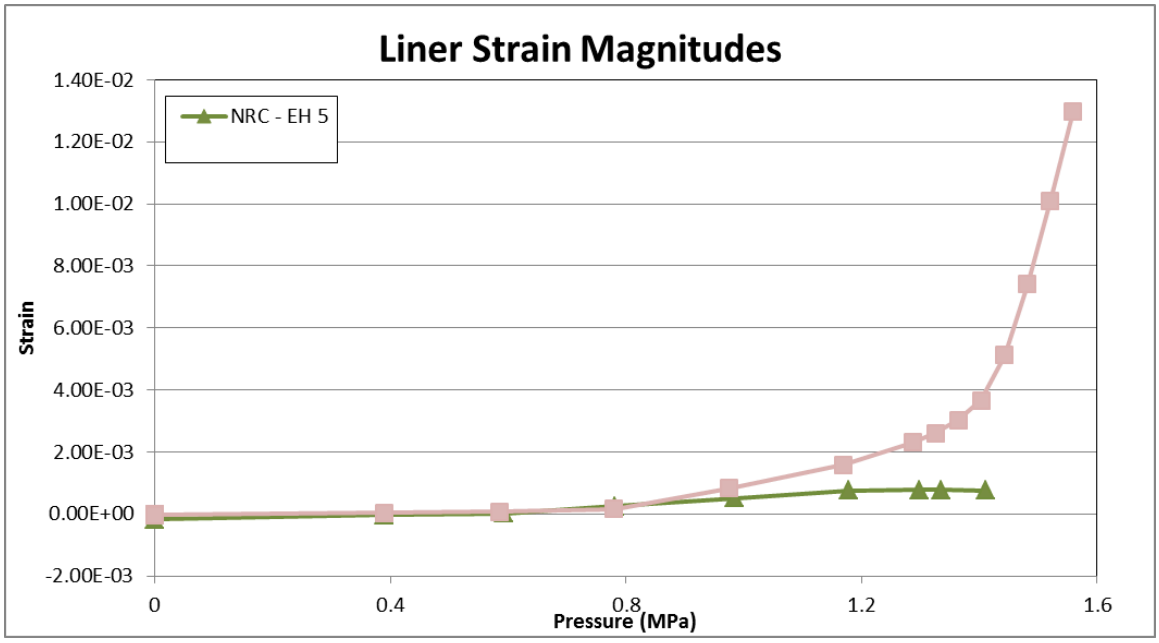

Figure 268: Strain over Gauge Length at Location 5 Near Equipment Hatch

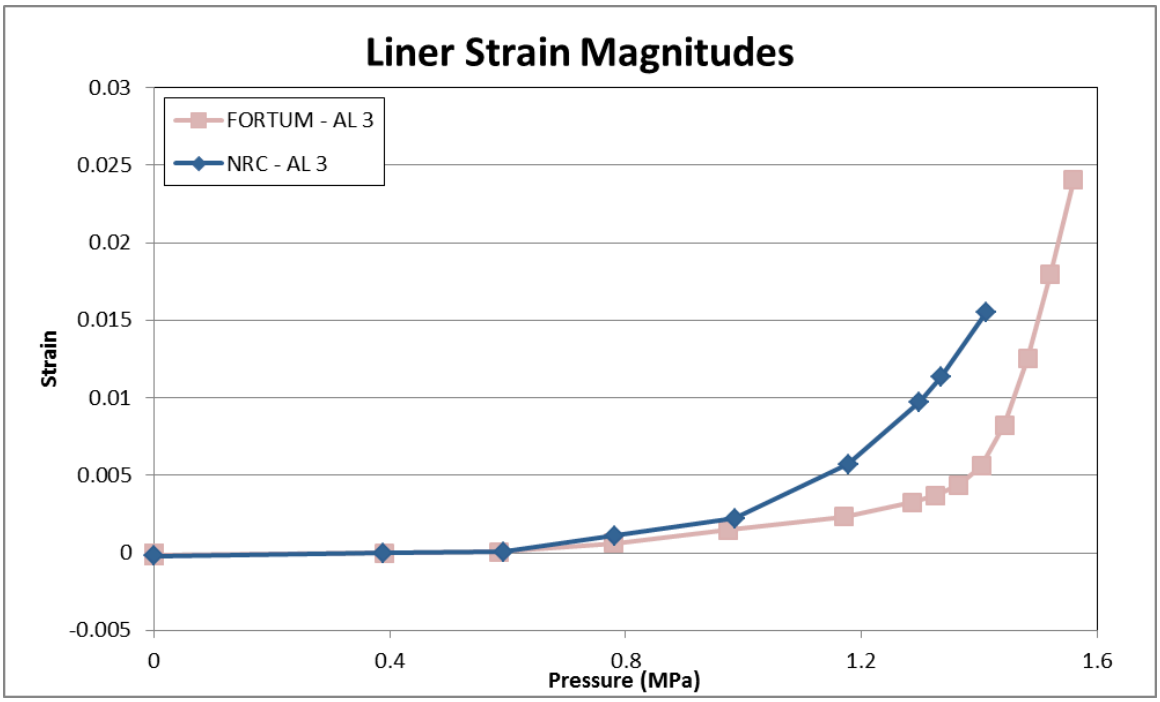

Figure 269: Strain over Gauge Length at Location 3 Near Air Lock

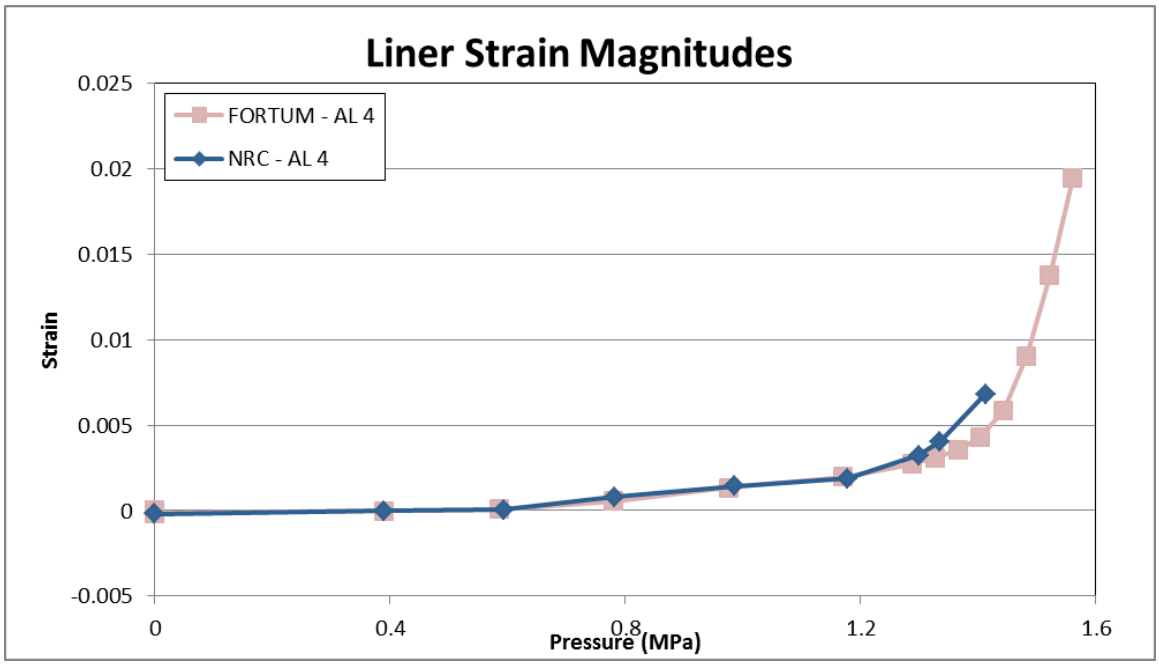

Figure 270: Strain over Gauge Length at Location 4 Near Air Lock

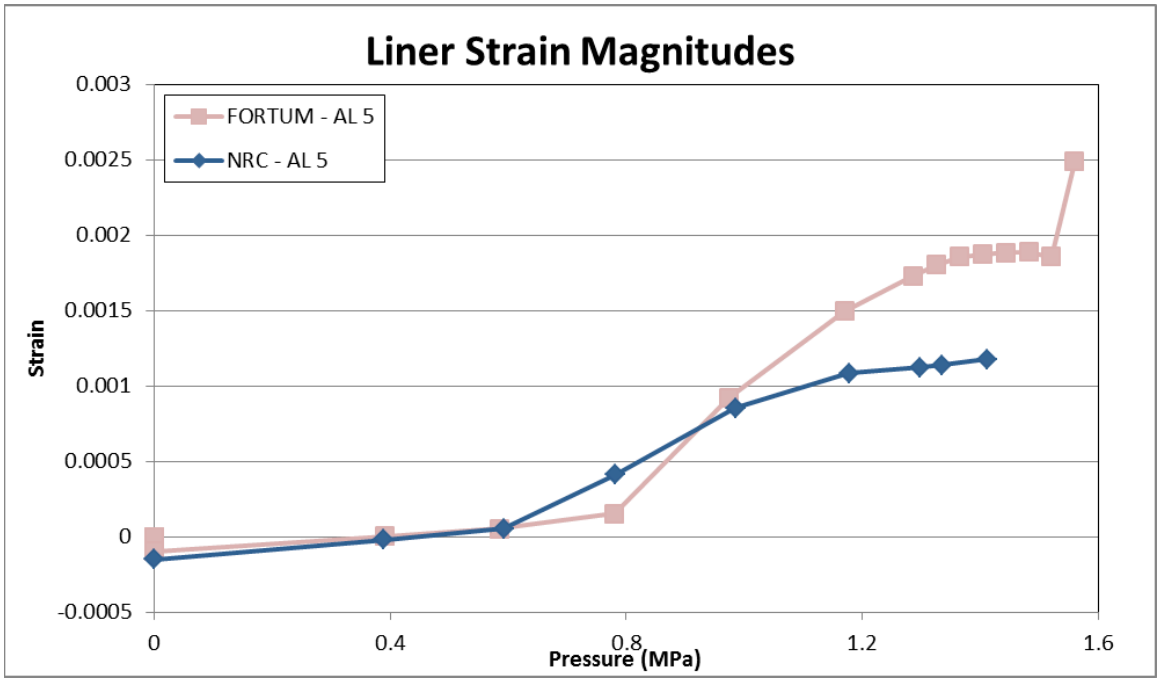

Figure 271: Strain over Gauge Length at Location 5 Near Air Lock

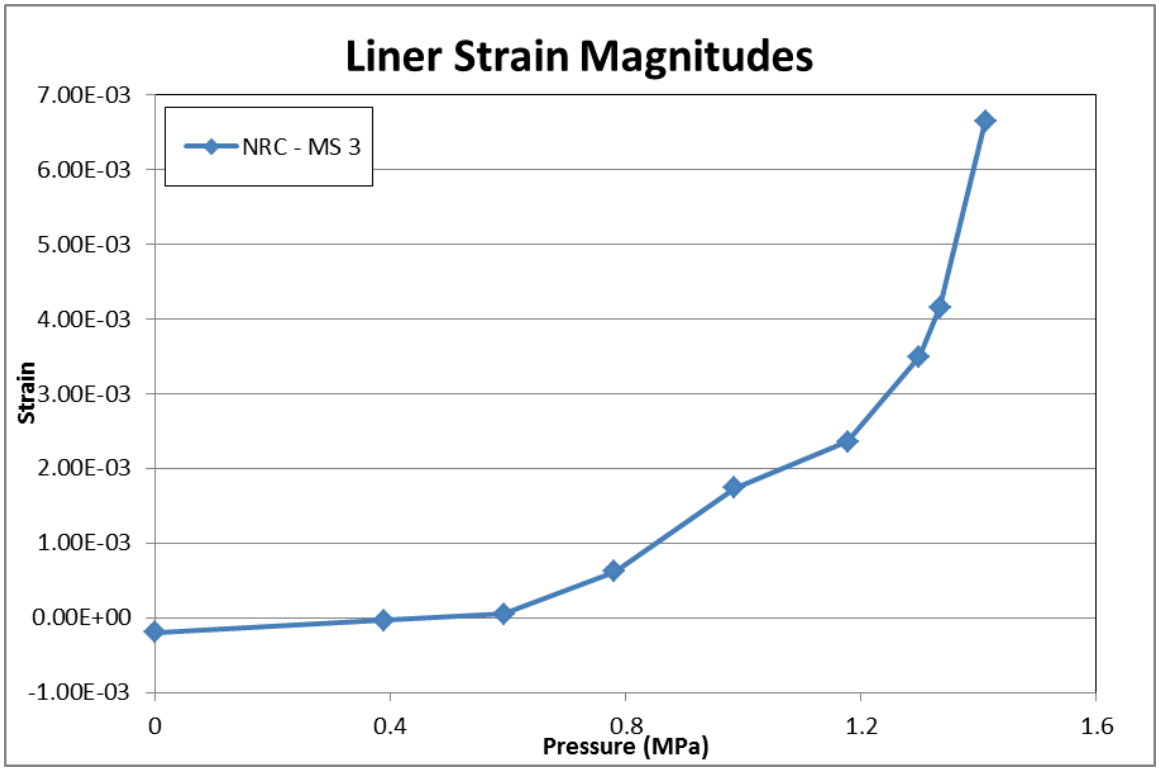

Figure 272: Strain over Gauge Length at Location 3 Near Mainsteam

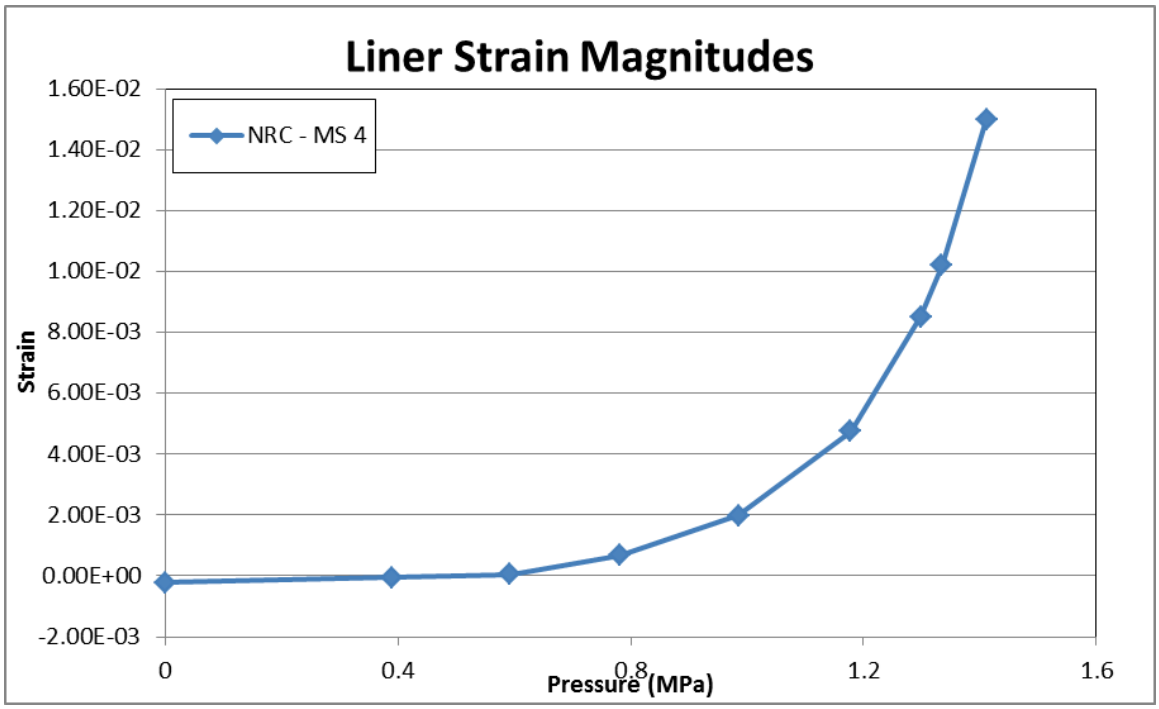

Figure 273: Strain over Gauge Length at Location 4 Near Mainsteam

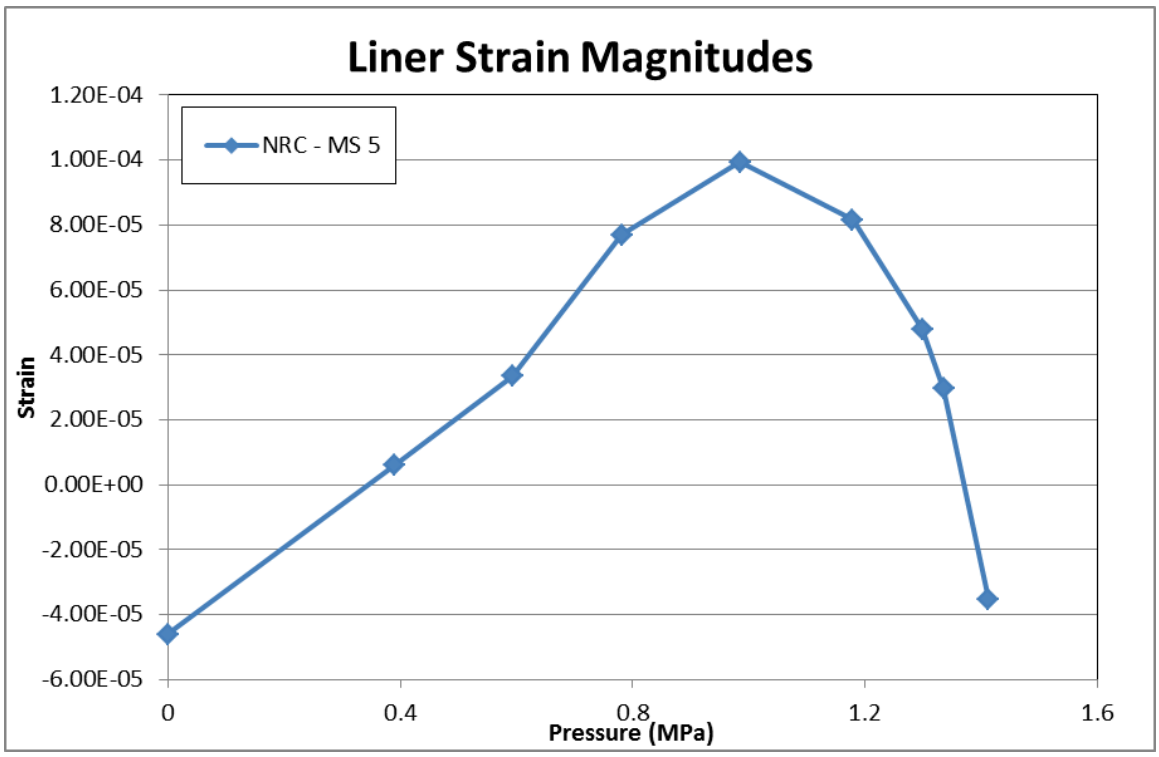

Figure 274: Strain over Gauge Length at Location 5 Near Mainsteam

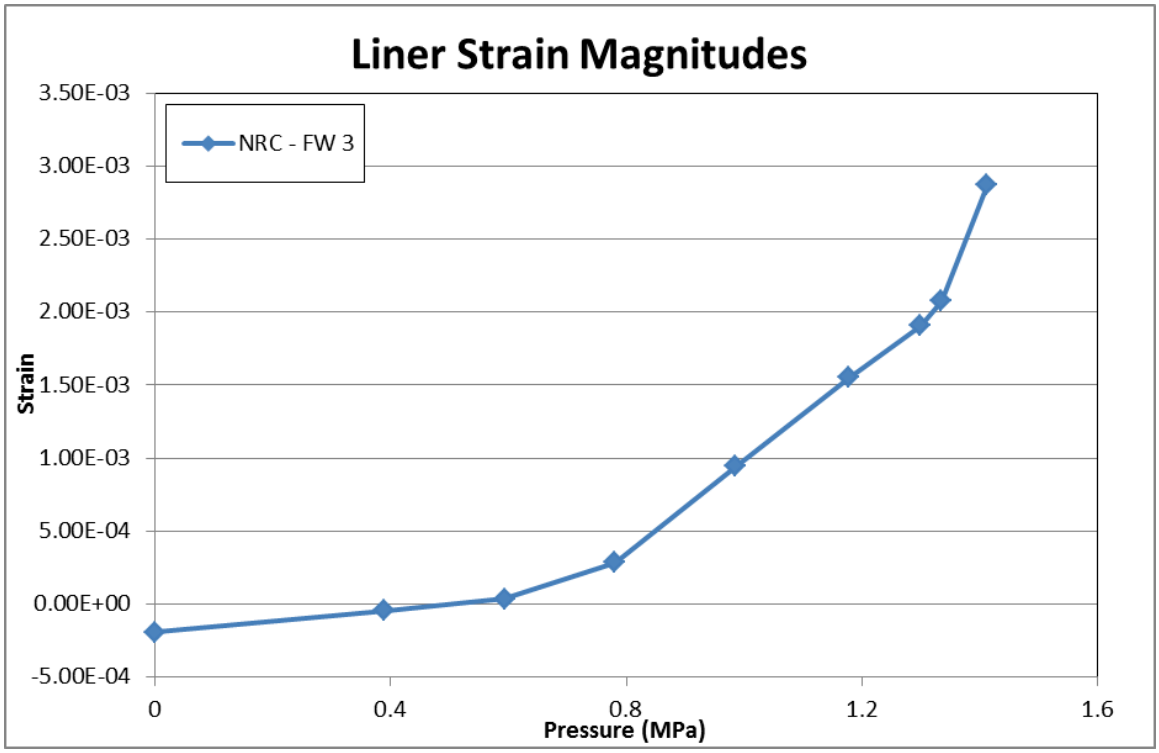

Figure 275: Strain over Gauge Length at Location 3 Near Feed Water

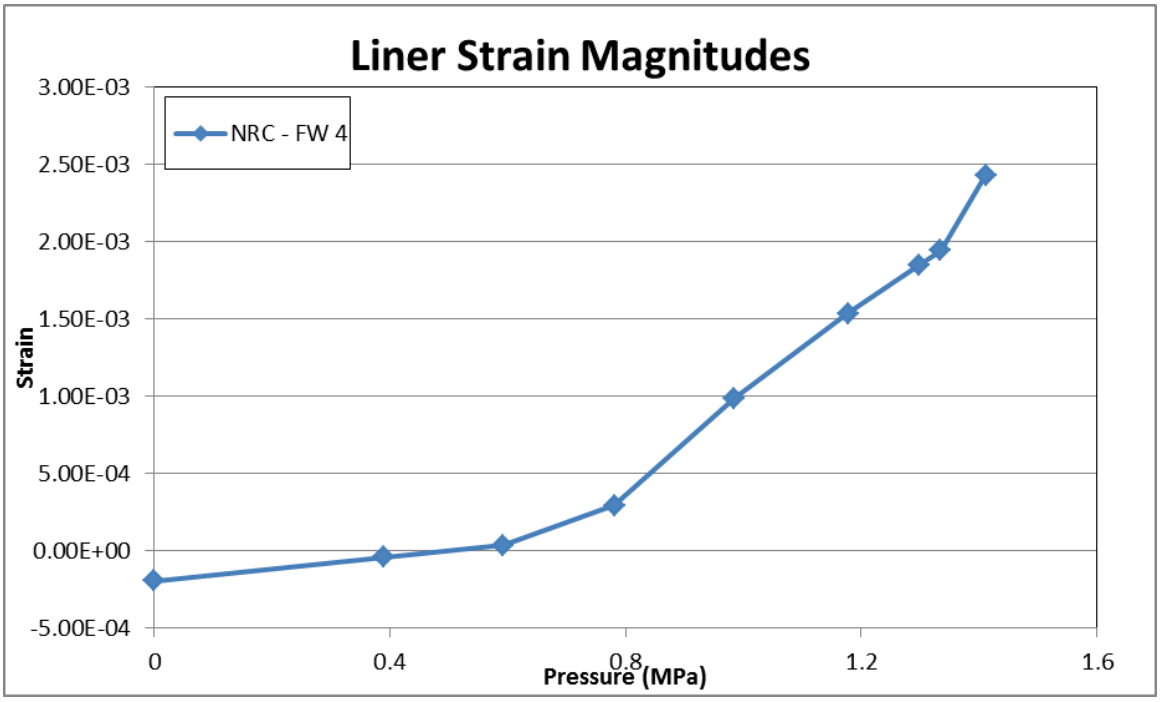

Figure 276: Strain over Gauge Length at Location 4 Near Feed Water

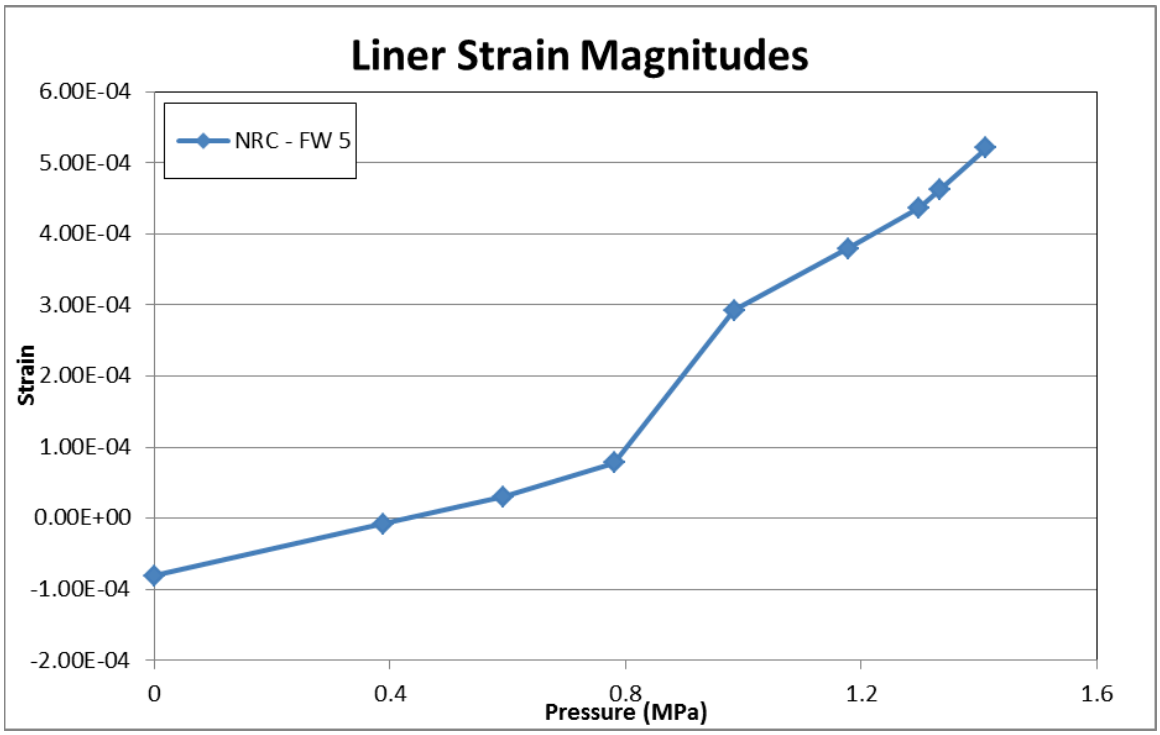

Figure 277: Strain over Gauge Length at Location 5 Near Feed Water

4.5. Tendon Stress Distribution

The tendon stress distribution plots from the participants are presented in Figure 278 through Figure 322. As was the case in previous sections, the abscissa and ordinate are plotted on constant scales through this subsection in order to facilitate comparison between the plots.

4.6.4. Hoop Tendons

The hoop tendons plotted in this subsection correspond to tendons #H35, H53, and H68 from the PCCV test. The selection of these tendons for analysis will help to facilitate comparison with the most instrumented tendons from the 1:4 scale test. The hoop tendon stress profiles can be found in Figure 278 through Figure 304. In general the tendon stress distributions from the participants agree reasonably well with the exception of the AERB provided data which seems to deviate from the shape of the other participant's data.

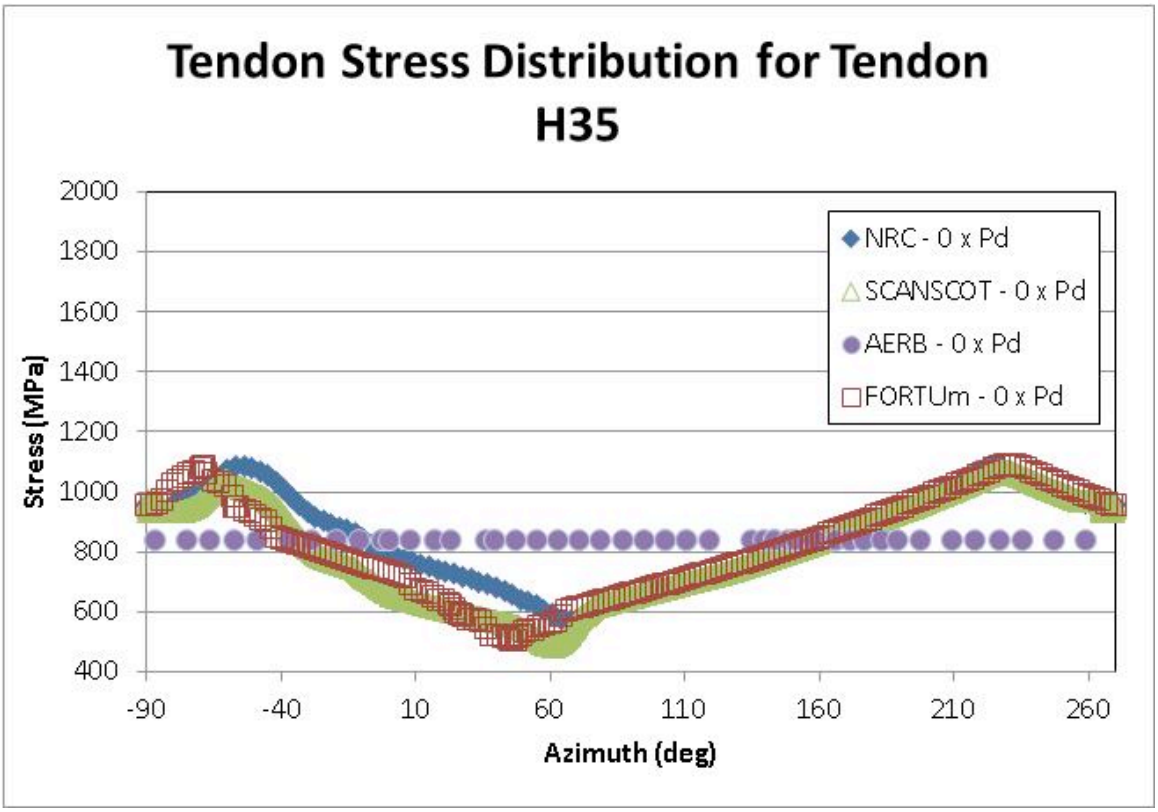

Figure 278: Tendon Stress Distribution for Tendon #H35 at 0 x P_d

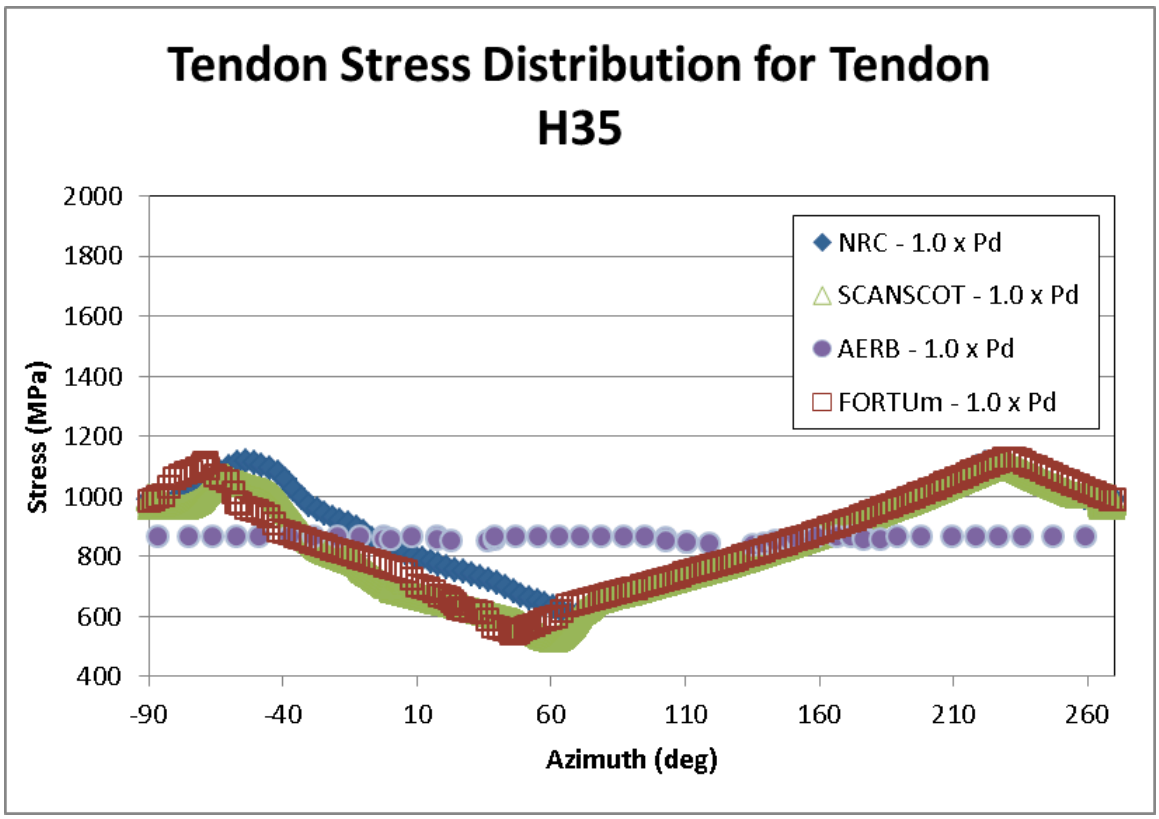

Figure 279: Tendon Stress Distribution for Tendon #H35 at 1.0 x P_d

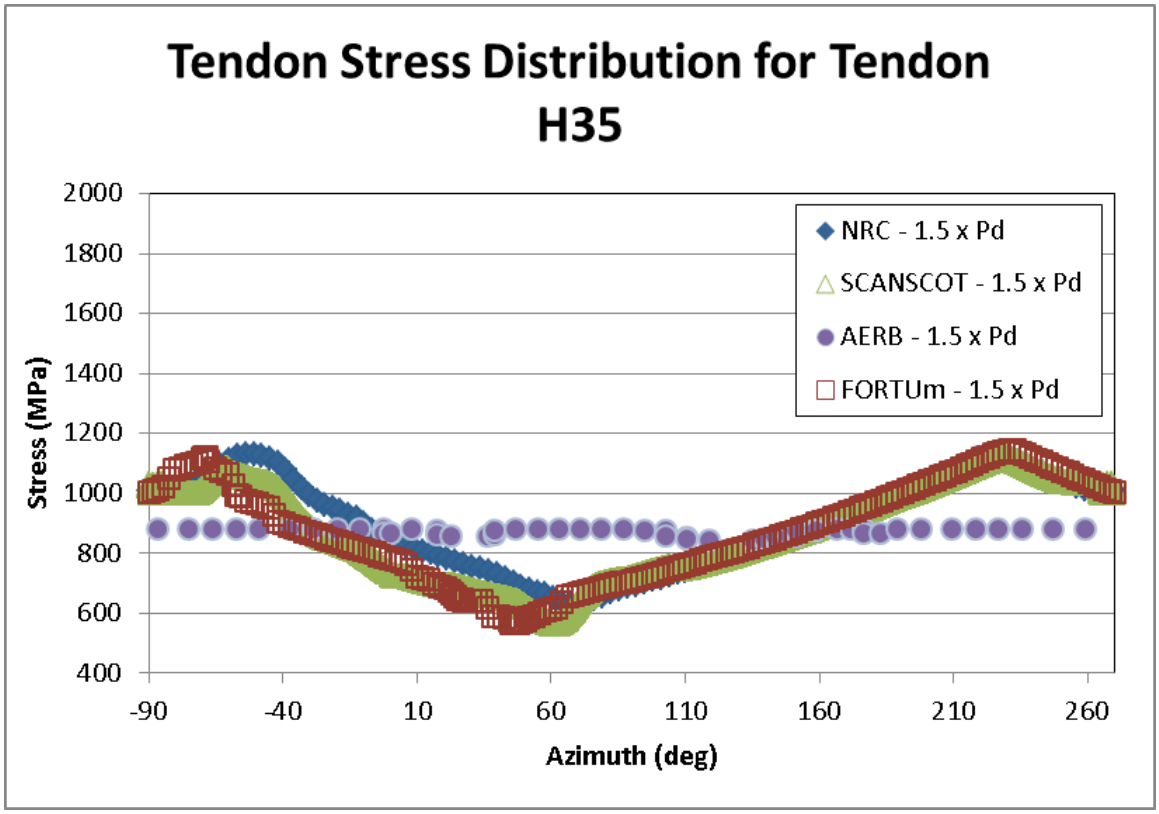

Figure 280: Tendon Stress Distribution for Tendon #H35 at 1.5 x P_d

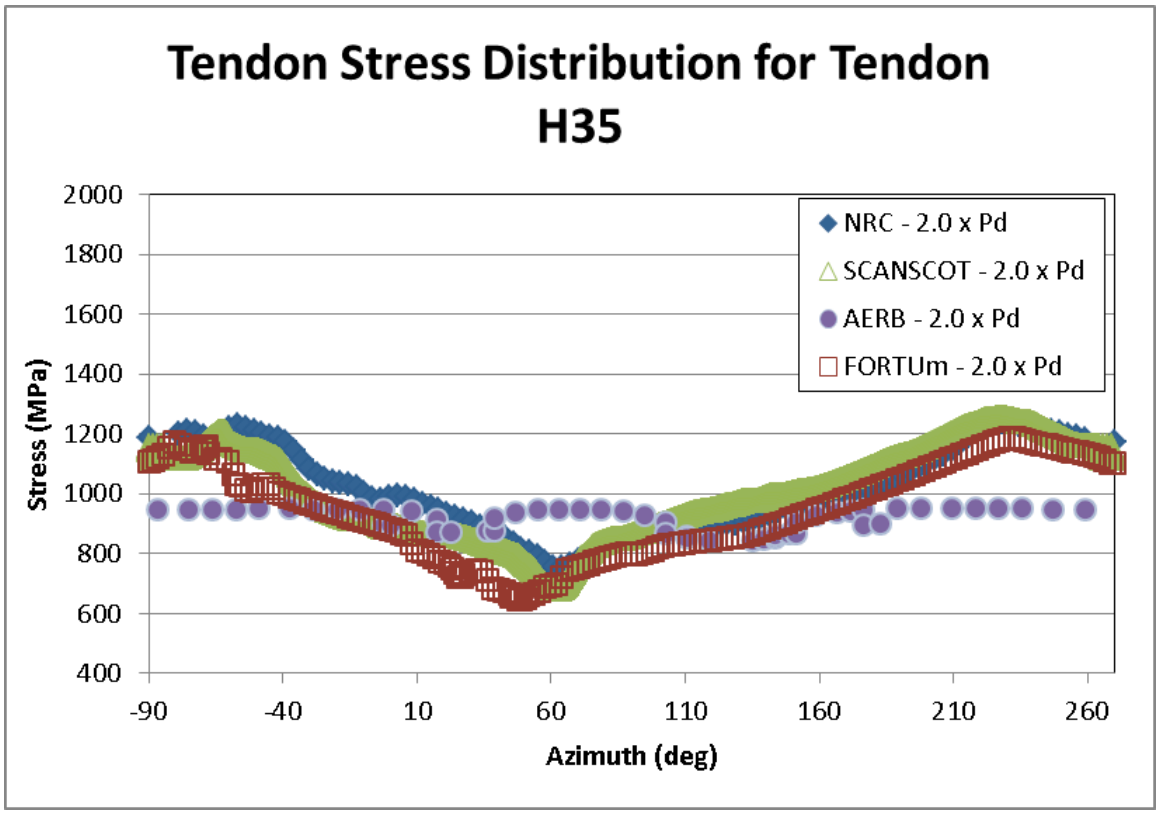

Figure 281: Tendon Stress Distribution for Tendon #H35 at 2.0 x P_d

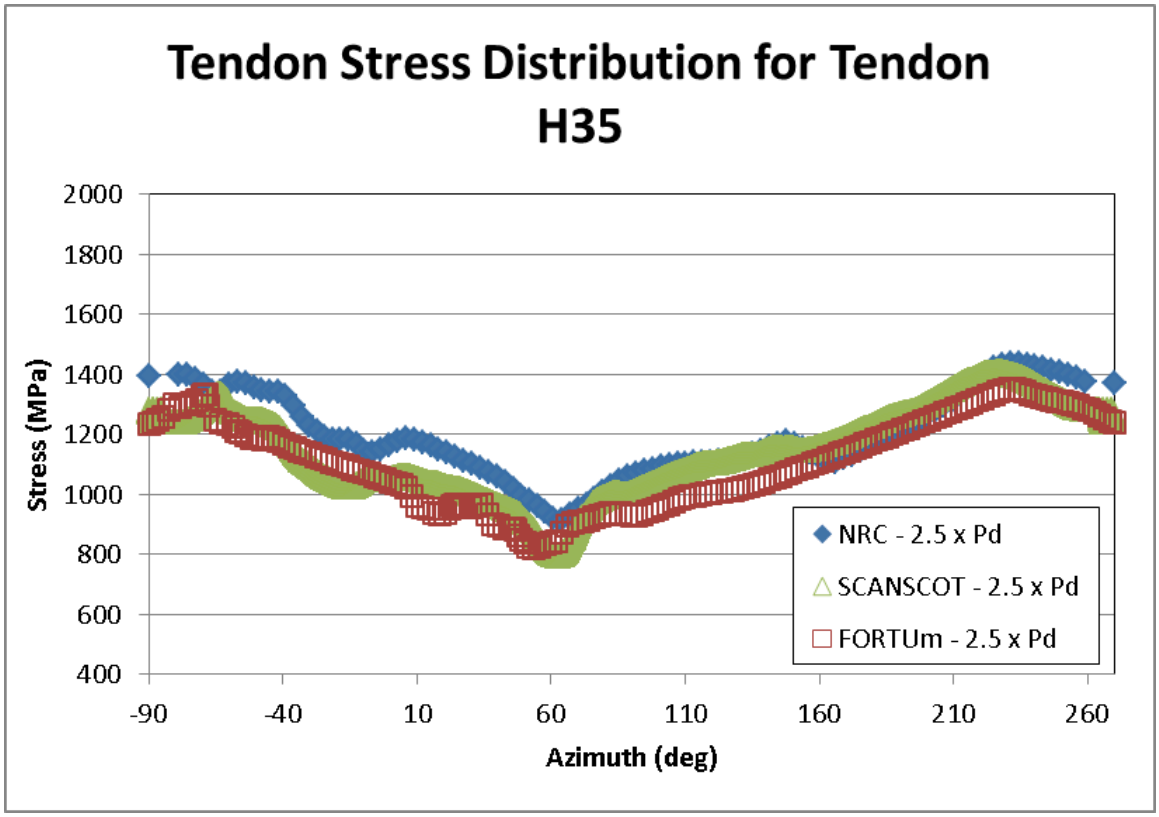

Figure 282: Tendon Stress Distribution for Tendon #H35 at 2.5 x P_d

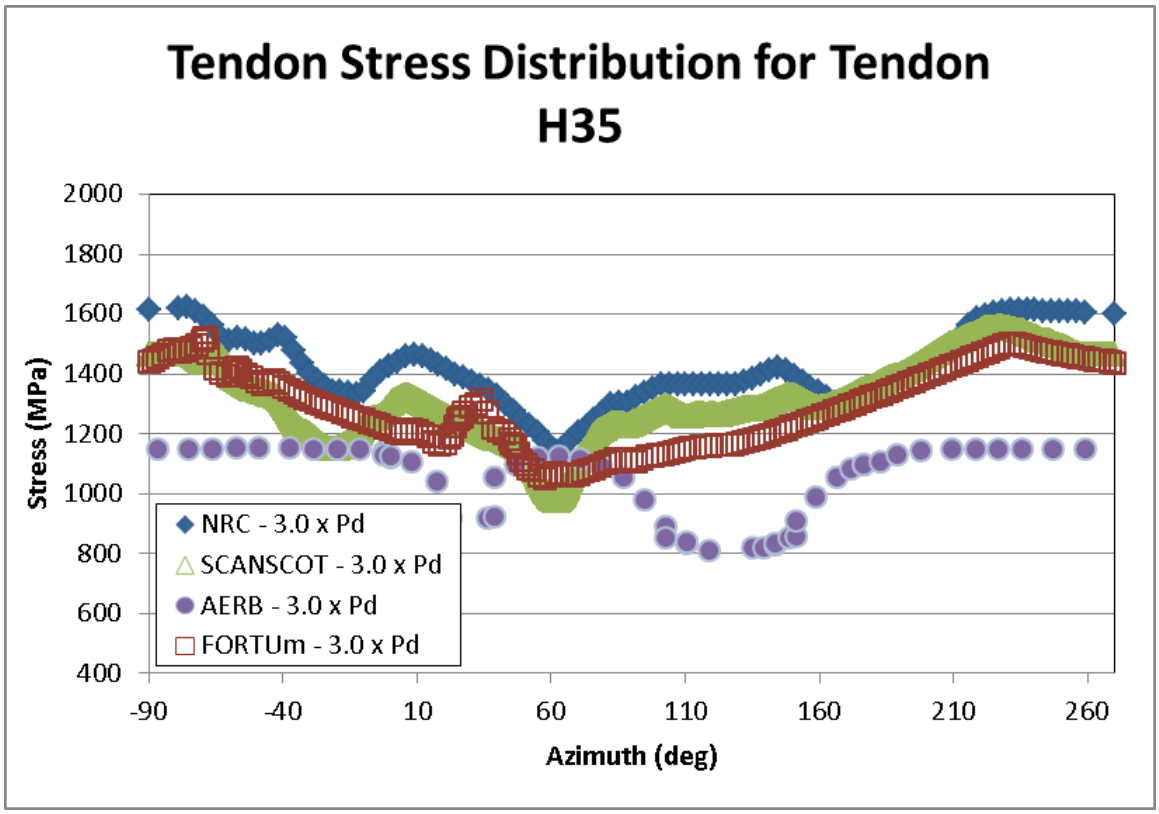

Figure 283: Tendon Stress Distribution for Tendon #H35 at 3.0 x P_d

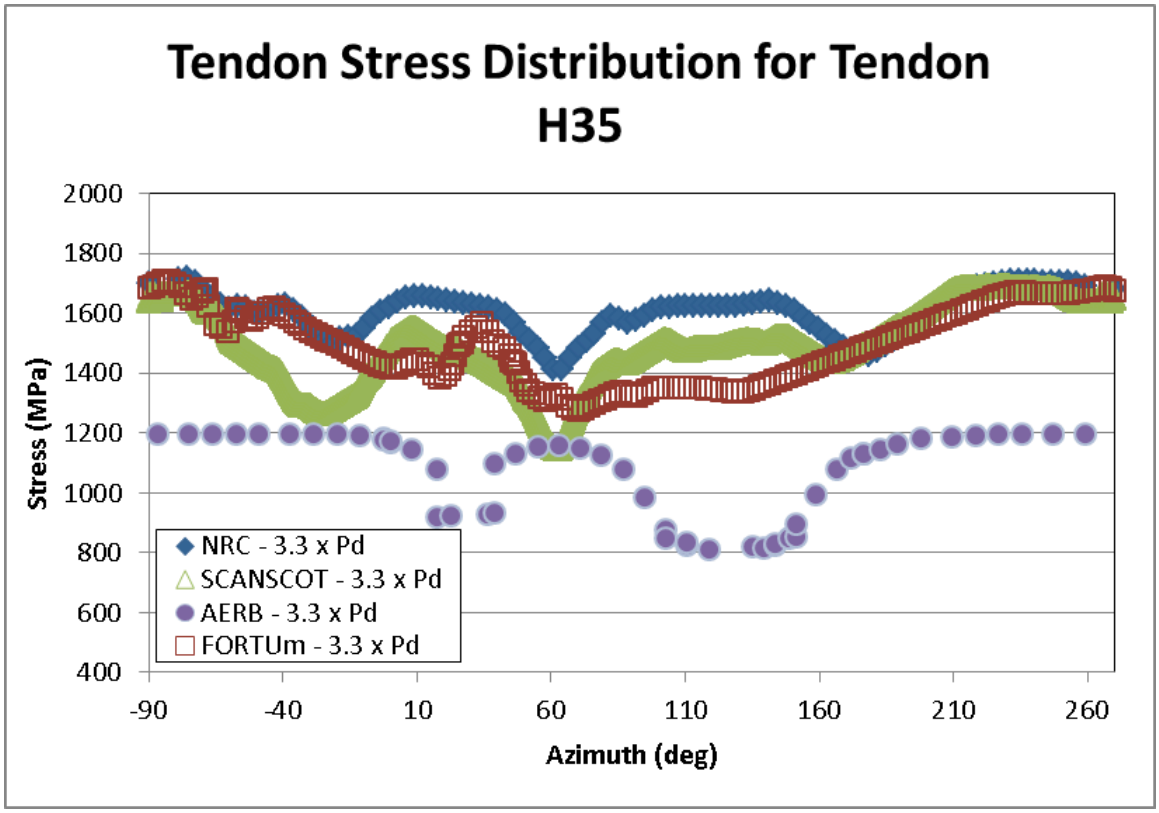

Figure 284: Tendon Stress Distribution for Tendon #H35 at 3.3 x P_d

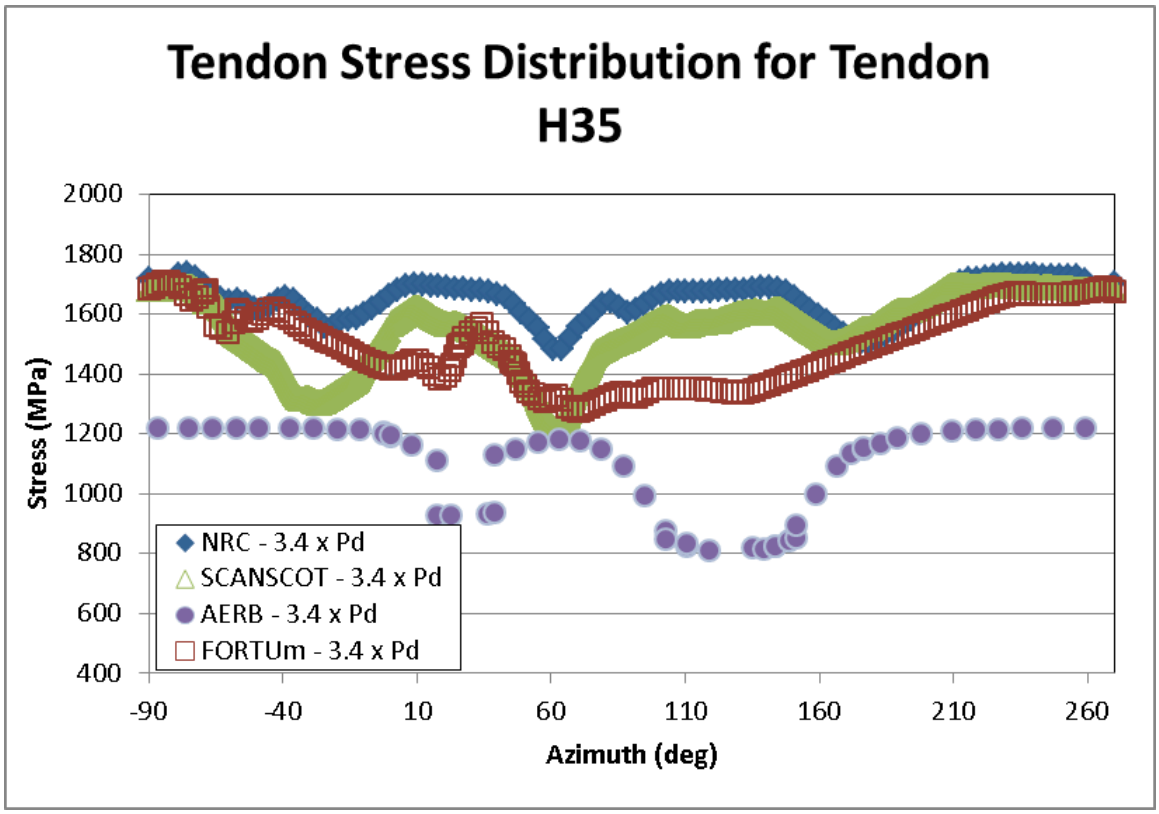

Figure 285: Tendon Stress Distribution for Tendon #H35 at 3.4 x P_d

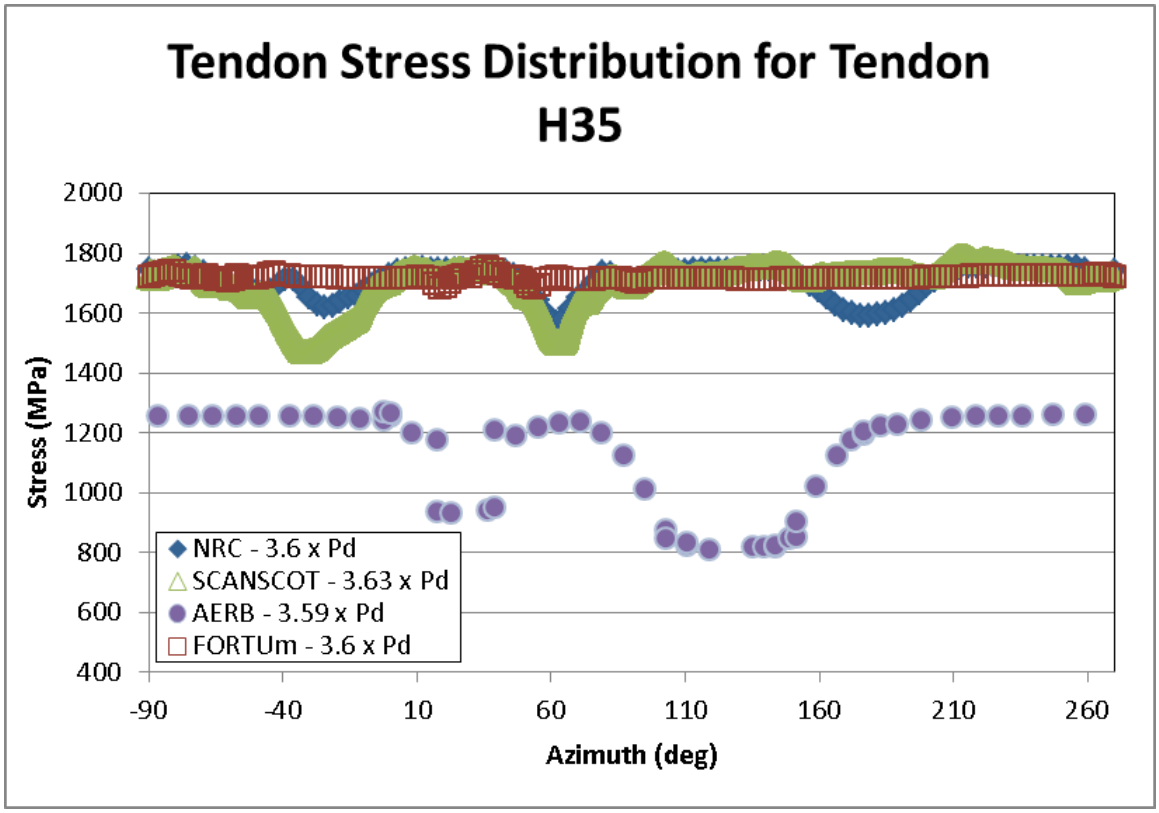

Figure 286: Tendon Stress Distribution for Tendon #H35 at Ultimate Pressure

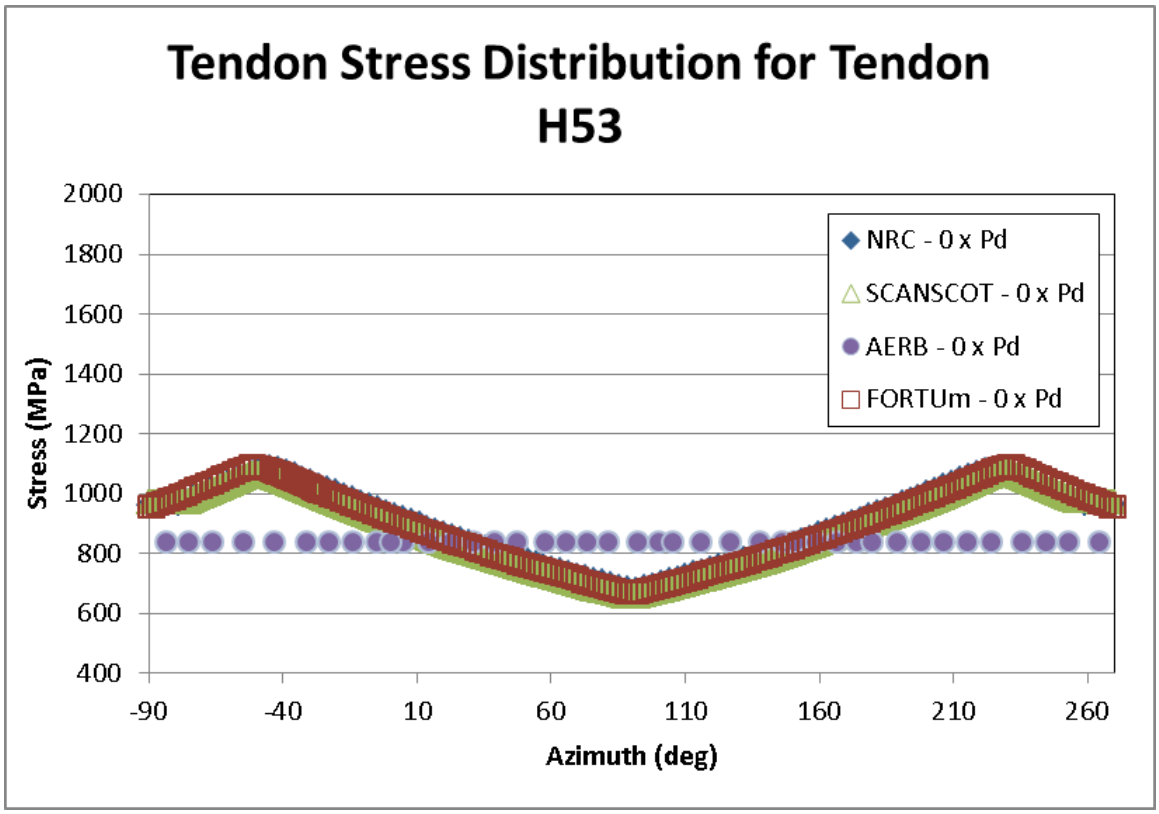

Figure 287: Tendon Stress Distribution for Tendon #H53 at 0 x P_d

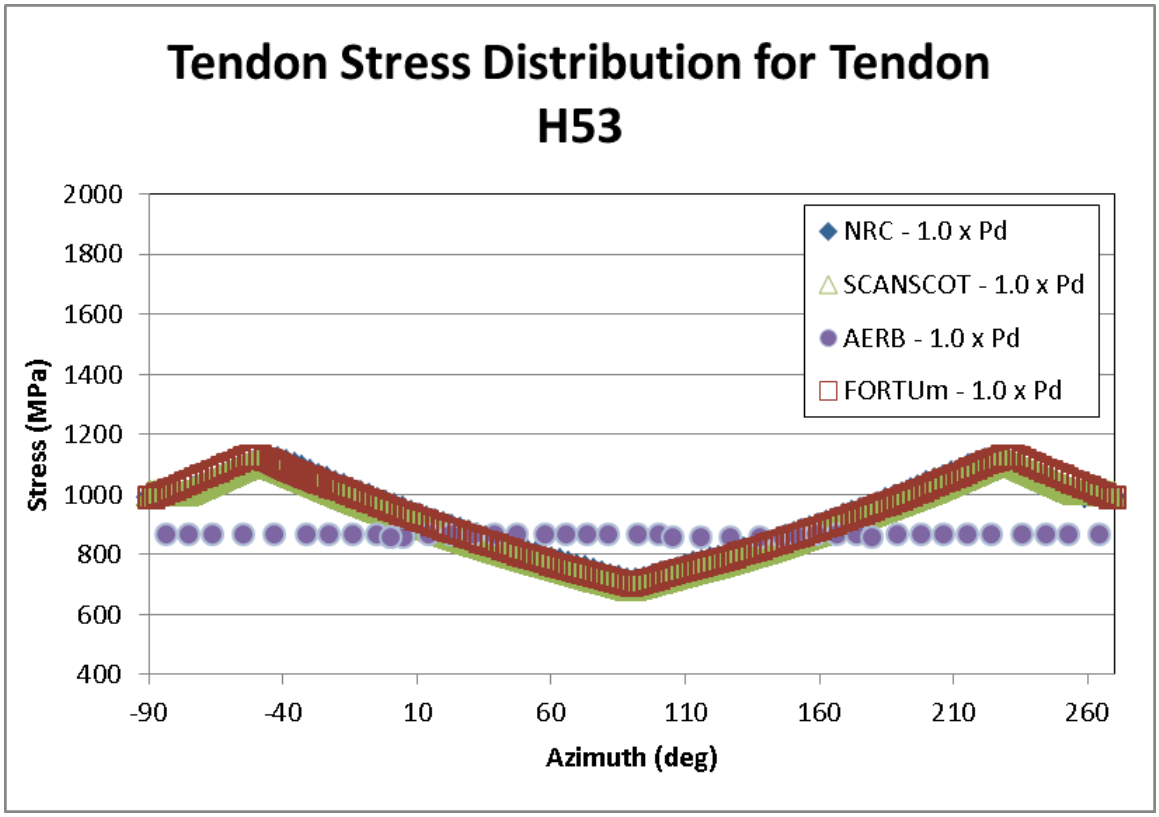

Figure 288: Tendon Stress Distribution for Tendon #H53 at 1.0 x P_d

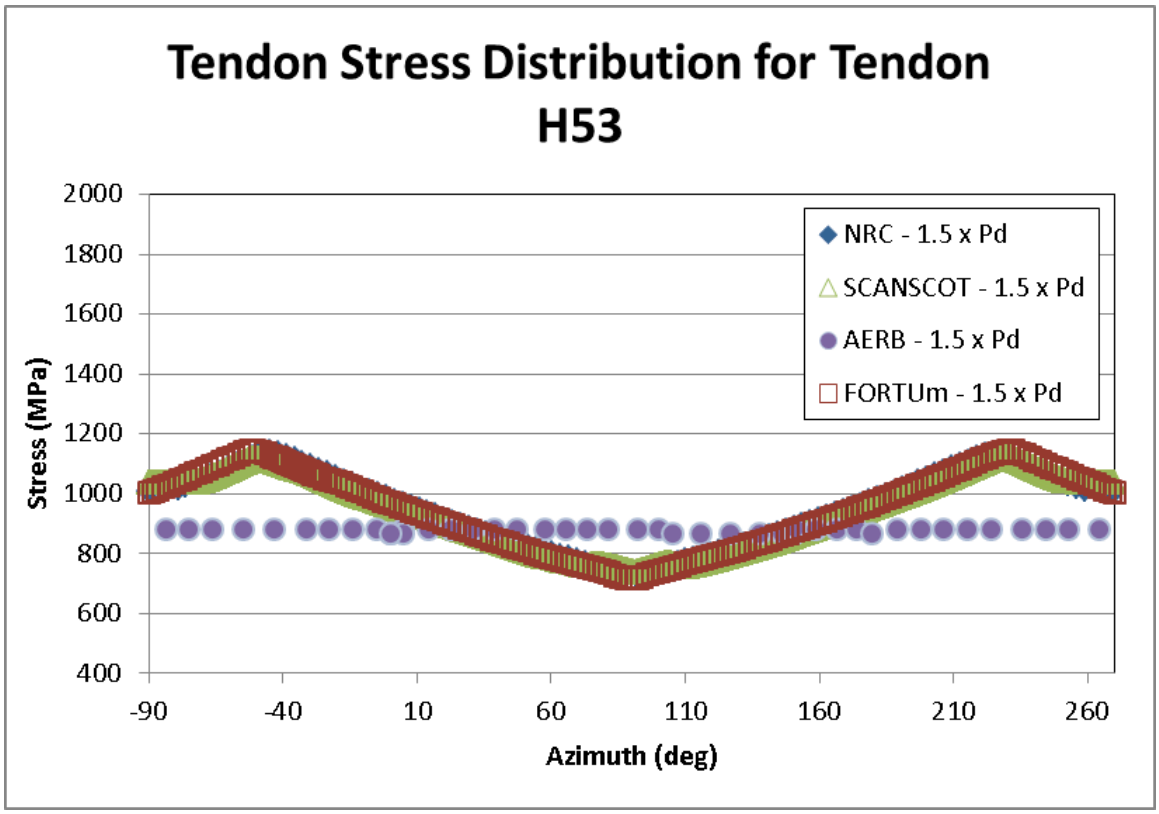

Figure 289: Tendon Stress Distribution for Tendon #H53 at 1.5 x P_d

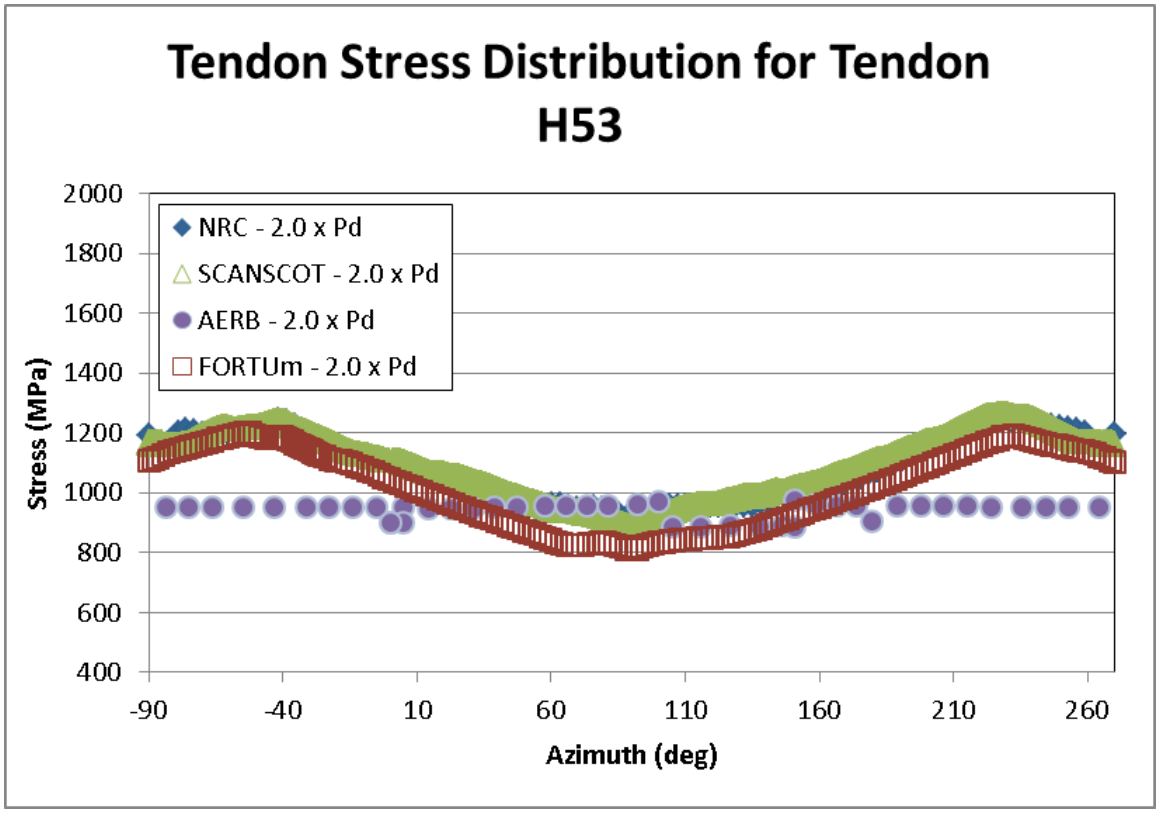

Figure 290: Tendon Stress Distribution for Tendon #H53 at 2.0 x P_d

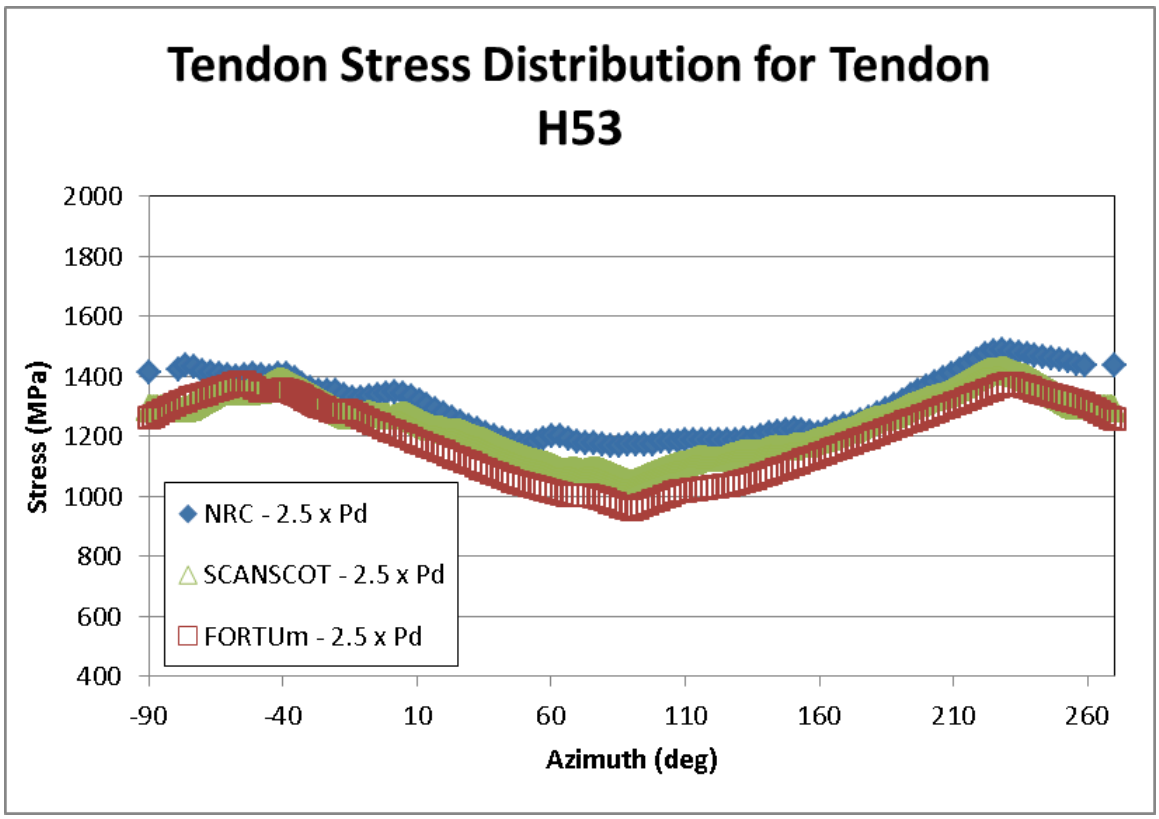

Figure 291: Tendon Stress Distribution for Tendon #H53 at 2.5 x P_d

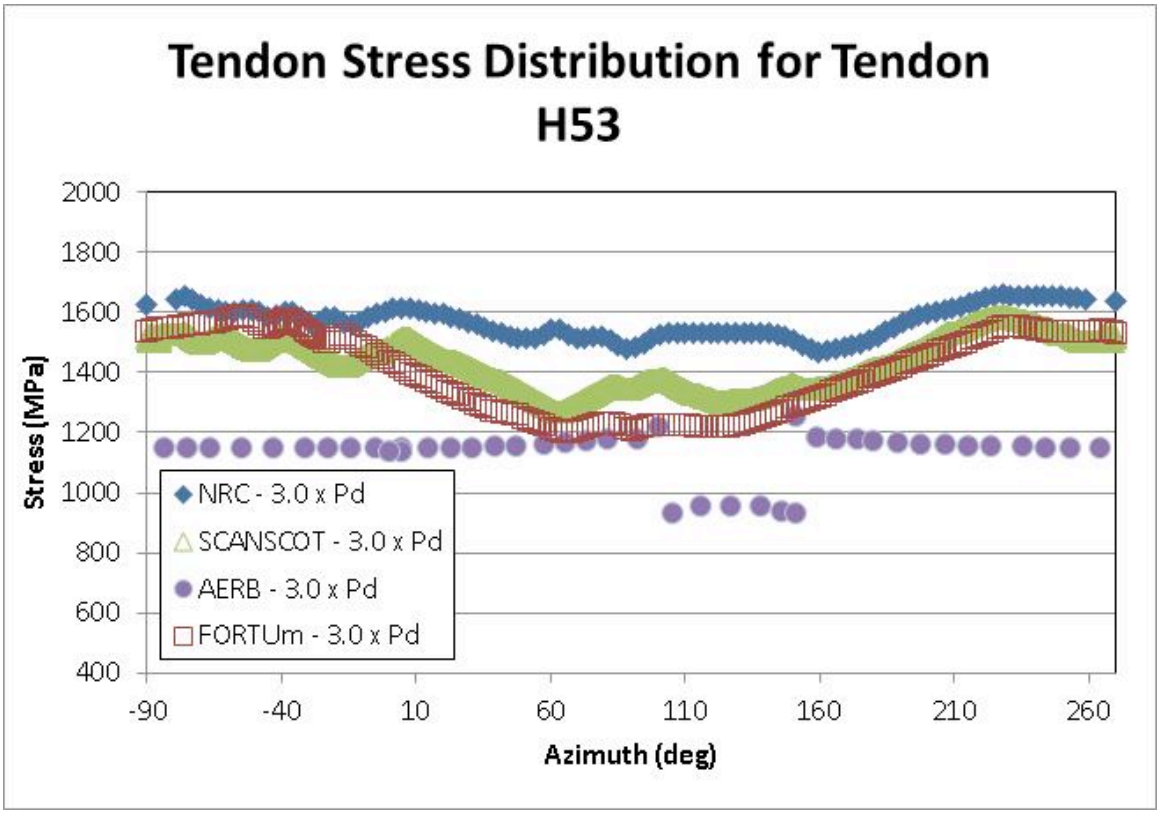

Figure 292: Tendon Stress Distribution for Tendon #H53 at 3.0 x P_d

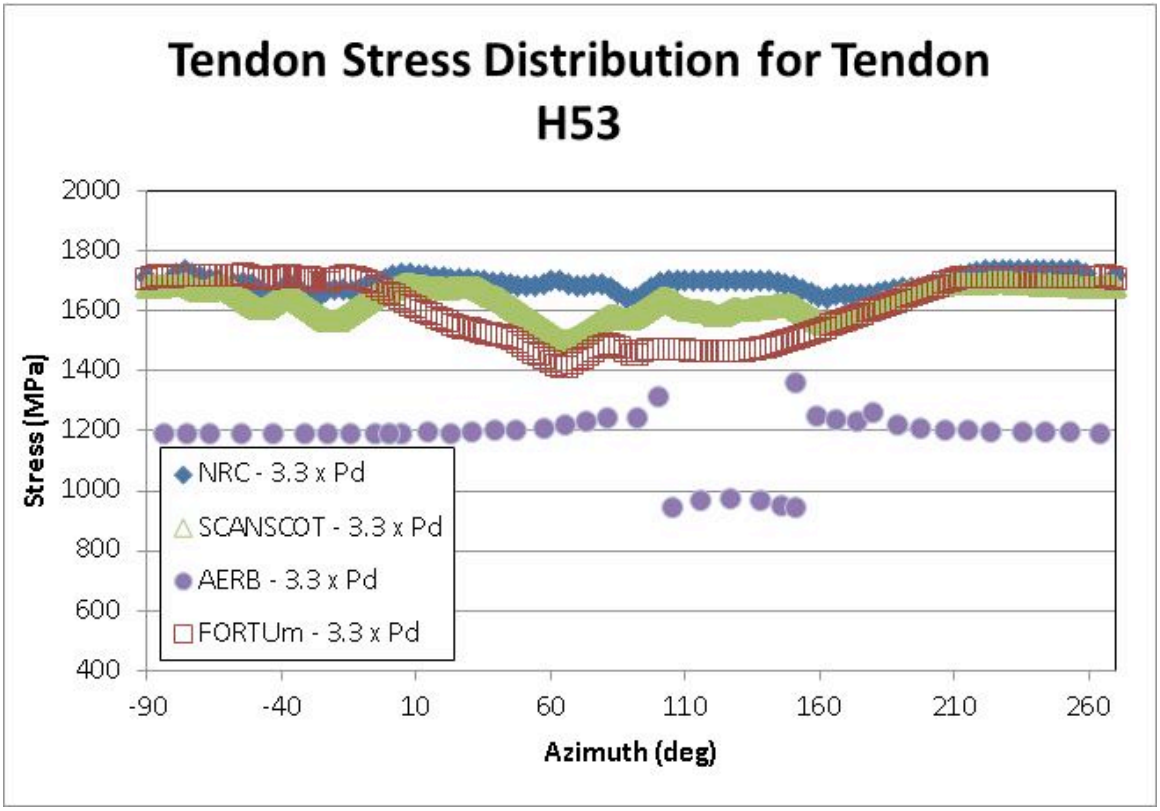

Figure 293: Tendon Stress Distribution for Tendon #H53 at 3.3 x P_d

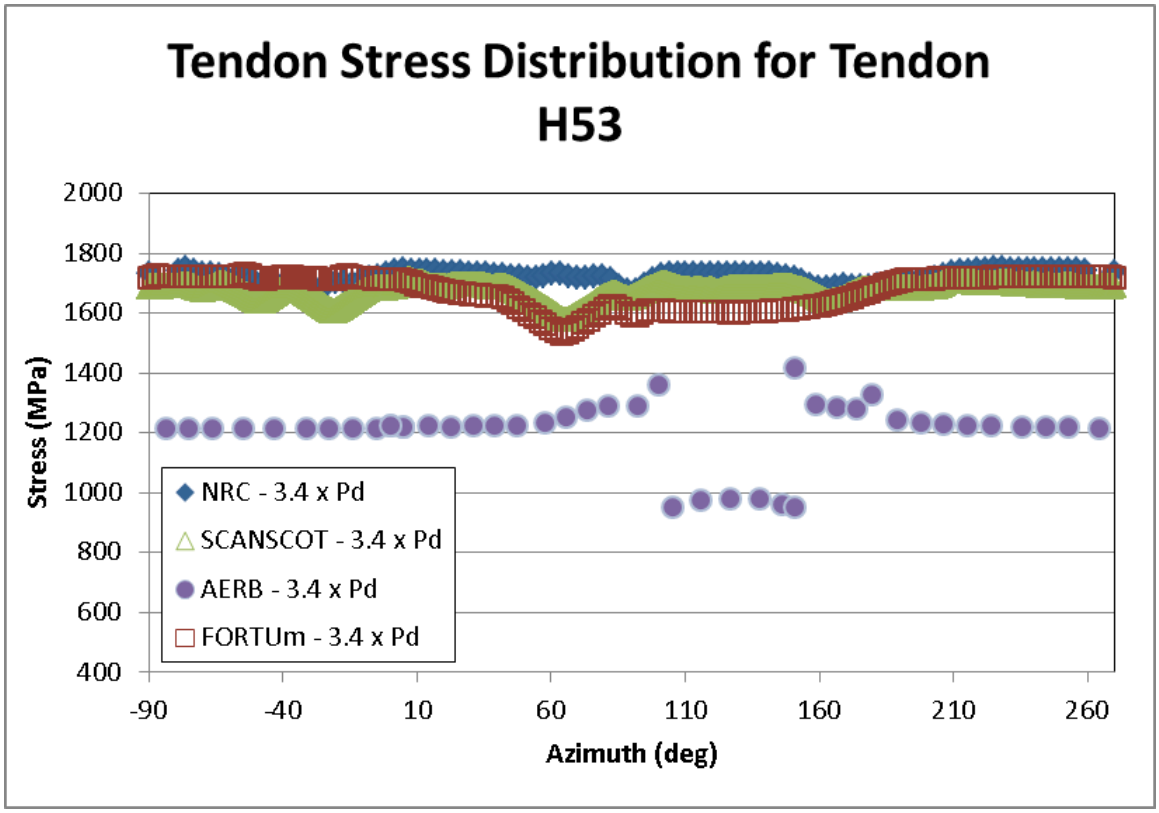

Figure 294: Tendon Stress Distribution for Tendon #H53 at 3.4 x P_d

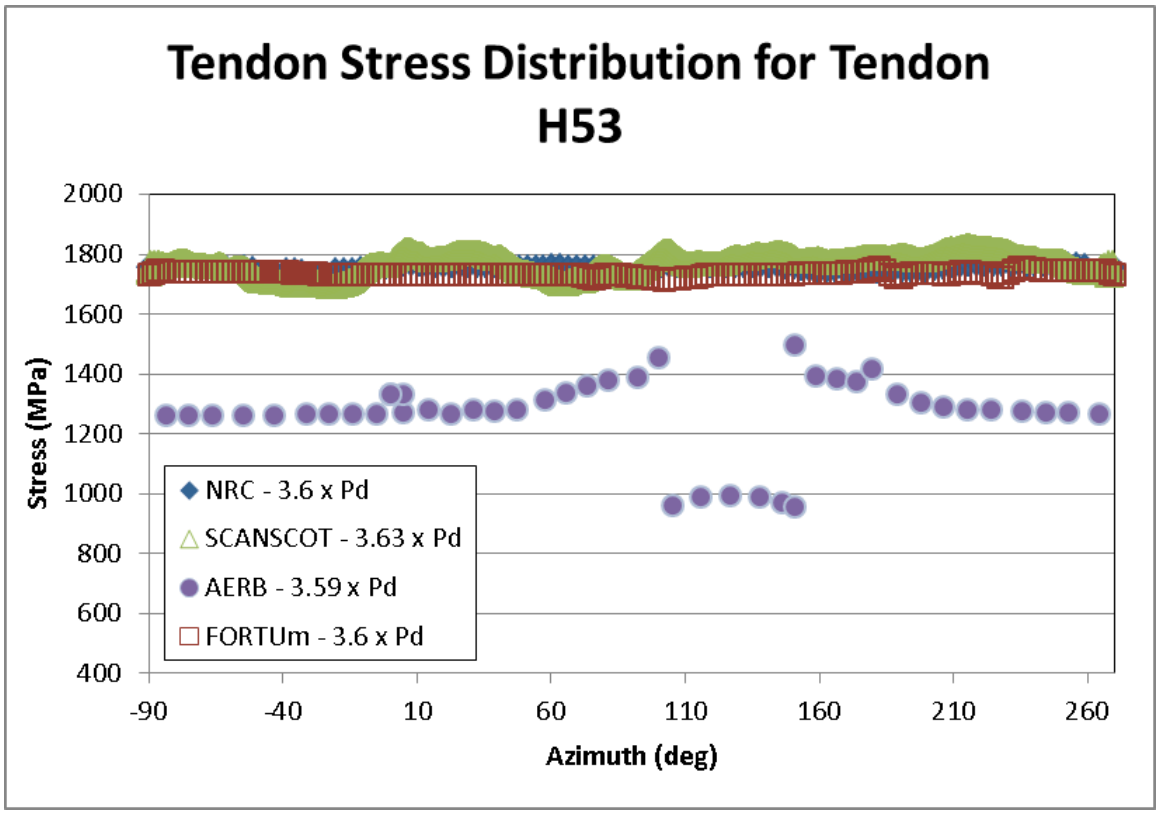

Figure 295: Tendon Stress Distribution for Tendon #H53 at Ultimate Pressure

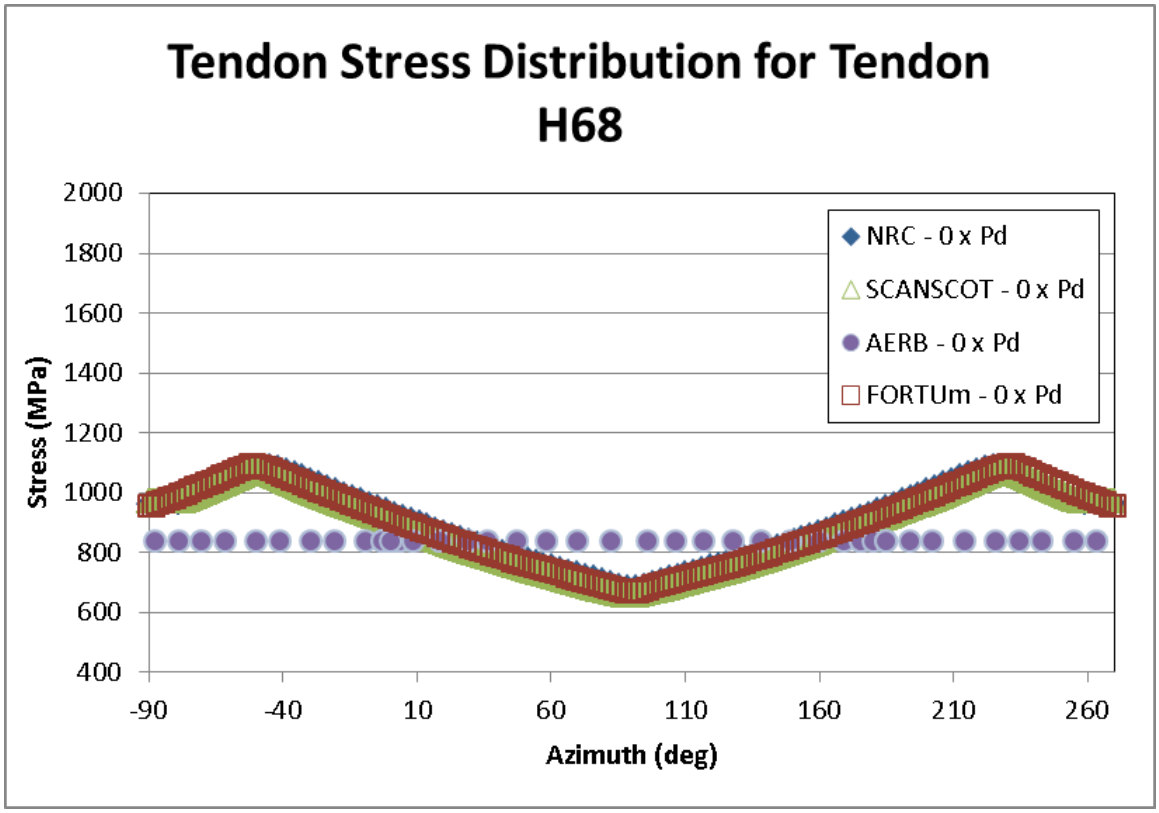

Figure 296: Tendon Stress Distribution for Tendon #H68 at 0 x P_d

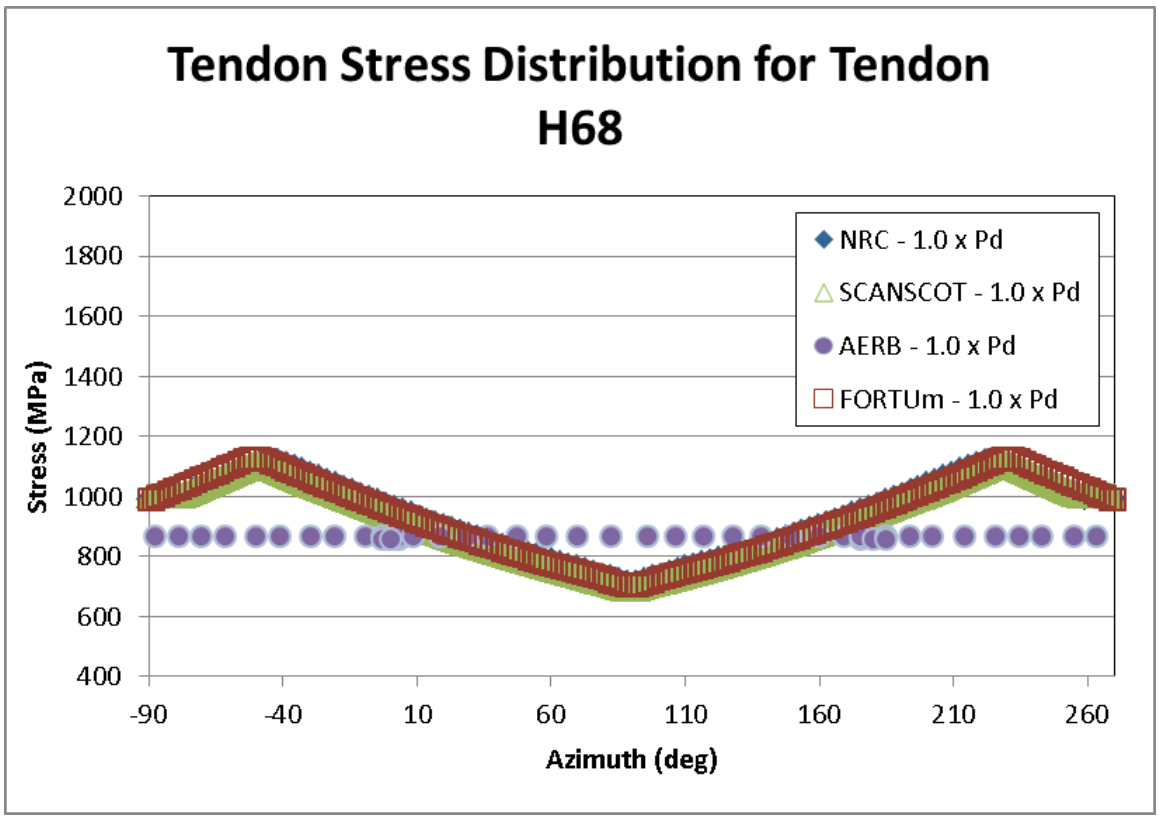

Figure 297: Tendon Stress Distribution for Tendon #H68 at 1.0 x P_d

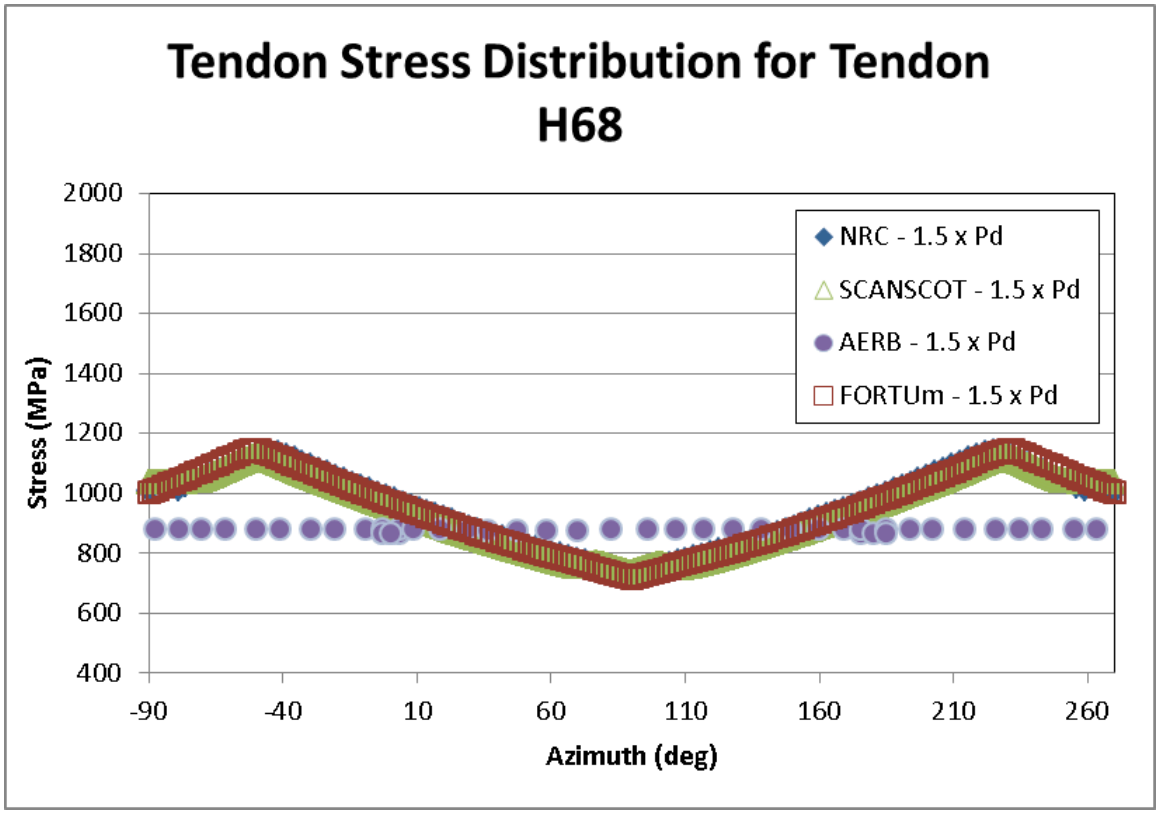

Figure 298: Tendon Stress Distribution for Tendon #H68 at 1.5 x P_d

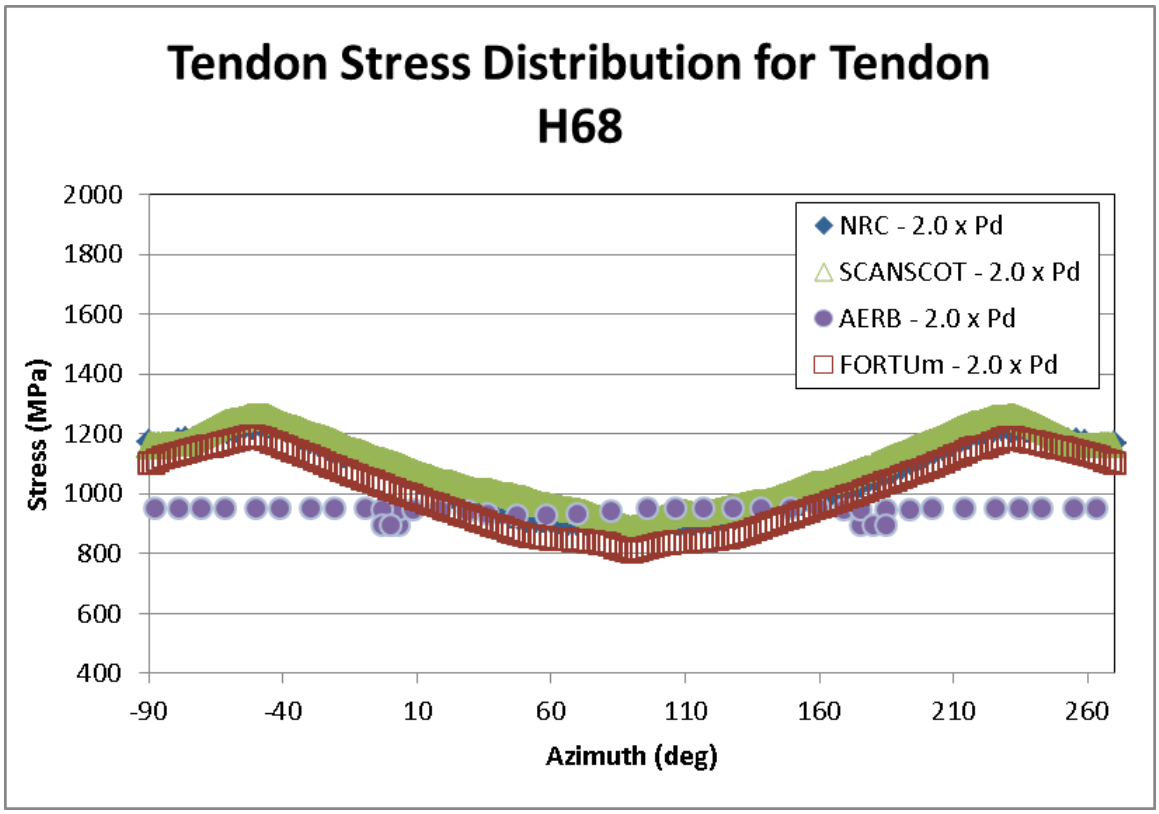

Figure 299: Tendon Stress Distribution for Tendon #H68 at 2.0 x P_d

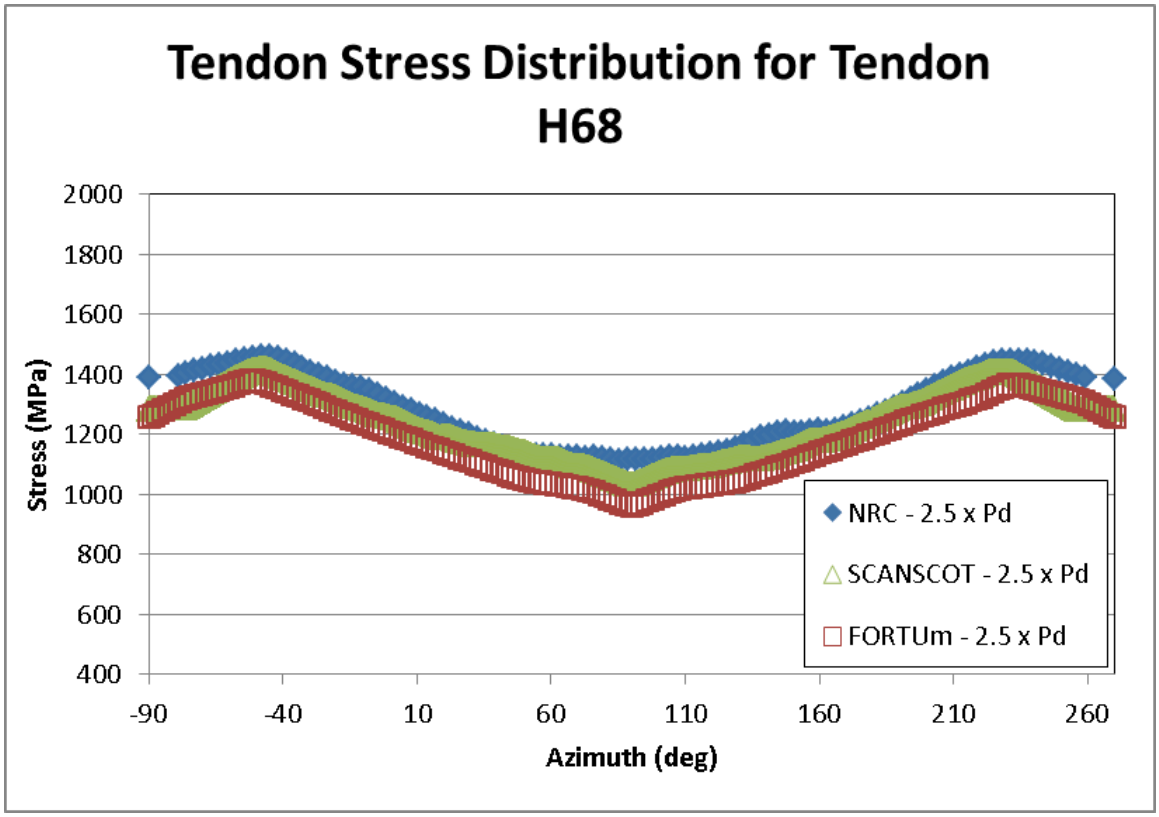

Figure 300: Tendon Stress Distribution for Tendon #H68 at 2.5 x P_d

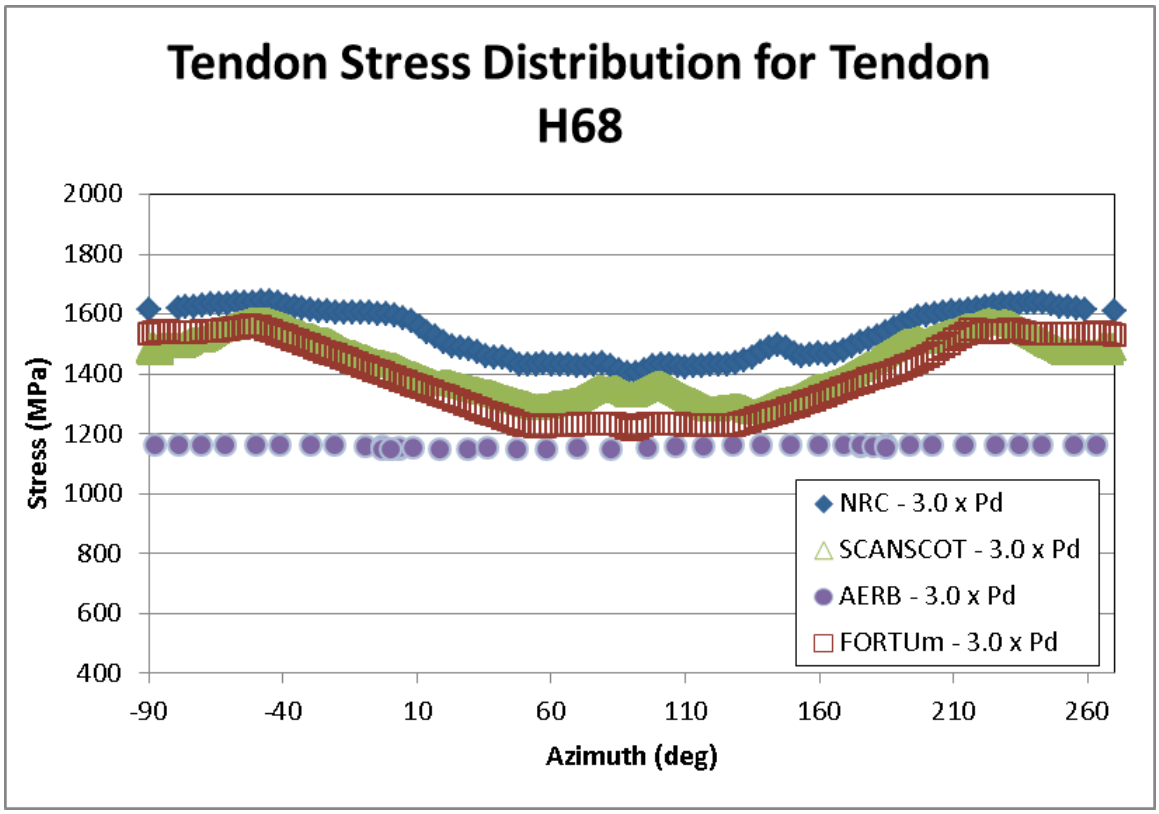

Figure 301: Tendon Stress Distribution for Tendon #H68 at 3.0 x P_d

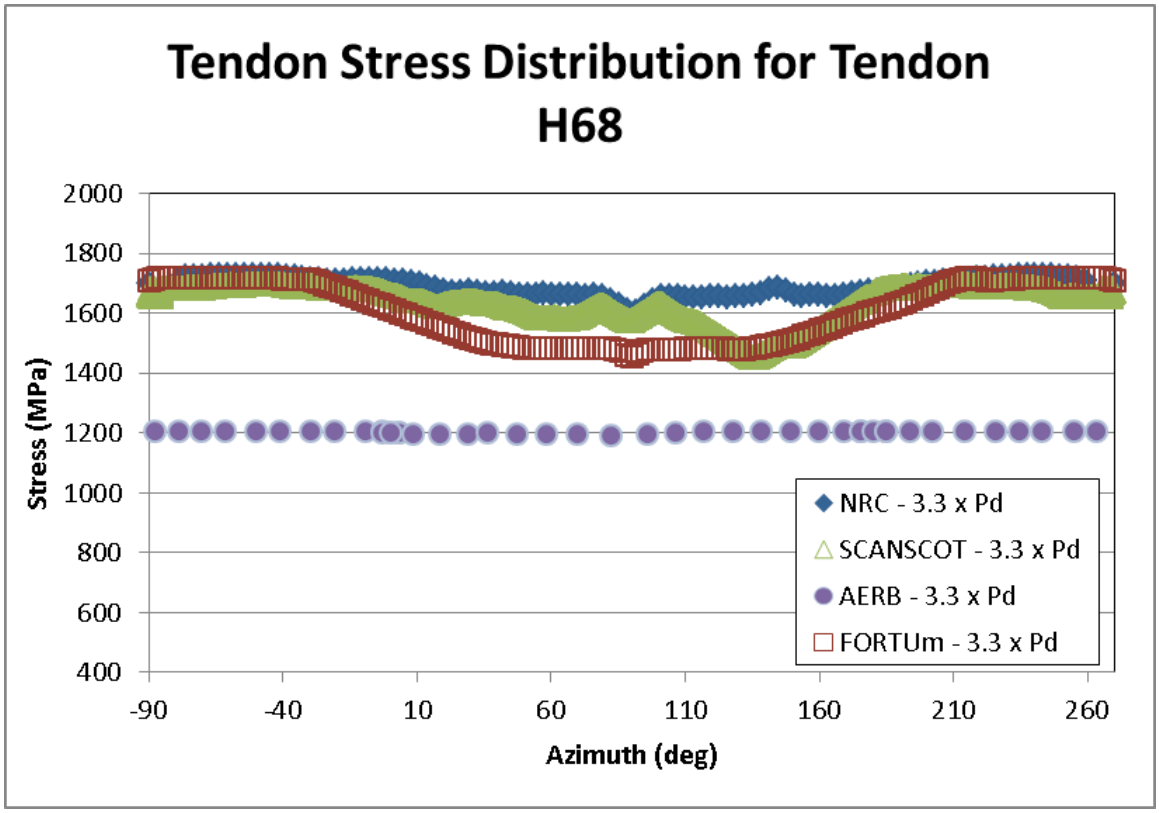

Figure 302: Tendon Stress Distribution for Tendon #H68 at 3.3 x P_d

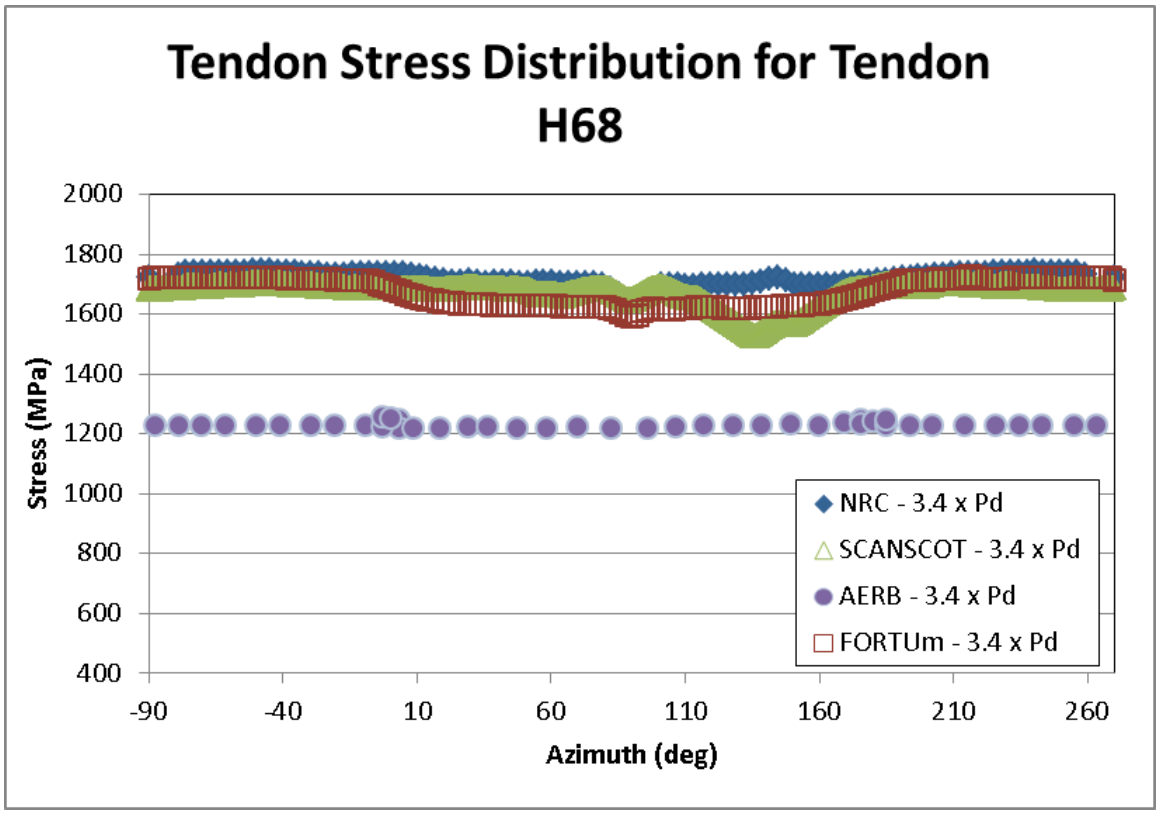

Figure 303: Tendon Stress Distribution for Tendon #H68 at 3.4 x P_d

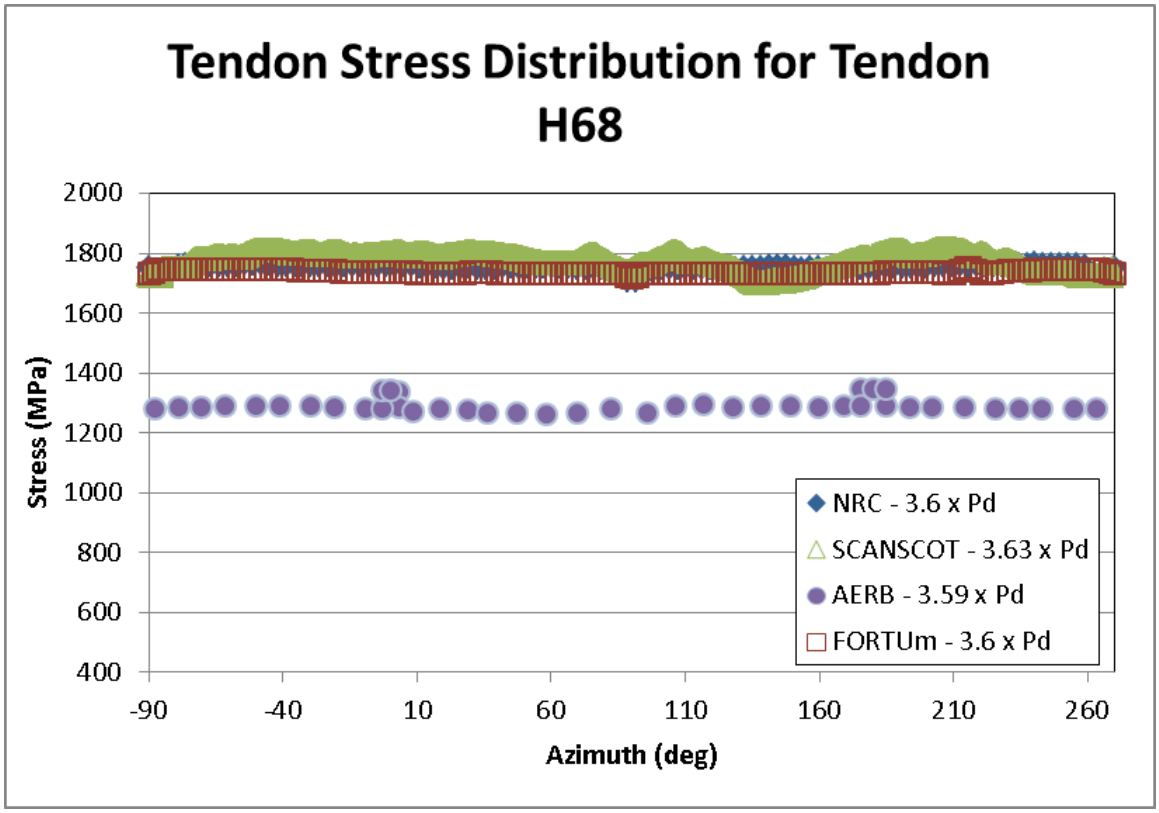

Figure 304: Tendon Stress Distribution for Tendon #H68 at Ultimate Pressure

4.6.5. Vertical Tendons

The vertical tendons selected for analysis correspond with tendons #V37, V46 from the PCCV test, and as stated earlier, this selection facilitates comparison with the most instrumented tendons from the test. There appears to be less agreement between the participants for the vertical tendons when compared with the hoop tendons in the previous section. The source of this deviation is not immediately known. The tendon stress versus location plots for the vertical tendons can be found in Figure 305 through Figure 322.

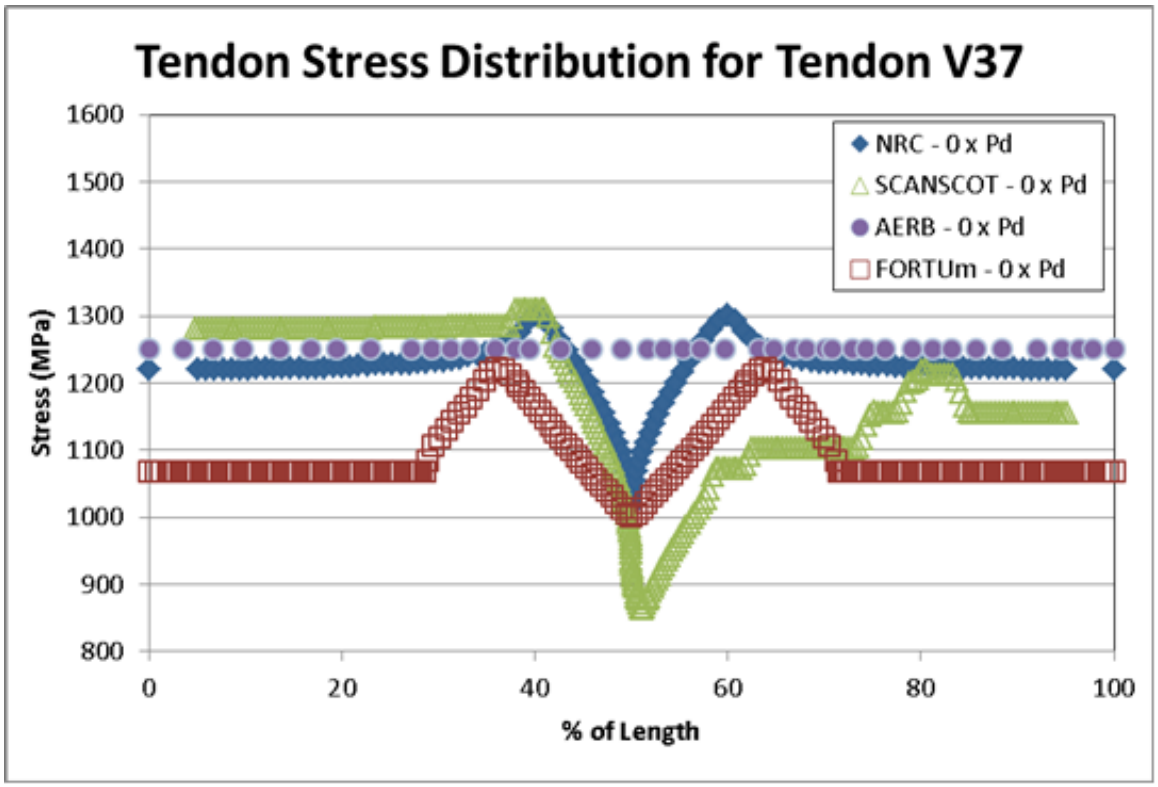

Figure 305: Tendon Stress Distribution for Tendon #V37 at 0 x P_d

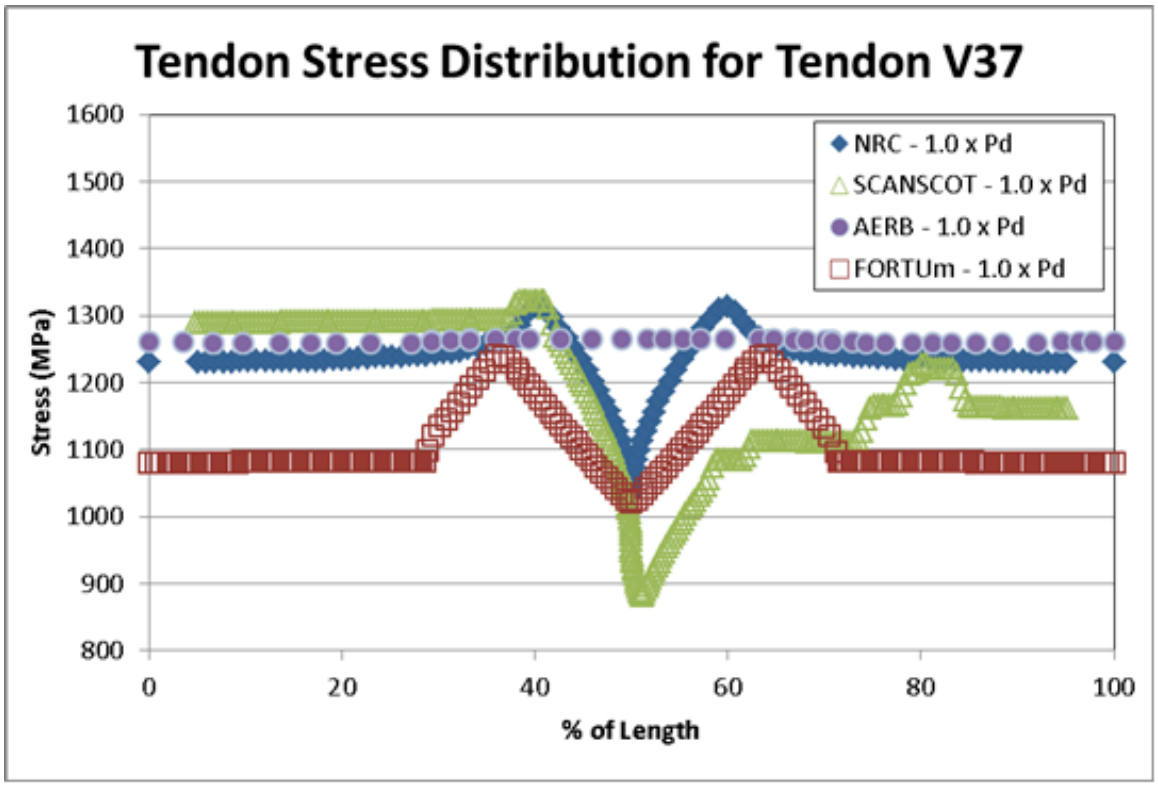

Figure 306: Tendon Stress Distribution for Tendon #V37 at 1.0 x P_d

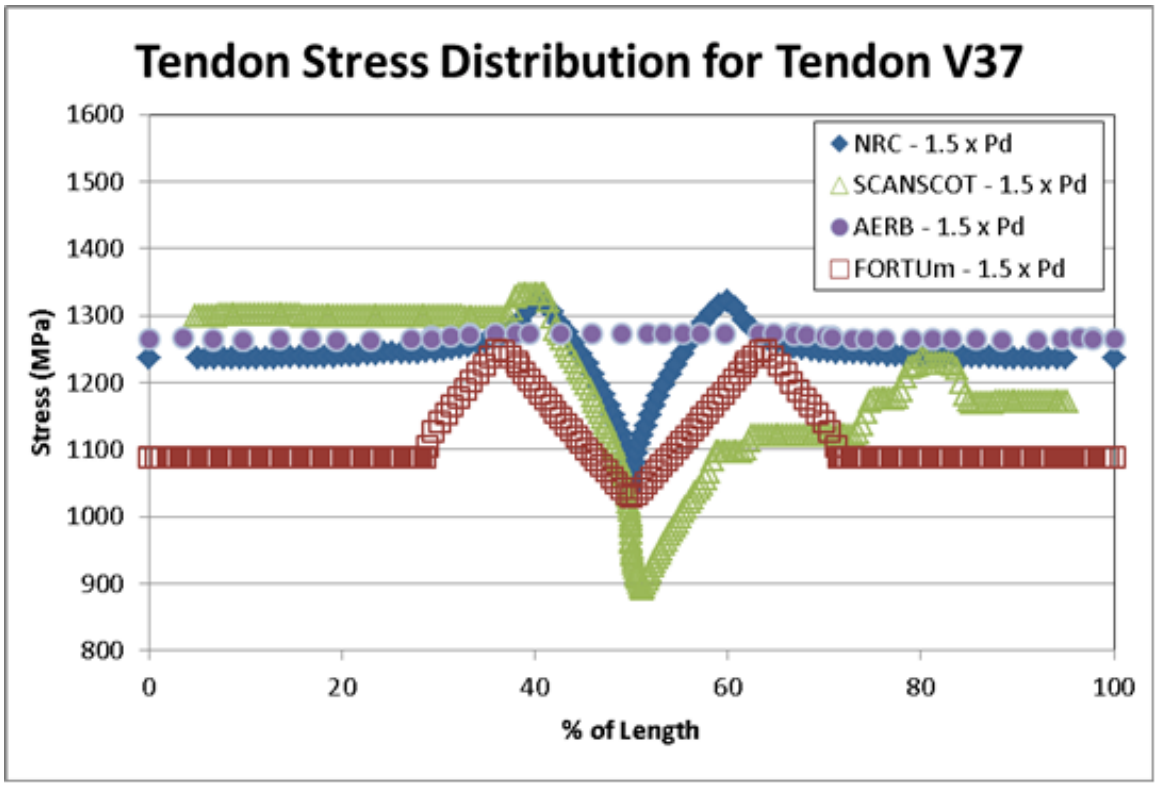

Figure 307: Tendon Stress Distribution for Tendon #V37 at 1.5 x P_d

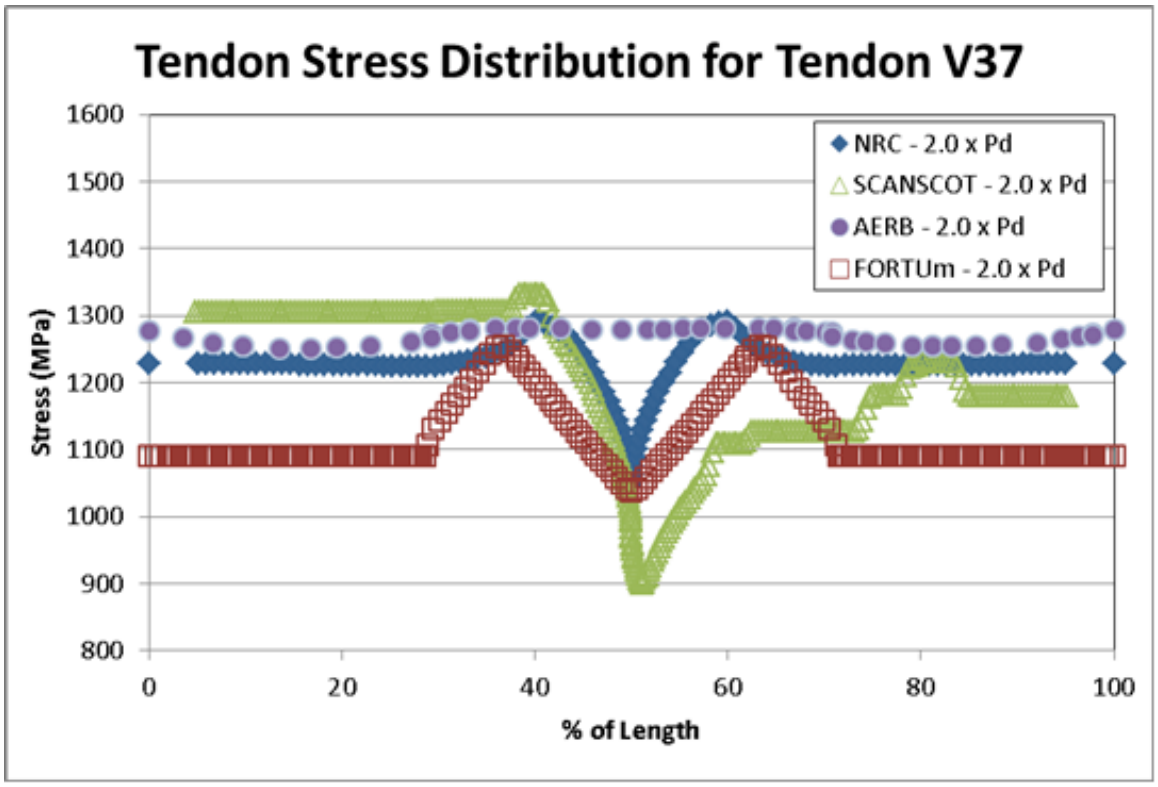

Figure 308: Tendon Stress Distribution for Tendon #V37 at 2.0 x P_d

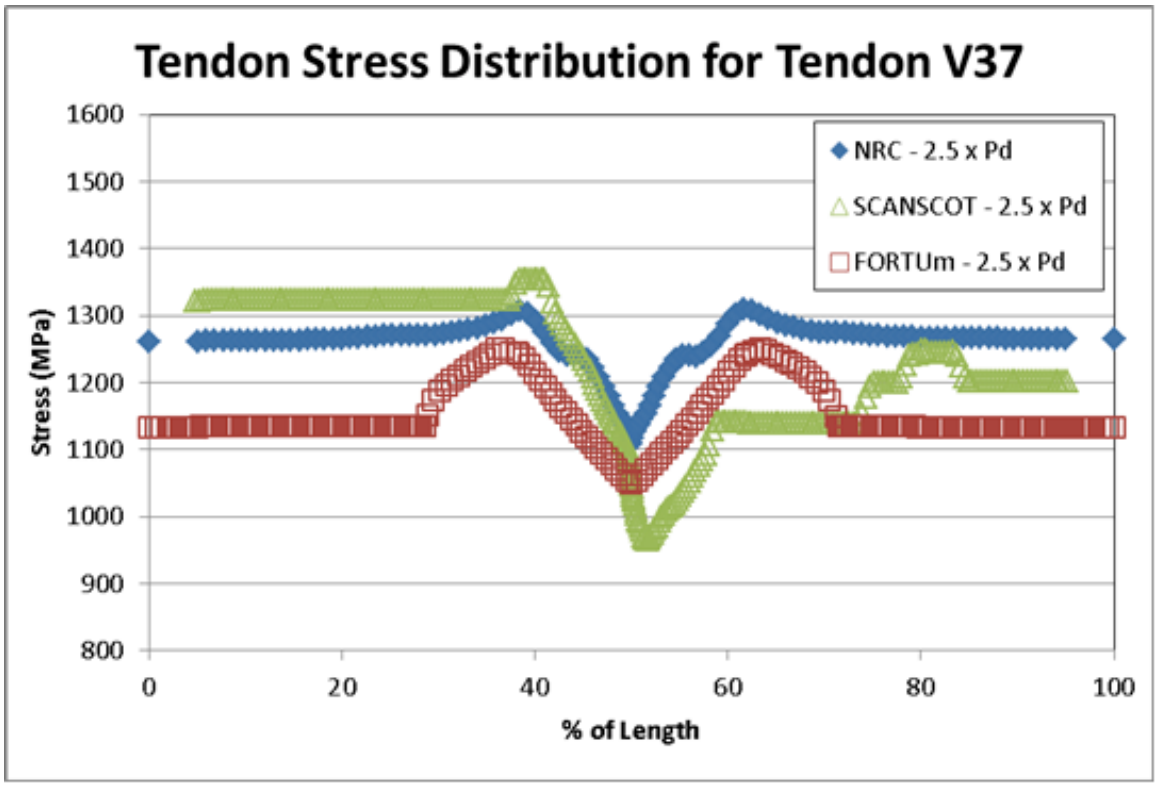

Figure 309: Tendon Stress Distribution for Tendon #V37 at 2.5 x P_d

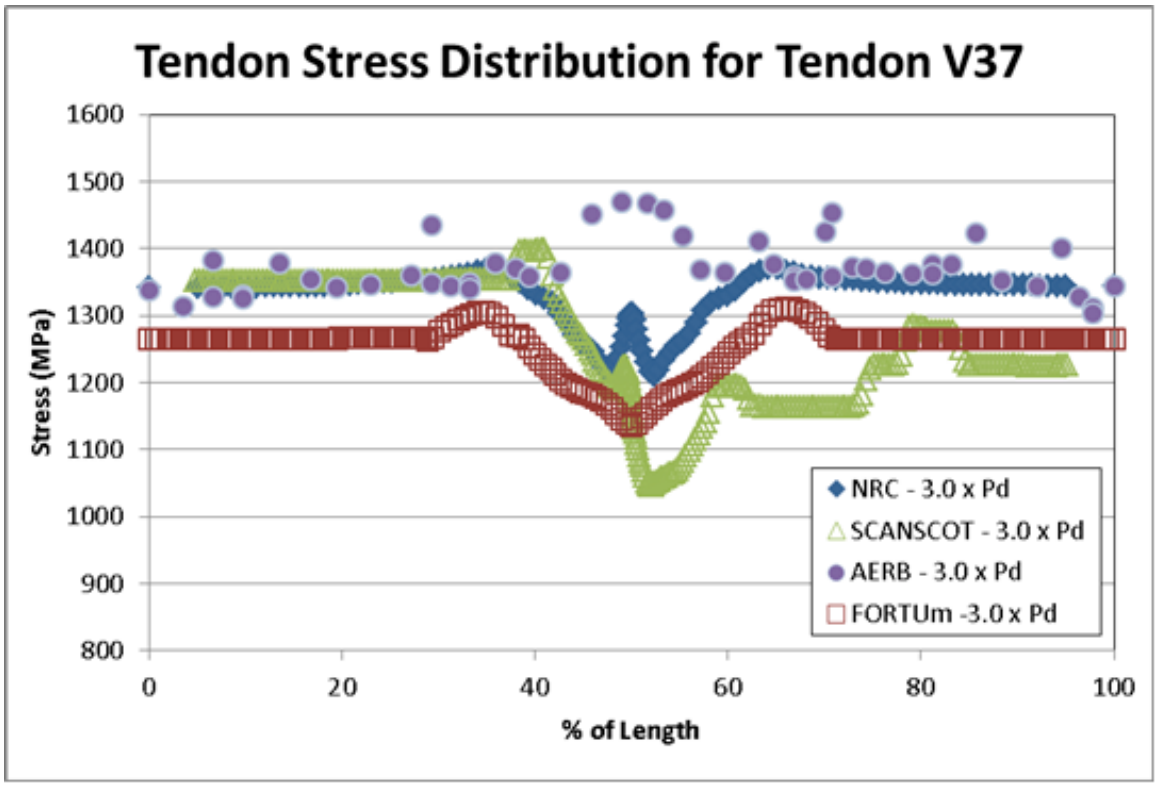

Figure 310: Tendon Stress Distribution for Tendon #V37 at 3.0 x P_d

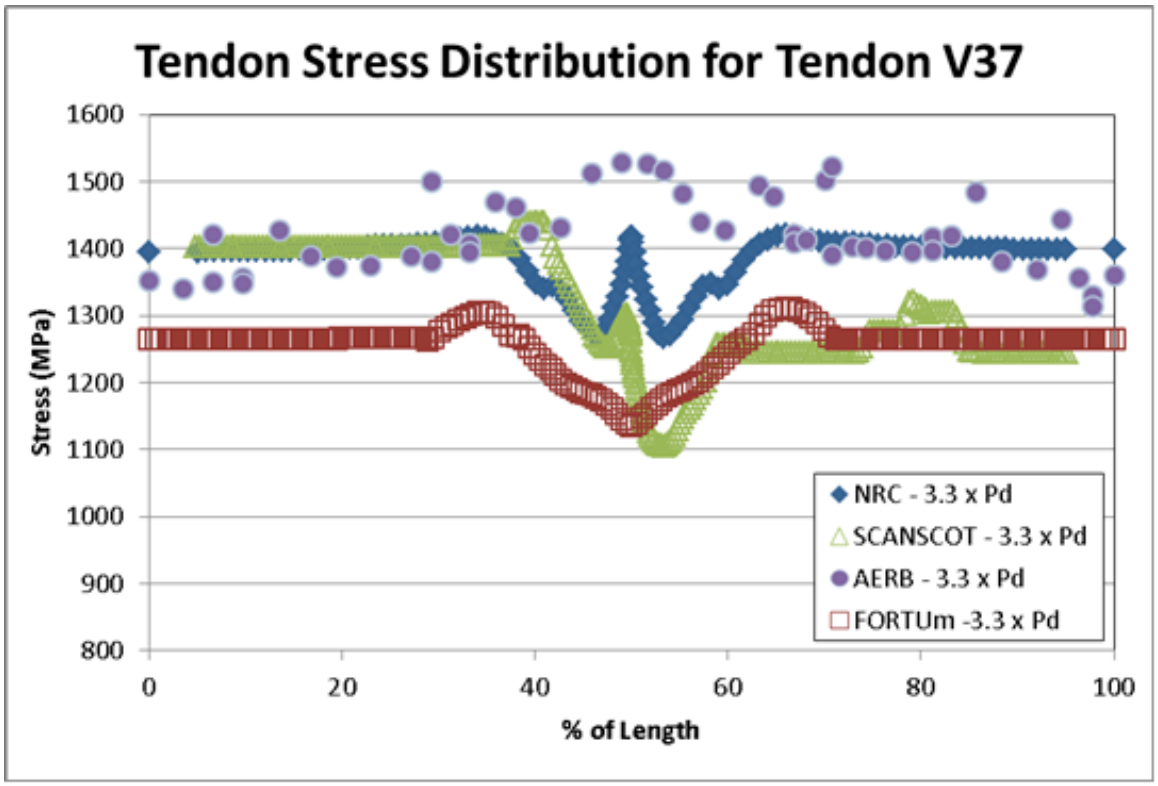

Figure 311: Tendon Stress Distribution for Tendon #V37 at 3.3 x P_d

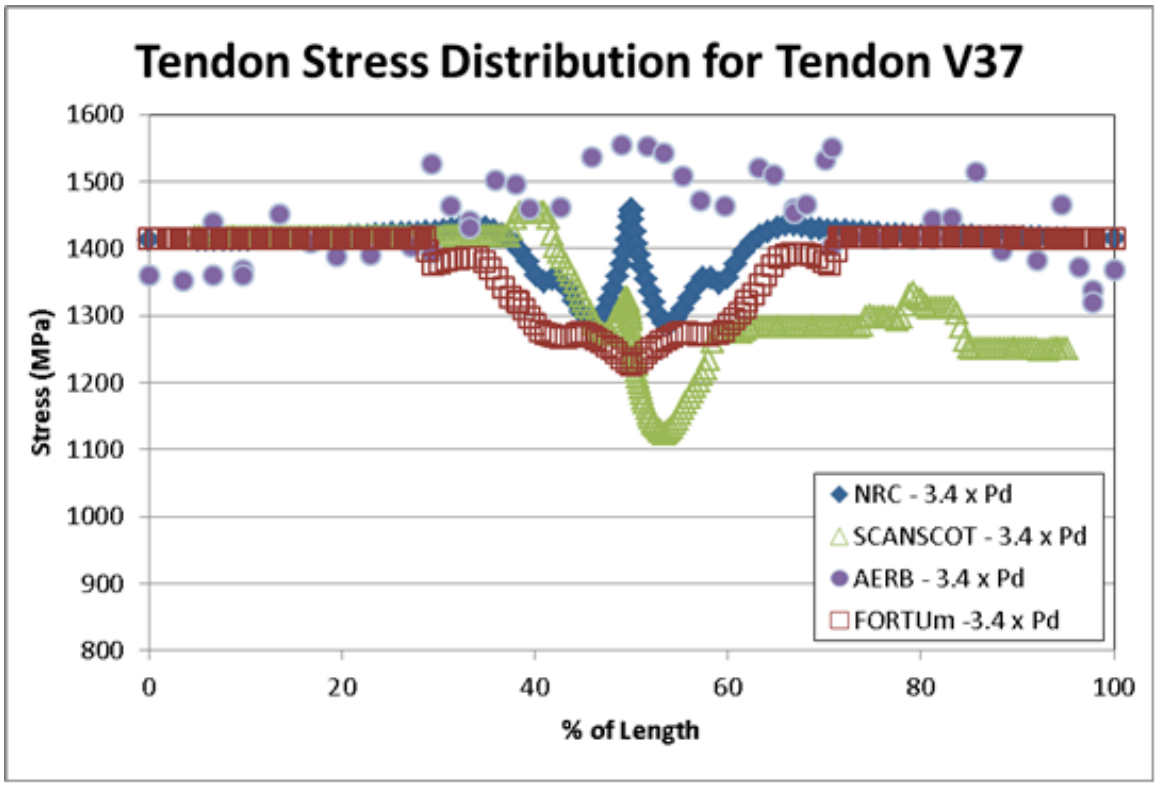

Figure 312: Tendon Stress Distribution for Tendon #V37 at 3.4 x P_d

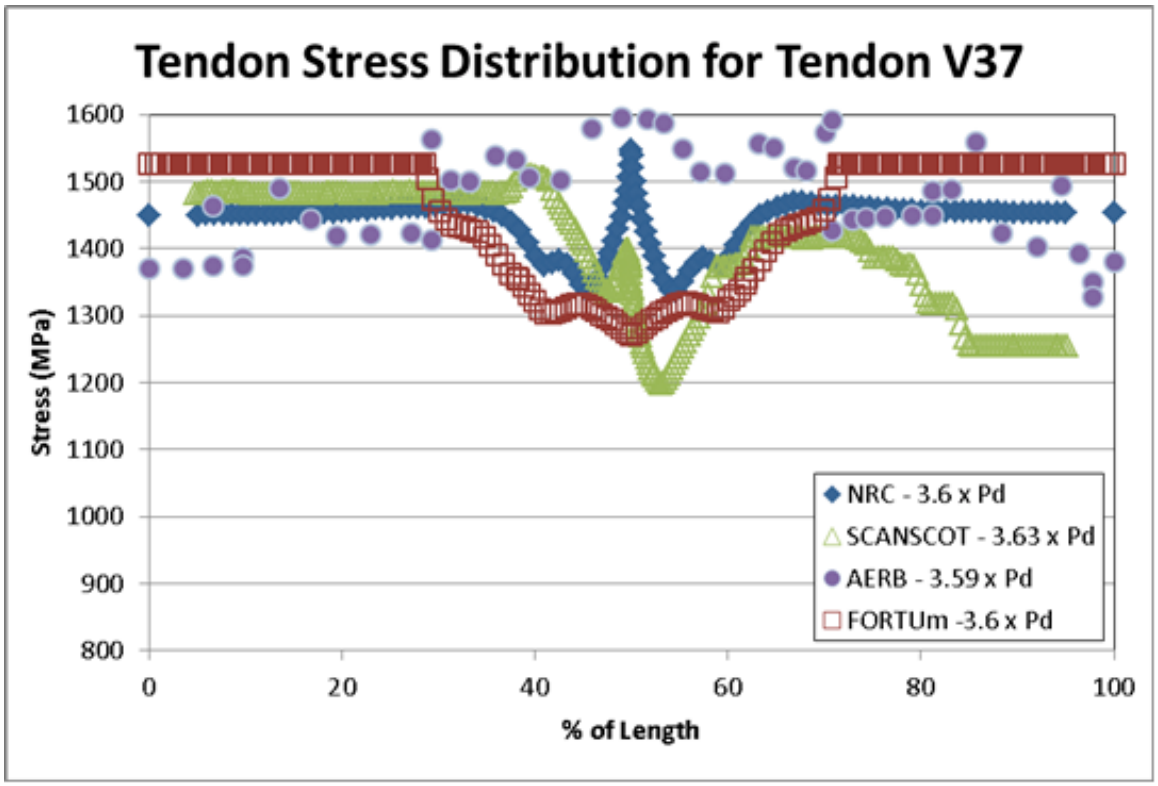

Figure 313: Tendon Stress Distribution for Tendon #V37 at 3.6 x P_d

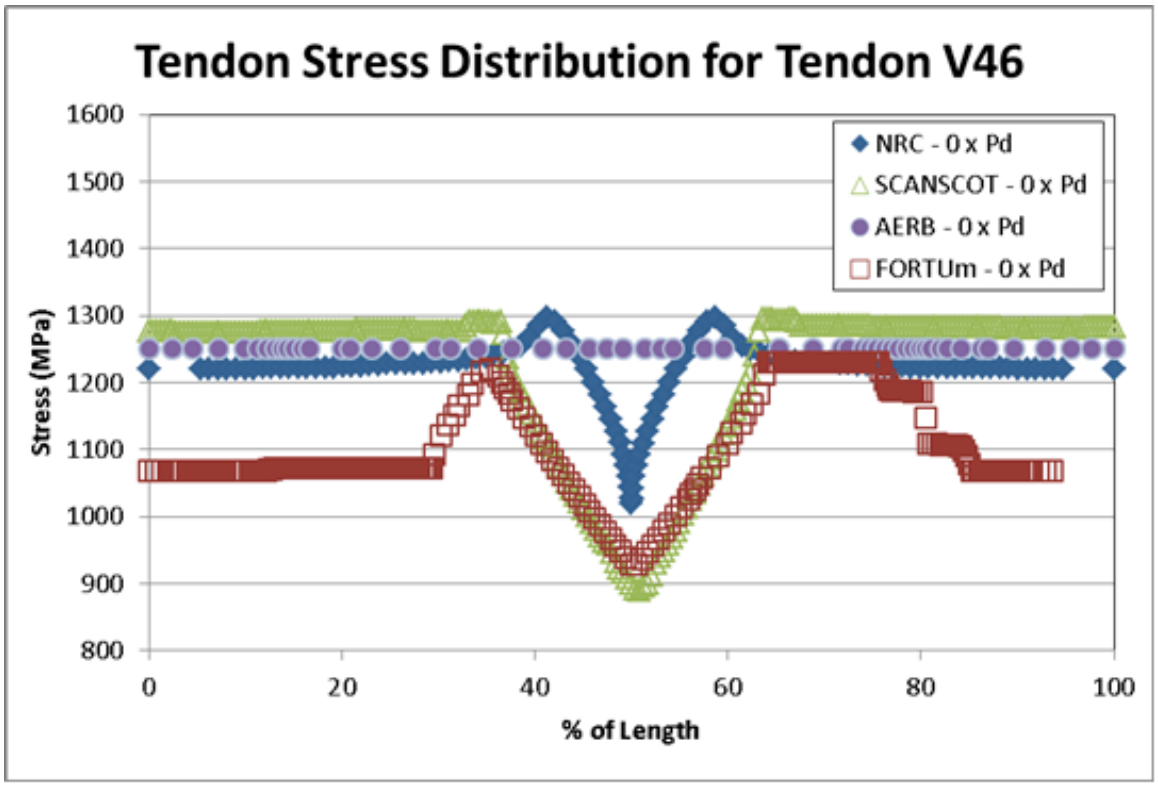

Figure 314: Tendon Stress Distribution for Tendon #V46 at 0 x P_d

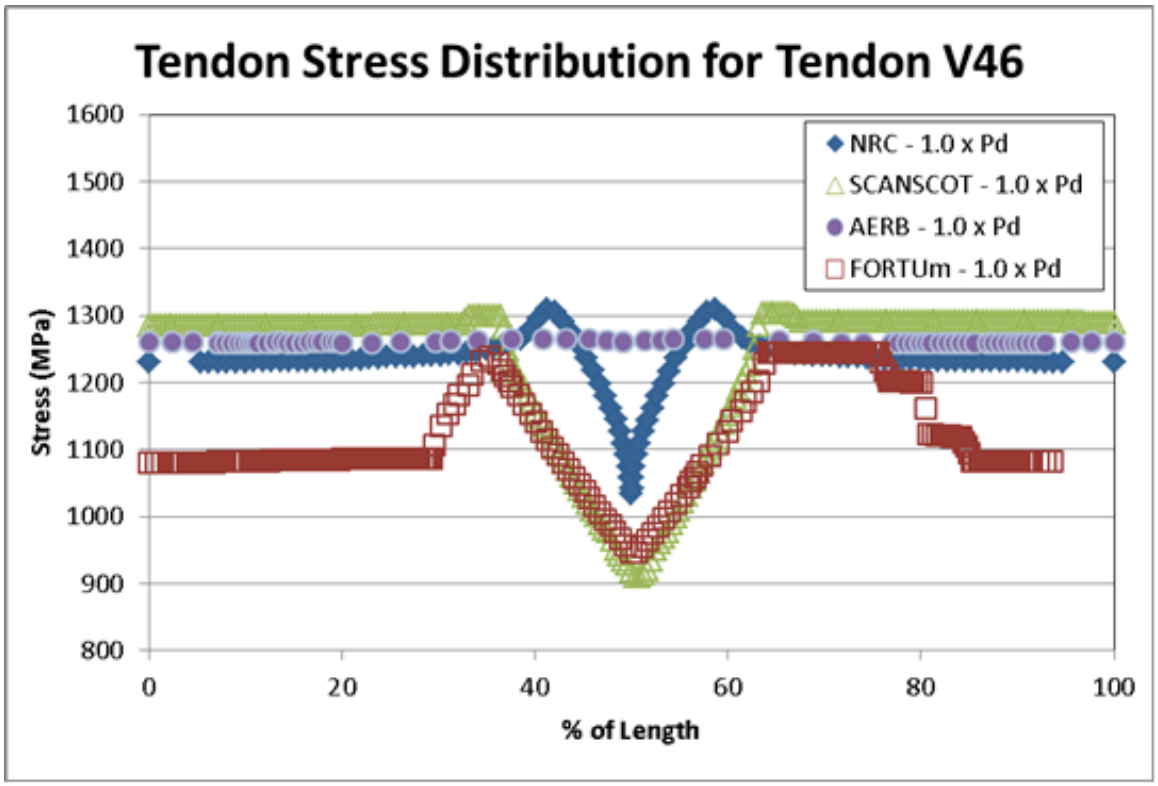

Figure 315: Tendon Stress Distribution for Tendon #V46 at 1.0 x P_d

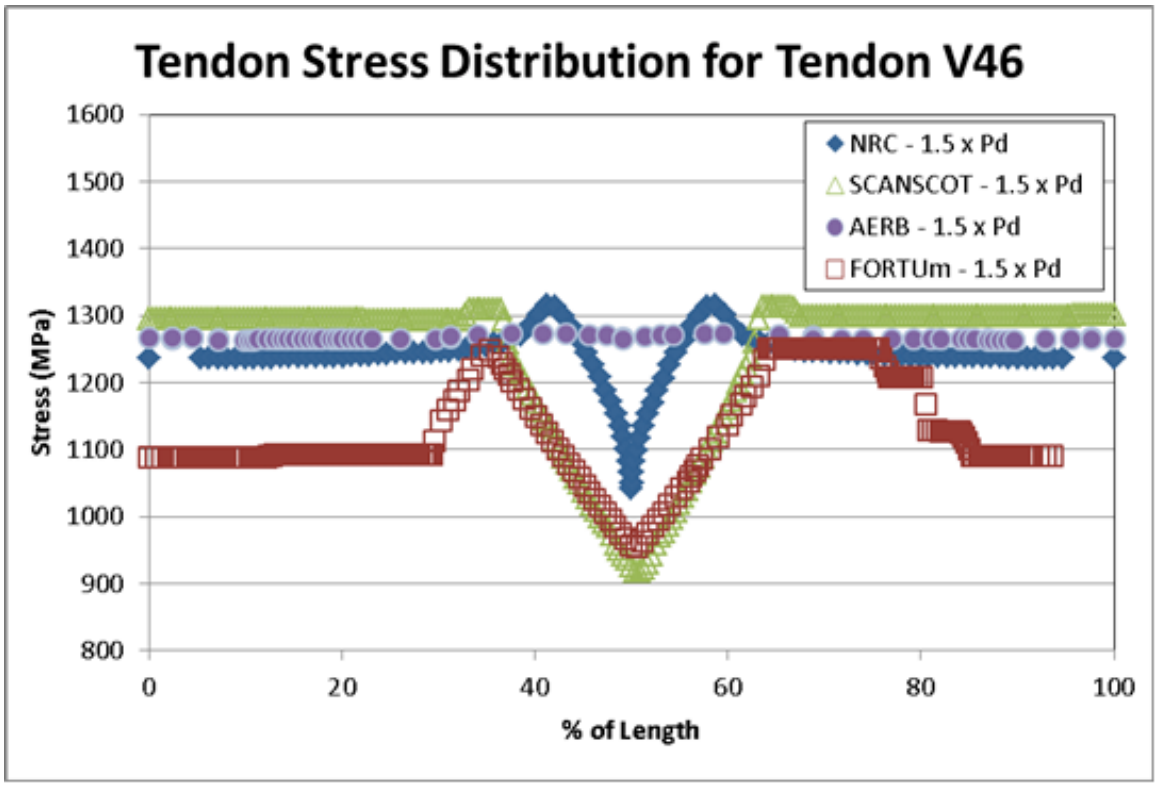

Figure 316: Tendon Stress Distribution for Tendon #V46 at 1.5 x P_d

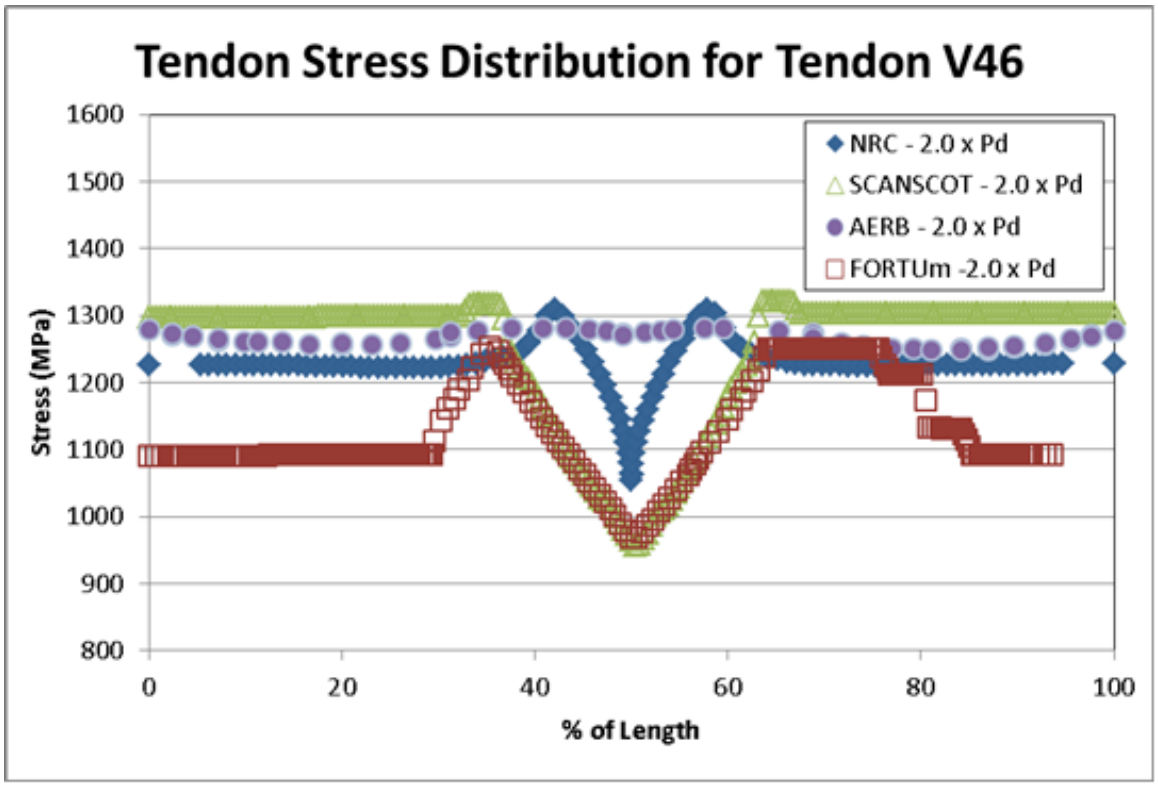

Figure 317: Tendon Stress Distribution for Tendon #V46 at 2.0 x P_d

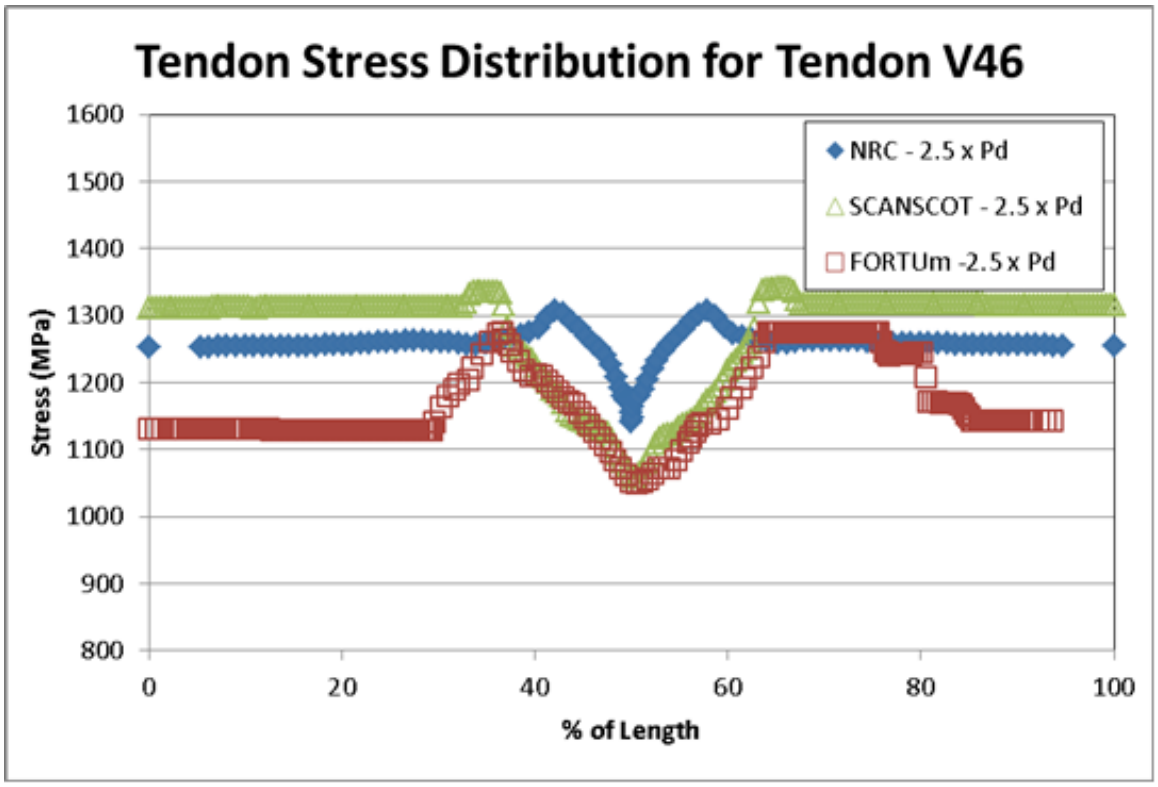

Figure 318: Tendon Stress Distribution for Tendon #V46 at 2.5 x P_d

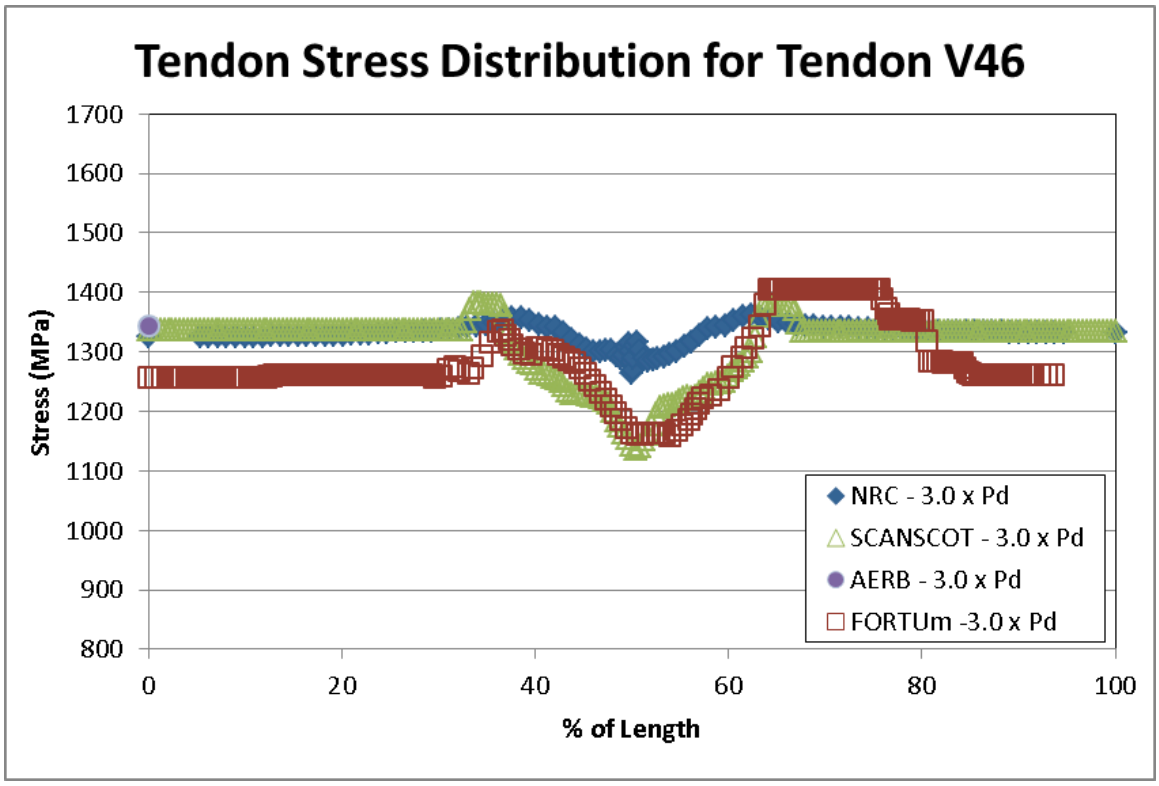

Figure 319: Tendon Stress Distribution for Tendon #V46 at 3.0 x P_d

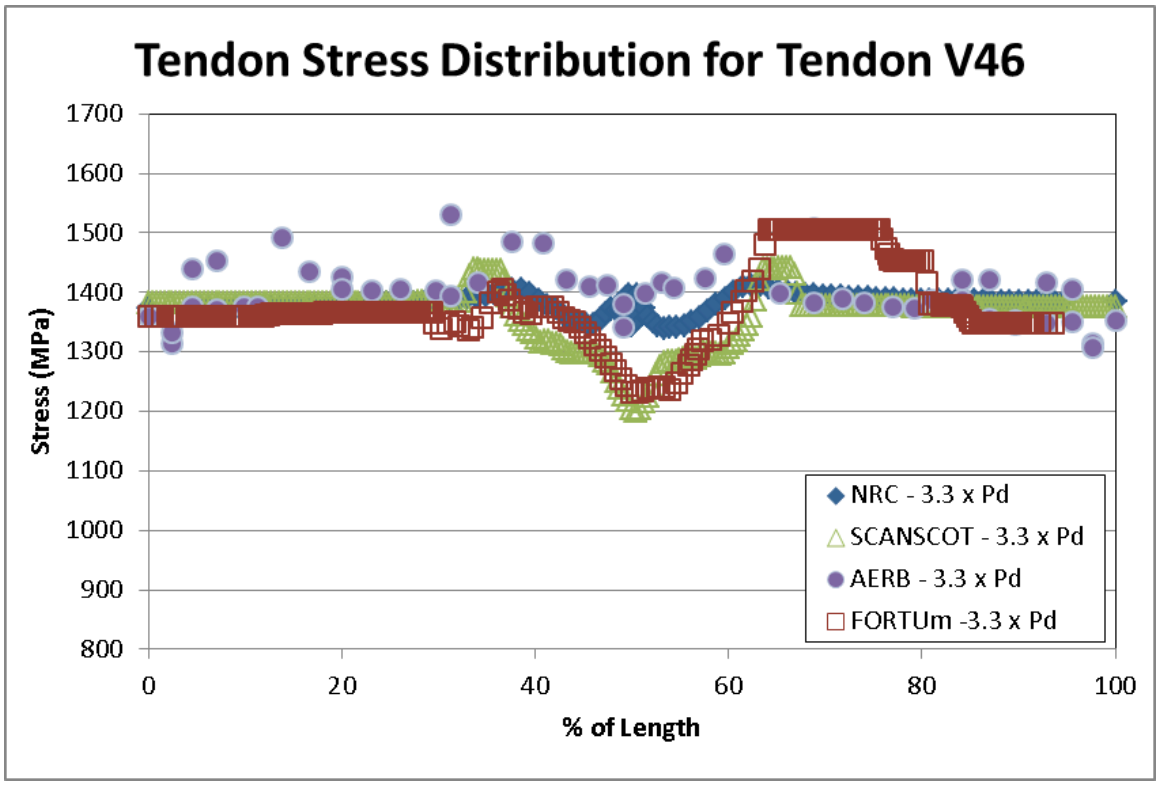

Figure 320: Tendon Stress Distribution for Tendon #V46 at 3.3 x P_d

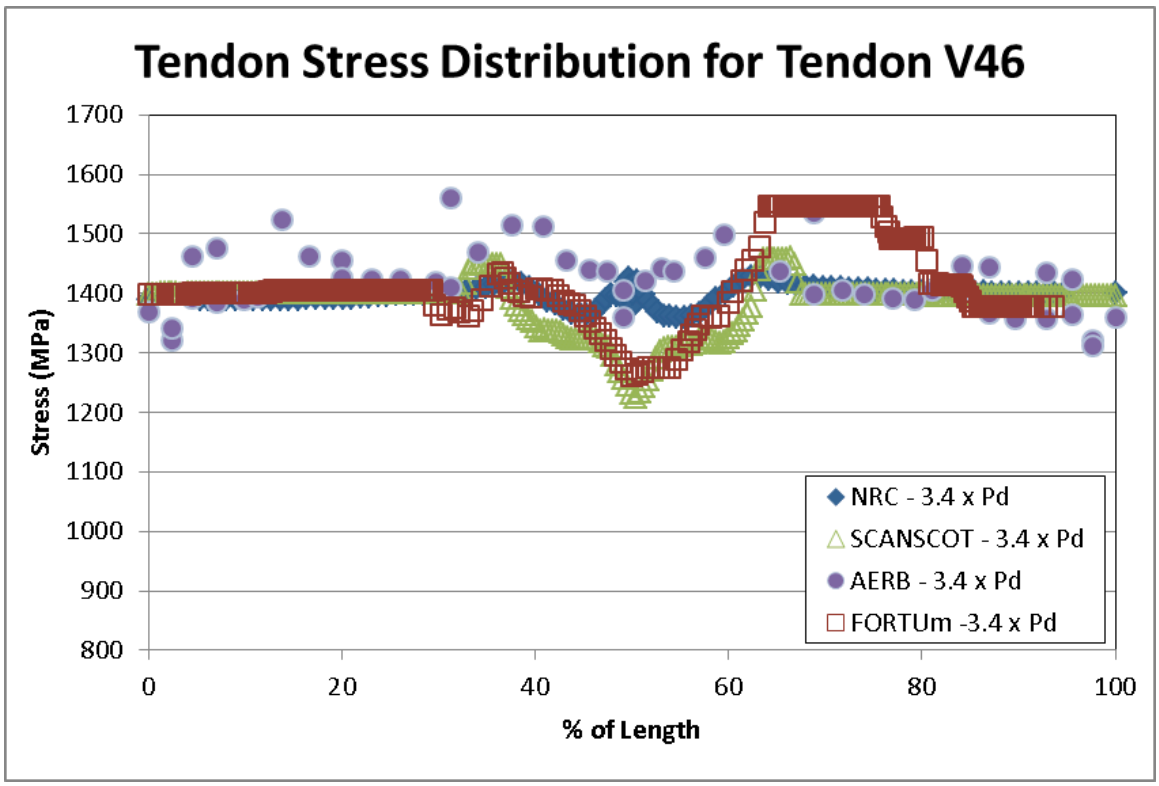

Figure 321: Tendon Stress Distribution for Tendon #V46 at 3.4 x P_d

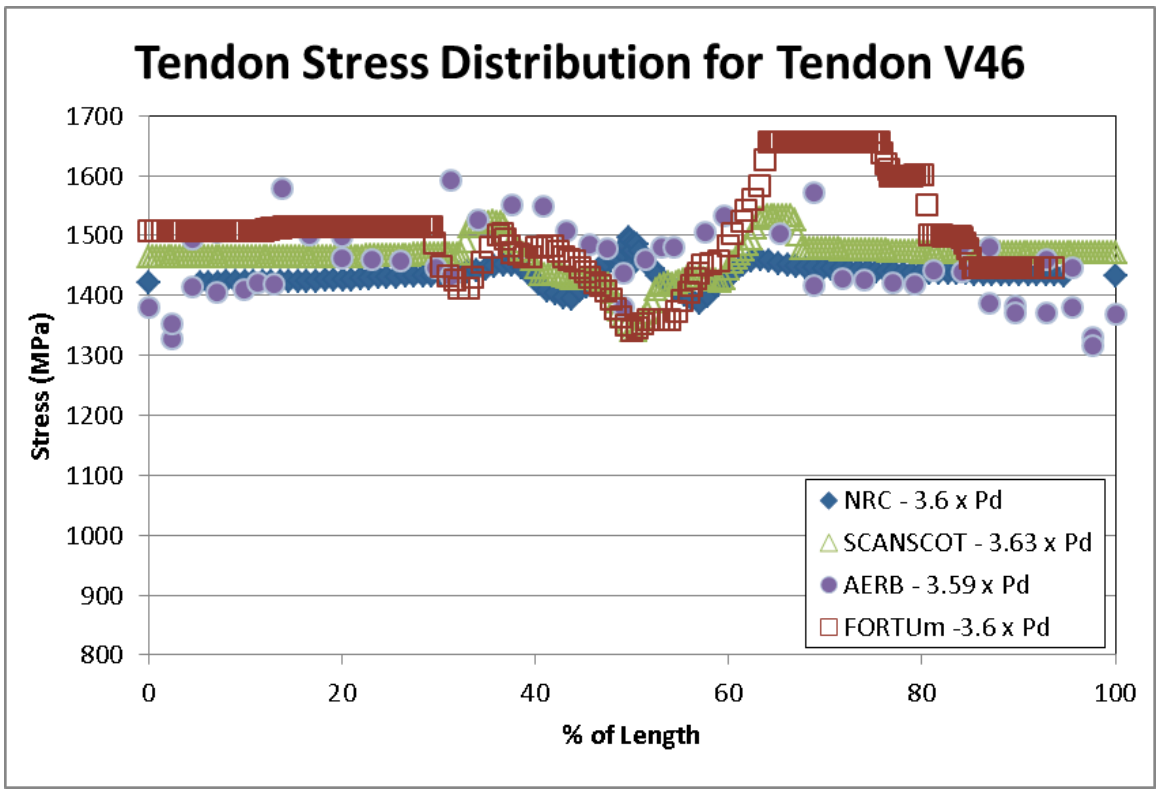

Figure 322: Tendon Stress Distribution for Tendon #V46 at Ultimate Pressure

4.6. Standard Output Location Comparisons

This section of the report compares the modeled results from the participants with the standard output locations (SOLs) from the PCCV test. This section serves to provide the most direct comparison to the experimental results and is therefore considered very valuable for evaluating the modeling of the participants.

4.6.1. Displacements

The first 15 SOLs involve displacement measurements both in the radial and meridional directions. The nature of the displacement is indicated in the figure caption for each figure in this section and the plots comparing the participants data with test data for SOLs 1-15 can be found in Figure 323 through Figure 337. As before, the participants' data agree well with test data, particularly well at the lower pressure levels. As the internal pressure approaches the failure level more divergence both between the participants and between the modeled and test data is noted.

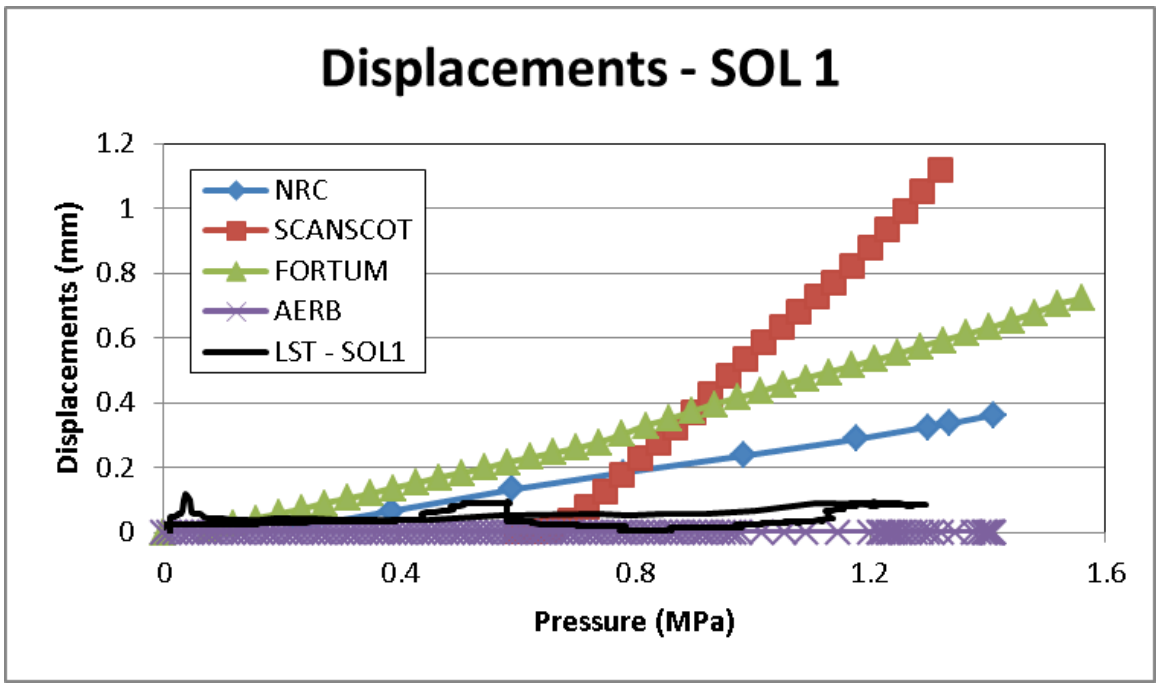

Figure 323: Displacement Versus Pressure at SOL #1 (Vertical Displacement at Top of Basemat)

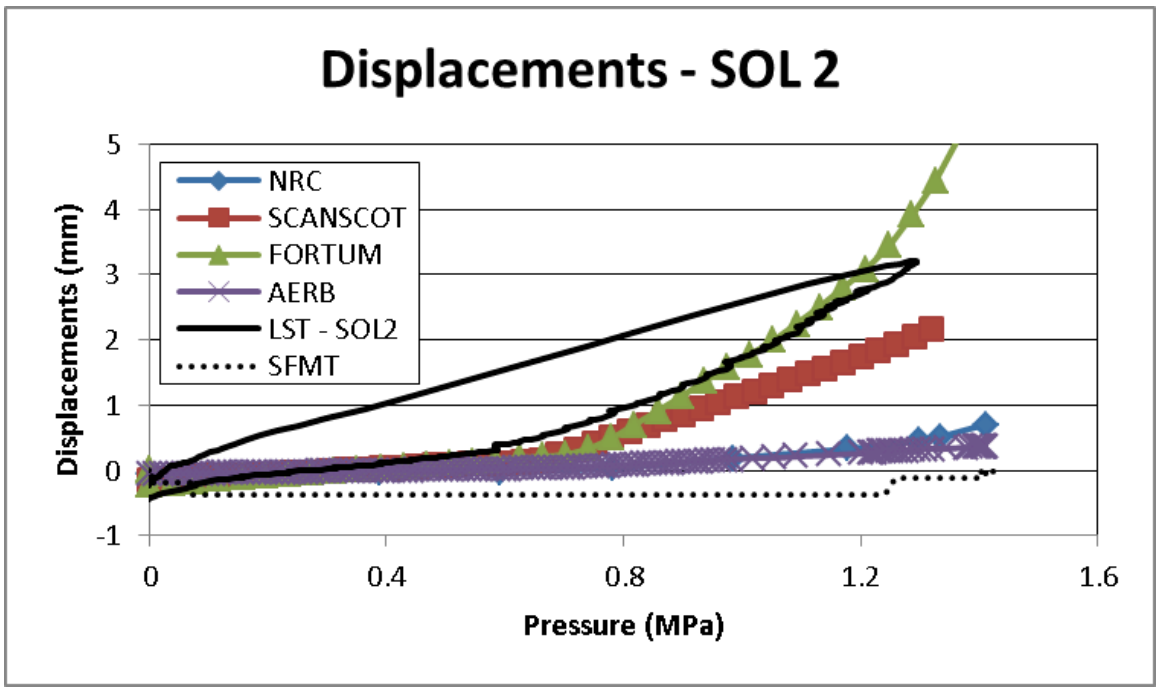

Figure 324: Displacement Versus Pressure at SOL #2 (Radial Displacement at Base of Cylinder)

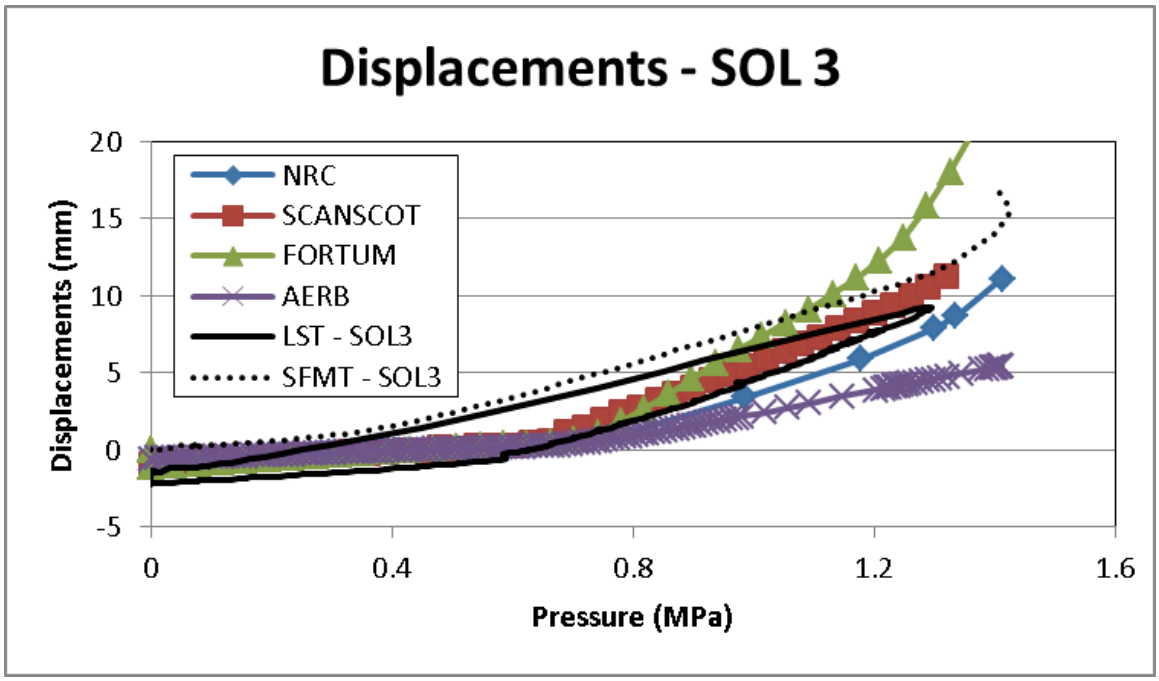

Figure 325: Displacement Versus Pressure at SOL #3 (Radial Displacement at Base of Cylinder)

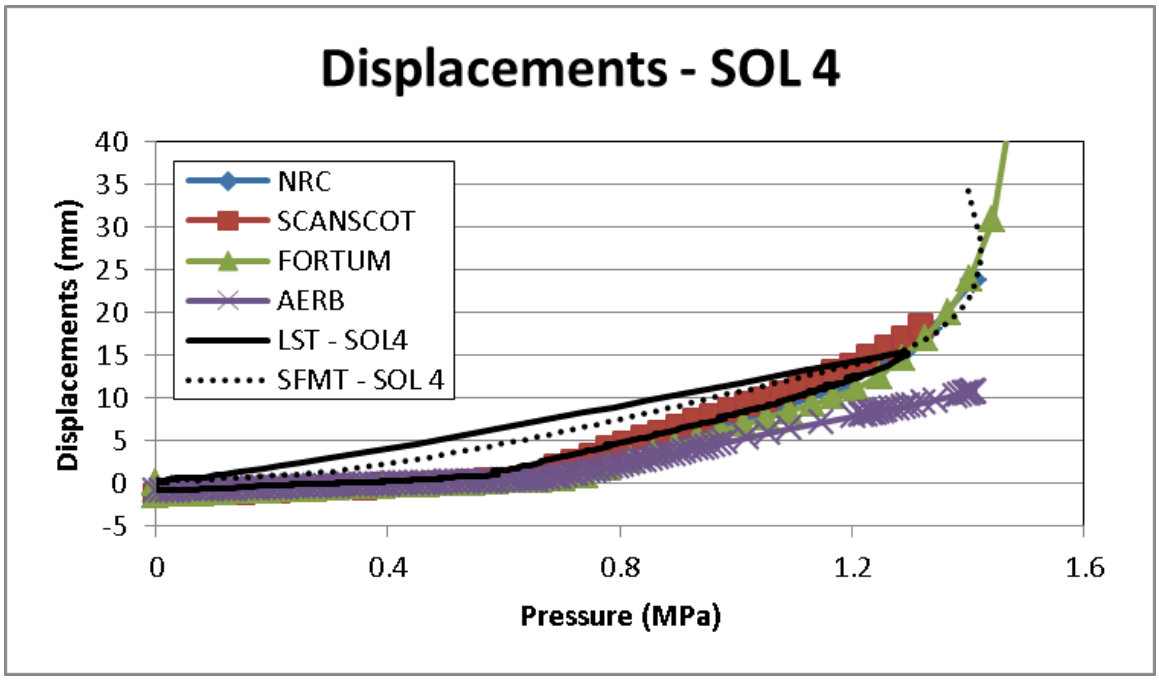

Figure 326: Displacement Versus Pressure at SOL #4 (Radial Displacement at Base of Cylinder)

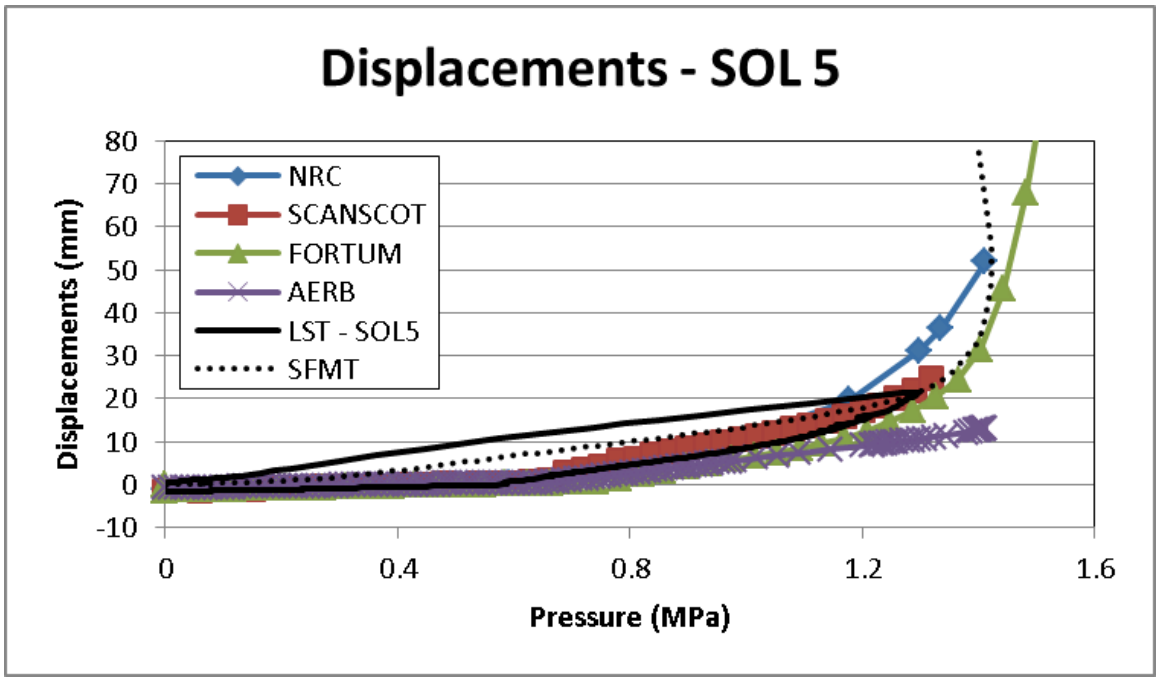

Figure 327: Displacement Versus Pressure at SOL #5 (Radial Displacement at E/H Elevation)

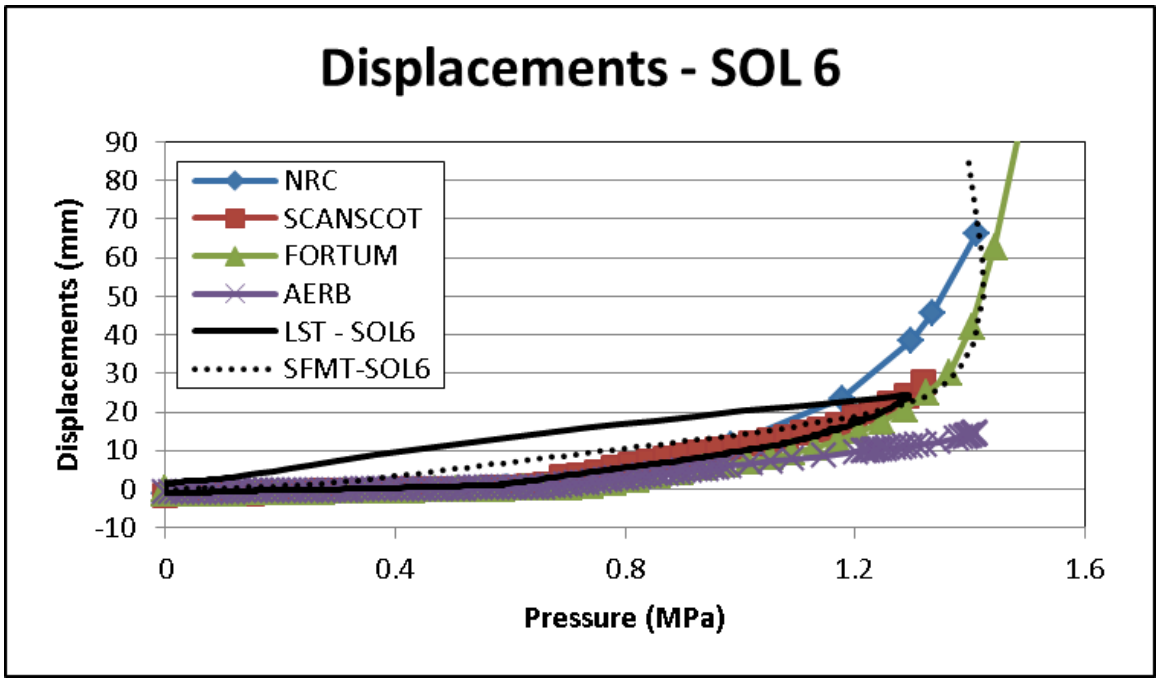

Figure 328: Displacement Versus Pressure at SOL #6 (Radial Displacement at Midheight)

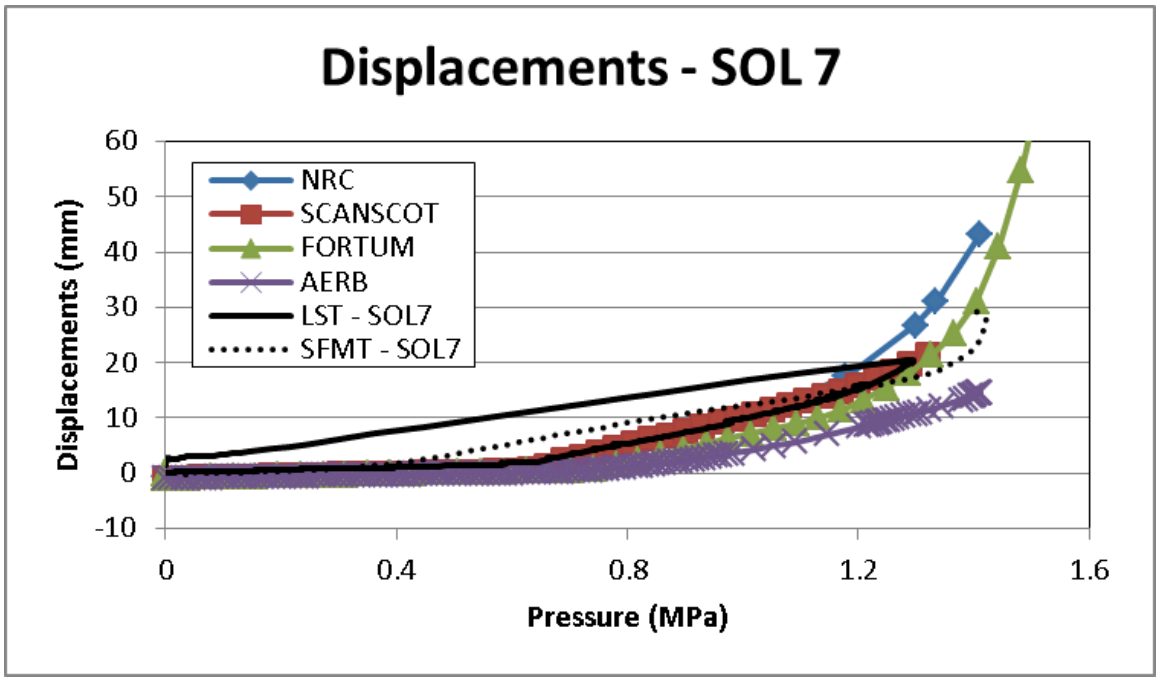

Figure 329: Displacement Versus Pressure at SOL #7 (Radial Displacement at Springline)

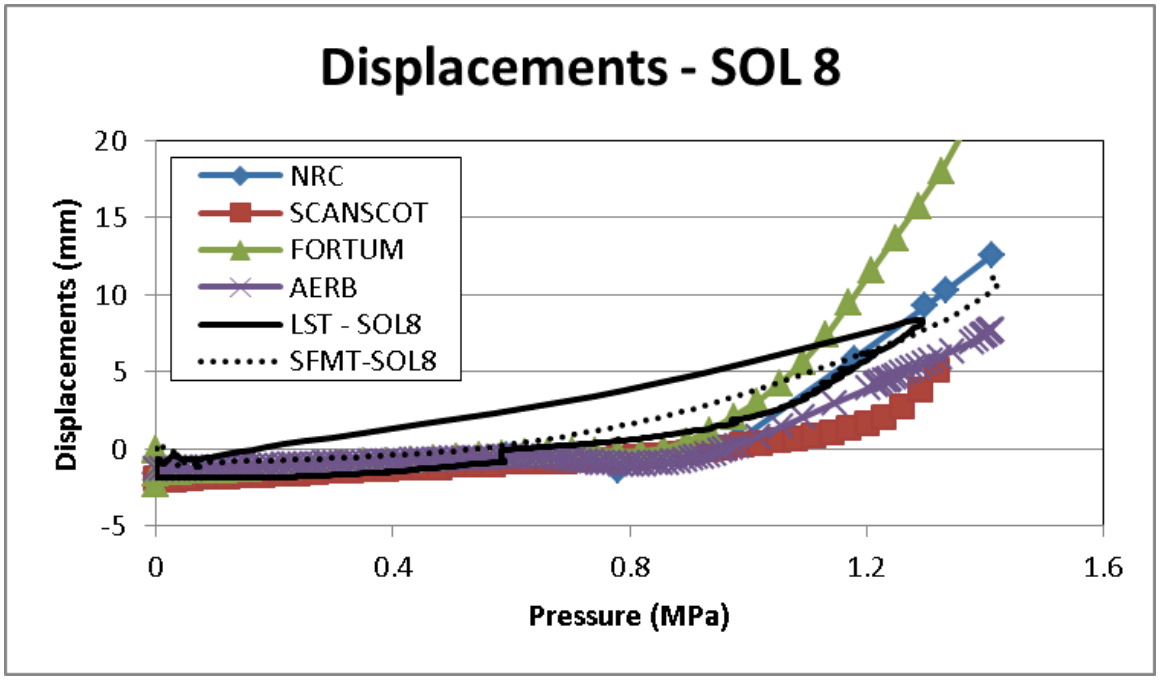

Figure 330: Displacement Versus Pressure at SOL #8 (Vertical Displacement at Springline)

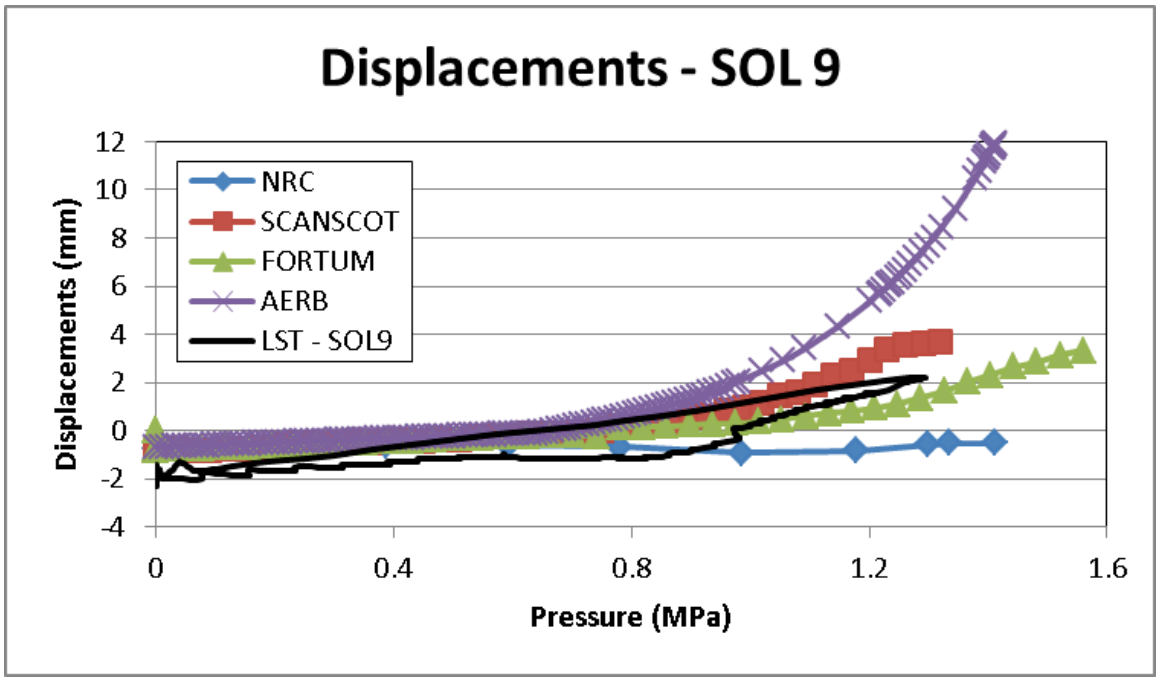

Figure 331: Displacement Versus Pressure at SOL #9 (Radial Displacement at Dome 45°)

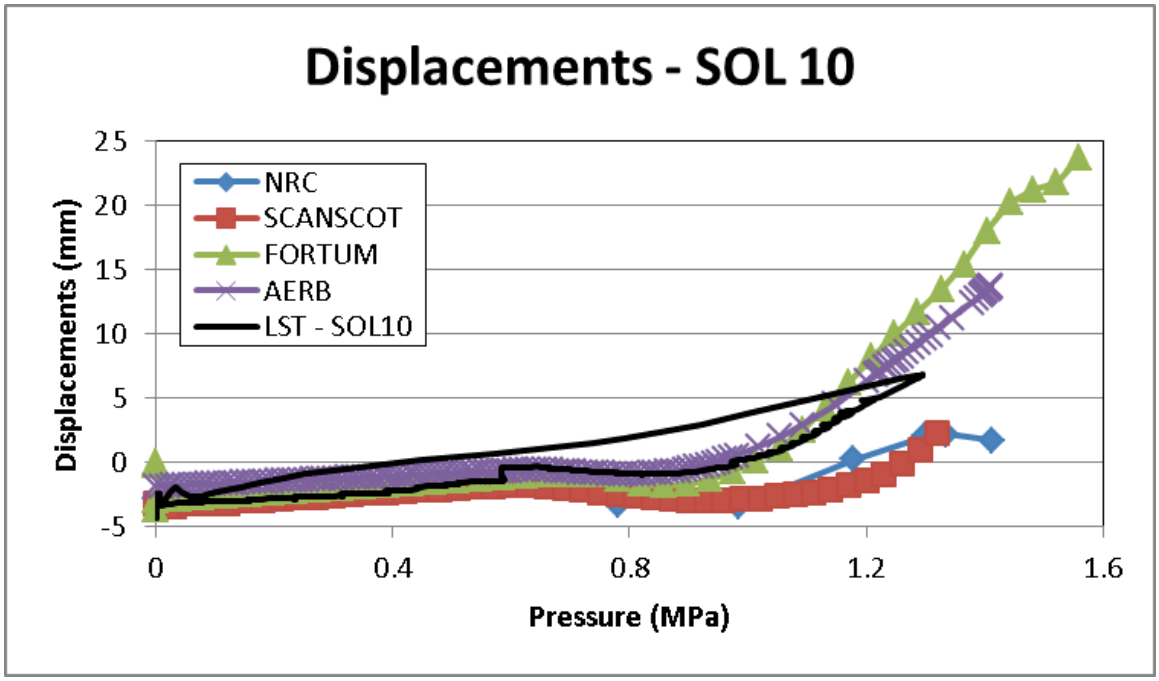

Figure 332: Displacement Versus Pressure at SOL #10 (Vertical Displacement at Dome 45°)

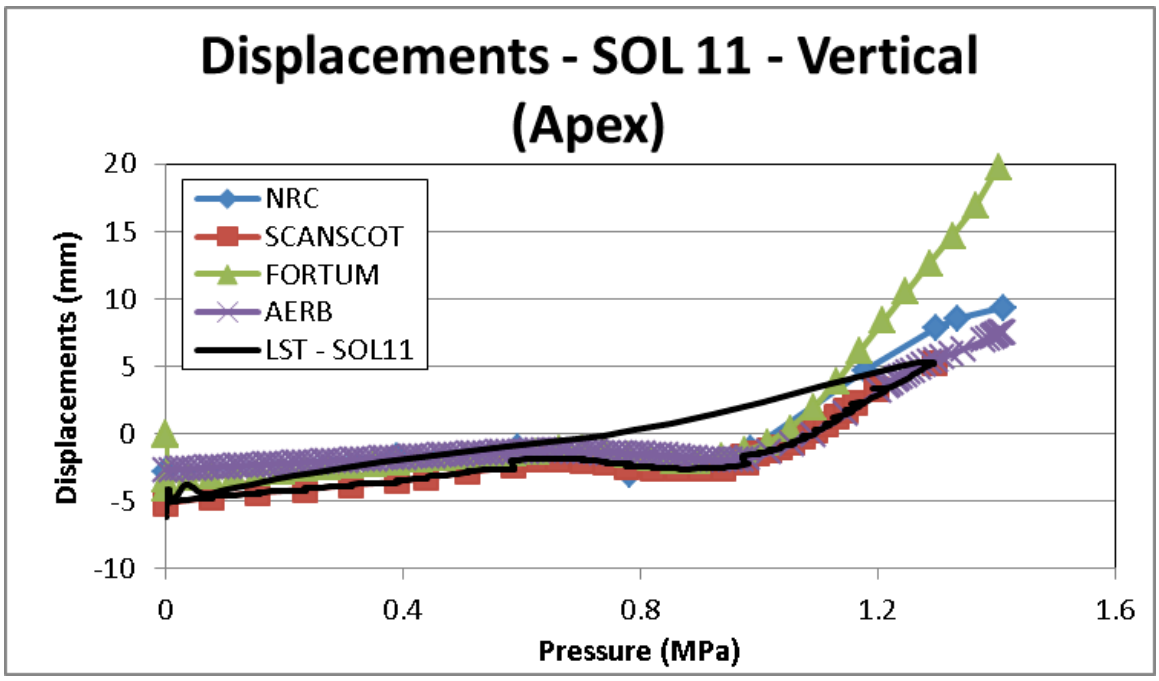

Figure 333: Displacement Versus Pressure at SOL #11 (Vertical Displacement at Dome Apex)

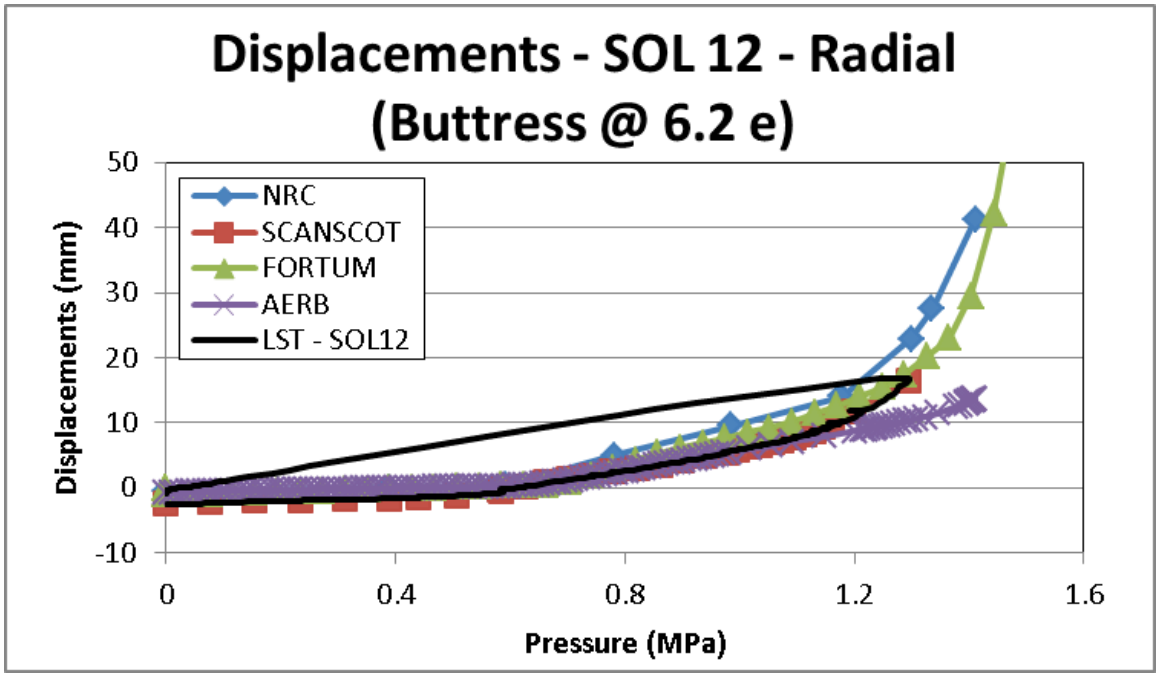

Figure 334: Displacement Versus Pressure at SOL #12 (Radial Displacement at Midheight of Buttress)

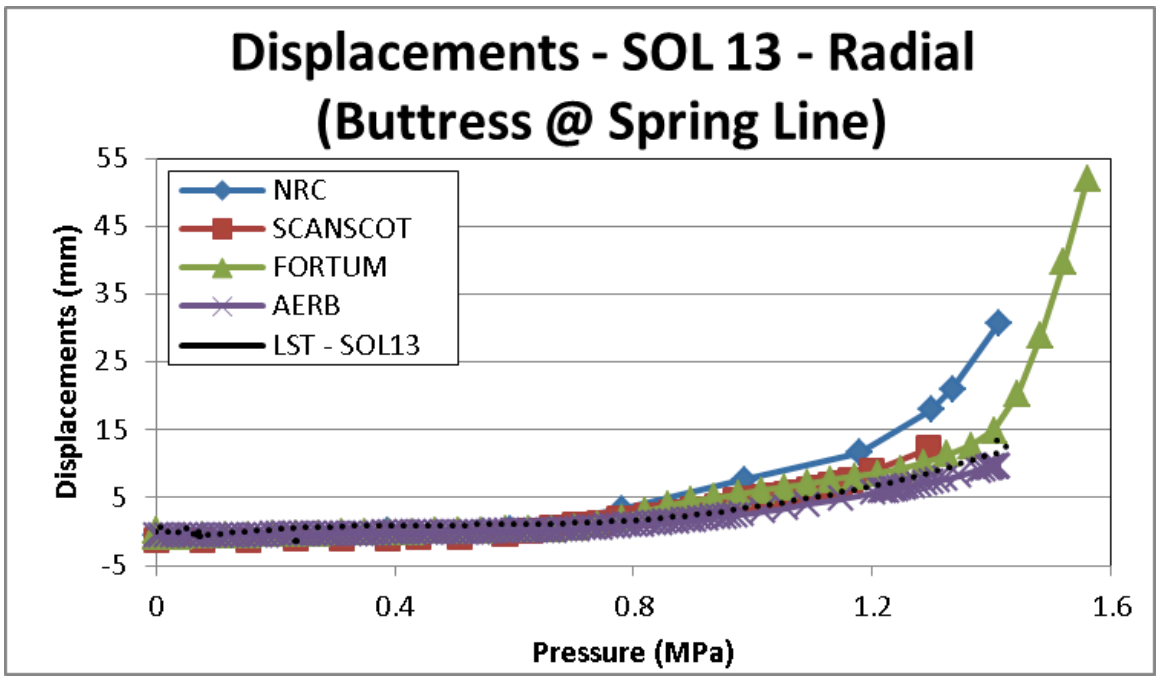

Figure 335: Displacement Versus Pressure at SOL #13 (Radial Displacement at Springline of Buttress)

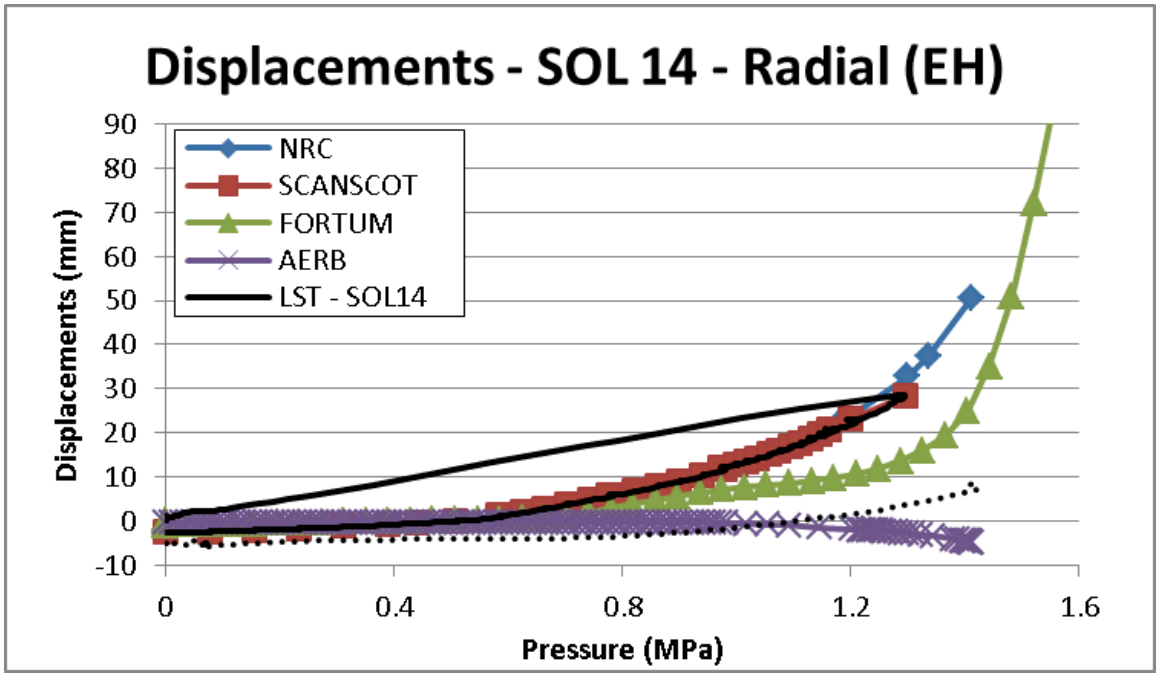

Figure 336: Displacement Versus Pressure at SOL #14 (Radial Displacement at Center of E/H)

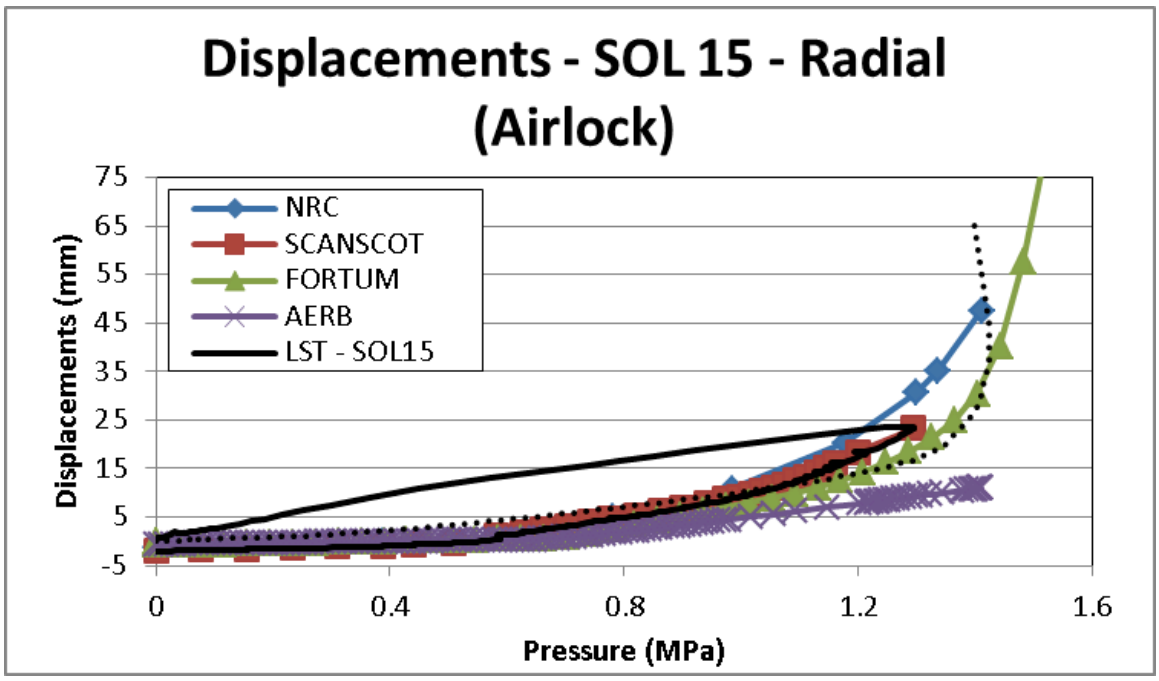

Figure 337: Displacement Versus Pressure at SOL #15 (Radial Displacement at Center of A/L)

4.6.2. Rebar Strains

The participants were asked to report results for rebar strains at locations SOL 22-29. FORTUM and AERB reported results for SOL 16-21 and 30-33. These results have been included as well. The rebar strain modeling results were generally good for the requested SOLs and somewhat less so for the additional points provided by FORTUM and by AERB. The rebar SOL comparison plots can be found in Figure 338 through Figure 355.

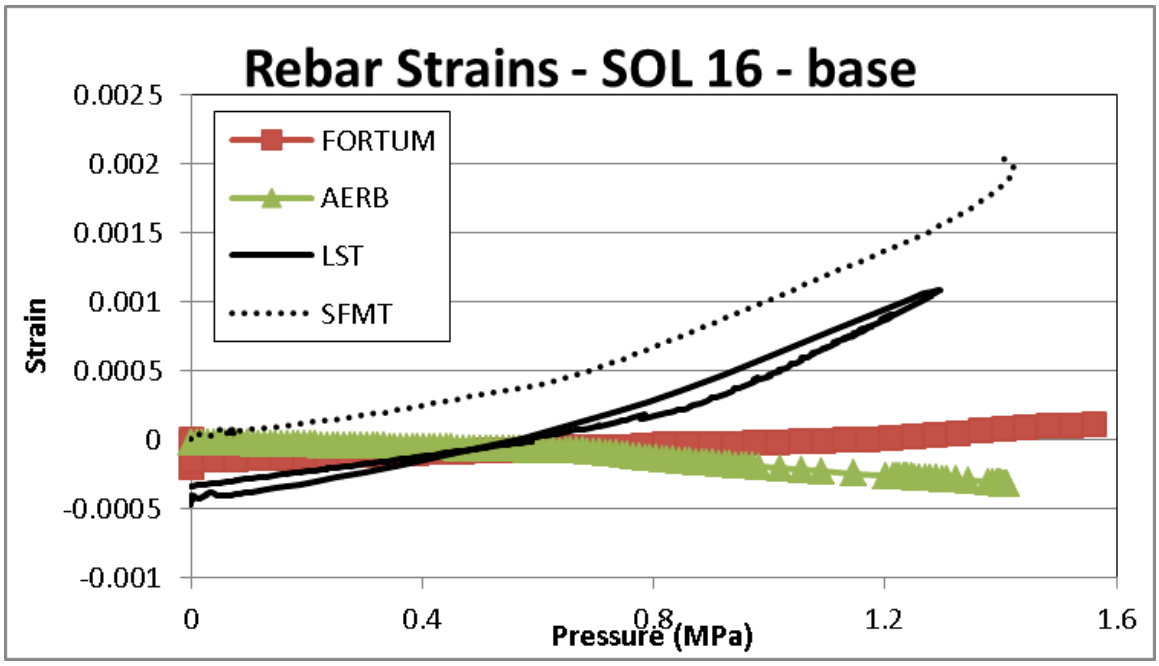

Figure 338: Rebar Strain Versus Pressure at SOL #16

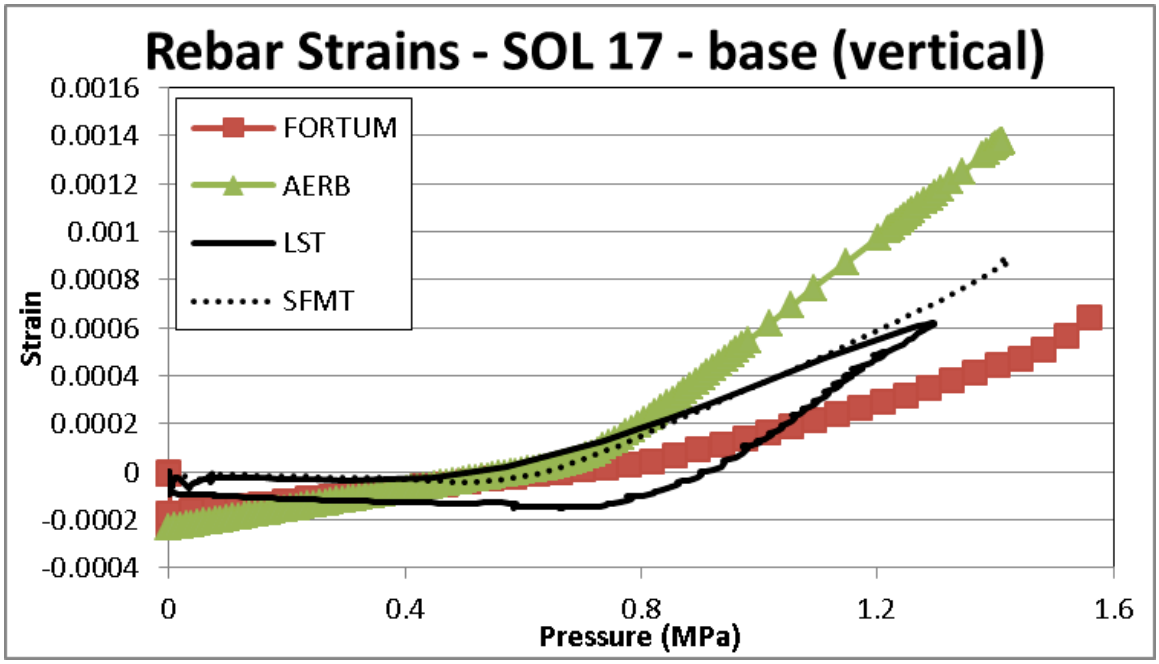

Figure 339: Rebar Strain Versus Pressure at SOL #17

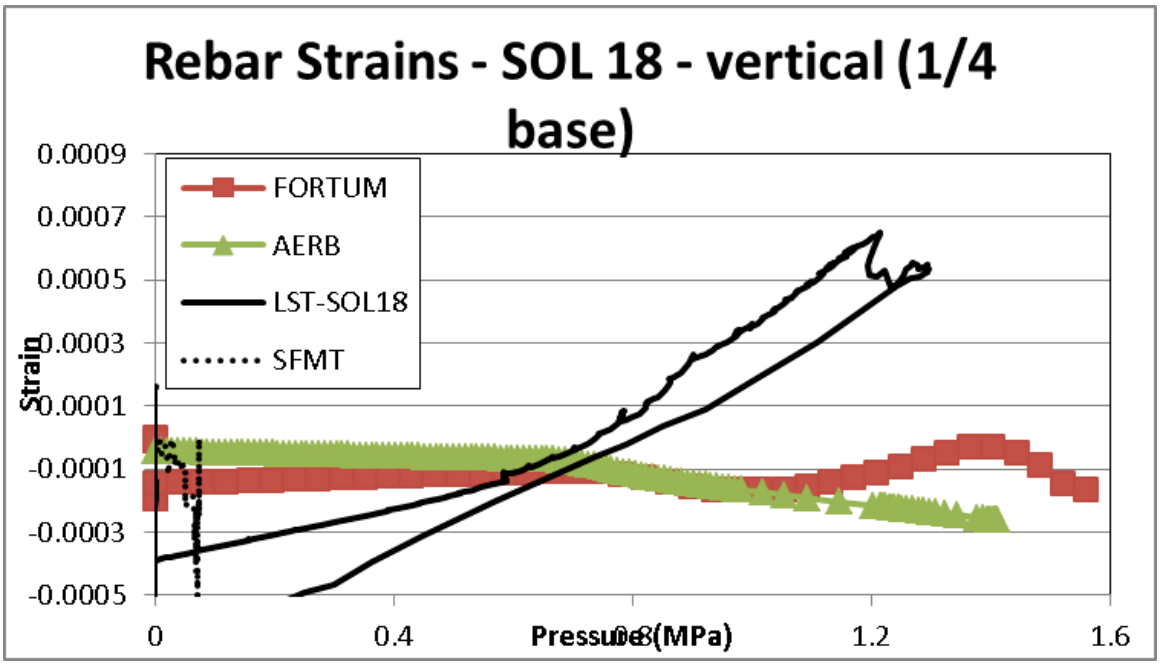

Figure 340: Rebar Strain Versus Pressure at SOL #18

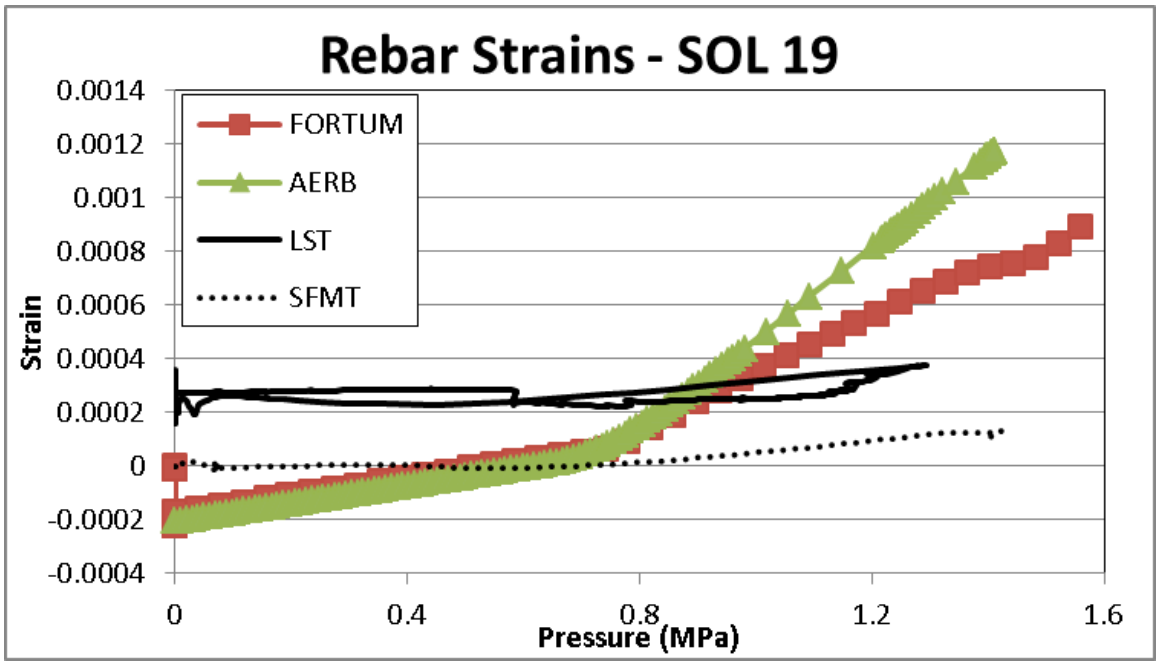

Figure 341: Rebar Strain Versus Pressure at SOL #19

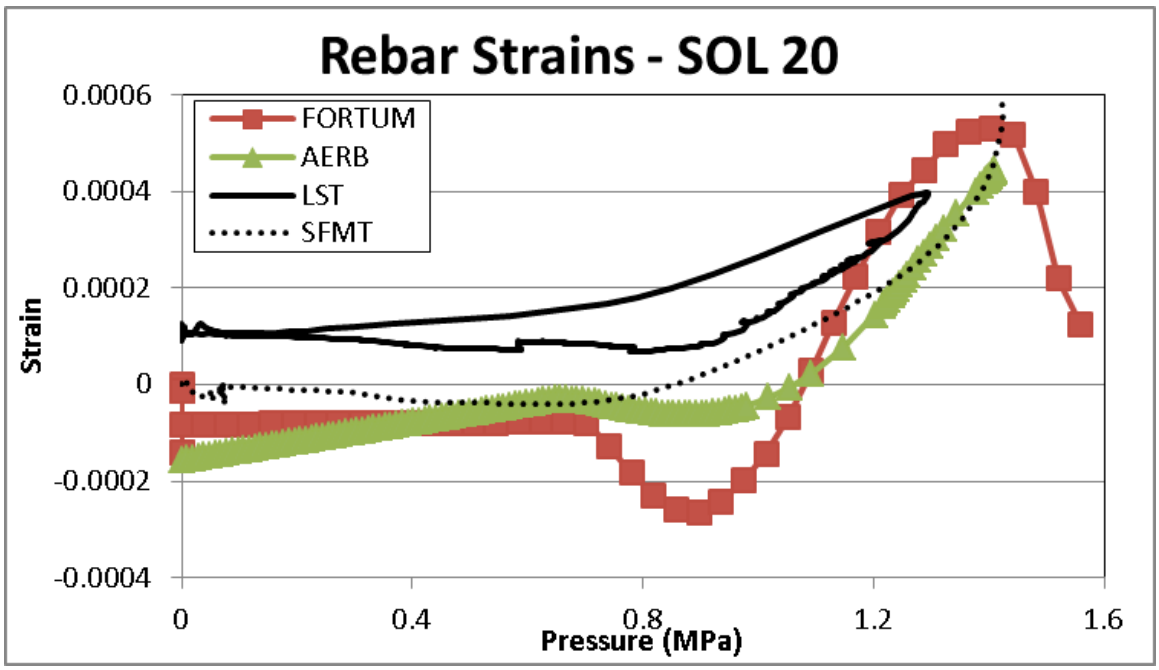

Figure 342: Rebar Strain Versus Pressure at SOL #20

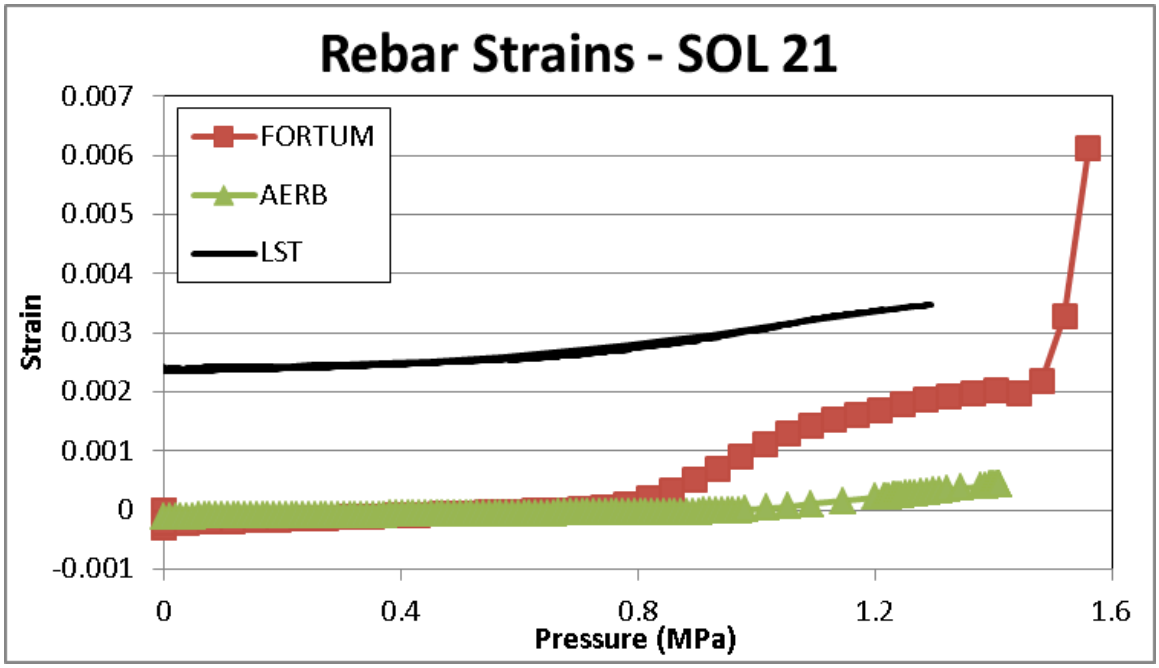

Figure 343: Rebar Strain Versus Pressure at SOL #21

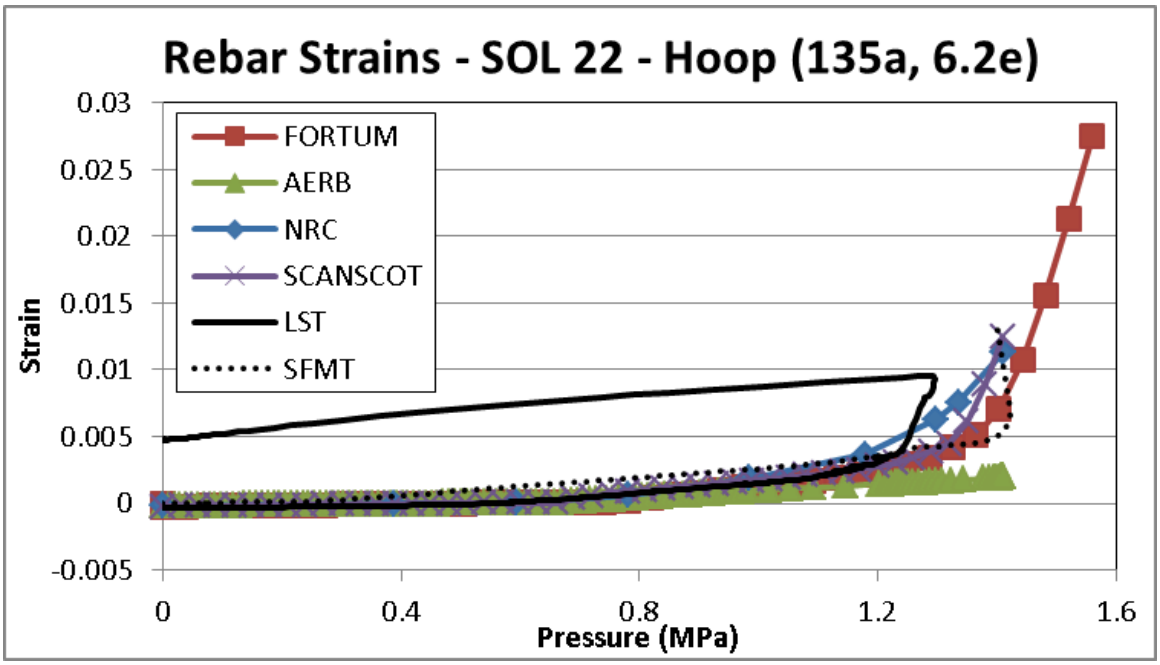

Figure 344: Rebar Strain Versus Pressure at SOL #22 (Hoop Strain of Outer Rebar at Midheight)

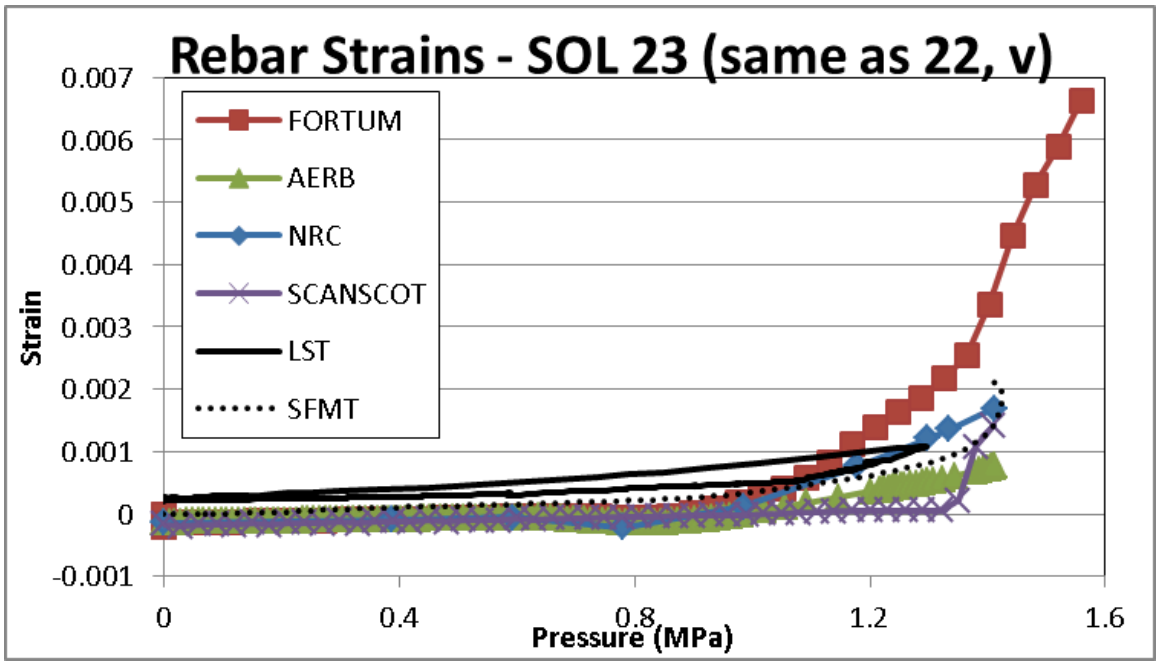

Figure 345: Rebar Strain Versus Pressure at SOL #23 (Meridional Strain of Outer Rebar at Midheight)

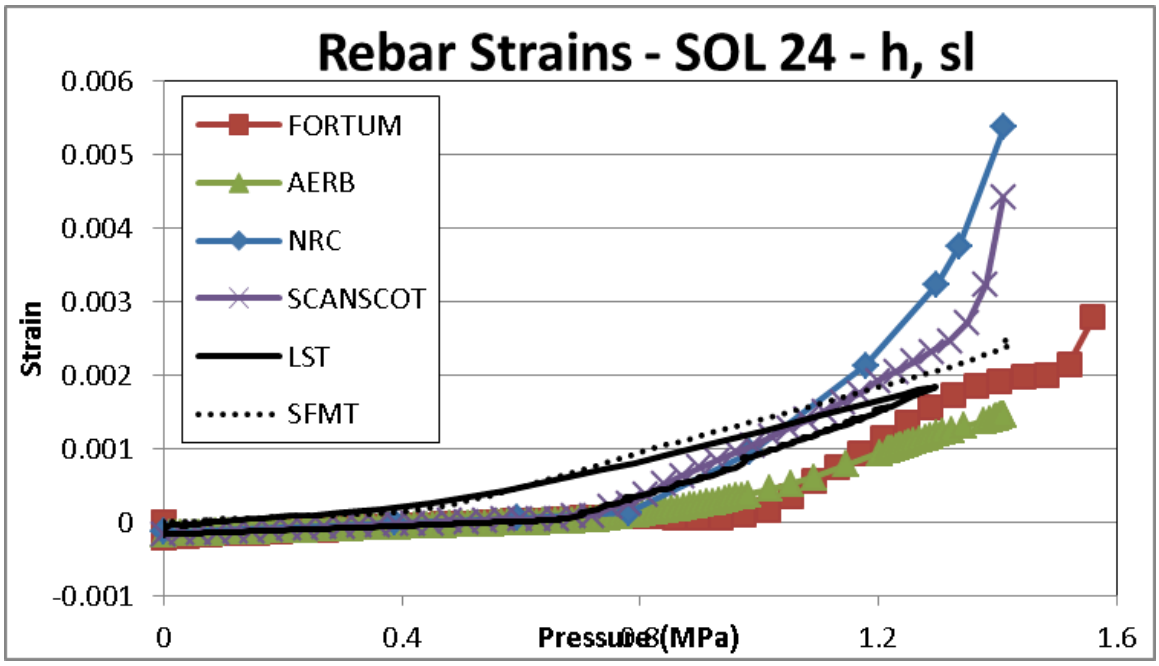

Figure 346: Rebar Strain Versus Pressure at SOL #24 (Hoop Strain of Outer Rebar at Springline)

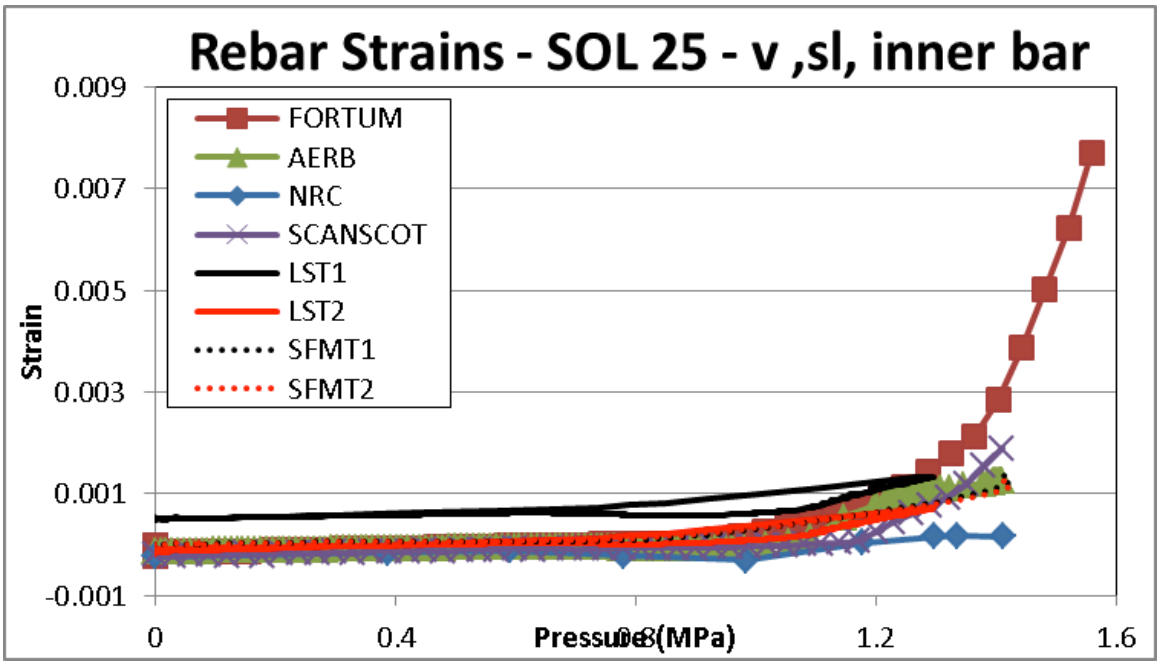

Figure 347: Rebar Strain Versus Pressure at SOL #25 (Meridional Strain of Inner Rebar at Springline)

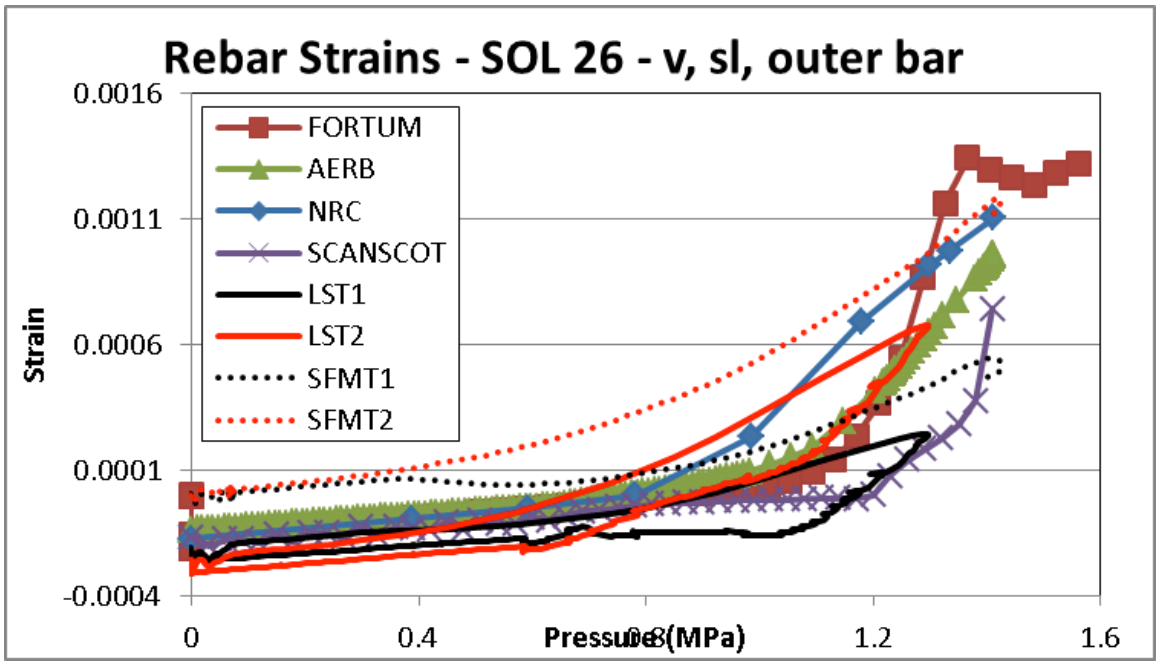

Figure 348: Rebar Strain Versus Pressure at SOL #26 (Meridional Strain of Outer Rebar at Springline)

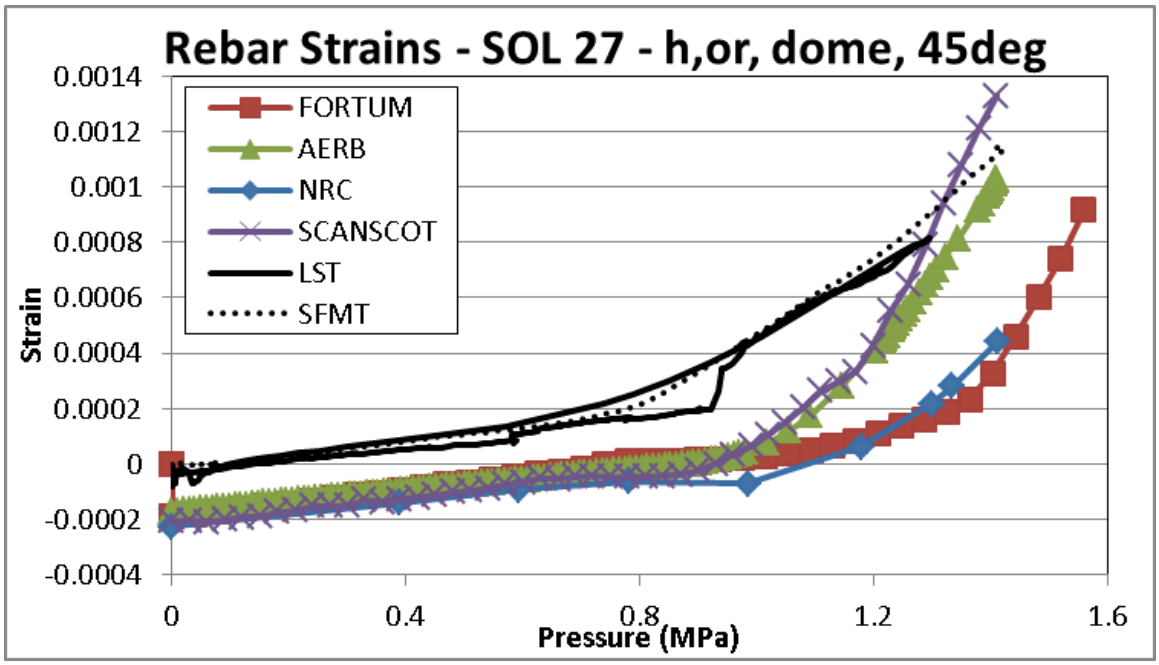

Figure 349: Rebar Strain Versus Pressure at SOL #27 (Hoop Strain of Outer Rebar at Dome 45°)

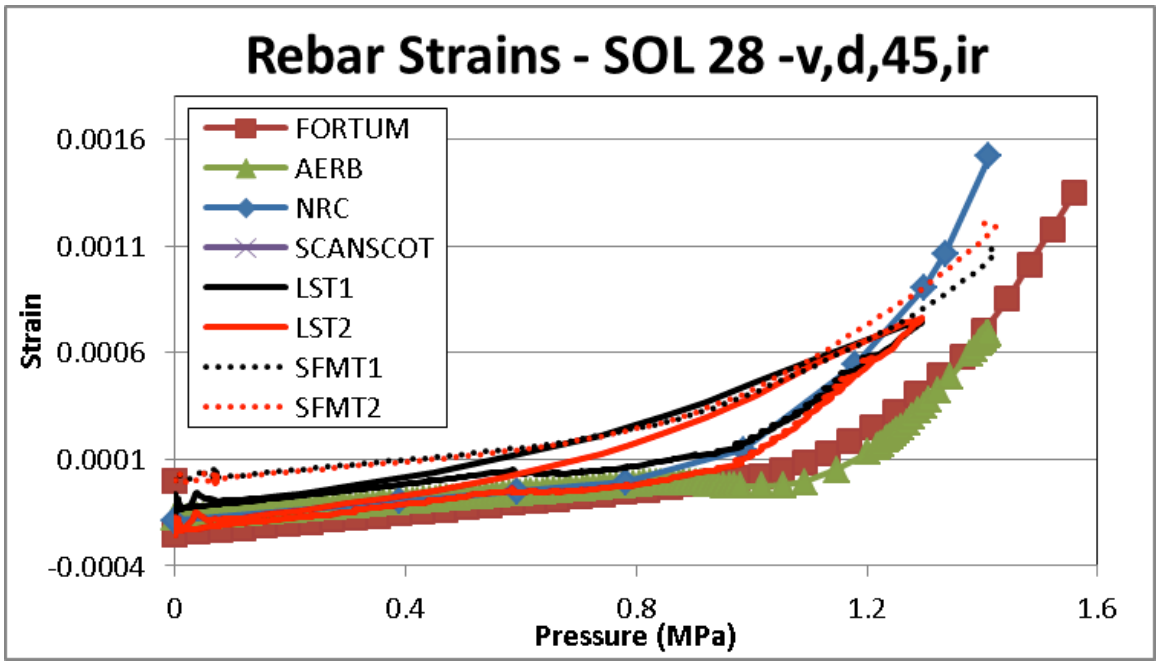

Figure 350: Rebar Strain Versus Pressure at SOL #28 (Meridional Strain of Inner Rebar at Dome 45°)

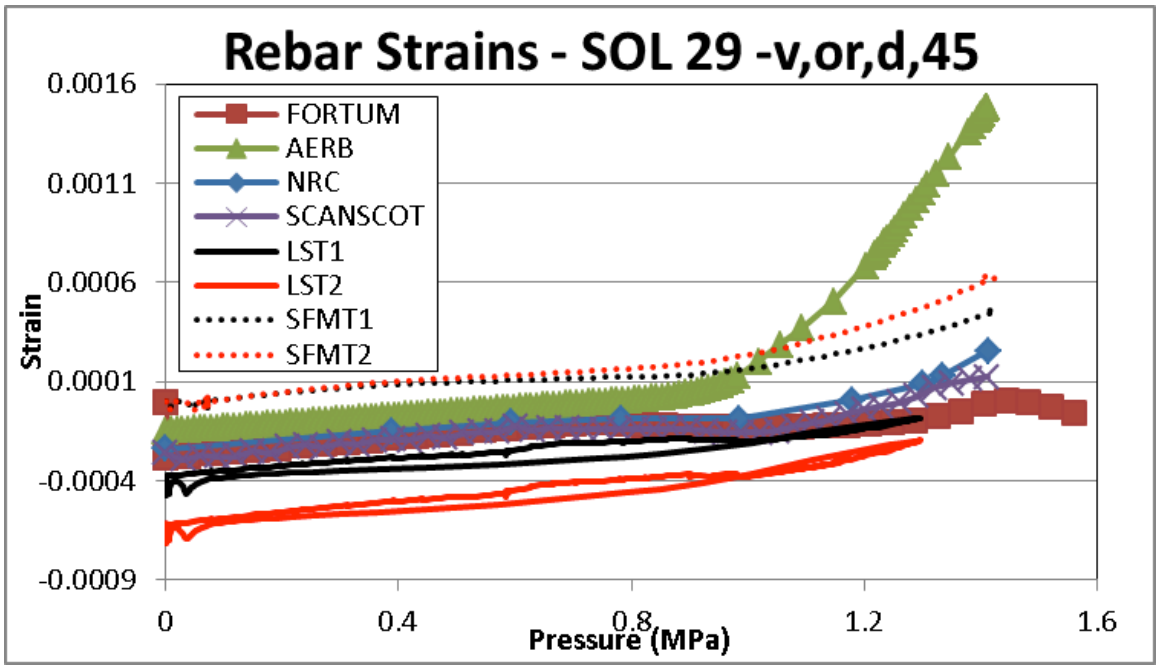

Figure 351: Rebar Strain Versus Pressure at SOL #29 (Meridional Strain of Outer Rebar at Dome 45°)

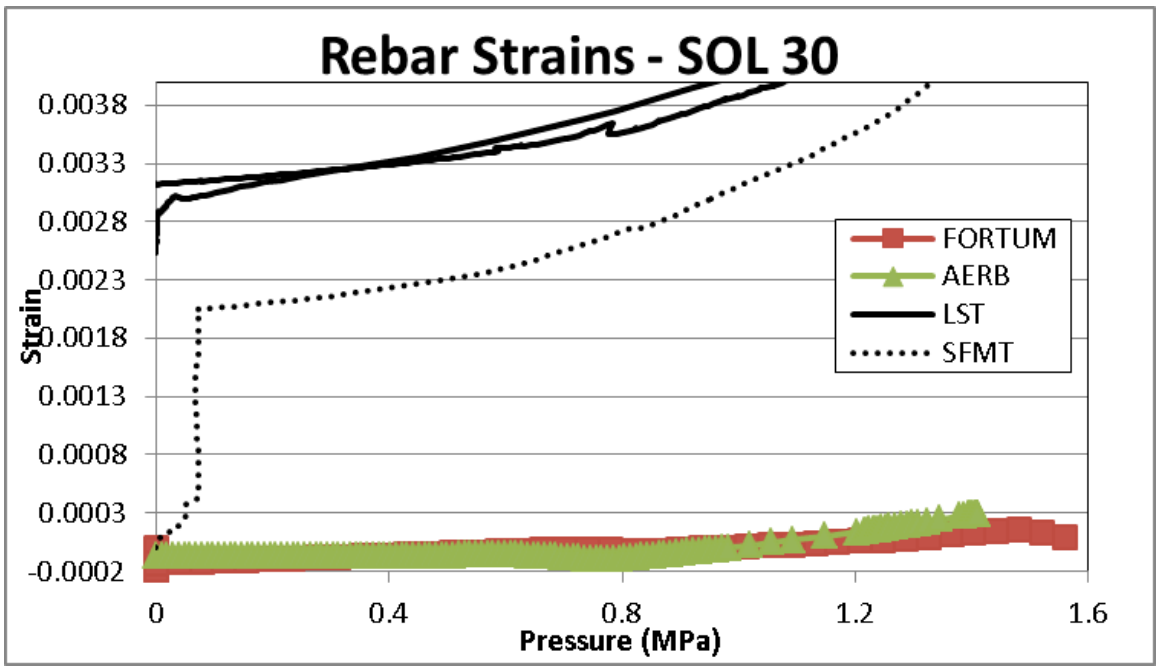

Figure 352: Rebar Strain Versus Pressure at SOL #30

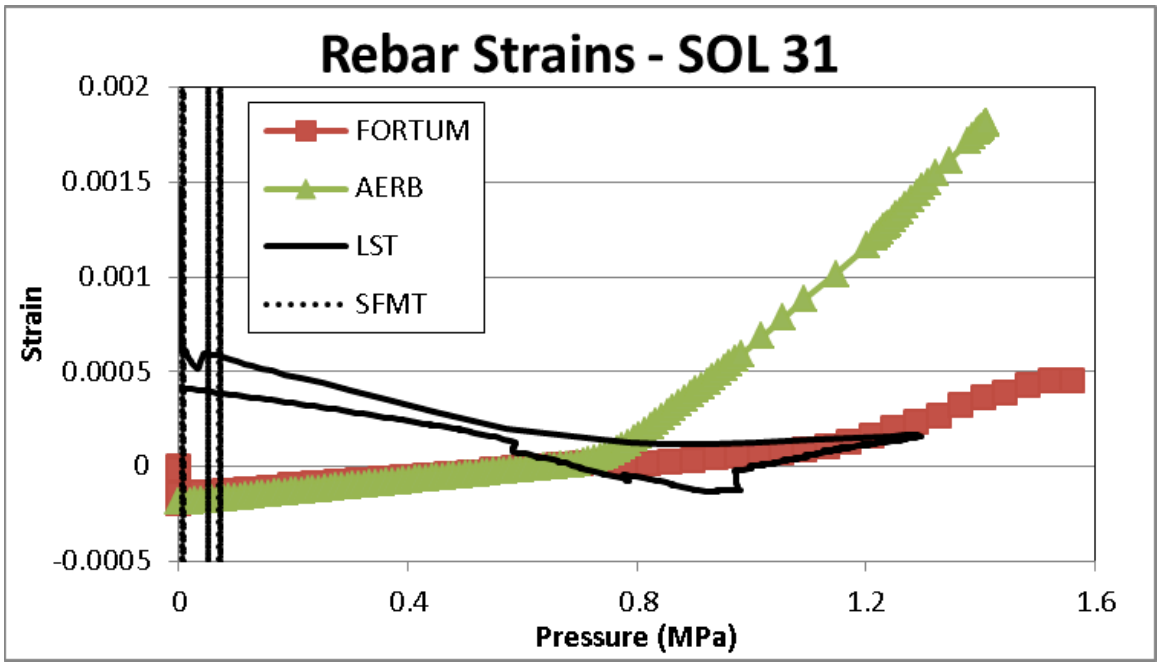

Figure 353: Rebar Strain Versus Pressure at SOL #31

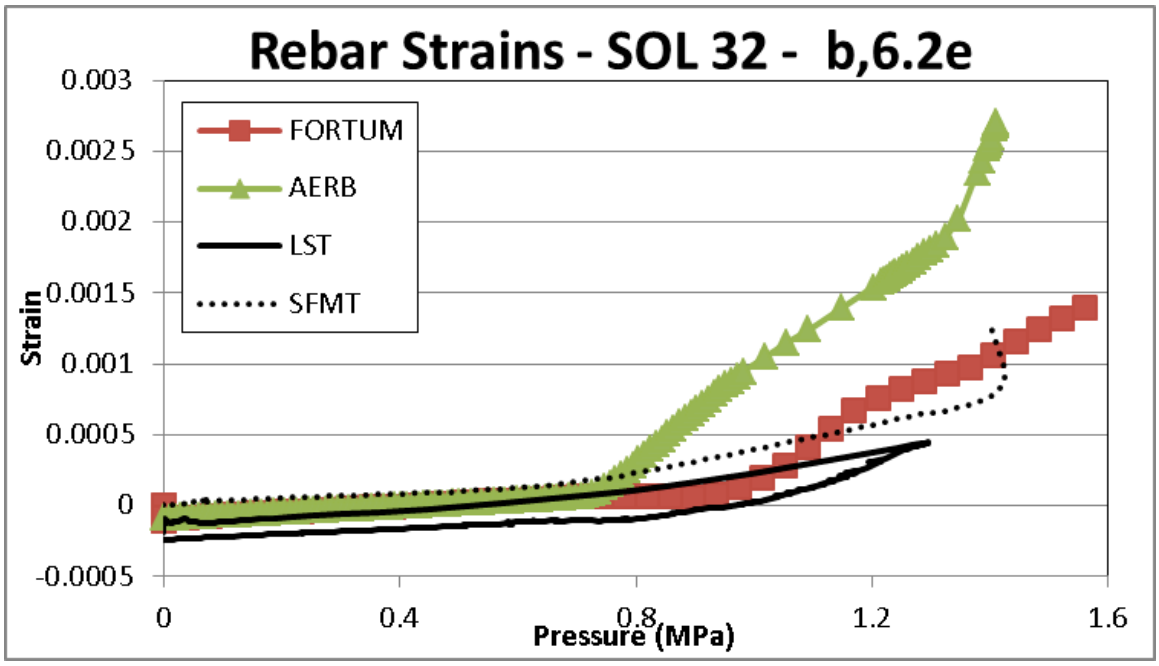

Figure 354: Rebar Strain Versus Pressure at SOL #32

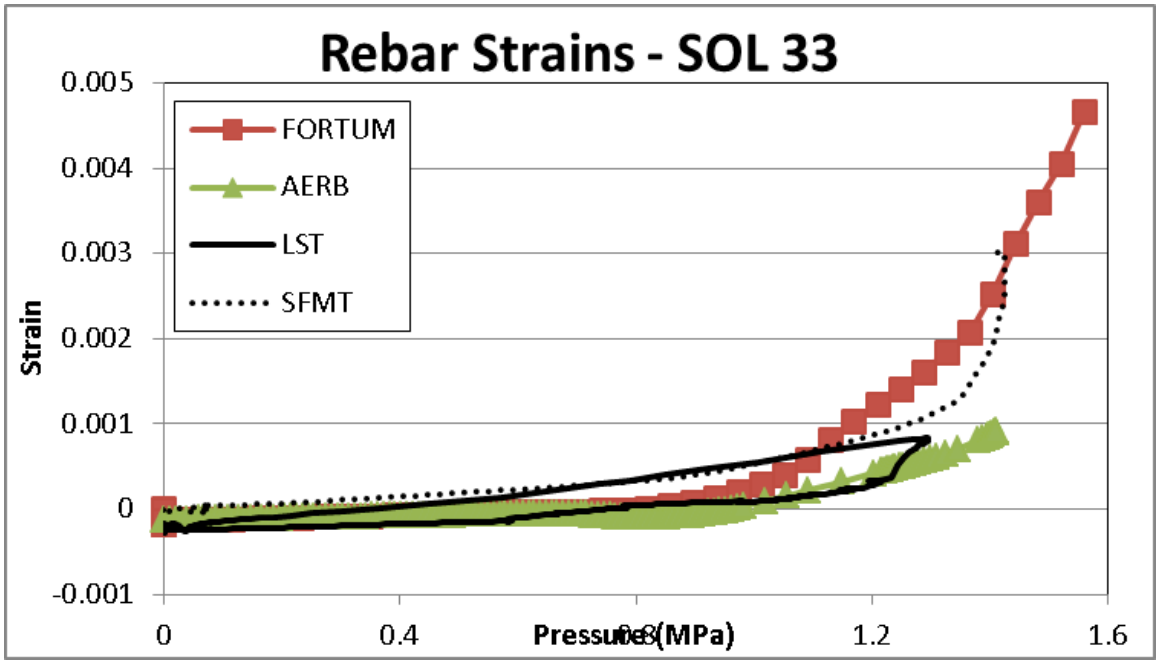

Figure 355: Rebar Strain Versus Pressure at SOL #33

4.6.3. Liner Strains

The participants were asked to report liner strains at locations SOL 36-42. FORTUM and AERB also reported results at SOL 34-35 and 43-46. These comparisons have been included. The comparison plots for the liner strain data and for the modeled results are presented in Figure 356 through Figure 368.

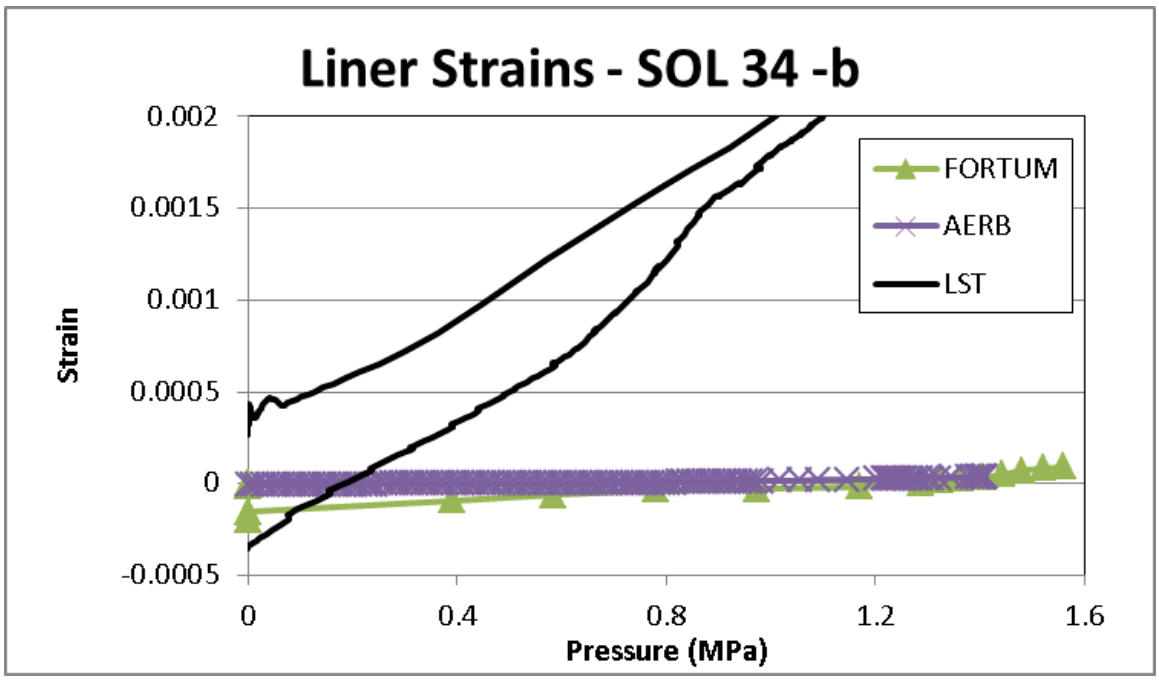

Figure 356: Liner Strain Versus Pressure at SOL #34

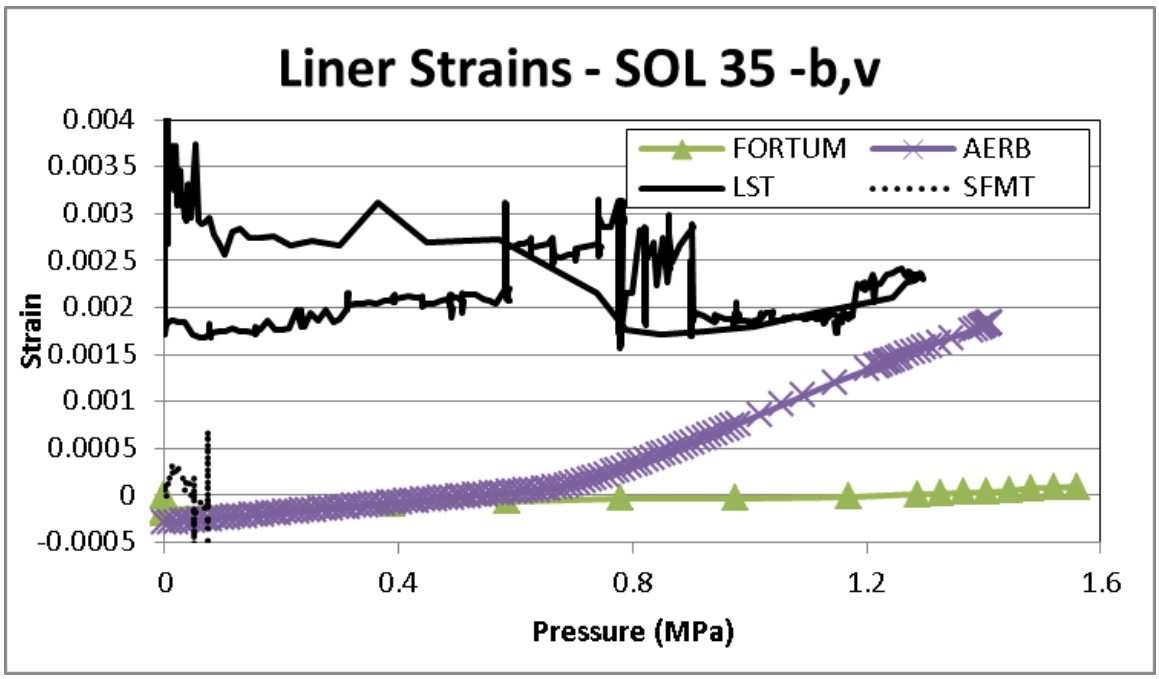

Figure 357: Liner Strain Versus Pressure at SOL #35

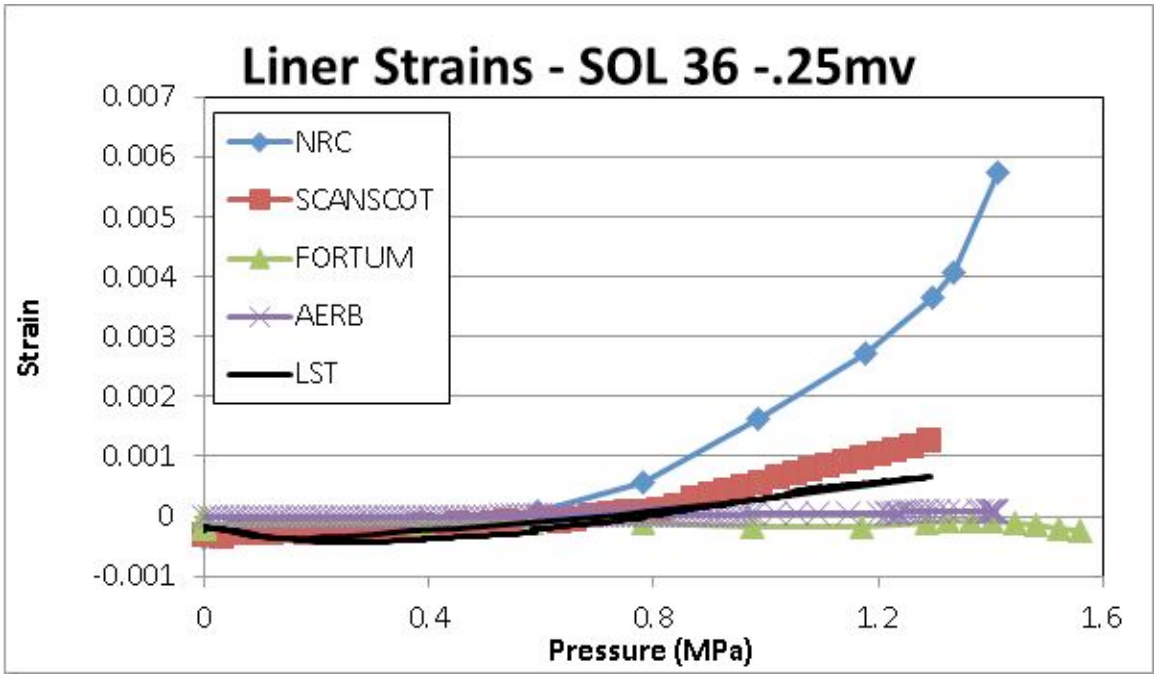

Figure 358: Liner Strain Versus Pressure at SOL #36 (Meridional Strain of Inside of Liner at Base of Cylinder)

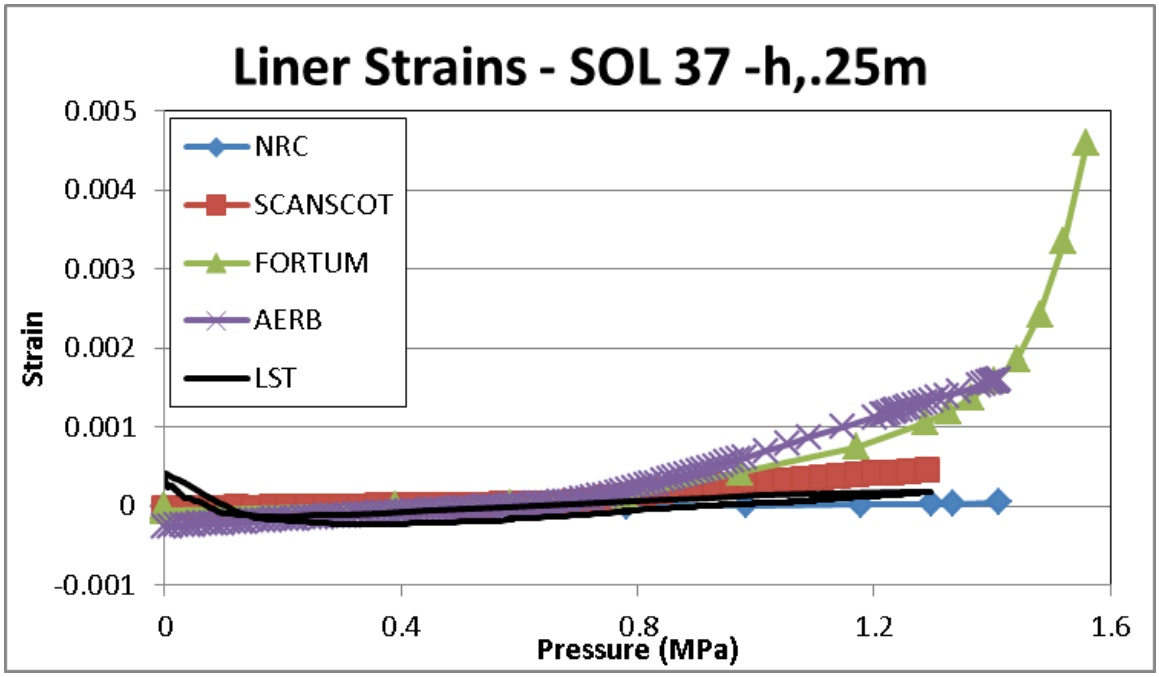

Figure 359: Liner Strain Versus Pressure at SOL #37 (Hoop Strain of Inside of Liner at Base of Cylinder)

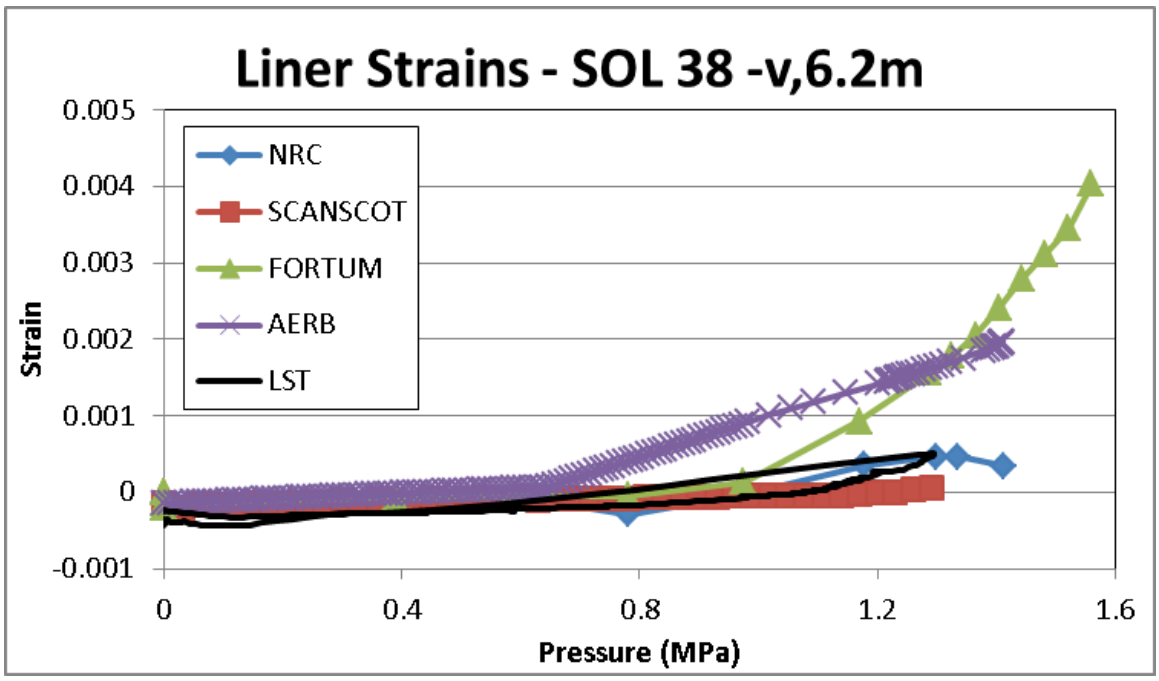

Figure 360: Liner Strain Versus Pressure at SOL #38 (Meridional Strain of Inside of Liner at Midheight)

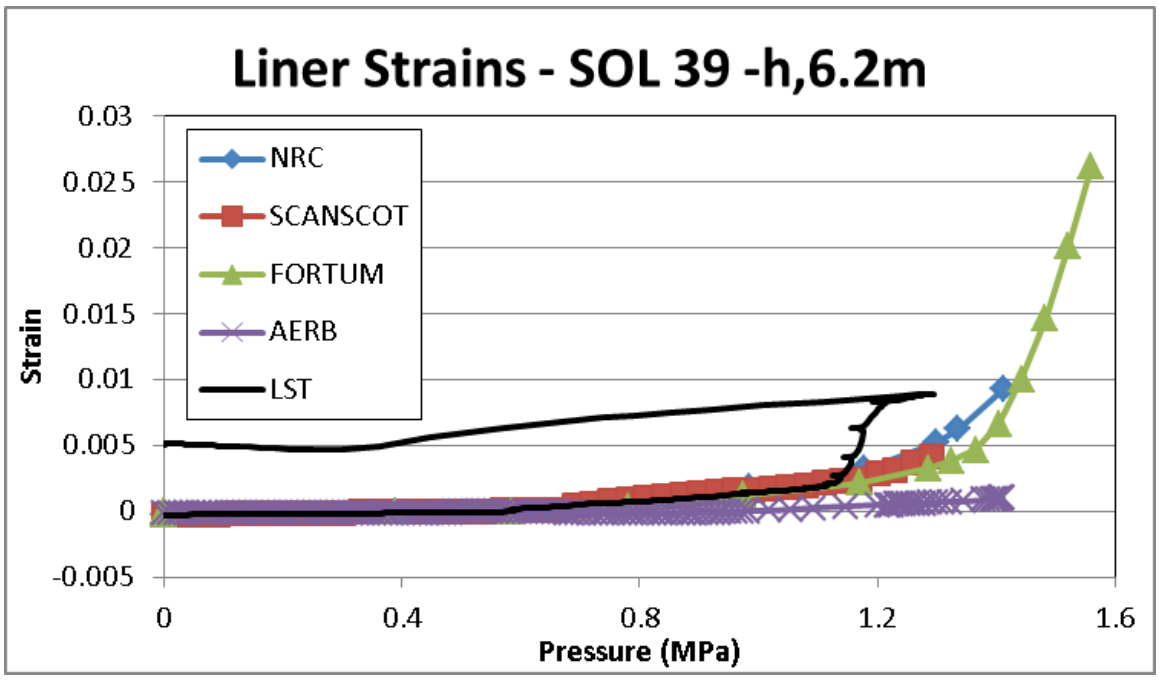

Figure 361: Liner Strain Versus Pressure at SOL #39 (Hoop Strain of Inside of Liner at Midheight)

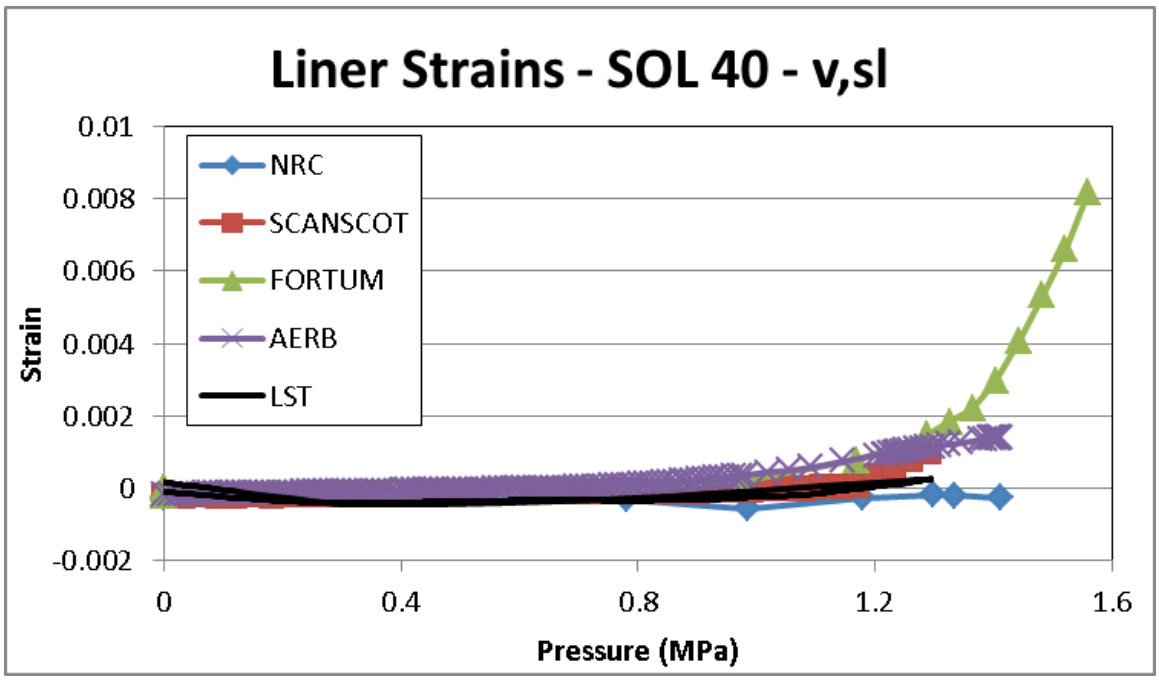

Figure 362: Liner Strain Versus Pressure at SOL #40 (Meridional Strain of Inside of Liner at Springline)

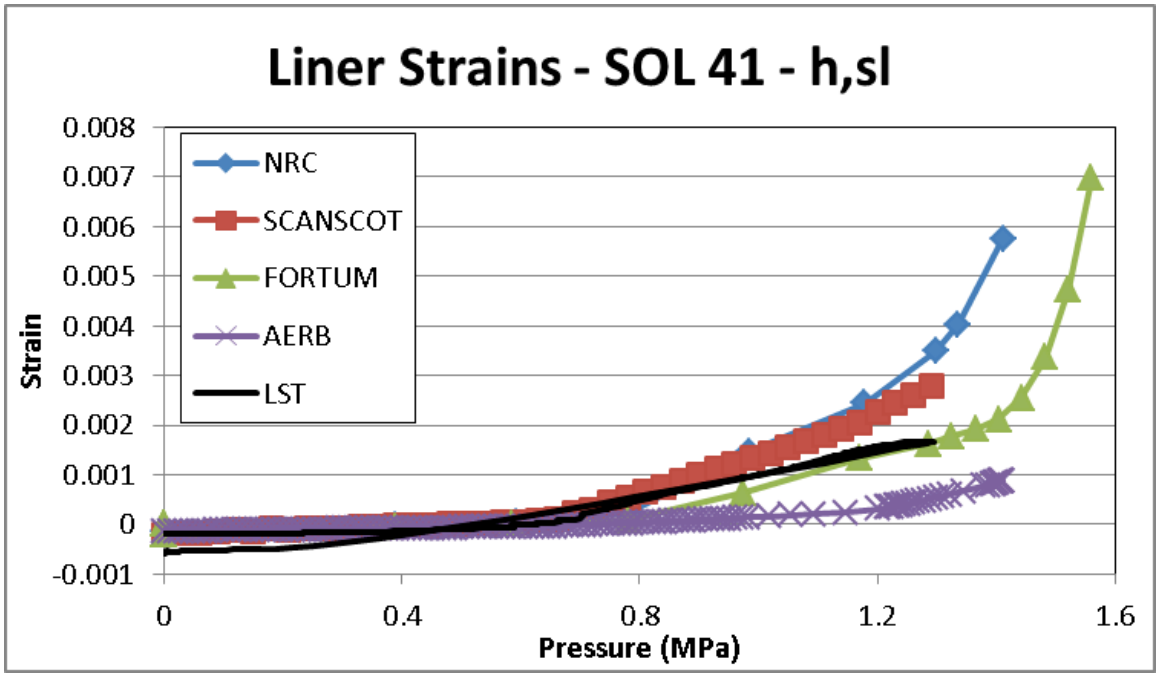

Figure 363: Liner Strain Versus Pressure at SOL #41 (Hoop Strain of Inside of Liner at Springline)

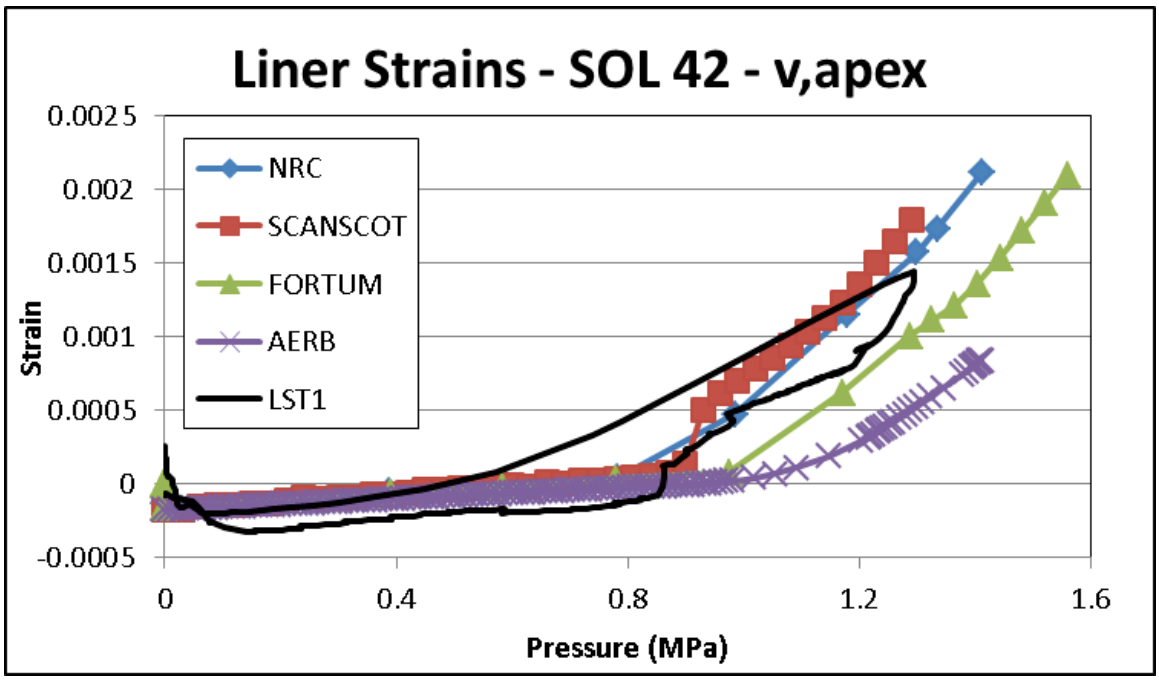

Figure 364: Liner Strain Versus Pressure at SOL #42 (Meridional Strain of Inside of Liner at Dome Apex)

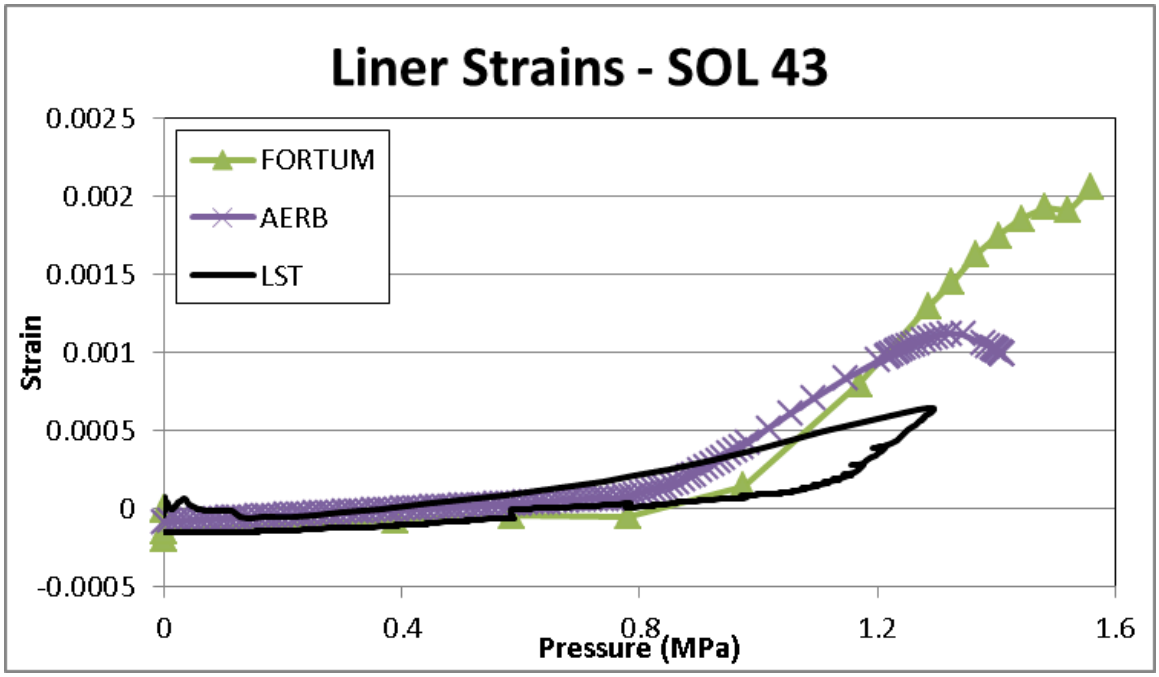

Figure 365: Liner Strain Versus Pressure at SOL #43

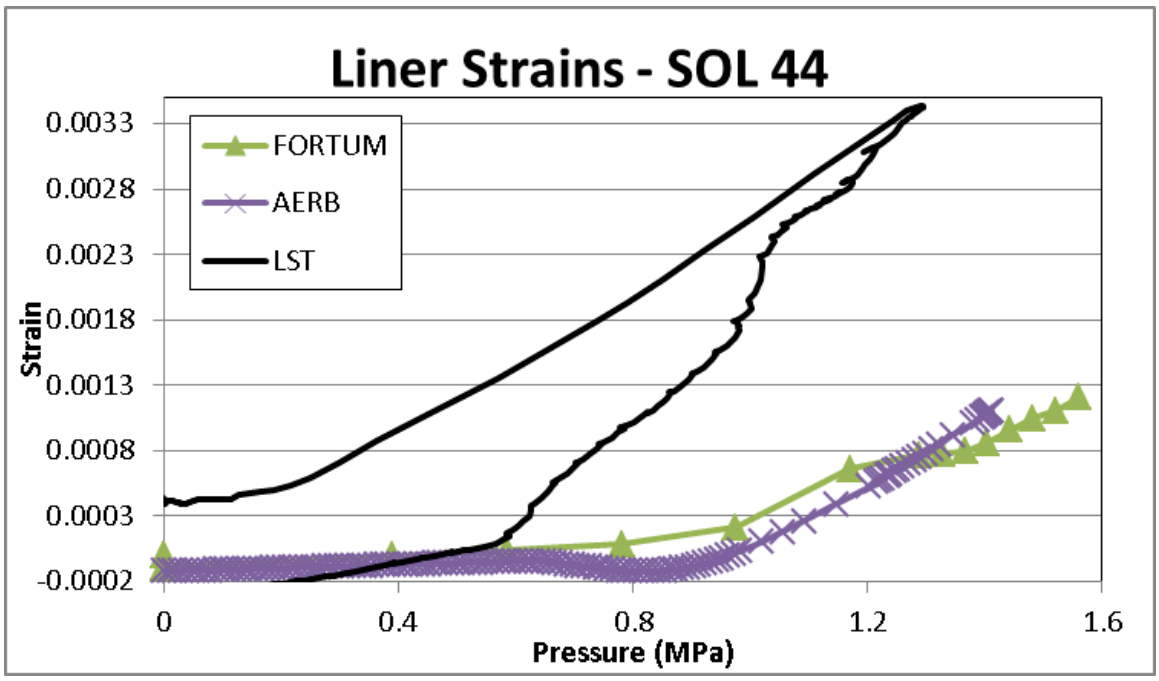

Figure 366: Liner Strain Versus Pressure at SOL #44

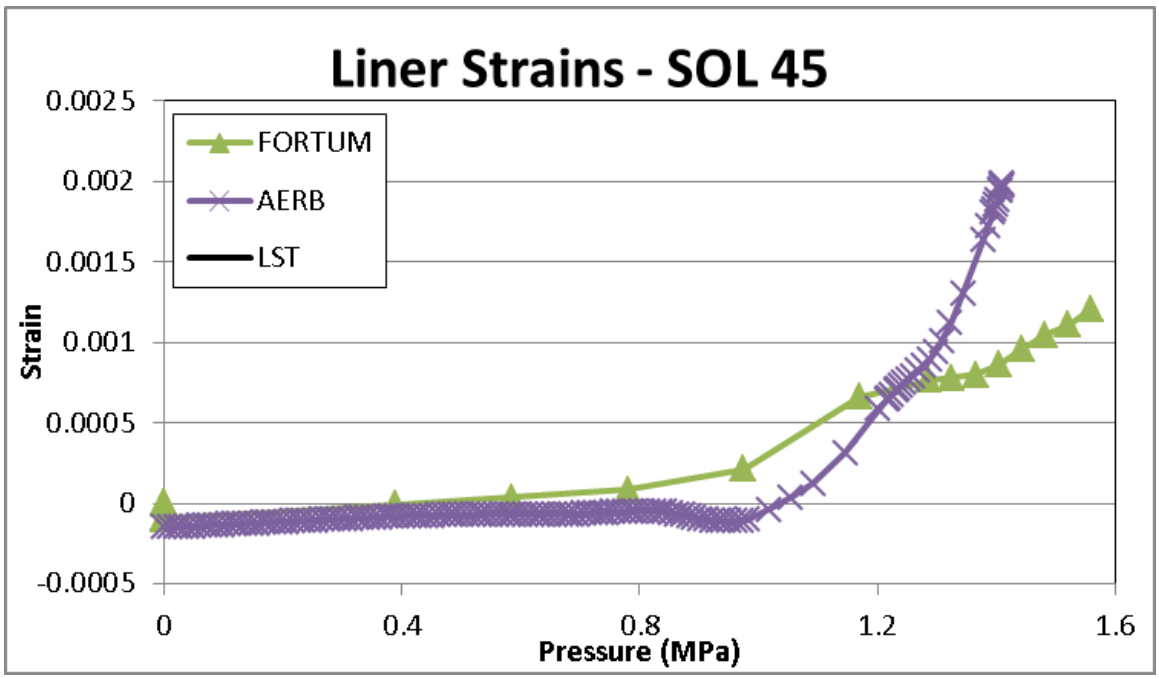

Figure 367: Liner Strain Versus Pressure at SOL #45

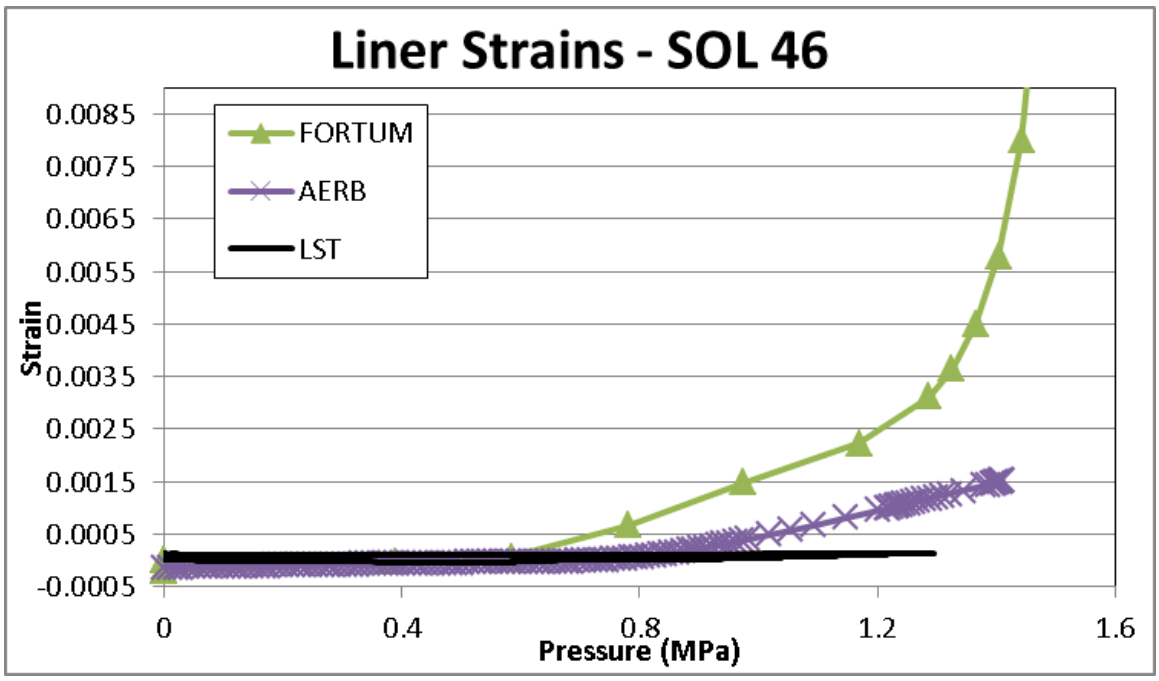

Figure 368: Liner Strain Versus Pressure at SOL #46

4.6.4. Tendon Strain

The tendon strain data comparison plots can be found in Figure 369 through Figure 374. The modeling results from the participants matched the test data somewhat well. For these data it should be noted that the strain test data corresponding to the SFMT has been zeroed since the strain gauges were replaced upon an already prestressed structure. As has been mentioned the modeling seems to better predict the behavior at lower pressure levels likely owing to the relative instability of the models as failure is approached. Participants FORTUM, SCANSCOT, and the NRC tended to match well with the LST data, while AERB's strains matched the SFMT data.

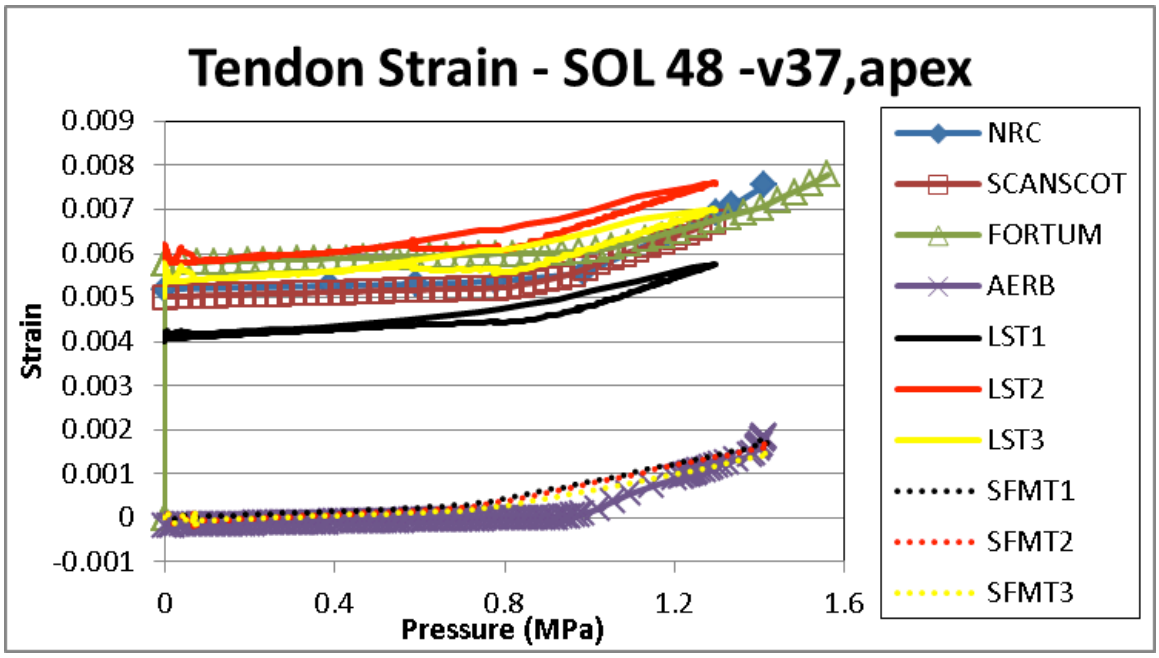

Figure 369: Tendon Strain Versus Pressure at SOL #48 (Hairpin, Tendon V37 at Tendon Apex)

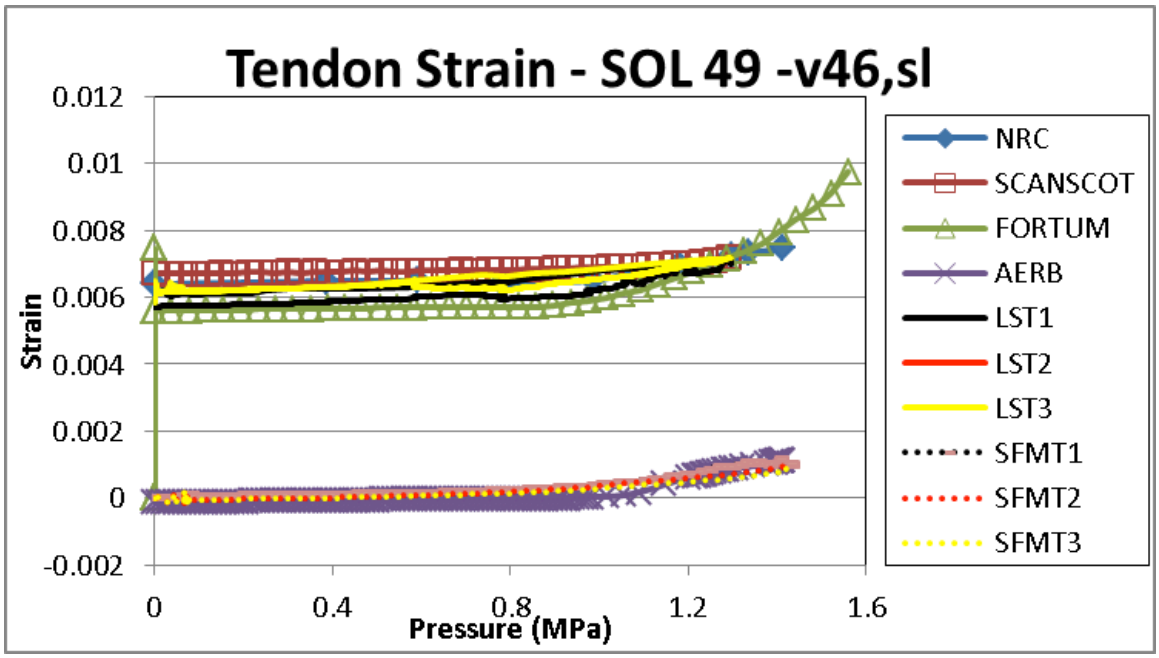

Figure 370: Tendon Strain Versus Pressure at SOL #49 (Hairpin, Tendon V46 at Tendon Springline)

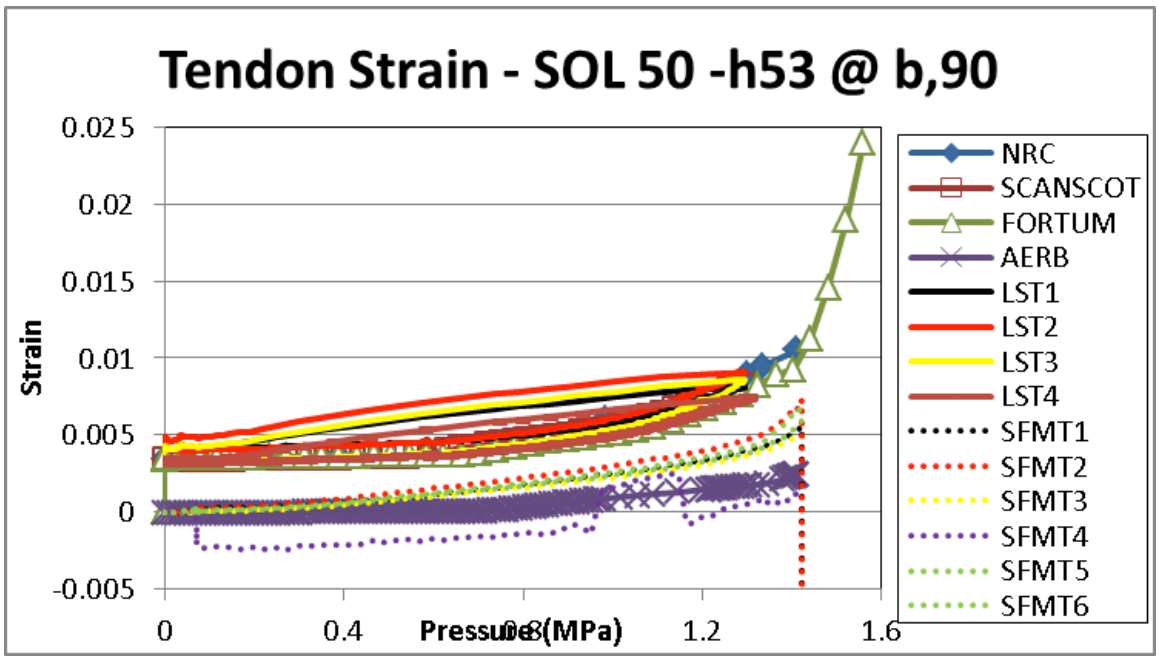

Figure 371: Tendon Strain Versus Pressure at SOL #50 (Hoop, Tendon H53 at Mid-Tendon)

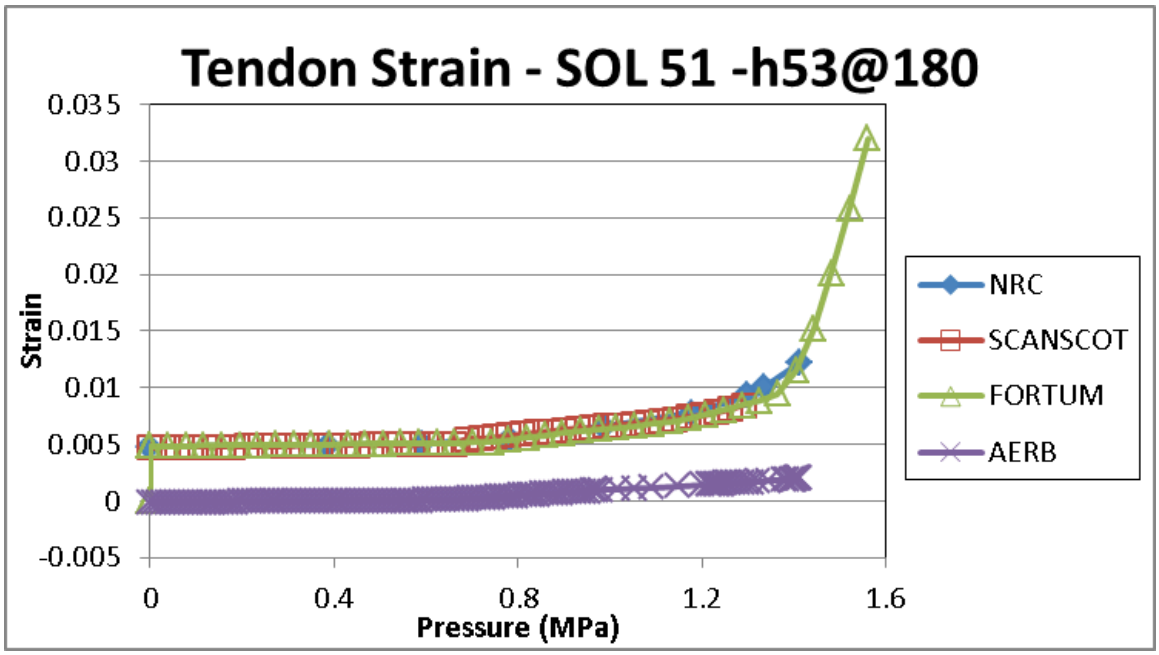

Figure 372: Tendon Strain Versus Pressure at SOL #51 (Hoop, Tendon H53 at ¼ Tendon)

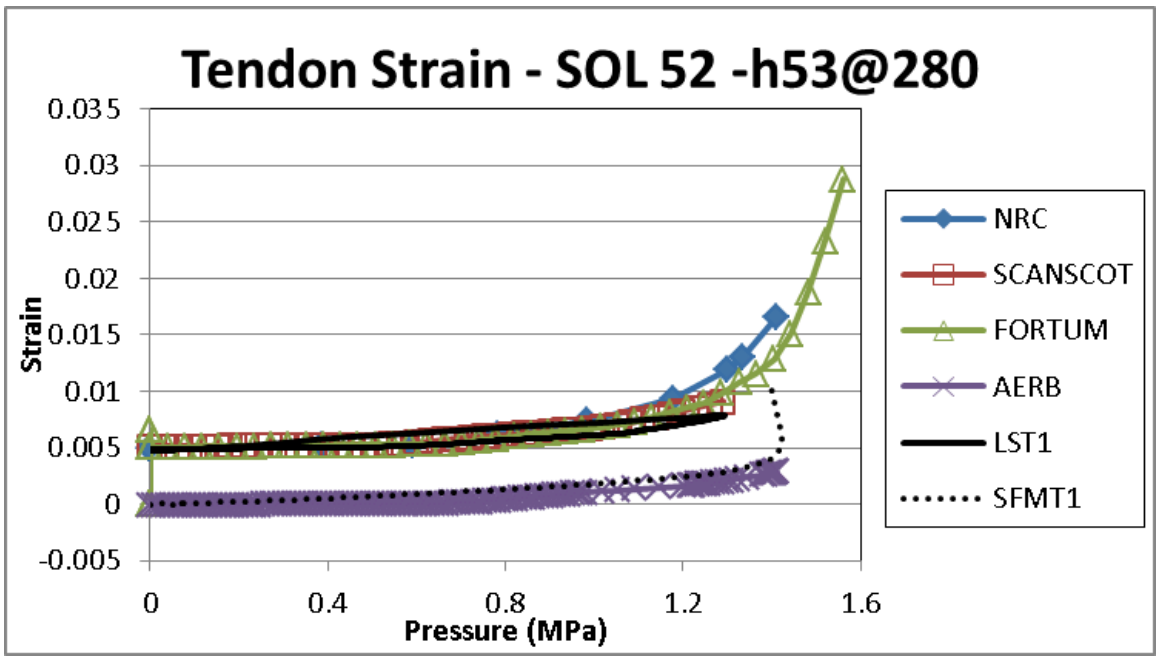

Figure 373: Tendon Strain Versus Pressure at SOL #52 (Hoop, Tendon H53 Near Buttress)

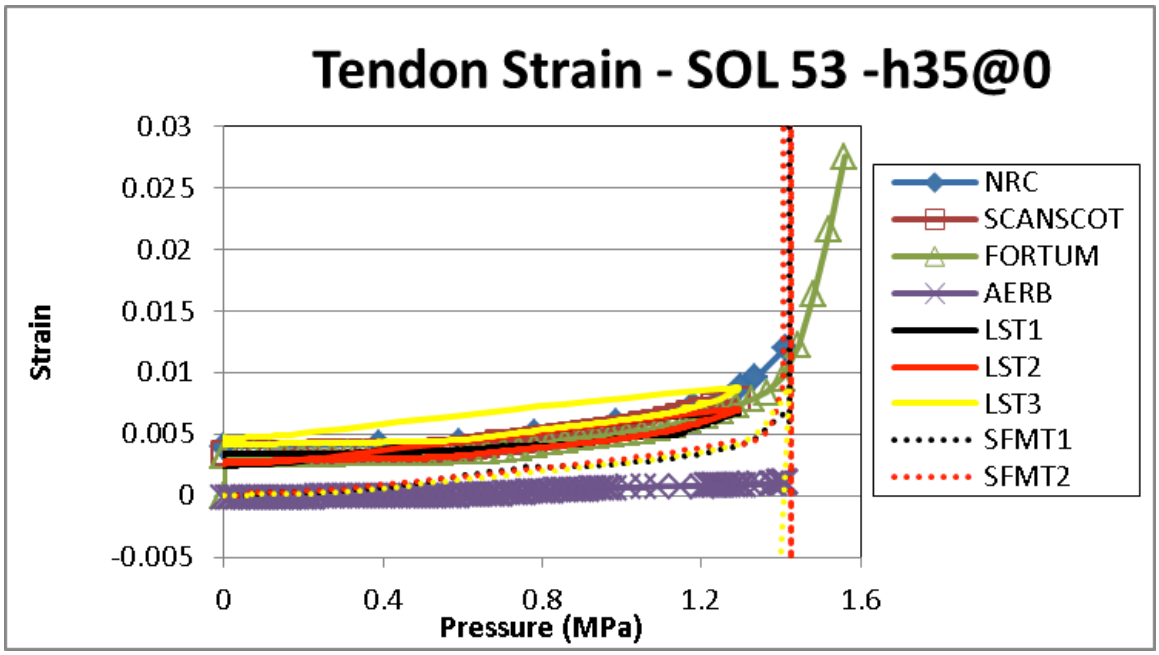

Figure 374: Tendon Strain Versus Pressure at SOL #53 (Hoop, Tendon H35 Between E/H and A/L)

4.6.5. Tendon Forces

The final SOLs measure tendon force and the comparison plots can be found in Figure 375 and Figure 376. Interestingly the model data matches the test data very well for these two SOLs.

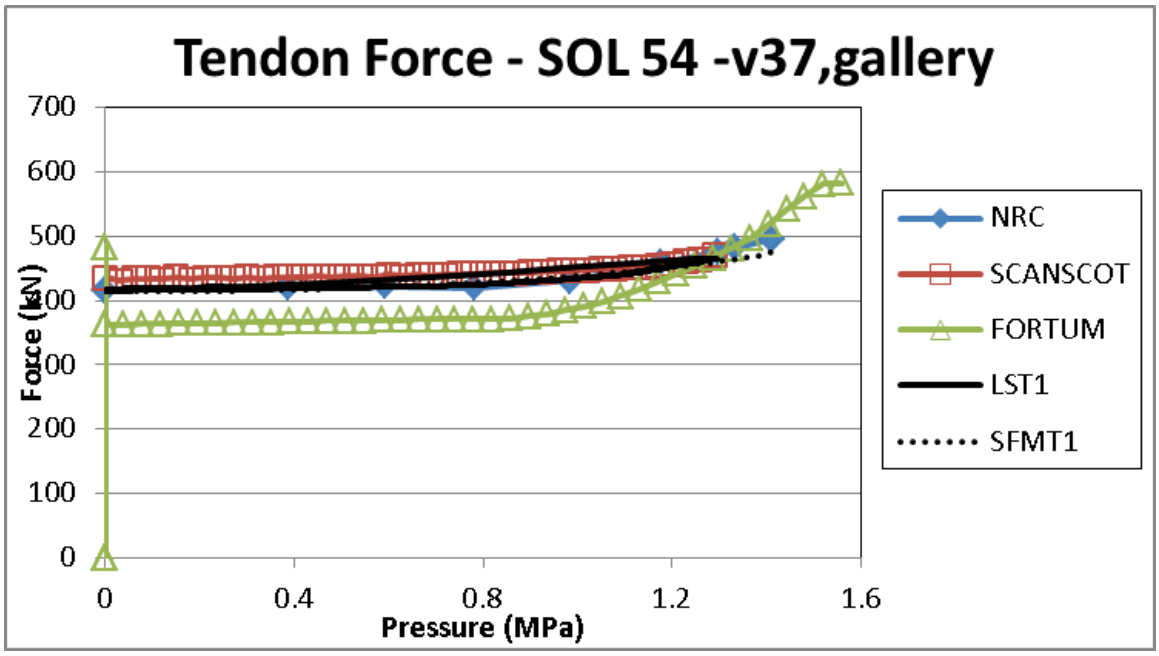

Figure 375: Tendon Force Versus Pressure at SOL #54 (Hairpin, Tendon V37 at Tendon Gallery)

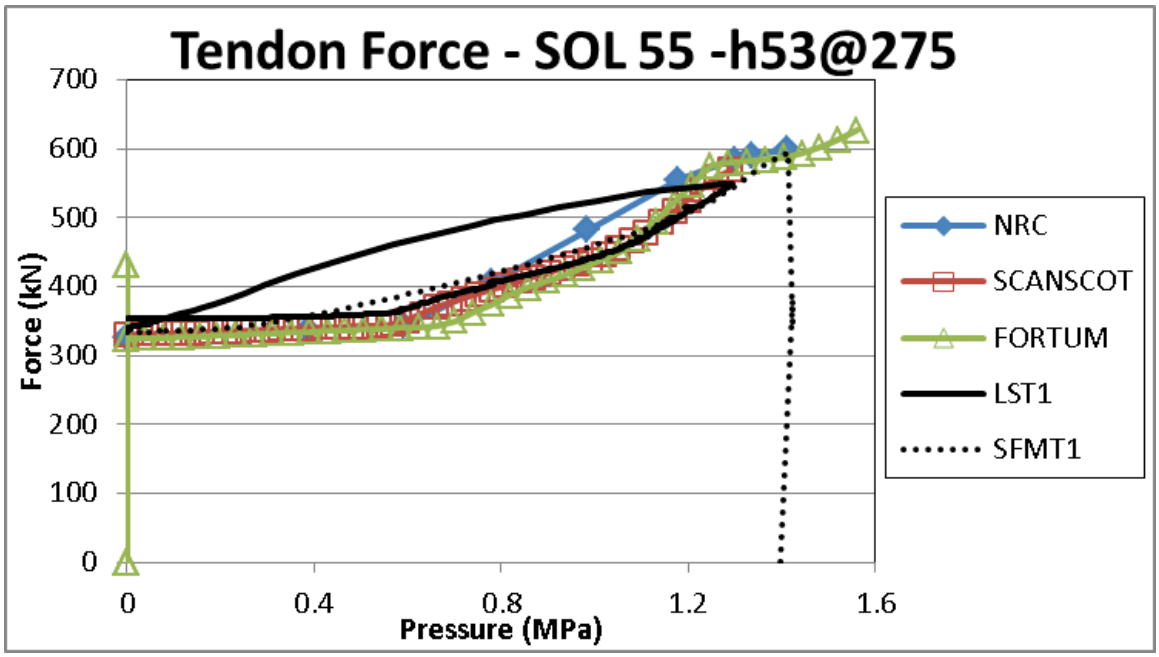

Figure 376: Tendon Strain Versus Pressure at SOL #55 (Hoop, Tendon H53 at Buttress)

4.7. Model 3 Conclusions

Model 3 results were submitted by AERB, FORTUM, NRC, and SCANSCOT. Some variability in modeling technique was observed between the participants, most notably in the method of modeling the tendons. AERB modeled the tendons as embedded in the concrete while FORTUM, NRC, and SCANSCOT allowed the tendons to move relative to the concrete. Additionally relatively minor differences were observed in the specific values used for the

material properties for Model 2. It is suspected that the variation in modeling approach and the minor differences in the input material properties likely account for the variations noted in the results for Model 1.

The deformed shape and liner strain comparisons indicated good agreement between all participants, particularly near the design pressure for the structure. The variations between the participants in the deformed shape at all pressure levels are small, however, and the agreement between participants for the deformed shapes are good.

The Standard Output Location comparisons indicate reasonably good agreement between the participants, particularly up to approximately 3.0-3.3 x P_d. Past this point in the pressurization, the models begin to become somewhat unstable as supported by the termination of the Limit State Test in the NUPEC/NRC 1:4 Scale PCCV Test at 3.3 x P_d. Additionally, several participants verified the slipping of the tendons with internal pressure as the source of the observed flattening of the tendon force versus location plots at high pressures.

5. PHASE TWO ANALYSIS DEFINTION

This chapter includes the analysis specification plan for Phase Two of the SPE #3 effort. This problem definition was determined and agreed to at the Phase One Concluding Meeting, held in April of 2011 in Washington, D.C.

5.1. Introduction

At the SPE Phase 1 Results Discussion Meeting for the Standard Problem Exercise (SPE) on the performance of containment vessels under severe accident conditions (Washington DC, April 13-14, 2011), consensus was reached on some of the details for the Phase 2 SPE program. This chapter is meant to specify the results of discussions held during the meeting, specifying those details of the SPE Phase 2 analyses to be performed, and identifying the results which are requested of the participants. It should be noted that a goal, continuing from discussions held in 2010, is to focus on questions still unanswered by the ISP-48, but to follow most of the temperature and loading definitions of ISP-48.

The current round-robin program consists of two rounds of analyses, and three review meetings. Currently, the first round of analysis and the second review meeting have been completed. The primary source of physical test data remains the Sandia/NRC/NUPEC 1:4 Scale PCCV Test [1], but the introduction of other research or published ancillary test data is welcomed in furthering the aims of the SPE work.

This chapter is organized as follows. The work phases and topics of study printed in the original SPE invitation are shown in italics. The actual FE model definitions are presented in normal typeface, as Models 1, 2, 3.

5.2. Phase Two SPE #3 Analyses

This phase of work has two distinct parts. Following the first phase of the Round Robin Analyses, the participants are asked to examine methods to estimate leakage rate as a function of pressure. These methods will be evaluated relative to the PCCV test results, and incorporate lessons learned from the first phase of the Round Robin Analysis. This would constitute the first part. The second part will consist of enumeration of methods for predicting leakage of prestressed concrete containment vessels as function of pressure and temperature; apply these methods to characterize the performance, in terms of leakage rate, under pressure and temperature; and transition them to probabilistic space.

Phase Two shall require the participants to re-investigate Model 3 from Phase 1. We will refer to this additional investigation as Model 4. It is, essentially, Model 3, but with all modifications the participant may wish to introduce based on lessons-learned from Phase 1 and modifications suitable to introducing temperature into the solution. The participants will apply two different temperature loading cases to the global Model 4. The loading cases are shown below in Figure 377 and Figure 378. At the initial workshop, the participants agreed to use the ISP-48 cases, but

to remove the H2 burn because of its lack of effect on leak rate. For Case 2, the "simplified" curves are used.

For Temp Cases 1 & 2, a heat transfer solution was performed by Dameron et al for the 1:4 Scale PCCV to develop the temperature profiles through the containment wall at different elevations of the containment [2]. This information (and the derivation) is provided herein. (It is the same as was used for the ISP-48 Exercise.) More information about the ISP-48 analyses are available in the reports published from that exercise, and these are available on the SPE website. The temperature profiles through the wall are provided in Excel Files along with this White Paper. Nodal point temperatures should be interpolated between the section points given. For Temperature Case 2, note: to NOT consider the hydrogen burn, ignore the data between Time=260 min. to Time=285 min.

Development of a third temperature case was also discussed in Washington, aimed at incorporating recent information becoming available from the last several years of study of Containment Accident Scenarios. At the time of this writing, this case is still under development, and may be added later. We suggest that participants complete Cases 1 and 2 as soon as possible, without waiting for the information for Case 3.

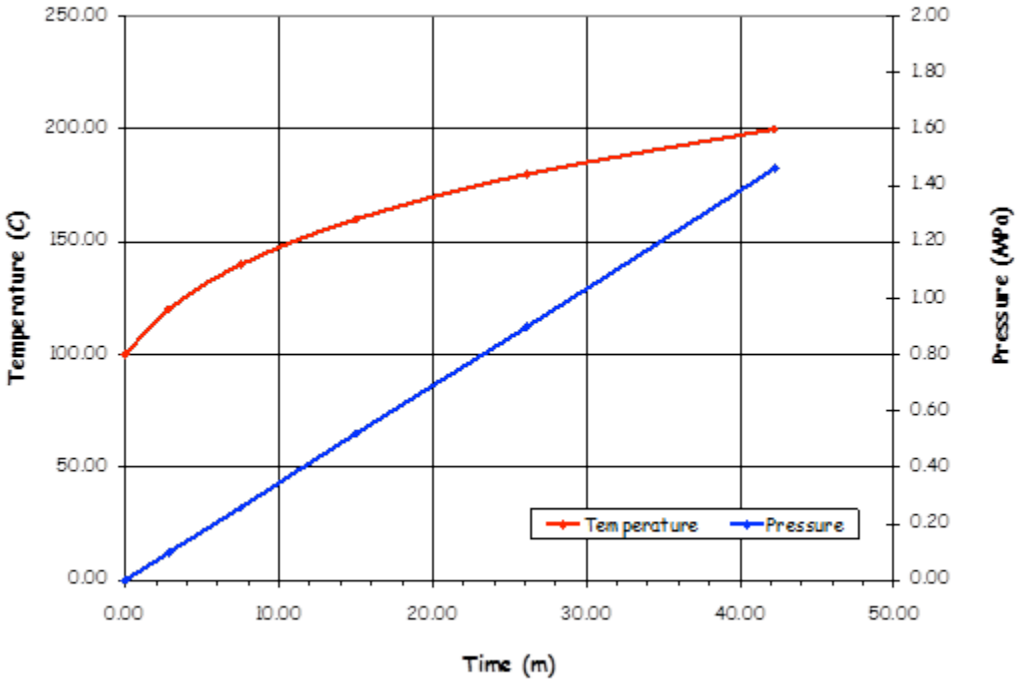

Figure 377: Model 4 – Case 1 Saturated Steam Pseudo-Time History

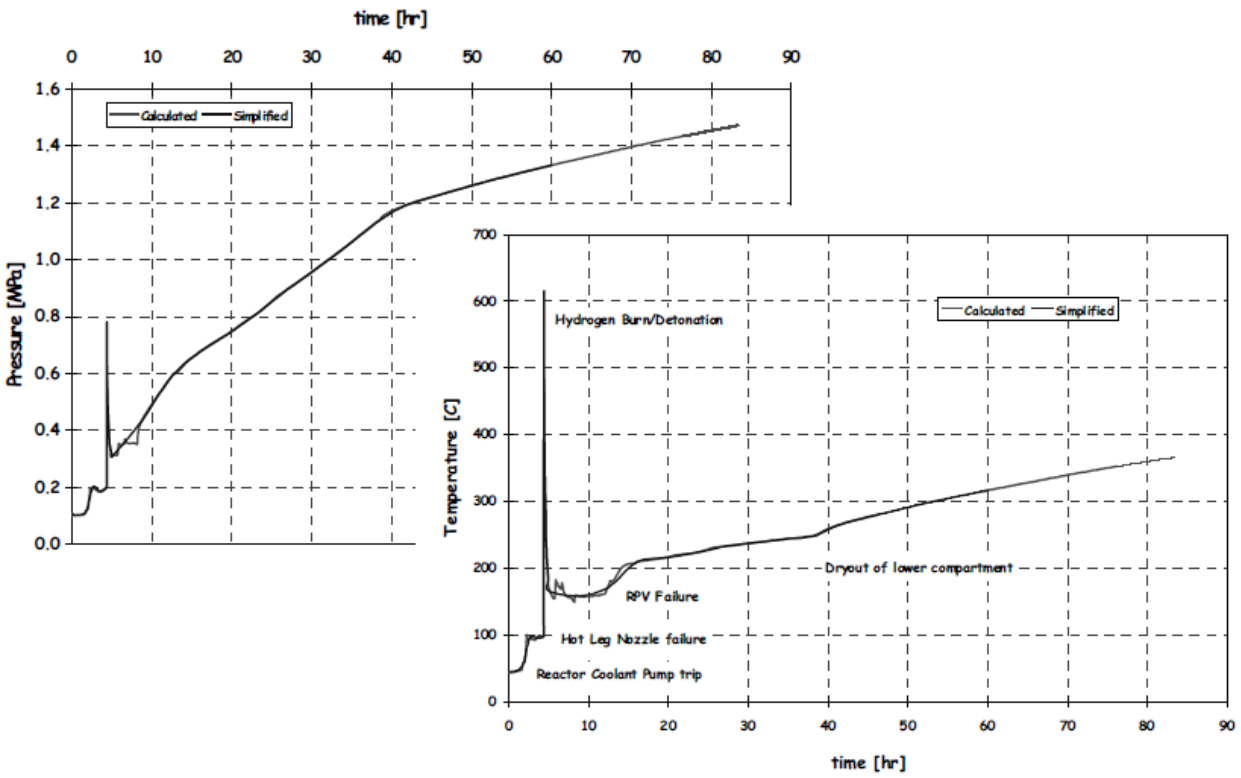

Figure 378: Model 4 – Case 2 Station Black-Out Time History

The thermal and mechanical analyses were de-coupled from the heat transfer calculations performed first using a full-scale axisymmetric model and a combination of applied temperature (liner), convection (cylinder wall and dome), and conduction (basemat/soil) boundary conditions. Thermal material properties and temperature dependent mechanical properties were based on handbook data.

A set of temperature-dependent concrete and steel mechanical properties are also provided, though these properties only enter into the mechanical (stress) portion of the solution, not into the purely thermal solution. All of these properties are offered as a baseline suggestion and documentation of the source of the thermal gradients, but SPE-3 participants are free to use properties from their own research if desired.

5.2.1. Assumptions for Heat Transfer Analysis

A full scale version of the PCCV axisymmetric model was used to conduct the thermal analysis since the thermal response does not scale geometrically. The resulting gradients are then scaled and applied to the 1:4-scale models for combined thermal-mechanical analysis.

To conduct the Heat Transfer analysis in ABAQUS, all elements relevant for thermal analysis were changed to diffusive heat transfer element types which only have temperature degrees of freedom. Thermal boundary conditions were imposed at the outer surface of the PCCV cylinder

and dome wall consisting of free convection with air with a sink temperature ($T_{f,\infty}$) of 25°C. For free convection with air, the heat transfer coefficient, h, varies with temperature according to the following relationship:

$h = 0.00382(\Delta T)^{1/3}$ lbf/in-s-°F (T in °F) for the full scale PCCV analysis, and

$h = 0.0153(\Delta T)^{1/3}$ lbf/in-s-°F for the 1:4 scale analysis. (These convert to 1.20 and 4.80 W-m^{-2}-°K.)

This is input to ABAQUS as a "non-uniform film coefficient" (FNU) through the User-defined subroutine related to the SFILM option.

The boundary condition on the basemat foundation consists of heat conduction with soil with a sink temperature ($T_{f,\infty}$) of 25°C. The heat transfer coefficient was developed for the horizontal surface of the foundation in contact with the soil to be:

$h = 5.76x10^{-5}$ lbf/in-s-°F for the full scale PCCV analysis,

and $h = 2.30x10^{-4}$ lbf/in-s-°F for the 1:4 scale PCCV.

(These convert to 0.0181 and 0.0724 W-m^{-2}-°K.)

This is input to ABAQUS as a constant film coefficient using the SFILM option and no User-defined subroutine. The temperature input for the thermal analysis was applied through prescribed temperature boundary conditions on the nodes of the inner surface of the basemat, cylinder wall, and dome (i.e., on the liner). For Case 2, a steady-state heat transfer analysis step preceded the dynamic heat transfer analysis with the time history temperature input. The steady state heat transfer step was used to bring the model up to an ambient/operating temperature of 25°C. Figure 379 shows the location of the prescribed boundary conditions for the axisymmetric model. Figure 380 shows the temperature contours for various steps in the heat transfer analysis. Also shown in Figure 381 are the sections through the containment wall and basemat where the temperature gradients are provided.

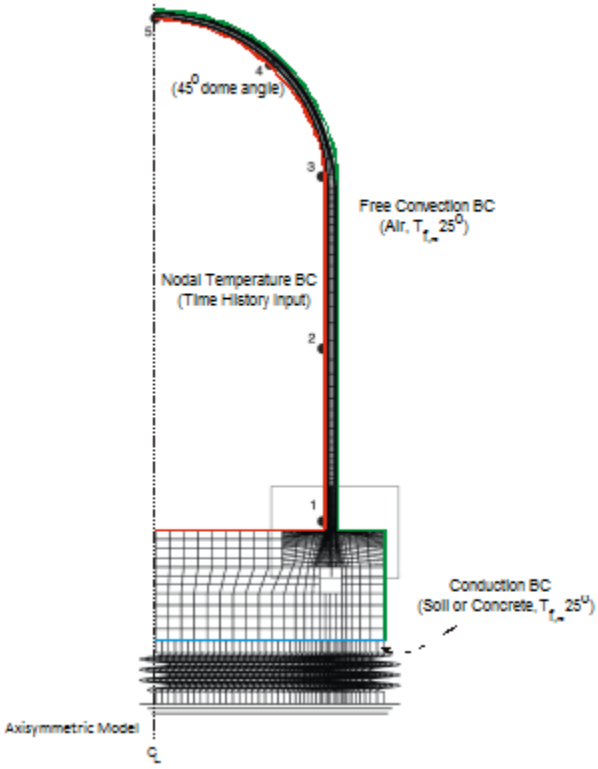

Figure 379: Axisymmetric Model with Thermal Boundary Conditions

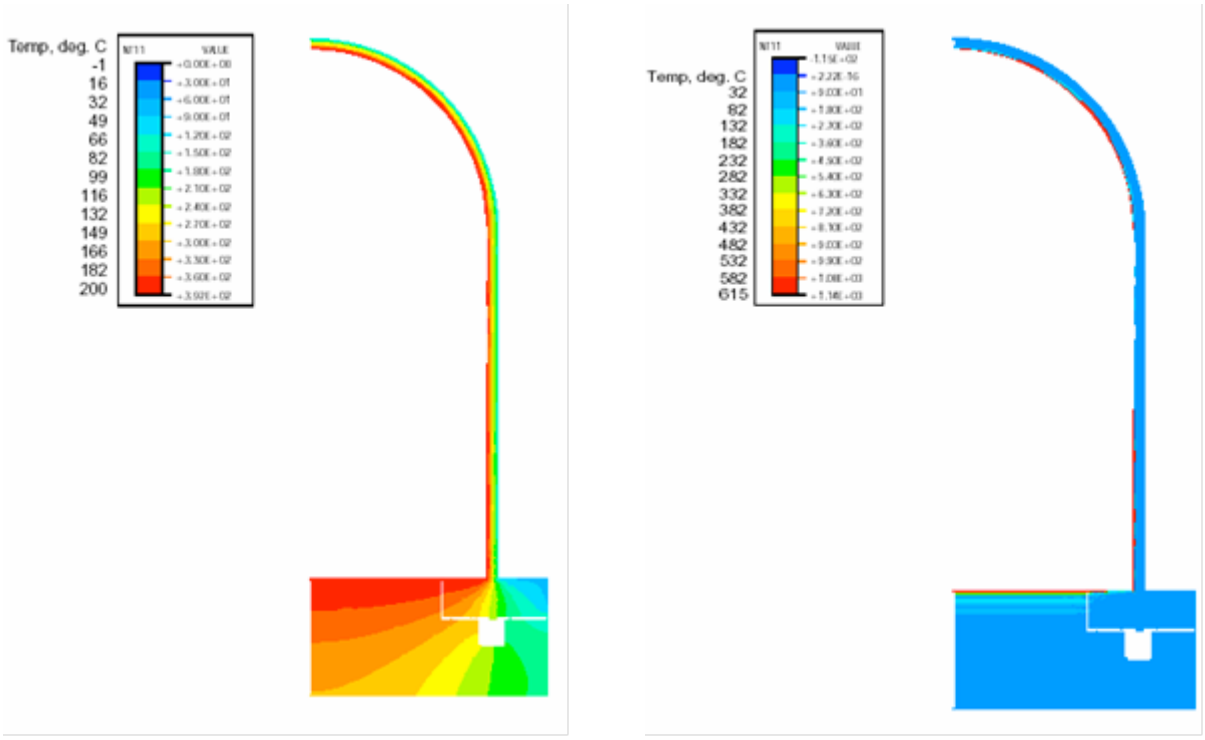

Case 1 Thermal Gradients @ T = 200°C

Case 2 Thermal Gradients @ T = 615°C

Figure 380: Axisymmetric Model Thermal Gradients

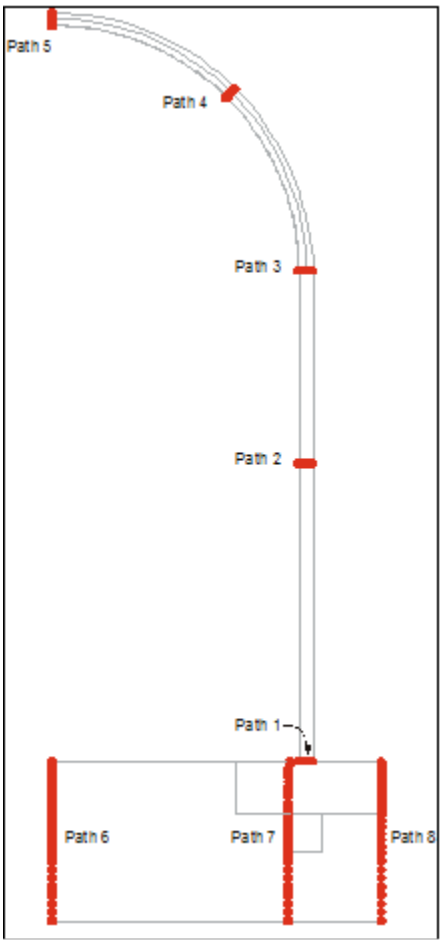

Figure 381: Thermal Gradient Locations

5.2.2. Material Properties and Variations Due to Temperature

A literature review was conducted during the ISP-48 work to choose and substantiate assumptions for concrete thermal properties, and for degradation of concrete and steel material properties. The final outcome of this work is summarized in Figure 382 and Figure 383. However, when the ISP-48 work was published, the literature review was still lacking in stress-strain information for steel at elevated temperature. Since that time, more data has been found, particularly with the research interest in design for fire- resistance conducted in the last decade (for example [3]). In order to consolidate the many research findings, we suggest that SPE participants use the stress-strain property versus temperature relationships published in the 2005 Euro-Code [4]; these are summarized in Figures Figure 384 through Figure 388.

5.2.3. Concrete Strength Degradation Versus Temperature Used in ISP – 48

Concrete Strength Ratio, $S_{Rc} = \exp^{-}(T/632)^{1.8}$ where T is in degrees C

The derivation of this curve was based on assumption of a basic shape as observed from the data, and then pegging the curve to the following points.

Table 19: Data Points for Strength Degradation Versus Temperature

T (°C)	S_R
0	1.00
200	0.88
600	0.40
1000	1.10

Further, based on the literature, it appears reasonable to base the modulus on the standard ACI formula: $E = 57{,}000\sqrt{fc'}$ (English Units) such that a Modulus Reduction Ratio can be defined as:

$$M_R = (S_R)^{\frac{1}{2}}$$

It should be noted, however, that the peak strain at which the concrete compressive strength limit is reached also shifts with increasing temperature. While at 25°C, this strain is approximately 0.002, it can reach two to three times this value at high temperatures.

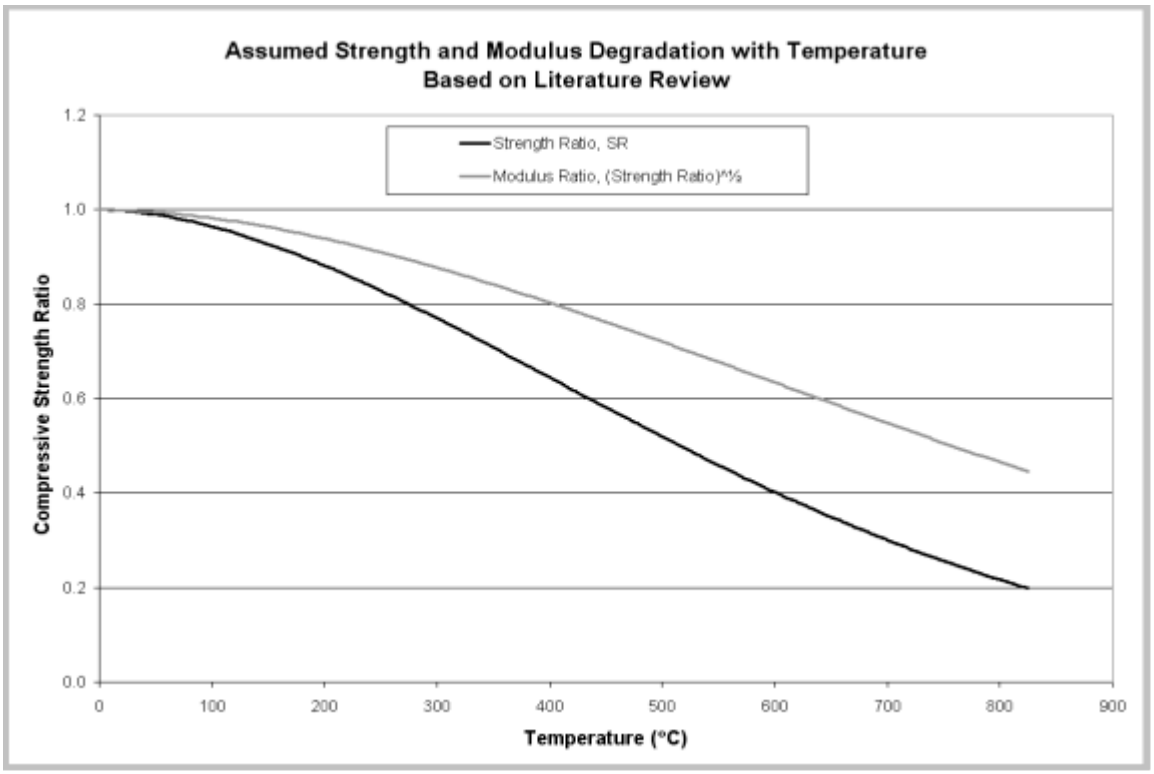

Figure 382: Concrete Compression Strength Ratio vs. Temperature (Used for ISP-48)

Temperature variation of steel is also included in the mechanical solution. This variation has been idealized based on curves and trends is observed in other texts and papers:

Steel Yield Strength Ratio, $S_{Rs} = \exp^{-}((T-340)/300)^{1.9}$ where T is in degrees C.

$$S_{Rs} = 1.0, T \le 340C$$

For steel, the Young's Modulus tends to follow the yield strength one-to-one, rather than the square-root relationship found in concrete.

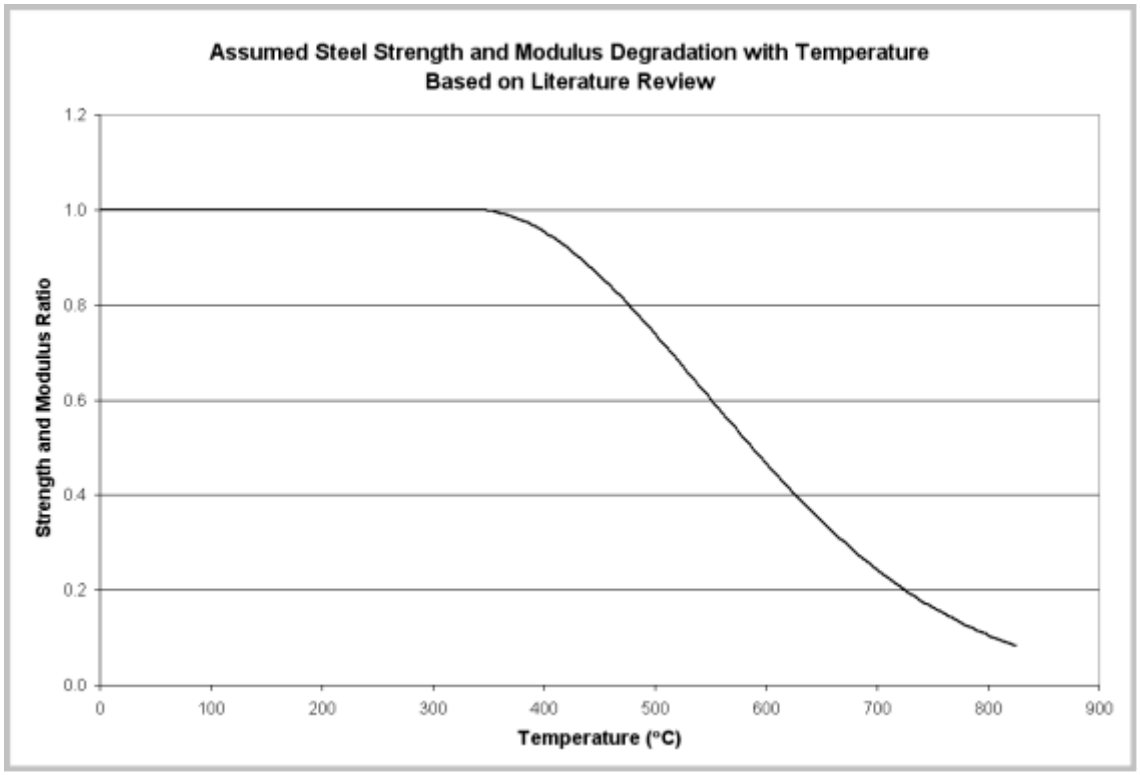

Figure 383: Steel Yield Strength and Modulus Ratio vs. Temperature (used for ISP-48)

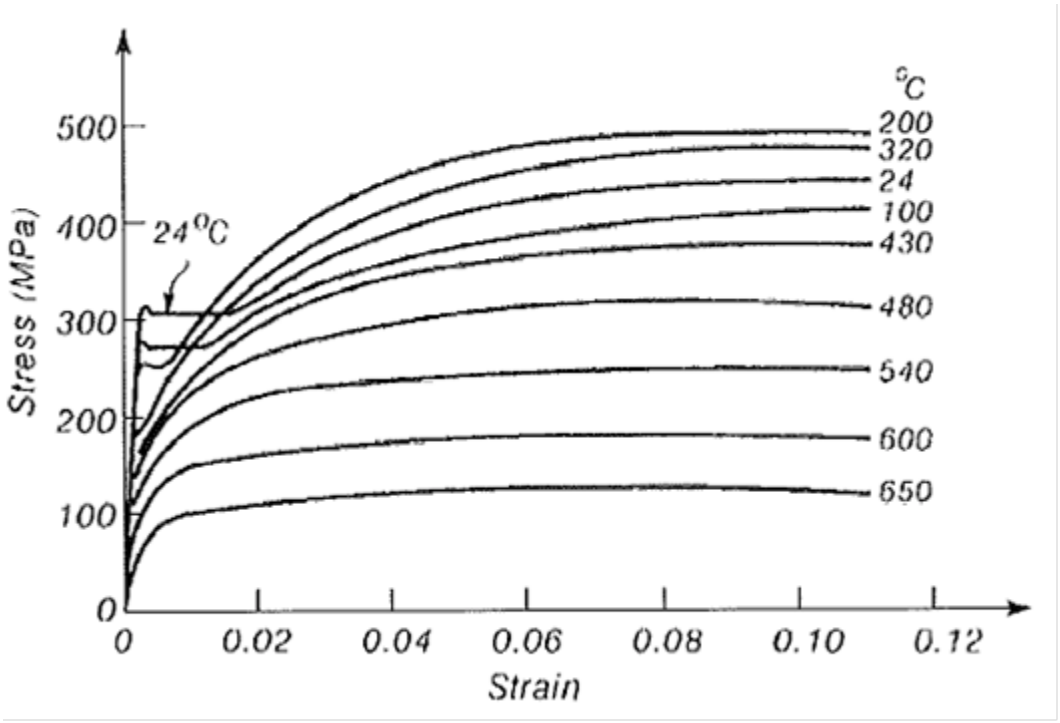

Figure 384: Stress-Strain Curves for Typical Hot-Rolled Steel at Elevated Temperatures

Table 20: Reduction Factors for Stress-Strain Relationship of Carbon Steel at Elevated Temperatures

Steel Temperature θ_λ	Reduction factors at temperature θ_λ relative to the value of f_y or E_λ at 20°C		
	Reduction factor (relative to f_y) for effective yield strength $k_{y\theta} = f_{y\theta}/f_y$	Reduction factor (relative to f_y) for proportional limit $k_{v\theta} = f_{v\theta}/f_y$	Reduction factor (relative to E_λ) for the slope of the linear elastic range $k_{\varepsilon\theta} = E_{\lambda\theta}/E_\lambda$
20°C	1.000	1.000	1.000
100 °C	1.000	1.000	1.000
200 °C	1.000	0.807	0.900
300 °C	1.000	0.613	0.800
400 °C	1.000	0.420	0.700
500 °C	0.780	0.360	0.600
600 °C	0.470	0.180	0.310
700 °C	0.230	0.075	0.130
800 °C	0.110	0.050	0.090
900 °C	0.060	0.0375	0.0675
1000 °C	0.040	0.0250	0.0450
1100 °C	0.020	0.0125	0.0225
1200 °C	0.000	0.0000	0.0000

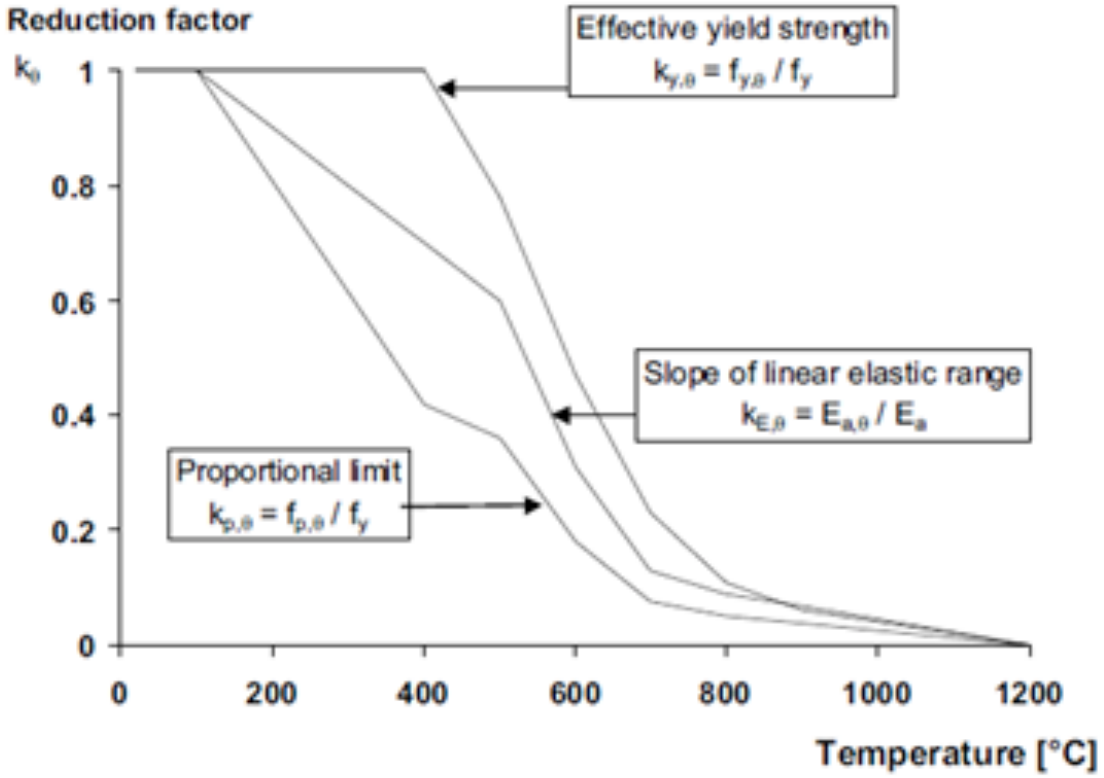

Figure 385: Reduction Factors for the Stress-Strain Relationship of Carbon Steel at Elevated Temperatures

Annex A [normative] Strain-hardening of carbon steel at elevated temperatures

(1) For temperatures below 400°C , the alternative strain-hardening option mentioned in 3.2 may be used as follows:

- for $0,02 < \varepsilon < 0,04$:

$$\sigma_a = 50(f_{u,\theta} - f_{y,\theta})\varepsilon + 2f_{y,\theta} - f_{u,\theta} \quad \text{(A.1a)}$$

- for $0,04 \leq \varepsilon \leq 0,15$:

$$\sigma_a = f_{u,\theta} \quad \text{(A.1b)}$$

- for $0,15 < \varepsilon < 0,20$:

$$\sigma_a = f_{u,\theta}[1 - 20(\varepsilon - 0,15)] \quad \text{(A.1c)}$$

- for $\varepsilon \geq 0,20$:

$$\sigma_a = 0,00 \quad \text{(A.1d)}$$

where:

$f_{u,\theta}$ is the ultimate strength at elevated temperature, allowing for strain-hardening.

NOTE: The alternative stress-strain relationship for steel, allowing for strain hardening, is illustrated in figure A.1.

(2) The ultimate strength at elevated temperature, allowing for strain hardening, should be determined as follows:

- for $\theta_a < 300°C$:

$$f_{u,\theta} = 1,25f_{y,\theta} \quad \text{(A.2a)}$$

- for $300°C \leq \theta_a < 400°C$:

$$f_{u,\theta} = f_{y,\theta}(2 - 0,0025\,\theta_a) \quad \text{(A.2b)}$$

- for $\theta_a \geq 400°C$:

$$f_{u,\theta} = f_{y,\theta} \quad \text{(A.2c)}$$

NOTE: The variation of the alternative stress-strain relationship with temperature is illustrated in figure A.2.

Figure 386: Determination of Strain-Hardening of Carbon Steel at Elevated Temperatures (Figure A.2 Refers to A.2 in Figure 387)

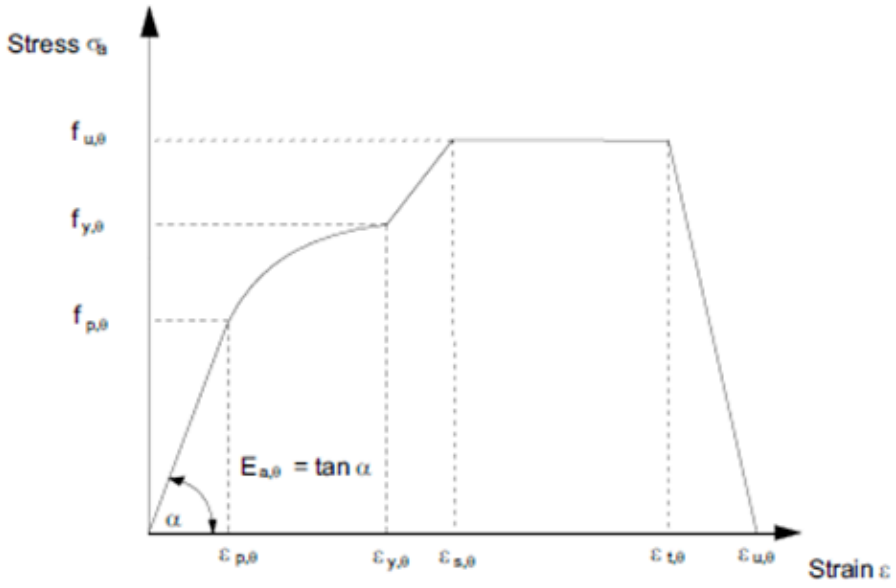

Figure A.1: Alternative stress-strain relationship for steel allowing for strain-hardening

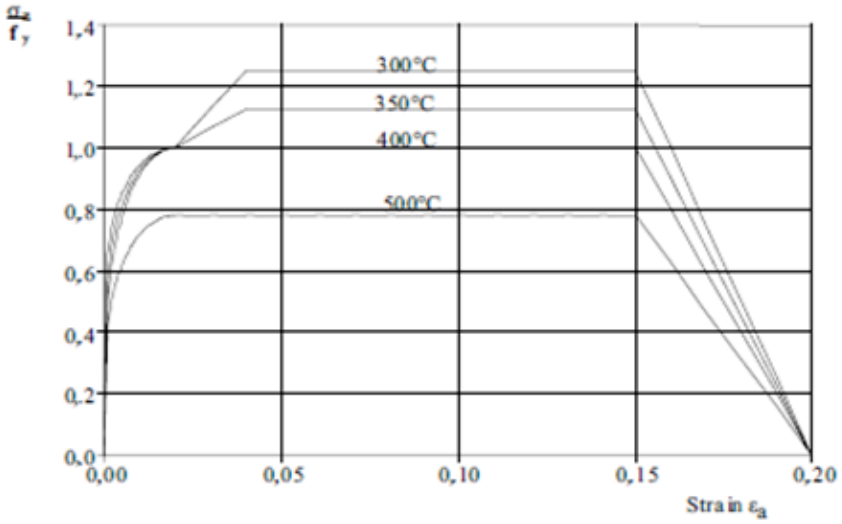

Figure A.2: Alternative stress-strain relationships for steel at elevated temperatures, allowing for strain hardening

Figure 387: Alternate Stress-Strain Relationships for Steel

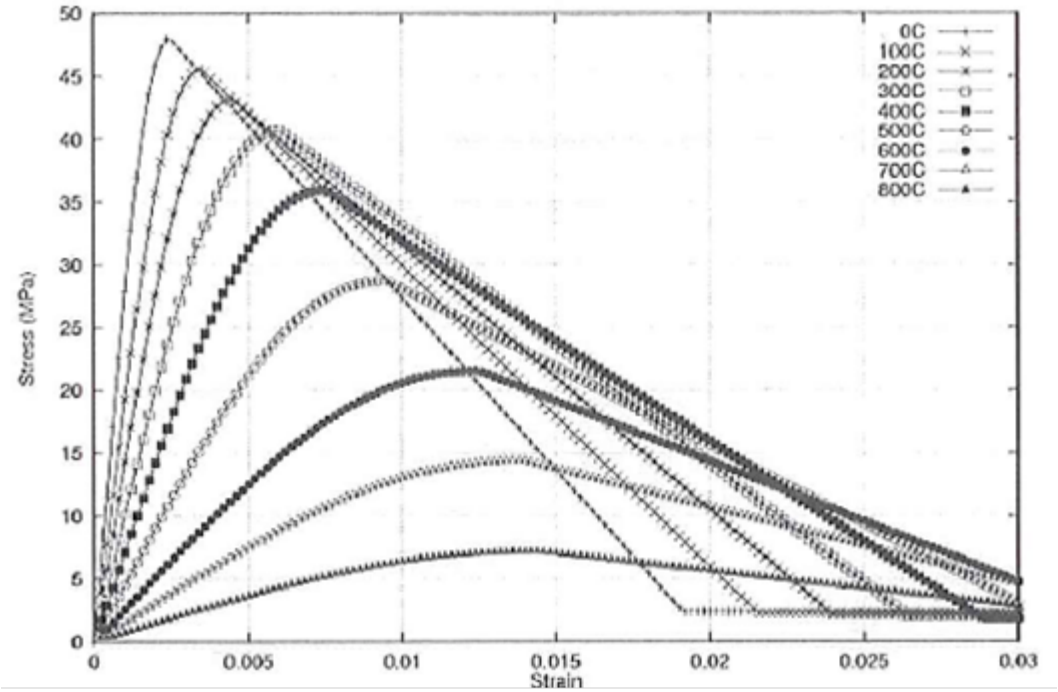

Figure 388: Idealization of Stress-Strain For Concrete at Elevated Temperatures per Eurocode 2

Table 21: Values for the Main Parameters of the Stress-Strain Relationships of Normal Weight Concrete with Siliceous or Calcareous Aggregates Concrete at Elevated Temperatures

Concrete	Siliceous aggregates			Calcareous aggregates		
temp.θ	$f_{c,\theta} / f_{ck}$	$\varepsilon_{c1,\theta}$	$\varepsilon_{cu1,\theta}$	$f_{c,\theta} / f_{ck}$	$\varepsilon_{c1,\theta}$	$\varepsilon_{cu1,\theta}$
[°C]	[-]	[-]	[-]	[-]	[-]	[-]
1	2	3	4	5	6	7
20	1,00	0,0025	0,0200	1,00	0,0025	0,0200
100	1,00	0,0040	0,0225	1,00	0,0040	0,0225
200	0,95	0,0055	0,0250	0,97	0,0055	0,0250
300	0,85	0,0070	0,0275	0,91	0,0070	0,0275
400	0,75	0,0100	0,0300	0,85	0,0100	0,0300
500	0,60	0,0150	0,0325	0,74	0,0150	0,0325
600	0,45	0,0250	0,0350	0,60	0,0250	0,0350
700	0,30	0,0250	0,0375	0,43	0,0250	0,0375
800	0,15	0,0250	0,0400	0,27	0,0250	0,0400
900	0,08	0,0250	0,0425	0,15	0,0250	0,0425
1000	0,04	0,0250	0,0450	0,06	0,0250	0,0450
1100	0,01	0,0250	0,0475	0,02	0,0250	0,0475
1200	0,00	-	-	0,00	-	-

5.2.4. Required Outputs/Results

The ISP-48 instructions can be used to guide the list of deliverables from the analysis related to temperature, but the basic list of Required Outputs/Results for the analysis are the same as for Model 3, as follows:

1. Description of failure prediction model or criteria selected
2. Assumptions made in geometric modeling, and model description
3. A subset of the response information defined by the "55 standard output locations" of the 1:4 Scale PCCV round-robin exercise; subset is to be determined later, but participants should plan models accordingly. At a minimum, the displacement transducer/data plots portion of the 55 Standard Output Locations are required.
4. Contour plot of peak strains in the liner during the LST at the pressure milestones: P = 0 (prestress applied); 1 x P_d; 1.5 P_d; 2 P_d; 2.5 P_d; 3 P_d; 3.3 P_d; 3.4 P_d; Ultimate Pressure
5. A subset of the response information defined by the "55 standard output locations" of the 1:4 Scale PCCV round-robin exercise; see below for the specific list.
6. Contour plots of peak strains in the liner during the LST at the pressure milestones: P = 0 (prestress applied); 1 x P_d; 1.5 P_d; 2 P_d; 2.5 P_d; 3 P_d; 3.3 P_d; 3.4 P_d; Ultimate Pressure
7. Liner strain map of entire liner surface; this has been discussed at the April 13-14 Meeting, and an Excel format for this is under development. But participants are asked to plan for outputting this from their Model 4 Analysis. The "map" will have a location format using the azimuths and

elevations of the model as shown in Figure 389. It will not matter how fine is the spacing of the data points, because participants model mesh sizes vary, but participants are asked to plan for a minimum spacing for liner strain data of 450 mm, which corresponds to the liner-anchor spacing.

For direct comparison amongst participants, please also plot (Using Excel):

1. Liner strain magnitudes (hoop direction) at locations indicated in Figure 11 (of SPE problem statement), versus pressure
2. Tendon stress distribution at P = 0 (prestress applied); 1 x P_d; 1.5 P_d; 2 P_d; 2.5 P_d; 3 P_d; 3.3 P_d; 3.4 P_d; Ultimate Pressure for
   - Hoop tendons # H35, H53, H68
   - Vertical tendon # V37 and V46
3. Plots of response versus pressure for Standard Output Locations:
   - 1-15 (displacements);
   - 22-29 (rebar strains);
   - 36-42 (liner strains);
   - 48-55 (tendon strains and stresses)

(see Table 22 for exact locations and definitions of SOL's)

Table 22: Standard Output Location Definitions

Loc. #	Type	Orientation	Az. (deg)	El. (m)	Comments	General Location	Instr. ID (1st)	ID (2nd gage)
1	Displacement	Vertical	135	0	Outside Cylinder	Top of Basemat	DL-M-Z0-01	
2	Displacement	Radial	135	0.25	Inside Liner Surface	Base of Cylinder	DL-R-Z2-01	
3	Displacement	Radial	135	1.43	Inside Liner Surface	Base of Cylinder	DL-R-Z3-01	
4	Displacement	Radial	135	2.63	Inside Liner Surface	Base of Cylinder	DT-R-Z4-01	
5	Displacement	Radial	135	4.68	Inside Liner Surface	E/H elev.	DT-R-Z5-01	
6	Displacement	Radial	135	6.2	Inside Liner Surface	Approximate Midheight	DT-R-Z6-01	
7	Displacement	Radial	135	10.75	Inside Liner Surface	Springline	DT-R-Z9-01	
8	Displacement	Vertical	135	10.75	Inside Liner Surface	Springline	DT-M-Z9-01	
9	Displacement	Horiz. (Rad)	135	14.55	Inside Liner Surface	Dome 45 deg	CP-R-Z11-01	
10	Displacement	Vertical	135	14.55	Inside Liner Surface	Dome 45 deg.	DT-M-Z11-01	
11	Displacement	Vertical	135	16.13	Inside Liner Surface	Dome apex	DT-M-Z13-01	
12	Displacement	Radial	90	6.2	Inside Liner Surface	Midheight @ Buttress	CP-R-D6-01	
13	Displacement	Radial	90	10.75	Inside Liner Surface	Springline @ Buttress	CP-R-D9-01	

Table 22: Standard Output Location Definitions (continued)

Loc. #	Type	Orientation	Az. (deg)	El. (m)	Comments	General Location	Instr. ID (1st)	ID (2nd gage)
14	Displacement	Radial	324	4.675	Inside Liner Surface	Center of E//H	CP-R-L5-01	
15	Displacement	Radial	62	4.525	Inside Liner Surface	Center of A/L	CP-R-C5-01	
16	Rebar Strain	Meridional	135	0.05	Inner Rebar Layer	Base of Cylinder	RS-M-Z1-01	
17	Rebar Strain	Meridional	135	0.05	Outer Rebar Layer	Base of Cylinder	RS-M-Z1-02	
18	Rebar Strain	Meridional	135	0.25	Inner Rebar Layer	Base of Cylinder	RS-M-Z2-01	
19	Rebar Strain	Meridional	135	0.25	Outer Rebar Layer	Base of Cylinder	RS-M-Z2-02	
20	Rebar Strain	Meridional	135	1.43	Inner Rebar Layer	Base of Cylinder	RS-M-Z3-01	
21	Rebar Strain	Meridional	135	1.43	Outer Rebar Layer	Base of Cylinder	RS-M-Z3-02	
22	Rebar Strain	Hoop	135	6.2	Outer Rebar Layer	Midheight	RS-C-Z6-02	
23	Rebar Strain	Meridional	135	6.2	Outer Rebar Layer	Midheight	RS-M-Z6-02	
24	Rebar Strain	Hoop	135	10.75	Outer Rebar Layer	Springline	RS-C-Z9-02	
25	Rebar Strain	Meridional	135	10.75	Inner Rebar Layer	Springline	RS-M-Z9-01	RS-M-Z9-03
26	Rebar Strain	Meridional	135	10.75	Outer Rebar Layer	Springline	RS-M-Z9-02	RS-M-Z9-04
27	Rebar Strain	Hoop	135	14.55	Outer Rebar Layer	Dome 45 deg.	RS-C-Z11-02	
28	Rebar Strain	Meridional	135	14.55	Inner Rebar Layer	Dome 45 deg.	RS-M-Z11-01	RS-M-Z11-03
29	Rebar Strain	Meridional	135	14.55	Outer Rebar Layer	Dome 45 deg.	RS-M-Z11-02	RS-M-Z11-04
30	Rebar Strain	Meridional	90	0.05	Inner Rebar Layer	Base of Cylinder @ Buttress	RS-M-D1-01	
31	Rebar Strain	Meridional	90	0.05	Outer Rebar Layer	Base of Cylinder @ Buttress	RS-M-D1-02	
32	Rebar Strain	Hoop	90	6.2	Outer Rebar Layer	Midheight @ Buttress	RS-C-D6-02	
33	Rebar Strain	Meridional	90	6.2	Outer Rebar Layer	Midheight @ Buttress	RS-M-D6-02	
34	Liner Strain	Meridional	0	0.01	Inside Liner Surface	Base of Cylinder	LSI-M-A1-01	
35	Liner Strain	Meridional	0	0.01	Outside Liner Surface	Base of Cylinder	LSO-M-A1-03	
36	Liner Strain	Meridional	135	0.25	Inside Liner Surface	Base of Cylinder	LSI-M-Z2-01	

Table 22: Standard Output Location Definitions (continued)

Loc. #	Type	Orientation	Az. (deg)	El. (m)	Comments	General Location	Instr. ID (1st)	ID (2nd gage)
37	Liner Strain	Hoop	135	0.25	Inside Liner Surface	Base of Cylinder	LSI-C-Z2-01	
38	Liner Strain	Meridional	135	6.2	Inside Liner Surface	Midheight	LSI-M-Z6-01	
39	Liner Strain	Hoop	135	6.2	Inside Liner Surface	Midheight	LSI-C-Z6-01	
40	Liner Strain	Meridional	135	10.75	Inside Liner Surface	Springline	LSI-M-Z9-01	
41	Liner Strain	Hoop	135	10.75	Inside Liner Surface	Springline	LCI-C-Z9-01	
42	Liner Strain	Meridional	135	16.13	Inside Liner Surface	Dome apex	LSI-M-Z13-01	LSI-C-Z13-01
43	Liner Strain	Meridional	90	6.2	Inside Liner Surface	Midheight @ Buttress	LSI-M-D6-01	
44	Liner Strain	Hoop	90	6.2	Inside Liner Surface	Midheight @ Buttress	LSI-C-D6-01	
45	Liner Strain	Hoop	334	4.675	Inside Liner Surface	10 mm from thickened plate	LSI-C-A5-03	
46	Liner Strain	Hoop	58	4.525	Inside Liner Surface	10 mm from thickened plate	LSI-C-C5-03	
47	Base Liner	Radial	135	0	100 mm Inside Cylinder	FF Basemat Liner Strain	LSI-R-Z1-08	
48	Tendon Strain	Hairpin	180	15.6	Tendon - V37	Tendon Apex	TT-M-G12-01	TF-M-G12-01
49	Tendon Strain	Hairpin	135	10.75	Tendon - V46	Tendon Springline	TT-M-Z9-01	TF-M-Z9-01
50	Tendon Strain	Hoop	90	6.58	Tendon - H53	Mid. Tendon	TT-C-D6-01	TT-C-D6-02
51	Tendon Strain	Hoop	180	6.58	Tendon - H53	¼ - Tendon	TT-C-G6-01	TF-C-G6-01
52	Tendon Strain	Hoop	280	6.58	Tendon - H53	Tendon Near Buttress	TT-C-K6-01	TF-C-K6-01
53	Tendon Strain	Hoop	0	4.57	Tendon - H35	Tendon between E/H and A/L	TT-C-A5-01	TT-C-A5-02
54	Tendon Force	Hairpin	241	-1.16	Tendon - V37	Tendon Gallery	TL—10-03	
55	Tendon Force	Hoop	275	6.58	Tendon - H53	@ Buttress	TL-C-J6-02	

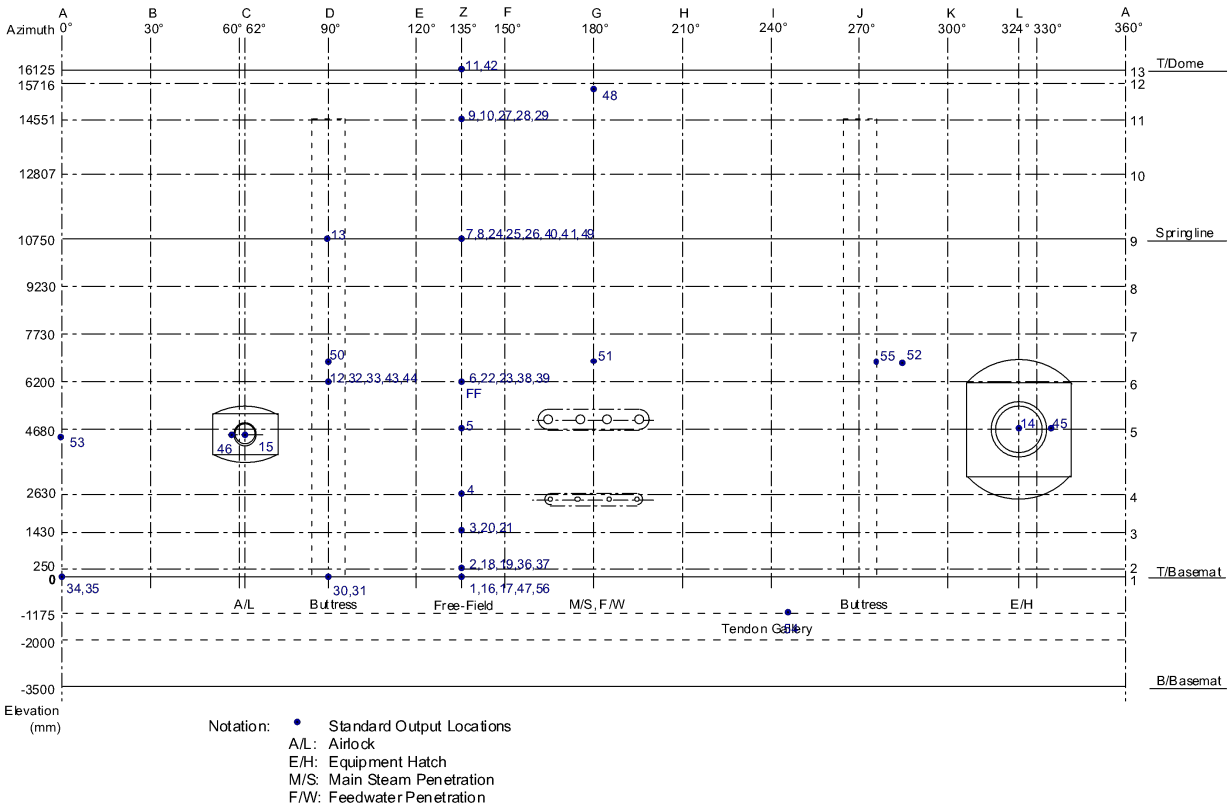

Figure 389: Liner View Showing SOL Strain Reports – Also Shown for Reference in Planning Global Liner Strain Map

5.2.5. Estimating Crack Size and Leak Areas

Model 4 and adjunct submodels should also be planned to estimate crack size and leak area, as this is one of the primary goals of the Phase 2 work. In conjunction with this, the Indian participants will continue their investigation into leak rates as a function of crack size, and this will be provided to the participants sometime during the execution of Phase 2. A plot of leak-rates at different stages of testing of the 1:4 Scale PCCV is provided for reference in Figure 390 through Figure 392.

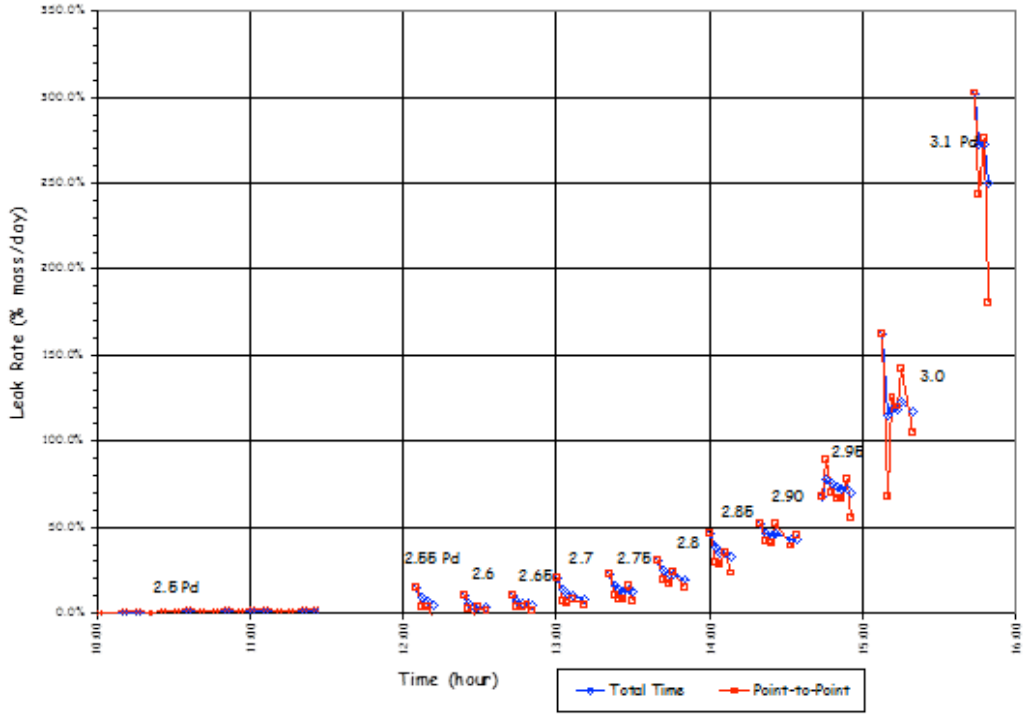

Figure 390: LST Calculated Leak Rates at 1.5, 2.0, and 2.5 P_d

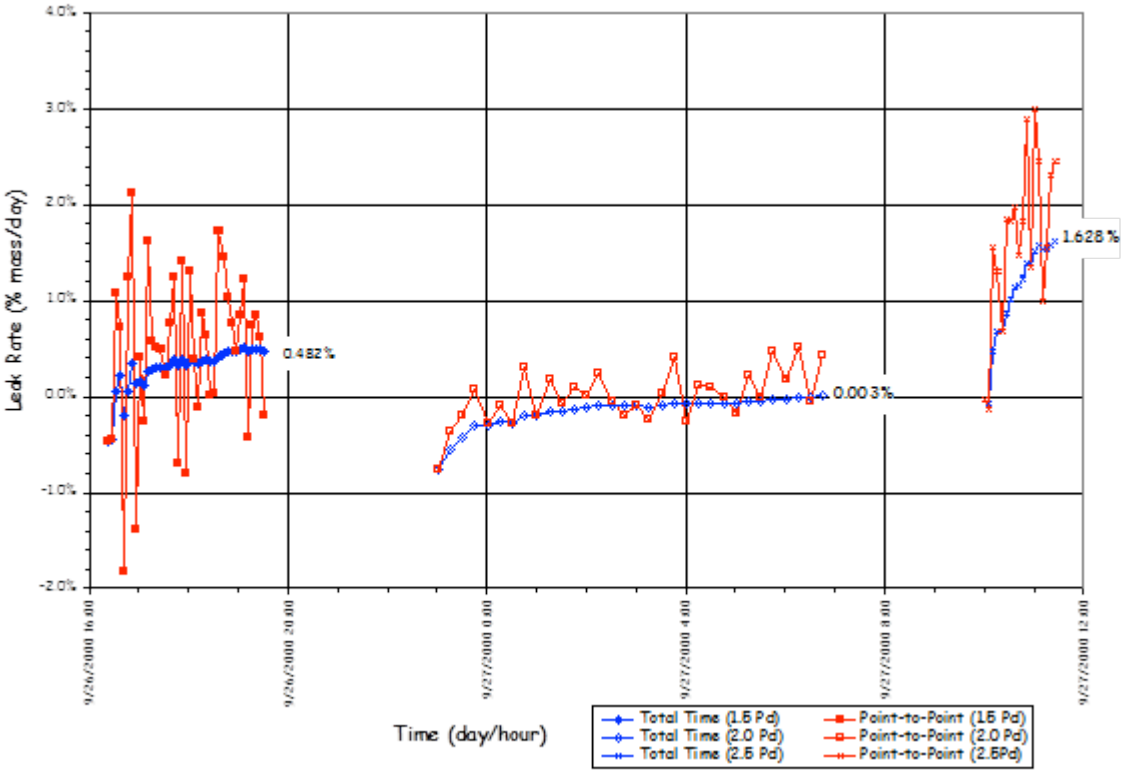

Figure 391: LST – Estimated Leak Rates (2.5-3.1 P_d)

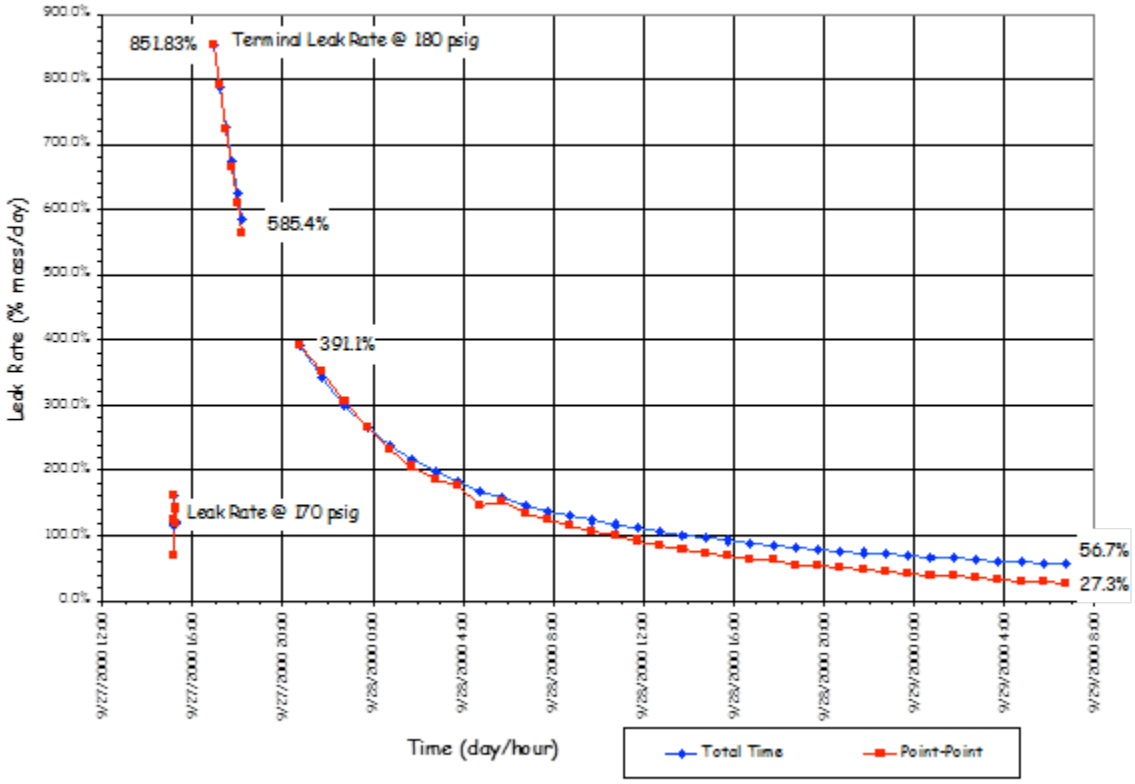

Figure 392: Estimated Terminal Leak Rates

Since the April 13-14 Meeting, renewed study has been made of the 1:4 Scale Model liner tears, and liner metallurgical properties. The liner and the regions at or near all 26 observed tears were studied in [?5]. Some SPE-3 participants may wish to expand on previously used liner failure criterion in their Phase 2 analyses and conclusions about failure and leakage, as for example, a few participants did in Phase 1, considering a fracture mechanics approach. For Phase 1, a fracture Jcritical of 350 psi-inch was assumed, without benefit of specific data, but as a "typical" value for mild carbon structural steel. Unfortunately, on further examination, we do not have measured toughness data for the 1:4 Scale Model liner, but Sandia is currently looking into the possibility of conducting some Charpy V-Notch testing for stored remnants of the liner material. From Ref. [5], we do have Vickers Hardness data (using 100 gram load), and this was found to be in the following range:

Base metal: 160 kgf/mm^2

Heat Affected Zones (depending on grain size): 151 to 164 kgf/mm^2

Fusion Zone: 173-180 kgf/mm^2

Based on a brief literature review, hardness testing does provide approximate indication of ultimate-tensile-strength (it is roughly the Vickers hardness divided by 3), and very approximate

indication of fracture toughness (KIc or Jcr). In the absence of conducting specific fracture-toughness testing, we recommend using the following.

Median J_{cr} = 500 psi-inch

Median + 1 std deviation J_{cr} = 800 psi-inch

Median – 1 std deviation J_{cr} = 200 psi-inch

If more data becomes available, it will be sent to participants right away. Fracture toughness data is often presented as a statistical distribution, so even if these hypothetical values are used for final predictions (in the absence of further data), we believe that framing a tearing criteria in this way can serve to advance the technology of our predictions toward a probabilistic leakage prediction basis. Indeed, the second task of Phase 2 will be to transition the results of Model 4 into probabilistic space. The participants are requested to provide leak rate versus pressure curves for a suite of temperatures. An example of the desired output is shown in Figure 393. The pressure range should vary from 0 to 4 times the design pressure.

One approach to both aspects of this (the estimation of crack size, and the estimation of probabilistic distribution on leakage and crack size versus pressure) is the methodology developed through EPRI research in the 1990's. References for more information on this are [6 and 7]. Ref. [6] provides a general description of the methodology, and is publicly available; Ref. [7] provides more detail, but is only available on a limited basis. Another approach that is gaining momentum (as presented and discussed by participants in our April 13-14 meeting) is a modified version of the EPRI approach where uncertainty distributions are still placed on a number of variables, but the fracture occurrence and tear areas could be based on a fracture mechanics approach. We look forward to the creative ways in which the SPE-3 participants will approach this last, all important, task for the SPE-3 project.

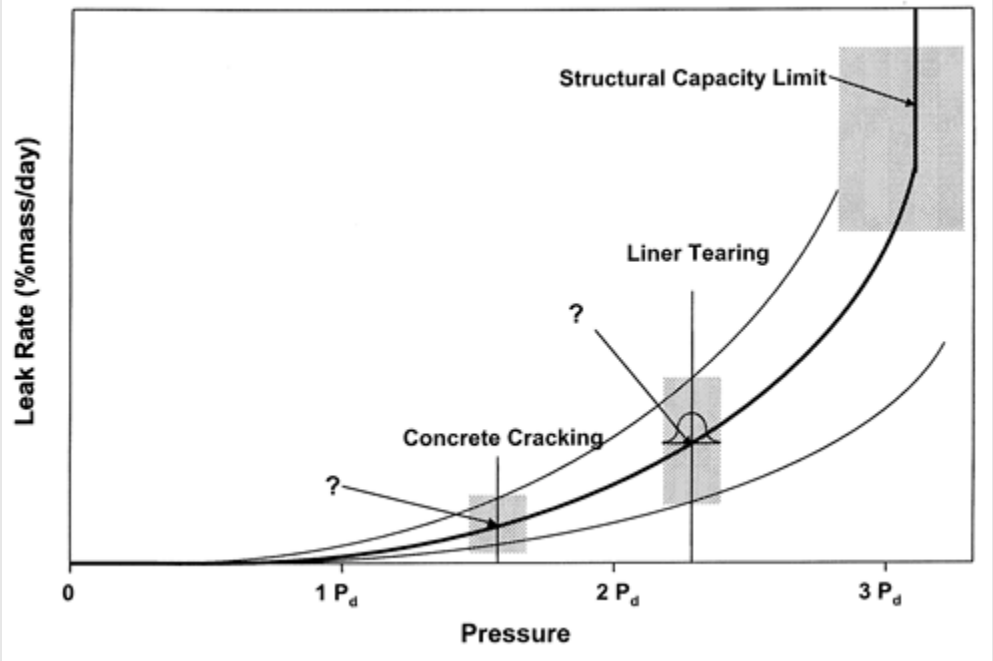

Figure 393: Schematic of a Containment Performance Model

5.3. Documents of SPE #3 Phase Two

In conjunction with completing the aforementioned analyses, participants will be asked to document, in the form of a report, results from Phase 2 of the Round Robin Analyses. The reports will provide the input for the final document of the SPE, which at a minimum, will be combined, edited, and published as a NUREG report, and will also, possibly, form the basis for a paper submittal to the refereed journal – Nuclear Engineering & Design.

5.4. Organizational Schedule

The schedule for the meetings and calculations for the overall SPE program is as follows (as now modified and agreed to at the April, 2011 meeting):

Event	Dates
Initial Workshop (Mumbai, India)	June 30-July 2, 2010
White Paper Finalization	August 6, 2010
Milestone Verification of Tendon and Equipment Hatch	December 1, 2010
Return Results from Milestone Evaluation	December 21, 2010
Format For Documentation Sent Out	December 21, 2010
Phase 1 Meeting After Completion of Phases 1.1-1.3 (**Tentative** – San Diego, USA)[3]	January 6-8, 2011 (not conducted)
Phase One Calculations and Documentation Due	March 15, 2011
Phase One Review Meeting (Washington, D.C.)	April 13-15, 2011
Phase Two Calculations and Documentation Due	April 27, 2012
Final Workshop (Washington, D.C.)	March 27-29, 2012
Final Report	June 2012

DISTRIBUTION

1 United States Nuclear Regulatory Commission
Attn: M. Sircar (1)
Washington, DC 20555-0001

1	MS0899	Technical Library	9536 (electronic copy)


Sandia National Laboratories